Фізика і хімія твердого тіла

№ 2
2023
Том 24
Vol.

Physics and Chemistry of Solid State

Міністерство освіти і науки України
Прикарпатський національний університет імені Василя Стефаника
Фізико-хімічний інститут
Навчально-дослідний центр напівпровідникового матеріалознавства

Ministry of Education and Science of Ukraine
Vasyl Stefanyk Precarpathian National University
Physical-Chemical Institute
Research & Education Center of Semiconductor Material Science

ISSN 1729-4428

ФІЗИКА І ХІМІЯ ТВЕРДОГО ТІЛА

PHYSICS AND CHEMISTRY OF SOLID STATE

№ 2
2023
Том 24
Vol.

Журнал ФХТТ індексується міжнародними наукометричними базами WoS (починаючи із 2017 р.) та Scopus (індексація матеріалів із 2018 р.)

Журнал включено у категорію А Реєстру фахових видань України:
Галузь науки: хімічні (02.07.2020), технічні (02.07.2020), фізико-математичні (24.09.2020)
Спеціальності: 102 (02.07.2020) 132 (02.07.2020) 104 (24.09.2020) 105 (24.09.2020)

Рекомендовано до друку Вченою радою
Прикарпатського національного університету імені Василя Стефаника

Свідоцтво про державну реєстрацію
КВ № 24247-14087ПР від 27.09.2019

Certificate of State Registration
KB No. 24247-14087 ПР from 27.09.2019

Передплатний індекс: 22938

Subscription index: 22938

Адреса редакції:
Прикарпатський національний університет
імені Василя Стефаника,
вул. Шевченка, 57,
Івано-Франківськ,
76018, Україна
Тел.: +380 (342) 596082
Факс.: +380 (342) 531574
E-mail: pcss@pnu.edu.ua
https://journals.pnu.edu.ua/index.php/pcss

Editorial address:
Vasyl Stefanyk Precarpathian National University,
57, Shevchenko Str.,
Ivano-Frankivsk,
76018, Ukraine
Tel.: +380 (342) 596082
Fax.: +380 (342) 531574
E-mail: pcss@pnu.edu.ua
https://journals.pnu.edu.ua/index.php/pcss

Vasyl Stefanyk Precarpathian National University
Physical-Chemical Institute
Research & Education Center of Semiconductor Material Science

Scientific Journal
"Physics and Chemistry of Solid State"

Physics and Chemistry of Solid State
2023. – Vol. 24. – No 2

Features of technological synthesis and properties of ZnO-Cd based materials for photocatalytic applications. Review **219**
R. I. Didus, D. V. Myroniuk, L. A. Myroniuk, A. I. Ievtushenko
Effect of the crystal structure and chemical bonding on the electronic and thermal transport in $Cu_2MeHf_3S_8$ (Me – Mn, Fe, Co, Ni) thiospinels **235**
O. Smitiukh, O. Soroka, O. Marchuk
Synthesis, magnetic, AC conductivity and dielectric properties of hematite nanocrystallites **244**
N. B. Gatchakayala , R. S. R. Dachuru
Fractal analysis of fractograms of aluminum alloys irradiated with high current electron beam **249**
S.Ye. Donets, V.V. Lytvynenko, O.A. Startsev, Yu.F. Lonin, A.G. Ponomarev, V.T. Uvarov
Bacteria inactivation using spinel cobalt ferrite catalyst **256**
N. Danyliuk, I. Lapchuk, T. Tatarchuk, R. Kutsyk, V. Mandzyuk
Physical properties of nanocrystaline PbS synthesized by electrolytic method **262**
O.A. Kapush, N.V. Mazur, A.V. Lysytsya, M.V. Moroz, B.D. Nechyporuk, B.P. Rudyk, V.M. Dzhagan, M.Ya. Valakh , V.O. Yukhymchuk
Quantum-chemical studies of the interaction of partially oxidized graphene-like planes with each other **269**
Y.V. Hrebelna, E.M. Demianenko, M.I. Terets, Y.I. Sementsov, V.V. Lobanov, A.G. Grebenyuk, V.S. Kuts, S.V. Zhuravskyi, O.V. Khora, M.T. Kartel
Development of high-precision hardware and software tools for automated determination of the characteristics of thermoelectric devices **278**
B. S. Dzundza, O.B. Kostyuk, U.M. Pysklynets, Z.M. Dashevsky
Structural studies and magnetism of $Dy_6Ni_{2.43}Sn_{0.5}$ stannide **284**
L. Romaka, Kh. Miliyanchuk, V.V. Romaka, L. Havela, Y. Stadnyk
Frequency shifts of surface plasmon resonances in calculating the absorption coefficient of a composite based on bimetallic 1D-systems **290**
A.O. Koval
Formation of submicron relief structures on the surface of sapphire substrates **298**
V.V. Petrov, A.A. Kryuchyn, I.V. Gorbov, A.V. Pankratova, D.Yu. Manko, Yu.O. Borodin, O.V. Shikhovets
The features of chemo-mechanical activation technology of polymer composite materials production **304**
O.V. Komashko, H.O. Sirenko, M.B. Skladaniuk
Sandwiched Plate Vibration Analysis with Open and Closed Lattice Cell Core **312**
H. Raad, E. K. Njim, M. J. Jweeg, M. Al-Waily
Properties of silica porous glasses with the nanoparticle ensembles of some compounds **323**
Y.I. Lepikh, I.K. Doycho
The influence of mercury vapor on the electrical resistance of chalcogenide amorphous films **335**
V.M. Rubish, V.K. Kyrylenko, M.O. Durkot, V.V. Boryk, R.O. Dzumedzey, I.M. Yurkin, M.M. Pop, Yu.M. Myslo
Manufacturing of nitinol-based alloys by using modern technology: A short review **341**
Ch. Imamalizade
Structural and sorption properties of nanoporous carbon materials obtained from walnut shells **348**
S.A. Lisovska, R.V. Ilnytskyy, R.P. Lisovskyy, N.Ya. Ivanichok, Kh.V. Bandura, B.I. Rachiy
The epitaxial iron-yttrium garnet films with homogeneous properties and narrow FMR line width **354**
S.I. Yushchuk, S.A. Yur`ev, V.V. Moklyak
The ternary system Hf–Re–Al at 1000 °C **361**
L. Zinko, G. Nychyporuk, O. Matselko, R. Gladyshevskii
Low-temperature anomalies and nanosized levels formation of self-organized structures in the non-crystalline solids of As(Ge)-S(Se) systems **367**
M. Mar'yan, N. Yurkovych, V. Seben
Structural, morphological and photocatalytic properties of nanostructured TiO_2/AgI photocatalyst **374**
I. Mironyuk, N. Danyliuk, L. Turovska, I. Mykytyn, V. Kotsyubynsky
The influence of the plates on the effectiveness of penetrating thermoelements in the cooling regime **385**
V.A. Semeshkin, R.G. Cherkez, A.S. Zhukova, V.V. Stefiuk
Spectroscopic, Magnetic and Morphological studies of $MgFe_2O_4$ Nanopowder **392**
F. Naaz, P. Lahiri, Cha. Kumari; H. K. Dubey
Stimulation of the metal doping process of nanoporous carbon material by laser irradiation **403**
I.M. Budzulyak, L.S. Yablon, M.M. Khemii, V.O. Kotsyubynsky, B.I. Rachiy, R.V. Ilnytskyi, R.I. Kryvulych
Information for authors **410**

PHYSICS AND CHEMISTRY OF SOLID STATE
V. 24, No. 2 (2023) pp. 219-234
Section: Physics

DOI: 10.15330/pcss.24.2.219-234

Vasyl Stefanyk Precarpathian National University

ФІЗИКА І ХІМІЯ ТВЕРДОГО ТІЛА
Т. 24, № 2 (2023) С. 219-234
Фізико-математичні науки

PACS: 68.55.ag, 68.55.Ln, 78.66.Hf, 82.65.r ISSN 1729-4428

R. I. Didus, D. V. Myroniuk, L. A. Myroniuk, A. I. Ievtushenko

Features of technological synthesis and properties of ZnO-Cd based materials for photocatalytic applications. Review

I.M. Frantsevich Institute for Problems of Materials Science, National Academy of Sciences of Ukraine, 3 Krzhyzhanovsky Str., 03142, Kyiv, Ukraine, romanik619@gmail.com

Abstract: In this review, the current state of ZnO-Cd based materials for photocatalytic applications is summarized. Relevant technological synthesis methods such as pulsed laser deposition, magnetron sputtering, electrodeposition, sol-gel, metalorganic chemical vapor deposition, evaporating, spray pyrolysis, reflux are considered, and recent developments in effective and reproducible synthesis technology of nano- and microstructured zinc oxide, doped with cadmium and solid solutions of $Zn_{1-x}Cd_xO$ for photodecomposition of organic pollutant molecules are discussed. The synthesis technology and level of Cd doping has a significant effect on the structure and morphology of zinc oxide and, as a result, on the optical and photocatalytic properties. The figures of merit, the theoretical limitations and rational control of the concentration of the cadmium alloying impurity is necessary to create a material with balanced optical properties and photocatalytic activity. Lastly, the importance of doping ZnO by isovalent Cd impurity significantly improves its photocatalytic properties due to a narrowing of the band gap, a decrease in the rate of recombination of electron-hole pairs, which increases the efficiency of spatial charge separation, the formation of active oxide radicals and an increase in the specific surface area. Thus, ZnO-Cd based materials are the most promising photocatalytic materials for organic pollutants.

Keywords: zinc oxide; cadmium doping; morphology; nanostructures; optical properties; photocatalysis.

Received 26 December 2023; Accepted 23 March 2023.

Introduction

Toxic organic air and water pollutants pose a significant danger to both human health and the eco-fauna as a whole. In this regard, the development of the latest environmental technologies for quick and safe deactivation of organic pollutants is a particularly relevant scientific task. Currently, the main efforts of the world scientific community are focused on the development of photocatalysis technology as a highly productive process of decomposition of organic compounds under the influence of light. Therefore, the realization of a reliable and reproducible synthesis of materials with high photocatalytic properties becomes important.

Due to its unique physico-chemical properties, biocompatibility and availability of synthesis methods, wide bandgap (~ 3.3 eV) zinc oxide is one of the most promising photocatalytic materials of the future [1]. Due to its multifunctional properties, ZnO is promising for use in solar cells, medical equipment, automotive industry, semiconductor industry, optoelectronics, biomaterials and for photocatalytic applications [2,3,4,5,6]. From an industrial point of view, ZnO is considered a very important material due to a number of advantages, such as low production cost, efficiency and non-toxic catalyst and environmental safety [7]. ZnO has high radiation resistance, good thermal properties, structural stability, biological compatibility, and effective optical absorption in the UV range [8]. It can be doped with impurity elements to obtain films with high conductivity and optical transparency [9,10]. However, the main disadvantage of zinc oxide is that this semiconductor material is able to effectively absorb light exclusively in the ultraviolet region of the optical spectrum, which significantly limits its use for photocatalysis.

Over the past 20 years, researchers have studied the alloying effect of Cd, Cu, Mg, Mn, Ni in zinc oxide on its optical properties. Among the above-mentioned alloying

elements, especially Cd provides the smallest bandgap value in the material, so it has many applications in industry and the environment protection. Bandgap tuning is desirable for wavelength stability and achieving a bandgap that matches the visible spectrum. Mosquera et al. [11] found that the band gap decreased from 3.21 eV to 3.11 eV as the evidence of influence Cd on the sample increased. With the correct Zn/Cd ratio, the band gap can be reduced to 2.92 eV [12,13,14].

I. Technological methods of synthesis of ZnO-Cd thin films (nanomaterials)

To date, several research articles have been published on the synthesis of the ZnO-Cd system using a variety of deposition methods, such as pulsed laser deposition (PLD) [5,15,16,17,18,19], electrodeposition [20,21,22], hydrothermal synthesis [21,20], sol-gel process [11,12,22,20,21,22,23,24], direct current [13,14,25] and radiofrequency magnetron deposition [27,28], spray pyrolysis (SP) [3,22,26,27,28,29], thermal co-evaporation [22, 36], molecular beam epitaxy (MBE) [2,5,36], remote plasma-enhanced metalorganic chemical vapor deposition (RPE-MOCVD) [5,37,38], ion layering (SILAR) [34,39], spin-coating [4,40] and even reflux method [42] (Fig. 1, 2).

The article [22] describes the production of ZnO-Cd films by the SP method. This method is based on the preparation of homogeneous precursor solutions from salts, thin films of which are deposited on preheated substrates (Fig. 3). During the processes of deposition of thin oxide film, both chemical and thermal reactions occur. Using SP, relatively uniform films are grown with very high growth rates of the order of several hundreds of nanometers per minute. Therefore, it is an attractive and widely used method in industry for covering large areas.

Among the listed methods, sol-gel is a simple and suitable for large-area deposition method, which is useness for almost any transparent conductive films. The spin-coating technique is simple, as it does not require a vacuum or high temperature to deposit the films. The technology of films deposition by this method is shown in Fig. 4.

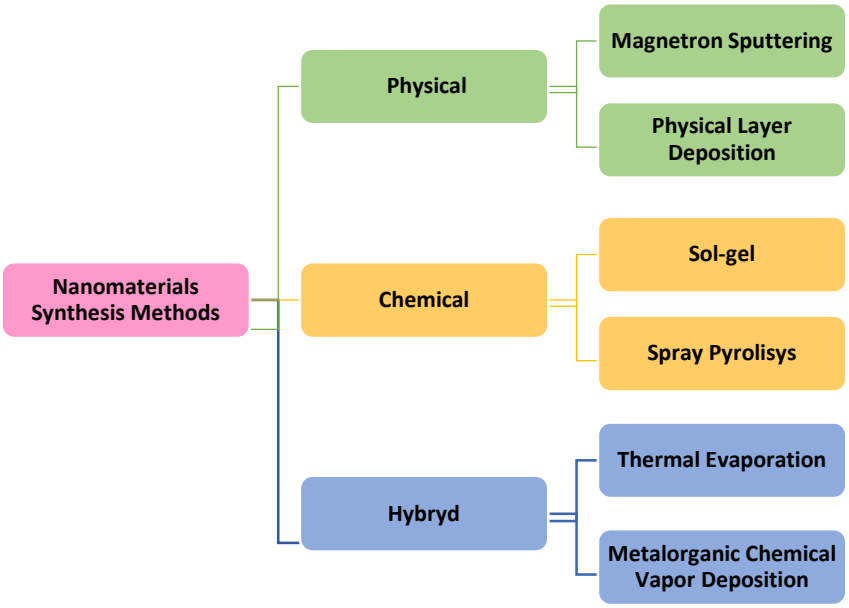

Fig. 1. General scheme of nanomaterial synthesis methods [43].

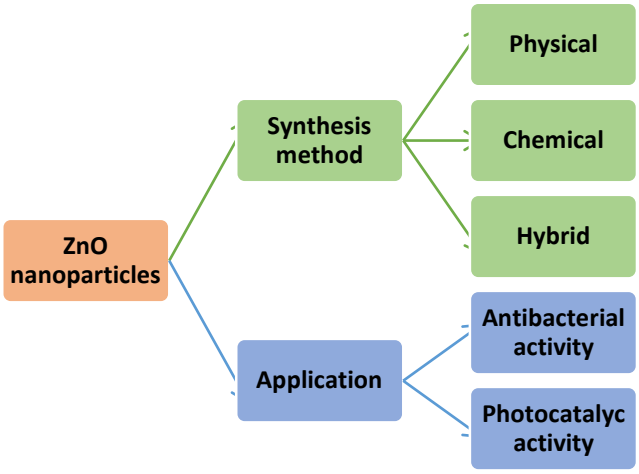

Fig.2. Synthesis methods of zinc NPs and their potential use [43].

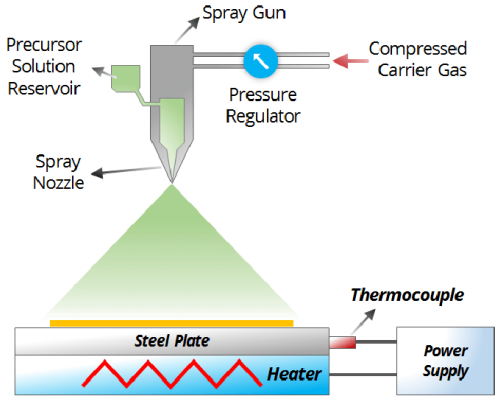

Fig. 3 Scheme of the installation for obtaining thin films by the spray pyrolysis method [22].

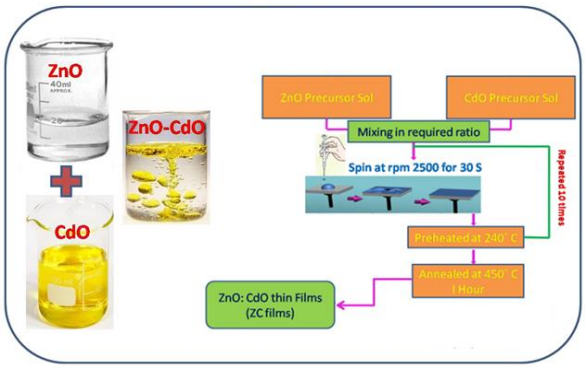

Fig. 4. Block diagram of deposition of ZnO:CdO sol-gel thin films by the spin-coating method [27].

II. Physical properties of thin films of the ZnO-Cd system

2.1.Microstructure and chemical composition of ZnO-Cd thin films.

The article [43] proposes growing nanostructures (NS) by the evaporation method on anodic aluminum oxide (AOA) substrates with gold (Au) particles deposited on it. SEM images of the obtained NS are shown at Fig. 5.

It was established that temperature is a key factor in the morphology of catalytically grown ZnO NS. At the higher temperature (700 °C), only ZnO nanowires were formed. At the lower temperature (680 °C) nanobelts appeared. ZnO nanocombs were formed when the temperature was 660 °C.

Undoped and doped ZnO samples (Fig. 6) with different doping concentrations (1–5% by weight of Cd) are labeled CZO-0, CZO-1, CZO-2, CZO-3, CZO-4, and CZO-5, respectively. Sample CZO-0 deposited at 450 °C on a glass substrate (Fig. 6, a), consists of various tiny spherical grains. A similar morphology is observed for sample CZO-1. For the CZO-2 sample, the morphology of which is shown in Fig. 6, c, the grain density is higher, and the grain size is 50 nm. Surface morphology changes with 3 % Cd doping (Fig. 6, d). Agglomeration of grains is observed on the surface of CZO-3 films. With a higher cadmium doping of CZO-4 and CZO-5 samples, a smooth surface covered with many spherical grains of 80-100 nm in size was observed. Among all the samples, the CZO-2 film shows a well-distributed granular morphology [40].

SEM images presented in the article [39] for undoped and Cd-doped ZnO films are shown in Fig. 7. It can be seen from this figure that the surface of the zinc oxide film is rough and consists of large and faceted grains (Fig. 7, a), and the thin ZnO-Cd film consists of almost hexagonal crystallites, mainly oriented perpendicular to the surface of the substrate, that is, along the *c* axis (Fig. 7, b). This change in the shape of the grains is probably related to the inclusion of cadmium, which disrupts the arrangement of atoms.

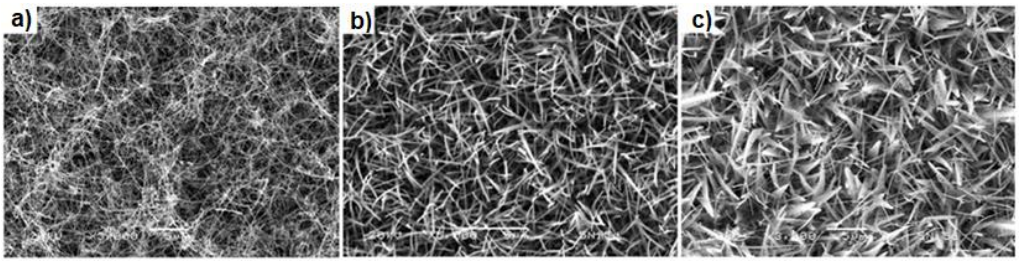

Fig. 5. SEM images of ZnO NS grown on substrates filled with Au particles at: a – 700 °C; b – 680 °C; c - 660 °C [44].

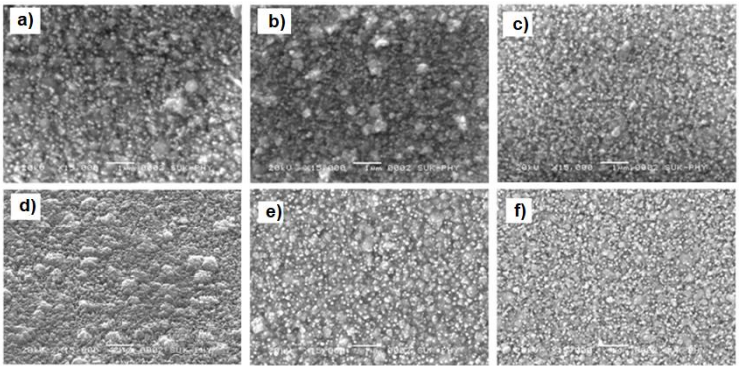

Fig. 6. SEM images of Cd-ZnO thin films deposited by pyrolysis sputtering with different concentrations of Cd doping: a – CZO-0; b – CZO-1; c – CZO-2; d – CZO-3; e – CZO-4; f – CZO-5 [40].

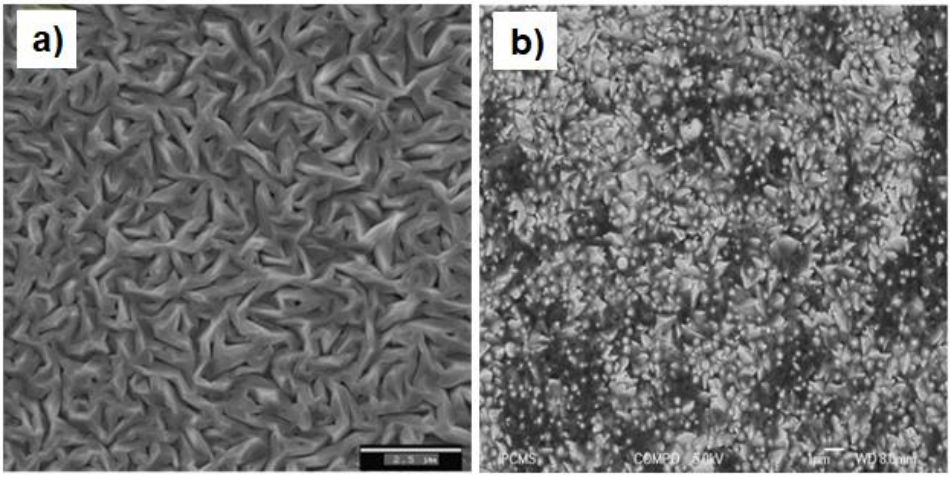

Fig. 7. SEM images of thin films: a – ZnO; b – ZnO-Cd [39].

The authors [42] synthesized ZnO and ZnO-Cd nanoparticles by the reflux method. ZnO nanoparticles were obtained, as well as nanoparticles with 5 % and 10 % by weight fraction of cadmium doping.

In Fig. 8 shows X-ray patterns of synthesized undoped ZnO and doped ZnO with different Cd content. All the obtained peaks are in good agreement with the hexagonal crystal structure of ZnO. No other impurity peak was observed in the X-ray pattern, indicating ZnO nanocrystals that have a pure hexagonal crystal structure. No impurity peaks were observed. The observed ZnO diffraction reflections appear at 31.71 °, 34.41 °, 36.24 °, 47.52 °, 56.6 °, 62.8 °, 66.3 °, 67.9 °, 69.1 °, 72.4 ° and 76.9 ° and correspond to the orthogonal planes (100), (002), (101), (102), (110), (103), (200), (112), (201), (004) and (202), respectively.

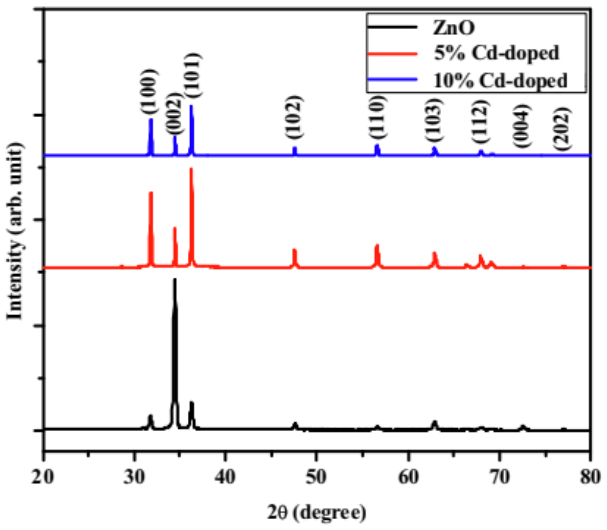

Fig. 8. Combined X-ray patterns of synthesized thin films [42].

An increase in the Cd content causes decreasing in the intensity of all diffraction peaks. This decrease is explained by the effect of defects created by cadmium ions included in the structure of the ZnO lattice. Compared to the pure ZnO film, the intensity of the (002) peak decreases for Cd-doped ZnO films, which is confirmed by the X-ray patterns in Figure 8. It is worth noting that the relative intensity of the (101) peak increases for Cd-doped ZnO films. Thus, doping with cadmium leads to the loss of the predominant orientation along the *c axis* . These observations, combined with a decrease in the relative intensity of the (002) peak, confirm that the inclusion of Cd increases the degree of polycrystallinity of the films. Therefore, the synthesized nanocrystals retain a stable hexagonal ZnO phase.

The grain size of the samples was calculated using Scherrer's formula. The obtained crystallite sizes of the (002) plane of pure ZnO, ZnO doped with 5 % Cd, and the ZnO sample doped with 10 % Cd are 32.19, 48.23, and 57.94 nm, respectively. It is shown that doping with cadmium leads to an increase in the size of crystallites.

To investigate the overall morphology, the as-grown undoped and cadmium-doped ZnO nanoparticles were examined by SEM, and the results are shown in Fig. 9.

In Fig. 9, a, shown that undoped ZnO is synthesized in nanocrystalline structures of high density. The SEM image shows a polycrystalline morphology of nanocrystalline size with interconnected grains present on undoped ZnO nanoparticles. In Fig. 9, b shows highly agglomerated particles with a size of 400–500 nm for ZnO samples doped with 5 % Cd. It should be noted that the samples look like particles oriented in different directions. In Fig. 9, c shows highly agglomerated quasi-spherical particles with a size of 600–700 nm for a ZnO sample doped with 10 % Cd. Some of them connected together to form secondary particles derived from tiny particles with a high surface tendency to cluster. It is obvious that the crystallite size gradually increases with increasing Cd doping. The full array of one crystal structure is in the range of 2 μm [42].

Quite the opposite result, in contrast to those shown in Fig. 8 [42] demonstrated the samples synthesized in [35] by the SP method. The samples in this paper demonstrated an increase in the intensity of the (002) peak when doped with cadmium (Fig. 10). This behavior indicates a decrease in the level of crystallinity of the structure.

In Fig. 11 shows that the positions of the diffraction peaks systematically shift towards smaller angles with increasing cadmium concentration. This testifies to the successful replacement of Zn^{2+} by Cd^{2+} ions .

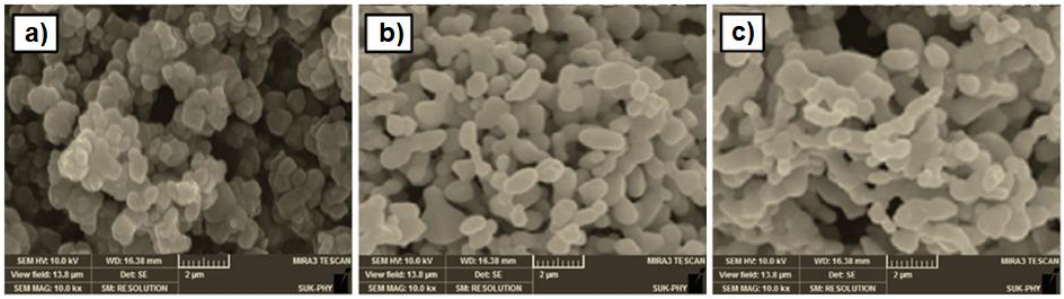

Fig.9. SEM photograph of nanoparticles synthesized by the method dephlegmation: a – undoped ZnO; b – ZnO doped with 5 % Cd; c – ZnO doped with 10 % Cd [42].

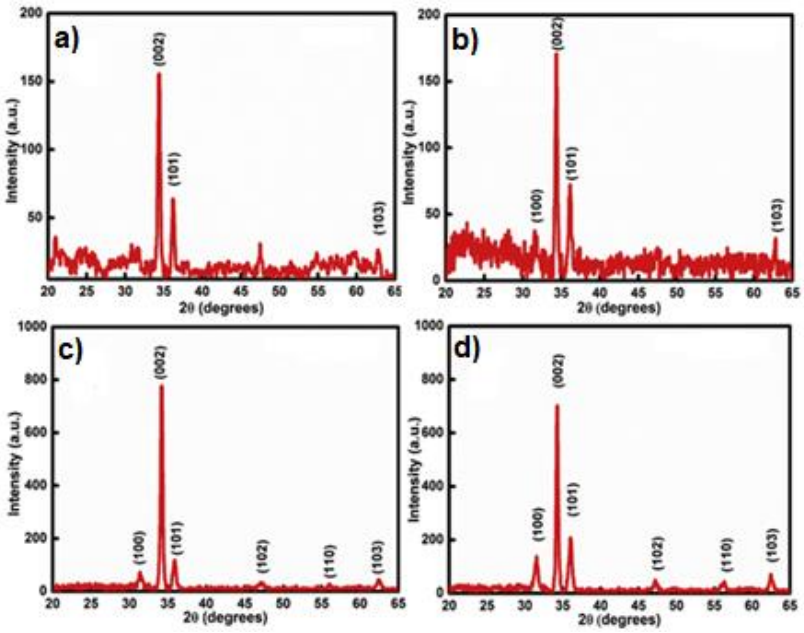

Fig. 10. X-ray diffraction of $Zn_{1-x}Cd_xO$ thin films with different atomic fractions of doping: a – 0%; b – 5%; c - 10 %; d – 20 % [35].

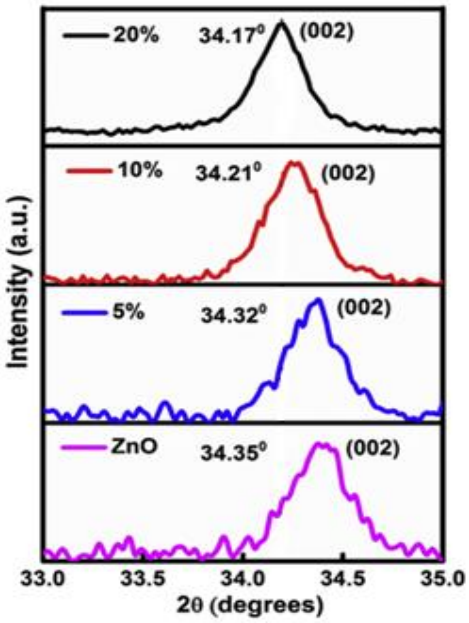

Fig. 11. Shift of the (002) peak position of $Zn_{1-x}Cd_xO$ when the level of cadmium doping changes [35].

The resulting structure was studied by SEM. The low-magnification image shows the uniformity of the formation of the microstructure without any holes or cracks. At higher magnification, it can be observed that the film consists of densely packed and randomly arranged lamellar structures. When adding 5 molar Cd %, the surface is modified with grains of arbitrary shape, as shown in Fig. 12, b. Increasing the cadmium concentration to 10 and 20 molar % results in a thin films with a grainy morphology. This granularity in structures can be observed in Fig. 12, c,d . These results show that the concentration of cadmium changes the surface morphology of the films. The resulting structures are of great importance due to their high specific surface area and adsorption capacity. In general, SEM image in Fig. 12 can be called similar to the results shown in Fig. 7 [39].

2.2. Optical properties

Optical transmission spectra of Cd-doped ZnO thin films synthesized by the sol-gel method is considered in the article [28]. In Fig. 13 shows the transmission spectra of samples with different molar Cd %, as well as PL spectra.

The films are 198, 205, 180, and 140 nm thick with a cadmium weight fraction of 0 %, 0.45 %, 0.51 %, and 0.56 %, respectively. All films demonstrate transparency of 80-90 % in the visible and infrared regions of the spectrum. High transparency is associated with good structural homogeneity, crystallinity and thickness.

It was found that the transparency decreases if the

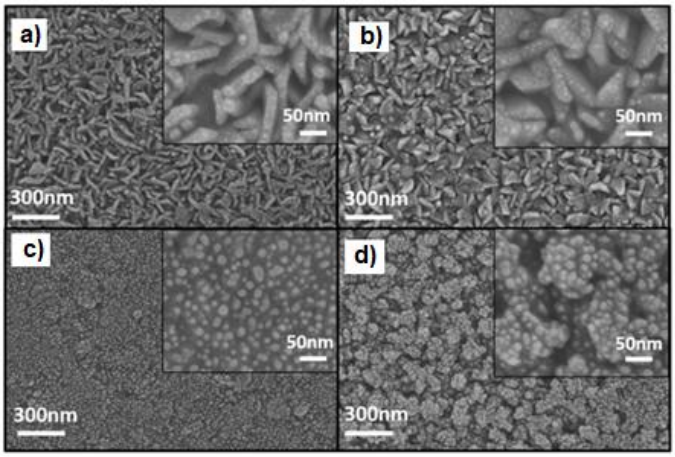

Fig. 12. SEM image of $Zn_{1-x}Cd_xO$ with different atomic fraction of doping: a) – 0 %; b) – 5 %; c) - 10 %; d) - 20 % [35].

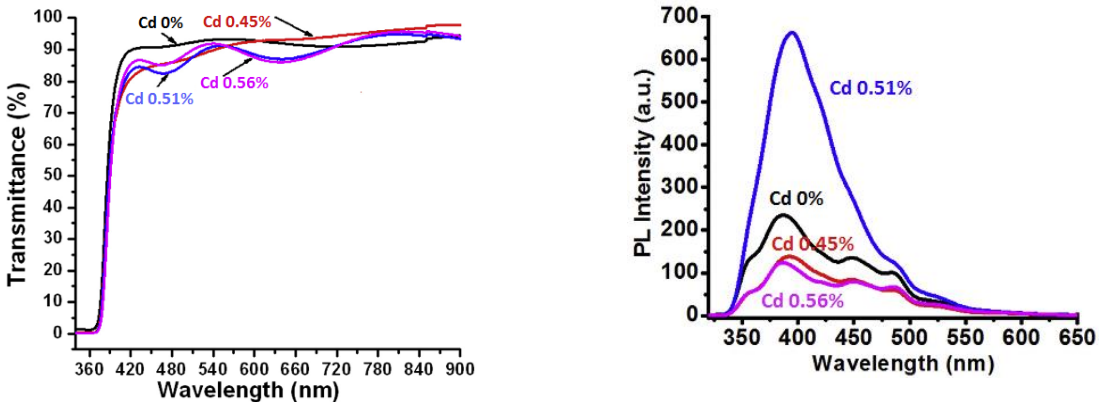

a) b)

Fig. 13. Spectra of ZnO thin films with different levels of Cd doping: a) – optical transmission spectra; b) - PL spectra [28].

annealing temperature is more than 450 °C. On the optical transmission spectra at cadmium concentrations of 0.51 % and 0.56 % in Fig. 13, a, an interference pattern is observed, which is characteristic of thin films [16]. Also at 370 nm, a sharp absorption edge is observed, which shifts towards a higher wavelength with doping increasing. This red shift of the absorption edge indicates a decrease in the optical bandwidth of ZnO thin films [28].

PL excitation spectra were recorded for emission at 385 nm, equivalent to the optical transmission band of 3.22 eV of the ZnO film in this study. The corresponding photoluminescence spectra are shown in Fig. 13, b.

A similar PL spectrum is observed when studying the sample that was synthesized in [17] by the method of pulsed laser deposition on a quartz substrate.

Experimental PL spectra of $Zn_{1-x}Cd_xO$ with different concentrations of Cd are shown in Fig. 14. At Cd x = 0.074 and less, the near band edge (NBE) emission peak shows a red shift from 381 nm to 426 nm or from 3.252 eV to 2.908 eV. When the Cd concentration is further increased to 0.151, a very broad emission band extending from 400 nm to 530 nm in visible range of the PL spectra.

PL spectra of undoped and Cd-doped ZnO nanostructures synthesized by the evaporation method were measured and shown in Fig. 15 [44]. The curve in Fig. 15, a with the center of the emission band at 494 nm and the curve in Fig. 15, b with the center at 505 nm refer to undoped ZnO samples and ZnO-Cd in accordance.

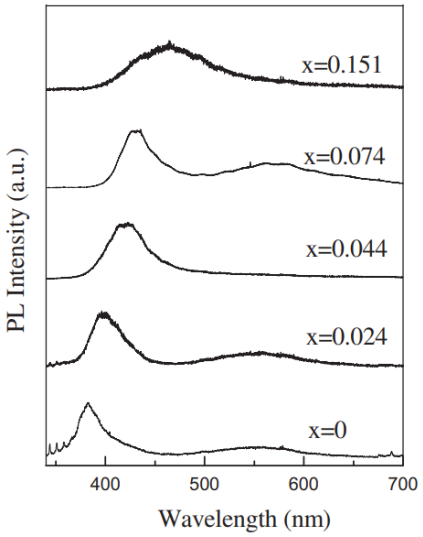

Fig. 14. PL spectra of $Zn_{1-x}Cd_xO$ films with different concentrations of Cd [17].

The green emission band around 500 nm arises as a result of the recombination of holes with electrons occupying a singly ionized oxygen vacancy. According to the PL emission band on the ZnO curve, the emission band

of ZnO nanostructures doped with cadmium has a red shift. In opposite to [17] at [28], no emission in the 375 nm region was detected, which could be a consequence of the high density of oxygen vacancies.

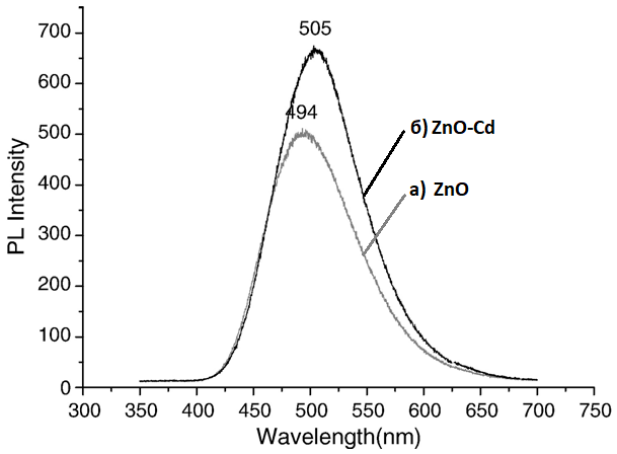

Fig. 15. PL spectra of undoped and Cd-doped ZnO nanostructures [44].

In Fig. 16, all samples show similar broad emission bands with different maxima associated with exciton recombination [29], edge emission (NBE), as well as maxima from transitions from deep defect levels, such as oxygen vacancy traps. The specific peak, its position and the corresponding mechanism observed in the resulting $Zn_{1-x}Cd_xO$ ($0 \le x \le 1$) structure are given in table 1.

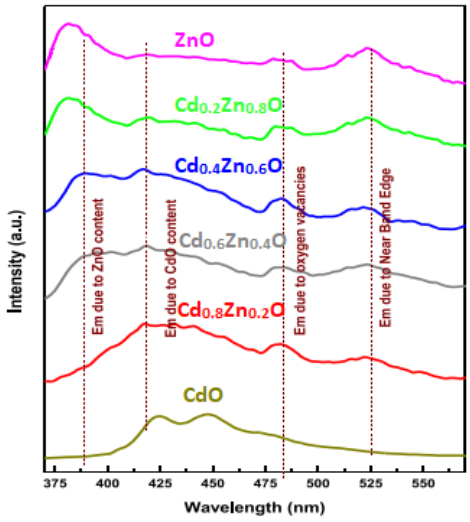

Fig. 16. PL spectra structure of $Cd_{1-x}Zn_xO$ ($0 \le x \le 1$) [45].

PL spectra of the $Zn_{1-x}Cd_xO$ structure with cadmium content $0 \le x \le 1$, can be seen in Fig. 20. More detailed information on PL mechanisms and peaks is given in table 1.

CdO sample has two peaks at 422 and 448 nm, which correspond to undoped CdO. Since CdO is a direct-band semiconductor nanomaterial, a slight shift of the exciton emission peaks is observed when substituted with zinc. In addition, with increasing Zn content, the emission edge by recombination of excitons in ZnO (sample $Zn_{0.2}Cd_{0.8}O$), shifts toward shorter wavelengths. In Fig. 16, it can be seen that the shift of the emission peak of CdO is insignificant compared to the shift of the exciton peak of ZnO [45].

Table 1.

Description of observed PL peaks in the structure $Zn_{1-x}Cd_xO$ ($0 \le x \le 1$) [1]

	Peaks of FL						Mechanism radiation
	CdO	$Cd_{0.8}Zn_{0.2}O$	$Cd_{0.6}Zn_{0.4}O$	$Cd_{0.4}Zn_{0.6}O$	$Cd_{0.4}Zn_{0.6}O$	ZnO	
1	–	–	387	382	380	378	The edge emission of undoped ZnO is associated with the recombination of excitons
2	422	420	419	417	415	–	The emission is associated with charge transfer in undoped CdO
3	448	–	–	–	–	–	The emission is associated with transitions of charge carriers from the defect level of internodal cadmium to the valence band
4	–	486	486	486	486	486	The emission is associated with the transitions of charge carriers from the defective level of internodal zinc to the valence band
5	–	520	520	520	520	520	The emission is associated with singly ionized oxygen vacancies (Vo) existing in $Zn_{1-x}Cd_xO$

In Fig. 17 shows the transmission and absorption spectra of ZnO and $Zn_{0.9}Cd_{0.1}O$ films, which were synthesized by the spin-coating method. It can be seen that both films have a transparency of 80-90 %. It was also found that cadmium doping causes a slight decrease in transmission in the visible region. ZnO-Cd film shows a shift of the absorption edge by about 80 nm compared to the ZnO film [30]. A similar result was obtained in [17], where the films were synthesized by pulsed laser deposition method.

Undoped ZnO shows absorption at 367 nm. This is shown in Fig. 18. After adding 5 % and 10 % Cd to ZnO, it shows a higher absorption band at 377 and 385 nm, respectively. Undoped ZnO and ZnO doped with cadmium have a large optical transmission window in the region of 400–800 nm. No visible absorption band was detected in this region. A wide transparency area is nessessary for fabrication nanodevices and is applicable to optoelectronics.

The energy gap width (E_g) of undoped ZnO and Cd-doped ZnO nanoparticles is shown in Fig. 19, were calculated according to the formula:

$$E_g = \frac{hc}{\lambda} \quad (1)$$

where h – Planck's constant,

c – speed of light,

λ – wavelength.

The appropriate values of the energy gap width of undoped ZnO and Cd-doped ZnO nanorods are shown in Fig. 19. It can be seen that with an increasing level of cadmium doping, the edge of the fundamental absorption decreases. The value of E_g for undoped ZnO is 3.24 eV. It decreases to 3.21 eV for ZnO doped with 5 % Cd and to 3.18 eV for ZnO doped with 10 % Cd. This decrease can be explained by the large difference in E_g values for zinc oxide and cadmium oxide [34,37,38,40].

The effect of an increased dose of doping, which was considered in [37] on optical properties, can be seen in Fig. 20 and Fig. 21.

Optical analysis in the wavelength range of 200–800 nm at room temperature of CdO-ZnO films deposited on a glass substrate is shown in Fig. 20, a. All films have a high transmittance in the visible area, which decreases with an increasing concentration of cadmium impurity. This change was a consequence of the large gap in electronic band structure of CdO and ZnO. The ZnO thin film has the highest transmittance, while the minimum transmittance was observed in the CdO film in the visible region.

From the dependence $(\alpha h\upsilon)^2$ to $h\upsilon$ for the films shown in Fig. 20, b, received values of 2.10, 2.40, 3.01 and 3.20 eV. This sequence corresponds to thin films of CdO, No.1,

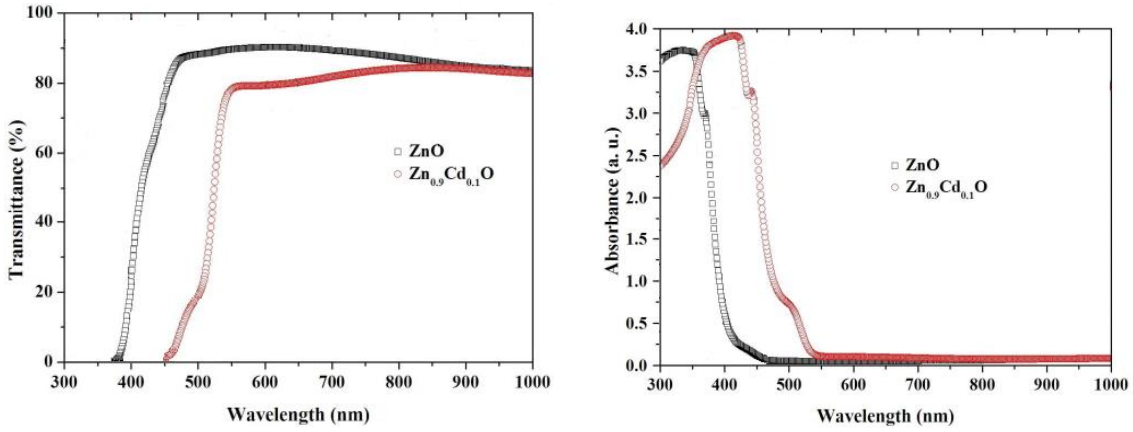

a) b)

Fig. 17. Spectra of $ZnO_{0.9}Cd_{0.1}O$ thin films : a) – optical transmission; b) – absorption spectra [41].

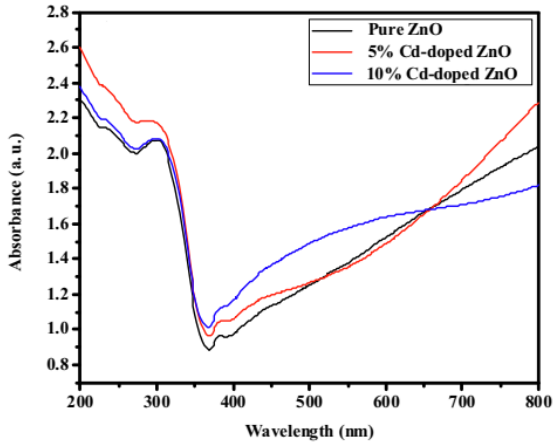

Fig.18. Absorption spectra of undoped and Cd-doped ZnO nanoparticles [42].

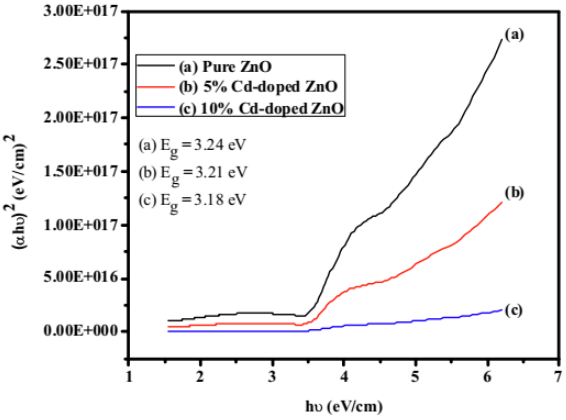

Fig. 19. The width of the energy gap of undoped and cadmium-doped ZnO synthesized by reflux method [42].

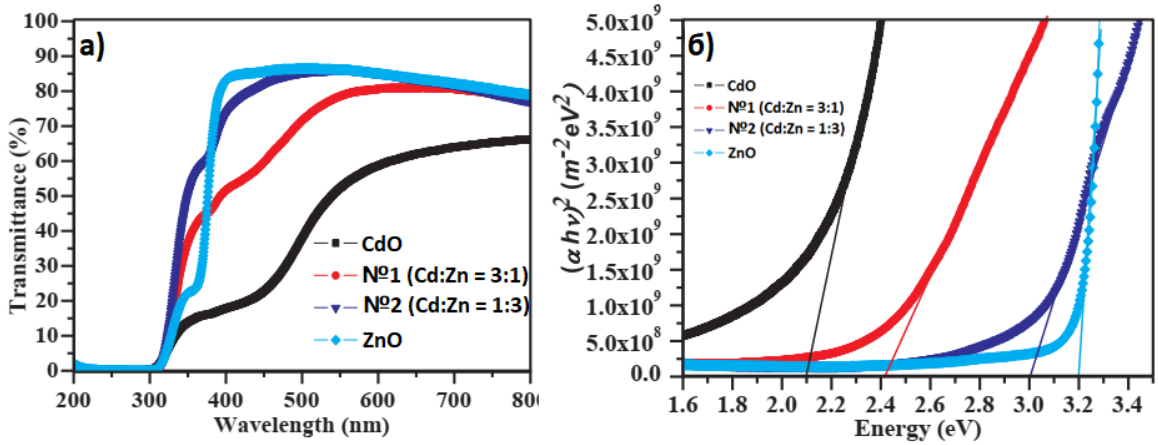

Fig. 20. Summary graphs of the optical characteristics of the obtained samples: a – optical transmission spectra; b – dependence of $(\alpha h\upsilon)^2$ to $h\upsilon$ [25].

No.2 and ZnO. The width of the energy gap is inversely proportional to the concentration of Cd in the thin film. The electron binding energy of CdO may be responsible for the narrowing of the bandgap because, due to the large atomic radius, conduction electrons require less energy to move into the valence band compared to ZnO.

PL spectra of CdO-ZnO at room temperature are shown in Fig. 21. Wide mission peaks were observed in the 380–440 nm region, which corresponds to excitonic emission near the band edge. The spectrum also shows emission in the visible region centered around 720 nm (red light), as shown in Fig. 21. The maximum intensity of the PL peak for red light was observed for thin film №1 with a ratio of Zn:Cd = 3:1. This emission occurs due to the transition of electrons from the bottom of the conduction zone to the level of vacancies - defects in the crystal structure of CdO and ZnO.

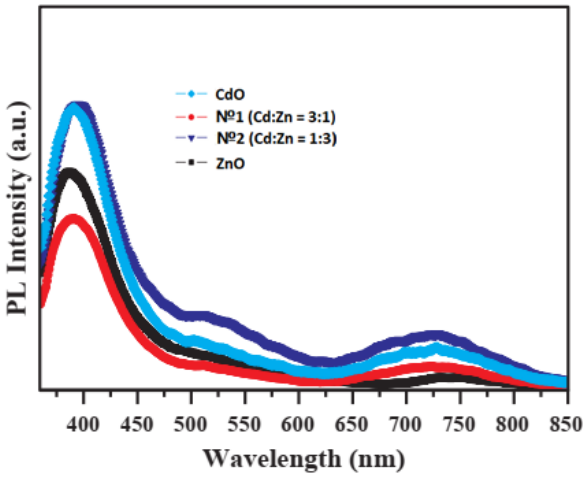

Fig.21. PL spectra of CdO-ZnO thin films [25].

It is also appropriate to consider the study optical properties of $Zn_{1-x}Cd_xO$ thin films in the article [36], in particular to investigate the spectra of optical transmittance and the dependence of $(\alpha h\upsilon)^2$ to $h\upsilon$ for the films that were deposited by spray pyrolysis method. The corresponding curves are shown in Fig. 22.

Comparing the graphs shown in Fig. 20, a, and Fig. 22, a, you can see the similarity of the results obtained by different methods and at different doping concentrations. In addition, films synthesized by the spray pyrolysis method show greater transparency in the ultraviolet spectrum (Fig. 22, a, c).

Thin films were deposited by synthesized by the DC and RF reactive magnetron co-sputtering $Zn_{1-x}Cd_xO$ in the article [30]. The peculiarity of this work is that it used two metal targets made of undoped zinc and cadmium. 80 W was applied to the zinc target and to modulate the molar fraction of cadmium in the structure, the power applied to the cadmium target was varied from 0 to 120 W. Table 2 shows the ratio of the composition of elements in $Zn_{1-x}Cd_xO$ films applied at different powers of sputtering a cadmium target (P_{Cd}). Using the method of energy dispersive X-ray spectroscopy, it was found that the Cd content increases with an increase P_{Cd}.

As a result of increasing the proportion of cadmium in the structure, the width of the energy gap decreases. This is demonstrated in Fig. 23.

On the basis of all considered materials and synthesis methods, a summary table can be compiled that will demonstrate the effect of cadmium doping on the width of the energy gap (Table 3).

2.3 Photocatalytic activity

Photocatalysis appears to be an interesting approach to water purification with the possibility of using sunlight as a sustainable and renewable energy source (Fig. 24). This technology is based on the use of a semiconductor that can be excited by light with an energy higher than the band gap, inducing the formation of electron-hole pairs that can participate in redox reactions. Nanoscale semiconductors typically have high activity and high degree of functionality, large specific surface area, and size-dependent properties, which making them suitable for water treatment applications.

In recent years, most photocatalysts have been specifically designed for applications under sunlight, but many researchers have focused their attention on UV-active systems. Thus, nanoscale semiconductors sensitive to UV and visible or sunlight should be considered.

Some publications have demonstrated a better photoresponse for ZnO compared to TiO_2 for the photocatalytic decomposition of some dyes in water [43].

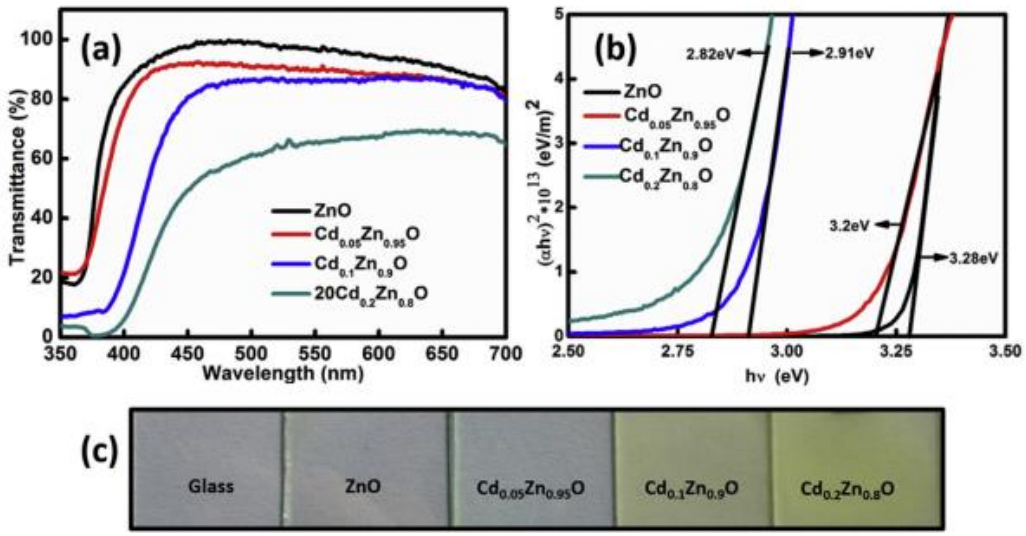

Fig. 22. Optical transmission spectra (a), dependence $(\alpha h\upsilon)^2$ to $h\upsilon$ (b) and appearance of deposited $Zn_{1-x}Cd_xO$ thin films (c) [35].

Table 2.

Composition of $Zn_{1-x}Cd_xO$ films according to energy dispersive analysis [30**Ошибка! Закладка не определена.**]

	Atomic fraction, %		
P_{Cd},W	O	Zn	Cd
20	50.68	48.67	0.65
40	51.24	47.45	1.31
60	51.59	46.07	2.34
120	51.99	40.48	7.53

Table 3.

Comparative analysis of different doping concentrations and different synthesis methods [18]

Cadmium content in the film $Zn_{1-x}Cd_xO$, %	Synthesis technique	Band gap width, eV	Link
x = 0.45 atomic	Sol-gel method	3.20	[28]
x = 0.51 atomic		3.19	
x = 0.56 atomic		3.15	
x = 16 atomic	Pulsed laser deposition	2.75	[17]
x = 25 atomic		2.4	
x = 50 atomic		2.19	
x = 10 atomic	Sol-gel spin coating	2.66	[41]
x = 5 molar	Reflux method	3.21	[42]
x = 10 molar		3.18	
x = 67 voluminous	Sol-gel spin coating method	2.4	[25]
x = 33 voluminous		3	
x = 0.65 atomic	High-frequency reactive magnetron sputtering	3.21	[30]
x = 31 atomic		3.16	
x = 2.34 atomic		3.07	
x = 7.53 atomic		2.82	
x = 5 atomic	Pulsed laser deposition	3.2	[19]
x = 10 atomic		2.97	
x = 5 atomic	Spray pyrolysis method	3.2	[35]
x = 10 atomic		2.91	
x = 20 atomic		2.82	

Several literature studies determined the method of doping ZnO-Cd to achieve a good photocatalytic effect. Despite this, the properties and the mechanism behind have not been fully explained [43]. It should be noted that the improvement of photocatalytic efficiency is closely related to structural properties, such as morphology, particle size, crystal orientation, degree of crystallization and oxygen defects, which greatly affect the activity and stability of photocatalysts [44].

Effect of doping with Cd ions on the photocatalytic

properties of ZnO nanoparticles obtained by the deposition method is described in [47].

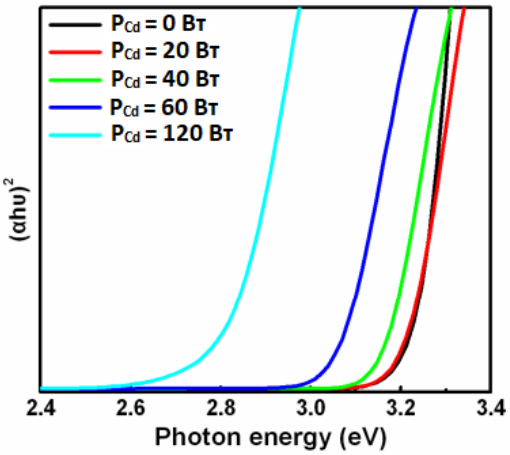

Fig. 23. Dependences $(\alpha h\nu)^2$ to $h\nu$ for $Zn_{1-x}Cd_xO$ films at different sputtering powers of the cadmium target [30].

To study the photocatalytic activity of ZnO-Cd nanostructures, the absorption spectra obtained during the degradation of crystal violet in an aqueous solution at ambient temperature were used (Fig. 25). The dye solution containing photocatalyst was exposed to UV irradiation with a 6 W mercury lamp and samples were collected at regular intervals to determine the photocatalytic behavior. The sample was centrifuged for 3 minutes at 2500 rpm to separate the catalyst particles from the aqueous phase to determine the degree of discoloration.

In Fig. 25, and in the Table 3 shows the percentage degradation of crystal violet for undoped ZnO and Cd doped ZnO with different molar fractions during 120 min of illumination.

The results showed that the best dye degradation in cadmium-doped ZnO catalysts occurs in the following order: 0.5 mol %, 0 mol %, 2 mol %, 1.5 mol %, 1.0 mol % cadmium doping. It can be concluded that the

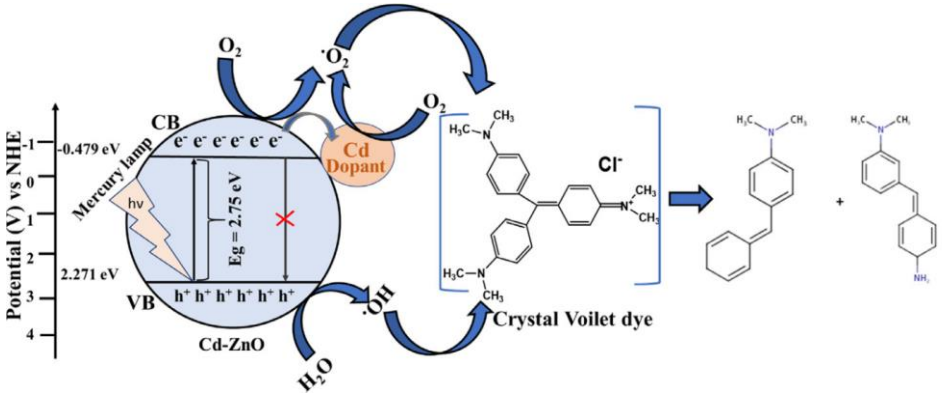

Fig. 24. Photocatalytic mechanism of degradation of crystal violet using ZnO - Cd nanoparticles [47].

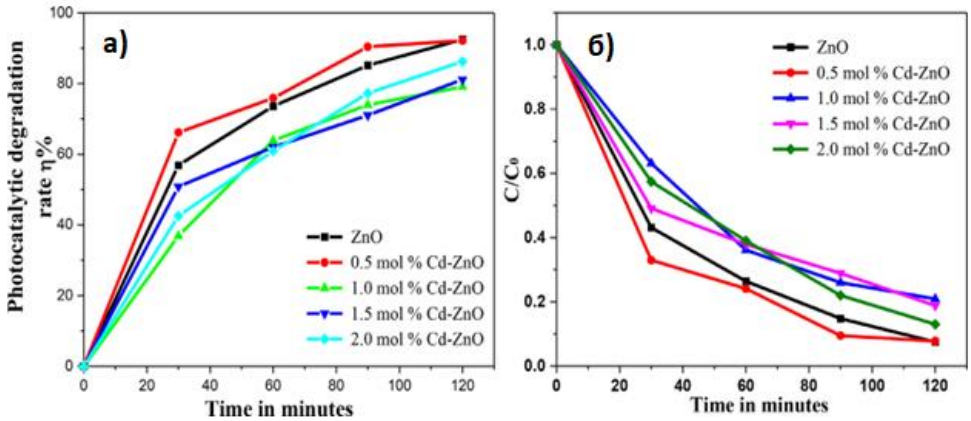

Fig. 25. a – diagram of photocatalytic degradation of crystal violet depending on the time of irradiation; b – a graph of the dependence of the concentration of crystal violet at different molar ratios of ZnO doped with Cd [47].

Table 3.

Influence of molar fraction of cadmium on photodegradation of samples [47]

		Duration of photocatalysis, min			
		30	60	90	120
		Biodegradation, %			
Molar fraction of Cd, mol %	Cd = 0 %	56.88	73.57	85.17	92.47
	Cd = 0.5 %	66.14	75.87	90.4	92.13
	Cd = 1 %	36.88	63.85	73.94	79.08
	Cd = 1.5 %	5.82	62.0	71.0	81.0
	Cd = 2 %	42.56	60.91	77.24	86.23

implantation of 0.5 mol % cadmium improves the photocatalytic activity of ZnO in the crystal violet due to the increased charge separation potential. Excessive inclusion of Cd leads to an increase in the rate of recombination of electrons and holes, which leads to a loss of photocatalytic activity. The authors of the article [47] suggested that this may be due to the presence of cadmium nanoparticles in the volume of zinc. The presence of a Cd impurity of more than 0.5 molar % in the photocatalyst leads to a decrease in the efficiency of the photocatalyst.

Undoped and cadmium doped ZnO samples were able to degrade the crystal violet dye, as seen by the decrease in concentration, which indicated that the chromophoric groups of the dye were converted to intermediate products. Fig. 25, b shows that more than 80 % of the dye decomposes within 120 minutes in ZnO-Cd nanoparticles.

The results in Fig. 26, and showed that nanoparticles of the ZnO-Cd series can destroy approximately from 53 to 67 % of alizarin red (AR) dye during irradiation with an ultraviolet lamp. In Fig. 26, it is shown that a significant decomposition was observed in the ultraviolet in the absence of a catalyst. The rate of decomposition reached 84 % in 120 minutes. These results show that a series of ZnO-Cd compounds can be effectively used to destroy cationic dyes, but not anionic ones.

The work also investigated the influence of the catalyst dose in the range from 0.5 mg to 3.0 mg on the decomposition of crystal violet. In the Table 4 shows the efficiency of dye degradation. Increasing the amount of catalyst in the range from 0.5 mg to 2.0 mg led to an increase in photocatalytic degradation. This suggests that the rate of degradation improves with increasing amount of catalyst. In turn, this result can be caused by an increase in the number of active centers on the surface of the catalyst. Since a higher dose of catalyst blocks the rays of the ultraviolet lamp from penetrating the solution, it also leads to a decrease in catalytic activity.

The pH level is one of the most important factors that can affect the process of dye degradation on the surface of the photocatalyst. The influence of different pH values in the range from 2 to 12 (in acidic, neutral and alkaline pH environments) on the efficiency of dye degradation was investigated. The obtained dependencies were presented in the Table 5.

In an acidic environment, the degradation efficiency of crystal violet was 90%, but in an alkaline environment it was higher and amounted to 100 % for 12 pH (Fig. 27). The efficiency of crystal violet decomposition was increased from 85% at pH 8 to 100% at pH 10 in pure ZnO solution. 100% decomposition was achieved in less than 60 min at pH 12. During the same time, 0.5 mol % Cd in the ZnO structure allows the dye to be decomposed by

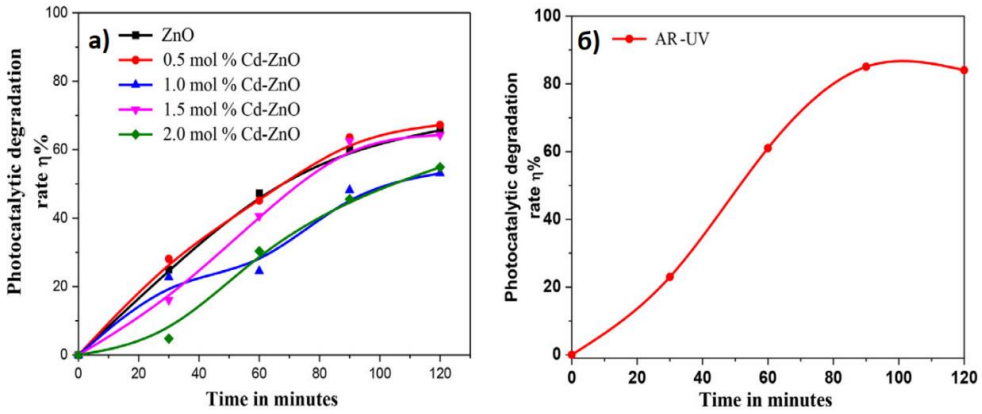

Fig. 26. Percentage diagram of the photocatalytic decomposition of alizarin red with: a – different concentration of the catalyst in UV; b – only in UV without catalyst [47].

Table 4.

Influence of the catalyst content on the photodegradation of samples [47]

		Duration of photocatalysis, min			
		30	60	90	120
		Biodegradation, %			
Catalyst content, mg	0,5	69.2	77.6	87.2	90.4
	1	66.14	75.87	90.4	92.15
	2	79.6	86.2	95.6	100
	3	69.6	77.7	88.5	88.5

Table 5.

Influence of the acidity of the medium on photodegradation of samples [47]

		Duration of photocatalysis, min			
		30	60	90	120
		Biodegradation, %			
pH level	2	71.28	82.12	88.26	92.15
	4	48.62	73.39	83.3	93.76
	6	44	80	85.13	86.23
	8	59.81	85.87	88.44	94.31
	10	64.4	100	100	100
	12	100	100	100	100

approximately 94 % at pH 8, 100% at pH 10 and 12 in 60 and 30 minutes respectively.

Fig. 27. Results of photodegradation of crystal violet [47].

From the Table 4 and 5 clearly show that 2 mg of the catalyst doped with 0.5 mol % Cd at pH 10 and 12 have a higher decomposition efficiency for 60 min and 30 min compared to 1, 1.5 and 2 mol % Cd in the ZnO structure.

The photocatalytic activity was also studied in the article [23]. ZnO and ZnO-Cd nanoparticles were synthesized by the hydrothermal method.

The photocatalytic activity of hydrothermally synthesized ZnO doped with cadmium was evaluated by testing the degradation of rhodamine B. The diagram of the decomposition of the ZnO-Cd photocatalyzed dye is shown in Fig. 28. Also, for comparison, a graph of dye decay on a sample of undoped ZnO is given. The time diagrams demonstrate a significant enhancement of the photocatalytic activity when ZnO is doped with cadmium using the hydrothermal method.

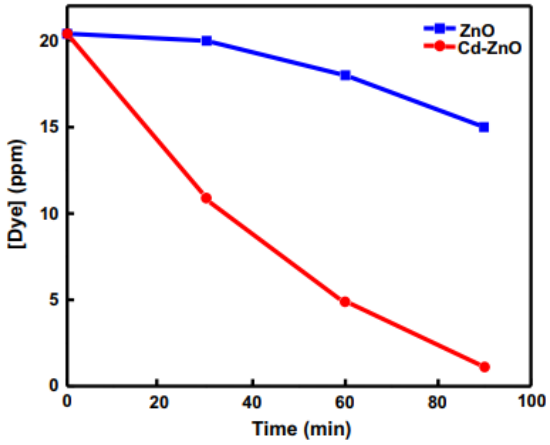

Fig. 28. Photocatalytic degradation of rhodamine B [23].

In Fig. 29 residual concentration of methylene blue (MB) was obtained for all samples and compared with the results decomposition of MB without a photocatalyst. It was observed that the MB dye decomposed by 99% within 180 minutes using the $Cd_{0.2}Zn_{0.8}O$ sample as catalyst, while only 28, 48, 65, 88 and 94 % of the dye decomposed when the zinc samples were used x = 0; 0.2; 0.4; 0.6 and 1 in $Cd_{1-x}Zn_xO$, respectively, as a catalyst under the same experimental conditions [45].

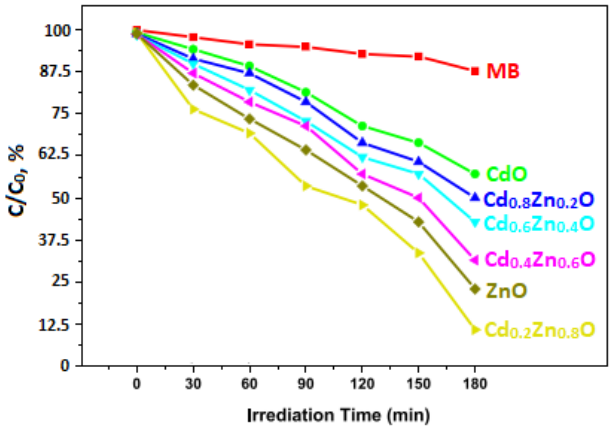

Fig.29. Graph of the residual concentration of methylene blue (MB) during photocatalysis by structures with different content of cadmium doping [45].

Conclusions

Materials based on ZnO and cadmium, are gaining increased attention as promising photocatalytic material and can be successfully applied for organic dyes degradation. This review considers the influence of cadmium doping on morphology, structure and optical properties of ZnO obtained by various techniques. It was discussed that Cd-doping modifies the characteristics of ZnO and enhances its suitability for photocatalysis due to suppressing the recombination rate of electron-hole pairs, increasing charge separation efficiency, and improving the production rate of hydroxyl radicals. The band engineering of ZnO toward visible range by Cd-doping leads to the increased ability to absorb more irradiation of the solar spectrum. Additional research is needed to evaluate how photocatalyst properties of Cd-doped ZnO correlate with their optical properties. It was shown that Cd-doped ZnO is the perspective multifunctional material for wide-scale environmental, technological, and biomedical applications.

Acknowledgements

This work was supported by the project of research works of young scientists of NAS of Ukraine "Creation of effective photocatalytic materials based on ZnO-Cd system for water purification from organic pollutants".

Didus R.I. – Senior Engineer of Department of Physics and Technology of Photoelectronic and Magnetoactive Materials;
Myroniuk D.V. – Candidate of Physical and Mathematical Sciences, Senior Researcher of Department of Physics and Technology of Photoelectronic and Magnetoactive Materials;
Myroniuk L.A. – Candidate of Chemical Sciences, Researcher of Department of Physics and Technology of Photoelectronic and Magnetoactive Materials;
Ievtushenko A.I. – Candidate of Physical and Mathematical Sciences, Senior Researcher, Head of Department of Physics and Technology of Photoelectronic and Magnetoactive Materials.

[1] O. E. Baibara, M.V. Radchenko, V.A. Karpyna, A.I. Ievtushenko, *A Review of the Some Aspects for the Development of ZnO Based Photocatalysts for a Variety of Applications*, Physics and Chemistry of Solid State, 22 (3), 585 (2021); https://doi.org/10.15330/pcss.22.3.585-594.
[2] S. P. Hoffmann, C. Meier, T. Zentgraf, W.-G. Schmidt, H. Herrmann, Zinc-Oxide Based Photonic Crystal Membranes, University of Paderborn, (2018).
[3] A. Antony, I. V. Kityk, G. Myronchuk, G. Sanjeev, V. C. Petwal, V. P. Verma, J. Dwivedi, *A study of 8 meV e-beam on localized defect states in ZnO nanostructures and its role on photoluminescence and third harmonic generation*, Journal Lumin, 207, 321 (2019); https://doi.org/10.1016/j.jlumin.2018.11.043.
[4] A. Sevik, B. Coskun, M. Soylu, *The effect of molar ratio on the photo-generated charge activity of ZnO–CdO composites*, Eur. Phys. J., 135, 65 (2020); https://doi.org/10.1140/epjp/s13360-020-00129-w.
[5] Rahman, *Zinc oxide light-emitting diodes: a review*, Opt. Eng., 58(1), 010901 (2019); https://doi.org/10.1117/1.OE.58.1.010901.
[6] Y. J. Noh, J. G. Kim, S. S. Kim, H. K. Kim, S. I. Na, *Efficient semitransparent perovskite solar cells with a novel indium zinc tin oxide top electrode grown by linear facing target sputtering*, Journal of Power Sources. 437, 226894 (2019); https://doi.org/10.1016/j.jpowsour.2019.226894.
[7] S. Golovynskyi, A. Ievtushenko, S. Mamykin, M. Dusheiko, I. Golovynska, O. Bykov, O. Olifan, D. Myroniuk, S. Tkach, J. Qu, *High transparent and conductive undoped ZnO thin films deposited by reactive ion-beam sputtering*, Vacuum, 153, 204 (2018); https://doi.org/10.1016/j.vacuum.2018.04.019.
[8] M. Pirsaheb, H. Hossaini, N. Simin, A. Nahid, S. Behzad, K. Toba, *Optimization of photocatalytic degradation of methyl orange using immobilized scoria-Ni/TiO2 nanoparticles*, Journal of Nanostructure in Chemistry, 10, 143 (2020); https://doi.org/10.1007/s40097-020-00337-x.
[9] V. Karpyna, A. Ievtushenko, O. Kolomys, O. Lytvyn, V. Strelchuk, V. Tkach, S. Starik, V. Baturin, O. Karpenko, *Raman and Photoluminescence Study of Al,N-Codoped ZnO Films Deposited at Oxygen-Rich Conditions by Magnetron Sputtering*, Phys. Status Solidi B., 257, 1900788 (2020); https://doi.org/10.1002/pssb.201900788.
[10] A. Ievtushenko, O. Khyzhun, I. Shtepliuk, O. Bykov, R. Jakieła, S. Tkach, E. Kuzmenko, V. Baturin, O. Karpenko, O. Olifan, G. Lashkarev, *X-Ray photoelectron spectroscopy study of highly-doped ZnO:Al,N films grown at O-rich conditions*, Journal of Alloys and Compounds, 722, 683 (2017); https://doi.org/10.1016/j.jallcom.2017.06.169.
[11] E. Mosquera, I. del Pozo, M. Morel, *Structure and redshift of optical band gap in CdO–ZnO nanocomposite synthesized by the sol-gel method*, Journal of Solid State Chemistry, 203, 265 (2013); https://doi.org/10.1016/j.jssc.2013.08.025.
[12] E. Ozugurlu, *Cd-doped ZnO nanoparticles: An experimental and first-principles DFT studies*, Journal of Alloys and Compounds, 861, 158620 (2020); https://doi.org/10.1016/j.jallcom.2021.158620.
[13] I. Shtepliuk, G. Lashkarev, V. Khomyak, P. Marianchuk, P. Koreniuk, D. Myroniuk, V. Lazorenko, I. Timofeeva, *Effects of Ar/O_2 Gas Ratio on the Properties of the $Zn_{0.9}Cd_{0.1}O$ Films Prepared by DC Reactive Magnetron Sputtering*, Acta Physica Polonica A, 120, A-61 (2011); https://doi.org/10.12693/APhysPolA.120.A-61.
[14] I.Shtepliuk, V.Khranovskyy, G.Lashkarev, V.Khomyak, V.Lazorenko, A.Ievtushenko, ... & R.Yakimova, *Electrical properties of n-Zn0.94Cd0.06O/p-SiC heterostructures*, Solid-State Electronics, 81, 72-77 (2013); https://doi.org/10.1016/j.sse.2013.01.015.
[15] S.Y. Lee, Y. Li, J.S. Lee, J.K. Lee, M. Nastasi, S.A. Crooker, ... & J.S. Kang, *Effects of chemical composition on the optical properties of Zn 1− x Cd x O thin films*, Applied physics letters, 85(2), 218-220 (2004); https://doi.org/10.1063/1.1771810.
[16] P.Misra, P. K. Sahoo, P. Tripathi, V. N. Kulkarni, R. V. Nandedkar, L. M. Kukreja, *Sequential pulsed laser deposition of $Cd_xZn_{1-x}O$ alloy thin films for engineering ZnO band gap*, Appl. Phys. A, 78, 37 (2004); https://doi.org/10.1007/s00339-003-2296-0.
[17] L. N. Bai, B. J. Zheng, J. S. Lian, Q. Jiang, *First-principles calculations of Cd-doped ZnO thin films deposited by pulse laser deposition*, Solid State Sciences, 14, 698 (2012); https://doi.org/10.1016/j.solidstatesciences.2012.03.018.
[18] S.Sharma, B. Saini, R. Kaur, M. Tomar, V. Gupta, A. Kapoor, *Low resistivity of pulsed laser deposited $Cd_xZn_{1-x}O$ thin films*, Ceramics International, 45, 1900 (2019); https://doi.org/10.1016/j.ceramint.2018.10.082.
[19] S.Chen, Q. Li, I. Ferguson, T. Lin, L. Wan, Z. C. Feng, L. Zhu, Z. Ye, *Spectroscopic ellipsometry studies on ZnCdO thin films with different Cd concentrations grown by pulsed laser deposition*, Applied Surface Science, 42, 383 (2017); https://doi.org/10.1016/j.apsusc.2017.02.264.
[20] M. Tortosa, M. Mollar, B. Mari, *Synthesis of ZnCdO thin films by electrodeposition*, Journal of Crystal Growth, 304, 97 (2007); https://doi.org/10.1016/j.jcrysgro.2007.02.010.
[21] O. Lupan, T. Pauporté, L. Chow, G. Chai, B. Viana, V. V. Ursaki, E. Monaico , I. M. Tiginyanu, *Comparative study of the ZnO and $Zn_{1-x}Cd_xO$ nanorod emitters hydrothermally synthesized and electrodeposited on p-GaN*, Applied Surface Science, 259, 399 (2012); https://doi.org/10.1016/j.apsusc.2012.07.058.
[22] S.-I. Park, Y. -J. Quan, S. -H. Kim, H. Kim, S. Kim, D. -M. Chun, S. -H. Ahn, *A review on fabrication processes for electrochromic devices*, International Journal of Precision Engineering and Manufacturing-Green Technology, 3, 397 (2016); https://doi.org/10.1007/s40684-016-0049-8.

[23] C.Karunakaran, A. Vijayabalan, G. Manikandan, *Photocatalytic and bactericidal activities of hydrothermally synthesized nanocrystalline Cd-doped ZnO*, Superlattices and Microstructures, 5, 443 (2012); https://doi.org/10.1016/j.spmi.2012.01.008.
[24] Y.Caglar *Morphological, optical and electrical properties of CdZnO films prepared by sol–gel method*Journal of Physics D: Applied Physics, 42, 065421 (2009); http://dx.doi.org/10.1088/0022-3727/42/6/065421.
[25] J.K. Rajput, T.K. Pathak, V. Kumar, H.C. Swart, L.P. Purohit, *CdO:ZnO nanocomposite thin films for oxygen gas sensing at low temperature*, Materials Science and Engineering: B., 228, 241 (2018); https://doi.org/10.1016/j.mseb.2017.12.002.
[26] F. Yakuphanoglu, S. Ilican, M. Caglar, Y. Caglar, *Microstructure and electro-optical properties of sol–gel derived Cd-doped ZnO films*, Superlattices and Microstructures, 47, 732 (2010); https://doi.org/10.1016/j.spmi.2010.02.006.
[27] T. K. Pathak, J. K. Rajput, V. Kumar, L. P. Purohit, H. C. Swart, R. E. Kroon, *Transparent conducting ZnO-CdO mixed oxide thin films grown by the sol-gel method*, Journal of Colloid and Interface Science, 487, 378 (2017); https://doi.org/10.1016/j.jcis.2016.10.062.
[28] N. Kumar, A. Srivastava, *Faster photoresponse, enhanced photosensitivity and photoluminescence in nanocrystalline ZnO films suitably doped by Cd*, Journal of Alloys and Compounds, 706, 438(2017); http://dx.doi.org/10.1016/j.jallcom.2017.02.244.
[29] I.Shtepliuk, V. Khranovskyy, G. Lashkarev, V. Khomyak, A. Ievtushenko, V. Tkach, V. Lazorenko, I. Timofeeva, R. Yakimova, *Microstructure and luminescence dynamics of ZnCdO films with high Cd content deposited on different substrates by DC magnetron sputtering*, Applied Surface Science, 276, 550 (2013); https://doi.org/10.1016/j.apsusc.2013.03.132.
[30] Y. R. Sui, Y. J. Wu, Y. P. Song, S. Q. Liv, B. Yao, X. W. Meng, L. Xiao, *A study on structural formation and optical properties of $Zn_{1-x}Cd_xO$ thin films synthesized by the DC and RF reactive magnetron co-sputtering*, Journal of Alloys and Compounds, 678, 383 (2016); https://doi.org/10.1016/j.jallcom.2016.03.302.
[31] A.Ievtushenko, V. Tkach, V. Strelchuk, L. Petrosian, O. Kolomys, O. Kutsay, V. Garashchenko, O. Olifan, S. Korichev, G. Lashkarev, V. Khranovskyy, *Solar Explosive Evaporation Growth of ZnO Nanostructures*, Applied Science, 7(4), 383 (2017); https://doi.org/10.3390/app7040383.
[32] S. Vijayalakshmi, S. Venkataraj, R. Jayavel, *Characterization of cadmium doped zinc oxide (Cd:ZnO) thin films prepared by spray pyrolysis method*, Journal of Physics D: Applied Physics, 41, 7 (2008); http://dx.doi.org/10.1088/0022-3727/41/24/245403.
[33] D. Acharya, S. Moghe, R. Panda, S. B. Shrivastava, M. Gangrade, T. Shripathi, D. M. Phase, V. Ganesan, *Effect of Cd dopant on electrical and optical properties of ZnO thin films prepared by spray pyrolysis route*, Thin Solid Films, 525, 49 (2012); https://doi.org/10.1016/j.tsf.2012.10.100.
[34] N. L. Tarwal, A. R. Patil, N. S. Harale, A. V. Rajgure, S. S. Suryavanshi, W. R. Bae, P. S. Patil, J. H. Kim, J. H. Jang, *Gas sensing performance of the spray deposited Cd-ZnO thin films*, Journal of Alloys and Compounds, 598, 282 (2014); https://doi.org/10.1016/j.jallcom.2014.01.200.
[35] S. P. Bharath, K. V. Bangera, G. K. Shivakumar, *Properties of $Cd_xZn_{1-x}O$ thin films and their enhanced gas sensing performance*, Journal of Alloys and Compounds, 720, 39 (2017); http://dx.doi.org/10.1016/j.jallcom.2017.05.240.
[36] Q. Wan, Q. H. Li, Y. J. Chen, T. H. Wang, X. L. He, X. G. Gao, J. P. Li, *Positive temperature coefficient resistance and humidity sensing properties of Cd-doped ZnO nanowires*, Appl. Phys. Lett, 84, 3085 (2004); https://doi.org/10.1063/1.1707225.
[37] S.Sakurai, T. Kubo, D. Kajita, T. Tanabe, H. Takasu, S. Fujita, S. Fujita, *Blue Photoluminescence from ZnCdO Films Grown by Molecular Beam Epitaxy*, Japanese Journal of Applied Physics, 39, 1146 (2000); http://dx.doi.org/10.1143/JJAP.39.L1146.
[38] S. Shigemori, A. Nakamura, J. Ishihara, T. Aoki, J. Temmyo, *$Zn_{1-x}Cd_xO$ film growth using remote plasma-enhanced metalorganic chemical vapor deposition*, Japanese Journal of Applied Physics, 43(8), 1088 (2004); http://dx.doi.org/10.1143/JJAP.43.L1088.
[39] M. Souissi, A. Fouzri, G. Schmerber, *Highlighting of ferromagnetism above room temperature in Cd-doped ZnO thin films grown by MOCVD*, Solid State Communications, 218, 40 (2015); https://doi.org/10.1016/j.ssc.2015.06.013.
[40] S. Mondal, P. Mitra, *Preparation of cadmium-doped ZnO thin films by SILAR and their characterization*, Bulletin of Materials Science, 35, 751 (2012); https://doi.org/10.1007/s12034-012-0350-2.
[41] Jacob, L. Balakrishnan, S. R. Meher, K. Shambavi, Z. C. Alex, *Structural, optical and photodetection characteristics of Cd alloyed ZnO thin film by spin coating*, Journal of Alloys and Compounds, 695, 3753 (2017); https://doi.org/10.1016/j.jallcom.2016.11.265.
[42] U. D. Babar, N. M. Garad, A. A. Mohite, B. M. Babar, H. D. Shelke, P. D. Kamble, U. T. Pawar, *Study the photovoltaic performance of pure and Cd-doped ZnO nanoparticles prepared by reflux method*, Materials Today: Proceedings, 43, 2780 (2021); https://doi.org/10.1016/j.matpr.2020.08.008.
[43] G. K. Weldegebrieal, *Synthesis method, antibacterial and photocatalytic activity of ZnO nanoparticles for azo dyes in wastewater treatment: A review*, Inorganic Chemistry Communications. 120, 108140 (2020); https://doi.org/10.1016/j.inoche.2020.108140.
[44] Z. Liu, P. X. Yan, G. H. Yue, J. B. Chang, R. F. Zhuo, D. M. Qu, *Controllable synthesis of undoped/Cd-doped*

ZnO nanostructures, Materials Letters, 60, 3122 (2006); https://doi.org/10.1016/j.matlet.2006.02.056.
[45] C.Bhukkal, R. Vats, B. Goswami, N. Rani, R. Ahlawat, *Zinc content (x) induced impact on crystallographic, optoelectronic, and photocatalytic parameters of $Cd_{1-x}Zn_xO$ (0≤x≤1) ternary nanopowder*, Materials Science and Engineering: B., 265, 11500 (2021); https://doi.org/10.1016/j.mseb.2020.115001.
[46] C.Belver, J. Bedia, A. Gómez-Avilés, M. Peñas-Garzón, J. J. Rodriguez, *Semiconductor photocatalysis for water purification in micro and nano technologies*, Nanoscale Materials in Water Purification, 581 (2019); https://doi.org/10.1016/B978-0-12-813926-4.00028-8.
[47] F. Sanakousar, C. C Vidyasagar, V. M. Jiménez-Pérez, B. K. Jayanna, Mounesh, A. H. Shridhar, K. Prakash, *Efficient photocatalytic degradation of crystal violet dye and electrochemical performance of modified MWCNTs/Cd-ZnO nanoparticles with quantum chemical calculations*, Journal of Hazardous Materials Advances, 2, 100004 (2021); https://doi.org/10.1016/j.hazadv.2021.100004.
[48] H. A. Azqhandi, B. F. Vasheghani, F. H. Rajabi, M. Keramati, *Synthesis of Cd doped ZnO/CNT nanocomposite by using microwave method: Photocatalytic behavior, adsorption and kinetic study*, Results in Physics, 7, 1106 (2017); https://doi.org/10.1016/j.rinp.2017.02.033.

Р. І. Дідусь, Д. В. Миронюк, Л. А. Миронюк, А. І. Євтушенко

Особливості технологічного синтезу та властивості матеріалів на основі ZnO-Cd для фотокаталітичного застосування. Огляд

Інститут проблем матеріалознавства ім. І.М. Францевича НАН України, Київ, Україна, romanik619@gmail.com

У цьому огляді узагальнено поточний стан матеріалів на основі ZnO-Cd для фотокаталітичних застосувань. Розглядаються відповідні технологічні методи синтезу, такі як імпульсне лазерне осадження, магнетронне розпилення, електроосадження, золь-гель, металоорганічне хімічне осадження з парової фази, випаровування, розпилювальний піроліз, а також останні розробки в ефективній та відтворюваній технології синтезу нано- та мікроструктурованого оксиду цинку, обговорюються леговані кадмієм тверді розчини $Zn_{1-x}Cd_xO$ для фоторозпаду молекул органічних забруднювачів. Технологія синтезу та рівень легування кадмієм істотно впливає на структуру та морфологію оксиду цинку і, як наслідок, на оптичні та фотокаталітичні властивості. Показники добротності, теоретичні обмеження та раціональний контроль концентрації легуючої домішки кадмію необхідні для створення матеріалу зі збалансованими оптичними властивостями та фотокаталітичною активністю. Нарешті, важливість легування ZnO ізовалентною домішкою Cd значно покращує його фотокаталітичні властивості за рахунок звуження забороненої зони, зниження швидкості рекомбінації електронно-діркових пар, що підвищує ефективність просторового розділення зарядів, утворення активних оксидних радикалів і збільшення питомої поверхні. Таким чином, матеріали на основі ZnO-Cd є найбільш перспективними фотокаталітичними матеріалами для органічних забруднювачів.

Ключові слова: оксид цинку; легування кадмієм; морфологія; наноструктури; оптичні властивості; фотокаталіз.

PHYSICS AND CHEMISTRY OF SOLID STATE
V. 24, No. 2 (2023) pp. 235-243
Section: Chemistry

DOI: 10.15330/pcss.24.2.235-243

Vasyl Stefanyk Precarpathian National University

ФІЗИКА І ХІМІЯ ТВЕРДОГО ТІЛА
Т. 24, № 2 (2023) С. 235-243
Хімічні науки

PACS: 61.66.Fn ISSN 1729-4428

Oleksandr Smitiukh[1], Oksana Soroka[2], and Oleg Marchuk[1]

Effect of the crystal structure and chemical bonding on the electronic and thermal transport in $Cu_2MeHf_3S_8$ (Me – Mn, Fe, Co, Ni) thiospinels

[1]*Department of Chemistry, Ecology and Pharmacy,Lesya Ukrainka Volyn National University, Lutsk, Ukraine, Smitiukh.Oleksandr@vnu.edu.ua*
[2]*Ivano-Frankivsk National Medical University, Ivano-Frankivsk, Ukraine*

Establishing the relationship between crystal structure and transport properties is an important issue that is directly connected with the applicability of functional materials. In this work, we present the analysis of the crystal structure, chemical bonding, and electronic and thermal transport properties of $Cu_2MeHf_3S_8$ (*Me* – Mn, Fe, Co, Ni) compounds. The increase of weighted mobility in the Mn → Fe → Co → Ni series as well as the change of the dominant scattering mechanism of charge carriers from scattering on point defects to the scattering on acoustic phonons explains the best electronic transport in $Cu_2NiHf_3S_8$. Moreover, bonding inhomogeneity between the covalent δ(Co – S) and δ(Hf – S) from one side, and more ionic δ(Cu – S) interactions from the other side leads to low lattice thermal conductivity in $Cu_2MeHf_3S_8$ (*Me* – Mn, Fe, Co, Ni) materials. The work also suggests the link between the occupation of the octahedral 16*d* site and the thermoelectric performance of the investigated thiospinels. Particularly, the best thermoelectric performance is observed in the case of the presence of two valence electrons in the *d*-level of atoms in octahedral voids, which can be essential for further enhancement of the thermoelectric performance in thiospinels.

Keywords: bonding inhomogeneity; crystal structure; weighted mobility; thermal conductivity; quaternary sulfides.

Received 30 August 2022; Accepted 24 March 2023.

Introduction

Development of the new materials with ultralow thermal conductivity for thermoelectrics and thermal barrier coatings is among the hot topics in modern materials science [1–4]. However, materials with low thermal conductivity usually contain heavy and hazardous elements [5–8], which is in contradiction with the required low weight of thermoelectric devices [9,10] and even more crucial for the thermal barrier coatings used for the protection of aircraft turbines [4]. However, a lot of recent works show that ultralow thermal conductivity can be achieved even in materials consisting of lightweight elements through the crystal structure complexity engineering and chemical bonding hierarchy [3,11–15]. Among the most successful approaches for the reduction of lattice thermal conductivity are the phonon-liquid electron-crystal (PLEC) concept (which is based on the liquid-like behavior of superionic conductors) [2,12,13,16], bonding anisotropy in layered structures [8,17,18], lattice anharmonicity induced by the lone-pair-electrons [5,19–21] and bonding inhomogeneity [22–24]. Following the market requirements, sulfides attract more attention recently and they are frequent objects of current investigations [25–28].

A lot of promising environmental-friendly sulfides with low thermal conductivity were explored recently. Among them, special attention was devoted to the binary copper-based sulfides $Cu_{2-x}S$ [29], chalcopyrites [30,31], ternary Cu-Sn-S semiconductors [32,33], colusites [34], tetrahedrites [13,35], argyrodites [12,36], and some others [37]. However, often low thermal conductivity in these

compounds is caused by weak chemical bonding which in turn leads to the low thermal stability of the majority of these compounds (e.g. $Cu_{2-x}S$, Cu-rich tetrahedrites, and argyrodites) [2]. This reason restricts the wide utilization of such materials for energy converters and thermal barrier coatings due to the structural degradation of the materials at elevated temperatures [38,39]. Therefore, the effective compromise between disturbed phonon transport and the thermal stability of materials is still a great challenge. Ternary and quaternary transition metal thiospinels are the perspective materials that can effectively meet both requirements [40,41].

The phases based on the $MgAl_2O_4$ crystal structure type attract special attention. The structure of spinels with the general formula AB_2X_4 is based on the diamond structure. The 8*a* site of *A* atoms corresponds to the diamond structure, *B* atoms occupy the 16*d* site, and X atoms are in the 32*e* site. The unit cell of the AB_2X_4 structures can be expressed as $A_8B_{16}X_{32}$. The cations occupy one-eighth of the tetrahedral sites and half of the octahedral sites. Such a structure favors the low thermal conductivity in the $Cu_2MeHf_3S_8$ materials (*Me* = Mn, Fe, Co, Ni) [9]. However, the finding of the correlation between the crystal structure and the transport properties of the spinel structure is an important task.

Aiming to find stable materials with low thermal conductivity, this study is dedicated to the investigation of the relations between the crystal structure of $Cu_2MeHf_3S_8$ and electronic and thermal transport properties. With this goal, we performed the analysis of structural parameters, chemical bonding, charge carrier mobility, and lattice thermal conductivity. The effective engineering of carrier mobility is crucial for designing electronic devices, while low thermal conductivity is necessary for efficient energy converters and thermal barrier coatings.

I. Experimental details

The concentration tetrahedron of the sulfide systems Cu – *Me* – Hf – S (*Me* – Mn, Fe, Co, Ni) is presented in Fig. 1.

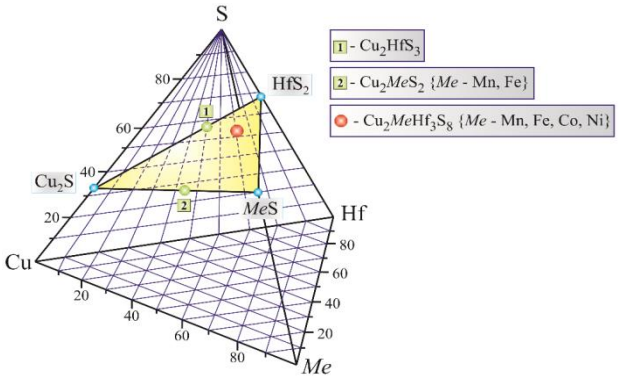

Fig. 1. Quaternary diagram Cu – *Me* – Hf – S and the quasi-ternary section Cu_2S – *Me*S – HfS_2 (*Me* – Mn. Fe, Co, Ni).

The quaternary sulfides $Cu_2MeHf_3S_8$ are formed in the quasi-ternary systems Cu_2S – *Me*S – HfS_2 that are one of the possible sections of the concentration tetrahedron. The $Cu_2MeHf_3S_8$ sulfides can be obtained by various techniques:

a) synthesis from the elementary substances Cu, Mn, Fe, Co, Ni, Hf and S;

b) interaction of the binary sulfides Cu_2S, *Me*S (*Me* – Mn, Fe, Co, Ni) and HfS_2 taken in the ratio of 1:1:3;

c) the $Cu_2MnHf_3S_8$ and $Cu_2FeHf_3S_8$ sulfides can be synthesized from the Cu_2MeS_2 (*Me* – Mn, Fe) and HfS_2 sulfides taken in the ratio of 1:3.

In the present work, we obtained the samples for investigation from high-purity elements. The total mass of a sample was 3g. Co-melting of the elements was held in evacuated ampoules (residual pressure 10^{-2} Pa) in an MP-30 programmable electric muffle furnace in two stages. The first stage was heating to 1423 K (heating rate 12 K/h); exposure to 1423 K for 4 h; cooling to room temperature (cooling rate 12 K/h). At the second stage to obtain homogeneous samples, pre-synthesized ingots were ground into powder and pressed into tablets. These were again placed in evacuated containers, reheated to 773 K at the rate of 12 K/h, annealed at this temperature for 500 h, and quenched into room-temperature water (without depressurizing the containers).

Phase identification was performed with a BRUKER D8 Advance X-ray diffractometer using Cu*K*α-radiation (λ = 1.5418 Å, $\Delta 2\Theta$ = 0.005°, 2Θ range 10 – 120°) with Bragg-Brentano geometry. Rietveld refinement of the crystal structure was performed in the WinCSD program package [42]. Visualization of the crystal structure utilized VESTA program [43].

Quantum chemical (QC) calculations were performed using the Firefly QC program package [44], which is based on the GAMESS (US) source code [45]. The calculations were performed based on the hybrid functional B3LYP that used the Becke GGA functional for the exchange energy, and the Lee-Yang-Parr GGA functional for the correlation energy [46,47]. For the calculations, we employed lattice parameters, symmetry information, and atomic coordinates obtained during the crystal structure refinement of the $Cu_2CoHf_3S_8$ and using literature data for $CuCo_2S_4$ and $CuHf_2S_4$ compounds. The basis sets for the self-consistent calculations can be obtained from the authors. The analysis of the chemical bonding for the investigated materials was performed by the electron localization function. For this purpose, the electron localization function (ELF) maps were calculated and visualized using the specialized module implemented in ChemCraft [48] and Vesta [43] software.

II. Results and discussion

2.1. Chemical bonding analysis in the $Cu_2MeHf_3S_8$ (*Me* – Mn, Fe, Co, Ni) sulfides

Multicomponent chalcogenides are interesting objects from the point of view of the nature of chemical bonding. To a large extent, the nature of the bond is determined by the features of the crystal structure. It is known that the spinel structure can be represented as a stacking of face-centered unit cells in which sulfur atoms form a three-layer closest packing of the ABCABC type (Fig. 2).

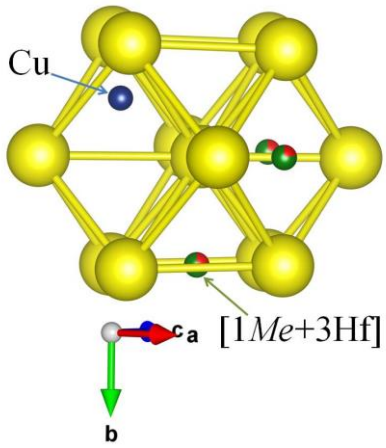

Fig. 2. Closest-packed structure of $Cu_2MeHf_3S_8$ (*Me*–Mn, Fe, Co, Ni) compounds.

To consider the nature of chemical bonding in the $Cu_2MeHf_3S_8$ (*Me* – Mn, Fe, Co, Ni) structure, we employed the data on atomic and ionic radii (Table 1). From the results of the calculation of experimental diffraction patterns, it can be seen that the Cu – S bond has mostly covalent component, with the bond ionicity increasing in the Mn → Fe → Co → Ni series of the $Cu_2MeHf_3S_8$ compounds. The opposite situation is observed for the Hf – S bonds where the covalent component increases in this series. For the *Me* – S bond, the ionicity fraction increases in the Mn → Fe → Co → Ni series. Considering the above analysis, an important role in the structure plays the *Me* metal atoms, which cause the strengthening of the ionic component. If we consider the formation of these phases from the point of view of a three-component system, it is appropriate to compare the values of interatomic distances (Table 2) of the experimentally obtained starting phases Cu_2S, HfS_2, MnS, FeS, CoS, and NiS (Table 3). Hence, in binary compounds, the covalent component prevails.

The crystal structure of the quaternary phases $Cu_2MeHf_3S_8$ (*Me* – Mn, Fe, Co, Ni) has cubic symmetry. The calculated and experimental diffractograms of the compounds are presented in Fig.3. Having the crystal structure with high symmetry of the structural elements, it is simplier to find the relationship between crystal structure and properties because each elements (atomic site, plane etc.) is responsible for appropriate properties

The lattice parameter *a* changes substantially in the Mn→Fe transition. The stable d^5-state in which all electrons of the *d*-sublevel are valence electrons transforms to d^6-state with 4 valence electrons with subsequent reduction of valence electrons (Co–d^7, Ni–d^8). Thus, Ni atoms have only two valence electrons. Hf atoms also have a d^2-state (two-valence electron state).

Table 1.

Data for analysis of the nature of chemical bonds

	Electron configuration of atoms	**r^*_{cov}, Å**	**r^*_{metal}, Å**	**r^*_{ion}, Å**	**Electron configuration of ions**	**r(Me) + r(S)**	**$r(Me^{+x})+ r(S^{2-})$**
Cu	$[Ar]3d^{10}4s^1$	1.17	1.28	0.98 (Cu^{+1})	$[Ar]3d^{10}4s^0$	2.19	2.8
Mn	$[Ar]3d^5 4s^2$	1.17	1.30	0.91 (Mn^{+2})	$[Ar]3d^3 4s^2$	2.19	2.73
Fe	$[Ar]3d^6 4s^2$	1.17	1.26	0.80 (Fe^{+2})	$[Ar]3d^4 4s^2$	2.19	2.62
Co	$[Ar]3d^7 4s^2$	1.16	1.25	0.78 (Co^{+2})	$[Ar]3d^5 4s^2$	2.18	2.6
Ni	$[Ar]3d^8 4s^2$	1.15	1.24	0.74 (Ni^{+2})	$[Ar]3d^6 4s^2$	2.17	2.56
Hf	$[Xe]4f^{14}5d^2 6s^2$	1.44	1.59	0.82 (Hf^{+4})	$[Xe]4f^{14}5d^0 6s^2$	2.46	2.64
S	$[Ne]3s^2 3p^4$	1.02	–	1.82 (S^{-2})	$[Ne]3s^2 3p^6$	–	–

**- Bokiy G. B. Kristallokhimiya. Izd. Tretye. pererabotannoye i dopolnennoye. izdalstvo «Nauka». 1971 g.. str. 400*

Table 2.

Interatomic distances in the $Cu_2MeHf_3S_8$ (*Me* – Mn, Fe, Co, Ni) structure

Bond	**$\delta(Me - X)_{exp}$, Å**			
	$Cu_2MnHf_3S_8$	**$Cu_2FeHf_3S_8$**	**$Cu_2CoHf_3S_8$**	**$Cu_2NiHf_3S_8$**
Cu – S	2.302	2.318	2.334	2.344
Hf – S	2.571	2.538	2.524	2.511
Mn – S	2.571			
Fe – S		2.538		
Co – S			2.524	
Ni – S				2.511

Table 3.

Interatomic distances Me – S

Compound	**Bond**	**$\delta(Me - X)_{exp}$, Å**
Cu_2S (*Fm*–3*m*)	Cu – S	2.3155
HfS_2 (*P*6$_3$/mmc)	Hf – S	2.51278
MnS (*P*6$_3$/mmc)	Mn – S	2.4264
FeS (*P*6$_3$/mmc)	Fe – S	2.4529
CoS (*P*6$_3$/mmc)	Co – S	2.3412
NiS (*P*6$_3$/mmc)	Ni – S	2.3779

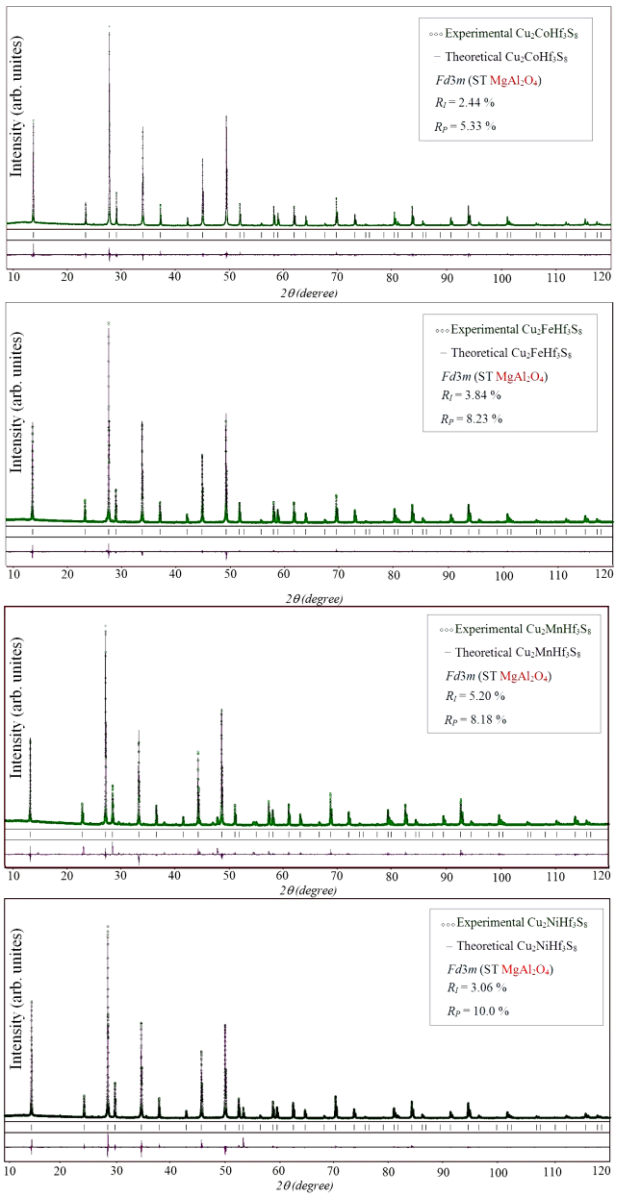

Fig.3. The calculated and experimental diffractograms of $Cu_2MeHf_3S_8$ (*Me* – Mn, Fe, Co, Ni) compounds.

Accordingly, the filling of the 16*d* site with Hf and Ni atoms contributes to the reduction of the thermal conductivity of $Cu_2MeHf_3S_8$ thiospinels. The change of lattice parameters, interatomic distances, atomic coordinates, and bond angles of the compounds are presented in Fig.4(a)(b).

The interatomic distances δ(*Me*/Hf – S) decrease with the decrease of *Me* atomic radii, whereas the δ(Cu–S) distance increases which indicates increasing bond ionicity. The arrangement of atoms in this structure indicates that the change in the 32*e* site coordinates should be considered since the first coordination environment for this site consists of (*Me*/Hf) and Cu atoms. The analysis of graphical dependence (Fig. 4(b)) indicates that the 32*e* site shifts in the direction of the 16*d* site in which the *Me*/Hf statistical mixture is located. Moreover, the Cu – S – (*Me*/Hf) angle decreases in the Mn → Fe → Co → Ni series, and the decrease is almost linear. At the same time, the value of the (*Me*/Hf) – S – (*Me*/Hf) angles increases linearly in the Mn → Fe → Co series, stabilizing at 90° for $Cu_2NiHf_3S_8$.

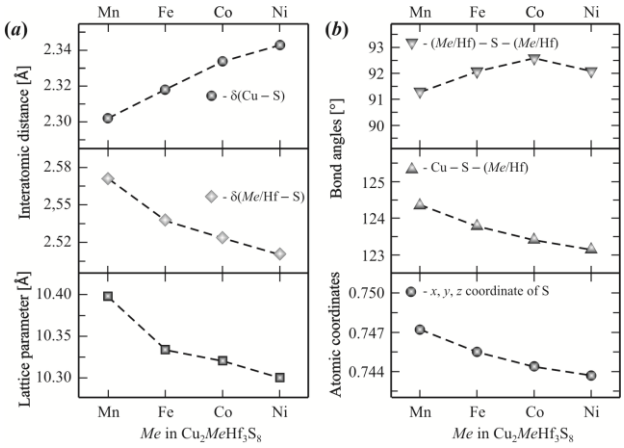

Fig.4. The change of lattice parameter and interatomic distances (a), atomic coordinates and bond angles (b) of $Cu_2MeHf_3S_8$ (*Me* – Mn, Fe, Co, Ni).

The nature of the change in isovalent parameters of atoms is ambiguous. This can be ascertained by analyzing the dependence of thermal oscillations of atoms on the qualitative composition of the studied sulfides (Fig. 5). It can be concluded from the presented dependences that the largest oscillations are shown by copper atoms. It is worth noting that the respective B_{iso} value is stabilized at 1.03 Å^2 in the $Cu_2NiHf_3S_8$ structure. Expectedly, the lowest B_{iso} value is for heavy Hf atoms. The value of the isovalent parameter of S atoms has a tendency to increase in the structure of $Cu_2MnHf_3S_8$, $Cu_2FeHf_3S_8$, and $Cu_2CoHf_3S_8$ while this parameter is decreasing to 0.70 Å^2 in the $Cu_2NiHf_3S_8$ structure. Clearly, copper atoms will have the largest effect on weighted mobility.

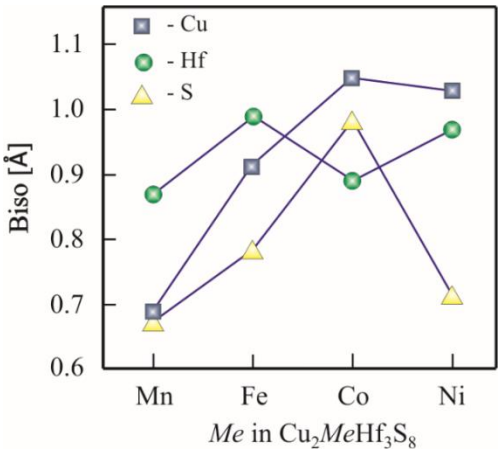

Fig. 5. Dependence of isovalent atomic parameter on composition.

The weighted mobility of state-of-the-art thermoelectric materials decreases with temperature as $T^{-3/2}$ because the electrons are scattered by phonons [49]. To calculate the weighted mobility for $Cu_2MeHf_3S_8$ samples, we used numerical data of temperature-dependent Seebeck coefficient and electrical conductivity from our previous work [9]. The change of weighted mobility of the $Cu_2MeHf_3S_8$ phases (Fig. 6(a)) shows that the increase of mobility with temperature indicates, that the carrier scattering on defects (ionized impurities or grain boundaries) is dominating [49]. The low mobility

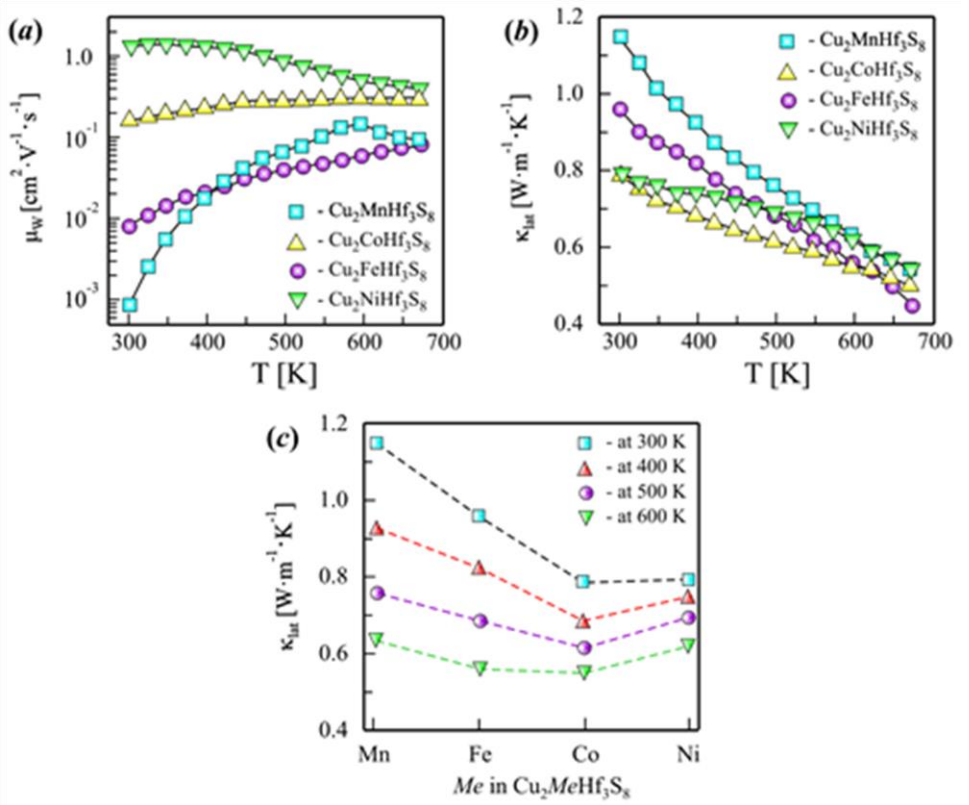

Fig.6. The properties of $Cu_2MeHf_3S_8$ (*Me* – Mn, Fe, Co, Ni): a) weighted mobility, b) thermal conductivity, and (c) the composition and thermal conductivity at 300, 400, 500, and 600 K.

below room temperature could be a sign of grain boundary scattering. However, in contrast with $Cu_2MeHf_3S_8$ (*Me* – Mn, Fe, Co) phases, $Cu_2NiHf_3S_8$ shows decreasing tendency of weighted mobility above 400 K, suggesting that electrons are mainly scattered by phonons as in the state-of-the-art thermoelectric materials [50]. Such a tendency of weighted mobility together with its highest values in the series indicates the best electronic transport in $Cu_2NiHf_3S_8$.

Fig. 6(b) shows the lattice thermal conductivity (κ_{lat}) of the studied $Cu_2MeHf_3S_8$ samples after sintering. All specimens possess very low thermal conductivities, in the range of 0.7–1.2 W m^{-1} K^{-1} at 300 K, decreasing to 0.4–0.7 W m^{-1} K^{-1} at 673 K which are among the lowest values observed in spinel-type materials. Fig. 6(c) shows the compositional dependence of lattice thermal conductivity at selected temperatures for $Cu_2MeHf_3S_8$. The values of κ_{lat} decrease in series Mn → Fe → Co and slightly increase for the Ni-contained sample.

Interestingly, such a compositional dependence of lattice thermal conductivity reflects well the deviations in bond angles and atomic coordinates from its ideal values, as it is shown in Fig. 4(b). This observation suggests a very strong interconnection between the crystal structure distortion and lattice thermal conductivity in the investigated materials. For the deeper analysis of electronic and thermal transport in $Cu_2MeHf_3S_8$ materials and their structural origin, we performed the analysis of chemical bonding between atoms in studied thiospinels.

We decided to start the analysis of chemical bonding from the ternary thiospinels $CuCo_2S_4$ and $CuHf_2S_4$. In the $CuCo_2S_4$ structure, the overlapping of electron clouds between Cu-S atoms is weaker than for Co-S, suggesting a more covalent nature of Co-S bonds. However, in the case of $CuHf_2S_4$, the overlapping of electron clouds between different cations and anions is very similar, suggesting small bonding inhomogeneity. To understand the chemical bonding environment in $Cu_2MeHf_3S_8$ (*Me* – Mn, Fe, Co, Ni), we calculated the electron localization function (ELF). The visualized 3D maps of the ELF sliced on the planes [1 0 1] and [1 0 -1] are shown in Fig. 7.

In order to calculate the electron localization function (ELF) maps for disordered $Cu_2CoHf_3S_8$ with the statistical occupation of the 16*d* site by Co/Hf, we created a structural model with a random distribution of Co and Hf over this site.

This analysis indicates that the electron clouds of Co and Hf atoms strongly overlap with chalcogen atoms highlighting the existence of strong covalent bonding between δ(Co – S) and δ(Hf – S). In this pair of bonds, δ(Co – S) shows slightly stronger overlapping of electron clouds than δ(Hf – S) in $Cu_2CoHf_3S_8$. The overlapping of electron clouds between δ(Co – S) and δ(Hf – S) is much stronger in $Cu_2CoHf_3S_8$ compared to $CuCo_2S_4$ [51] and $CuHf_2S_4$ (Fig. 6 a-c). On the other hand, the weaker overlapping of electron clouds between Cu and S atoms reveals a more ionic nature of chemical bonding between them. Such bonding inhomogeneity between the covalent δ(Co – S) and δ(Hf – S) from one side, and more ionic δ(Cu – S) interactions leads to low lattice thermal conductivity in $Cu_2MeHf_3S_8$ (*Me* – Mn, Fe, Co, Ni) materials.

Moreover, even if the bonding inhomogeneity is present in the $CuCo_2S_4$ structure, this material shows quite high values of sound velocity (v_l = 4377 m s^{-1}, v_t = 2367 m s^{-1}) which leads also to relatively high lattice

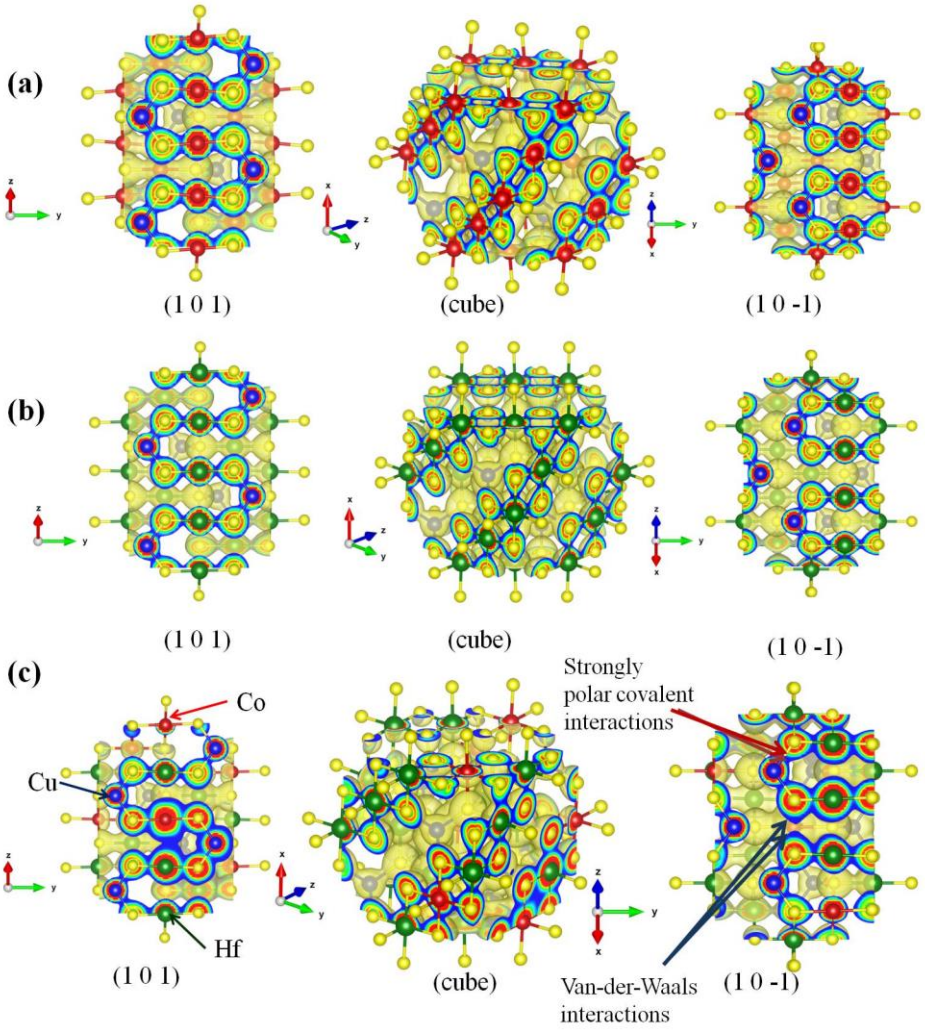

Fig.6. Bonding analysis in $Cu_2CoHf_3S_8$ (a), $CuCo_2S_4$ (b), and $CuHf_2S_4$ (c) by means of electron localization function (ELF) with isosurface value of 0.02 e bohr^{-3} sliced on the planes [1 0 1] and [1 0 -1], respectively.

thermal conductivity in this material (ranging from 1.48 W m^{-1}K^{-1} at 323 K to 0.57 W m^{-1}K^{-1} at 723 K) [51]. Interestingly, strong bonding inhomogeneity observed in $Cu_2CoHf_3S_8$ leads to the lowering of its sound velocity (v_l= 4072 m s^{-1}, v_t = 2172 m s^{-1}) as was hypothesized by Grin [22], this fact causes a significant lowering of lattice thermal conductivity in the material (ranging from 0.78 W m^{-1}K^{-1} at 298 K to 0.50 W m^{-1}K^{-1} at 673 K). This work confirms that bonding inhomogeneity can be effectively used to disturb thermal transport in functional materials.

Conclusions

The analysis of the crystal structure of $Cu_2MeHf_3S_8$ (*Me* – Mn, Fe, Co, Ni) sulfides indicates that if the 16*d* site in spinel structures is occupied by a *d*-element, then the number of electrons in the *d*-sublevel is important. Additionally, the formation of a statistical mixture in this site has an important effect on the electronic properties. Specifically, it was established that the best electronic transport is observed in the presence of the same two valence *d* electrons in both [1Ni:3Hf] atoms. Moreover, random occupation of the 16*d* site by *Me*/Hf atoms in $Cu_2MeHf_3S_8$ (*Me* – Mn, Fe, Co, Ni) leads to a strong bonding inhomogeneity and one of the lowest lattice thermal conductivity in materials with spinel structure type. The best thermoelectric performance of $Cu_2NiHf_3S_8$ can be explained by its highest weighted mobility described by electron scattering on phonons and the low lattice thermal conductivity due to strong bonding inhomogeneity.

Smitiukh Oleksandr – Candidate of Chemical Sciences, Senior Laboratory Technician of the Department of Chemistry and Technologies;
Soroka Oksana **–** Ph.D, Associate Professor of the Department of Forensic Medicine, Medical and Pharmaceutical Law;
Marchuk Oleg – Candidate of Chemical Sciences, Associate Professor of the Department of Chemistry and Technologies.

[1] Z. Chen, X. Zhang, Y. Pei, *Manipulation of Phonon Transport in Thermoelectrics*, Adv. Mater., 30, 1705617 (2018); https://doi.org/10.1002/adma.201705617.

[2] K. Zhao, P. Qiu, X. Shi, L. Chen, *Recent Advances in Liquid-Like Thermoelectric Materials*, Adv. Funct. Mater., 30, 1903867 (2020); https://doi.org/10.1002/adfm.201903867.

[3] T. Ghosh, M. Dutta, D. Sarkar, K. Biswas, I*nsights into Low Thermal Conductivity in Inorganic Materials for Thermoelectrics*, J. Am. Chem. Soc., 144, 10099 (2022); https://doi.org/10.1021/JACS.2C02017/ASSET/IMAGES/LARGE/JA2C02017_0008.JPEG.

[4] R.A. Miller, *Thermal barrier coatings for aircraft engines: History and directions*, J. Therm. Spray Technol., 6, 35 (1997); https://doi.org/10.1007/BF02646310/METRICS.

[5] O. Cherniushok, R. Cardoso-Gil, T. Parashchuk, R. Knura, Y. Grin, K.T. Wojciechowski, *Lone-Pair-Like Interaction and Bonding Inhomogeneity Induce Ultralow Lattice Thermal Conductivity in Filled β-Manganese-Type Phases*, Chem. Mater. 34, 6389 (2022); https://doi.org/10.1021/acs.chemmater.2c00915.

[6] T. Parashchuk, A. Shabaldin, O. Cherniushok, P. Konstantinov, I. Horichok, A. Burkov, Z. Dashevsky, *Origins of the enhanced thermoelectric performance for p-type Ge1-xPbxTe alloys*, Phys. B Condens. Matter. 596, 412397(2020); https://doi.org/10.1016/J.PHYSB.2020.412397.

[7] T. Parashchuk, B. Wiendlocha, O. Cherniushok, R. Knura, K.T. Wojciechowski, *High Thermoelectric Performance of p-Type PbTe Enabled by the Synergy of Resonance Scattering and Lattice Softening*, ACS Appl. Mater. Interfaces, 13, 49027 (2021); https://doi.org/10.1021/acsami.1c14236.

[8] T. Parashchuk, R. Knura, O. Cherniushok, K.T. Wojciechowski, *Ultralow Lattice Thermal Conductivity and Improved Thermoelectric Performance in Cl-Doped Bi2Te3–xSex Alloys*, ACS Appl. Mater. Interfaces. 14, 33567 (2022); https://doi.org/10.1021/acsami.2c08686.

[9] O. Cherniushok, O. V. Smitiukh, J. Tobola, R. Knura, O. V. Marchuk, T. Parashchuk, K.T. Wojciechowski, *Crystal Structure and Thermoelectric Properties of Novel Quaternary Cu2MHf3S8(M-Mn, Fe, Co, and Ni) Thiospinels with Low Thermal Conductivity*, Chem. Mater. 34, 2146 (2022); https://doi.org/10.1021/acs.chemmater.1c03593.

[10] M. Maksymuk, K. Zazakowny, A. Lis, A. Kosonowski, T. Parashchuk, K.T. Wojciechowski, *Development of the anodized aluminum substrates for thermoelectric energy converters*, Ceram. Int. 49, 4816(2023); https://doi.org/10.1016/J.CERAMINT.2022.09.371.

[11] W.G. Zeier, A. Zevalkink, Z.M. Gibbs, G. Hautier, M.G. Kanatzidis, G.J. Snyder, *Thinking Like a Chemist: Intuition in Thermoelectric Materials*, Angew. Chemie Int. Ed. 55, 6826 (2016); https://doi.org/10.1002/ANIE.201508381.

[12] O. Cherniushok, T. Parashchuk, J. Tobola, S.D.N. Luu, A. Pogodin, O. Kokhan, I. Studenyak, I. Barchiy, M. Piasecki, K.T. Wojciechowski, *Entropy-Induced Multivalley Band Structures Improve Thermoelectric Performance in p-Cu7P(SxSe1- x)6Argyrodites*, ACS Appl. Mater. Interfaces., 13, 39606 (2021); https://doi.org/10.1021/acsami.1c11193.

[13] K. Zazakowny, A. Kosonowski, A. Lis, O. Cherniushok, T. Parashchuk, J. Tobola, K.T. Wojciechowski, *Phase Analysis and Thermoelectric Properties of Cu-Rich Tetrahedrite Prepared by Solvothermal Synthesis*, Materials (Basel)., 15, 849(2022); https://doi.org/10.3390/MA15030849.

[14] J. Yang, Y. Wang, H. Yang, W. Tang, J. Yang, L. Chen, W. Zhang, *Thermal transport in thermoelectric materials with chemical bond hierarchy*, J. Phys. Condens. Matter., 31, 183002 (2019); https://doi.org/10.1088/1361-648X/AB03B6.

[15] F. Kateusz, T. Korzec, M. Zambrzycki, O. Cherniushok, M. Gubernat, *Influence of montmorillonite nanoparticles on thermal and mechanical properties of carbon-carbon hybrid composites based on phenolic-formaldehyde resin*, Compos. Theory Pract., 2021, 96 (2021).

[16] H. Liu, X. Shi, F. Xu, L. Zhang, W. Zhang, L. Chen, Q. Li, C. Uher, T. Day, G. Snyder Jeffrey, *Copper ion liquid-like thermoelectrics*, Nat. Mater., 11, 422 (2012); https://doi.org/10.1038/nmat3273.

[17] L.D. Zhao, S.H. Lo, Y. Zhang, H. Sun, G. Tan, C. Uher, C. Wolverton, V.P. Dravid, M.G. Kanatzidis, *Ultralow thermal conductivity and high thermoelectric figure of merit in SnSe crystals*, Nature., 508, 373 (2014); https://doi.org/10.1038/nature13184.

[18] X.L. Shi, J. Zou, Z.G. Chen, *Advanced Thermoelectric Design: From Materials and Structures to Devices*, Chem. Rev., 120, 7399 (2020); https://doi.org/10.1021/acs.chemrev.0c00026.

[19] E.J. Skoug, D.T. Morelli, *Role of lone-pair electrons in producing minimum thermal conductivity in nitrogen-group chalcogenide compounds*, Phys. Rev. Lett., 107, 235901(2011); https://doi.org/10.1103/PHYSREVLETT.107.235901/FIGURES/4/MEDIUM.

[20] C. Chang, L.D. Zhao, *Anharmoncity and low thermal conductivity in thermoelectrics*, Mater. Today Phys., 4, 50 (2018); https://doi.org/10.1016/J.MTPHYS.2018.02.005.

[21] O. V. Smitiukh, O. V. Marchuk, Y.M. Kogut, V.O. Yukhymchuk, N. V. Mazur, G.L. Myronchuk, S.M. Ponedelnyk, O.I. Cherniushok, T.O. Parashchuk, O.Y. Khyzhun, T. Wojciechowski, A.O. Fedorchuk, *Effect of rare-earth doping on the structural and optical properties of the Ag3AsS3 crystals*, Opt. Quantum Electron., 54, (2022); https://doi.org/10.1007/S11082-022-03542-W.

[22] Y. Grin, *Inhomogeneity and anisotropy of chemical bonding and thermoelectric properties of materials*, J. Solid State Chem., 274, 329 (2019); https://doi.org/10.1016/J.JSSC.2018.12.055.

[23] A. Ormeci, Y. Grin, *Coexistence of ionic and covalent atomic interactions (bonding inhomogeneity) and thermoelectric properties of intermetallic clathrates*, J. Thermoelectr., 6, 16 (2015).
[24] M. Dutta, K. Pal, U. V. Waghmare, K. Biswas, *Bonding heterogeneity and lone pair induced anharmonicity resulted in ultralow thermal conductivity and promising thermoelectric properties in n-type AgPbBiSe3*, Chem. Sci., 10, 4905(2019); https://doi.org/10.1039/C9SC00485H.
[25] F. Huiying, *Environmentally friendly and earth-abundant colloidal chalcogenide nanocrystals for photovoltaic applications*, J. Mater. Chem. C., 6, 414 (2018).
[26] F.T. Farheen F.Jaldurgam, Zubair Ahmad, *Low-Toxic, Earth-Abundant Nanostructured Materials for Thermoelectric Applications*, Nanomaterials. 11, 895 (2021); https://doi.org/10.3390/nano11040895.
[27] M.R. Huch, L.D. Gulay, I.D. Olekseyuk, *Crystal structures of the R3Mg0.5GeS7 (R = Y, Ce, Pr, Nd, Sm, Gd, Tb, Dy, Ho and Er) compounds*, J. Alloys Compd., 424, 114 (2006); https://doi.org/10.1016/j.jallcom.2005.12.025.
[28] L.D. Gulay, M. Daszkiewicz, M.R. Huch, A. Pietraszko, *Ce3Mg0.5GeS7 from single-crystal data*, Acta Crystallogr. Sect. E Struct. Reports Online. 63 (2007); https://doi.org/10.1107/S1600536807048593.
[29] Y. He, T. Day, T. Zhang, H. Liu, X. Shi, L. Chen, G.J. Snyder, *High thermoelectric performance in non-toxic earth-abundant copper sulfide*, Adv. Mater., 26, 3974 (2014); https://doi.org/10.1002/adma.201400515.
[30] R. Ang, A.U. Khan, N. Tsujii, K. Takai, R. Nakamura, T. Mori, *Thermoelectricity Generation and Electron-Magnon Scattering in a Natural Chalcopyrite Mineral from a Deep-Sea Hydrothermal Vent*, Angew. Chemie - Int. Ed. 54, 12909 (2015); https://doi.org/10.1002/anie.201505517.
[31] Y. Kim, S.-W. Kang, H.-U. Kim, al -, N. Kryzhanovskaya, A. Zhukov, E. Moiseev, D. Zhang, H.-C. Bai, Z.-L. Li, J.-L. Wang, G.-S. Fu, S.-F. Wang, *Multinary diamond-like chalcogenides for promising thermoelectric application**, Chinese Phys. B., 27, 047206 (2018); https://doi.org/10.1088/1674-1056/27/4/047206.
[32] S. Fiechter, M. Martinez, G. Schmidt, W. Henrion, Y. Tomm, *Phase relations and optical properties of semiconducting ternary sulfides in the system Cu–Sn–S*, J. Phys. Chem. Solids., 64,) 1859 (2003); https://doi.org/10.1016/S0022-3697(03)00172-0.
[33] V. Pavan Kumar, P. Lemoine, V. Carnevali, G. Guélou, O.I. Lebedev, P. Boullay, B. Raveau, R. Al Rahal Al Orabi, M. Fornari, C. Prestipino, D. Menut, C. Candolfi, B. Malaman, J. Juraszek, E. Guilmeau, *Ordered sphalerite derivative Cu5Sn2S7: a degenerate semiconductor with high carrier mobility in the Cu–Sn–S diagram*, J. Mater. Chem. A., 9, 10812 (2021); https://doi.org/10.1039/D1TA01615F.
[34] C. Bourgès, Y. Bouyrie, A.R. Supka, R. Al Rahal Al Orabi, P. Lemoine, O.I. Lebedev, M. Ohta, K. Suekuni, V. Nassif, V. Hardy, R. Daou, Y. Miyazaki, M. Fornari, E. Guilmeau, *High-Performance Thermoelectric Bulk Colusite by Process Controlled Structural Disordering*, J. Am. Chem. Soc., 140, 2186 (2018); https://doi.org/10.1021/jacs.7b11224.
[35] R. Chetty, A. Bali, R.C. Mallik, T*etrahedrites as thermoelectric materials: An overview*, J. Mater. Chem. C., 3, 12364 (2015); https://doi.org/10.1039/c5tc02537k.
[36] S. Lin, W. Li, Y. Pei, *Thermally insulative thermoelectric argyrodites*, Mater. Today., 48, 198(2021); https://doi.org/10.1016/J.MATTOD.2021.01.007.
[37] P. Lemoine, G. Guélou, B. Raveau, E. Guilmeau, *Crystal Structure Classification of Copper-Based Sulfides as a Tool for the Design of Inorganic Functional Materials*, Angew. Chemie Int. Ed., 61, e202108686 (2022); https://doi.org/10.1002/ANIE.202108686.
[38] X. Shen, C.C. Yang, Y. Liu, G. Wang, H. Tan, Y.H. Tung, G. Wang, X. Lu, J. He, X. Zhou, *High-Temperature Structural and Thermoelectric Study of Argyrodite Ag 8 GeSe 6*, ACS Appl. Mater. Interfaces. 11, 2168 (2019); https://doi.org/10.1021/acsami.8b19819.
[39] F. Baumer, T. Nilges, *Phase Segregation of Polymorphic Solid Ion Conducting Cu7PSe6 during Thermoelectric Experiments*, Zeitschrift Für Anorg. Und Allg. Chemie. 644, 1519(2018); https://doi.org/10.1002/ZAAC.201800108.
[40] G. Strick, G. Eulenberger, H. Hahn, *Über einige quaternäre Chalkogenide mit Spinellstruktur*, ZAAC - J. Inorg. Gen. Chem. 357, 338 (1968); https://doi.org/10.1002/zaac.19683570421.
[41] J.J. Snyder, T. Caillat, J.P. Fleurial, *Thermoelectric properties of chalcogenides with the spinel structure*, Mater. Res. Innov., 5, 67 (2001); https://doi.org/10.1007/s100190100133.
[42] L. Akselrud, Y. Grin, *WinCSD: Software package for crystallographic calculations (Version 4)*, J. Appl. Crystallogr., 47, 803 (2014); https://doi.org/10.1107/S1600576714001058.
[43] K. Momma, F. Izumi, *VESTA 3 for three-dimensional visualization of crystal, volumetric and morphology data*, J. Appl. Crystallogr., 44, 1272 (2011); https://doi.org/10.1107/S0021889811038970/FULL.
[44] The PC GAMESS/Firefly - REFERENCE, (n.d.).
[45] G.M.J. Barca, C. Bertoni, L. Carrington, D. Datta, N. De Silva, J.E. Deustua, D.G. Fedorov, J.R. Gour, A.O. Gunina, E. Guidez, T. Harville, S. Irle, J. Ivanic, K. Kowalski, S.S. Leang, H. Li, W. Li, J.J. Lutz, I. Magoulas, J. Mato, V. Mironov, H. Nakata, B.Q. Pham, P. Piecuch, D. Poole, S.R. Pruitt, A.P. Rendell, L.B. Roskop, K. Ruedenberg, T. Sattasathuchana, M.W. Schmidt, J. Shen, L. Slipchenko, M. Sosonkina, V. Sundriyal, A. Tiwari, J.L. Galvez Vallejo, B. Westheimer, M. Włoch, P. Xu, F. Zahariev, M.S. Gordon, *Recent developments in the general atomic and molecular electronic structure system*, J. Chem. Phys. 152, 154102 (2020); https://doi.org/10.1063/5.0005188.

[46] I. V. Horichok, L.I. Nykyruy, T.O. Parashchuk, S.D. Bardashevska, M.P. Pylyponuk, *Thermodynamics of defect subsystem in zinc telluride crystals*, Mod. Phys. Lett. B., 30, (2016); https://doi.org/10.1142/S0217984916501724.
[47] D. Freik, T. Parashchuk, B. Volochanska, *Thermodynamic parameters of CdTe crystals in the cubic phase*, J. Cryst. Growth., 402, 90 (2014); https://doi.org/10.1016/J.JCRYSGRO.2014.05.005.
[48] Chemcraft - Graphical program for visualization of quantum chemistry computations, (n.d.).
[49] G.J. Snyder, A.H. Snyder, M. Wood, R. Gurunathan, B.H. Snyder, C. Niu, *Weighted Mobility*, Adv. Mater. 32, 2001537 (2020); https://doi.org/10.1002/ADMA.202001537.
[50] T. Parashchuk, I. Horichok, A. Kosonowski, O. Cherniushok, P. Wyzga, G. Cempura, A. Kruk, K.T. Wojciechowski, *Insight into the transport properties and enhanced thermoelectric performance of n-type Pb1−xSbxTe*, J. Alloys Compd., 860, 158355 (2021); https://doi.org/10.1016/J.JALLCOM.2020.158355.
[51] Y. Lang, L. Pan, C. Chen, Y. Wang, *Thermoelectric Properties of Thiospinel-Type CuCo2S4*, J. Electron. Mater. 48, 4179 (2019); https://doi.org/10.1007/s11664-019-07182-x.

Олександр Смітюх[1], Оксана Сорока[2], Олег Марчук[1]

Вплив кристалічної структури та хімічних зв'язків на електронні та теплові властивості у шпінелях $Cu_2MeHf_3S_8$ (Me – Mn, Fe, Co, Ni)

[1]*Факультет хімії, екології та фармації, Волинський національний університет імені Лесі Українки, м. Луцьк, Україна, Smitiukh.Oleksandr@vnu.edu.ua*
[2]*Івано-Франківський національний медичний університет, Івано-Франківськ, Україна*

Встановлення взаємозв'язків між кристалічною структурою та транспортними властивостями є важливою проблемою, що безпосередньо пов'язана із застосуванням функціональних матеріалів. У цій роботі нами представлено аналіз кристалічної структури, хімічних зв'язків, електронних та теплових транспортних властивостей сполук $Cu_2MeHf_3S_8$ (*Me* – Mn, Fe, Co, Ni). Збільшення рухливості носіїв заряду в ряду Mn → Fe → Co → Ni, а також зміна домінуючого механізму розсіювання носіїв заряду від росіювання на точкових дефектах до розсіювання на акустичних фононах пояснює найкращий рух електронів у сполуці $Cu_2NiHf_3S_8$. Окрім цього, неоднорідність зв'язків між ковалентним для δ(Co – S) і δ(Hf – S) з одного боку та більш іонним для δ(Cu – S) з іншої сторони призводить до низької теплопровідності в матеріалах $Cu_2MeHf_3S_8$ (*Me* – Mn, Fe, Co, Ni). У роботі також пропонується оглях зв'язку між зайнятістю октедричної 16*d* ПСТ і термоелектричними параметрами досліджених тіошпінелей. Варто зазначити, що найкращі термоелектричні параметри спостерігаються у тому випадку, коли в суміші присутні два валентних електрони на *d*-підрівні атомів, що займають октаедричні позиції, що може бути важливим для подальших досліджень з метою покращення термоелектричних параметрів тіошпінелей.

Ключові слова: неоднорідність зв'язків; кристалічна структура; рухливість носіїв заряду; теплопровідність; тетрарні сульфіди.

PHYSICS AND CHEMISTRY OF SOLID STATE
V. 24, No. 2 (2023) pp. 244-248
Section: Chemistry

DOI: 10.15330/pcss.24.2.244-248

Vasyl Stefanyk Precarpathian National University

ФІЗИКА І ХІМІЯ ТВЕРДОГО ТІЛА
Т. 24, № 2 (2023) С. 244-248
Хімічні науки

PACS: 75.75.Fk ISSN 1729-4428

Naresh Babu Gatchakayala, D. Rama Sekhara Reddy*

Synthesis, magnetic, ac conductivity and dielectric properties of hematite nanocrystallites

Department of Chemistry Krishna University, Machilipatnam 521004, Andhra Pradesh, India.dachuru@gmail.com

We are reporting the synthesis along with magnetic, ac conductivity and dielectric properties of hematite nanocrystallites. The prepared Fe_2O_3 is crystallizing in corundum structure which belongs to the rhombohedron system with the space group R3-c.The magnetization data shows a typical Morin transition, T_N = 265 K for 110 nm crystallites, whereas this transition is decreasing with decrease in crystallite size, T_N = 252 K for 33 nm. The value of magnetization is increased with increasing crystallite size. The enhanced dielectric permittivity and ac conductivity were observed in higher hematite crystallite size. The overall dielectric response has revealed conduction mechanism is due to the extrinsic contribution from the dominant Maxwell-Wagner polarization.

Keywords: hematite nanoparticles; Cole-Cole plot; Dielectric properties; Ac conductivity; Impedance.

Received 2 September2022; Accepted 10 March 2023.

Introduction

Recently, iron (Fe) and its oxides (Fe_3O_4 and Fe_2O_3) have attracted the field of research due to their potential applications [1-10]. The most stable known Fe state due to having lower Gibbs free energy and wide spread oxide phase of iron is *a*-Fe_2O_3. They have been employed in technology due to their non-toxicity and low cost as the members of catalysis, magnetic storage, anticorrosive agents and gas sensors. The crystal structure of *a*-Fe_2O_3 is rhombohedral or hexagonal with the space group R3c or D^6_{3d} [11]. The magnetic state of bulk *a*-Fe_2O_3 particles is "canted antiferromagnetic (weak ferromagnetism)" between 263 K and Neel temperature (~ 950 K) [12,13]. It is because of their unique structural property of hematite that the rhombohedral (1 1 1) planes form the layers of Fe^{3+} ions (T = 950 K to 260 K). These planes are separated by layers of oxygen (O^{2-}) ions. The spins of Fe^{3+} ions remained parallel in any (1 1 1) plane, i.e., ferromagnet, but adjacent planes are antiparallel, i.e., antiferromagnet. The canting between (1 1 1) plane produces uncompensated magnetic moments of Fe^{3+} spins between adjacent planes. Thus a weak ferromagnetism (or canted antiferromagnetism) is observed in hematite. The spin moments are completely turned perpendicular to the (1 1 1) plane below a typical temperature T_M ~ 260 K, known as Morin temperature, and *a*-Fe_2O_3 becomes a normal antiferromagnet [12,13]. This transition is a first order magnetic phase transition, which is dependent upon strain, particle size, crystallite, change at lattice parameters, and particle shape. Compared with bulk *a*-Fe_2O_3, the effects of lattice expansion, strain, defects, unpaired spins and broken symmetries have a grounded new magnetic behavior in nano sized *a*-Fe_2O_3. In this paper, we present the synthesis along with the magnetic, ac conductivity and dielectric properties of hematite nanocrystallites.

I. Experimental Details

Fe_2O_3 nanoparticles were synthesized by co-precipitation method. The metal nitrate $Fe(NO_3)_3$ 0.02 mole were added into 100 ml distilled water. A water solution of sodium hydroxide 50 ml with molarity 2 M were slowly added into the iron solution above. Precipitate is formed immediately. The precipitate was washed thoroughly with distilled water then filtered and dried at 80°C for overnight. After drying, the hydroxed precipitate flakes were ground into powder. This

powder was segregated into different parts and heated for 3 h at different temperatures ranging from 550ºC to 1000ºC in air. The ramping rate was set 2ºC/min. and the cooling rate was 5ºC/min. After above procedure, the powders were pressed into pellets (10 mm diameter and 1~2 mm thickness) and annealed at the corresponding temperatures. These pellet samples were polished to produce a flat uniform surface and electrode with silver paint, then applied an AC voltage source for dielectric measurement.

II. Results and discussions

The *a*-Fe_2O_3 samples were prepared by co-precipitation method, and annealed in five different annealing temperatures T_A (550, 650, 750, 900, and 1000ºC). The obtained nanocrystallites are of Rhombohedral structure with space group *R3-c* [11]. X-ray diffraction pattern of the different annealing temperatures T_A (550, 650, 750, 900, and 1000ºC) samples are shown in Fig. 1 and no impurity being revealed. All the obtained samples are revealed Rhombohedral structure with space group *R3-c* [11]. The refined lattice constants are decreasing slightly from a = 5.028 Å, and c = 13.744 Å for T_A = 550ºC to a = 5.024 Å, c = 13.713 Å for T_A = 1000ºC as shown in Table I. The average crystallite sizes (determined from the XRD peak width employing the Scherrer relation) were found to be ~ 33 nm to ~ 110 nm with increasing annealing temperature from 550ºC to 1000ºC, which is indicated in Fig 1.

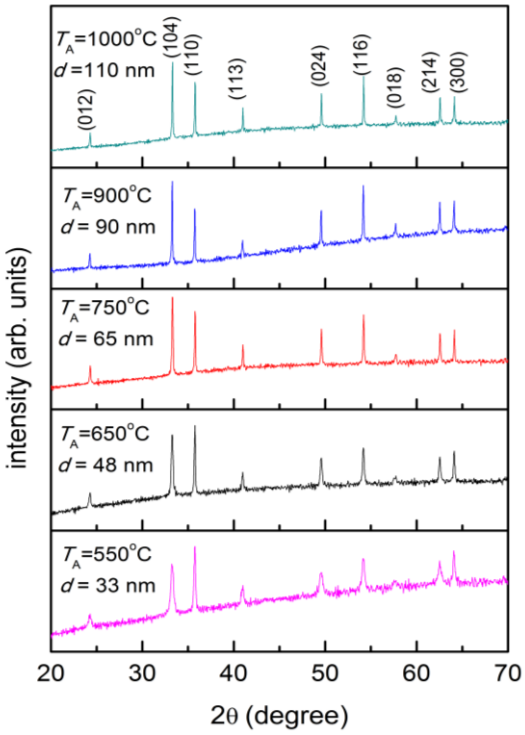

Fig. 1. X-ray diffraction pattern of the α-Fe_2O_3 nanocrystallites with different annealing temperatures and corresponding crystallite sizes.

Figure 2 shows the typical SEM micrographs for *a*-Fe_2O_3 particles prepared at different T_A's (a) 550ºC and (b) 1000ºC. The particle size and the morphology changes with T_A were observed. These microstructures were strongly influenced by T_A for all the particles.

The temperature dependence of magnetization of

Table 1.

The lattice constants of α-Fe_2O_3nanocrystallites

T_A = 550ºC d = 33 nm	T_A = 650 ºC d = 48 nm	T_A = 750 ºC d = 65 nm	T_A = 900 ºC d = 90 nm	T_A = 1000 ºC d = 110 nm
a = 5.028 Å b = 5.028 Å c = 13.744 Å V= 347.459 Å^3	a = 5.027 Å b = 5.027 Å c = 13.726 Å V= 346.866 Å^3	a = 5.027Å b = 5.027Å c = 13.721 Å V = 346.739 Å^3	a = 5.024 Å b = 5.024 Å c = 13.714 Å V = 346.149 Å^3	a = 5.024 Å b = 5.024 Å c = 13.713 Å V = 346.124 Å^3

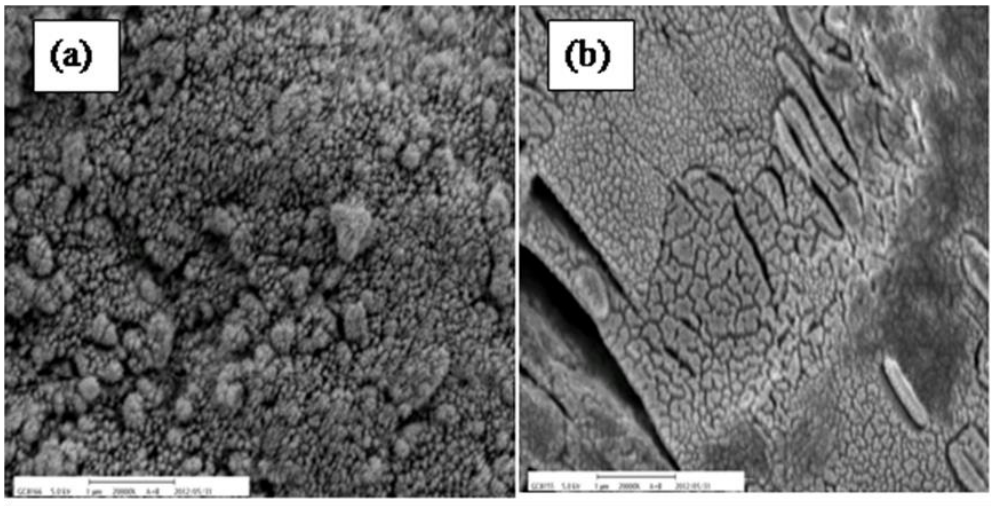

Fig. 2. SEM photos of theα-Fe_2O_3 samples of (a) 33 nm and (b) 110 nm.

a-Fe_2O_3 with different T_A's was depicted in Fig. 3. It revealed a magnetic transition around 265 K, named Morin transition for higher crystallites size of 110 nm (Figure 3a) whereas this transition is decreased with decrease in crystallites size for 33 nm particles the transition is at 252 K as shown in Fig. 3(b) [12,13]. Moreover, the magnetization value has increased with increase in crystallite size as observed in these nanocrystallites, which is related to quantum effects like surface effects.

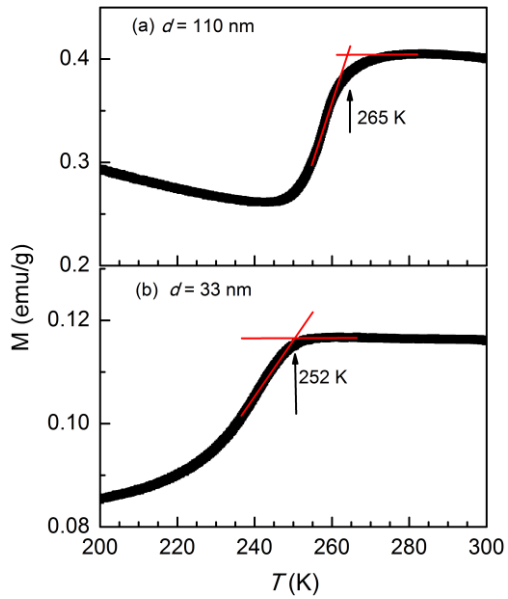

Fig. 3. Temperature dependent magnetization of α-Fe_2O_3(a) 110 nm and (b) 33 nm size crystallites.

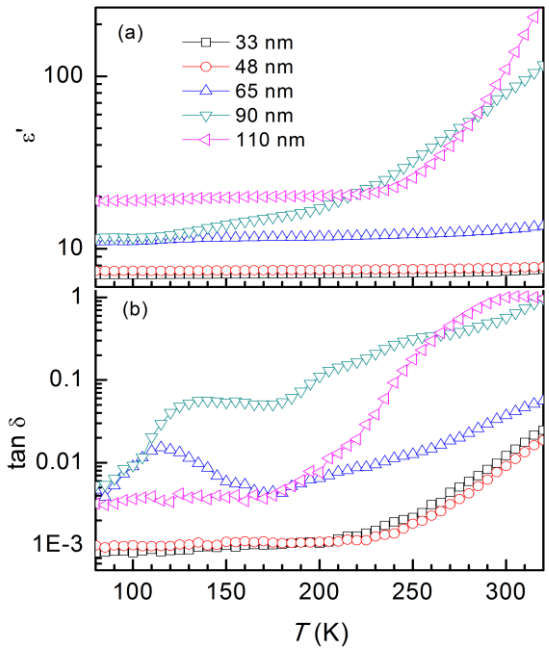

Fig. 4. ε'-*T* and tanδ-*T* relation of all nanocrsytallites of α-Fe_2O_3 at 1.5 kHz frequency.

Figure 4(a) shows the temperature dependent dielectric permittivity $\varepsilon'(T)$ at 1.5 kHz frequency for *a*-Fe_2O_3 with all crystallites sizes. $\varepsilon'(T)$ curves indicate that the ε' value increases with increasing crystallite size, which indicates the enhanced grain boundary. The imaginary part of dielectric loss $\tan\delta(T)$ as a function of temperature at 1.5 kHz frequency for *a*-Fe_2O_3 with all crystallites sizes as depicted in Fig. 4(b).

Figure 5(a) shows the temperature dependent dielectric permittivity at different fixed frequencies for *a*- Fe_2O_3 with crystallites size of 33 nm. Below 250 K, $\varepsilon'(T)$ is independent of temperature and frequency, indicates intrinsic static dielectric constant value of $\varepsilon_S \sim 7.1$. Above 250 K, small increase in $\varepsilon'(T)$ is observed. Figure 4(b) shows the data of loss tangent (*tan*δ) as a function of temperature with selected test frequencies for 33 nm size crystallites of *a*-Fe_2O_3. The *tan*δ(*T*) curves also exhibit similar behavior like $\varepsilon'(T)$ curves and absence of peak below measured temperature range.

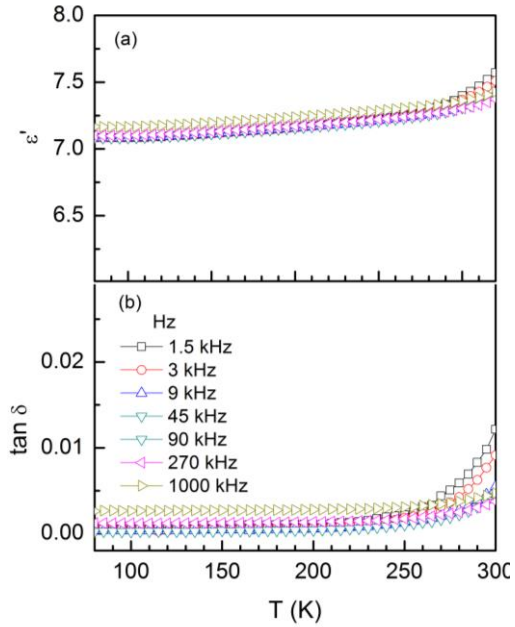

Fig. 5. ε''-*T* and tanδ-*T* relation of 33 nm nanocrystallites of *a*-Fe_2O_3.

Figure 6 shows the temperature dependent dielectric permittivity at different fixed frequencies for *a*-Fe_2O_3 with crystallite size of 110 nm. Below 250 K, $\varepsilon'(T)$ is independent of temperature and frequency and a small increase of intrinsic static dielectric constant value were observed of $\varepsilon_S \sim 19$. Above 250 K, small increase in $\varepsilon'(T)$ is observed. Figure 6 shows the data of loss tangent (*tan*δ) as a function of temperature with selected test frequencies for 110 nm size crystallites of *a*-Fe_2O_3. The *tan*δ(*T*) curves show a dielectric relaxation, where the step like increase in $\varepsilon'(T)$ curves. The relaxation is shifted to higher frequency with increasing temperature.

Increase in ε' of all samples rapidly with temperature at low frequencies could be either due to interfacial polarization or due to the accumulation of charged species at grain boundaries or dipolar polarizations which are strongly temperature dependent. The dispersion occurring in lower frequency regime may be attributed to interfacial polarization due to the charge accumulated at grain boundaries. The other reasons for dispersion may be due to space charge polarization, Maxwell Wagner, long range structural order and defect relaxations. The shifting of step

like dispersion to higher frequency region in the real part of the complex dielectric constant indicates that Maxwell Wagner relaxation mechanism was responsible for dispersive and large dielectric constant at low frequencies [14]. The dielectric behavior of such a material consists of a conducting or (semiconducting) grain separated by a more insulating grain boundary. The permittivity dispersion is insignificant at higher frequencies because atomic, electronic and molecular polarizations are responsible for high frequency permittivity which is independent of measured frequency range. The increase of ε' with the rise in temperature over the entire frequency range could be attributed related to the thermally activated process like charge carrier transportation.

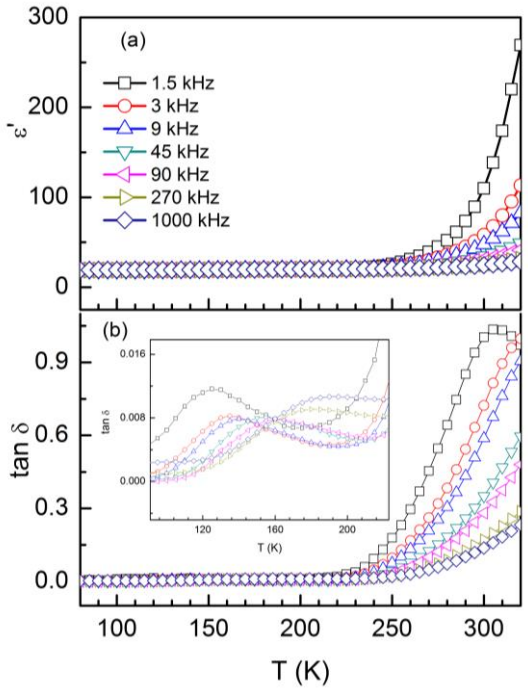

Fig. 6. ε'-T and tanδ-T relation of 110 nm nanocrystallites of α-Fe_2O_3.

The AC conductivity σ_{AC} as a function of test frequency *f* for different temperatures are shown in Figure 7 for *a*-Fe_2O_3 with crystallite size of (a) 33 nm and (b) 110 nm. The $\sigma_{AC}(f)$curves show different behavior in two ranges in all crystallite sizes. First, there is a strong rise at low frequencies. This is the grain-boundary blocking effect. Secondly, the conductivity does not increase as rapidly at high frequency. It is the bulk conductivity relaxation in which we are primarily interested. The σ_{AC} in the high frequency range can be described by "universal dielectric response" (UDR) [15]

$$\sigma_{AC} = \sigma_{DC} + \sigma_0 f^s \qquad (1)$$

Where σ_{DC} is the dc bulk conductivity, σ_0 is a constant, *f* is the rest frequency, and the exponent *s* is smaller than 1. Equation (1) is a common feature for all amorphous semiconductors and some other disordered systems. It is typical of thermal assisted tunneling between localized states.

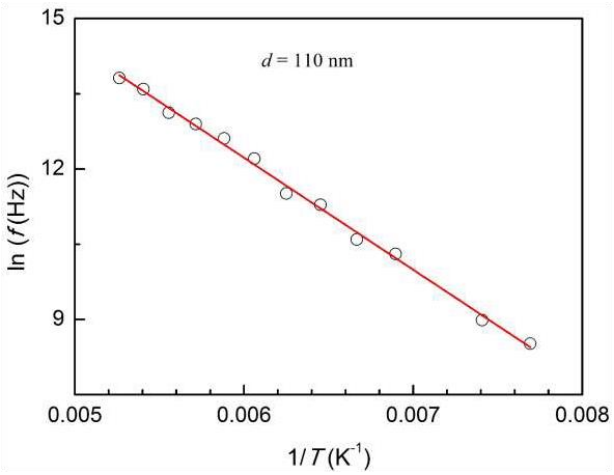

Fig. 7. Arrhenius plots for the observed relaxations of α-Fe_2O_3 of 110 nm size crystallites.

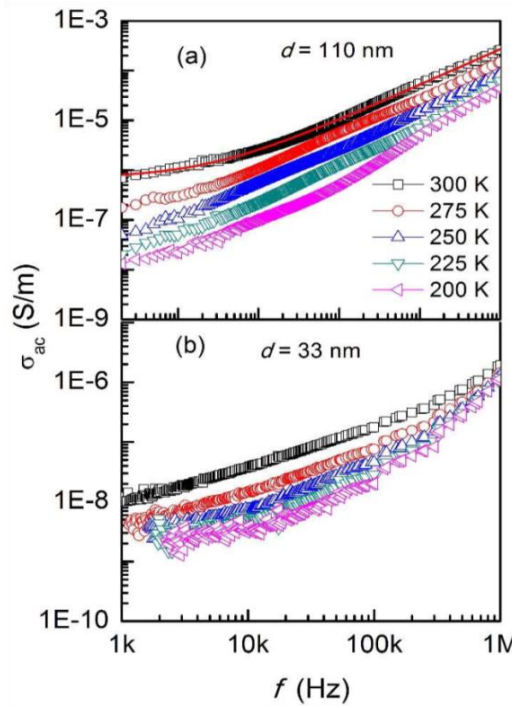

Fig. 8. Frequency dependent AC conductivity at fixed temperature of α-Fe_2O_3nanocrystallites (a) 110 nm and (b) 33 nm.

Conclusion

We report synthesis along with magnetic, ac conductivity and dielectric properties of hematite nanoparticles. As prepared Fe_2O_3 crystallizes in corundum structure which belongs to the rhombohedron system (space group *R3-c*). The magnetization data shows a typical Morin transition, T_N = 265 K for 110 nm crystallites, whereas this transition is decreasing with decreasing crystallite size, T_N = 252 K for 33 nm. The value of magnetization is increased with increasing crystallite size. The enhanced dielectric permittivity was observed in higher hematite crystallite size. The overall dielectric response has revealed conduction mechanism is due to the extrinsic contribution from the dominant Maxwell-Wagner polarization.

Acknowledgement

This research did not receive any specific grant from funding.

Declaration of competing interest

The authors declare that they have no known competing financial interests.

Naresh Babu Gatchakayala– Research Scholar of Krishna University;
D. Rama Sekhara Reddy– Asst.Professor at Krishna University.

[1] O.V. Salata, *Applications of nanoparticles in biology and medicine*, J. Nanobiotechnology, 2(1), 3 (2004); https://doi.org/10.1186/1477-3155-2-3.
[2] D.L. Huber, *Synthesis, properties, and applications of iron nanoparticles*, Small., 1(5), 482 (2005); https://doi.org/10.1002/smll.200500006.
[3] R.M. Cornell, U. Schwertmann, *The Iron Oxides: Structure, Properties, Reactions, Occurrences and Uses*. 2nd ed. John Wiley & Sons; (2006).
[4] S. Laurent, D. Forge, M. Port, et al. *Magnetic iron oxide nanoparticles: synthesis, stabilization, vectorization, physicochemical characterizations, and biological applications*, Chem Rev., 108(6), 2064 (2008); https://doi.org/10.1021/cr068445e.
[5] A.S. Teja,P-Y. Koh, *Synthesis, properties, and applications of magnetic iron oxide nanoparticles*, Prog Crystal Growth Char Mat., 55(1), 22(2009); http://dx.doi.org/10.1016/j.pcrysgrow.2008.08.003.
[6] M. De Cuyper, M. Joniau, *Magnetoliposomes*, Eur Biophys J., 15(5), 311 (1988);https://doi.org/10.1007/BF00256482.
[7] S. Hasany, I. Ahmed, J. Rajan, A. Rehman, *Systematic review of the preparation techniques of iron oxide magnetic nanoparticles*, Nanosci Nanotechnol, 2(6):148 (2012); https://doi.org/10.5923/j.nn.20120206.01.
[8] C-T. Wang, S-H. Ro, *Nanocluster iron oxide-silica aerogel catalysts for methanol partial oxidation*, Appl Catal A Gen., 285(1), 196 (2005); https://doi.org/10.1016/j.apcata.2005.02.029.
[9] A.K. Gupta, M. Gupta, *Synthesis and surface engineering of iron oxide nanoparticles for biomedical applications*, Biomaterials, 26(18), 3995(2005); https://doi.org/10.1016/j.biomaterials.2004.10.012.
[10] Attarad Ali, Hira Zafar, Muhammad Zia, Ihsan ul Haq, Abdul Rehman Phull, Joham Sarfraz Ali, Altaf Hussain, *Synthesis, characterization, applications, and challenges of iron oxide nanoparticles*, Nanotechnol Sci Appl. 9, 49 (2016); https://doi.org/10.2147/NSA.S99986.
[11] R.M. Cornell, U. Schwertmann, *Iron Oxides in the Laboratory: Preparation and Characterization*, 2nd ed.; Wiley-VCH: New York, NY, USA, 2000.
[12] J. G. Kim, K. H. Han, C. H. Lee and J. Y. Jeong, *Crystallographic and Magnetic Properties of Nanostructured Hematite Synthesized by the Sol-Gel Process*. J. Korean Phys. Soc., 38, 798 (2001);
[13] F. Bødker, M. F. Hansen, C. B. Koch, K. Lefmann and S. Mørup, *Magnetic properties of hematite nanoparticles*, Phys. Rev. B: Condens. Mater. Phys. 61, 6826 (2000); https://doi.org/10.1103/PhysRevB.61.6826.
[14] P. Lunkenheimer, V. Bobnar, A. V. Pronin, A. I. Ritus, A. A. Volkov, and A. Loidl, *Origin of apparent colossal dielectric constants*, Phys. Rev. B, 66, 052105 (2002); https://doi.org/10.1103/PhysRevB.66.052105.
[15] A. K. Jonscher, *Universal Relaxation Law*, (Chelsea Dielectrics Press, London, 1996).

Н.Б. Гатчакаяла,Р.С.Д. Дакуру

Синтез, магнітні, провідність змінного струму та діелектричні властивості та характеристики нанокристалітів гематиту

Хімічний факультет, Університету Крішни, Мачіліпатнам 521004, Андхра-Прадеш, Індія; dachuru@gmail.com

У статті наведено інформацію про синтез та магнітні властивості, провідність змінного струму, а також діелектричні властивості нанокристалітів гематиту. Отриманий Fe_2O_3 кристалізується в структурі корунду, що належить до системи ромбоедрів із просторовою групою *R3-c*. Дані намагніченості показують типовий перехід Моріна, T_N = 265 K для кристалітів 110 нм, тоді як цей перехід зменшується зі зменшенням розміру кристаліту, T_N = 252 K для 33 нм. Величина намагніченості збільшується зі збільшенням розміру кристалітів. Підвищені діелектрична проникність і провідність змінного струму спостерігалися у кристалів гематиту більших розмірів. Загальна діелектрична відповідь показала, що механізм провідності зумовлений зовнішнім внеском домінуючої поляризації Максвелла-Вагнера.

Ключові слова: нанокристали гематиту; точки Cole-Cole; діелектричні властивості; змінна провідність; імпеданс.

PHYSICS AND CHEMISTRY OF SOLID STATE
V. 24, No. 2 (2023) pp. 249-255
Section: Physics

DOI: 10.15330/pcss.24.2.249-255

Vasyl Stefanyk Precarpathian National University

ФІЗИКА І ХІМІЯ ТВЕРДОГО ТІЛА
Т. 24, № 2 (2023) С. 249-255
Фізико-математичні науки

PACS: 41.75.Ht, 61.25.Mv, 61.43.Hv ISSN 1729-4428

S.Ye. Donets[1], V.V. Lytvynenko[1], O.A. Startsev[1], Yu.F. Lonin[2], A.G. Ponomarev[2], V.T. Uvarov[2]

Fractal analysis of fractograms of aluminum alloys irradiated with high current electron beam

[1]*Institute of Electrophysics and Radiation Technologies, Kharkiv, 61002, Ukraine, vvlytvynenko@ukr.net*
[2]*NSC Kharkiv Institute of Physics and Technology, Kharkiv, 61108, Ukraine*

The aluminum alloys D16 and AMg6 were irradiated using the high-current relativistic electron beam in vacuum. Intense electron irradiation of the materials modified their physical properties. The fractal character of the fracture surfaces' images was studied. The change of the fractality is a distinguished descriptor of the materials modification. The characteristic ductile and brittle fractures are accompanied with the change of the fractal dimension.

Keywords: aluminum alloy, fractal, electron beam, irradiation, modification.

Received 14 December 2023; Accepted 22 March 2023.

Introduction

Obtaining protective surfaces is one of the key tasks for ensuring the safety of both human health and technical systems. Among the many existing approaches to tackle this problem for metals, the irradiation treatment of surfaces can be selected. The popular approaches in this domain are: (i) laser treatment, (ii) irradiation with ions, (iii) processing with electron beams. The focus of current research is on obtaining hardened surfaces of metal plates by irradiating them with high-current relativistic electron beams (HCEB). Relativistic energy of electrons provides a deeper influence into the material (a hundred microns at 0.3-0.5 MeV for light metals), while intensive currents induce extreme volumetric thermo-mechanical conditions [1,2]. This technology can be an efficient tool of modification of the metallic surface to the required performance characteristics: microhardness, abrasion resistance, corrosion resistance, etc. Also, they could be further combined with additional techniques like electro-erosive alloying to enhance the surface properties [3].

At the same time, it is known [2, 4] that the HCEB treatment has a heterogeneous impact on the metals due to its radiation, temperature, and shock-wave effects. In this case, the depth of the modified layer significantly exceeds the average range of electrons in the material. Thus, the microstructure together with such an indicator as the value of microhardness, change significantly along the depth. It is stipulated, that interlayers can dampen possible external impacts. It is also found that the pretreatment of aluminum alloys with HCEB leads to a significant improvement in their superplastic deformation [5]. The dislocation density distribution over the volume of the irradiated material and their spatial orientation change even more unpredictably. Considering the above list of effects that occur during the irradiation of HCEB metal plates from the point of view of the possibility of obtaining impact-resistant materials, we can say that they represent certain technological prospects. The protective property of the material depends on its ability to convert the kinetic energy of the striking object into its own internal energy, as well as into the energy of its own deformations in all directions, with the exception of the direction in which the protected object is located. It is possible to approach the implementation of such requirement by creating an anisotropy in the microstructure of a solid material utilizing HCEB.

Since we are dealing with a non-homogeneous distribution of the characteristics of an object, it is possible to use the apparatus of fractal analysis as a macro tool to

evaluate the effect the HCEB irradiation by examining the fractures of the irradiated materials and the reference material. The fractal analysis can provide quantitative descriptors of the objects under study. The relative change of those descriptors actually is a result of the change in the microstructures and their corresponding fracture mechanisms. A common fractal descriptor is a fractal dimension *D*. It denotes changes in complexity in the surface under study. The more complex is the surface (e.g., roughness, visible features), the more complex is the distribution of the fractal dimension [6]. However, one should be aware about that changes in *D* may not actually result in changes in particular mechanical properties and vice-versa as the techniques used to calculate *D* can be insensitive to the provided changes. For example, a hardness could change while a fractal dimension stays almost the same.

2 aluminum alloys were selected for study: AMg6 alloy of the Al-Mg system and D16 of the Al-Cu-Mg system. These alloys are commonly used in aerospace domain and for special light-vehicle production. These alloys were also studied by our team and results were presented in [7], and thus suited for this case study to investigate their fractures using fractal analyses.

I. Materials and methods

The aluminum alloys D16 (91.9% Al; 4.8% Cu; 1.5% Mg; 0.8% Mn; impurities Fe and Si up to 0.5%, wt.%) and AMg6 (92.197% Al, 0.1% Cu; 6% Mg; 0.6% Mn; 0.4% Fe; 0.4% Si; 0.2% Zn; 0.1% Ti; 0.003% Be, wt.%) were used in the current research [7]. The samples of irradiated materials were prepared in a form suitable for subsequent mechanical deformations in various modes.

Irradiation was carried out on the TEMP-A pulsed electron accelerator NSC KIPT [1] with the current –2 kA, electron energy of 0.3 MeV, and the pulse duration around 5 μs. The irradiation was conducted in the vacuum.

To prepare the samples for fractographic analyses, the samples were broken at a room temperature and the fractures were studied using a JEOL JSM-840 scanning electron microscope.

Fractal character of the SEM images of fractures was studied as per methodology described in [8]. Variation of intensity in the grayscale SEM images of microstructures is a composite characteristic property which depends on the fracture roughness, grain structure, and on the scanning properties such as illumination (signal) and focus. If it may be assumed that the microscope imaging conditions are optimal, then the fractal analysis can be performed for the SEM images to describe the target microstructures.

Fractal dimension analyses were conducted using the in-house software package based on the Clarke's triangular prism surface area method (TPSAM) and spin-off methods [9, 10]. Basically, Clarke extended the Mandelbrot approach to an area grid. TPSAM enables calculation of the fractal dimension of a digital surface by plotting virtual prisms on the surface using the pixel gray-level values. The surface area *A* is covered with the triangular prisms on a square window with a step size δ. Then, a least square regression of *A*- δ though the data points is plotted for multiple δ on the log-log scale [11]:

$$A(\delta) = \mathrm{N}(\delta)\delta^2 = K\delta^{2-D} \quad (1)$$

$$Log(A) = \mathrm{K} + (2 - \mathrm{D})Log(\delta) \quad (2)$$

$$D = 2 - \beta \quad (3)$$

where $N(\delta)$ is a number of steps performed, K is a constant, D is a fractal dimension, while β is a slope of the regression line. If there is no slope of the line *log(D)*-*log(*δ*)*, then *D* tends to the theoretical value of 2. In other terms, a grayscale image is considered as a matrix of certain $x \times y$ pixel size, while a gray-scale intensity (1..256) of an image is considered as a height. Thus, it is possible to cover the image with virtual prisms and calculate a fractal dimension map as described above.

The corresponding software package was previously developed in Pascal/Delphi [12]. For calculations in this research, the original TPSAM method was selected on the squared windows 4x4 pixels with a sliding step of 1 px. The data *A*- δ was calculated increasing the step size δ from 1 to 4 px. A starting point for a 1 px prism was taken as a top left corner of an image, selection of such starting point was assumed to have a negligible effect as the calculation was done with a sliding step of 1 px in x & y directions. Next, a slope of a regression line was calculated. Small window size minimized blurring and smoothing of the features. TPSAM method is known to underestimate or distort the fractal dimension *D*, thus the tests were conducted to establish such effects. In general, the possible over- or underestimations of the fractal dimension are of less importance because the fractal analyses are used for comparison between samples, and in the case if we need to make a correction for the underestimation, it is advised to refer to the study in [13]. Regarding error of calculations of fractal dimensions, it is possible to estimate it directly from computations, however, it makes the computations more complex, and it is harder to relate to them. It was recommended to do actual tests on images, if a fractal dimension tends to some theoretical expected value. The authors followed the latter approach.

The necessary visualizations and data post-processing were performed in Python 3, incl. the library plotly v5.11. The scripts were written in the Jupyter notebooks which facilitates development due to user friendliness and collaboration between the developers.

II. Discussion

Prior to analyses, the tests of fractal calculations were performed. As the data objects for analyses are SEM images, it was necessary to establish how the algorithm calculate the fractal dimension *D* for some simple cases. For example, Fig. 1a shows the test sample 1 which is a cropped piece of the SEM image of the relatively flat fracture surface and the test sample 2 which is also a piece of SEM image but out-of-focus sample surface. The sample 1 was actually taken from Fig. 2b and the sample 2 was from Fig. 2a. Having calculated the fractal dimensions, the fractal maps were obtained. As the

sampling window was 4x4 pixels, the actual smoothing effect was not large compared to the cases with large sampling windows like 10x10. However, as the algorithm slides across 2 dimensions of the SEM image while processing the grayscale intensity, some blurring appears. The blurring effect is noticeable on the sharp boundaries. For example, the sample 1 has a white background due to cropping. This boundary blurs on the fractal map. Thus, it is important to have high-resolution images and to minimize a sampling window size while trying to explore small objects with higher accuracy.

When the fractal maps are calculated, one can plot a distribution of fractal dimensions against number of pixels. Such fractal distributions are presented on Fig. 1b, but they are also normalized on the maximum value of frequency of pixels in each distribution to enable relative comparison between the samples. The bin size of fractal dimension for all our distributions is 0.01. The sharp peak at D~2 for the sample 1 corresponds to the white background of the cropped image. Basically, a flat 2-dimensional surface should have no features and no complexity. When the pixel intensities start to variate, D grows. The flat fracture surface of the sample 1 has a second peak at D~2.37. The sample 2 has a wide peak at 2.46, which is characterizes a more chaotic object. It appears, that the method is sensitive to the small variations of intensities or noise as expected [10]. Noisier SEM images will have a wider peak at D~2.5. It is seen that the calculated value at the peak D~2, tends to the theoretical value at D~2. A calculation error can be estimated as a full width at a half maximum, and it was around ~ 0.01 (however, for that particular test a bin size for a fractal dimension distribution was taken at 0.002). The relative error of all calculations of fractal dimensions in this research was assumed to be around ~ 0.01.

During calculations of D, the actual values are not limited within a max theoretical value of 3 and a min value of 2. The Clarke's algorithm may not fit properly the actual surface with the virtual prisms, thus, leaving for some errors. So, the values might be a little lower than 2 or higher than 3 for few points on the large SEM image. With those assumptions, it is now possible to proceed to analyses of the real fractograms.

Fig. 2 shows the fractogram of the AMg6 alloy. On the left side of Fig. 2a, the target surface is melted by the beam, which is characterized by grain elongated perpendicular to the surface. This is a common recrystallized microstructure of the melted zone (MZ) due to directional crystallization. The thickness of the recrystallized MZ reaches ~ 100 μm at the epicenter of

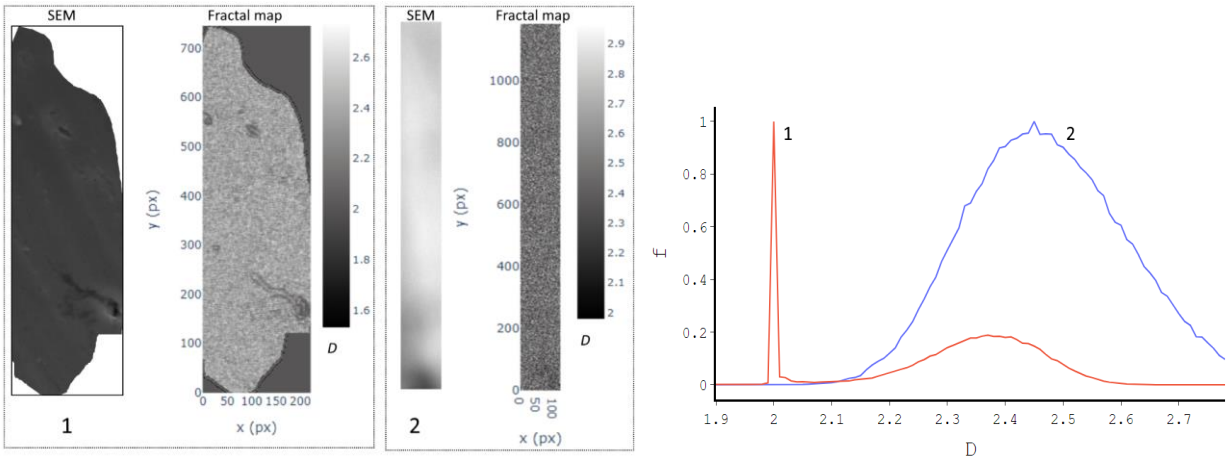

a b

Fig. 1. Tests on pieces of SEM images (a) and their corresponding (b) distribution of the normalized frequency of the calculated fractal dimensions of the SEM images, where (1) is the test sample 1, (2) is the test sample 2.

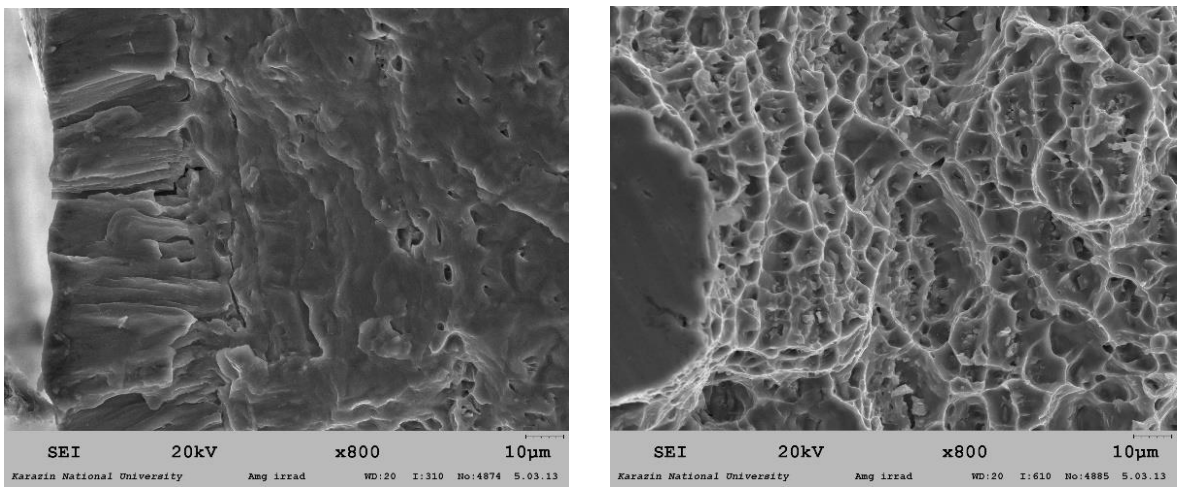

a b

Fig. 2. Fractograms of the fracture of the AMg6 alloy. (a) irradiated material, near-surface area, (b) reference material in the central part of the sample

irradiation, however, the beam melts up to the depth of around 500-600 μm but most of the material is lost due to ablation into the environment. The elongated grains have a thickness of ~1-5 μm, and traversing the whole MZ. On the right side of Fig. 2a, there is a rough globular microstructure. This is a heat-affected zone (HAZ), which was impacted by the thermal and shock-wave effects of the beam. The microhardness of such irradiated area is 20% higher compared to the reference material as reported elsewhere [7]. Apart from recrystallization effects, the formation of compression-tension waves in the target volume contributes to the change of microstructure as it was discussed in [14]. The fracture mechanism of MZ is brittle with clear intercrystalline cracks and between MZ and HAZ. In the latter case, the cracks appeared confirming a poor adhesion between the recrystallized layer and HAZ base, Fig. 2a.

Fig. 2b shows a fragment of the central part of the plate. This part was not affected by the HCEB irradiation and it represents the reference material. The reference alloy AMg6 has the faceted microstructure of a size 2-8 μm. Its fracture mechanism is of predominantly ductile mode with elements of brittle fracture. There are many fine independent dimples with a diameter ~2 μm, uniformly distributed across the fractogram. Presence of hardening phase in terms of small particles with a size 0.5-3 μm was noticed on the facet boundaries. It is assumed that those are Al_2Mg_3, (Fe, Mn)A_{l6}, Mg_2Si as found in [15].

In general, the HCEB irradiation resulted in formation of the thin brittle surface layer of recrystallized material. The mechanical properties at MZ deteriorated in terms as a protective layer. It is known, that HCEB processing of the materials results in some residual compressive stresses, which actually lead to lower adhesion of the melted zone of material to the bulk material. The stresses were estimated to reach around 80-150 MPa [16].

The fractal dimension maps of the SEM images on Fig. 2, are presented on Fig. 3a-b. The gray scale color bar is characteristic similar for both, and it is omitted for Fig. 3b. It is seen, the fractal analysis is a powerful tool for edge detection. It clearly highlighted the grain boundaries and the fracture cracks as the dark features which are visible on the gray 'noise' background. The normalized frequency distributions revealed the differences in the fractal dimension for the MZ, HAZ and the reference material. It appeared, the faceted microstructure of the reference material has a larger contribution of the edge boundaries, thus leading to a shift to lower *D* values. The melted zone itself has the highest contribution of the background noise as it is featureless compared to others judging on its peak position and width with trails. HAZ with the faceted-globular microstructure has intermediate distribution of fractal dimensions due to its nature of formation. To illustrate the difference between 'noise' background and the edge features, Fig. 3d was built by

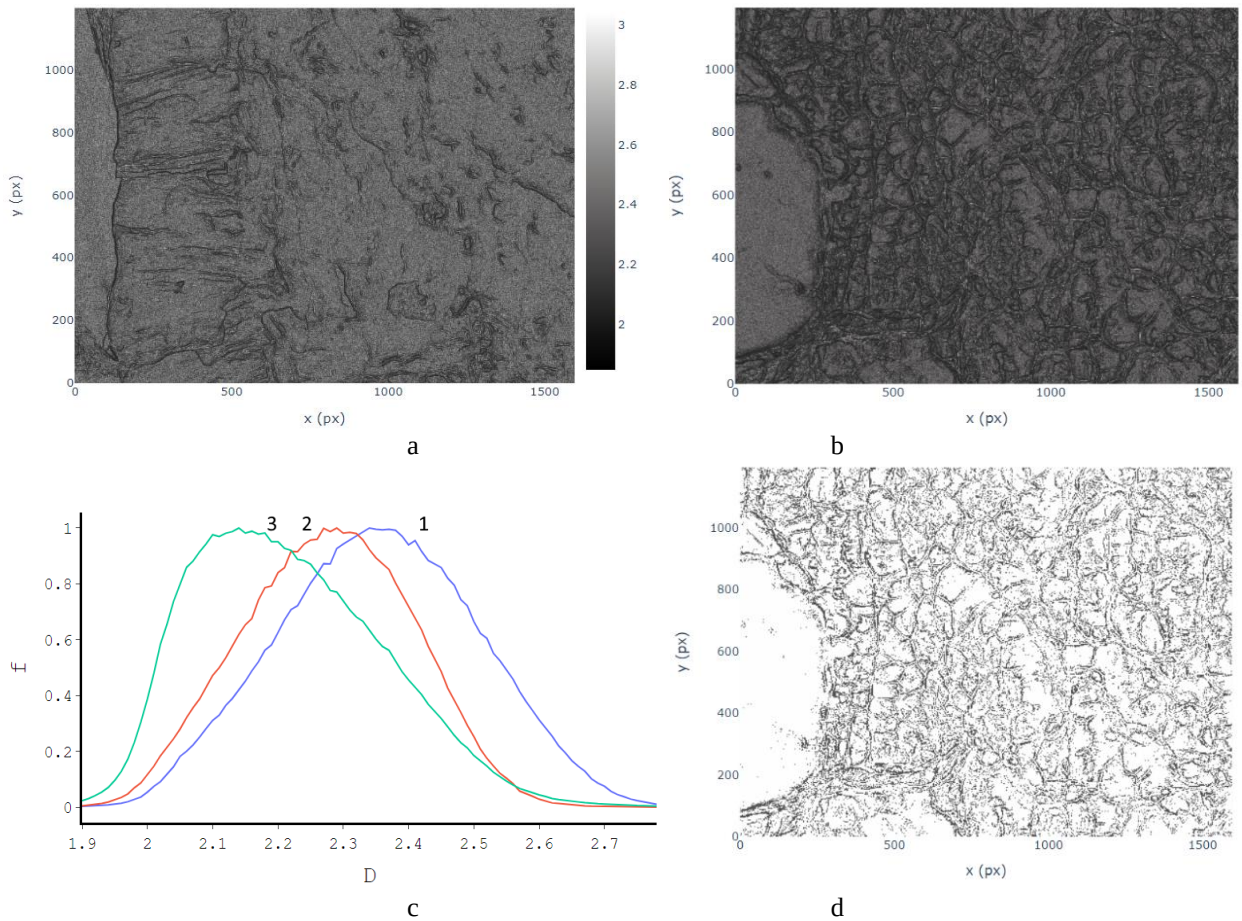

Fig. 3. Calculated fractal dimensions of the SEM images for the AMg6 alloy: (a) irradiated material, (b) reference non-irradiated material. The color bar of the fractal dimension *D* is included in (a) for illustrative purposes. (c) shows the distribution of the normalized frequency in the areas: 1) MZ, 2) HAZ, 3) non-irradiated reference. (d) illustrates a filtered fractal dimension map for (b), where $D < 2.2$.

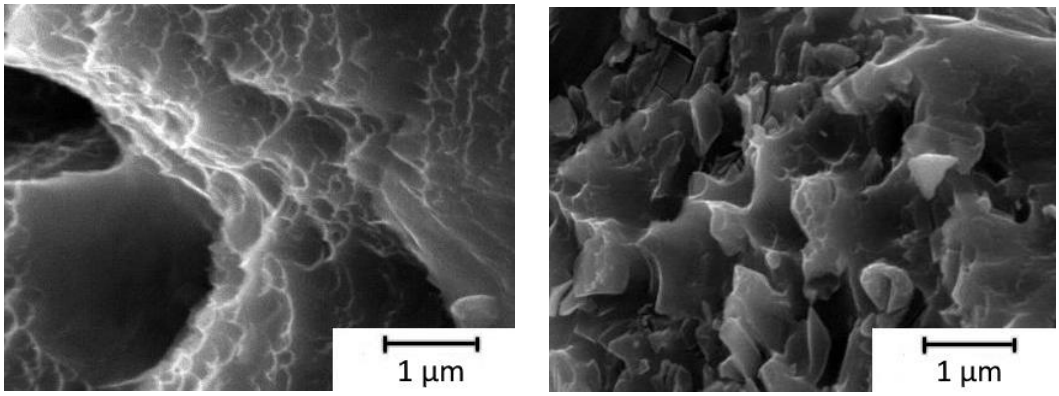

a b

Fig. 4. Fractograms of the D16 alloy: a) irradiated (HAZ) zone, b) non-irradiated reference.

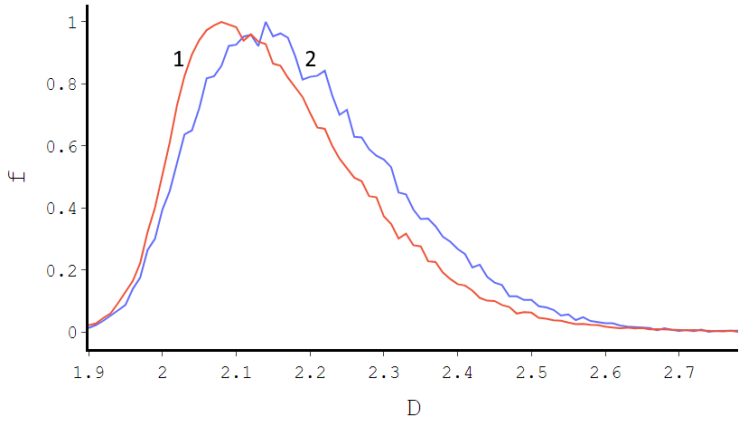

Fig. 5. Distribution of the normalized frequency of the calculated fractal dimensions of the SEM images in the areas: 1) irradiated (HAZ) zone, 2) non-irradiated reference of the D16 alloy.

filtering the Fig. 3b data set for $D < 2.2$. Some differences between the backgrounds ($D>2.2$) for all zones can be found, but it is currently unclear what is an actual effect of the SEM imaging conditions and the actual microstructures, and it requires some future investigations.

The study of the fractures of the D16 aluminum alloy were started earlier by the team in [7]. As it can be seen in Fig. 4a, the fracture of the irradiated part of the target was accompanied by the release of internal stress energy, which manifested itself in the deformation at the mesoscale level. The reference material is presented on Fig. 4b, the fracture went in a predominantly brittle mode with intergranular fracture and fine dimples. The irradiated material has the ductile mechanism of fracture in the heat-affected zone, accompanied with large deep dimples and tear ridges. From the point of view of absorption of external shock energy, the irradiated material may be better as a protection layer. Fractal dimension analyses (Fig. 5) revealed the shift of the distribution to lower D values, both in terms of a peak position and a higher-D trail. The shift in the fractal dimension distribution is basically contributed by the change in the fracture mode and thus, in a presence of more edge features. Based on the results from the AMg6 alloy and the D16 alloy, it appeared that the more brittle aluminum alloys are, the higher is the contribution of noise, and the higher ductile microstructures have the SEM fractograms with the distributions significantly contributing at D~2.

It is suggested, that the nonlinearity of the behavior of the mechanical properties of the aluminum alloys can be extended by considering the fractal dimension of the microstructure, i.e. their fractures. In such case, the behavior may follow the modified Hall-Petch expression as described by Tian et al. in [17]:

$$\sigma = \frac{F}{A}\left(1 + \frac{k}{r^{2\alpha-2}}\right) \quad (4)$$

where F is the applied force to the crystalline object with a section of size A, k is a constant, r is a size of crystallites or grains, and α is a fractal dimension. It becomes the classic Hall-Petch relationship when $\alpha=5/4$. In general, it is hypothesized, that the fractal dimension influences on the local mechanical properties, and it could be useful to do tensile testing, or pico- or nano-hardness testing in future to confirm the relation. Also, more solid understanding of the fractal descriptors of the fractures and the microstructure, could assist with prediction of materials failure. However, it is still unclear how the calculated fractal dimensions should be used as the distributions have large contribution of noise, chaotic variations of SEM imaging conditions. A possible improvement is extraction of components from the fractal dimension distributions as on Fig. 3: noise/background as a gaussian distribution with a peak around D~2.4-2.5, and contribution of other features with peaks at D~2-2.3. More studies are planned to be conducted in this field by our team.

The possible application domains of fractal analyses of microstructure images could be extended to more simple matters as it simplifies the edge detection for the grain boundaries and other high-contrast features. For example, the automated analyses of microstructure can be implemented if combined with other methods. Such approach may provide the details on the fracture mechanisms, comparisons of microstructures, quantitative description of the microstructures.

Conclusions

Modification of the surfaces of aluminum alloys by processing with high-current relativistic electron beams changes the microstructural nature of their near-surface layer. HCEB processing of the AMg6 alloy caused embrittlement of the melted area. The heat-affected zone of the materials also went through substantial changes in microstructure. HAZ in D16 alloy became more ductile compared to the reference material. The fractal analyses revealed the distinct differences of the alloys before and after modification in terms of fractal dimension of the SEM images of their fracture surfaces. More ductile sample areas appeared to have a larger contribution of fractal dimension close to 2, compared to more brittle microstructures due to abundance of edge features in the former case.

Acknowledgements

The research presented in this article was performed by financial support of the Ukrainian state budget program "Support for the development of the priority areas of scientific researches" (Budget Financial Code 6541230).

Donets S.Ye. – PhD, Senior Scientist Research Fellow, Institute of Electrophysics & Radiation Technologies National Academy of Sciences of Ukraine;
Lytvynenko V.V. – Dr. Tech. Sc., Director, Institute of Electrophysics & Radiation Technologies, National Academy of Sciences of Ukraine;
Startsev O.A. – PhD, Research Fellow, Institute of Electrophysics & Radiation Technologies, National Academy of Sciences of Ukraine;
Lonin Yu.F. – Dr. Tech. Sc., Head of Department, NSC Kharkiv Institute of Physics and Technology National Academy of Sciences of Ukraine;
Ponomarev A.G. – PhD, Head of Laboratory, NSC Kharkiv Institute of Physics and Technology National Academy of Sciences of Ukraine;
Uvarov V.T. **–** PhD, Senior Scientist, NSC Kharkiv Institute of Physics and Technology National Academy of Sciences of Ukraine.

[1] V.T. Uvarov et al., *Radiation acoustic control over the thermal parameter of construction materials irradiated by intense relativistic electron beam*. Physics of Particles and Nuclei Letters. 11(3) (2014); https://doi.org/10.1134/S1547477114030157.
[2] V.V. Bryukhovetsky et al., *The structural phase state and strength properties of the surface layer of AA6111-T4 aluminum alloy irradiated by the high-current electron beam*, Nuclear Instruments and Methods in Physics Research, Section B: Beam Interactions with Materials and Atoms, 519 (2022); https://doi.org/10.1016/j.nimb.2022.03.008.
[3] V. Tarelnyk et al., *New sulphiding method for steel and cast iron parts*, IOP Conference Series: Materials Science and Engineering, 233(1), 012049; https://doi.org/10.1088/1757-899X/233/1/012049.
[4] V.V. Bryukhovetsky et al., *The features of the structural state and phase composition of the surface layer of aluminum alloy Al-Mg-Cu-Zn-Zr irradiated by the high current electron beam*, Nuclear Instruments and Methods in Physics Research, Section B: Beam Interactions with Materials and Atoms, 499 (2021); https://doi.org/10.1016/j.nimb.2021.02.011.
[5] V. V. Bryukhovetskii et al., *Effect of pulsed electron irradiation on the parameters of duraluminum superplasticity*, Fiz. Khim. Obrab. Mater., 4 (2002); https://www.researchgate.net/publication/292062571_Effect_of_the_pulsed_electron_irradiation_on_superplasticity_properties_of_duraluminum.
[6] M. Tarafder et al., *Fractal analysis of microstructural images for evaluation of HSLA steel*. Supplemental Proceeding, TMS, 2 (2010); https://eprints.nmlindia.org/3309/.
[7] M.I. Bazaleev et al., *Aluminum alloys shock protective surfaces modified by high current electron beam*, Journal of Surface Physics and Engineering, 1 (2017); http://dspace.nbuv.gov.ua/handle/123456789/122608.
[8] V.F. Klepikov et al., *Fractality of Fractures of Aluminum and Titanium Alloys Irradiated by Intensive Electron Beam*, Journal of Nano- and Electronic Physics, 8(3) 03009 (2016); https://doi.org/ 10.21272/jnep.8(3).03009.
[9] K.C. Clarke, *Computation of the fractal dimension of topographic surfaces using the triangular prism surface area method*, Computers & Geosciences, 12(5) (1986); https://doi.org/10.1016/0098-3004(86)90047-6.
[10] W. Sun et al., *Three New Implementations of the Triangular Prism Method for Computing the Fractal Dimension of Remote Sensing Images*. Photogrammetric Engineering and Remote Sensing, 72(4) (2006); https://doi.org/10.1080/01431160600676695.
[11] C. Nayak, *Comparing various fractal models for analyzing vegetation cover types at different resolutions with the change in altitude and season*, MSc Thesis, ITC, IIRS (2008); https://webapps.itc.utwente.nl/librarywww/papers_2008/msc/gfm/nayak.pdf.
[12] A. Startsev, *Calculation of fractal maps for data sets*, IERT NAS of Ukraine (2014); https://github.com/oleksandrstartsev/FractalsDimPRGs.

[13] M.K. Rathore et al., *Estimation of Fractal Dimension of Digital Images*, International Journal of Engineering and Technical Research (IJETR), 2(9) (2014); https://www.erpublication.org/published_paper/IJETR022497.pdf.
[14] V.V. Bryukhovetskii et al., *Features of gelation of surface of industrial aluminium alloy 6111 in the area of influence of impulsive bunch of electrons in the mode of pre-melting*, Problems of Atomic Science and Technology, 72(2) (2011); https://vant.kipt.kharkov.ua/ARTICLE/VANT_2011_2/article_2011_2_28.pdf.
[15] G.I. Prokopenko et al., *Hardening of Surface Layer on Al—6Mg Aluminium Alloy, Using Complex Effects of Electric Spark and Ultrasonic Impact Treatments*, Metallofiz. Noveishie Tekhnol. 35(10) (2013).
[16] V.F. Klepikov et al., *Physical and mechanical properties of titanium alloy VT1-0 after high-current electron beam irradiation*, Problems of Atomic Science and Technology 96(2) (2015); https://vant.kipt.kharkov.ua/ARTICLE/VANT_2015_2/article_2015_2_39.pdf.
[17] Dan Tian et al. *Hall–Petch effect and inverse Hall–Petch effect: a fractal unification*, Fractals, 26(06) (2018); https://doi.org/10.1142/S0218348X18500834.

С.Є. Донець[1], В.В. Литвиненко[1], О.А. Старцев[1], Ю.Ф. Лонін[2], А.Г. Пономарьов[2], В.Т. Уваров[2]

Фрактальний аналіз фрактограм алюмінієвих сплавів, модифікованих сильнострумовим електронним пучком

[1]*Інститут електрофізики та радіаційних технологій, м. Харків, 61002, Україна, vvlytvynenko@ukr.net*
[2]*ННЦ Харківський фізико-технічний інститут, м. Харків, 61108, Україна*

Алюмінієві сплави Д16 і АМг6 опромінено сильнострумовим релятивістським електронним пучком у вакуумі. Інтенсивне електронне опромінення матеріалів зумовило зміну фізичних властивостей сплавів. Досліджено фрактальний характер зображень поверхонь зламів. Зміна фрактальності є відмінним параметром опису модифікації матеріалів. Характерні пластичні та крихкі руйнування супроводжуються зміною розподілу фрактальної розмірності.

Ключові слова: алюмінієвий сплав, фрактал, електронний пучок, опромінення, модифікація.

PHYSICS AND CHEMISTRY OF SOLID STATE
V. 24, No. 2 (2023) pp. 256-261
Section: Chemistry

DOI: 10.15330/pcss.24.2.256-261

Vasyl Stefanyk Precarpathian National University

ФІЗИКА І ХІМІЯ ТВЕРДОГО ТІЛА
Т. 24, № 2 (2023) С. 256-261
Хімічні науки

UDC: 579.61 + 544.47 ISSN 1729-4428

Nazarii Danyliuk[1], Ivanna Lapchuk[1], Tetiana Tatarchuk[1],
Roman Kutsyk[2], Volodymyr Mandzyuk[1]

Bacteria inactivation using spinel cobalt ferrite catalyst

[1]*Educational and Scientific Center of Material Science and Nanotechnology, Vasyl Stefanyk Precarpathian National University, Ivano-Frankivsk, Ukraine, danyliuk.nazariy@gmail.com*
[2] *Microbiology Department, Ivano-Frankivsk National Medical University, Ivano-Frankivsk, Ukraine, rkutsyk@ifnmu.edu.ua*

The *E. coli* inactivation using hydrogen peroxide (H_2O_2) and cobalt ferrite granulated catalyst was investigated in a fixed-bed flow reactor. The $CoFe_2O_4$ catalyst was synthesized by the co-precipitation method, granulated, and annealed at 1150°C. X-ray diffraction analysis was used to identify the crystal structure of the catalyst. $CoFe_2O_4$ catalyst demonstrates good catalytic activity for bacteria inactivation in the presence of H_2O_2. An increase in the hydrogen peroxide concentration increases the inactivation efficiency. The reactor demonstrates the *E. coli* inactivation of 99.94% at the H_2O_2 hydrogen peroxide concentration of 15 mM and initial bacterial concentration of $6 \cdot 10^3$ CFU/L. The water disinfection using a fixed-bed reactor demonstrates the broad prospects for industrial use.

Keywords: fixed-bed reactor; *E. coli*; cobalt ferrite; hydrogen peroxide; bacteria inactivation.

Received 16 January 2023; Accepted 13 March 2023.

Introduction

Clean water is becoming less available to people [1]. Contamination of water with chemical and microbiological pollutants prompts people to solve this problem, namely to find new effective methods of cleaning and disinfection. Chemical pollutants are quite dangerous, but microbiological ones, which include bacteria and viruses, pose a greater danger due to their rapid spread among humans. That is why it is important to use innovative and highly effective methods for wastewater disinfection, which contains a large number of various pathogenic microorganisms.

Advanced oxidation processes are promising for polluted water disinfection [2,3]. Reactive oxygen species effectively neutralize the microorganisms that can harm people [2,4]. Fenton systems, as demonstrated by recent studies, are more effective, ecological, and economical compared to ozonation, UV irradiation, electrochemical oxidation, and sonolysis [5,6]. The catalyst plays an important role in the Fenton processes. It should be non-toxic, and effectively decompose used oxidants into free radicals (•OH, •OOH), which are responsible for the pathogens' inactivation. The most common option for hydroxyl and hydroperoxyl radicals generating is the decomposition of hydrogen peroxide [1,7]. Iron oxides and spinel ferrites have met these requirements [6,8]. For example, cobalt ferrite has been tested in real wastewater and found to be excellent in peroxymonosulfate (PMS) activation and *Escherichia coli* and *Enterococcus sp* bacteria disinfection [1].

The hydroxyl radicals formed during the catalytic decomposition of H_2O_2 possess a strong oxidizing effect, are toxic for biomolecules, and, therefore, easily damage the cell walls of microbes, organelles, and DNA. In addition, these radicals show a much higher reaction rate than chlorine, ozone, or potassium permanganate [5,9]. The effect of hydrogen peroxide on bacteria inactivation is evidenced by many studies [2,10–12]. L. Fernández et al. [2] inactivated *E. coli* bacteria using magnetite-based nanoparticles. It was shown that the inactivation percentage increased with increasing H_2O_2 concentration. Copper ferrite also actively generates hydroxyl radicals, which resulted in cell membrane damage and inactivation of *E. coli* (100 %) and *S. aureus* (96.4 %) bacteria [10].

I. de la Obra Jiménez et al. [8] have chosen iron oxides (hematite, magnetite) as heterogeneous catalysts for Fenton processes. The disinfection of municipal wastewater in reactors with natural catalysts was evaluated. The research was carried out at neutral pH, in the periodic and continuous flow modes. As a result, the authors obtained a complete inactivation of *E. coli* bacteria, namely a reduction of *E. coli* by 5-log. It is important to note that different types of inactivation mechanisms were observed in this case, but the heterogeneous Fenton process is the key. Therefore, water disinfection using the Fenton processes effectively solved the polluted water problems.

The complete wastewater treatment technology includes two processes: the degradation of organic toxicants and water disinfection. To date, there is a very small amount of research dedicated to *E. coli* inactivation using fixed-bed flow reactors. G.D.L.P. Vargas et al. [13] have shown that the rate of *Escherichia coli* inactivation increases with an increase in pH and H_2O_2 concentration. The presence of dissolved pollutants in domestic wastewater decreases the effectiveness of *E. coli* inactivation.

The key factors in evaluating whether a treatment technology is suitable for industrial use are cost and energy consumption. The paper [14] describes a microbubble-gas plasma reactor that produces a large amount of oxygen reactive species and nitrogen reactive species for the bacteria inactivation in sewage. The reactor reduces more than a 5-log of *E. coli* after 30 minutes at an energy consumption of 68 kJ/L. The addition of humic acid reduces the rate of *E. coli* inactivation: the inactivation of *E. coli* at the humic acid concentration of 0.0015% was less than 50% compared to the inactivation in pure water. L.Y. Ozer et al. [15] have used a fixed-bed reactor to investigate the antimicrobial properties of the nano-silver-4 wt.%-kaolin (nAg-4-Kn) composite deposited onto borosilicate glass beads (BGB). The tests were conducted in a fixed-bed reactor on effluent taken from a secondary sewage treatment plant. The results showed complete disinfection of the wastewater, which was maintained for several days. The nAg-4-Kn/BGB composites demonstrated high stability, which was confirmed by the composites' stability on the BGB surface. C. Pablos et al. [16] investigated the photocatalytic inactivation of *Escherichia coli* bacteria by titanium dioxide in a fixed-bed reactor. The efficiency of the reactor was studied and compared with the results obtained in batch mode. In both cases, photocatalytic inactivation was successfully achieved, for a 6-fold reduction in bacterial concentration. A fixed-bed reactor increases the rate of inactivation with increasing treatment time. It can be explained by the fact that the fixed bed reactor requires a longer irradiation time to completely inactivate the bacteria. It allows the use of a continuous process without the need for particle removal, making this immobilized system a good alternative for the successful scale-up of water disinfection technology. I. Thakur et al [17] have presented a low-cost Fe-TiO_2 composite for *E. coli* disinfection prepared by mixing clay with foundry sand and fly ash. The constant leaching of iron ions in acidic conditions into the solution led to the double effect of photocatalysis and photo-Fenton in the purification system. The composite beads were used 30 times and accompanied by a decrease in their photoactivity by only 11%. The corresponding results represent high prospects for dual technology for *E. coli* inactivation. The study [18] describes a reliable device for water disinfection using silver nanoparticles (AgNP), immobilized on the glass surface, in a continuous flow mode. It was found that the cleaning efficiency increases with an increase in the reactor contact time. A minimal release of silver (100 μg/L) into the treated water was observed throughout the test period.

Thus, the effectiveness of flow reactors depends on various factors such as reactor volume, catalyst nature, and treatment time. Bacterial inactivation is influenced by a range of different parameters: temperature, pH, and hydrogen peroxide concentration [19]. The peroxide technique has already demonstrated high efficiency in wastewater treatment due to the reactive oxygen species (ROS) formation [11]. Today, it is important to evaluate the suitability of the flow mode for industrial-scale use, maintaining the high efficiency of bacterial inactivation. It is assumed that the integration of flow reactors into the wastewater treatment system will ensure efficient and rapid treatment of effluents. Therefore, the aim of this work is to investigate a flow fixed-bed reactor filled with $CoFe_2O_4$ catalyst and H_2O_2 for water disinfection.

I. Experimental

1.1. Chemicals and microorganisms

$CoCl_2 \cdot 6H_2O$ (Carlo Erba reagents), $FeCl_3 \cdot 6H_2O$ (Carlo Erba reagents), NaOH, and hydrogen peroxide (31.5 %) were obtained from SferaSim (Ukraine). The model bacteria were Gram-negative, non-spore-forming bacteria *Escherichia coli (ATCC 35218)*.

1.2. Catalyst preparation and characterization

$CoFe_2O_4$ nanoparticles were synthesized by the co-precipitation method. The precise amounts of iron(III) chloride (27.05 g) and cobalt(II) chloride (11.91 g) were used as a source of Fe^{3+} and Co^{2+} cations, respectively. Metal salts were dissolved in 500 mL of water and the resulting solution was stirred for 30 minutes at 90°C. After that, a NaOH solution (5 M) was added dropwise as a precipitant to obtain a solution pH of 14. The mixture was further stirred with an overhead stirrer at 600 rpm for 30 min to complete the reaction. During the entire synthesis process, the solution was heated at 90°C in a water bath. The resulting black precipitate of $CoFe_2O_4$ was separated using a magnet, washed three times with distilled water, and dried at room temperature. The obtained $CoFe_2O_4$ powder was pressed into pellets, the pressing process is described in detail in our previous work [11]. Pellets with a diameter of 10 mm and a thickness of 3 mm were sintered for 6 hours at 1150 °C. The sintered tablets were crushed into granules with a size of 0.2-3 mm and filled into a flow-through reactor with an inner diameter of 21 mm and a length of 60 cm. The total mass of granules in the flow-through reactor was 445 g, and the filling volume was 130.5 mL.

The phase analysis of the catalyst was performed by X-ray diffraction analysis (XRD) using a Rigaku MiniFlex

600 diffractometer. The CuKα radiation at a wavelength of 1.5406 Å with the scan step of 0.02° (2θ) and the scan speed of 1°/min was applied.

1.3. Bacterial inactivation tests

Gram-negative *Escherichia coli* bacteria were plated on a sterile nutrient medium and cultivated for 24 hours at 37°C. The bacterial dilution was used to prepare the desired concentration of the bacterial solution. A bacterial suspension was prepared from the former colonies, serial dilutions were carried out, and 1 mL of the suspension was added to 1 L of distilled water. As a result, concentrations of 10^2 and 10^3 CFU/L were obtained. To inactivate *E. coli*, a series of hydrogen peroxide solutions with a concentration of 2.5, 5, 10, and 15 mM were used in the experiments. The initial bacterial solution and H_2O_2 solution were simultaneously fed into the reactor at a constant speed of 1.25 mL/min. To study the effect of temperature on *E. coli* inactivation, the experiments were performed at 20°C and 25°C. Residual bacteria were cultivated for 24 hours at 37°C. Endo's medium helps identify *E. coli* bacteria by forming red colonies. Colonies were counted and the inactivation percentage was calculated according to the formula:

$$\% \text{ inactivation} = [1 - N_{out}/N_{in}] \times 100\% \quad (1)$$

where N_{in} and N_{out} are the concentration of bacteria at the inlet and outlet of the reactor.

II. Results and discussion

2.1. X-ray analysis

X-ray diffractograms of as-prepared and calcined at 1150 °C $CoFe_2O_4$ samples are shown in Fig. 1. The diffractograms contain peaks with indices (111), (220), (311), (222), (400), (422), (511), (440), (533) and (622), which belong to the face-centered cubic crystal structure of spinel [20,21]. It can be seen that the rise in annealing temperature leads to significant peaks' narrowing. The narrow peaks of the $CoFe_2O_4$ (1150 °C) sample confirm the formation of particles with a high degree of crystallinity. The detected XRD peaks correspond to the space group Fd3m. The lattice parameters equal a = 8.3749 Å and a = 8.3628 Å for as-synthesized $CoFe_2O_4$ and $CoFe_2O_4$-1150°C, respectively. The crystallite size (D) was calculated by the Scherrer method using the formula: $D = k \cdot \lambda/(\beta_{1/2} \cdot \cos\theta)$, where k is the Scherrer constant that takes into account the shape of the particles (k = 0.94), λ is the X-ray wavelength (nm); $\beta_{1/2}$ is the width of the peak at its half maximum (in radians); θ is an angle for peak (311) (in radians). The calculated crystallite sizes of $CoFe_2O_4$ and $CoFe_2O_4$-1150°C samples are approximately 14 and 98 nm, respectively.

2.2. Inactivation of bacteria *E. coli* using the catalytic decomposition of H_2O_2

The catalytic activity of $CoFe_2O_4$ was studied on opportunistic bacteria *Escherichia coli*. The work focuses on water disinfection using a reactor filled with a spinel ferrite catalyst using low concentrations of peroxide, which will reduce the negative effects on human health [1,22]. It is known that the $CoFe_2O_4$ catalyst can effectively decompose H_2O_2 to aggressive free radicals. These reactive oxygen species, as researchers have shown, are the main reason for the destruction of bacteria, their cell walls, DNA, and internal organelles [16]. Figs. 2a-f show the main results of this study. The initial bacterial suspensions contained $7 \cdot 10^2$ and $6 \cdot 10^3$ CFU/L of *E. coli* bacteria. The concentration of hydrogen peroxide varied from 2.5 to 15 mM. Studies at room temperature showed a reduction of *E. coli* bacteria in water by 1.81-log and 1.96-log at a concentration of 15 mM H_2O_2 for $7 \cdot 10^2$ and $6 \cdot 10^3$ CFU/L *E. coli*, respectively (Fig. 2a-b). The inactivation percentage increases with increasing concentration of hydrogen peroxide and is equal to more than 98 % at 15 mM of H_2O_2 (Fig. 2e). Thus, the higher the concentration of H_2O_2, the greater the number of ROS generated on the catalyst's surface [16].

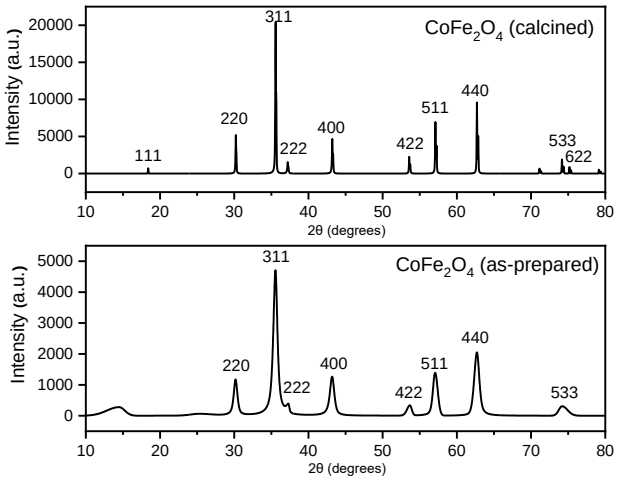

Fig. 1. XRD patterns for as-prepared and calcined at 1150 °C cobalt ferrites.

In addition, it was found that temperature change has a significant effect on bacteria inactivation. Conducting research on the catalytic activity of cobalt ferrite under conditions of elevated temperature, namely 25°C, is more favorable for *E. coli* inactivation (Fig. 2c-d). This is evidenced by the inactivation %, which is equal 99.89% at the initial concentration of *E. coli* $7 \cdot 10^2$ CFU/L and 99.94% at $6 \cdot 10^3$ CFU/L in the presence of 15 mM H_2O_2 (Fig. 2f). Presumably, as the temperature increases, the catalyst more actively decomposes H_2O_2 and generates a higher amount of hydroxyl and hydroperoxyl radicals, which inactivate gram-negative *E. coli* bacteria.

Fig. 3 shows the impact of experimental parameters (initial H_2O_2 concentration and temperature) on the *E. coli* inactivation. An increase in the H_2O_2 concentration and temperature from 20 to 25 °C causes a gradual increase in the inactivation effectiveness. The maximum efficiency of *E. coli* inactivation is observed at $[H_2O_2]_0$ = 15 mM and T = 25°C. The *E. coli* inactivation was mostly caused by hydrogen peroxide, which is a ROS source. It should be emphasized that the catalyst, prepared from sintered $CoFe_2O_4$ granules, requires rather low concentrations of H_2O_2 (10-15 mM) for the complete inactivation of *E. coli* bacteria.

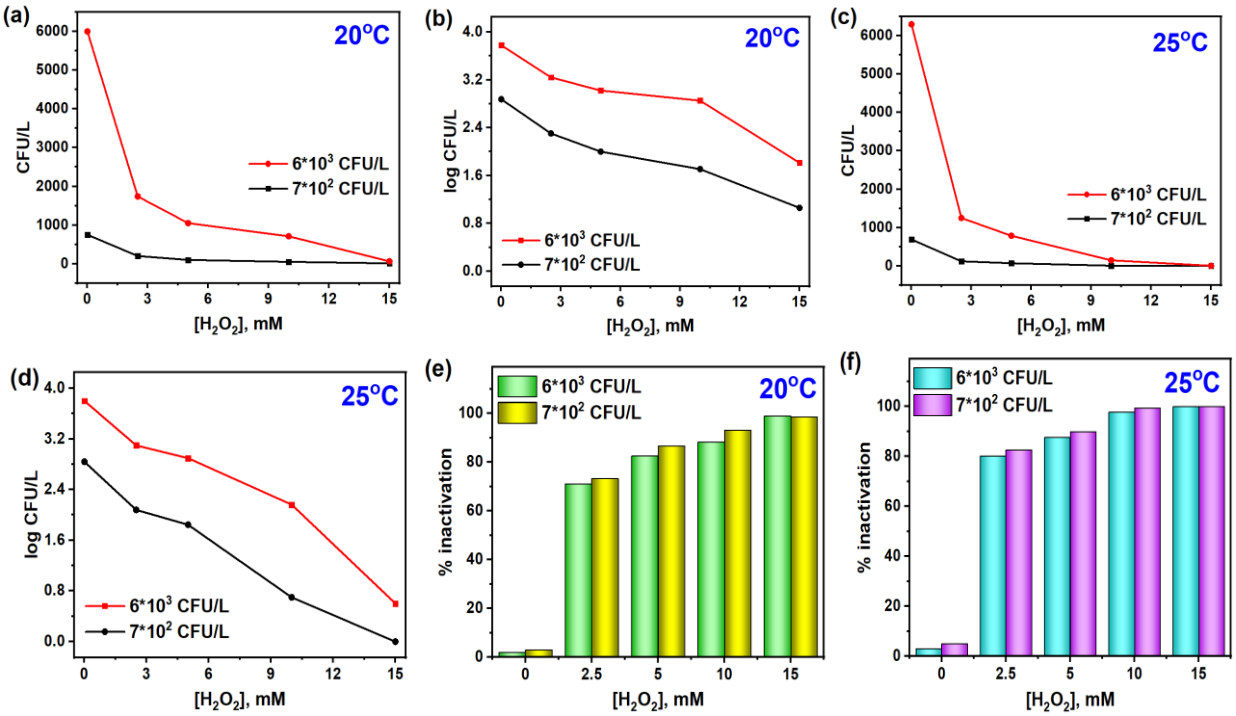

Fig. 2. (a) The *E. coli* bacteria inactivation at (a, c, e) 20 °C and (b, d, f) 25 °C: (a, c) bacteria count at the outlet of the reactor depending on the H_2O_2 concentration; (b, d) the log inactivation; (e, f) disinfection efficiency.

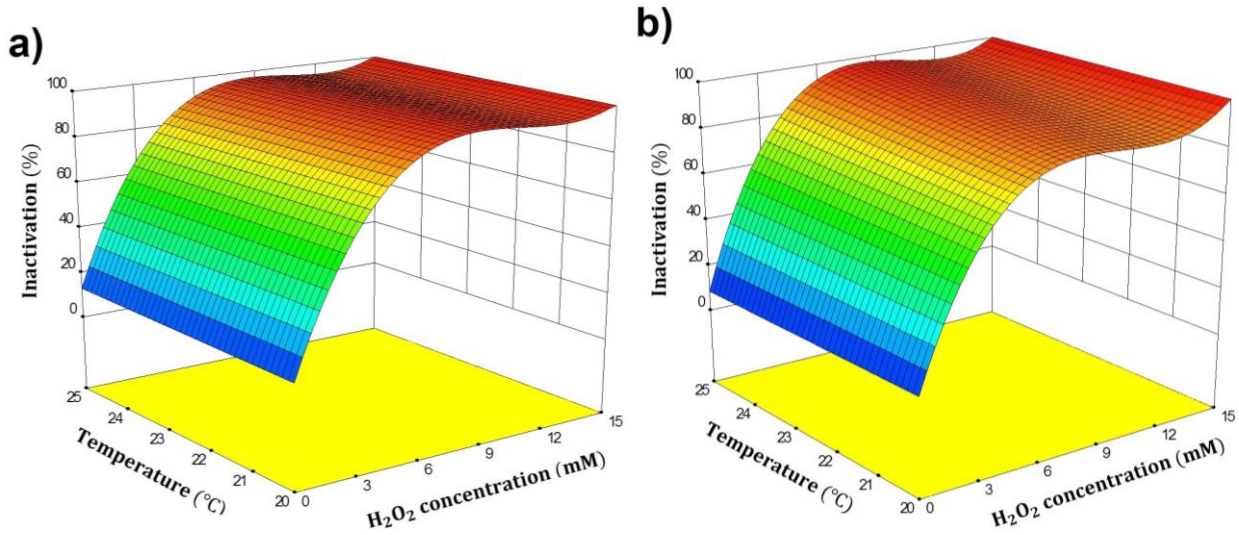

Fig. 3. (a, b) 3D graphs showing the impact of experimental parameters ($[H_2O_2]_0$ and T) on the *E. coli* inactivation: (a) $[E.\ coli]_0 = 7 \cdot 10^2$ CFU/L; (b) $[E.\ coli]_0 = 6 \cdot 10^3$ CFU/L.

Conclusions

Water disinfection using a flow fixed-bed reactor filled with $CoFe_2O_4$ granules showed good efficiency at an initial bacterial concentration of $7 \cdot 10^2$ and $6 \cdot 10^3$ CFU/L. The tests were performed at different hydrogen peroxide concentrations (0, 2.5, 5, 10, and 15 mM) and different temperatures (20°C and 25°C). The maximum efficiency of the flow reactor is observed using 15 mM H_2O_2: the inactivation of *E. coli* is more than 99 % at the initial *E. coli* concentration of $7 \cdot 10^2$ CFU/L and $6 \cdot 10^3$ CFU/L. The contact time of 52.5 min was sufficient for the *E. coli* inactivation. This approach can be used to treat industrial wastewater without adverse effects on the environment.

Acknowledgment

The authors thank the Ministry of Education and Science of Ukraine for financial support (project 0121U109476).

Nazarii Danyliuk **–** Ph.D. student, a leading specialist at the Educational and Scientific Center of Materials Science and Nanotechnology, Vasyl Stefanyk Precarpathian National University;
Ivanna Lapchuk – M.Sc., a leading specialist at the Educational and Scientific Center of Materials Science and Nanotechnology, Vasyl Stefanyk Precarpathian National University;
Tetiana Tatarchuk – Associate Professor of the Chemistry Department, Director of Educational and Scientific Center of Materials Science and Nanotechnology, Vasyl Stefanyk Precarpathian National University;
Roman Kutsyk – Doctor of Medical Sciences, Head of the Department of Microbiology, Ivano-Frankivsk National Medical University.
Volodymyr Mandzyuk – Doctor in Physics and Mathematics, Professor of Department of Computer Engineering and Electronics, Vasyl Stefanyk Precarpathian National University.

[1] J. Rodríguez-Chueca, E. Barahona-García, V. Blanco-Gutiérrez, L. Isidoro-García, A.J. Dos santos-García, *Magnetic $CoFe_2O_4$ ferrite for peroxymonosulfate activation for disinfection of wastewater*, Chem. Eng. J., 398, 125606 (2020); https://doi.org/10.1016/j.cej.2020.125606.
[2] L. Fernández, J. González-Rodríguez, M. Gamallo, Z. Vargas-Osorio, C. Vázquez-Vázquez, Y. Piñeiro, J. Rivas, G. Feijoo, M.T. Moreira, *Iron oxide-mediated photo-Fenton catalysis in the inactivation of enteric bacteria present in wastewater effluents at neutral pH*, Environ. Pollut., 266, (2020); https://doi.org/10.1016/j.envpol.2020.115181.
[3] P. V. Nidheesh, *Heterogeneous Fenton catalysts for the abatement of organic pollutants from aqueous solution: A review*, RSC Adv., 5, 40552 (2015); https://doi.org/10.1039/c5ra02023a.
[4] N. Verma, S. Vaidh, G.S. Vishwakarma, A. Pandya, *Antimicrobial nanomaterials for water disinfection*, Nanotoxicity,) 365(2020); https://doi.org/10.1016/b978-0-12-819943-5.00018-x.
[5] J.A.Z. and J.J.R. P Bautista, A F Mohedano, J A Casas, *An overview of the application of Fenton oxidation to industrial wastewaters treatment*, J. Chem. Technol. Biotechnol., 83, 1323 (2008); https://doi.org/doi:10.1002/jctb.1988.
[6] A. Basu, M. Behera, R. Maharana, M. Kumar, N.K. Dhal, A.J. Tamhankar, A. Mishra, C. Stålsby Lundborg, S.K. Tripathy, *To unsnarl the mechanism of disinfection of Escherichia coli via visible light assisted heterogeneous photo-Fenton reaction in presence of biochar supported maghemite nanoparticles*, J. Environ. Chem. Eng., 9 (2021); https://doi.org/10.1016/j.jece.2020.104620.
[7] N. Thomas, D.D. Dionysiou, S.C. Pillai, *Heterogeneous Fenton catalysts: A review of recent advances*, J. Hazard. Mater., 404, 124082 (2021); https://doi.org/10.1016/j.jhazmat.2020.124082.
[8] I. de la Obra Jiménez, S. Giannakis, D. Grandjean, F. Breider, G. Grunauer, J.L. Casas López, J.A. Sánchez Pérez, C. Pulgarin, *Unfolding the action mode of light and homogeneous vs. heterogeneous photo-Fenton in bacteria disinfection and concurrent elimination of micropollutants in urban wastewater, mediated by iron oxides in Raceway Pond Reactors*, Appl. Catal. B Environ., 263 (2020); https://doi.org/10.1016/j.apcatb.2019.118158.
[9] C.S. Nóbrega, S.R. Pauleta, *Reduction of hydrogen peroxide in gram-negative bacteria – bacterial peroxidases*, Adv. Microb. Physiol. 74, 415 (2019); https://doi.org/10.1016/bs.ampbs.2019.02.006.
[10] Y. Liu, Z. Guo, F. Li, Y. Xiao, Y. Zhang, T. Bu, P. Jia, T. Zhe, L. Wang, *Multifunctional Magnetic Copper Ferrite Nanoparticles as Fenton-like Reaction and Near-Infrared Photothermal Agents for Synergetic Antibacterial Therapy*, ACS Appl. Mater. Interfaces, 11, 31649 (2019); https://doi.org/10.1021/acsami.9b10096.
[11] T. Tatarchuk, N. Danyliuk, I. Lapchuk, W. Macyk, A. Shyichuk, R. Kutsyk, V. Kotsyubynsky, V. Boichuk, *Oxytetracycline removal and E . Coli inactivation by decomposition of hydrogen peroxide in a continuous fixed bed reactor using heterogeneous catalyst*, J. Mol. Liq., 366, 120267 (2022); https://doi.org/10.1016/j.molliq.2022.120267.
[12] X. Huang, X. Hou, J. Zhao, L. Zhang, *Hematite facet confined ferrous ions as high efficient Fenton catalysts to degrade organic contaminants by lowering H_2O_2 decomposition energetic span*, Appl. Catal. B Environ, 181, 127 (2016); https://doi.org/10.1016/J.APCATB.2015.06.061.
[13] G.D.L.P. Vargas, U. Federal, C. Erechim, A. Dom, J. Hoffmann, E. Rs, *Kinetics of Escherichia coli and total coliform inactivation by oxidation with hydrogen peroxide*, Quím. Nova, 36, 252 (2013); https://doi.org/10.1590/S0100-40422013000200009.
[14] A. Wright, B. Uprety, A. Shaw, G. Shama, F. Iza, *Effect of humic acid on E. coli disinfection in a microbubble-gas plasma reactor*, J. Water Process Eng., 31, 100881 (2019); https://doi.org/10.1016/j.jwpe.2019.100881.
[15] L.Y. Ozer, A. Yusuf, J.M. Uratani, B. Cabal, L.A. Díaz, R. Torrecillas, J.S. Moya, J. Rodríguez, G. Palmisano, *Water microbial disinfection via supported nAg/Kaolin in a fixed-bed reactor configuration*, Appl. Clay Sci., 184 (2020); https://doi.org/10.1016/j.clay.2019.105387.

[16] C. Pablos, R. Van Grieken, J. Marugán, B. Moreno, *Photocatalytic inactivation of bacteria in a fixed-bed reactor: Mechanistic insights by epifluorescence microscopy*, Catal. Today, 161, 133 (2011); https://doi.org/10.1016/j.cattod.2010.10.051.
[17] I. Thakur, A. Verma, B. Örmeci, *Mathematical modeling of E. coli inactivation in water using Fe-TiO_2 composite in a fixed bed reactor*, Sep. Purif. Technol., 260 (2021); https://doi.org/10.1016/j.seppur.2020.118242.
[18] S. Bharti, S. Mukherji, S. Mukherji, *Water disinfection using fixed bed reactors packed with silver nanoparticle immobilized glass capillary tubes*, Sci. Total Environ., 689, 991 (2019); https://doi.org/10.1016/j.scitotenv.2019.06.482.
[19] S. Raffellini, M. Schenk, S. Guerrero, S.M. Alzamora, *Kinetics of Escherichia coli inactivation employing hydrogen peroxide at varying temperatures, pH and concentrations*, Food Control., 22, 920 (2011); https://doi.org/10.1016/j.foodcont.2010.11.027.
[20] S. Mitra, P.S. Veluri, A. Chakraborthy, R.K. Petla, *Electrochemical Properties of Spinel Cobalt Ferrite Nanoparticles with Sodium Alginate as Interactive Binder*, ChemElectroChem., 1, 1068 (2014); https://doi.org/10.1002/celc.201400026.
[21] S. Zhao, D. Ma, *Preparation of $CoFe_2O_4$ nanocrystallites by solvothermal process and its catalytic activity on the thermal decomposition of ammonium perchlorate*, J. Nanomater., 2010, (2010); https://doi.org/10.1155/2010/842816.
[22] M.I.A. Abdel Maksoud, G.S. El-Sayyad, A.M. El-Khawaga, M. Abd Elkodous, A. Abokhadra, M.A. Elsayed, M. Gobara, L.I. Soliman, H.H. El-Bahnasawy, A.H. Ashour, *Nanostructured Mg substituted Mn-Zn ferrites: A magnetic recyclable catalyst for outstanding photocatalytic and antimicrobial potentials*, J. Hazard. Mater., 399, 123000 (2020); https://doi.org/10.1016/j.jhazmat.2020.123000.

Назарій Данилюк[1], Іванна Лапчук[1], Тетяна Татарчук[1],
Роман Куцик[2], Володимир Мандзюк[1]

Інактивація бактерій за допомогою шпінельного кобальт-феритного каталізатора

[1] *Прикарпатський національний університет імені Василя Стефаника, Івано-Франківськ, Україна, danyliuk.nazariy@gmail.com*
[2] *Івано-Франківський національний медичний університет, Івано-Франківськ, Україна, rkutsyk@ifnmu.edu.ua*

В роботі досліджено інактивацію бактерій *E. coli* з використанням пероксиду водню (H_2O_2) і гранульованого каталізатора фериту кобальту в протічному реакторі з нерухомим шаром. Каталізатор $CoFe_2O_4$ синтезували методом співосадження, гранулювали та відпалювали при 1150°C. Для аналізу кристалічної структури каталізатора використовували Х-променевий аналіз. Каталізатор $CoFe_2O_4$ продемонстрував хорошу каталітичну активність щодо інактивації бактерій у присутності H_2O_2. Збільшення концентрації пероксиду водню підвищує ефективність інактивації. Реактор демонструє інактивацію бактерій *E. coli* на рівні 99.94% при концентрації пероксиду водню 15 мМ і початковій концентрації бактерій $6 \cdot 10^3$ КУО/л. Знезараження води за допомогою реактора з нерухомим шаром демонструє широкі перспективи для його промислового використання.

Ключові слова: реактор з нерухомим шаром; *E. coli*; кобальтовий ферит; пероксид водню; інактивація бактерій.

PHYSICS AND CHEMISTRY OF SOLID STATE
V. 24, No. 2 (2023) pp. 262-268
Section: Physics

DOI: 10.15330/pcss.24.2.262-268

Vasyl Stefanyk Precarpathian National University

ФІЗИКА І ХІМІЯ ТВЕРДОГО ТІЛА
Т. 24, № 2 (2023) С. 262-268
Фізико-математичні науки

PACS: 33.20.Fb; 73.20.Mf; 78.30.-j ISSN 1729-4428

N.V. Mazur[1], A.V. Lysytsya[2], M.V. Moroz[3], B.D. Nechyporuk[2], B.P. Rudyk[3], V.M. Dzhagan[1,4], O.A. Kapush[1], M.Ya. Valakh[1], V.O. Yukhymchuk[1]

Physical properties of nanocrystaline PbS synthesized by electrolytic method

[1]*Lashkaryov Institute of Semiconductors Physics, National Academy of Sciences of Ukraine, Kyiv, Ukraine,* kapush-olga@ukr.net
[2] *Rivne State University of* Humanities, *Rivne, Ukraine*
[3]*National University of Water Management and Environmental Management, Rivne, Ukraine*
[4] *Physics Department, Taras Shevchenko National University of Kyiv, Kyiv, Ukraine*

The possibility of obtaining nanocrystaline lead sulfide by an electrolytic method using lead electrodes is demonstrated, and the influence of temperature on the synthesis process is investigated. Based on the results of X-ray diffraction studies, the chemical and phase composition of the obtained samples is determined, as well as the parameters of the unit cell of the crystals lattice. The size of the nanocrystallites and the magnitude of residual mechanical strain in them is determined using the methods of Debye-Scherrer and Williamson-Hall. The results of X-ray diffraction are in agreement with the results of the Raman scattering on phonons.

Keywords: lead sulfide, X-ray diffraction, nanocrystals, Debye-Scherrer formula, Williamson-Hall method, Raman scattering, phonons.

Received 18 November 2022; Accepted 3 April 2023.

Introduction

Lead sulfide (PbS) belongs to narrow-bandgap chalcogenide semiconductors, it has a band gap of 0.41 eV and crystallizes in a cubic crystal system [1]. Due to this, PbS bulk crystals and thin films are widely used in IR detectors, in particular for detecting radiation in the wavelength regions from 1 to 3 μm, which can operate in the temperature range from 77 to 300 K [2]. Due to its unique optoelectronic properties, lead sulfide is also one of the traditional photovoltaic materials [3], and promising for numerous applications in modern optoelectronic devices [3-5], for applications in global positioning systems, software radio systems, environmental monitoring satellites, etc.

In recent years, interest in the development of semiconductor nanostructured materials has been growing rapidly due to their unique physical and chemical properties [6-12]. This is due to their potential application in the field of solar cells of a new generation, optoelectronic devices, photoconductors, sensors, and infrared detector devices. The attractiveness of PbS nanocrystals stems from the dependence of their properties on size, shape, doping, tunable surface chemistry, and the low cost synthesis. The synthesis of PbS nanocrystals with different morphologies and the corresponding effect on material properties is of great importance in the process of finding new applications in electroluminescent devices, such as light-emitting diodes [7-9]. PbS nanocrystals are especially attractive for devices related to infrared radiation since the energy of their first exciton transition can be easily varied from visible to infrared ranges [7]. Lead sulfide has a large Bohr radius (18 nm) [7], and therefore strong quantization effects can be achieved even for relatively large sizes. The possibility of multiphoton absorption in PbS is extremely useful for the efficiency increase of photoelectronic devices [10]. PbS has a huge potential also in the field of electrochemical biosensors, as well as effective antimicrobial drugs [6, 11].

Semiconductor nanocrystals are obtained by various methods, such as laser sputtering, electrochemical deposition, thermal and magnetron sputtering, mechanical-chemical crushing, chemical deposition, molecular beam epitaxy, synthesis in colloidal solutions, hydrothermal synthesis, electric discharge in water, etc. [12, 13]. In the synthesis of nanomaterials, the choice of research methods is of great importance, especially for controlling dimensional and structural characteristics. It is known that transmission scanning microscopy, optical studies, and X-ray structural analysis are the main methods of studying the dispersion of particles [1,14-17].

I. Experiment and materials

Lead sulfide was obtained by the electrolytic method in an open glass electrolyzer with lead electrodes. A stabilized direct current source was used to power the electrolyzer. Distilled water and the following reagents were used to prepare the electrolyte: sodium thiosulfate ($Na_2S_2O_3$ $5H_2O$), sodium chloride (NaCl), and sodium carbonate (Na_2CO_3). Electrolyte concentration was the next: 12.5 g/l in the case of using $Na_2S_2O_3$; 0.625 g/l in the case of NaCl; 6.25 g/l in the case of Na_2CO_3. The synthesis process was carried out at the temperature of the electrolyte, which varied from room temperature to 100 C. The duration of the synthesis process was 3 hours, and the current density was 1.3×10^{-2} A/cm^2. For uniform use of the electrode material, the direct current was reversed after 30 min. After the end of the electrolysis process, the electrolyte was filtered using a paper filter and the resulting powder was washed with five times the volume of distilled water. Samples were air-dried at room temperature.

X-ray studies were carried out on a DRON-4 diffractometer using CuK_α radiation at room temperature. Scanning of XRD pattern was performed according to the Bragg-Brentano scheme (θ-2θ). The anode voltage and current were 41 kV and 21 mA, respectively. The scanning step of the XRD pattern is 0.05, and the exposure time is 5 s.

For a detailed analysis of experimental XRD patterns, each experimental reflex was described by a Gaussian function, as a result of which the following information was obtained: angular position 2θ, FWHM (full width at half maximum) β, the integrated intensity I. Obtained results were used to interpret experimental XRD patterns and calculate the sizes of nanocrystallites.

Raman light scattering spectra of samples were studied in the backscattering geometry at room temperature. Experimental spectra were recorded using a single-stage spectrometer MDR-23 (LOMO) equipped with a cooled CCD detector (Andor iDus 420, UK). Laser radiation with a wavelength of 457 nm (diode-pumped solid-state laser, CNI Laser) was used as an excitation source for Raman spectra.

II. Results and discussion

Figure 1 shows experimental XRD patterns of samples obtained by the electrolytic method using different compositions and temperatures of the electrolyte. Using the known interplanar distances and the Wulff-Bragg formula [17,18]:

$$2d \cdot \sin\theta = k \cdot \lambda,$$

where d – interplanar distance; θ – diffraction angle; k – order of the diffraction maximum; λ – wavelength of X-ray radiation, the angular positions of the 2θ reflexes for lead sulfide were calculated. Experimental characteristics of X-ray pattern reflexes (angular position and intensity) were compared with calculations and literature data [6, 17, 19, 20]. It was established that the XRD patterns of the samples shown in Fig. 1 (a) and Fig. 1 (b), contain intense reflexes corresponding to PbS and, accordingly, have the following angular positions 2 θ with Miller indices: 26.1 (111); 30.2 (200); 43.2 (220); 51.1; (311); 53.5 (222); 62.7 (400). Thus, using an electrolyte based on $Na_2S_2O_3$ at room and 98 C temperatures allows obtaining lead sulfide without a noticeable content of other compounds.

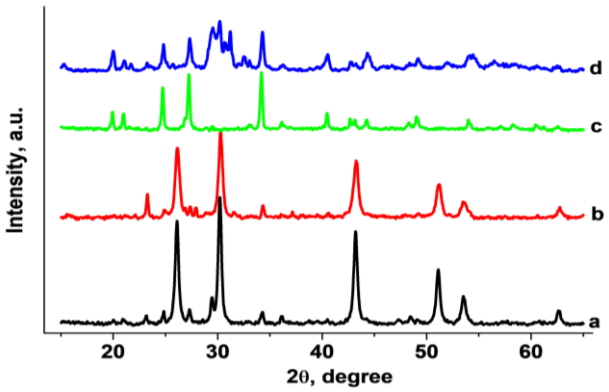

Fig. 1. XRD patterns of samples synthesized by the electrolytic method: a – electrolyte is made using $Na_2S_2O_3$, electrolyte temperature is 98 C; b – electrolyte is made using $Na_2S_2O_3$, the temperature of electrolyte is 23 C; c – electrolyte made using Na_2CO_3, the electrolyte temperature 20 C; d – electrolyte is made using NaCl, the temperature of the electrolyte is 98 C.

The above XRD patterns (a) and (b) show low-intensity reflexes that do not belong to PbS. It can be assumed that they may refer to lead carbonate and oxide, since we previously showed [21, 22] that when trying to keep cadmium sulfide and zinc oxide by the electrolytic method at room temperature, in addition to these semiconductor nanocrystals, cadmium carbonate and hydrozincite are formed, respectively. Therefore, in this work, two control samples were synthesized - when using an electrolyte based on sodium carbonate and sodium chloride. The XRD patterns of these samples are shown in Fig. 1 (c) and Fig. 1 (d), respectively. A detailed analysis of these patterns showed that there are reflections on them that belong to $PbCO_3$ and two modifications of lead oxide. Thus, when obtaining lead sulfide by the electrolytic method, carbonate and lead oxide are minor impurities. Carbon dioxide, which is necessary for the lead carbonate formation, is one of the gases dissolved in electrolytes during the electrolysis process since an open electrolyzer is used in our case.

Parameters of the elementary cell are fundamental

values in the identification of crystalline substances, as well as in the determination of chemical bond lengths, the study of transitions from one crystalline phase to another, component composition of solid solutions, and the nature of defects in crystals. The accuracy of determining crystallographic parameters of the sample is affected by several factors, including absorption and refraction of X-rays in the sample, a divergence of the primary beam, dispersion, Lorentz factor and polarization, temperature, etc. [18]. Therefore, it is best to use single crystals to determine the crystallographic parameters of alloys. In the case of nanocrystalline samples, the task is complicated by the large FWHM and low intensity of the peaks in the XRD pattern. In addition, even in the region of large diffraction angles, separation of $K_{\alpha 12}$ doublet is not observed. Therefore, we used the extrapolation method to estimate the parameters of elementary cells, since almost all systematic errors of X-ray measurements tend to zero at the diffraction angle θ = 90 [18]. Nanocrystalline PbS obtained in this work, the XRD patterns of which are shown in Fig. 1 (a)-(b), crystallizes in the sphalerite structure, and therefore, using the Wulff-Bragg formula and the quadratic form for cubic crystal system [18], it is possible to calculate the value of unit cell parameter:

$$1/d^2 = (h^2 + k^2 + l^2)/\alpha^2,$$

where a is the crystal lattice parameter; h, k, l are indices of Miller planes.

As an extrapolation function, we used the function [17, 18]

$$f(\theta)=0.5(\cos^2\theta / \sin\theta + \cos^2\theta /\theta).$$

Figure 2 shows the dependence of the unit cell parameter of PbS nanocrystals determined from various reflections on the value of the extrapolation function. A slight deviation of experimental points from linear dependence is visible, and therefore extrapolation line was found by the method of least squares. Calculated values of unit cell parameter are equal to a = 0.5938 nm and a = 0.5935 nm for samples obtained at electrolyte temperatures of 98 °C and 23 °C, respectively, which is in good agreement with the literature data for single-crystal lead sulfide a = 0.5936 nm [20].

The results of processing experimental XRD patterns were also used to calculate the size of nanocrystals using Debye–Scherrer formula [23]:

$$D = 0.89\lambda/(\beta \cdot \cos\theta),$$

where λ is the wavelength of X-ray radiation; β is the FWHM of the reflex; θ is the diffraction angle. The physical value of the FWHM is calculated by the formula:

$$\beta = (\beta_1^2 - \beta_2^2)^{1/2},$$

where β_1 is the experimental value of the FWHM of the XRD reflex FWHM; β_2 is the instrumental value of the X-ray reflex FWHM. The instrumental value of the X-ray reflexes FWHM was determined based on the analysis of XRD patterns of silicon and Al_2O_3 reference powders, which were obtained under the same conditions.

Using Debye–Scherrer formula, the nanocrystallite size was calculated from all six reflexes and the average value of obtained results was found. As a result, the following sizes of nanocrystals were obtained: 25.9 nm for the sample synthesized at a temperature of 98 °C and 18.8 nm for the case of 23 °C.

The use of Debye–Scherrer formula is based on X-ray reflex FWHM dependence on the particle size, and FWHM increases as size decrease. In addition, it is known that FWHM is affected by mechanical stresses that arise due to defects in a crystal structure. In the case of nanocrystals, defects can appear because a significant part of atoms in them is on the surface, therefore, as the size of nanocrystals decreases, the contribution of surface atoms (surface stress) will increase.

Therefore, to determine the size and mechanical stresses that may be inherent in PbS nanocrystals, we used Williamson-Hall method [24]. In this method, the FWHM of the reflex is described by the following formula:

$$\beta = 0.89\,\lambda/(D\,\cos\theta) + 4\,\varepsilon\,tg\,\theta,$$

where λ is the wavelength of X-ray radiation, and ε is the relative elongation. In the last formula, the first term shows contribute to the FWHM is caused by the dimensional effect and the second – by mechanical stresses. We write the last dependence in the form:

$$\beta\,\cos\theta = 0.89\lambda/D + 4\,\varepsilon\sin\theta.$$

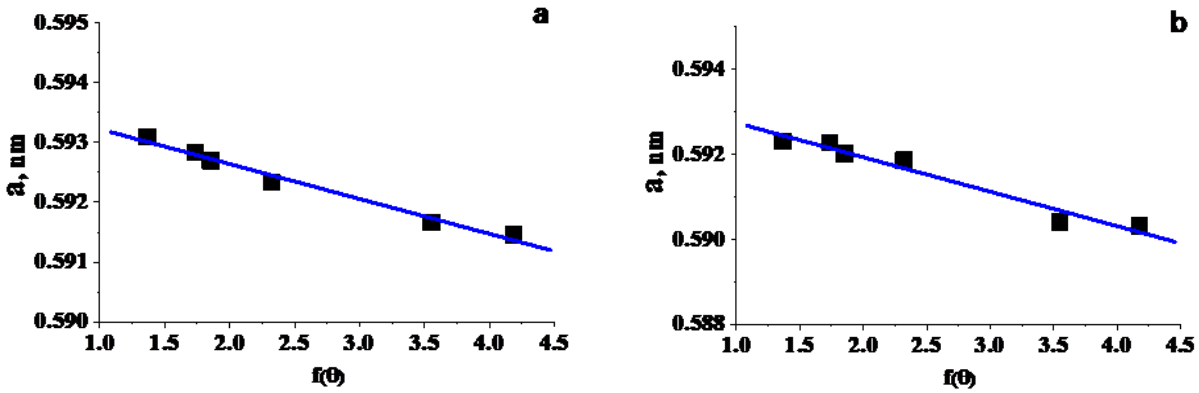

Fig. 2. Graphical extrapolation to determine the crystal lattice parameter of nanocrystalline lead sulfide, obtained at the temperature of the electrolyte: 98 C – a, 23 C – b.

According to Hooke's law, during elastic deformations, the magnitude of mechanical stress is equal to:

$$\sigma = E \cdot \varepsilon,$$

where E is Young's modulus. Having determined the relative elongation from Hooke's law, we obtain the dependence:

$$\beta \cdot \cos\theta = 0.89\lambda/\mathrm{D} + 4 \cdot \sigma \cdot \sin\theta/E.$$

If this dependence is plotted in the coordinate system <4 sinθ/E, β cosθ>, then we get a straight line from which we can find the nanocrystal size D and the magnitude of mechanical stress σ. For single crystals, Young's modulus will depend on the direction inside the single crystal, that is, on the values of the Miller indices (h k l) and the type of crystal system. This dependence for the cubic system is described by the formula [18]:

$$E^{-1} = s_{11} - (2\,s_{11} - 2\,s_{12} - s_{44})(h^2\,k^2 + k^2\,l^2 + l^2\,h^2)/(h^2 + k^2 - l^2)^2\,,$$

where s_{11}, s_{12}, s_{44} are coefficients of elastic compliance. Using the known values of the coefficients of elastic compliance for the cubic modification of lead sulfide $s_{11} = 1.23 \cdot 10^{-12}$ Pa^{-1}, $s_{12} = -0.33 \cdot 10^{-12}$ Pa^{-1}, $s_{44} = 4.0 \cdot 10^{12}$ Pa^{-1} [25], as well as the Miller indices of reflections observed on the experimental XRD pattern, we previously calculated the values of Young's moduli depending on the direction inside the single crystal.

Figure 3 shows the use of the Williamson-Hall method to determine the size of nanocrystals and mechanical stresses for two samples. The figure shows the deviation of experimental points from the linear dependence, and therefore the extrapolation line was found by the method of least squares. As a result of using the Williamson-Hall method, the size of PbS nanocrystals was found to be 36.6 nm and the value of mechanical stresses was 1.3×10^8 Pa (tensile stress) for the samples obtained at a temperature of 98 C, as well as 39.4 nm and 2.5×10^8 Pa for a temperature of 23 C. The sizes of nanocrystals calculated by Williamson-Hall method are larger than the sizes obtained based on Debye–Scherrer formula. Mechanical tensile stresses for the sample synthesized at a temperature of 23 C are almost two times higher than for the sample obtained at a temperature of 98 C. The latter may indicate that nanocrystals obtained at room temperature have significantly more defects.

Similar results were obtained by the authors of [1], who studied the properties of PbS thin films formed on glass substrates by a chemical method using solutions of lead acetate and thiourea at room temperature. The sizes of nanoparticles in work [1] were also determined by Debye–Scherrer and Williamson–Hall methods and their values varied from 19 to 23 nm. The authors of the paper [11] studied nanoparticles of lead sulfide obtained by centrifugation of a lead chloride solution and sulfur powder. When the temperature changed from 10 to 40 C, an increase in size from 10 to 25 nm was observed.

Figure 4 represents Raman spectra of two samples of lead sulfide nanocrystals synthesized by the electrolytic method at temperatures of 98 and 23 C, XRD patterns of which are shown in Fig. 1 (a, b), respectively. The figure shows that the spectra of these samples are quite similar. the observed Raman bands were best fitted with a Gaussian function, from which frequency, FWHM, and integral intensity was obtained. The spectra contain two intense scattering bands with a frequency position of 153 and 218 cm^{-1}, as well as bands of low intensity – 88, 191, and 243 cm^{-1}. In addition, the FWHMs are slightly larger at the synthesis temperature of 23 C than at the temperature of 98 C: 11.4 and 10.7 cm^{-1}, respectively, for the band of 88 cm^{-1}, 8.2, and 7.9 cm^{-1} for band 153 cm^{-1}. In the case of a band with a frequency of 218 cm^{-1}, they are the same and equal to 5.2 cm^{-1}.

Bands with frequencies of 88 and 218 cm^{-1} can be attributed to scattering by transverse (TO) and longitudinal (LO) optical phonons at the center of Brillouin zone [26]. The scattering band of LO phonons for PbS is not active in Raman light scattering spectra but is active in IR spectra. It can be manifested in Raman spectra, as noted by the authors of works [27-29], under

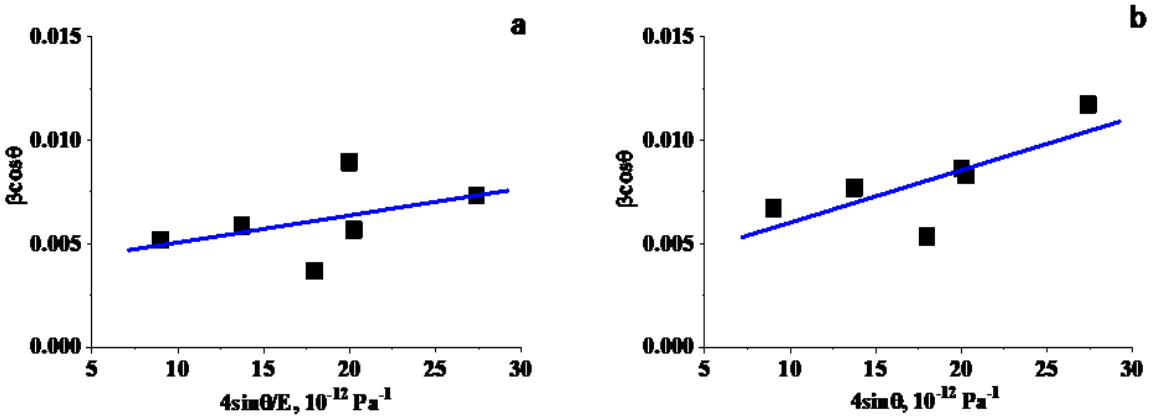

Fig. 3. Results of using Williamson-Hall method for PbS nanocrystals obtained at the temperature of the electrolyte: 98 C – a, 23 C – b.

conditions of resonant or quasi-resonant excitation of Raman spectra due to electron-phonon interaction. In addition, the authors of [30] observed an absorption band at LO phonons (210 cm^{-1}) in the IR spectra. The same opinion on the nature of these scattering bands is held by the authors of works [30, 31].

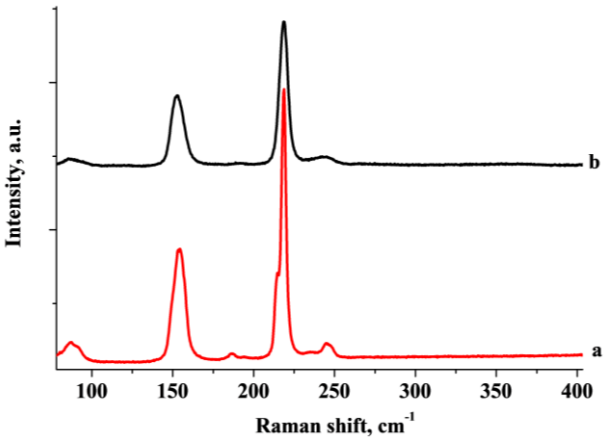

Fig. 4. Raman spectra of samples synthesized using $Na_2S_2O_3$-based electrolyte at temperatures:
a – 98 C; b – 23 C.

In [27], the authors studied Raman spectra of natural PbS and calculated the dispersion curves of lead sulfide for three important directions of Brillouin zone: [100], [111], and [110], as well as the total density of phonon states based on the dispersion curves. They suggested that the band at 190 cm^{-1} is due to the combination of TO + LA phonons along the Δ or Σ direction, and the band at 155 cm^{-1} is due to the combination of TO + TA phonons along the Σ direction. The authors of the work [31] compared Raman spectra of polycrystalline and nanocrystalline PbS and observed a higher value of the scattering frequency for LO phonons in NC, 210 cm^{-1}, compared to a bulk crystal, from 206 cm^{-1}. In our samples, the frequency of the corresponding band is even higher, 218 cm^{-1}, although the size of NC is much larger than in [31], about 20 nm. Therefore, the frequency position of this band in our nanostructures can be determined not by the size effect, but by the dominant contribution of phonons from different dispersion branches of phonons [27].

In [31], thin films of lead sulfide obtained by the chemical method were studied, and scattering bands with frequencies of 148, 192, and 201 cm^{-1} were recorded in Raman spectra. The authors of this paper believe that the band with a frequency of 201 cm^{-1} corresponds to scattering by LO phonons of the center of Brillouin zone, and the band with a frequency of 192 cm^{-1} corresponds to scattering by surface phonons. The nature of the band with a frequency of 148 cm^{-1} is not discussed in [32].

In [33], it is believed that the scattering band of 151 cm^{-1} is due to the combination of TO + TA phonons, and 194 cm^{-1} is due to surface phonons. When studying PbS films in [34], Raman spectra were interpreted as scattering by LO phonons (210 cm^{-1}) and surface phonons (205 cm^{-1}). An alternative explanation for the origin of the band at 153 cm^{-1} could be the PbO phase [35], but its spectrum is expected to contain a band in the region of 270-280 cm^{-1}, almost equally intense, which is not observed in the spectra of our samples.

For the weak band at 243 cm^{-1}, it is currently impossible to establish the origin. In some works, weak bands in the range of 240-260 cm^{-1} were also observed, but their nature was not discussed [28].

It is known that PbS nanostructures can undergo significant oxidation, both during synthesis and measurement of Raman spectra since the oxidation is a photostimulated process [36]. However, in the spectra of nanocrystalline PbS obtained in this work by the method of electrolytic synthesis, there are no bands of any of the oxide forms, at least for samples synthesized using an electrolyte based on $Na_2S_2O_3$ (Fig. 4).

Conclusions

This work shows the possibility of synthesizing nanocrystalline lead sulfide by the electrolytic method using lead electrodes and an electrolyte based on sodium thiosulfate. When the temperature of synthesis (electrolyte) increases, the size of PbS nanocrystals increases, and the mechanical tensile stresses acting in the them decrease. The results of Raman scattering spectra are correlated with the results of X-ray structural studies.

Mazur N. – Ph D;
Lysytsya A. – Ph D., Associate Professor of the department of ecology, geography and tourism of Rivne State University of Humanities;
Moroz M. – Dr. Sci, Associate Professor of the Department of Chemistry and Physics of National University of Water Management and Environmental Management;
Nechyporuk B. – Ph D., Associate Professor of the Department of Physics and Astronomy and Teaching Methods of Rivne State University of Humanities;
Rudyk B. – Ph D., Associate Professor of the Department of Chemistry and Physics of National University of Water Management and Environmental Management.
Dzhagan V. - Doctor of Physical and Mathematical Sciences, Professor at Department of Optics and Spectroscopy of Institute of Semiconductor Physics NAS of Ukraine;
Kapush O. – Ph D;
Valakh M. - Doctor of Physical and Mathematical Sciences, Professor at Department of Optics and Spectroscopy of Institute of Semiconductor Physics NAS of Ukraine;
Yukhymchuk V. - Doctor of Physical and Mathematical Sciences, Professor at Department of Optics and Spectroscopy of Institute of Semiconductor Physics NAS of Ukraine.

[1] N. Choudhury and B.K. Sarma, *Structural characterization of lead sulfide thin films by means of X-ray line profile analysis*, Bull. Mater. Sci., 32 (1), 43 (2009); https://doi.org/10.1007/s12034-009-0007-y.

[2] A.B. Rohom, P.U. Londhe, P.R. Jadhav, G.R. Bhand, and N.B. Chaure. *Studies on chemically synthesized PbS thin films for IR detector application*, J. Mater. Sci. 28, 17107 (2017); https://doi.org/10.1007/s10854-017-7637-4.

[3] M.H. Jameel, S. Saleem, M. Hashim, [et al], *A comparative study on characterizations and synthesis of pure lead sulfide (PbS) and Ag-doped PbS for photovoltaic applications*, Nanotechnology Reviews, 10, 1484 (2021); https:doi.org/10.1515/ntrev-2021-0100.

[4] Th. Bielewicz, S. Dogan, and Ch. Klinke. Tailoring the Height of Ultrathin PbS Nanosheets and Their Application as Field-Effect Transistors. *Small* 11(7), 826 (2015); https:doi.org/10.1002/smll.201402144.

[5] D.J. Asunskis, I.L. Bolotin, A.T. Wroble, A.M. Zachary, L. Hanley. Lead Sulfide Nanocrystal-Polymer Composites for Optoelectronic Applications. Macromol. Symp., 268, 33 (2008); https:doi.org/10.1002/masy.200850807.

[6] L.F. Koao, F.B. Dejene, H.C. Swart, *Synthesis of PbS Nanostructures by Chemical Bath Deposition Method*, Int. J. Electrochem. Sci., 9, 1747 (2014);

[7] I. Moreels, K. Lambert, D. Smeets, D. De Muynck, T. Nollet, J. C. Martins, F. Vanhaecke, A. Vantomme, C. Delerue, G. Allan, and Z. Hens, S*ize-Dependent Optical Properties of Colloidal PbS Quantum Dots*, ACS Nano, 3(10), 3023 (2009); https://doi.org/10.1021/nn900863a.

[8] M. Mozafari, F. Moztarzadeh, *Controllable synthesis, characterization and optical properties of colloidal PbS/gelatin core–shell nanocrystals*, Journal of Colloid and Interface Science, 351, 442 (2010); https://doi.org/10.1016/j.jcis.2010.08.030.

[9] M. Scheele, D. Hanifi, D. Zherebetskyy, S. T. Chourou, S. Axnanda, B. J. Rancatore, K. Thorkelsson, T. Xu, Z. Liu, L.-W. Wang, Y. Liu, and A. P. Alivisatos, *PbS Nanoparticles Capped with Tetrathiafulvalenetetracarboxylate: Utilizing Energy Level Alignment for Efficient Carrier Transport*, ACS Nano, 8(3), 2532 (2014); https://doi.org/10.1021/nn406127s.

[10] L. Cheng, Y. Cheng, J. Xu, H. Lin, Y. Wang, *Near-infrared two-photon absorption upconversion of PbS/CdS quantum dots prepared by cation exchange method*, Materials Research Bulletin 140, 111298 (2021); https://doi.org/10.1016/j.materresbull.2021.111298.

[11] A.K. Mishra, S. Saha, *Synthesis and characterization of PbS nanostructures to compare with bulk*, Chalcogenide Letters, 17(3), 147 (2020); https://doi.org/10.15251/CL.2020.173.147.

[12] D.V. Talapin, J.-S. Lee, M.V. Kovalenko and E.V. Shevchenko, *Prospects of Colloidal Nanocrystals for Electronic and Optoelectronic Applications*, Chem. Rev., 110, 389 (2010); https://doi.org/10.1021/cr900137k.

[13] S.V. Kershaw, L. Jing, X. Huang, M. Gao and A.L. Rogach, *Materials aspects of semiconductor nanocrystals for optoelectronic applications*, Mater. Horizons, 4, 155 (2017); https://doi.org/10.1039/C6MH00469E.

[14] M.T. Dieng, B.D. Ngom, P.D. Tall, M. Maaza, *Biosynthesis of $Zn_5(CO_3)_2(OH)_6$ from Arachis Hypogaea Shell (Peanut Shell) and Its Conversion to ZnO Nanoparticles*, American Journal of Nanomaterials, 7(1), 1 (2019); https://doi.org/10.12691/ajn-7-1-1.

[15] Ankita, S. Kumar, S. Saralch, D. Pathak, *Nanopowder and Thin Films of ZnO by Sol Gel Approach*, J. Nano - Electron. Phys., 11(4), 04027 (2019); https://doi.org/10.21272/jnep.11(4).04027.

[16] O.Z. Didenko, P.E. Strizhak, G.R. Kosmambetova, N.S. Kalchuk, *Synthesis and Morphology of the ZnO/MgO Low-Dimensional Quantum Systems*, Physics and Chemistry of Solid State, 10(1), 106 (2009);

[17] M. Basak, Md. L. Rahman, Md. F. Ahmed, B. Biswas, N. Sharmin. *The use of X-ray diffraction peak profile analysis to determine the structural parameters of cobalt ferrite nanoparticles using Debye-Scherrer, Williamson-Hall, Halder-Wagner and Size-strain plot: Different precipitating agent approach*,. Journal of Alloys and Compounds 895, 162694 (2022); https://doi.org/10.1016/j.jallcom.2021.162694.

[18] A. Guinier, X-ray Diffraction in Crystals, Imperfect Crystals, and Amorphous Bodies. Dover publication incorporation, New York, 1994.

[19] S. Rajathi, K. Kirubavathi, K. Selvaraju, *Structural, morphological, optical, and photoluminescence properties of nanocrystalline PbS thin films grown by chemical bath deposition*, Arabian Journal of Chemistry 10, 1167 (2017); https://doi.org/10.1016/j.arabjc.2014.11.057.

[20] M. Wati and K. Abraha, *A Study on Fabrication and Structural Characterization of PbS Thin Films*, American Journal of Biochemistry and Biotechnology, 13(4), 208 (2017); https://doi.org/10.3844/ajbbsp.2017.208.214.

[21] N.B. Danilevska , M.V. Moroz , B.D. Nechyporuk , N.E. Novoseletskiy, V.O. Yukhymchuk, *The Influence of Technological Modes on the Physical Properties of Cadmium Sulfide Nanocrystals Derived by the Electrolyte Method*, Journal of Nano- and Electronic Physics, 8(2), 02041 (2016); https://doi.org/10.21272/jnep.8(2).02041.

[22] A.V. Lysytsya, M.V. Moroz, B.D. Nechyporuk, B.P. Rudyk, B.F. Shamsutdinov, *Physical Properties of Zinc Compounds Obtained by Electrolytic Method*, Physics and Chemistry of Solid State, 22(1), 160 (2021); https://doi.org/10.15330/pcss.22.1.160-167.

[23] N.B. Danilevska, M. Moroz, N. Yu. Novoseletskyy, B.D. Nechyporuk, Б B.P. Rudyk, *The influence of technological modes on the physical properties of zinc oxide nanocrystals derived electrolyte method*, Journal of Physical Studies, 20(3), 3601-1 (2016); https://doi.org/10.30970/jps.20.3601.

[24] V.D. Mote, Y. Purushotham, B.N. Dole, *Williamson-Hall analysis in estimation of lattice strain in nanometer-sized ZnO particles*, Journal of theoretical and applied physics, 6(1), 2251 (2012); https://doi.org/10.1186/2251-7235-6-6.

[25] B. Huntington. *The Elastic Constants of Crystals*. Solid State Physics. 7, 213-351 (1958).

[26] T. D. Krauss, F.W. Wise, *Raman-scattering study of exciton-phonon coupling in PbS nanocrystals*, Phys. Rev. B, 15(55), 9860 (1997); https://doi.org/10.1103/PhysRevB.55.9860.
[27] P. G. Etchegoin, M. Cardona, R. Lauck, R. J. H. Clark, J. Serrano, and A. H. Romero, *Temperature-dependent Raman scattering of natural and isotopically substituted PbS*, Phys. stat. sol. (b) 245(6), 1125 (2008); https://doi.org/10.1002/pssb.200743364.
[28] A.G. Kontos, V. Likodimos, E. Vassalou, I. Kapogianni, Y.S. Raptis, C. Raptis, P. Falaras, *Nanostructured titania films sensitized by quantum dot chalcogenides*, Nanoscale Research Letters, 6(1), 266 (2011); https://doi.org/10.1186/1556-276X-6-266.
[29] A. Milekhin, L. Sveshnikova, T. Duda, N. Surovtsev, S. Adichtchev, D. R. T. Zahn, *Optical Phonons in Nanoclusters Formed by the Langmuir-Blodgett Technique*, Chinese Journal of Physics, 49(1), 63 (2011);
[30] J.S. Arunashree, N. P. Suresh, S. Sujesh, K.P. Vaishnav, Vishnu, S. Vishnu, M. Prabhakaran, V.V. Ison and C.O. Sreekala, *Surface Modified Lead Sulphide Quantum Dots for In Vitro Imaging of Breast Cancer Cells Adopting Confocal Raman Spectroscopy*, Int. J. Chem. Sci.: 14(4), 1844 (2016);
[31] A. V. Baranov, K. V. Bogdanov, E. V. Ushakova, S. A. Cherevkov, A. V. Fedorov, and S. Tscharntke, *Comparative Analysis of Raman Spectraof PbS Macro- and Nanocrystals*, Optics and Spectroscopy, 109(2), 268 (2010); https://doi.org/10.1134/S0030400X10080199.
[32] O. Portillo-Moreno, R. Gutierrezerez, M. Chavez Portillo, M.N. Marquez Specia, G. Hernandez-Telleza, M. Lazcano Hernandez, A. Moreno Rodrıguez, R. Palomino-Merino, E. Rubio Rosas, *Growth of doped PbS:Co^{2+} nanocrystals by Chemical Bath*, Revista, Mexicana de Fısica, 62, 456 (2016);
[33] M. Cheraghizade, R. Yousefi, F. Jamali-Sheini, A. Saaedi, *Comparative study of Raman properties of various lead sulfide morphologies*, Majlesi Journal of Telecommunication Devices, 2(1), 163 (2013);
[34] K. K. Nanda, S. N. Sahu, R. K. Soni and S. Tripathy, *Raman spectroscopy of PbS nanocrystalline semiconductors*, PHYSICAL REVIEW B, 58(23), 15405 (1998); https://doi.org/10.1103/PhysRevB.58.15405.
[35] M. Cortez-valadez, A. Vargas-ortiz, L. Rojas-blanco, H. Arizpe-chávez, M. Flores-Acosta, R. Ramírez-Bon, *Additional Active Raman Modes in α-PbO Nanoplates*, Physica E: Low-dimensional Systems and Nanostructures, 53, 146 (2013); https://doi.org/10.1016/j.physe.2013.05.006.
[36] J. L. Blackburn, H. Chappell, J. M. Luther, A. J. Nozik, J. C. Johnson, *Correlation between Photooxidation and the Appearance of Raman Scattering Bands in Lead Chalcogenide Quantum Dots*, J. Phys. Chem. Lett., 2 (6), 599 (2011); https://doi.org/10.1021/jz2000326.

Н.В. Мазур[1], А.В. Лисиця[2], М.В. Мороз[3], Б.Д. Нечипорук[2], Б.П. Рудик[3], В.М. Джаган[1], О.А. Капуш[1], М.Я. Валах[1], В.О. Юхимчук[1]

Фізичні властивості нанокристалічного сульфіду свинцю отриманого електролітичним методом

[1] Інститут фізики напівпровідників імені В.Є. Лашкарьова НАН України, м. Київ, Україна
kapush-olga@ukr.net
[2] Рівненський державний гуманітарний університет, м. Рівне, Україна
[3]Національний університет водного господарства і природокористування, Рівне, Україна
[4] Факультет фізики, Київський національний університет імені Тараса Шевченка, Київ, Україна

Досліджено можливість отримання нанокристалічного сульфіду свинцю електролітичним методом з використанням свинцевих електродів та встановлено вплив температури на процес синтезу. На основі проведених рентгеноструктурних досліджень визначено хімічний та фазовий склад отриманих сполук та розмір нанокристалітів методами Дебая-Шеррера та Вільямсона-Холла, а також визначено параметр елементарної комірки досліджуваних кристалів. Результати рентгеноструктурних досліджень порівнюються з даними, отриманими зі спектрів комбінаційного розсіювання світла цих зразків.

Ключові слова: сульфід свинцю, рентгеноструктурні дослідження, розміри нанокристалів, формула Дебая-Шеррера, метод Вільямсона-Холла, комбінаційне розсіювання світла.

PHYSICS AND CHEMISTRY OF SOLID STATE
V. 24, No. 2 (2023) pp. 269-277
Section: Chemistry

DOI: 10.15330/pcss.24.2.269-277

Vasyl Stefanyk Precarpathian National University

ФІЗИКА І ХІМІЯ ТВЕРДОГО ТІЛА
Т. 24, № 2 (2023) С. 269-277
Хімічні науки

PACS: 546.26:544.18 ISSN 1729-4428

Yu.V. Grebelna[1], E.M. Demianenko[1], M.I. Terets[1], Yu.I. Sementsov[1,2], V.V. Lobanov[1], A.G. Grebenyuk[1], V.S. Kuts[1], S.V. Zhuravskyi[1], O.V. Khora[1], M.T. Kartel[1]

Quantum-chemical studies of the interaction of partially oxidized graphene-like planes with each other

[1]*Chuiko Institute of Surface Chemistry of National Academy of Sciences of Ukraine, Kyiv, Ukraine, teretsmariya@gmail.com*
[2]*Ningbo University of Technology, Ningbo, China, ysementsov@ukr.net*

Using the methods of quantum chemistry, the energy effects of the interaction of partially oxidized graphene-like planes with each other and the effect on this characteristic of the nature of the functional groups present in the oxidized graphene-like planes, as well as the dimensions of the graphene-like planes themselves, were clarified. It was established that the reaction between the hydroxyl and aldehyde groups of two interacting graphene-like planes is the most thermodynamically probable, regardless of the dimensions of the graphene-like planes. The reaction between two carboxyl groups of different graphene-like planes is the least thermodynamically probable. To create nanocomposites by interacting graphene-like planes with each other, it is necessary that the graphene-like planes contain hydroxyl and aldehyde groups.

Keywords: oxidized graphene-like planes, chemical reaction, pyrene, coronene, density functional theory method, cluster approximation.

Received 22 January 2023; Accepted 16 May 2023.

Introduction

Creation of sp^2-hybridized carbon-carbon composite nanomaterials is a promising direction of modern science [1–4]. Nanocomposites with the specified properties, as evidenced by the literature, can be created in a wide variety of ways, in particular, in the interaction of sp^2-hybridized carbon materials with inorganic compounds and metals [5, 6], with polymers [7, 8], as well as with low molecular weight organic substances [9, 10]. Also, when obtaining new sp^2-hybridized carbon-carbon composite materials with unique properties, it was recently possible to obtain functionalized carbon materials [11–14], in particular, partially oxidized forms of graphene [15, 16]. One of the promising ways of creating carbon nanocomposites presented in [17] is its result in the production of large-scale graphene sheets by dispersing graphene particles with certain functional groups in organic solvents.

Another approach to the experimental creation of carbon nanocomposites is based on the so-called crosslinking of graphene sheets [18–20], that is, on the covalent interaction of different graphene-like planes (GLP). In particular, work [21] even proposed the concept of so-called conformational engineering, which consists in the construction of new composites from sheets of oxidized graphene. It was reported in [22] that dehydration, for example, by vacuum drying an aqueous solution of graphene oxide (GO), causes irreversible spontaneous cross-linking of its sheets. Dehydrated GO films retain their structural integrity in water, and they can no longer re-disintegrate into individual layers after stirring. At the bilayer level, after dehydration, folded GO sheets are fixed, which do not dissociate together even after sonication. Spectroscopic studies confirm the formation of new chemical bonds, suggesting a condensation-esterification reaction between GO sheets.

To find out the features of the creation of new carbon nanocomposites, computer modeling methods are successfully used, in particular, calculation schemes of quantum chemistry [23–26], as well as molecular dynamics [27–29].

It is known that the process of creating a composite material based on thermally expanded graphite (TRG) and carbon nanotubes (CNTs) consists in simultaneous deagglomeration of CNTs and intercalation of natural graphite [30]. This procedure can be carried out in two ways: electrochemical (anodic) or chemical oxidation. In our previous works [31–33], it was shown that the process of creating a carbon nanocomposite TRG-CNT occurs as follows: graphite oxidized to the first stage was hydrolyzed, washed to neutral pH, dried and heat-treated at a temperature of ~1000°C in a gas horizontal industrial furnace. Next, the obtained TRG nanocomposite powder was rolled on horizontal rolls. It was assumed that the formation of sp^2-hybridized carbon-carbon composites is related not only to the effect of physical factors (pressure, temperature) on the starting material, but also to the chemical interaction of individual partially oxidized GLPs with each other. Since there are various oxygen-containing functional groups on the surface of partially oxidized carbon graphene materials, which are capable of exhibiting significant chemical activity [34]. But it remains unknown how covalent bonding of GLPs is possible during the formation of sp^2-hybridized carbon-carbon composite materials. Therefore, the goal of the work was to find out the interaction energy of partially oxidized graphene-like planes with each other and the effect on this characteristic of the nature of functional groups that are present in oxidized GLPs using quantum chemistry methods.

I. Objects and calculation methods

Polyaromatic pyrene molecules with different functional groups on their periphery were considered as models of partially oxidized GLPs, while the functional groups were chosen so that the carbon atom near them had a different degree of oxidation, the lowest near the hydroxyl group (Fig. 1, *a*,*d*,*g*), higher - in carbonyl (Fig. 1, *b*,*e*,*h*). and the largest - in carboxyl (Fig. 1, *c*,*f*,*i*).

In addition, in order to take into account the size effect of GLP on the energy parameters of the studied reactions, graphene-like planes with a gross composition of $C_{24}H_{12}$ (coronene) were used (Fig. 1, *d*–*e*). and $C_{42}H_{16}$ (Fig. 1, *e*–*g*).

Calculations were performed using the GAMESS program (US) [35] within the framework of the density functional theory (DFT) with the B3LYP functional [36, 37] and the 6-31G(d,p) basis set, taking into account the Grimme D3 dispersion correction [38, 39] . This calculation method has proven itself well in modeling graphene-like clusters [40].

II. Results and their discussion

The first of the considered reactions consists in the interaction of GLP with a hydroxyl group on the periphery with the same graphene-like plane (Fig. 2). At the same time, there is an interaction of two hydroxyl groups of different GLPs with the release of a water molecule and the formation of a reaction product in which the GLPs are

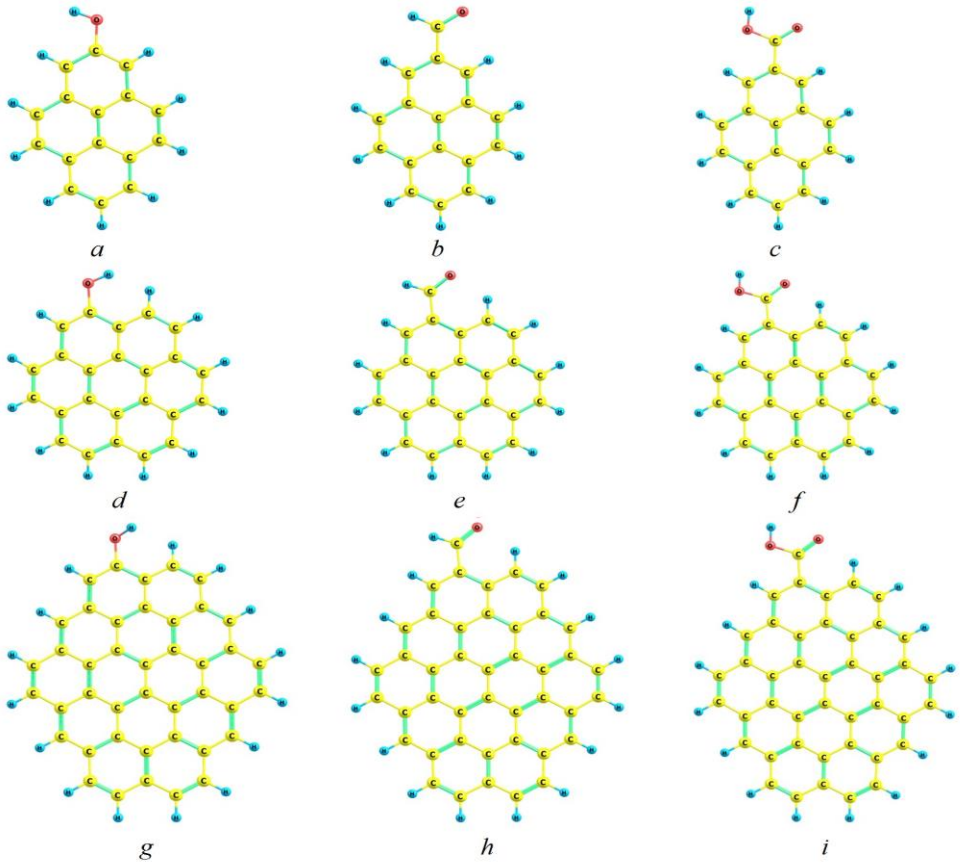

Fig. 1. Equilibrium geometry of partially oxidized GLPs of different sizes, with hydroxyl (*a*, *d*, *g*), aldehyde (*b*, *e*, *h*), and carboxyl (*c*, *f*, *i*) groups.

covalently connected to each other by an oxygen bridge. This reaction can be represented by scheme 1:

$$GLP–OH + HO–GLP \rightarrow GLP–O–GLP + H_2O. \quad \text{(Scheme 1)}$$

According to (Scheme 1), a hydrogen atom of one hydroxyl group (Fig. 2, *a*) interacts with an oxygen atom of another hydroxyl group (Fig. 2, *b*), as a result of which the bond between C–O atoms of the last group is broken and a water molecule is formed (Fig. 2, *d*), and the oxygen atom of the other hydroxyl group forms a covalent bond with the carbon atom of the second GLP. In this way, a product is formed (Fig. 2, *c*), which consists of two chemically bonded GLP planes with the help of an oxygen bridge.

The energy effect of reactions was calculated according to formula (1):

$$\Delta E_{react} = [E_{tot}(GLP–O–GLP) + E_{tot}(H_2O)] - 2\,E_{tot}(GLP–OH), \quad (1)$$

where $E_{tot}(GLP–O–GLP)$ is the total energy of the interaction product of two GLPs with hydroxyl groups, $E_{tot}(H_2O)$ is the total energy of the reaction product – H_2O, $E_{tot}(GLP–OH)$ is the total energy of the GLP with a hydroxyl group.

The energy effect of this reaction (Scheme 1), calculated by formula (1), has a positive value and is +22.2 kJ/mol (see Table).

When using larger GLP models, the reaction products are localized (Fig. 3), similar in structure to the previous case (Fig. 2, *c*).

As can be seen from Figures3, a and 3, b, despite the different sizes of the GLP, the reaction products obtained are similar to each other. It should be noted that the two GLPs in the reaction products are not located in a common plane, but placed at a small angle. For the smallest model (Fig. 2, *c*), the angle between the planes is 64.4°, for the product consisting of two coronene planes (Fig. 3, *a*), this angle is much larger and reaches 90.2°, and for the largest by the size of the reaction product (Fig. 3, *b*), the angle between the GLPs is similar to the previous one and is equal to 90.3°. This may indicate that the further increase in the size of GLPs with hydroxyl groups will have almost no effect on the angle between the planes. Therefore, in the reaction products (Scheme 1), the GLPs are located almost perpendicular to each other, regardless of the size of the initial GLPs. This non-coplanarity of the two GLPs is apparently caused by a significant repulsion of a pair of closely spaced hydrogen atoms of neighboring graphene-like planes, one from each of them (see Figs. 2 and 3). As the size of the graphene-like planes in the reaction product increases, their mutual repulsion increases, as can be seen from the distances between the hydrogen atoms of different GLPs (2.8 Å for pyrene, 3.3 Å for coronene, and 3.5 Å for the maximum size GLP).

The energy effect of the reaction during product formation (Fig. 3, *a*), calculated according to formula (1), also has a positive, but much smaller value, as in the previous case, and is +1.3 kJ/mol. A similar value of the energy of the formation of the product of the reaction involving the maximum-sized GLP among those considered in the work is even closer to 0, but it is slightly

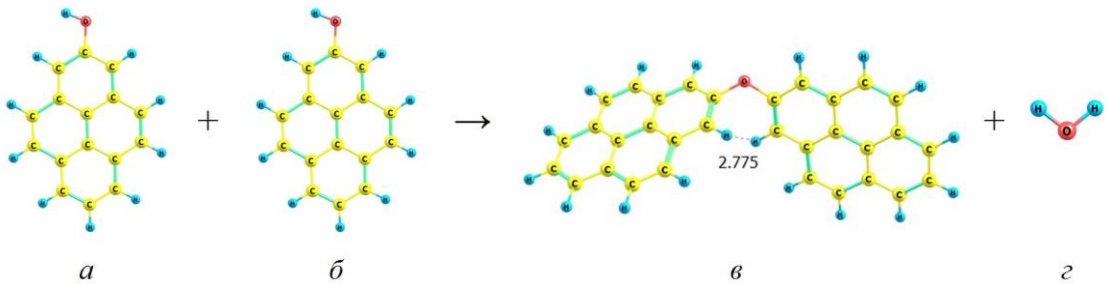

Fig. 2. Equilibrium geometry of the molecules of the starting substances *(a, b)* and reaction products (*c, d*) of the interaction of two GLPs with a hydroxyl group on the periphery,
(here and further the distances between atoms are given in Å).

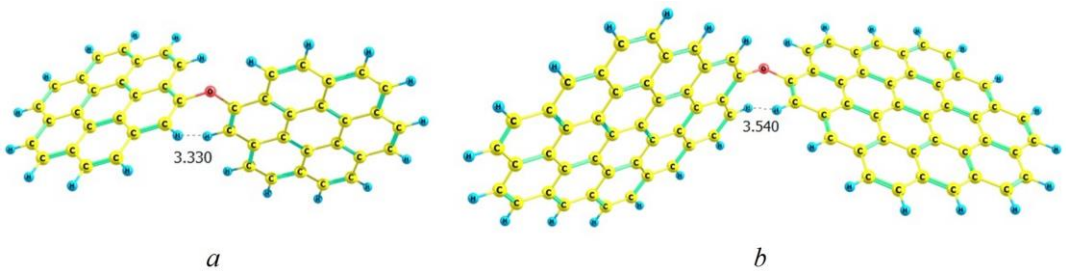

Fig. 3. Equilibrium geometry of the molecules of the reaction products of two graphene-like planes ($C_{24}H_{12}$ – (*a*), $C_{42}H_{16}$ – (*b*)) with hydroxyl groups.

smaller than the previous one and is only +0.1 kJ/mol (see the Table).

Next, the reaction between GLP with a hydroxyl group on the periphery and a graphene-like plane containing an aldehyde group was considered (Fig. 4). In this reaction, the hydroxyl group of one GLP interacts with the aldehyde group of another GLP according to scheme 2:

$$GLP–OH + HOC–GLP \rightarrow GLP–OC–GLP + H_2O. \quad \text{(Scheme 2)}$$

According to this scheme, the oxygen atom of the hydroxyl group (Fig. 4, *a*) interacts with the hydrogen atom of the aldehyde group (Fig. 4, *b*). As a result, the C–O bond between the hydroxyl group and GLP is broken, and, in turn, the H–C bond in the aldehyde group is broken with the formation of a water molecule. At the same time, the carbon atom of the first GLP (Fig. 4, *a*) interacts with the carbon atom of the aldehyde group of the second graphene-like plane (Fig. 4, *b*) with the formation of a reaction product (Fig. 4, *c*), in which the two GLPs are covalently linked between themselves through the carbonyl group (>C=O).

The energy effect of reactions was calculated according to formula (2):

$$\Delta E_{react} = [E_{tot}(GLP –OC– GLP) + E_{tot}(H_2O)] - [E_{tot}(GLP –OH) + E_{tot}(HOC–GLP)], \quad (2)$$

where E_{tot}(GLP –OC– GLP) is the total energy of the interaction product of the hydroxyl group of one GLP with the aldehyde group of another GLP, $E_{tot}(H_2O)$ is the total energy of the H_2O molecule, E_{tot} (GLP–OH) is the total energy of the GLP with a hydroxyl group, E_{tot}(HOC – GLP) is the total energy of GLP with an aldehyde group.

As the results of the calculation according to formula (2) show, the energy effect of the reaction (Scheme 2), in contrast to similar values for the reaction (Scheme 1), has a negative value, for the product of the reaction, in which the graphene-like planes are the smallest, is -17.1 kJ /mol (see Table).

When using the coronene molecule (Fig. 1, *d*, *e*) and the molecule with the composition $C_{42}H_{16}$ (Fig. 1, *e*, *c*) as starting GLPs for the reaction (Scheme 2), reaction products are formed (Fig. 5), the molecules of which are similar in structure to those considered above (Fig. 4, *c*). In the molecules of the reaction products (Scheme 2), as can be seen from these figures, the GLPs are located relative to each other not perpendicularly, as in the reaction products (Scheme 1), and not parallel, but at an acute angle. In particular, for the structure depicted in fig. 4, c, this angle is 47.8°, for the product from coronene derivatives (Fig. 5, *a*) it is slightly larger and has a value of 53.3°, and for the product of the reaction with GLP of the maximum size (Fig. 5, *b*) , is 54.2°.

The energy effect of the reaction (Scheme 2), calculated according to formula 2, during the formation of a product from coronene derivatives (Fig. 5, *a*), in contrast to the similar value (-17.1 kJ/mol), where in the molecule of the reaction product (Scheme 2) graphene-like planes are the smallest, has a value close to 0 and is +0.5 kJ/mol.

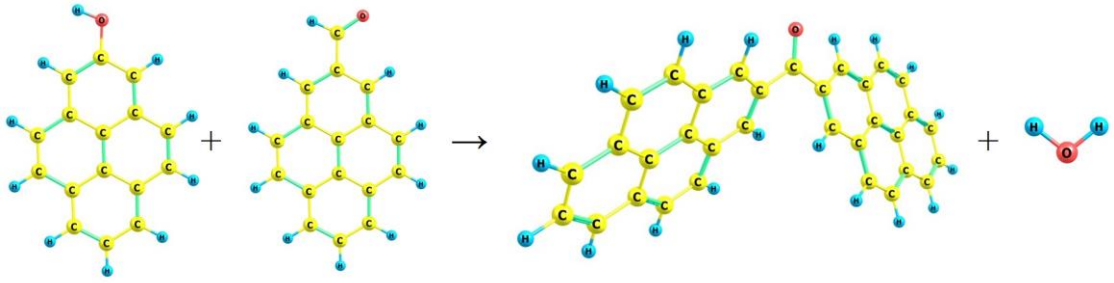

a *b* *c* *d*

Fig. 4. Equilibrium geometry of the molecules of the starting substances and reaction products of the interaction of two GLPs that contain hydroxyl and aldehyde groups.

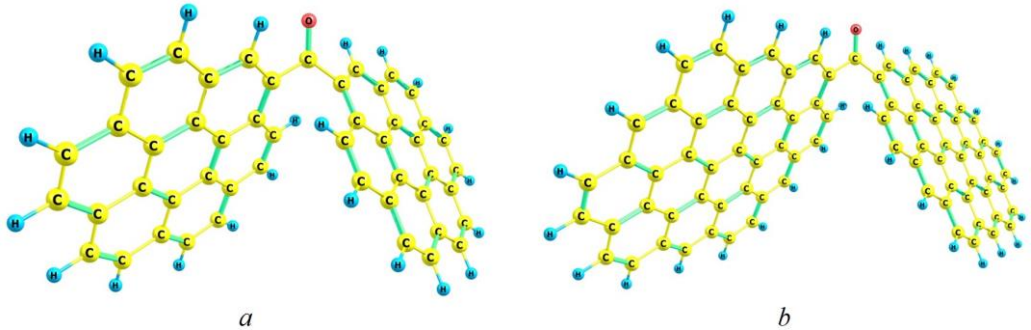

a *b*

Fig. 5. Equilibrium geometry of the molecules of the reaction products of two graphene-like planes ($C_{24}H_{12}$ – (*a*), $C_{42}H_{16}$ – (*b*)) with hydroxyl and aldehyde groups.

With a further increase in the size of the GLP during product formation (Fig. 5, *b*), the energy effect slightly decreases in absolute value to -0.9 kJ/mol.

Subsequently, the reaction between GLP with a hydroxyl group on the periphery and GLP with a carboxyl group on the periphery was investigated. In it, the hydroxyl group of one GLP interacts with the carboxyl group of another GLP according to Scheme 3:

$$GLP–OH + HOOC–GLP \rightarrow GLP–O–OC–GLP + H_2O. \quad \text{(Scheme 3)}$$

According to this scheme, similar to the reaction discussed above (Scheme 2), the oxygen atom of the hydroxyl group (Fig. 6, *a*) interacts with the hydrogen atom of the carboxyl group (Fig. 6, *b*), as a result of which the C–O bond between the hydroxyl group and GLP in the molecule of the starting substance (Fig. 6, *a*), while the H–O bond in the carboxyl group breaks with the formation of a water molecule. At the same time, the carbon atom of the first GLP (Fig. 6, *a*) interacts with the oxygen atom of the carboxyl group of the second graphene-like plane (Fig. 6, *b*) with the formation of a reaction product (Fig. 6,*c*), in which the two GLPs are covalently linked between themselves through the ester group (–O–C(=O)–).

The energy effect of reactions was calculated according to the formula:

$$\Delta E_{react} = [E_{tot}(GLP–O–OC–GLP) + E_{tot}(H_2O)] - [E_{tot}(GLP–OH) + E_{tot}(HOOC–GLP)], \quad (3)$$

where E_{tot}(GLP–O–OC–GLP) is the total energy of the interaction product of the hydroxyl group of one GLP with the carboxyl group of another GLP, $E_{tot}(H_2O)$ is the total energy of the H_2O molecule, E_{tot}(HOOC–GLP) is the total energy of the GLP with the carboxyl group.

As the results of the calculation according to formula (3) show, the energy effect of the reaction (Scheme 3), similar to the analogous reaction values (Scheme 1), has a positive value, which is for the product of the reaction, in which the GLP is the smallest (Fig. 6, *c*), +26.0 kJ/mol (see Table).

When using larger GLP models ($C_{24}H_{12}$ and $C_{42}H_{16}$), molecules of the reaction products are formed (Fig. 7), similar in structure to the previous one (Fig. 6, *c*).

An interesting feature of the molecular geometry of these reaction products is that the GLPs are located in one plane, regardless of the size of the graphene-like planes used, which is due to the occurrence of a hydrogen bond between the hydrogen atom of one GLP and the carbonyl oxygen atom of the other. The length of this bond is 2.152 Å, which is characteristic of the case when the hydrogen atom of the C–H bond takes part in the hydrogen bond. This approximately O•••H distance is also preserved when using larger GLPs, in particular, in the product where coronane is used as the GLP, this distance is 2.118 Å (Fig. 7, *a*), and for the product in which the GLPs are of the maximum size - 2.110 Å (Fig. 7, *b*).

The energy effect of the reaction (Scheme 3) when a coronene molecule is used as a GLP is also positive and is 4.1 kJ/mol smaller than the similar value for the same

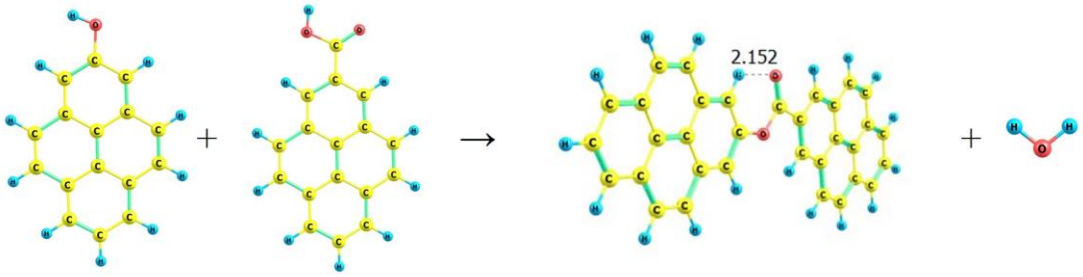

Fig. 6. Equilibrium geometry of molecules of starting substances and reaction products of the interaction of two graphene-like planes containing hydroxyl and carboxyl groups.

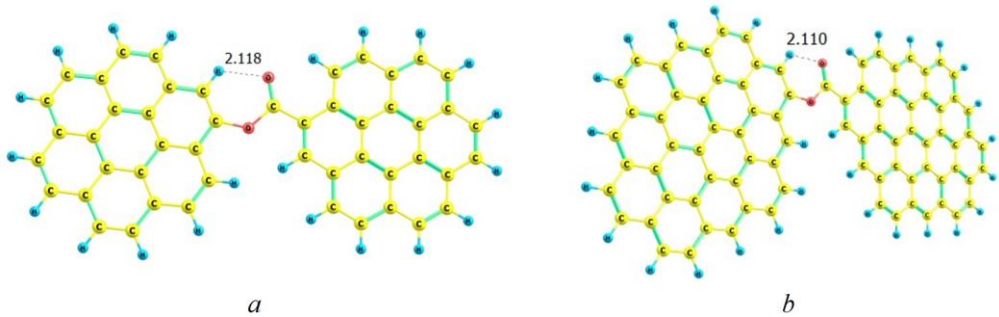

Fig. 7. Equilibrium geometry of the molecules of the reaction products of two graphene-like planes ($C_{24}H_{12}$ – (*a*), $C_{42}H_{16}$ – (*b*)) with hydroxyl and carboxyl groups.

reaction, in which a pyrene molecule was used as graphene-like planes, and is +21.9 kJ/mol. If the GLP is dominated by a larger molecule, in particular $C_{42}H_{16}$ (Fig. 7, *b*), then the energy effect is also a positive value, which has a value of +19.9 kJ/mol (see Table).

And finally, for comparison, the interaction of two GLPs with carboxyl groups on the periphery of each of them is considered. This reaction can be represented by scheme 4:

$$\text{GLP –COOH + HOOC– GLP} \rightarrow \text{GLP –CO–O–OC– GLP} + H_2O. \qquad \text{(Scheme 4)}$$

According to this scheme, the hydrogen atom of the carboxyl group of the molecule of the first starting substance (Fig. 8, *a*) interacts with the oxygen atom of the acid center of the carboxyl group of the molecule of the second starting substance (Fig. 8, *b*). As a result, the C–O bond between the hydroxyl group and the carbon atom in the carboxyl group of the molecule of the second starting substance is broken, while the H–O bond in the carboxyl group of the molecule of the first starting substance is broken (Fig. 8, *a*) with the formation of a water molecule. At the same time, the oxygen atom of the acid center of the carboxyl group of the molecule of the first starting substance interacts with the carbon atom of the carboxyl group of the molecule of the second starting substance (Fig. 8, *b*) with the formation of a molecule of the reaction product (Fig. 8, *c*), in which two GLPs are covalently connected connected to each other through a symmetric group (–C(=O)–O–C(=O)–).

The energy effect of reactions was calculated according to formula (4):

$$\Delta E_{react} = [E_{tot}(\text{GLP –CO–O–OC–GLP}) + E_{tot}(H_2O)] - 2\,E_{tot}(\text{GLP –COOH}), \qquad (4)$$

where E_{tot}(GLP –CO–O–OC– GLP) is the total energy of the interaction product of two GLP s with carboxyl groups, $E_{tot}(H_2O)$ is the total energy of the reaction product – H_2O, E_{tot}(GLP –COOH) is the total energy of the GLP with a carboxyl group.

The energetic effect of the GLP reaction with two carboxyl groups (Scheme 4) when using pyrene molecules as graphene-like planes, calculated according to formula (4), is the maximum of all previously considered and amounts to +74.5 kJ/mol.

When the size of these graphene planes increases, molecules of the reaction products are formed (Scheme 4), which are also similar in spatial structure to each other (Fig. 9,*a* and 9, *b*) and the reaction product molecule with carboxylatedpyrene molecules (Fig. 8).

As can be seen from these figures, in contrast to the molecules of the products of the HP reaction with hydroxyl and carboxyl groups (Scheme 3), in all these molecules of the reactio n products (Scheme 4), the graphene-like planes are not parallel to each other, but form some angle between them, like and in the molecules of products of the reaction of HP with hydroxyl and aldehyde groups (Scheme 2) (Fig. 4, c and Fig. 5). In particular, the angle between graphene-like planes in the smallest pyrene-containing reaction product (Fig. 8,*c*) is 77.2°. In the larger product, in which the GLP was

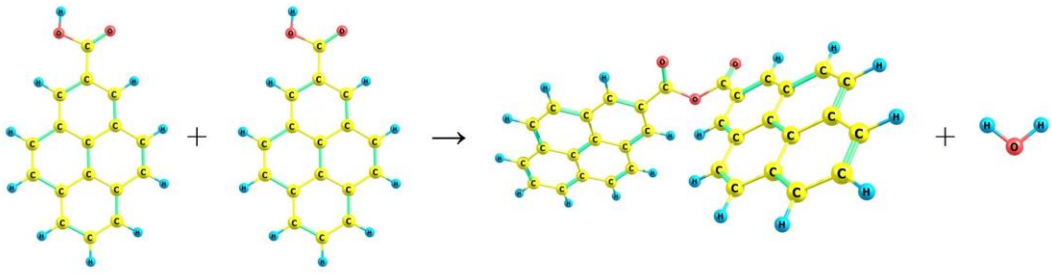

a *b* *c* *d*

Fig. 8. Equilibrium geometry of molecules of starting substances and reaction products of the interaction of two graphene-like planes with a carboxyl group on the periphery.

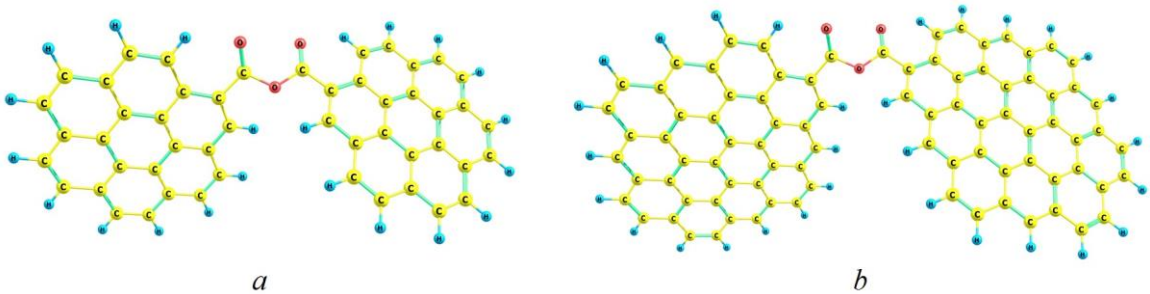

a *b*

Fig. 9. Equilibrium geometry of the molecules of the reaction products of two graphene-like planes ($C_{24}H_{12}$ – (*a*), $C_{42}H_{16}$ – (*b*)) with two carboxyl groups.

Table

Energy effects of the interaction of partially oxidized graphene-like planes with each other.

No. reaction scheme	Interaction scheme	ΔE_{react}, (kJ/mol)		
		$C_{16}H_{10}$	$C_{24}H_{12}$	$C_{42}H_{16}$
1	GLP –OH + HO–GLP→GLP–O–GLP + H_2O	+22.2	+1.3	+0.1
2	GLP–OH + HOC–GLP→GLP–OC–GLP + H_2O	-17.1	+0.5	-0.9
3	GLP–OH + HOOC–GLP→GLP–O–OC–GLP + H_2O	+26.0	+21.9	+19.9
4	GLP–COOH+HOOC–GLP→GLP–CO–O–OC–GLP+H_2O	+74.5	+70.6	+69.3

dominated by coronene molecules, the corresponding angle is slightly smaller and has a value of 54.7°. For the reaction product of the maximum size, this angle is almost the same as the previous one and is 55.9°. Such non-coplanarity is caused by the presence of closely spaced oxygen atoms with a significant negative charge on each of them in the considered molecules.

The energy effect of the reaction (Scheme 4) for the crown-containing product also has a positive value, which is +70.6 kJ/mol, and for the reaction product of an even larger size, this value is even smaller and its value is +69.3 kJ/mol (see Fig. Table).

It can be seen from the table that, regardless of the size of the GLP, the lowest absolute value of the energy effect with the participation of the same oxygen-containing group is characteristic of the reaction of the interaction of the GLP with hydroxyl and aldehyde groups (Scheme 2). It should also be noted that for all the considered reactions except the reaction (Scheme 2), with an increase in the size of the GLP, the magnitude of the energy effect decreases. The greatest dependence of the energy effect on the size of the graphene-like planes is observed for the reaction (Scheme 1) of the interaction of the GLP with hydroxyl groups. In this case, the values of ΔE_{react}.decrease from 22.2 for pyrene-containing GLPs to 0.1 kJ/mol for $C_{42}H_{16}$ GLPs. For the reaction (Scheme 2), with an increase in the size of the graphene-like planes, on the contrary, the energy effect increases by 16.2 kJ/mol, from -17.1 to -0.9 kJ/mol. For the reaction of the interaction of a hydroxyl group with a carboxyl group in graphene-like planes, ΔE_{reacts} differ by 6.1 kJ/mol when the size of the GLP changes from the minimum to the maximum. And with the interaction between two carboxyl groups (Scheme 4), similar values change by only 5.2 kJ/mol.

Conclusions

Therefore, as evidenced by the analysis of the results of quantum chemical calculations, the reaction between the hydroxyl and aldehyde groups of two interacting GLPs is the most thermodynamically probable, regardless of the dimensions of the graphene-like planes.

The reaction of the interaction of hydroxyl groups of two adjacent graphene-like planes is slightly less thermodynamically probable.

The reaction between two carboxyl groups of different graphene-like planes is the least thermodynamically probable.

To create nanocomposites by interacting graphene-like planes with each other, it is necessary that the graphene-like planes contain hydroxyl and aldehyde groups.

Hrebelna Y.V. – senior engineer, Chuiko Institute of Surface Chemistry of National Academy of Sciences of Ukraine;
Demianenko E.M. – PhD. in chemistry, senior researcher, Chuiko Institute of Surface Chemistry of National Academy of Sciences of Ukraine;
Terets M.I. – PhD. in chemistry, senior researcher,researcher,Chuiko Institute of Surface Chemistry of National Academy of Sciences of Ukraine;
Sementsov Y.I. – doctor of physical and mathematical sciences, senior researcher, leading researcher, Chuiko Institute of Surface Chemistry of National Academy of Sciences of Ukraine;
Lobanov V.V. – professor, doctor of chemical Sciences head of the department, Chuiko Institute of Surface Chemistry of National Academy of Sciences of Ukraine;
Grebenyuk A.G. – PhD. in chemistry, senior researcher, senior researcher, Chuiko Institute of Surface Chemistry of Nationa lAcademy of Sciences of Ukraine;
Kuts V.S. – PhD. in physical and mathematical sciences, senior researcher, Chuiko Institute of Surface Chemistry of National Academy of Sciences of Ukraine;
Zhuravskyi S.V. – PhD. in chemistry, senior researcher, Chuiko Institute of Surface Chemistry of National Academy of Sciences of Ukraine;
Khora O.V. – junior researcher, Chuiko Institute of Surface Chemistry of National Academy of Sciences of Ukraine;
Kartel M.T. – academician, doctor of chemical sciences, chief researcher, Chuiko Institute of Surface Chemistry of National Academy of Sciences of Ukraine.

[1] F. Farjadian, S. Abbaspour, M.A.A. Sadatlu et al., *Recent Developments in Graphene and Graphene Oxide: Properties, Synthesis, and Modifications: A Review*, Chemistry Select, 5(33), 10200 (2020); https://doi.org/10.1002/slct.202002501.
[2] X. Liua, A.L. Miller, S. Parkc et al., *Covalent crosslinking of graphene oxide and carbon nanotube into hydrogels enhances nerve cell responses*, J. Mater. Chem. B., 4(43), 6930 (2016); https://doi.org/10.1039/c6tb01722c.

[3] X. Cui, S. Xu, X. Wang, C. Chen, *The nano-bio interaction and biomedical applications of carbon nanomaterials*, Carbon, 138, 436 (2018); https://doi.org/10.1016/j.carbon.2018.07.069.
[4] S. Bhattacharjee, R. Joshi, A. A. Chughtai, et al., *Graphene modified multifunctional personal protective clothing*, Adv. Mater. Interfaces, 6, 1900622 (2019); https://doi.org/10.1002/admi.201900622.
[5] S. I. Ahmad., H. Hamoudi, A. Abdala et al., *Graphene-Reinforced Bulk Metal Matrix Composites: Synthesis, Microstructure, and Properties*, Rev. Adv. Mater. Sci., 59, 67 (2020); https://doi.org/10.1515/rams-2020-0007.
[6] J. Wang, J. Zhou, Y. Hu, T. Regier, *Chemical interaction and imaging of single Co_3O_4/graphene sheets studied by scanning transmission X-ray microscopy and X-ray absorption spectroscopy*, Energy Environ. Sci., 6, 926 (2013); https://doi.org/10.1039/c2ee23844f.
[7] Z. Jia, Y. Wang, *Covalently crosslinkedgraphene oxide membranes by esterification reactions for ions separation*, J. Mater. Chem. A, 3, 4405 (2015); https://doi.org/10.1039/C4TA06193D.
[8] W. Xing, H. Li, G. Huang et al., *Graphene oxide induced crosslinking and reinforcement of elastomers*, Composites Science and Technology, 144, 223 (2017); http://dx.doi.org/10.1016/j.compscitech.2017.03.006.
[9] C. A. Amarnath, C. E. Hong, N. H. Kim et al., *Efficient synthesis of graphene sheets using pyrrole as a reducing agent*, Carbon 49, 3497 (2011); http://dx.doi.org/10.1016/j.carbon.2011.04.048.
[10] J. Su, M. Jia, W. Wu, et al. *Chemical vapor crosslinking of graphene oxide membranes for controlling nanochannels*, Environ. Sci.: Nano, 7, 2924 (2020); https://doi.org/10.1039/D0EN00710B.
[11] M. Chougan, F. R. Lamastra, D. Caschera, et al. *Cementitiousnanocomposites engineered with high-oxidized graphene oxide: Spotting the nano to macro correlation*, Ceramics International, 49, 964 (2023); https://doi.org/10.1016/j.ceramint.2022.09.070.
[12] W. Yu, L. Sisi, Y. Haiyana, L. Jie, *Progress in the functional modification of graphene/graphene oxide: a review*, RSC Adv., 10, 15328 (2020); https://doi.org/10.1039/d0ra01068e.
[13] A. Verma, A. Parashara, M. Packirisamy, *Effect of grain boundaries on the interfacial behaviour of graphenepolyethylenenanocomposite*, Applied Surface Science, 470(15) 1085 (2019); https://doi.org/10.1016/j.apsusc.2018.11.218.
[14] T. Seifi, A. R. Kamali, *Anti-pathogenic activity of graphene nanomaterials: A review*, Colloids and Surfaces B: Biointerfaces, 199, 111509 (2021); https://doi.org/10.1016/j.colsurfb.2020.111509.
[15] F. Nie, W. Jian, D. Lau, *An atomistic study on the thermomechanical properties of graphene and functionalized graphene sheets modified asphalt*, Carbon, 182, 615 (2021); https://doi.org/10.1016/j.carbon.2021.06.055.
[16] F. Tarannum, R. Muthaiah, S. Danayat, et al., *Chemically Edge-CarboxylatedGraphene Enhances the Thermal Conductivity of Polyetherimide–GrapheneNanocomposites*, ACS Appl. Mater. Interfaces, 14(12), 14753 (2022); https://doi.org/10.1021/acsami.1c25279.
[17] Y. Liang, D. Wu, X. Feng et al., *Dispersion of Graphene Sheets in Organic Solvent Supported by Ionic Interactions*, Adv. Mater., 21, 1679 (2009); https://doi.org/10.1002/adma.200803160.
[18] A. Vallin, D. Battegazzore, G. Damonte et al., *On the Development of Nanocomposite Covalent Associative Networks Based on Polycaprolactone and Reduced Graphite Oxide* Nanomaterials, 12, 3744 (2022); https://doi.org/10.3390/nano12213744.
[19] B. Li, C.-G. Wang, N. Erdeanna et al., *Microscopically tuning the graphene oxide framework for membrane separations: a review*, Nanoscale Adv., 3, 5265 (2021); https://doi.org/10.1039/d1na00483b.
[20] B. Wu, F. Du, W. A et al., *Graphene-based hemostatic sponge*, Chinese Chemical Letters, 33, 703 (2022); https://doi.org/10.1016/j.cclet.2021.06.029.
[21] Y. Jiang, Y. Wang, Z. Xu et al., *Conformation engineering of two-dimensional macromolecules: a case study with graphene oxide*, Acc. Mater. Res. 1(3), 175 (2020), – 187 https://doi.org/10.1021/accountsmr.0c00027.
[22] H. Huang, H. Park, J. Huang, *Self-crosslinking of graphene oxide sheets by dehydration*, Chem, 8(9), 2432 (2022); https://doi.org/10.1016/j.chempr.2022.05.016.
[23] E.M. Demianenko, M.I. Terets, L.M. Ushakova, et al., *A theoretical study on the effect of heteroatoms (N, B, Si) on the interaction of aluminum clusters with a carbon graphene-like plane*, Chemistry, Physics and Technology of Surface, 13(4) 391 (2022); https://doi.org/10.15407/hftp13.04.391.
[24] E.M. Demianenko, M.I. Terets, S.V. Zhuravskyi et al., *Theoretical simulation of the interaction of Fe_2 cluster with a N, B, Si-containing carbon graphene-like plane*, Surface, 14(29), 37 (2022); https://doi.org/10.15407/Surface.2022.14.037. [in Ukrainian].
[25] E.M. Demianenko, M.I. Terets, Yu.I. Sementsov et al., *Theoretical study on the effect of carbon graphenous nanoclusters on the stability and capacity of polyamide in a nanocomposite*, Chemistry, Physics and Technology of Surface. 10(4), 355 (2019); https://doi.org/10.15407/hftp10.04.355.
[26] E. Fuente, J. A. Menendez, M. A. Dıez et al., *Infrared Spectroscopy of Carbon Materials: A Quantum Chemical Study of Model Compounds*, J. Phys. Chem. B, 107 6350 (2003); https://doi.org/10.1021/jp027482g.
[27] J. P. Froning, P. Lazar, M. Pykal, et al., *Direct Mapping of Chemical Oxidation of Individual Graphene Sheets through Dynamic Force Measurements at Nanoscale*, Nanoscale, 9, 119 (2017); https://doi.org/10.1039/C6NR05799C.
[28] C. Jang, S. Nouranian, T.E. Lacy et al., *Molecular dynamics simulations of oxidized vapor-grown carbon nanofiber surface interactions with vinyl ester resin monomers*, Carbon, 50(3), 748 (2012); https://doi.org/10.1016/j.carbon.2011.09.013.

[29] J. L. Suter, R.C. Sinclair, P. V. Coveney, *Principles Governing Control of Aggregation and Dispersion of Graphene and Graphene Oxide in Polymer Melts*, Adv. Mater., 32(36), 2003213 (2020); https://doi.org/10.1002/adma.202003213.
[30] Y. Liu, J. Zhou, E. Zhu, et al., *A facile synthesis of bacterial cellulose fibers covalently intercalated graphene oxide by one-step cross-linking for robust supercapacitors*, J. Mater. Chem. C, 3, 1011 (2015); https://doi.org/10.1039/C4TC01822B.
[31] Yu. Sementsov, Yu. Grebel'na, V. Strelchuk et al., *Carbon-Carbon Composition "Expanded Graphite–Multiwalled Carbon Nanotubes"*, International Journal of Materials Science and Applications, 8(6) 127 (2019); https://doi.org/10.11648/j.ijmsa.20190806.16.
[32] M. Kartel, Yu. Sementsov, G. Dovbeshko et al., *Lamellar structures from graphene nanoparticles produced by anode oxidation*, Advanced Materials Letters, 8(3), 212 (2017); https://doi.org/10.5185/amlett.2017.1428.
[33] M. Kartel, Yu. Sementsov, S. Makhno et al., *Electrochemical reactor and process conditions for the continuous oxidation of natural graphite with a capacity of 10 kg/hour*, Intern. Journal of Innovative Science, Engineering & Technology, 4(7), 203 (2017); https://ijiset.com/vol4/v4s7/IJISET_V4_I07_25.pdf
[34] N.A. Havryliuk, E.N. Shevchuk, G.P. Prikhod'ko et al., *Grapheneoxide: preparation, properties, applications (review)*, Chemistry, Physics and Technology of Surface, 6 (4), 413 (2015); https://doi.org/10.15407/hftp06.04.413. [in Ukrainian].
[35] G. Barca, C. Bertoni, L.Carrington et al., *Recent developments in the general atomic and molecular electronic structure system*, J. Chem. Phys., 152, 154102-1 (2020); https://doi.org/10.1063/5.0005188.
[36] A.D. Becke*Density functional thermochemistry. III. The role of exact exchange*, J. Chem. Phys., 98(7), 5648 (1993); https://doi.org/10.1063/1.464913.
[37] C. Lee, W. Yang, R.G. Parr, *Development of the Colle-Salvetti correlation-energy formula into a functional of the electron density*, Phys. Rev. B., 37(2), 785 (1988); https://doi.org/10.1103/physrevb.37.785.
[38] S. Grimme, S. Ehrlich, L. Goerigk, *Effect of the damping function in dispersion corrected density functional theory*, J. Comput. Chem., 32(7), 1456 (2011); https://doi.org/10.1002/jcc.21759.
[39] S. Grimme, *Density functional theory with London dispersion corrections*, WIREs Comput. Mol. Sci., 1(2), 211 (2011); https://doi.org/10.1002/wcms.30.
[40] K.Voitko, A.Tóth, E.Demianenko, et al., *Catalytic performance of carbon nanotubes in H_2O_2 decomposition: Experimental and quantum chemical study*, J. Colloid Interf. Sci., 437, 283 (2015); https://doi.org/10.1016/j.jcis.2014.09.045.

Ю.В. Гребельна[1], Є.М. Дем'яненко[1], М.І. Терець[1], Ю.І. Семенцов[1,2], В.В. Лобанов[1], А.Г. Гребенюк[1], В.С. Куць[1], С.В. Журавський[1], О.В. Хора[1], М.Т. Картель[1]

Квантовохімічні дослідження взаємодії частково окиснених графеноподібних площин між собою

[1]*Інститут хімії поверхні ім. О.О. Чуйка Національної академії наук України, Київ, Україна, teretsmariya@gmail.com*
[2]*Ніньбо технологічний університет, Ніньбо, Китай*

Методами квантової хімії з'ясовані енергетичні ефекти взаємодії частково окиснених графеноподібних площин між собою і їхня залежність від природи оксигенвмісних функціональних груп, які наявні в них, а також від розмірів самих графеноподібних площин. Встановлено, що найбільш термодинамічно ймовірною є реакція між гідроксильною і альдегідною групами двох взаємодіючих графеноподібних площин незалежно від їхніх розмірів. Найменш термодинамічно ймовірною є реакція між двома карбоксильними групами різних графеноподібних площин. Для створення нанокомпозитів при взаємодії графеноподібних площин між собою, необхідно щоб у складі графеноподібних площин були наявні гідроксильні і альдегідні групи.

Ключові слова: окиснені графеноподібні площини, хімічна реакція, пірен, коронен, метод теорії функціонала густини, кластерне наближення.

PHYSICS AND CHEMISTRY OF SOLID STATE
V. 24, No. 2 (2023) pp. 278-283
Section: Technology

DOI: 10.15330/pcss.24.2.278-283

Vasyl Stefanyk Precarpathian National University

ФІЗИКА І ХІМІЯ ТВЕРДОГО ТІЛА
Т. 24, № 2 (2023) С. 278-283
Технічні науки

UDC: 537.323 ISSN 1729-4428

B.S. Dzundza[1], O.B. Kostyuk[1,2], U.M. Pysklynets[2], Z.M. Dashevsky[3]

Development of high-precision hardware and software tools for automated determination of the characteristics of thermoelectric devices

[1]*Vasyl Stefanyk Precarpathian National University, Ivano-Frankivsk, Ukraine, bdzundza@gmail.com*
[2]*Ivano-Frankivsk National Medical University, Ivano-Frankivsk, Ukraine, oksanakostuk@gmail.com*
[3]*Ben-Gurion University of the Negev, Beer-Sheva, Israel, zdashev@bgu.ac.il*

In this work, a high-accuracy setup was developed for the characterization of thermoelectric devices in the temperature range of 300-900 K. The output parameters of the thermoelectric devices, including the thermoelectric efficiency Z, Seebeck coefficient S, and internal resistance r, were measured. A technique, block diagram, and computer tools for automated measurement and preliminary processing of experimental data were developed for automated studies of the properties of semiconductor materials and thermoelectric power conversion modules. The developed tools were shown to have high efficiency. The complexity of the process of measuring the main electrical parameters of semiconductor materials was significantly reduced, and the accuracy of the obtained results was increased.

Keywords: thermoelectricity, thermoelectric materials, thermoelectric efficiency, measurement techniques, high-accuracy automated measurement.

Received 18 January 2023; Accepted 2 June 2023.

Introduction

Due to the increase in energy demand and depletion of natural resources, the development of energy harvesting technologies has become tremendously important [1]. The application of thermoelectric devices, which convert heat directly into electrical energy, has led to significant progress in the development of cost-effective, environmentally-friendly, and fuel-saving energy sources for power generation, refrigeration, temperature sensors, and thermal management [2–10]. The high reliability and long operational lifespan of thermoelectric (TE) energy converters make them ideal for use in the space industry, gas pipeline systems, medical devices, and consumer electronics [4,5,11,12].

The efficiency of such TE converter is determined by the following equation [4,12,13]:

$$\eta_{max} = \frac{\Delta T}{T_h} \frac{\sqrt{1+(ZT)_{av}}-1}{\sqrt{1+(ZT)_{av}}+\frac{T_c}{T_h}}, \quad (1)$$

where T_h and T_c are the hot and cold sides temperatures at the ends of TE converter, respectively, $\Delta T = T_h - T_c$, and $(ZT)_{av}$ is the average dimensionless TE figure of merit, which is determined as:

$$(ZT)_{av} = \frac{1}{T_h - T_c} \int_{T_c}^{T_h} ZT \cdot dT \quad (2)$$

$$ZT = \frac{S^2 \sigma}{\kappa} T, \quad (3)$$

where S is the Seebeck coefficient, σ and κ are electrical and thermal conductivity.

Theoretical studies have shown that the most accurate ZT value can be obtained using the Harman method [14]. There are many modifications of this method [15,16] that allow for the direct estimation of the TE figure of merit on a single sample. However, the use of measurements based on the Harman method, especially at high temperatures, has certain disadvantages [27]:

1. The effect of parasitic heat transfer between the

sample and its environment has been determined to be critical to the measurement accuracy.

2. This effect of parasitic thermal phenomena increases rapidly with increasing measurement temperature.

3. To determine thermoelectric parameters, it is necessary to use correction factors of up to 80% of the measured *ZT* value, which cannot be reliably estimated for arbitrary temperatures and sample sizes.

To measure parameters of the thermoelectric devices, direct methods were chosen, in which a heat flux is passed through the thermoelement due to a certain temperature gradient created between the heater and the cooler. Direct methods require a gradient heater, precise temperature gradient maintenance and measurement, and the accounting of heat fluxes and losses, which may introduce considerable errors in the estimate of the thermoelectric figure of merit. The design and analysis issues of devices concerning these problems are discussed in [18,19]. The use of general tools for studying thermoelectric properties poses several difficulties, primarily with regards to adapting measurement techniques and integrating such tools into pre-existing laboratory complexes [20].

The peculiarity of the developed method is the use of two identical samples placed on both sides of the heater and cooled by the same water radiators.

Due to the properties of semiconductors, n-type and p-type materials have Seebeck coefficients of opposite signs, respectively [21]. Consequently, thermoelectric modules are composed of two distinct semiconductor materials that are interconnected electrically in series and thermally in parallel [21], as shown in Fig. 1.

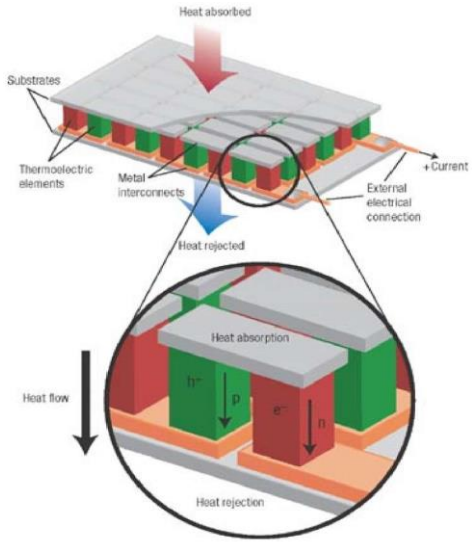

Fig 1. Thermoelectric module [21].

Thermoelectric devices available in the market typically comprise a series of thermocouples sandwiched between hot and cold plates that conduct heat. In order to maximize their efficiency, modern modules are sometimes segmented or cascaded, wherein a single leg can incorporate several materials consecutively. The rationale behind this approach lies in the fact that thermoelectric modules frequently experience temperature gradients of several hundred degrees, and given that the figure of merit of a given material may vary considerably across a range of temperatures, using more than one material becomes advantageous [21]. Additionally, the metal-semiconductor junctions present in a thermoelectric module are ohmic contacts, thereby rendering the device essentially symmetrical and enabling it to pump heat or current in either direction.

I. Development of setup

The development and widespread use of thermoelectric generation as a user-friendly technology for direct energy conversion is mainly limited by a small efficiency factor. Presently, scientists in the field of thermoelectricity are primarily focusing on increasing the thermoelectric efficiency Z across a wide range of operating temperatures (300-900 K). The quality of a thermoelectric material is determined by a set of key parameters, including the Seebeck coefficient, electrical conductivity, and thermal conductivity. Moreover, for a thermoelectric converter to be fully functional, it must also possess a range of electrical and operational characteristics, such as internal resistance, generated current and voltage, thermoelectric power, heat capacity, and other performance metrics.

For the purpose of measuring all the aforementioned parameters, direct methods have been selected, whereby a heat flow is directed through a thermoelement in response to a temperature gradient generated between the heating and cooling elements. A noteworthy aspect of the developed methodology lies in the use of two identical samples positioned on either side of the heating element, and subsequently cooled by identical water radiators. The measuring cell is shown schematically in Fig. 2.

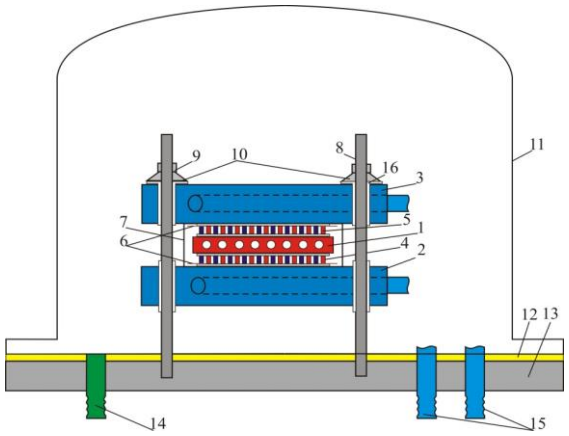

Fig. 2. Schematic representation of the measuring cell. 1 – copper electric heater with thermocouple, 2, 3 – copper water radiator with thermocouple, 4, 5 – thermocouples or single samples of thermoelectric material, 6 – electrical contacts, 7 – heat shield, 8 – clamping pins, 9 – nuts, 10 – spring washers, 11 – vacuum cap, 12 – vacuum gasket, 13 – base, 14 – fitting for pumping, 15 – fittings for water supply and drainage, 16 – fluoroplastic insulation.

The use of a water-based cooling system allowed to maintene the stable temperature of cold junction. To achieve uniform heating of cylindrical or rectangular samples, a miniature copper heater with low power output

was designed and coupled with a tubular heat shield made of tantalum. This configuration was effective in in reducing the impact of parasitic heat loss, which is often challenging to accurately account for in thermoelectric measurements.

To diagnose ready-made thermoelectric energy conversion modules with a size of 40x40 mm, a rectangular copper heater with a size of 40x40x8 mm is made, which contacts the hot surfaces of the thermocouple through the thermal interface. The general view of the measuring cell is shown in Fig. 3.

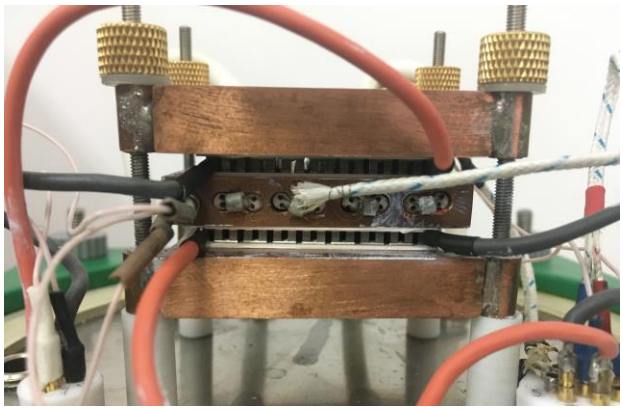

Fig. 3. General view of the measuring cell with installed thermoelectric elements.

The design further allows for the installation of an extra heater on two threaded racks, positioned at the interface level of the two radiators. This feature enables the investigation of film thermomodules, wherein the cold junction is secured between two radiators while the hot junction is pressed against an additional copper plate that is heated by the extra heater.

All electrical contacts are routed through two sealed connectors located in the base. The setup supports up to 5 thermocouples, with one placed in the heater, another in the radiators, and two more that can be drilled into the sample for additional control of heat fluxes. When investigating the electrical properties of semiconductors, fundamental parameters such as electrical conductivity, thermoelectric power, and thermoelectric EMF are measured.

The principle of determining the coefficient of thermal conductivity of stationary methods is based on the measurement of heat flux and temperature difference according to [22]

$$k = \frac{qd}{T_2 - T_1} = \frac{Pd}{S(T_2 - T_1)}$$

Here q is the heat flux; P - measured power of the electric heater; S is the area of the sample; T_2-T_1 is the temperature difference between two opposite surfaces of the sample; d is the thickness of the sample. Usually, the geometry of the sample and the configuration of the measuring system have the strongest effect on the value of the thermal conductivity. It is possible to implement comparative methods in which the amount of heat that has passed through the test sample is determined from the known parameters of the reference sample, which is in similar conditions. The method is quite well developed for different materials in a wide range of temperatures: from a few degrees to ~ 1000 K.

II. Design of software and hardware for automated studies of the properties of thermoelectric energy conversion modules

The computer system designed for measuring electrical parameters was developed with special attention given to the versatility of solutions, which allows for the study of both massive and film thermocouples, as well as the diagnosis of thermoelectric modules. The block diagram of the measuring system can be found in Fig. 4.

Cold water is running through two copper radiators, it can be both flowing tap water and water cooled by means of the cooling thermostat. The cooling thermostat is constructed on the basis of 12 V Peltier elements. The set temperature of the hot side is maintained by the microcontroller by means of a precision PID thermostat, the power of which is accurately measured and can be kept constant, regardless of changes in external conditions or the resistance of the heater. Feedback is carried out using chromel-alumel thermocouples. The thermostat maintains the set temperature with an accuracy of 0.1 K. It is also possible to connect additional thermocouples drilled in the sample, to accurately measure small temperature gradients.

The measuring system is based on the UNI-T UTM1805A digital multimeter, which supports data output to a computer and provides a resolution of 1 μV with an accuracy of 0.015% in the DC voltmeter mode and has an automatic range selection function. The control device for the system is a STM32F303 microcontroller, programmed in C language, and communication with the computer is enabled through the USB-UART converter, coupled with a text command interpreter that facilitates two-way data exchange between the device microcontroller and control programs on the computer.

The thermo-EMF recording process on the samples is executed sequentially with the aid of a switching unit integrated with a reed microrelay. The system allows for the measurement of voltage from each differential thermocouple individually, or to take an average of the readings. Furthermore, thermocouples can be connected in series to obtain the sum of the thermo-EMF of both thermocouples. The Seebeck coefficient is then automatically calculated.

The measurement of thermoelectric power is enhanced by the implementation of a load block, which enables the determination of the operational parameters of thermoelements. Additionally, studying the Peltier effect under load presents further opportunities for analyzing heat transfer parameters, particularly in determining thermal conductivity.

The computer program provides automated control of the measurement process, registration of data from a digital voltmeter, pre-processing and visualization of data. The program is developed in Delphi programming language. The measurement results of each sample are recorded in separate MS Excel-compatible files with the

possibility of further continuation of the experiment. The setup exhibits high reliability, stability, and precision of results during prolonged and regular operation.

III. Experimental research and discussion of the obtained results

Let us examine the operational capabilities of the computerized measuring system through a concrete illustration, where a series of industrial thermoelectric elements of the TEKB-1-1-(15.4-6.0-51.4)-40-71 type were studied. Experimental data on the thermoelectric power, maximum power, and efficiency concerning the temperature difference applied to the module for the studied modules are shown in Fig. 5.

In Table. 1. comparison of measured and passport data for two thermoelectric modules TECB-1-1-(15.4-6.0-51.4)-40-71 is presented. The relative measurement error does not exceed 2%.

Upon analysis of the results and comparison of the calculation results with experimental measurements, it was observed that the measurement methods selected, and their hardware and software implementation, despite the relative simplicity of the implemented algorithms, demonstrated high efficiency. The implementation of the

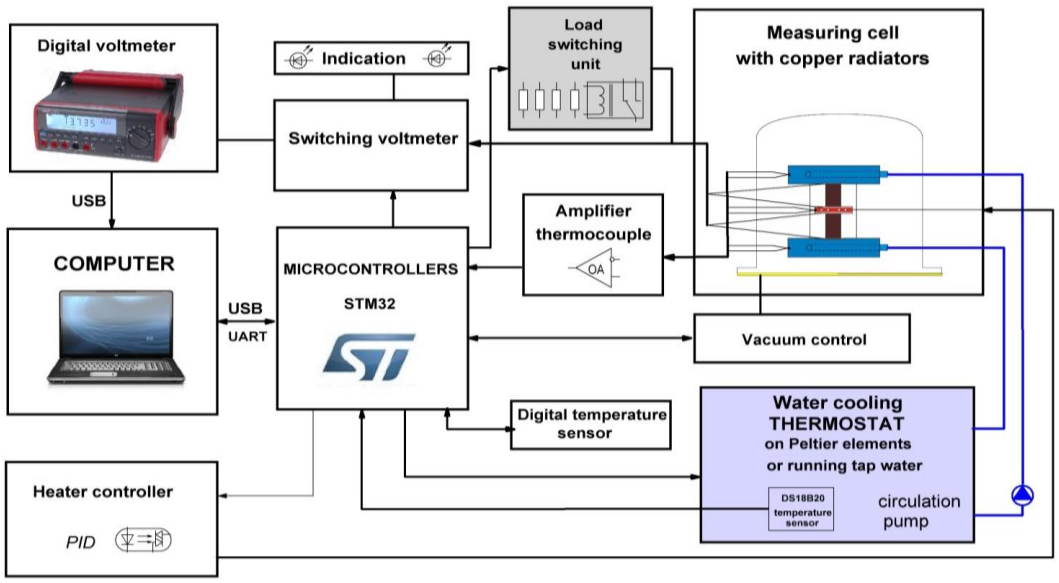

Fig. 4. Block diagram of a computer system for automated diagnostics of thermoelectric modules.

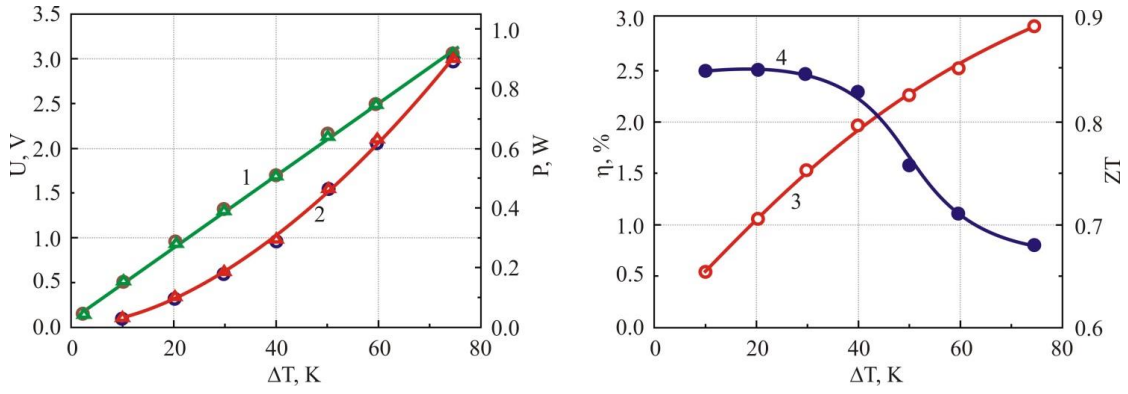

a *b*

Fig. 5. Dependences of thermoelectric power (curve 1), maximum thermoelectric power (curve 2), efficiency (curve 3) and *ZT* (curve 4) on the temperature difference applied to the module. Δ – corresponds to sample №3 placed at the bottom of heater, ○ – sample №4 placed at the top of the heater.

Table 1.

Measured and passport electrical parameters of industrial modules.

Sample	*s*, 1/Ω cm		*S*, μV/K		*r*, Ω (25 °C)		*r*, Ω (50 °C)		*Z* x10^{-3}, K^{-1}	
	Measured (M)	Passport (P)	M	P	M	P	M	P	M	P
3	1006	1000-1020	222.3	220-225	2.13	2.12	2.32	2.30	2.85	2.88
4	1005	1000-1020	222.8	220-225	2.17	2.17	2.34	2.34	2.85	2.84

computerized measuring system significantly reduced time and labor costs for experimental measurements, and facilitated automated diagnostics and fault detection of thermoelectric modules.

The advantage of the implemented research method is the automation of both the measurement process and the pre-processing of the result during the experiment, depending on the material under study. Furthermore, the representation of the acquired data through graphical dependencies makes it possible to visually detect errors, defective samples, even during the measurement process. In contrast to general-purpose tools and mathematical software packages, which offer much broader data processing capabilities, the development of specialized tools, despite the limited set of models, integrates well into the developed measuring system and provides information on electrical properties of the material with minimal effort and reduces time required. for measurement and processing.

Conclusions

1. A high-accuracy setup has been developed for the characterization of thermoelectric devices.

2. The method, flowchart, and computer tools for automated measurement and pre-processing of experimental data for automated studies of the properties of semiconductor materials and thermoelectric modules of energy conversion have been presented.

3. The developed tools were used for experimental research of thermoelectric modules with known characteristics, and their high efficiency was demonstrated. The use of these tools significantly reduced the complexity of the process of measuring the basic electrical parameters of semiconductor materials and increased the accuracy of the obtained results.

The work was partially performed within the project of the Ministry of Education and Science of Ukraine «Elements of hybrid sensor microsystems for biomedical applications» (State registration number 0122U000858).

Kostyuk O. – PhD, Senior Researcher;
Dzundza B. – PhD, Associate Professor;
Pysklynets U. – PhD, Associate Professor;
Dashevsky Z. – Doctor of Sciences, Professor.

[1] I. Petsagkourakis, K. Tybrandt, X. Crispin, I. Ohkubo, N. Satoh, T. Mori, *Thermoelectric materials and applications for energy harvesting power generation*, Science and technology of advanced materials, 19(1), 836 (2018); https://doi.org/10.1080/14686996.2018.1530938.

[2] D.M. Rowe, CRC Thermoelectrics Handbook : Macro to Nano (CRC Press, Taylor & Francis Group, 2006); ISBN 9781315220390; https://doi.org/10.1201/9781420038903.

[3] J. Chen, K. Li, C. Liu, M. Li, Y. Lv, L. Jia, S. Jiang, *Enhanced Efficiency of Thermoelectric Generator by Optimizing Mechanical and Electrical Structures*, Energies, 10, 1329 (2017); https://doi.org/10.3390/EN10091329.

[4] Z. Dashevsky, A. Jarashneli, Y. Unigovski, B. Dzundza, Feng Gao, R. Shneck, *Development of a high performance gas thermoelectric generator (TEG) with possible use of waste heat,* Energies, 15, 3960 (2022); https://doi.org/10.3390/en15113960.

[5] S. Mamykin, R. Shneck, B. Dzundza, Feng Gao and Z. Dashevsky, *A Novel Solar System of Electricity and Heat,* Energies. 16, 3036 (2023); https://doi.org/10.3390/en16073036.

[6] Y.P. Saliy, B.S. Dzundza, I.S. Bylina, O.B. Kostyuk, *The influence of the technological factors of obtaining on the surface morphology and electrical properties of the PbTe films doped Bi*, Journal of Nano- and Electronic Physics, 8(2), 02045 (2016); https://doi.org/10.21272/jnep.8(2).02045.

[7] M.A. Ruvinskii, O.B. Kostyuk, B.S. Dzundza, *The Influence of the Size Effects on the Termoelectric Properties of PbTe Thin Films*, Journal of Nano- and Electronic Physics, 8(2), 02051 (2016); https://doi.org/10.21272/jnep.8(2).02051.

[8] A. Druzhinin, I. Ostrovskii, Y. Khoverko, I. Kogut, V. Golota, *Nanoscale polysilicon in sensors of physical values at cryogenic temperatures*, Journal of Materials Science: Materials in Electronics, 29(10), 8364 (2018); https://doi.org/10.1007/s10854-018-8847-0.

[9] S. El Oualid, F. Kosior, A. Dauscher, C. Candolfi, G. Span, E. Mehmedovic, J. Paris, B. Lenoir, *Innovative design of bismuth-telluride-based thermoelectric micro-generators with high output power*, Energy Environ. Sci., 13, 3579 (2020); https://doi.org/10.1039/D0EE02579H.

[10] M. Maksymuk, B. Dzundza, O. Matkivsky, I. Horichok, R. Shneck, Z. Dashevsky, *Development of the high performance thermoelectric unicouple based on Bi_2Te_3 compounds* Journal of Power Sources, 530, 231301 (2022); https://doi.org/10.1016/j.jpowsour.2022.231301.

[11] M.A. Zoui, S. Bentouba, J.G. Stocholm, M. Bourouis, *A Review on Thermoelectric Generators: Progress and Applications*, Energies, 13, 3606 (2020); https://doi.org/10.3390/EN13143606.

[12] Y. Pei, X. Shi, A. LaLonde, H. Wang, L. Chen, G.J. Snyder, *Convergence of electronic bands for high performance bulk thermoelectrics*, Nature, 473, 66 (2011); https://doi.org/10.1038/nature09996.

[13] A. Elarusi, H. Fagehi, A. Attar, H. Lee, *Theoretical Approach to Predict the Performance of Thermoelectric Generator Modules*, J. Electron. Mater., 46, 872 (2016); https://doi.org/10.1007/s11664-016-4948-9.

[14] T.C. Harman, *Special Techniques for Measurement of Thermoelectric Properties*, J. Appl. Phys., 29, 1373 (1958); https://doi.org/10.1063/1.1723445.

[15] B. Kwon, S.-H. Baek, S.K. Kim, and J.-S. Kim, *Impact of parasitic thermal effects on thermoelectric property measurements by Harman method*, Rev. Sci.Instum., 85, 045108 (2014); https://doi.org/10.1063/1.4870413.
[16] H. Iwasaki, T. Yamamoto, H. Kim, and G. Nakamoto, *Development of a Measurement System for the Figure of Merit in the High-Temperature Region*, J. Electr. Mater., 42, 1840 (2013); https://doi.org/10.1007/s11664-012-2448-0.
[17] M.S. Kang, I.J. Roh, Y.G. Lee, S.H. Baek, S.K. Kim, B.K. Ju, D.B. Hyun, J.S. Kim, B. Kwon, *Correction of the electrical and thermal extrinsic effects in thermoelectric measurements by the harman method*, Sci. Rep., 6, 26507 (2016); https://doi.org/ 10.1038/srep26507.
[18] J. Martin, T. Tritt, C. Uher, *High temperature Seebeck coefficient metrology*, Journal of Applied Physics, 108, 14 (2010); https://doi.org/10.1063/1.3503505.
[19] J. De Boor, E. Müller, *Data analysis for Seebeck coefficient measurements*, Review of scientific instruments, 84, 065102 (2013); https://doi.org/10.1063/1.4807697.
[20] A. Kumar, A. Patel, S. Singh, K. Asokan, D. Kanjilal, *Apparatus for Seebeck coefficient measurement of wire, thin film and bulk materials in the wide temperature range (80 – 650 K)*, The Review of scientific instruments, September (2019); https://doi.org/10.1063/1.5116186.
[21] Y. David. *Modeling and Application of a Thermoelectric Generator.* A thesis submitted in conformity with the requirements for the degree of Masters of Applied Science Graduate Department of Electrical and Computer Engineering University of Toronto, 98 (2011).
[22] M.O. Haluschak , V.G. Ralchenko , A.I. Tkachuk , D.M. Freik, *Methods of Measuring the Thermal Conductivity of Bulk Solids and Thin Films (Review)*, Physics and Chemistry of Solid State, 14(2), 317 (2013).

Б. С. Дзундза[1], О. Б. Костюк [1,2], У.М. Писклинець,[2] З. М. Дашевський[3]

Розробка високоточних програмно-апаратних засобів для автоматизованого визначення характеристик термоелектричних пристроїв

[1]*Прикарпатський національний університет імені Василя Стефаника, Івано-Франківськ, Україна, bdzundza@gmail.com*
[2]*Івано-Франківський національний медичний університет, Івано-Франківськ, Україна, oksanakostuk@gmail.com*
[3]*Університет Бен-Гуріона в негеві, Беер-Шева, Ізраїль, zdashev@bgu.ac.il*

У роботі розроблено високоточну установку для визначення характеристик термоелектричних приладів в діапазоні температур 350-600 К. Були виміряні вихідні параметри термоелектричних приладів, включаючи термоелектричну добротність Z, коефіцієнт Зеєбека S і внутрішній опір r. Розроблено методику, структурну схему та комп'ютерні засоби автоматизованого вимірювання та попередньої обробки експериментальних даних для автоматизованих досліджень властивостей напівпровідникових матеріалів і модулів термоелектричного перетворення енергії. Показано високу ефективність розроблених засобів. Значно зменшено трудомісткість процесу вимірювання основних електричних параметрів напівпровідникових матеріалів, а також підвищено точність отриманих результатів.

Ключові слова: термоелектрика, термоелектричні матеріали, термоелектрична ефективність, вимірювальна техніка, високоточні автоматизовані вимірювання

PHYSICS AND CHEMISTRY OF SOLID STATE
V. 24, No. 2 (2023) pp. 284-289
Section: Chemistry

DOI: 10.15330/pcss.24.2.284-289

Vasyl Stefanyk Precarpathian National University

ФІЗИКА І ХІМІЯ ТВЕРДОГО ТІЛА
Т. 24, № 2 (2023) С. 284-289
Хімічні науки

UDC: 546:548.736.4 ISSN 1729-4428

L. Romaka[1], K. Miliyanchuk[1], V.V. Romaka[2], L. Havela[3], Yu. Stadnyk[1]

Structural studies and magnetism of $Dy_6Ni_{2.43}Sn_{0.5}$ stannide

[1]*Department of Inorganic Chemistry, Ivan Franko National University of Lviv, Lviv, Ukraine, lyubov.romaka@gmail.com*
[2]*Institute for Solid State Research, IFW-Dresden, Dresden, Germany*
[3]*Department of Condensed Matter Physics, Charles University, Prague 2, The Czech Republic*

Intermetallic compound $Dy_6Ni_{2.43}Sn_{0.5}$ was prepared by arc melting and annealing at 873 K. It was characterized by X-ray powder diffraction, differential thermal analysis, and electron probe microanalysis. The crystal structure of low temperature $Dy_6Ni_{2.43}Sn_{0.5}$ phase belongs to the orthorhombic Ho_6Co_2Ga structure type (space group *Immm*, a = 0.93116(1) nm, b = 0.94993(1) nm, c = 0.98947(1) nm). Crystal structure refinements showed the deviation from the ideal 6:2:1 stoichiometry corresponding to the formula $Dy_6Ni_{2.43}Sn_{0.5}$. It exhibits a sequence of magnetic phase transitions; antiferromagnetic ordering sets in at 60 K, while further order-order magnetic phase transitions take place at lower temperatures.

Keywords: Intermetallics; Crystal structure; Magnetic properties; Heat capacity.

Received 16 January 2023; Accepted 26 April 2023.

Introduction

The search of new intermetallics with useful magnetic properties has brought lot of attention to compounds containing rare earths (*R*), *d*-metals (*M*), and *p*-elements (*X*) such as Si, Ga, Ge, Sn, In, Pb. In the *R*-rich region of the *R*–*M*–*X* ternary systems (*M* = Co, Ni; *X* = Ga, In, Sn, Pb) two series of isotypic compounds $R_{12}M_6X$ (cubic $Sm_{12}Ni_6In$-type) and R_6M_2X (orthorhombic Ho_6Co_2Ga-type) were identified and studied previously [1-8]. Both types of crystal structures are characterized by the antiprismatic-tetragonal coordination of the smaller atoms (Co, Ni) and by significant shortening of interatomic distances between rare earths and *d*-elements and between *M* atoms. The relationship between $Sm_{12}Ni_6In$ and Ho_6Co_2Ga structure types is described in Ref. [8]. In the Ho_6Co_2Ga structure, the rare earth atoms form metal bonded framework yielding several types of high coordination polyhedra encapsulating the atoms of the transition metals and *X* elements [4]. Depending on the ratio of the size of the atoms *M* and *X*, the tendency for disorder in particular crystallographic sites is observed in these structures. For example, the compounds $Tb_6Co_{2.35}Sn_{0.65}$ [9], $Ho_6Co_{2.135}In_{0.865}$ [6], $Er_6Co_{2.19}In_{0.81}$ [10], and $R_6M_{2+x}Pb_{1-x}$ (*M* = Co, Ni) [8] are characterized by statistical mixture of *M* and *X* atoms in the 2*a* site, while in the original Ho_6Co_2Ga structure type it is occupied exclusively by Ga atoms. In $Dy_6Co_{2.5}Sn_{0.5}$, the Co atoms occupy three crystallographic sites, and only 2*c* position is occupied by the Sn atoms [11]. Study of isotypic compounds with bismuth [12] showed that unlike the Ho_6Co_2Ga prototype, the 2*a* position is occupied by Co atoms and authors propose the formula $R_{12}Co_5Bi$ (equal to $R_6Co_{2.5}Bi_{0.5}$) which reflects the occupancy of crystallographic positions in the structure.

Taking into account that the complex magnetic behavior arises from the connection of *f*- and *d*-electrons in rare-earth intermetallics with transition elements, the properties of stannides $R_{12}Ni_6Sn$ and R_6M_2Sn were explored. A study of magnetic properties revealed that the $R_{12}Ni_6Sn$ intermetallics exhibit ferromagnetic ordering for Gd and Tb compounds with T_C = 85 K and 95 K, respectively [1]. The temperature dependencies of the magnetic susceptibility measured earlier in the range 78-293 K for R_6Ni_2Sn compounds (*R* = Tb, Dy, Er, and Tm) showed that they obey the Curie-Weiss law with effective magnetic moments close to free R^{3+} ion values [5, 7].

The isotypic stannide Er_6Ni_2Sn has been investigated as potential material for the lower temperature stage of Gifford-McMahon cryocooler [13]. Refs. [14,15]

suggested, based on specific-heat data and magnetic measurements of Er_6Ni_2Sn giving estimates of isothermal entropy change and magnetocaloric effect, that this compound can serve as material for cryogenic devices. Neutron diffraction study of Er_6Ni_2Sn showed a complex non-collinear commensurate antiferromagnetic structure [16], in which the magnetic moment values of Er atoms are significantly reduced.

The present work aims to determine structure characteristics and magnetic properties of $Dy_6Ni_{2.43}Sn_{0.5}$. In addition, magnetic behaviour of the binary Dy_5Sn_3 is presented.

I. Experimental details

Polycrystalline samples for investigation were prepared by direct arc melting of the constituent metals (dysprosium, purity 99.9 wt.%; nickel, purity 99.99 wt.%; tin, purity 99.999 wt.%) under purified argon atmosphere (Ti as a getter) in a water-cooled copper crucible. Weight losses of the initial batch did not exceed 1 wt. %. Two pieces of the alloys were annealed separately in the evacuated quartz ampoules at T = 873 K and T = 1073 K for 720 hours and then quenched in cold water. The synthesized and annealed samples are stable under ambient conditions. The chemical composition of the prepared samples was examined by Scanning Electron Microscopy using JEOL-840A scanning microscope.

X-ray powder diffraction data were collected using STOE STADI P powder diffractometer (Cu $K\alpha_1$ radiation, angular range for data collection $6.000 \le 2\theta \le 110.625/0.015$). FullProf Suite program package [17] was used for the determination of the crystal structure parameters.

Differential thermal analysis (DTA) was used to check the temperature range of the stability of the compound (LINSEIS STA PT 1600 device, argon atmosphere). Sample was heated up to 1173 K, at a rate of 10 K/min. The weight losses during heating (TG) were less than 0.2%.

The magnetic susceptibility was measured in external magnetic fields up to 9 T in the temperature range from 2 K to 300 K using a Quantum Design PPMS extraction magnetometer. The grains of the sample were fixed in random orientation preventing rotation of individual grains under the influence of a magnetic field. The specific heat measurements were performed on a bulk sample in the same temperature range using a Quantum Design PPMS microcalorimetry setup.

The magnetic behavior of the Dy_5Sn_3 compound was measured using an extraction method in the magnetic fields up to 10 T in the temperature range 2 K to 300 K.

II. Results and discussion

2.1. Formation of compounds and crystal structure refinement

Taking into account the literature data and general stoichiometry 6:2:1 for the R_6Ni_2Sn series, a polycrystalline sample with nominal composition $Dy_{67}Ni_{22}Sn_{11}$ was prepared. X-ray phase analysis of the sample showed the presence of the main phase Dy_6Ni_2Sn with the Ho_6Co_2Ga structure type and a small amount of additional binary phase Dy_5Sn_3 (Mn_5Si_3 structure type, a = 0.88863(1), c = 0.64873(1) nm). According to the electron probe microanalysis (EPMA) data, the determined composition of the main phase is $Dy_{66.62}Ni_{27.67}Sn_{5.71}$, meaning lower Sn concentration in comparison with the ideal 6:2:1 stoichiometry. As the next step, we prepared a new sample with the nominal composition $Dy_{66}Ni_{28}Sn_6$. In order to synthesize a single-phase sample we used two different temperatures of annealing, namely 873 and 1073 K. The phase analysis of the sample annealed at 873 K proved the existence of orthorhombic phase with the Ho_6Co_2Ga structure type, while a phase with the cubic $Sm_{12}Ni_6In$ structure type was identified in the sample annealed at 1073 K. To confirm a polymorphic transition we have studied the sample by the differential thermal analysis. The DTA curve measured in the heating and cooling regimes is shown in Fig. 1. Two thermal peaks are more visible on the cooling curve at 1098.5 K and 1015.3 K, respectively, which can be associated with the formation of the cubic phase and next polymorphic transition to the orthorhombic one. Thus, we can stay that orthorhombic phase is stable up to ≈ 1015 K.

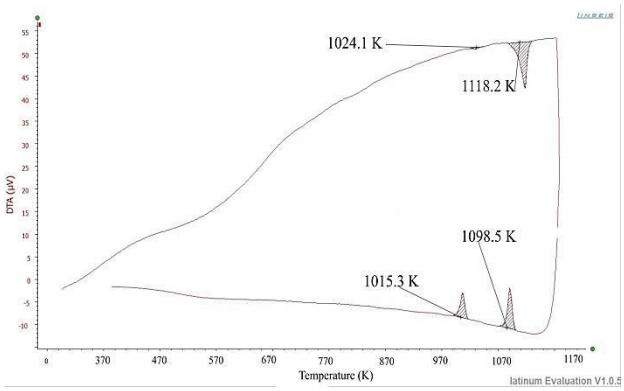

Fig. 1. DTA plot for $Dy_{66}Ni_{28}Sn_6$ sample.

Analysis of X-ray powder diffraction pattern of the $Dy_{66}Ni_{28}Sn_6$ sample annealed at T = 870 K showed the presence of a single phase with orthorhombic Ho_6Co_2Ga-type (space group *Immm*, a = 0.93116(1) nm, b = 0.94993(1) nm, c = 0.98947(4) nm). Refined atomic coordinates and displacement parameters for Ho_6Co_2Ga-type phase are listed in Table 1. The refinement of the site occupancies showed that in this structure Ni atoms fully occupy the 4*j* position and both 4*g* and 2*a* positions for Ni atoms are occupied partially (Table 1). Thus, the chemical formula should be written as $Dy_6Ni_{2.43}Sn_{0.5}$, what is in a good agreement with EPMA data ($Dy_{66.62}Ni_{27.67}Sn_{5.71}$). Obtained stoichiometry is close to the previously studied $Tb_6Co_{2.35}Sn_{0.65}$ [9] and $R_6M_{2+x}Pb(In)_{1-x}$ (M = Co, Ni) [6,8,10] compounds, which are characterized by a lower concentration of the *p*-element compared to the ordered Ho_6Co_2Ga-type phase.

Crystal chemical analysis of the stannide $Dy_6Ni_{2.43}Sn_{0.5}$ showed that this structure can be presented as a framework of Dy atoms forming prismatic and icosahedral polyhedra filled with the smaller Ni and Sn atoms (Fig. 2) The analysis of the interatomic distances in the $Dy_6Ni_{2.43}Sn_{0.5}$ structure showed a significant variations

Table 1.

Atomic coordinates and isotropic displacement parameters for the $Dy_6Ni_{2.43}Sn_{0.5}$ compound (R_{Bragg} = 0.039, R_p = 0.011, R_{wp} = 0.015)

Atom	Wyckoff position	*x*/*a*	*y*/*b*	*z*/*c*	$*B_{iso}\cdot10^2$ (nm^2)	Occupancy
Dy1	8*n*	0.2924(2)	0.1821(2)	0	1.17(8)	1
Dy2	8*m*	0.3030(2)	0	0.3233(1)	0.49(8)	1
Dy3	8*l*	0	0.1903(2)	0.2146(2)	0.84(8)	1
Ni1	4*j*	1/2	0	0.1233(6)	1.72(2)	1
Ni2	4*g*	0	0.3633(7)	0	1.57(6)	0.95(1)
Ni3	2*a*	0	0	0	1.62(1)	0.96(1)
Sn	2*c*	1/2	1/2	0	0.88(1)	1

of the sum of the corresponding atomic radii (r_a(Dy) = 0.177 nm, r_a(Ni) = 0.125 nm): for shorter Dy-Ni distances Dy1-Ni1 – 0.2849 nm; Dy2-Ni2 – 0.2847 nm; Dy3-Ni2 – 0.2821 nm and Ni1-Ni1 distance 0.2440 nm. The shortening in interatomic distances in $Dy_6Ni_{2.43}Sn_{0.5}$ is similar to the shortening in the prototype Ho_6Co_2Ga [4] and in other isotypic intermetallics with Sn or Pb [8, 9].

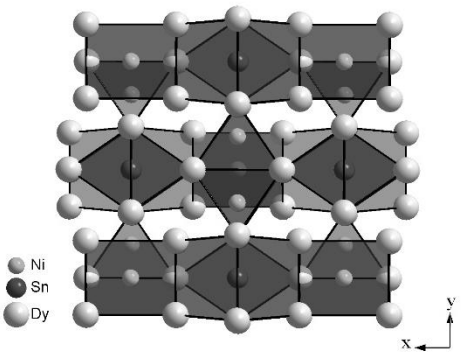

Fig. 2. Atomic columns in $Dy_6Ni_{2.43}Sn_{0.5}$ structure formed by Dy atoms. The smaller Ni and Sn atoms are inside prismatic and icosahedral voids.

It should be pointed out that the crystal structure of $Dy_6Ni_{2.43}Sn_{0.5}$ can be derived from the WAl_{12} structure type by an insertion of Ni and Sn atoms into binary WAl_{12} [7]. Both compounds are characterized by similar 3D-framework structure built by Dy and Al atoms, respectively (Fig. 3).

The analysis of the structures Ho_6Co_2Ga [4] and the isotypic $R_6M_{2+x}X_{1-x}$ intermetallics (*M* = Co, Ni and *X* = Ga, In, Sn, Pb, and Bi) [5-12] illustrated the role of the size of the *X* element in structural disorder. The Ho_6Co_2Ga structure is completely ordered, small Ga atoms occupy two crystallographic sites 2*c* and 2*a* fully. Crystal structures of the related compounds with larger *X* atoms show that the crystallographic position 2*a*, occupied only by Ga atoms in Ho_6Co_2Ga-type, is strongly susceptible to accommodate statistical mixtures with *d*-metals, what results in a deviation from the ideal stoichiometry 6:2:1. This fact was observed for the compounds $Tb_6Co_{2.35}Sn_{0.65}$, $Ho_6Co_{2.135}In_{0.865}$, $Er_6Co_{2.19}In_{0.81}$, $R_6M_{2+x}Pb(Bi)_{1-x}$ [6, 8-12], and finally for $Dy_6Ni_{2.43}Sn_{0.5}$.

2.2. Magnetic and heat capacity measurements

For the $Dy_{67}Ni_{22}Sn_{11}$ sample we performed magnetic susceptibility measurements in magnetic field of 0.05 T, 2 T, and 4 T in the temperature range 2-300 K. The field dependence of magnetization was measured in magnetic fields up to 9 T for temperatures *T* = 2, 20, and 40 K. Fig. 4 shows that the high temperature Curie-Weiss behavior extends down only to 60-70 K and below this temperature the values of $\chi(T)$ become field dependent. In the paramagnetic state the temperature dependence of the inverse magnetic susceptibility $\chi^{-1}(T)$ is well described by the Curie-Weiss law with the value of effective moment 10.60 μ_B/Dy, *i.e.* close to the value for free ion Dy^{3+}(10.65 μ_B) (Fig. 5). The paramagnetic Curie temperature θ_p = 26 K is lower than the transition temperature but still positive, which indicates predominant ferromagnetic interactions. Temperature behavior of the magnetic susceptibility exhibits a kink, pointing to an antiferromagnetic ordering below about

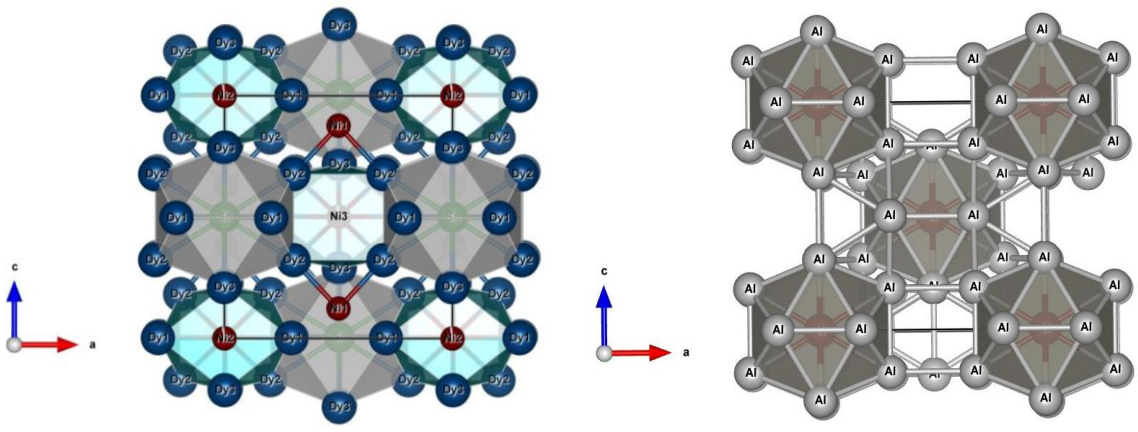

a b

Fig. 3. Model of $Dy_6Ni_{2.43}Sn_{0.5}$ (a) and WAl_{12} (b) structures.

60 K (see Fig. 4). However, $\chi(T)$ still increases below this temperature (at least in low magnetic fields) and another kink is visible at T = 27 K, which may suggest presence of a magnetic phase transition of the order-order type. A smaller anomaly see particularly for the 2 T data can be distinguished at 19 K. The $\chi(T)$ measurement in very low magnetic field (0.05 T) reveals a small ferromagnetic component developing below T = 60 K. As the size of the increment in the inset of Fig. 4 is $\approx 6\times10^{-5}$ m^3/mol f.u., i.e. < 0.5 μ_B/f.u., it means less than 0.1 μ_B/Dy. Hence we most likely encounter a defected antiferromagnetic structure with incomplete cancelation of sublattices, related most likely to the statistical occupancy of several crystallographic sites. Although the magnetism has be related to Dy only and no Ni moments are anticipated, the defected Dy environment brings randomness into the RKKY interaction, yielding certain features of magnetic glass, as magnetic history phenomena in antiferromagnet. This suggestion is corroborated by the fact that there is residual magnetization of 2 μ_B/f.u. when returning to zero field from a high field state in μ_0H = 9 T at T = 2 K (see Fig. 6).

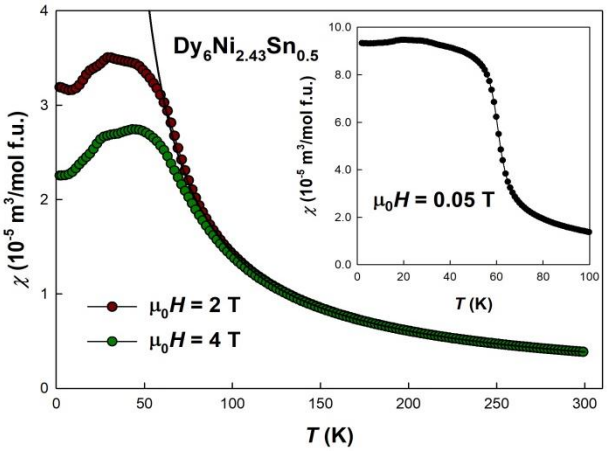

Fig. 4. Temperature dependences of the magnetic susceptibility χ(T) of $Dy_6Ni_{2.43}Sn_{0.5}$ in various magnetic fields. Detail of low-field data are shown in the inset.

The magnetization curve measured at T = 2 K (Fig. 6) exhibits a metamagnetic process starting at $\mu_0H \approx$ 3 T, which brings the total magnetization to the level of 25–30 μ_B/f.u. It is still only a half of the theoretical total magnetization of 60 μ_B/f.u. The related broad hysteresis becomes narrower but it is still observed at 20 K, shifting the metamagnetic transition to lower fields, while both hysteresis and metamagnetic transition disappear at 40 K. The total magnetization achieved can be naturally affected by anisotropy, the type and strength remain unknown. For example, only 50% of total magnetization is measured if a strongly anisotropic material with uniaxial anisotropy is measured in the form of randomly oriented polycrystal. Therefore it is also impossible to determine with certainty whether the metamagnetism is of the spin-flip or spin-flop type. Even in the first case, the distribution of orientation of individual grains with respect to the field direction can cause a spreading of the transition over a large field range.

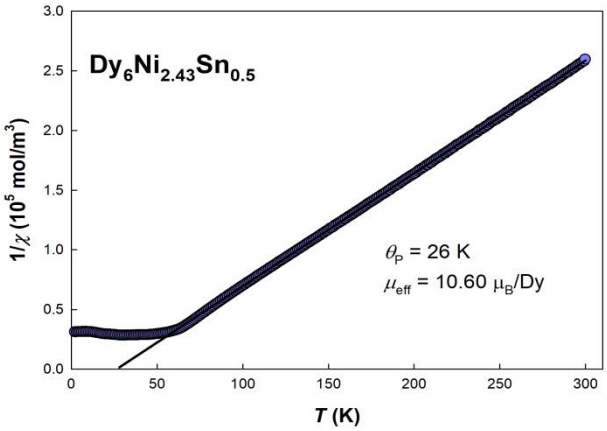

Fig. 5. Temperature dependence of the inverse magnetic susceptibility of the $Dy_6Ni_{2.43}Sn_{0.5}$ compound (μ_0H = 2T).

Complementary information can be obtained from the temperature dependence of specific heat at constant pressure, $C_p(T)$. It exhibits a clear phase transition at T = 62 K, which remains practically unchanged in magnetic field of 2 T (Fig. 7).

External magnetic field of 9 T, *i.e.* exceeding the critical metamagnetic field, removes the magnetic phase transition and the related entropy is displaced to higher temperatures as in ferromagnets. Therefore we can assume that the state above the metamagnetic transition corresponds to field-aligned paramagnetic state, however not necessarily with full collinearity of magnetic moments. The slope of $M(H)$ in 9 T indicates that the alignment process would continue even to much higher fields. At low temperatures one can use the $C_p/T(T^2)$ plot to determine the Sommerfeld coefficient of electronic specific hear γ as the intercept of extrapolated line with the vertical axis (see inset). For $Dy_6Ni_{2.43}Sn_{0.5}$ we can make only a very approximate estimate yielding $\gamma \approx$ 200 mJ/mol f.u. K^2. The linear part is actually short, limited from below probably by the nuclear heat capacity component of Dy [18].

As presence of a small amount of Dy_5Sn_3 in the sample has been indicated, a question is whether some of the anomalies observed can be associated with such spurious phase. Therefore we prepared Dy_5Sn_3 sample, annealed at T = 873 K, and its magnetic behavior determined. According to X-ray analysis, Dy_5Sn_3 crystallizes in the Mn_5Si_3 structure type (space group $P6_3/mcm$) with refined lattice parameters a = 0.88633(1), c = 0.64873(1) nm. The maximum in the temperature dependence of the magnetic susceptibility in the temperature range 2-100 K indicates an antiferromagnetic ordering at T_N = 20 K (Fig. 8,a). Analysis of the temperature dependence of the inverse magnetic susceptibility showed that the paramagnetic Curie temperature is Θ_P = 14 K, calculated effective moment 10.71 μ_B/Dy is close to Dy^{3+}. The field dependencies of the magnetization are displayed in Fig. 8,b. At low temperatures they reveal rather fast initial increase and a weak tendency to saturation in fields exceeding 5-6 T. It can be interpreted as canting of Dy moments starting from low fields already. Therefore the antiferromagnetic transition is eliminated in the field of 1 T. Hence Dy_5Sn_3 cannot be taken responsible low-temperature anomalies seen in $\chi(T)$ for $Dy_6Ni_{2.43}Sn_{0.5}$ in the field of 2 or 4 T.

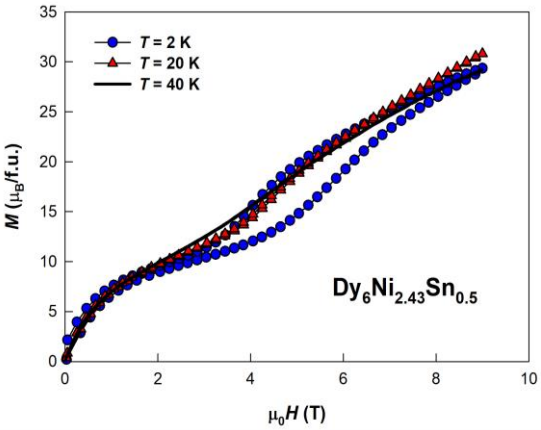

Fig. 6. Field dependence of magnetization of $Dy_6Ni_{2.43}Sn_{0.5}$ at various temperatures with field swept up and down.

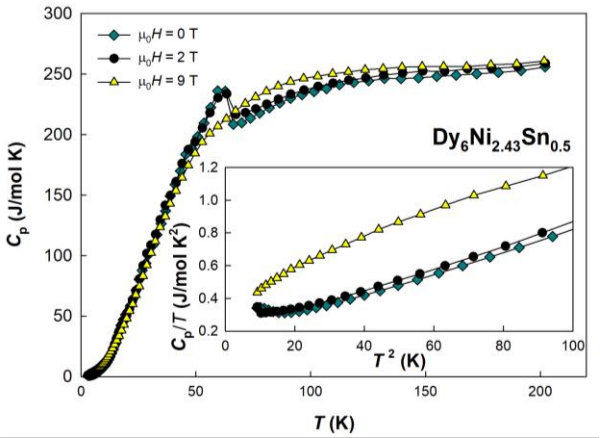

Fig. 7. Temperature dependence of the specific heat of $Dy_6Ni_{2.43}Sn_{0.5}$.

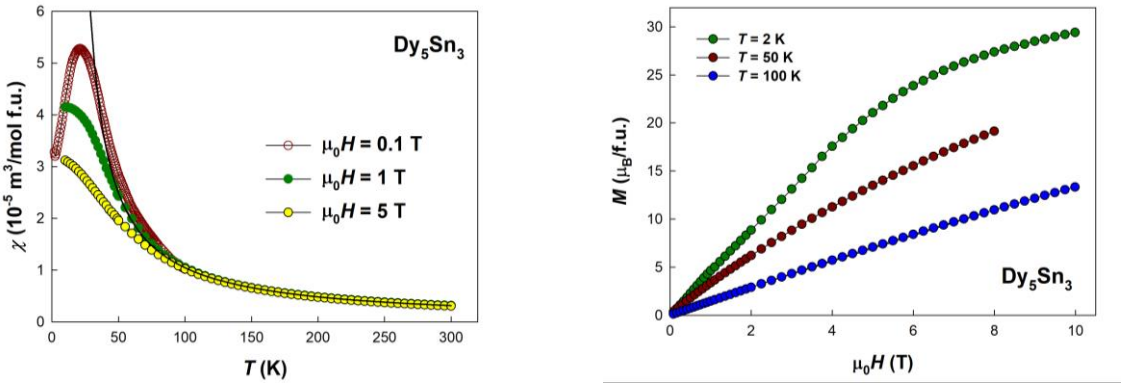

a b

Fig. 8. Temperature dependence of the magnetic susceptibility of Dy_5Sn_3 it various magnetic fields (a); magnetization vs magnetic field at different temperatures (b).

Considerable anomalies concerning the magnetic ordering of impurity phase Dy_5Sn_3 were not observed in the temperature dependence of magnetic susceptibility of $Dy_6Ni_{2.43}Sn_{0.5}$. Taking into account this result we can rule out contribution of impurity phase Dy_5Sn_3 in the magnetism of the $Dy_6Ni_{2.43}Sn_{0.5}$ stannide.

Conclusions

Structure refinements of the $Dy_6Ni_{2.43}Sn_{0.5}$ compound confirmed that this compound belongs to the orthorhombic Ho_6Co_2Ga structure type but contrary to the prototype Ho_6Co_2Ga compound a significant deviation from the 6:2:1 stoichiometry has been observed. This deviation is caused by the exclusive presence of Ni atoms at the 2*a* site and a partial occupation of the 4*g* and 2*a* sites by Ni atoms. The phase situation is, however, affected by annealing.

The results of the magnetic and heat capacity measurements indicated a magnetic transition at 60 K connected with antiferromagnetic ordering. Further order-order phase transitions have been observed at lower temperatures. The calculated effective magnetic moments in paramagnetic state is closed to the value for free ion Dy^{3+}, indicating a main role of rare earth in the magnetism of $Dy_6Ni_{2.43}Sn_{0.5}$. Statistical occupation of several Ni sites yields a glassy behavior and magnetic history phenomena.

Acknowledgements

We would like to acknowledge financial support of the Ministry of Education and Science of Ukraine under Grant No. 0121U109766. We also thank Prof. O. Isnard for assistance with collecting part of the magnetic data.

Romaka Lyubov – Ph.D., Senior Researcher, Ivan Franko National University of Lviv;
Miliyanchuk Khrystyna – Ph.D., Senior Researcher, Ivan Franko National University of Lviv;
Romaka Vitaliy – D.Sc., Doctor of material science, Institute for Solid State Research, Dresden, Germany;
Havela Ladislav – CSc., RNDr, Senior Researcher, Charles University, Prague, Czech Republic;
Stadnyk Yuriy – Ph.D., Senior Researcher, Ivan Franko National University of Lviv.

[1] L. Romaka, O. Senkovska, D. Fruchart, D. Gignoux, Gignoux, *Crystal structure and magnetic properties of new rare earth $R_{12}Ni_6Sn$ compounds*, J. Magn. Magn. Mater., 242-245, 854 (2002); https://doi.org/10.1016/S0304-8853(01)01342-7.

[2] Ya.M. Kalychak, *Composition and crystal structure of rare-earths-Co-In compounds*, J. Alloys Compd., 291, 80 (1999); https://doi.org/10.1016/S0925-8388(99)00290-X.
[3] L.D. Gulay, Ya.M. Kalychak, M. Wolcyrz, K. Lukaszewicz, *Crystal structure of $R_{12}Ni_6Pb$ (R = Y, Sm, Gd, Tb, Dy, Ho, Er, Tm, Lu) compounds*, J. Alloys Compd., 311, 238 (2000); https://doi.org/10.1016/S0925-8388(00)01115-4.
[4] R.E. Gladyshevskii, Yu.N. Gryn', Ya.P. Yarmolyuk, *The crystal structure of R_6GaCo_2 compounds (R = Y, Tb, Dy, Ho, Er, Tm, Lu)*, Dopov. Akad. Nauk Ukr. RSR A2, 67 (1983).
[5] O.M. Sichevich, L.P. Komarovskaja, Yu.N. Grin, Ya.P. Yarmolyk, R.V. Skolozdra, *Crystal structure and magnetic properties of $R_6Ga\{Co,Ni\}_2$ and R_6SnNi_2 compounds (R-rare earths)*, Ukr. J. Phyz., 29, 1342 (1984).
[6] J.M. Kalychak, V.I. Zaremba, P.Y. Zavalij, *Crystal structure of holmium cobalt indium (6/2/1) $Ho_6Co_{2+x}In_{1-x}$, x = 0.135*, Z. Kristallogr. 208, 380 (1993).
[7] R.V. Skolozdra, in: K.A. Gschneidner, Jr., L.Eyring (Eds.), *Handbook on the Physics and Chemistry of Rare-Earths*, Vol. 24, North-Holland, Amsterdam, 1997, chapt. 164.
[8] L.D. Gulay, M. Wolcyrz, *Crystal structure of $R_6Co_{2+x}Pb_{1-y}$ (R = Y, Gd, Tb, Dy, Ho, Er, Tm, Lu) and $R_6Ni_{2+x}Pb_{1-y}$ (R = Tb, Dy, Ho, Er, Tm, Lu) compounds*, J. Alloys Compd., 315, 164 (2001); https://doi.org/10.1016/S0925-8388(00)01281-0.
[9] A.V. Kolomiets, Ya. Mudryk, Yu. Stadnyk, V. Sechovsky, *Crystal structure and magnetic properties of $Tb_6Co_{2.35}Sn_{0.65}$*, J. Alloys Compd., 333, 34 (2002); https://doi.org/10.1016/S0925-8388(01)01715-7.
[10] V.I. Zaremba, Y.M. Kalychak, M.V. Dzevenko, U.C. Rodewald, R.D. Hoffmann, R. Pöttgen, *Syntheses and structure of $Er_6Co_{2.19(1)}In_{0.81(1)}$*, Monatsh. Chem., 138, 101 (2007); https://doi.org/10.1007/s00706-006-0572-3.
[11] A.V. Morozkin, R. Nirmala, S.K. Malik, *Magnetic and magnetocaloric properties of Ho_6Co_2Ga-type $Dy_6Co_{2.5}Sn_{2.5}$ compound*, J. Magn. Magn. Mater., 378, 174 (2015); https://doi.org/10.1016/j.jmmm.2014.11.011.
[12] A.V. Tkachuk, A. Mar, *Structure and physical properties of ternary rare-earth cobalt bismuth intermetallics $(RE)_{12}Co_5Bi$ (RE = Y, Gd, Tb, Dy, Ho, Er, Tm)*, Inorg. Chem., 44(7), 2272 (2005); https://doi.org/10.1021/ic048195p.
[13] K.A. Gschneidner, V.K. Pecharsky, M. Gailloux, in: R.G. Ross Ir. (Ed.), Cryocoolers 8, Plenum Press, New-York, 1995.
[14] O. Syshchenko, Yu. Stadnyk, L. Romaka, Ya. Mudryk, R.V. Dremov, V. Sechovsky, *Magnetic and transport properties of Er_6Ni_2Sn*, J. Alloys Compd., 319, 14 (2001); https://doi.org/10.1016/S0925-8388(01)00877-5.
[15] D. Vasylyev, O. Syshchenko, V. Sechovsky, J. Sebek, Yu. Stadnyk, Ya. Mudryk, L. Romaka, *Magnetocaloric effect in Er_6Ni_2Sn*, Czech. J. Phys., 52, A205 (2002); https://doi.org/10.1007/s10582-002-0049-5.
[16] K. Prokes, V. Sechovsky, O. Syshchenko, *Magnetic structure of Er_6Ni_2Sn*, J. Alloys Compd., 48-53, 467 (2009); https://doi.org/10.1016/j.jallcom.2007.12.022.
[17] T. Roisnel, J. Rodriguez-Carvajal, *WinPLOTR: a Windows tool for powder diffraction patterns analysis*, Mater. Sci. Forum, 378–381, 118 (2001). https://doi.org/10.4028/www.scientific.net/MSF.378-381.118
[18] O.V. Lounasmaa, R. A. Guenther, *Specific heat of dysprosium metal between 0.4 and 4°K*, Phys. Rev., 126, 1357 (1962); https://doi.org/10.1103/PhysRev.126.1357

Л. Ромака[1], Х. Міліянчук[1], В.В. Ромака[2], Л. Гавела[3], Ю. Стадник[1]

Структурні дослідження і магнетизм станіду $Dy_6Ni_{2,43}Sn_{0,5}$

[1]*Львівський національний університет ім. І.Франка, Львів, Україна, lyubov.romaka@gmail.com*
[2]*Інститут досліджень твердого тіла, IFW-Дрезден, Дрезден, Німеччина*
[3]*Кафедра фізики твердого тіла, Карлів університет, Прага 2, Чехія*

Інтерметалід $Dy_6Ni_{2,43}Sn_{0,5}$ отриманий методом електродугового плавлення і гомогенізуючого відпалювання за температури 873 K. Сполука досліджена методами рентгенівської дифрактометрії, диференціального термічного аналізу і енергодисперсійної спектроскопії. Кристалічна структура низькотемпературної фази $Dy_6Ni_{2,43}Sn_{0,5}$ належить до орторомбічного структурного типу Ho_6Co_2Ga (просторова група *Immm*, *a* = 0,93116(1) нм, *b* = 0,94993(1) нм, *c* = 0,98947(1) нм). Структурні розрахунки засвідчили відхилення від ідеальної стехіометрії 6:2:1, що відповідає формулі $Dy_6Ni_{2,43}Sn_{0,5}$. Для сполуки встановлено послідовність магнітних фазових переходів; антиферомагнітне впорядкування виникає при 60 K, подальші магнітні фазові переходи порядок-порядок відбуваються за нижчих температур.

Ключові слова: Інтерметаліди; Кристалічна структура; Магнітні властивості; Питома теплоємність.

PHYSICS AND CHEMISTRY OF SOLID STATE
V. 24, No. 2 (2023) pp. 290-297
Section: Physics

DOI: 10.15330/pcss.24.2.290-297

Vasyl Stefanyk Precarpathian National University

ФІЗИКА І ХІМІЯ ТВЕРДОГО ТІЛА
Т. 24, № 2 (2023) С. 290-297
Фізико-математичні науки

PACS: 61.46.-w, 62.23.Hj, 73.63.-b

ISSN 1729-4428

A.O. Koval[1,2]

Frequency shifts of surface plasmon resonances in calculating the absorption coefficient of a composite based on bimetallic 1d-systems

[1]*Zaporizhzhia Polytechnic National University, Zaporizhzhia, Ukraine*
[2]*Scientific and Production Complex "Iskra", Zaporizhzhia, Ukraine, andrej.koval@ukr.net*

In this paper analyzes the electromagnetic radiation absorption by a composite based on bimetallic nanowires. Using the Drude-Lorentz theory it was obtained the relationship for the polarizability frequency dependences, as well as real and imaginary parts of the dielectric function of layered 1D-systems was obtained. It is shown that the structure in the form of a metal core covered with a layer of another metal leads to splitting and the appearance of two maxima in the frequency dependence of the absorption coefficient. The positions of the maxima are determined by the composition of bimetallic nanowires and the volume content of metals. The influence of the dimensionality of the systems has been established by comparing the frequency dependences of the composite absorption coefficient based on bimetallic nanowires and nanoparticles. Calculations were performed for Ag@Au and Au@Ag nanowires immersed in Teflon.

Keywords: bimetallic nanowire, surface plasmon resonance, polarizability, dielectric function, absorption coefficient.

Received 5 November 2022; Accepted 15 May 2023.

Introduction

The widespread use of metal 1D-systems is due to their unique optical features associated with the regulation of electromagnetic radiation absorption by changing the size, shape and material of the studied samples [1]. Modern technologies allow experimentally obtaining and measuring the optical properties of metal nanowires in various spectral ranges. The theoretical study of the mentioned nanostructures is of interest in connection with the possibility of explaining the position and magnitude of the optical absorption maximum. The ability to adjust the energy and optical characteristics of 1D structures is a promising task from the point of view of using the latter in the form of high-speed switches in the creation of information transmission and processing systems, optical photosensors [2,3], etc.

Recently, studies of composite materials based on two-layer nanostructures have attracted considerable attention. The formation of an oxide layer on the metal wire surface makes it possible to regulate more effectively the position of the surface plasmon resonance (SPR) by changing both the oxide layer thickness and the metal core radius [4]. In turn, the application of a metal layer on the dielectric core leads to the appearance of two frequency maxima of optical absorption due to the surface plasmons hybridization [5]. An intuitively simple model (which is easily extended to multilayer structures) allows to explain the emergence of two resonance maxima due to the plasmon resonance splitting into low-energy symmetric and high-energy antisymmetric modes caused by the interaction of the dielectric core (hollow) with the metal shell inner wall on the one hand and, due to the connection of the metal layer outer wall with the surrounding dielectric medium on the other side. It is obvious that the plasmons interaction with each other directly depends on the metal shell thickness.

In contrast to the above-mentioned types of two-layer structures, bimetallic systems are characterized by a wide spectral range of the SPR shift due to the difference in the scattering and absorption of light by different metal fractions. Au and Ag are usually used as metals for bimetallic wires due to the ease of obtaining and

controlling the parameters of such structures. Experimental growth of Ag@Au nanowires with adjustable optical properties is presented in works [6,7]. A theoretical study of the light wave absorption cross-section of the Ag@Au and Au@Ag 1D-systems using the quasi-static theory is given in [8]. Along with Au and Ag, noble metals Pd and Pt are widely used as photocatalysts. In [9], the oxidase-like properties of Pd@Pt nanowires were experimentally studied. The chemical synthesis of Pt@Ag nanowires and their subsequent use as electrocatalysts are discussed in [10].

In connection with the broad prospects of using bimetallic 1D systems as light-stable color filters, polarizers, optical sensors [11], for biological labeling and surface Raman scattering [12], the study of their optical parameters is a relevant task. The purpose of this work is to calculate the composite absorption coefficient based on bimetallic nanowires and analytical estimates the plasmon resonance maxima shifts depending on the composition and sizes of the core and shell metal fractions.

I. Basic relations

Let's consider a composite that consists of a dielectric matrix with permeability ε_m and cylindrical bimetallic inclusions with a total radius of $R = R_c + R_{sh}$ (the length of the wire L is assumed to be much greater than R), where R_c is the radius of the metal core covered with a layer of another metal with a value of R_{sh}. The absorption coefficient of the composite is determined by the ratio [13]:

$$\eta(\omega) = \frac{\omega}{3c}\beta\varepsilon_m^{3/2}\sum_j \frac{1}{P_j^2}\frac{Im\,\varepsilon_{c-sh}}{\left(Re\,\varepsilon_{c-sh}+\frac{1-P_j}{P_j}\varepsilon_m\right)^2+Im\,\varepsilon_{c-sh}^2}, \qquad (1)$$

where ω is the frequency of the incident electromagnetic wave; c is the speed of light; β is the volume content of cylindrical layered systems; P_j is the depolarization factor; $j = x, y, z$; $Re\,\varepsilon_{c-sh}$ and $Im\,\varepsilon_{c-sh}$ are the real and imaginary parts of core-shell system dielectric function.

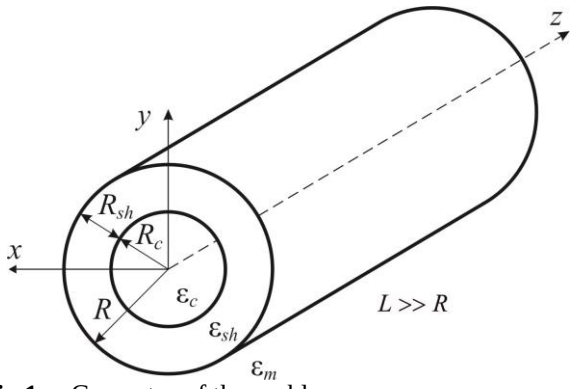

Fig.1. – Geometry of the problem.

Let us assume that an electromagnetic wave is incident on a cylindrical two-layer nanowire perpendicular to wire axis (the movement of electrons along the axis of the wire is neglected), as a result of which the wave vector lies in the plane xy and $P_z = 0,\ P_x = P_y = (1 - P_z)/2$. Then

$$\eta_{1D}(\omega) = \frac{8\omega}{3c}\beta\varepsilon_m^{3/2}\frac{Im\,\varepsilon_{1D(c-sh)}}{(Re\,\varepsilon_{1D(c-sh)}+\varepsilon_m)^2+Im\,\varepsilon_{1D(c-sh)}^2} \qquad (2)$$

The expression for the dipole polarizability of a cylindrical monosystem has the form:

$$\tilde{\alpha}_{1D(c-sh)} = \frac{\varepsilon_{1D(c-sh)}-\varepsilon_m}{\varepsilon_{1D(c-sh)}+\varepsilon_m}. \qquad (3)$$

On the other hand, the polarizability of such a system is found by solving the Laplace equation in a cylindrical coordinate system

$$\frac{\partial^2\varphi_i}{\partial r^2}+\frac{1}{r}\frac{\partial\varphi_i}{\partial r} = 0 \quad (i = 1,2,3)$$

taking into account the boundary conditions at the boundary of media

$$\varphi_1|_{r=R_c} = \varphi_2|_{r=R_c};\ \varphi_2|_{r=R} = \varphi_3|_{r=R};$$

$$\varepsilon_c\frac{\partial\varphi_1}{\partial r}\Big|_{r=R_c} = \varepsilon_{sh}\frac{\partial\varphi_2}{\partial r}\Big|_{r=R_c};\quad \varepsilon_{sh}\frac{\partial\varphi_2}{\partial r}\Big|_{r=R} = \varepsilon_m\frac{\partial\varphi_3}{\partial r}\Big|_{r=R},$$

where ε_c and ε_{sh} are the dielectric functions of the metal core and shell, respectively:

$$\varepsilon_c(\omega) = \varepsilon_1(\omega) + i\varepsilon_2(\omega) = \varepsilon_c^{\infty} - \frac{\omega_{pl(c)}^2\tau_{eff(c)}^2}{1+\omega^2\tau_{eff(c)}^2} + i\frac{\omega_{pl(c)}^2\tau_{eff(c)}}{\omega(1+\omega^2\tau_{eff(c)}^2)},$$

$$\varepsilon_{sh}(\omega) = \varepsilon_3(\omega) + i\varepsilon_4(\omega) = \varepsilon_{sh}^{\infty} - \frac{\omega_{pl(sh)}^2\tau_{eff(sh)}^2}{1+\omega^2\tau_{eff(sh)}^2} + i\frac{\omega_{pl(sh)}^2\tau_{eff(sh)}}{\omega(1+\omega^2\tau_{eff(sh)}^2)},$$

$\varepsilon_{c,sh}^{\infty}$ – the component responsible for the contribution of the ionic backbone of the core and shell metals, $i = \sqrt{-1}$, $\omega_{pl(c,\ sh)}^2 = \frac{\bar{n}_{c,sh}e^2}{\varepsilon_0 m_{c,sh}^*}$ – bulk plasma frequency, ε_0 – electric constant, $\bar{n}_{c,sh} = \left(4\pi r_{s(c,sh)}^3/3\right)^{-1}$ – concentration of conduction electrons, $r_{s(c,sh)}$ – average distance between conduction electrons, $m_{c,sh}^*$ – effective electron mass, $\tau_{eff(c,sh)}^{-1} = \tau_{bulk(c,sh)}^{-1} + \gamma_{1D(c,sh)}(\omega)$ – effective relaxation time, $\tau_{bulk(c,sh)}$ – relaxation time in the bulk metal, $\gamma_{1D(c,sh)}$ is the decrement of the attenuation of the dipole plasma oscillations of the cylindrical metal core and shell, respectively.

For a metal particle in the elongated ellipsoid form of rotation (that is, at $0 \le e_p \le 1$, where e_p is the eccentricity of the spheroid), the parameter γ based on the kinetic approach is calculated as [14]

$$\gamma_{c,sh}(\omega) = \frac{\upsilon_{F(c,sh)}}{4R_{c,sh}}\left(\frac{\omega_{pl(c,sh)}}{\omega}\right)^2 \frac{3}{16e_p^3}\left(e_p\left(1+2e_p^2\right)\left(1-e_p^2\right)^{1/2} - \left(1-4e_p^2\right)\arcsin e_p\right), \quad (4)$$

where $\upsilon_{F(c,sh)}$ is the Fermi velocity. At the boundary condition, when $e_p \to 1$, the expression for the attenuation decrement of dipole plasma oscillations of a metal nanowire takes the form:

$$\gamma_{1D(c,sh)}(\omega) = \frac{9\pi\upsilon_{F(c,sh)}}{128R_{c,sh}}\left(\frac{\omega_{pl(c,sh)}}{\omega}\right)^2. \quad (5)$$

Substituting the solutions of the Laplace equation into the boundary conditions for polarizability, we get

$$\tilde{\alpha}_{1D(c-sh)} = \frac{(\varepsilon_c+\varepsilon_{sh})(\varepsilon_{sh}-\varepsilon_m)+\beta_c^2(\varepsilon_c-\varepsilon_{sh})(\varepsilon_{sh}+\varepsilon_m)}{(\varepsilon_c+\varepsilon_{sh})(\varepsilon_{sh}+\varepsilon_m)+\beta_c^2(\varepsilon_c-\varepsilon_{sh})(\varepsilon_{sh}-\varepsilon_m)}, \quad (6)$$

where $\beta_c = R_c/R = 1 - R_{sh}/R$ is the volume content of the core material. When $\varepsilon_c = \varepsilon_{sh}$ expression (6) turns into a relation for the dipole polarizability of a continuous nanowire.

Equating (3) and (6), we have

$$\varepsilon_{1D(c-sh)} = \varepsilon_{sh}\frac{(\varepsilon_c+\varepsilon_{sh})+\beta_c^2(\varepsilon_c-\varepsilon_{sh})}{(\varepsilon_c+\varepsilon_{sh})-\beta_c^2(\varepsilon_c-\varepsilon_{sh})}. \quad (7)$$

By substituting the Drude function and separating the real and imaginary parts, we finally get

$$Re\ \varepsilon_{1D(c-sh)} = \frac{\chi_{(-)}\chi_{(+)}\varepsilon_3\left(\varepsilon_1^2+\varepsilon_2^2+\varepsilon_3^2+\varepsilon_4^2\right)+\chi_{(-)}^2\left(2\varepsilon_2\varepsilon_3\varepsilon_4+\varepsilon_1\left(\varepsilon_3^2-\varepsilon_4^2\right)\right)+\chi_{(+)}^2\varepsilon_1\left(\varepsilon_3^2+\varepsilon_4^2\right)}{\left(\varepsilon_1\chi_{(-)}+\varepsilon_3\chi_{(+)}\right)^2+\left(\varepsilon_2\chi_{(-)}+\varepsilon_4\chi_{(+)}\right)^2} \quad (8)$$

$$Im\ \varepsilon_{1D(c-sh)} = \frac{\chi_{(-)}\chi_{(+)}\varepsilon_4\left(\varepsilon_1^2+\varepsilon_2^2+\varepsilon_3^2+\varepsilon_4^2\right)+\chi_{(-)}^2\left(2\varepsilon_1\varepsilon_3\varepsilon_4-\varepsilon_2\left(\varepsilon_3^2-\varepsilon_4^2\right)\right)+\chi_{(+)}^2\varepsilon_2\left(\varepsilon_3^2+\varepsilon_4^2\right)}{\left(\varepsilon_1\chi_{(-)}+\varepsilon_3\chi_{(+)}\right)^2+\left(\varepsilon_2\chi_{(-)}+\varepsilon_4\chi_{(+)}\right)^2}, \quad (9)$$

where $\chi_{(\mp)} = 1 \mp \beta_c^2$.

At the boundary condition, when the layer thickness $R_{sh} \to 0$, we have $Re\ \varepsilon_{1D(c-sh)} = \varepsilon_1$ and $Im\ \varepsilon_{1D(c-sh)} = \varepsilon_2$; as $R_{sh} \to R$ and $\beta_c = 0$ we obtain $Re\ \varepsilon_{1D(c-sh)} = \varepsilon_3$ and $Im\ \varepsilon_{1D(c-sh)} = \varepsilon_4$.

II. Calculation results

The calculations of the absorption coefficient $\eta_{1D}(\omega)$ were carried out for bimetallic nanowires with the Ag@Au and Au@Ag structure, located in Teflon (ε_m = 2,3). The parameters of the metals are given in Table 1.

Let's trace the dimensional dependence of the composite absorption coefficient based on 1D-systems. Figure 2 shows the frequency dependences of $\eta_{1D}(\omega)$ which are calculated using relation (2) taking into account the formulas of the dielectric function real and imaginary parts (8)–(9) for a bimetallic Ag nanowire covered with a layer of Au (Ag@Au). For clarity, we introduce the following notations: $\hbar\omega_{sp(-)}$, $\hbar\omega_{sp(+)}$ – surface plasma frequencies of the first (low-frequency) and second (high-frequency) resonances. Figure 2 demonstrates the presence of one resonance maximum $\hbar\omega_{sp(+)} \approx 3{,}6$ eV (curve *1*), which corresponds to the Ag monowire R_{sh} = 0 nm. The presence of a Au metal layer at a constant value of the Ag core radius R_c causes the appearance of the second resonance peak $\hbar\omega_{sp(-)} \approx 2{,}8$ eV. An increase R_{sh} (curves *2→4*) leads to a slight shift of both maxima towards low frequencies. At the same time $\hbar\omega_{sp(-)}$ shifts slightly faster in contrast to $\hbar\omega_{sp(+)}$, as a result of which there is a "repulsion" of the absorption coefficient maxima. It is obvious when R_{sh} is fixed and R_c increases (curves *1'→4'*), a smooth shift of resonance peaks towards high frequencies should be expected.

The absorption coefficient of the composite based on Au@Ag 1D-systems is shown in Figure 3. The results of the calculations also demonstrate the presence of two resonance maxima in the considered frequency range. However, an increase in the R_{sh} value of the Ag shell (curves *2→4*), in contrast to the Ag@Au structure, leads to linear shift $\hbar\omega_{sp(+)}$ to the region of lower frequencies, while $\hbar\omega_{sp(-)}$ moves towards high frequencies. Thus, the frequency absorption peaks are "attracted" to each other. A significant increase in the thickness of the shell neutralizes the influence of the core and leads to a gradual merging of the maxima into one, which will correspond to the plasmon resonance frequency of the Ag monowire.

An increase in R_c of the Au core (curves *1'→4'*) leads to red shift of $\hbar\omega_{sp(-)}$. At the same time, $\hbar\omega_{sp(+)}$ undergoes a blue shift. The "repulsion" of resonance maxima from each other is observed.

Comparing Figures 2(*a*) and 3(*a*), we can conclude that the low-frequency peak $\hbar\omega_{sp(-)}$, which shifts from 2,76

Table 1.

Parameters of metals (a_0 – Bohr radius; m^* – the electron effective mass is given for a 3D metal; m_e – electron mass; $\hbar = h/2\pi$ – Planck's reduced constant)

Parameters	r_s, a_0 [15]	m^*/m_e [16]	ε^∞ [17]	τ_{bulk}, 10^{-15}s [15]	$\hbar\omega_{pl}$, eV
Au	3,01	0,99	9,84	29	9,07
Ag	3,02	0,96	3,70	40	9,17

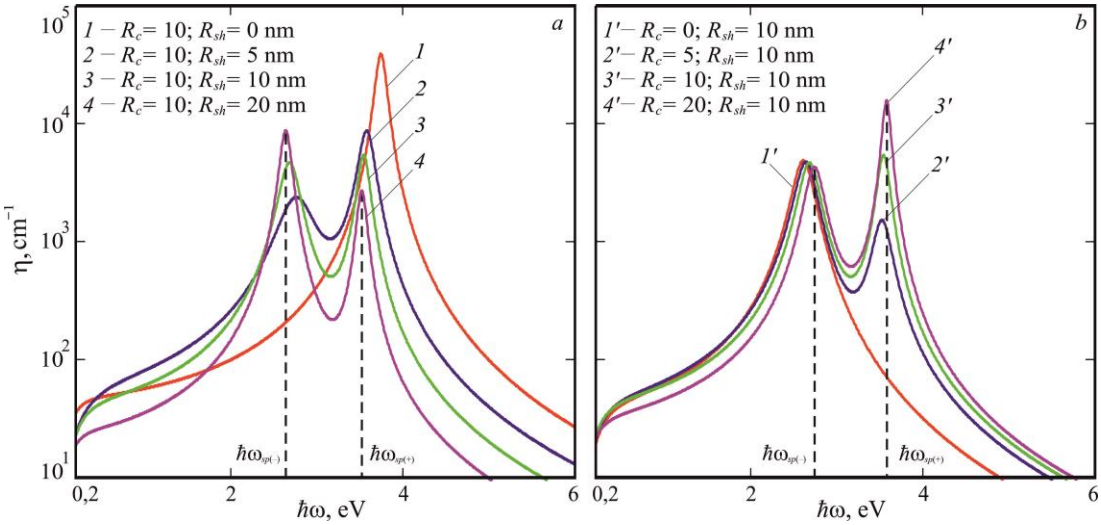

Fig. 2. – Frequency dependence of the absorption coefficient of the composite based on Ag@Au bimetallic nanowires: *a* – R_c = 10 nm; R_{sh} = 0; 5; 10; 20 nm; *b* – R_c = 0; 5; 10; 20 nm; R_{sh} = 10 nm.

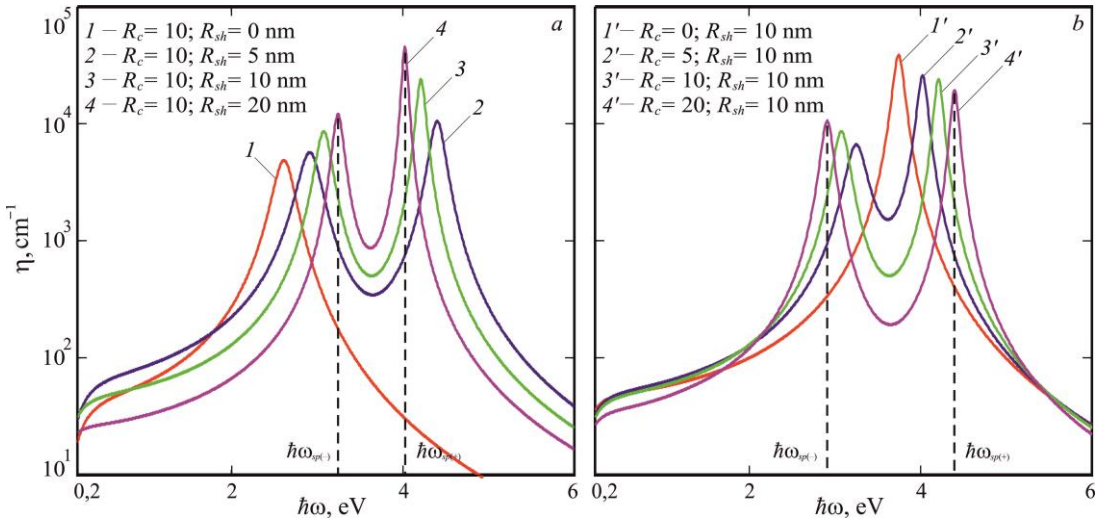

Fig. 3. – Frequency dependence of the absorption coefficient of the composite based on bimetallic Au@Ag nanowires: *a* – R_c = 10 nm; R_{sh} = 0; 5; 10; 20 nm; *b* – R_c = 0; 5; 10; 20 nm; R_{sh} = 10 nm.

to 2,62 eV in the Ag@Au nanowire, has the same origin as the high-frequency maximum $\hbar\omega_{sp(+)}$ in the Au@Ag structure, which shifts from 4,3 to 4 eV. Both maxima are a consequence of the plasmon interaction of the outer shell wall and the dielectric matrix ε_m. In turn, $\hbar\omega_{sp(+)}$ in the Ag@Au nanowire and $\hbar\omega_{sp(-)}$ in Au@Ag also have the same origin, which is the result of the surface charges induction of the inner shell wall and the core.

It is known that resonant oscillations of free electrons, which are weakly connected to the cation lattice, determine the frequency of SPR. As shown in [8], the stronger the bond between electrons is, the greater the energy of the SPR is and the higher the frequency is. On the contrary, weak electron coupling reduces the SPR value and shifts the resonance towards low frequencies. Thus, in the Ag@Au structure, Ag electrons move to the Au shell as a result of the "attraction" of positive charges. This leads to a decrease in electron coupling and a red shift of the maximum ($\hbar\omega_{sp(+)}$ in Figure2 (*a*)). Instead, the blue shift of the maximum of the Au@Ag nanowire ($\hbar\omega_{sp(-)}$ in Figure 3(*a*)) occurs due to the repulsion of the Au core electrons from the negative charges of the Ag shell.

Thus, a characteristic feature of a two-layer bimetallic nanowire is a frequency shift of resonance maxima due to variations in the ratio of the values of the core radius and the shell thickness. However, in order to be able to estimate the SPR position and their frequency shifts, it is possible to go another way. For this, it is sufficient to consider formula (6). It is known that the polarizability of the 1D-system will be zero if the following condition is

fulfilled for the numerator in (6):

$$\frac{\varepsilon_m - \varepsilon_{sh}}{\varepsilon_m + \varepsilon_{sh}} = \beta_c^2 \frac{\varepsilon_c - \varepsilon_{sh}}{\varepsilon_c + \varepsilon_{sh}}$$

The fact that polarizability is equal to zero means the invisibility of the wire metal core together with the shell. In the case of equating the denominator (6) to zero, we obtain the condition for the occurrence of plasmon resonance. Due to the large number of parameters, we will perform analytical calculations taking into account some approximations. Let us assume that $\omega\tau >> 1$ and the dielectric constant is also a real value (at the same time, $\varepsilon_m = 1$)

$$\varepsilon_{c,sh}(\omega) \approx 1 - \frac{\omega_{pl(c,sh)}^2}{\omega^2}$$

Substituting the last expression into the denominator (6), we have

$$4\omega_{sp}^4 - \omega_{sp}^2\left(4\omega_{pl(sh)}^2 + 2\omega_{pl(c)}^2\right) + \omega_{pl(sh)}^2\left(\omega_{pl(c)}^2(1+\beta_c^2) + \omega_{pl(sh)}^2(1-\beta_c^2)\right) = 0,$$

where the substitution $\omega = \omega_{sp}$ is introduced.

Then the resonance in (6) occurs at the following frequencies:

$$\omega_{sp(\mp)}^2 = \frac{1}{4}\left(2\omega_{pl(sh)}^2 + \omega_{pl(c)}^2 \mp \left(4\omega_{pl(sh)}^2\beta_c^2\left(\omega_{pl(sh)}^2 - \omega_{pl(c)}^2\right) + \omega_{pl(c)}^4\right)^{\frac{1}{2}}\right) \quad (10)$$

It follows from (10) the presence of two surface plasmon resonances in the bimetallic 1D-system. Considering boundary conditions $\beta_c = 0$ (absent core) and $\beta_c = 1$ (absent shell), we obtain the following results:

$$\omega_{sp(-)}\big|_{\beta_c=0} = \frac{\omega_{pl(sh)}}{\sqrt{2}} \text{ and } \omega_{sp(+)}\big|_{\beta_c=0} = \sqrt{\frac{\omega_{pl(sh)}^2+\omega_{pl(c)}^2}{2}};$$

$$\omega_{sp(-)}\big|_{\beta_c=1} = \frac{\omega_{pl(c)}}{\sqrt{2}} \text{ and } \omega_{sp(+)}\big|_{\beta_c=1} = \omega_{pl(c)}.$$

The minus sign "–" leads to the equality of the frequency of the first resonance $\omega_{sp(-)}$ with the frequencies of the localized surface plasmon of the shell and core. As a result, the frequency range for the first resonance at $0 \le \beta_c \le 1$ varies within $\omega_{pl(c)}/\sqrt{2} \le \omega_{sp(-)} \le \omega_{pl(sp)}/\sqrt{2}$. As for the last two results, they testify to the equality of the frequency of the second resonance $\omega_{sp(+)}$ to the value $\sqrt{\left(\omega_{pl(sh)}^2 + \omega_{pl(c)}^2\right)/2}$ and bulk plasma frequency of the shell $\omega_{pl(sh)}$. It is obvious that the solutions $\omega_{sp(+)}$ at $\beta_c = 0$ and $\beta_c = 1$, indicating the absence of a surface plasmon, have no physical meaning, since they are a consequence of the boundary conditions which are used to obtain relation (6). Therefore, the frequency range of the second resonance lies in the region $\omega_{pl(sh)} < \omega_{sp(+)} < \sqrt{\left(\omega_{pl(sh)}^2 + \omega_{pl(c)}^2\right)/2}$.

Let's continue further evaluation judgments for the Ag@Au bimetallic structure. By substituting the value of $\omega_{pl(c,sh)}$ (see Table 1), we obtain for $\omega_{sp(-)}$ a shift towards low frequencies when $\beta_c \to 0$ (increasing R_{sh}), while $\omega_{sp(+)}$ moves towards high frequencies. There is a "repulsion" of maxima from each other. On the contrary, when $\beta_c \to 1$ (increasing R_c), there is an "attraction" of resonance peaks. However, for Au@Ag, when $\beta_c \to 0$, the maxima converge, and when $\beta_c \to 1$, they move away from each other. It is obvious that the fulfillment of the condition $\omega_{pl(c)} > \omega_{pl(sh)}$ at $\beta_c \to 0$ leads to the "removal" of the maxima; $\omega_{pl(c)} < \omega_{pl(sh)}$ is responsible for their "convergence". It can be argued that to determine the SPR shifts depending on the value of β_c, it is sufficient to calculate the bulk plasmon frequencies $\omega_{pl(c)}$ and $\omega_{pl(sh)}$, while neglecting other constants (τ_{bulk}, ε_m and ε^∞).

It is interesting to compare the results of the study of the thin bimetallic wires absorption coefficient with similar results for bimetallic spheres. The starting point can be considered the polarizability formula for a layered 0D-system [18]:

$$\tilde{\alpha}_{0D(c-sh)} = \frac{(\varepsilon_c+2\varepsilon_{sh})(\varepsilon_{sh}-\varepsilon_m)+\beta_c^3(\varepsilon_c-\varepsilon_{sh})(2\varepsilon_{sh}+\varepsilon_m)}{(\varepsilon_c+2\varepsilon_{sh})(\varepsilon_{sh}+2\varepsilon_m)+2\beta_c^3(\varepsilon_c-\varepsilon_{sh})(\varepsilon_{sh}-\varepsilon_m)}. \quad (11)$$

Equating (11) to

$$\tilde{\alpha}_{0D(c-sh)} = \frac{\varepsilon_{0D(c-sh)}-\varepsilon_m}{\varepsilon_{0D(c-sh)}+2\varepsilon_m}$$

we get

$$\varepsilon_{0D(c-sh)} = \varepsilon_{sh}\frac{(\varepsilon_c+2\varepsilon_{sh})+2\beta_c^3(\varepsilon_c-\varepsilon_{sh})}{(\varepsilon_c+2\varepsilon_{sh})-\beta_c^3(\varepsilon_c-\varepsilon_{sh})}. \quad (12)$$

For the case of a spherical coordinate system ($P_x = P_y = P_z = 1/3$), the absorption coefficient of the composite takes the following form

$$\eta_{0D}(\omega) = \frac{9\omega}{c}\beta\varepsilon_m^{3/2}\sum_j \frac{Im\ \varepsilon_{0D(c-sh)}}{\left(Re\ \varepsilon_{0D(c-sh)}+2\varepsilon_m\right)^2+Im\ \varepsilon_{0D(c-sh)}^2} \tag{13}$$

and the real $Re\ \varepsilon_{0D(c-sh)}$ and $Im\ \varepsilon_{0D(c-sh)}$ imaginary parts of the bimetallic nanoparticle dielectric function

$$Re\ \varepsilon_{0D(c-sh)} = \frac{\xi\zeta\varepsilon_3(\varepsilon_1^2+\varepsilon_2^2)+2\xi^2\left(2\varepsilon_2\varepsilon_3\varepsilon_4+\varepsilon_1(\varepsilon_3^2-\varepsilon_4^2)\right)+\varsigma(\varepsilon_3^2+\varepsilon_4^2)(\varepsilon_1\zeta+2\varepsilon_3\xi)}{(\varepsilon_1\xi+\varepsilon_3\varsigma)^2+(\varepsilon_2\xi+\varepsilon_4\varsigma)^2}, \tag{14}$$

$$Im\ \varepsilon_{0D(c-sh)} = \frac{\xi\zeta\varepsilon_4(\varepsilon_1^2+\varepsilon_2^2)+2\xi^2\left(2\varepsilon_1\varepsilon_3\varepsilon_4-\varepsilon_2(\varepsilon_3^2-\varepsilon_4^2)\right)+\varsigma(\varepsilon_3^2+\varepsilon_4^2)(\varepsilon_2\zeta+2\varepsilon_4\xi)}{(\varepsilon_1\xi+\varepsilon_3\varsigma)^2+(\varepsilon_2\xi+\varepsilon_4\varsigma)^2}, \tag{15}$$

where the following notations are entered: $\xi = 1-\beta_c^3$, $\zeta = 1+2\beta_c^3$ i $\varsigma = 2+\beta_c^3$.

To calculate the attenuation decrement of spherical nanoparticle dipole plasma resonances, we use the expression given in [19]

$$\gamma_{0D(c,sh)}(\omega) = \frac{\nu_{c,sh}}{2}\left(\frac{\omega_{pl}}{\omega}\right)^2\left(1-\frac{\nu_{c,sh}}{\omega}sin\frac{\omega}{\nu_{c,sh}}+2\left(\frac{\nu_{c,sh}}{\omega}\right)^2\left(1-cos\frac{\omega}{\nu_{c,sh}}\right)\right), \tag{16}$$

where $\nu_{c,sh} = \upsilon_{F(c,sh)}/2R_{c,sh}$ is the frequency of electron oscillations from one potential wall to the opposite one. Note that for the case of a nanoparticle in vacuum at frequencies $\omega = \omega_{pl}/\sqrt{3}$ and $\nu_{c,sh} \ll \omega$ we obtain a well-known result $\gamma_{0D(c,sh)}(\omega) = 3\upsilon_{F(c,sh)}/4R_{c,sh}$.

The differences in the indicators of the bimetallic cylinder and the sphere (Fig. 4) are related to the dimensionality of the systems, which is expressed in a significant difference in the forms of the dielectric function real and imaginary parts. Small low-frequency "stochastic" oscillations $\eta_{0D}(\omega)$ are a consequence of the presence of a parenthesis in expression (16). As for the position of the resonance peaks, it is comprehensively explained by the conditions of the SPR, which follow from the denominators of ratios (2) and (13):

$$Re\ \varepsilon_{1D(c-sh)} = -\varepsilon_m; \quad Re\ \varepsilon_{0D(c-sh)} = -2\varepsilon_m.$$

It should be noted that the maximum $\hbar\omega_{sp(-)}$ in Figs.4(a) and 3(a) (at $R_{sh} \to \infty$) is the result of the interaction between the shell inner wall and the core, while $\hbar\omega_{sp(+)}$ arises as a result of the induction of surface charges at the separation boundary metal shell and external dielectric medium. However, when $R_c \to \infty$ (Figs.4(b) and 3(b)), similar regularities are not observed. Indeed, the interaction between the shell and the core is determined by the maxima of $\hbar\omega_{sp(-)}$ for the wire and $\hbar\omega_{sp(+)}$ for the particle. In turn, $\hbar\omega_{sp(+)}$ in the case of a cylinder and $\hbar\omega_{sp(-)}$ in the case of a sphere is responsible for the connection of the shell outer wall and ε_m. It is clear that the given regularities of bimetallic systems are "conditional". Real estimates of the position of the SPR maximum can be made only for monosystems. In the case of two-layer structures, the assessment of the predominance and influence of the shell and core metal fractions is a difficult task due to the consideration of a large number of constants included in the Drude formula and their subsequent "mixing" due to the substitution of the latest equation in the expression for the polarizability of bimetallic systems.

Figure 4 demonstrates the "merging" of $\eta_{0D}(\omega)$ maxima with increasing R_{sh}, while increasing R_c leads to their "repulsion". It is quite obvious that the given nature of shifts of the 0D-systems SPR is similar to that presented

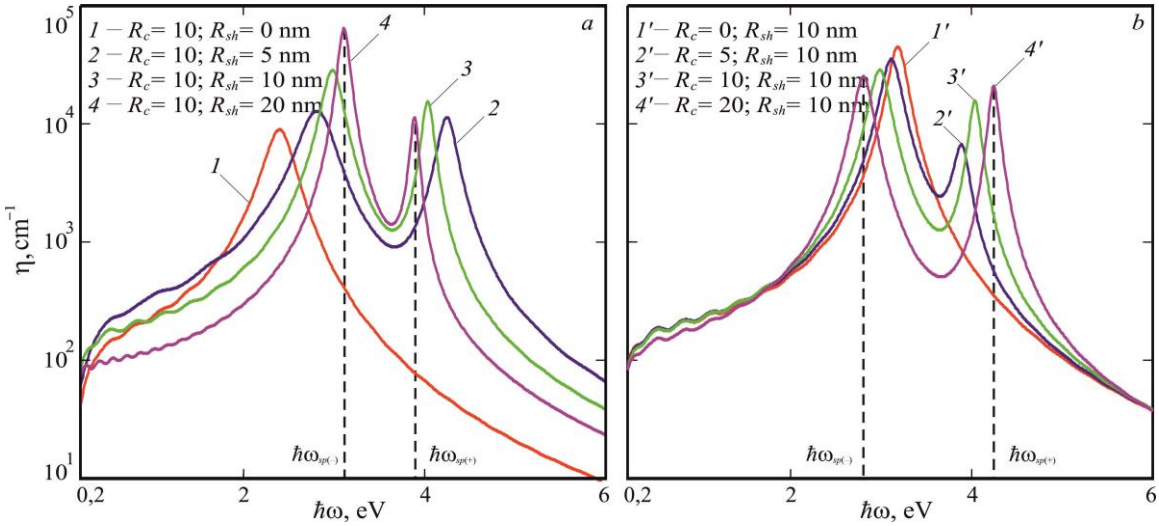

Fig. 4. – Frequency dependence of the absorption coefficient of the composite based on bimetallic Au@Ag nanoparticles: a – R_c = 10 nm; R_{sh} = 0; 5; 10; 20 nm; b – R_c = 0; 5; 10; 20 nm; R_{sh} = 10 nm.

in Figure 3 for the case of 1D-systems. Again, using the previous judgments and equating the denominator (11) to zero, we obtain the equation for the plasmon frequencies for a bimetallic nanoparticle

$$\omega_{sp(\mp)}^2 = \frac{1}{6}\left(3\omega_{pl(sh)}^2 + \omega_{pl(c)}^2 \mp \left(8\omega_{pl(sh)}^2\beta_c^3\left(\omega_{pl(sh)}^2 - \omega_{pl(c)}^2\right) + \left(\omega_{pl(sh)}^2 + \omega_{pl(c)}^2\right)^2\right)^{\frac{1}{2}}\right), \quad (17)$$

whence the conditions of plasmon resonances corresponding to the limiting cases are the following:

$$\omega_{sp(-)}\big|_{\beta_c=0} = \frac{\omega_{pl(sh)}}{\sqrt{3}}$$

and $\omega_{sp(+)}\big|_{\beta_c=0} = \sqrt{\frac{2\omega_{pl(sh)}^2+\omega_{pl(c)}^2}{3}}$;

$\omega_{sp(-)}\big|_{\beta_c=1} = \frac{\omega_{pl(c)}}{\sqrt{3}}$ and $\omega_{sp(+)}\big|_{\beta_c=1} = \omega_{pl(sh)}$.

Substitution of the values of the shell and core metals bulk plasma frequencies for the case of a bimetallic nanoparticle leads to similar conclusions about the SPR shifts that were obtained for the case of a nanowire. It is obvious that similar regularities in the position of resonance maxima should be expected for multilayer systems when calculating the optical characteristics of the composite.

Conclusions

Based on the Drude-Lorentz theory, the ratio of frequency dependences for polarizability, dielectric function real and imaginary parts of bimetallic 1D-systems was obtained. Taking into account the obtained expressions, the electromagnetic radiation absorption coefficient of the composite based on inclusions in the form of bimetallic nanowires was calculated. The presence of two frequency maxima of the absorption coefficient is shown, which is the result of the interaction of the shell inner wall surface charges and the core on the one hand, and the shell outer wall with the dielectric matrix on the other. The ability to control the composite optical characteristics by changing the core radius and the shell thickness is demonstrated.

The influence of the elemental composition on the optical characteristics of 1D-systems was investigated. When the shell thickness increases, for the Ag@Au structure optical absorption maxima are "repelled", while for Au@Ag the maxima are "converged". The resulting equation for the frequency shift of the surface plasmon resonances of bimetallic nanowires indicates the presence of two limiting cases that determine the position of the optical absorption peaks. Fulfillment of the condition $\omega_{pl(c)} > \omega_{pl(sh)}$ leads to "repulsion" of the maxima with an increase of the metal layer thickness. At the same time, when $\omega_{pl(c)} < \omega_{pl(sh)}$, there is a "convergence" of resonance maxima. As a result, the character of the shift of surface plasmon resonances is evaluated by comparing the values of the core and shell bulk plasma frequencies.

Analogous judgments can be extended to systems of other dimensions. In particular, for 0D-systems, the characters of the calculated dependences are similar to those obtained for the case of bimetallic nanowires.

Koval A.O. – PhD student.

[1] N.L. Dmitruk, S.Z. Malinich, *Surface Plasmon Resonances and Their Manifestation in the Optical Properties of Nanostructures of Noble Metals*, Ukrainian Journal of Physics, 9(1), 3 (2014); https://ujp.bitp.kiev.ua/index.php/ujp/article/view/2019664.

[2] N. Lawrence, L. Dal Negro, *Light scattering, field localization and local density of states in co-axial plasmonic nanowires*, Opt. Exp., 18(15), 16120 (2010); https://doi.org/10.1364/OE.18.016120.

[3] K. Mitamura, T. Imae, *Functionalization of Gold Nanorods Toward Their Applications*, Plasmonic, 4(1), 23(2009); https://doi.org/10.1007/s11468-008-9073-z.

[4] J. Zhu, S. Zhao, J.-W. Zhao, J.-J. Li, *Dielectric wall controlled resonance light scattering of coated long gold nanowire*, Curr. Nanosci., 7(3), 377 (2011); https://doi.org/10.2174/157341311795542480.

[5] E. Prodan, C. Radloff, N.J. Halas, P. Nordlander, *A Hybridization Model for the Plasmon Response of Complex Nanostructures*, Science, 302(5644), 419 (2003); https://doi.org/10.1126/science.1089171.

[6] H. Fu, X. Yang, X. Jiang, A. Yu, *Bimetallic Ag–Au Nanowires: Synthesis, Growth Mechanism, and Catalytic Properties*, Langmuir, 29(23), 7134 (2013); https://doi.org/10.1021/la400753q.

[7] S. E. Hunyadia, C. J. Murphy, *Bimetallic silver–gold nanowires: fabrication and use in surface-enhanced Raman scattering*, J. Mater. Chem., 16 (40), 3929 (2006); https://doi.org/10.1039/B607116C.

[8] J. Zhu, *Surface Plasmon Resonance from Bimetallic Interface in Au–Ag Core–Shell Structure Nanowires*, Nanoscale Res. Lett., 4 (9), 977 (2009); https://doi.org/10.1007/s11671-009-9344-4.

[9] L. Jin, Y. Sun, L. Shi, C. Lia, Y. Shena, *PdPt Bimetallic Nanowires with Efficient Oxidase Mimic Activity for the Colorimetric Detection of Acid Phosphatase in Acidic Media*, J. Mater. Chem., B 7 (29), 4561 (2019); https://doi.org/10.1039/C9TB00730J.

[10] X. Cao, N. Wang, Y. Han, C. Gao, Y. Xu, M. Li, Y. Shao, *PtAg bimetallic nanowires: Facile synthesis and their use as excellent electrocatalysts toward low-cost fuel cells*, Nano Energy, 12, 105 (2015); https://doi.org/10.1016/j.nanoen.2014.12.020.

[11] Q. Fu, D.G. Zhang, M.F. Yi, X.X. Wang, Y.K. Chen, P. Wang, H. Ming, *Effect of shell thickness on a Au–Ag core–shell nanorods-based plasmonic nano-sensor*, Journal of Optics, 14 (8), 085001 (2012); https://doi.org/10.1088/2040-8978/14/8/085001.
[12] W. Eberhardt, *Clusters as new materials*, Surface Science, 500 (1-3), 242 (2002); https://doi.org/10.1016/S0039-6028(01)01564-3.
[13] K.Chatterjee, S.Basu, D.Chakravorty, *Plasmon resonance absorption in sulfide-coated gold nanorods*, Journal of Materials Research, 21 (1), 34 (2006); https://doi.org/10.1557/jmr.2006.0032.
[14] P.M. Tomchuk, D.V. Butenko, *Dependences of Dipole Plasmon Resonance Damping Constants on the Shape of Metallic Nanoparticles*, Ukrainian Journal of Physics, 60 (10), 1042 (2015); https://doi.org/10.15407/ujpe60.10.1042.
[15] Neil W. Ashcroft, N. David Mermin. Solid state physics (Saunders College Publishing, 1976).
[16] P. B. Johnson, R. W. Christy, *Optical Constants of the Noble Metals*, Physical Review B, 6 (12), 4370 (1972); https://doi.org/10.1103/PhysRevB.6.4370.
[17] I.I. Shaganov, T.S.Perova, K. Berwick, *The effect of the local field and dipole-dipole interactions on the absorption spectra of noble metals and the plasmon resonance of their nanoparticles*, Photonics and Nanostructures - Fundamentals and Applications, 27, 24 (2017); https://doi.org/10.1016/j.photonics.2017.09.003.
[18] A.V. Korotun, A.A. Koval', I.N. Titov, *Optical Absorption of a Composite Based on Bilayer Metal–Dielectric Spherical Nanoparticles*, J. Appl. Spectrosc., 87 (2), 240 (2020); https://doi.org/10.1007/s10812-020-00991-7.
[19] N.I. Grigorchuk, P.M. Tomchuk, *Optical and transport properties of spheroidal metal nanoparticles with account for the surface effec*t, Phys. Rev. B, 84 (8), 085448 (2011); https://doi.org/10.1103/PhysRevB.84.085448.

А.О. Коваль[1,2]

Частотні зсуви поверхневих плазмонних резонансів при обчисленні коефіцієнту поглинання композиту на основі біметалічних 1d-систем

[1]*Національний університет "Запорізька політехніка", вул. Жуковського, 64, 60063 Запоріжжя, Україна*
[2]*Науково-виробничий комплекс "Іскра", вул. Магістральна, 84, 69071 Запоріжжя, Україна, andrej.koval@ukr.net*

В роботі проаналізовано поглинання електромагнітного випромінювання композитом на основі біметалічних нанодротів. З використанням теорії Друде-Лоренца одержано співвідношення для частотних залежностей поляризовності, дійсної та уявної частин діелектричної функції шаруватих 1D-систем. Показано, що структура у вигляді металевого ядра, покритого шаром іншого металу, призводить до розщеплення та появи двох максимумів у частотній залежності коефіцієнту поглинання. Положення максимумів визначаються складом біметалічних нанодротів і об'ємним вмістом металів. Вплив розмірності систем оцінюється шляхом порівняння частотних залежностей коефіцієнту поглинання композиту на основі біметалічних нанодротів та наночастинок. Розрахунки проведені для нанодротів Ag@Au та Au@Ag, занурених у тефлон.

Ключові слова: біметалічний нанодріт, поверхневий плазмонний резонанс, поляризовність, діелектрична функція, коефіцієнт поглинання.

PHYSICS AND CHEMISTRY OF SOLID STATE
V. 24, No. 2 (2023) pp. 298-303
Section: Physics

DOI: 10.15330/pcss.24.2.298-303

Vasyl Stefanyk Precarpathian National University

ФІЗИКА І ХІМІЯ ТВЕРДОГО ТІЛА
Т. 24, № 2 (2023) С. 298-303
Фізико-математичні науки

PACS: 81.07.-b ISSN 1729-4428

V.V. Petrov, A.A. Kryuchyn, I.V. Gorbov, A.V. Pankratova, D.Yu. Manko, Yu.O. Borodin, O.V. Shikhovets

Formation of submicron relief structures on the surface of sapphire substrates

Institute for Information Recording of the National Academy of Sciences of Ukraine, Kyiv, Ukraine, kryuchyn@gmail.com

An analysis of technologies that allow creating microrelief structures on the surface of sapphire substrates has been carried out. It is shown that the most effective method of forming relief structures with submicron dimensions is ion beam etching through a protective mask formed by photolithography. The main problems in creating a microrelief on the surface of sapphire substrates are the removal of static electric charge in the process of ion beam etching of the substrates, as well as obtaining a protective mask with windows of specified sizes, through which etching of the sapphire substrate is performed.

Keywords: sapphire substrates, selective etching, microrelief structures, protective mask, direct laser recording

Received 7 February 2023; Accepted 07 June 2023.

Analysis of the state of the problem

Microrelief structures on the surface of sapphire substrates are widely used in the manufacture of LEDs, diffractive optical elements and long-term data storage media. Most of epitaxial structures for LEDs are grown on profiled sapphire substrates allowing get high efficiency of light output from LEDs. It is known that the profiled substrate scatters the emitted light at the interface of GaN and sapphire and this improves the efficiency of light removal. The efficiency of LEDs grown on profiled sapphire substrates is about 1.5-2 times higher compared to the case of employing the flat sapphire substrates [1-3].

Microrelief diffraction optical elements (DOEs) are formed on sapphire substrates, designed to function at high radiation powers and temperatures [4-6]. To create the microrelief diffraction optical elements on the surface of sapphire substrates, both photolithography methods [4] and the method of laser ablation with femtosecond pulses of ultraviolet radiation are used [5,6]. The micro-profiled sapphire substrates are also proposed to be used to create media for long-term data storage. When creating micro-relief diffraction optical elements on the surface of sapphire substrates and long-term data storage media, special attention should be paid to the formation of elements with submicron strictly defined dimensions. The tolerance for the size of the elements in the horizontal plane should be 30-50 nm, and 20-30 nm in depth. Particularly strict requirements for the size of microrelief elements must be met when manufacturing media with a microrelief structure [7, 8].

The formation of relief on the surface of the sapphire substrate is difficult due to its high chemical resistance. In recent years, several methods of forming a microrelief on the surface of a sapphire substrate have been proposed. These methods of creating a relief on the surface of a sapphire substrate can be divided into two groups. The first one concludes in forming a microrelief in the material of the substrate itself. And the second one provides obtaining a microrelief image in the material applied to the surface of the sapphire substrate. In the first group of methods, the application of chemical etching to create microrelief structures on the surface of sapphire substrates should be highlighted. To profile sapphire one can use etching in a mixture of acids
H_2SO_4: H_3PO_4 (H_2SO_4: H_3PO_4 = 3: 1) with employing a mask made of SiO_2 (the temperature of the acid mixture is higher than 300°C). The output pattern on the surface of

the SiO_2 layer to be applied to the sapphire is formed either by the method of standard photolithography (to obtain microrelief elements of submicron sizes) or by annealing the deposited nickel layer which leads to the formation of submicron islands that served as a mask during SiO_2 etching [2].

The rate of chemical etching of sapphire is 1 μm/min. [9]. The method of nanosphere lithography can be used to create a microrelief on the surface of sapphire substrates [6]. A mask during sapphire etching can be quasi-ordered hemispherical gold drops of 0.5-3 μm in size, formed in a controlled manner on the surface of sapphire by heating the sputtered solid layer of gold above its melting temperature. The uniqueness of gold as a mask material for this technology should be especially emphasized. Gold is the only metal that combines the necessary chemical resistance with a fairly low melting point. Relief elements have the shape of triangular pyramids. The height of relief elements and their density on the surface can vary significantly depending on the process parameters [1, 2]. Although this method is effective, it is potentially dangerous for the health of operators [9]. To obtain relief structures in the material of sapphire substrates, dry etching in inductively coupled plasma through a mask formed by photolithography is also used [2]. High-frequency ion-chemical etching of sapphire (f_{hf} = 13.56 MHz) was also reported in CF_4 medium (Tetrafluoromethane) [4]. The high chemical resistance of sapphire makes it necessary to apply the dry etching of multilayer masks [9]. One of the layers of the mask is often a layer of metallic chromium, which is necessary to reduce the electrification of the processed sapphire substrate (the specific electrical resistance of sapphire is 10^{19} Ohm cm) [10]., A compensation of the charge on the surface in contact with the plasma is necessary during plasma etching of the sapphire substrates.

To obtain sapphire substrates with regular microrelief on the surface it is suggested to use methods that do not utilize the photolithography technique. Such methods are advisable to apply in the manufacture of diffractive optical elements and optical media for long-term data storage. In one of the options for manufacturing microrelief structures on the surface of sapphire substrates, there is proposed to apply metal to them through stencils with a diameter of holes in the range of 0.2-40 μm by the method of vacuum sputtering and subsequent annealing to form a regular microrelief of sprayed metal on the ultra-smooth surface of sapphire plates [11]. Long-term optical data storage media can be produced by direct laser writing on a layer of photoresist being deposited on a film of chromium on a sapphire substrate [12].

I. The research methods

Ion beam etching of sapphire substrates through windows in organic positive photoresist does not allow obtaining microrelief structures with a depth of more than 70-80 nm. Increasing the etching time leads only to an increase in the size of the elements in the horizontal plane. Such a problem does not arise during ion beam etching of substrates made of silicate glass, on which elements with a depth of 150-200 nm were being formed. The main problems in creating a microrelief on the surface of sapphire substrates are that its etching rate is much lower compared to other materials (for example, silicate and quartz glass). Accordingly, it takes more time to etch sapphire, which leads to a significant accumulation of charge on its surface. Thus, in the process of ion-beam etching of sapphire substrates in order to obtain microrelief structures of given sizes, it is necessary to ensure the avoidance or removal of such surface static electric charge.

To form microrelief structures with submicron dimensions on sapphire substrates by ion beam plasma etching there is proposed to use two-layer masks (conductive layer of chromium and layer of positive photoresist). The masks were being formed by the method of direct laser recording on positive photoresist films and subsequent selective chemical etching of photoresist and chromium layers in various etchants. The scheme of the process on obtaining microrelief structures on the surface of sapphire substrates is demonstrated in Fig. 1.

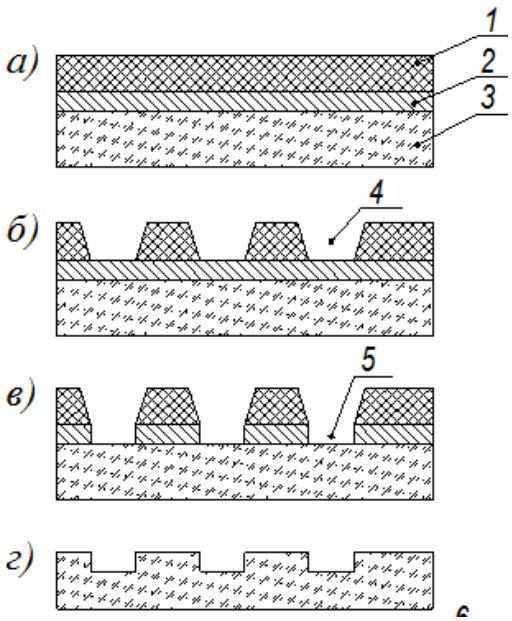

Fig. 1. The process of obtaining microrelief structures on the surface of sapphire substrates: 1- layer of photoresist; 2- chrome layer; 3- substrate; 4- windows in the photoresist; 5 - windows in chrome.

The process of obtaining microrelief structures on the surface of sapphire substrates includes several basic operations:

- direct laser recording on the layer of positive photoresist of the given structure;
- selective etching of the layer of positive photoresist in alkaline etchant;
- selective etching of the chromium layer through the windows in the photoresist layer;
- ion beam etching of the sapphire substrate through a double-layer mask.

The selective chemical etching of the photoresist layer on the surface of the sapphire substrate was carried out with an alkaline etching agent (0.7-1.0% KOH) for 10-20 seconds. The etching time was determined by obtaining the required value of the relative intensity of the diffracted laser beam on the microrelief structure. The

selective chemical etching of the chromium layer through the windows formed in the photoresist layer was performed with a standard etching agent based on cerium sulfate and sulfuric acid (cerium sulfate – 200 ml, hydrochloric acid – 100 ml, sulfuric acid – 10 ml, distilled water – up to 1000 ml) [13].

The plasma chemical etching was used to form a microrelief structure in the sapphire substrate. The scheme of the plasma chemical etching installation is presented in Fig. 2.

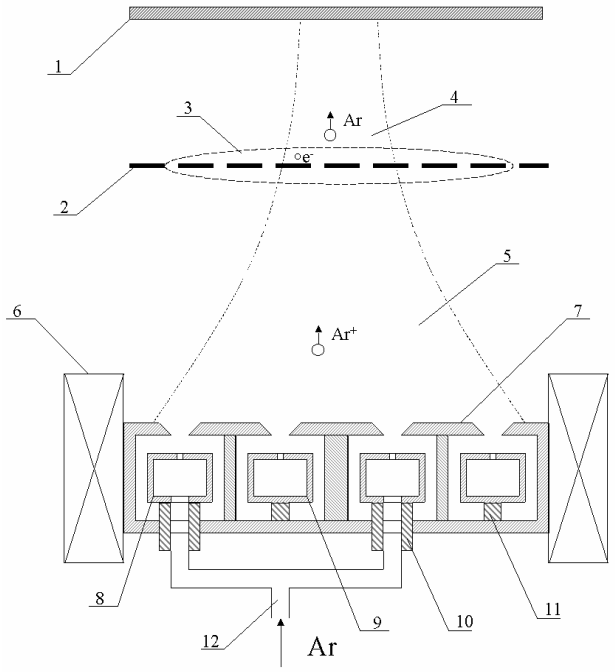

Fig.2. Scheme of the device of plasma chemical etching of sapphire substrates :
1 – work piece; 2 – electron emitter (tungsten filament); 3 – electron cloud; 4 – neutralized ion beam; 5 – ion beam; 6 – focusing coil; 7 – grounded electrode; 8 – alive external gas source; 9 – alive internal gas source; 10 – isolator with gas input; 11 – isolator; 12 – gas input.

The applied technology [14] differs from the known technology of forming microrelief structures in sapphire substrates [4] in that the etching was carried out using a direct current discharge.

II. Experimental studies on the formation of microrelief structures on sapphire substrates

The formation of the image in the layer of positive photoresist was carried out by the method of direct laser recording followed by selective chemical etching in an alkaline solution, and the control of recorded microrelief structures was made with using the analysis of the intensity of the diffracted beam. Fig. 3 shows the image of the surface of disks obtained by the method of direct laser recording on a layer of positive photoresist.

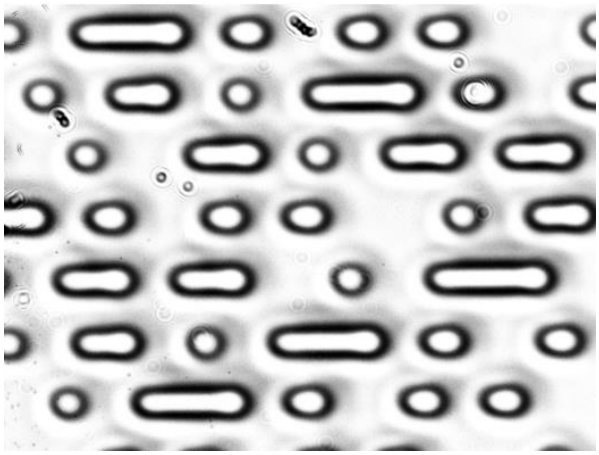

Fig. 3. The disk surface after direct laser recording of submicron structures on the photoresist layer and selective chemical etching of the photoresist.

The deviation of the length of the depressions formed in the process of direct laser recording and selective chemical etching does not exceed 40-50 nm, and the width of the depressions - 100 nm. One of the main problems of obtaining microrelief structures on the surface of sapphire substrates is the presence of a residual layer of positive photoresist in pits formed after recording and selective chemical etching of the photoresist layer with an alkaline etching agent. As our experiments have shown, the formation of microrelief structures of a given depth is strongly influenced by photoresist residues in micro-holes (pits), through which the chrome layer is etched. Increasing the time of selective etching of the chromium layer on samples with remnants of photoresist in the micro-holes does not allow obtain the recess of the required uniform depth. Etching in an ultrasonic field helps to the uniform chromium etching [15].

The use of ultrasound-assisted etching requires the use of substrates with minimal mechanical stresses. The presence of micro-cracks and significant mechanical stress leads to the destruction of the substrate in the process of ultrasonic treatment. Fig. 4 demonstrates the image of the surface of the sapphire substrate after selective etching of the chromium layer through the windows in the photoresist layer with remnants of the photoresist in the micro-holes.

The effect of incomplete removal of the photoresist is the reason for the distortion of the micro-relief structure and the formation of micro-holes with a stepped shape and different depths. The incomplete removal of the photoresist in the micro-holes is associated with insufficient exposure of the samples and a local change in the properties of the photoresist layer after exposure. The appearance of a residual layer of positive photoresist was observed during laser recording of ring chromium templates and is associated with the fact that due to the relatively high transparency of the photoresist layer.

Thus, a significant portion of the energy of the recording laser beam is absorbed by the chromium film under the photoresist. This leads to heating of the chrome film and, accordingly to a decrease in the sensitivity of the photoresist. As a result, the photoresist film may be underexposed near the chrome-photoresist border. As a result, a thin residual layer of acid-resistant positive

photoresist is formed on the bottom of the microelements, which prevents the etching of chromium by acid etching. The effect of the residual layer of photoresist on the bottom of the microelements on the etching process of the chromium layer can be almost completely eliminated by optimizing the concentration of the etching agent. Experiments have shown that for selective etching of elements recorded on a photoresist film with a thickness of 0.5 μm applied to a chromium film, the optimal concentration of KOH should be 1% [16]. To avoid the formation of a residual layer of photoresist on the bottom of the microelements, we also increased the concentration of KOH to 1%. This made it possible to carry out more homogeneous etching of chromium through the windows in the positive photoresist. Further selective chemical etching of the chromium layer made it possible to obtain a two-layer mask through which etching of the sapphire substrate was carried out (Fig. 5).

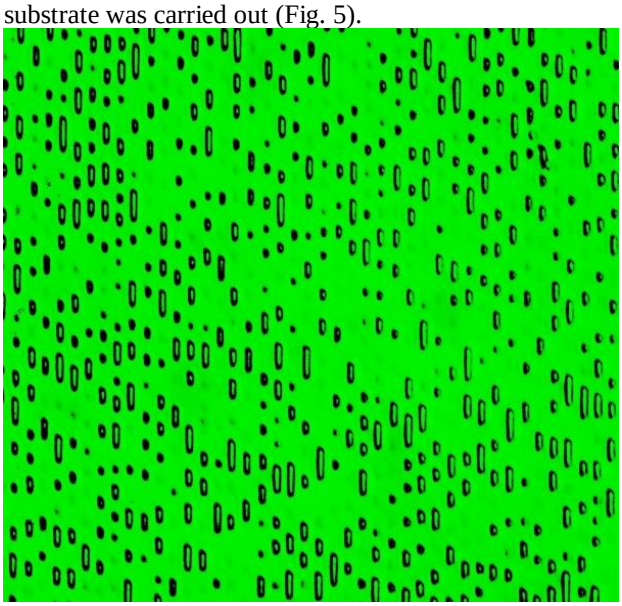

Fig.4. The surface of the sapphire substrate after selective etching of the chromium layer through the windows in the photoresist layer with photoresist remnants in the micro-holes.

Extraction of electric charge from the surface of the sapphire substrate during its plasma chemical etching was performed by grounding the metal layer of the protective mask using conductive paste. The compensation of the electric charge on the surface of the sapphire substrate made it possible to form relief structures with a depth of 120-200 nm by plasma chemical etching through a two-layer protective mask. The thickness of them was 160 nm of a layer of positive photoresist Shipley 1813 and a 30 nm layer of chromium. The plasma chemical etching of sapphire substrate through a two-layer protective mask was made in the following modes: residual pressure in the vacuum chamber- $2*10^{-2}$ Pa; the operating pressure of the Freon(CF_4) - $4*10^{-2}$ Pa; etching time -12.5 minutes; the current of ion beam - 1A; accelerating voltage - 2.2 kV; the lens current –76 mA; the angular speed of the carousel with substrates - 20 rpm. Fig. 6 shows the image of sapphire substrates after the plasma chemical etching through a two-layer mask - the layers of positive photoresist and chromium.

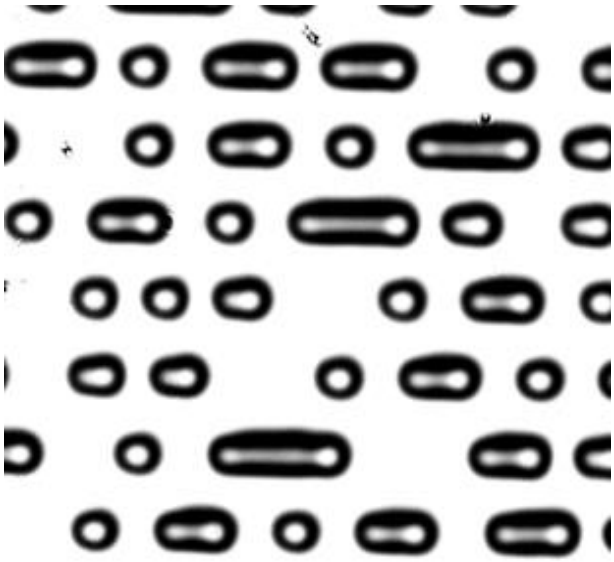

Fig. 5. The disk surface after chemical etching of the chrome layer (image of a two-layer mask on the surface of the sapphire substrate).

Fig. 6. Optical image of the surface of sapphire substrate after plasma chemical etching through a two-layer mask: a layer of positive photoresist and a layer of chromium (obtained with use of NEOPHOT 2).

Fig. 7 demonstrates the images of ASM from the surface of the sapphire substrate after plasma chemical etching. It shows that the depth of the microrelief structure is 157 nm.

After the plasma-chemical etching process was completed the double-layer mask was stored on the surface of the sapphire substrate which made it possible to obtain microrelief structures of greater depth.

Conclusions

1. The formation of submicron relief structures on the surface of sapphire substrates is an urgent problem. A significant number of technologies are proposed to solve them. In most of the proposed technical solutions, the use of multi-layer protective masks is proposed.

2. One of the main problems during the creation of a regular microrelief on the surface of sapphire substrates is the obtaining of a protective mask through which etching

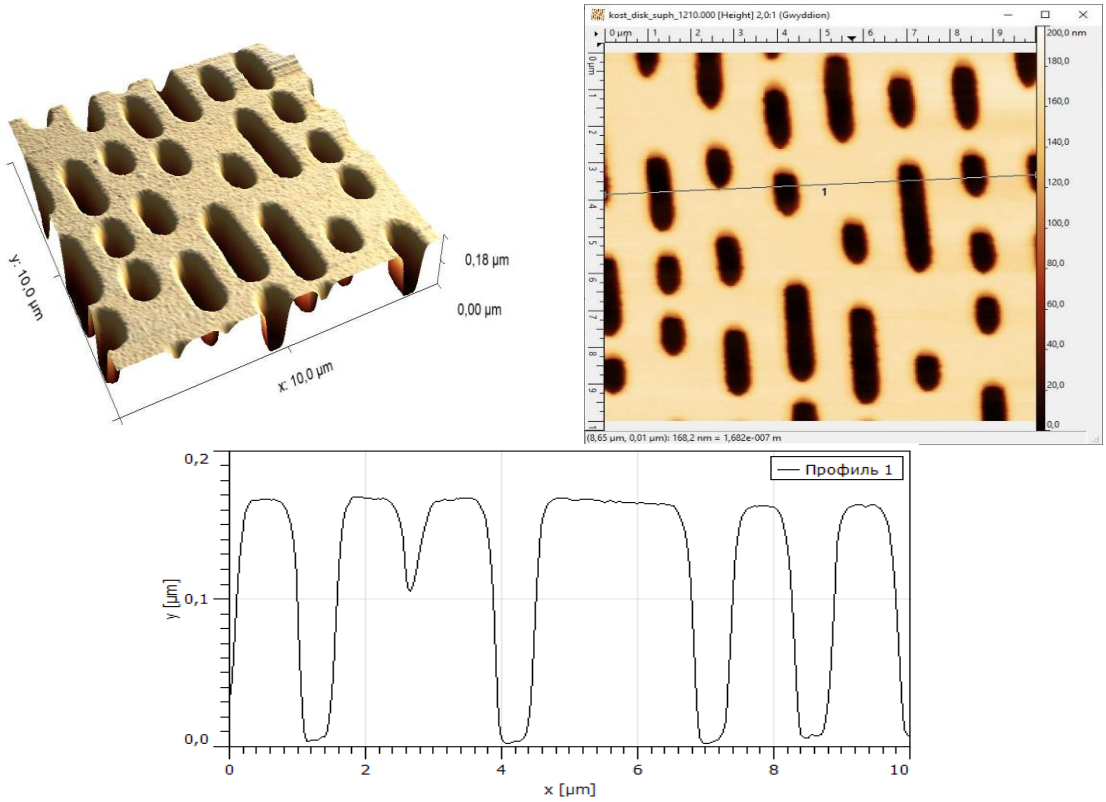

Fig.7. ASM image of the sapphire disk after the plasma-chemical etching (the pit depth is 159 nm).

of the sapphire substrate is being carried out. Deviations from the specified shape of the holes in the protective mask affect the quality of the micro-relief structure of the sapphire substrate.

3. The most promising and technological method of creating a regular microrelief on the surface of sapphire substrates is plasma chemical etching of sapphire substrates through windows in multilayer protective masks.

4. An alternative method for micro profiling of sapphire substrates is the technology of microrelief formation in an additional layer applied to the surface of the sapphire substrate. This technology can be considered promising for the creation of long-term data storage media.

Acknowledgments

The authors express their deep gratitude to the colleagues from the Institute for Information Recording of the National Academy of Sciences of Ukraine for their help in conducting experiments on the manufacture of sapphire substrates with a microrelief structure and to the employees of the Institute of Semiconductor Physics named after V.E. Lashkarev for researching microrelief structures using an atomic force microscope and a fruitful discussion of the research results.

Petrov V.V. – Doctor of Technical Sciences, Director of the Institute for Information Recording of the National Academy of Sciences of Ukraine;
Kryuchyn A.A. – Doctor of Technical Sciences, Deputy Director of the Institute for Information Recording of the National Academy of Sciences of Ukraine;
Gorbov I.V. **–** Candidate of Technical Sciences, Senior researcher at the Institute for Information Recording of the National Academy of Sciences of Ukraine;
Manko D.Yu. – Candidate of physical and mathematical sciences, senior researcher at the Institute for Information Recording of of the National Academy of Sciences of Ukraine;
Pankratova A.V. – Researcher at the Institute for Information Recording of the National Academy of Sciences of Ukraine;
Borodin Yu.O. **–** Researcher at the Institute for Information Recording of the National Academy of Sciences of Ukraine;
Shikhovets O.V. – Researcher at the Institute for Information Recording of the National Academy of Sciences of Ukraine**.**

[1] S.Watanabe, N. Yamada, M. Nagashima, Y. Ueki, C. Sasaki, Y. Yamada, H. Kudo, *Internal quantum efficiency of highly-efficient InxGa1−xN-based near-ultraviolet light-emitting diodes*, Applied Physics Letters, 83(24), 4906 (2003); https://doi.org/10.1063/1.1633672.

[2] H.Gao, F. Yan, Y. Zhang, J. Li, Y. Zeng., G. Wang, *Enhancement of the light output power of InGaN/GaN light-emitting diodes grown on pyramidal patterned sapphire substrates in the micro- and nanoscale*, Journal of Applied Physics, 103, 014314 (2008); https://doi.org/10.1063/1.2830981.

[3] S.-H.Chao, L.-H. Yeh, R. T.Wu, K.Kawagishi, S.-C. Hsu, *Novel patterned sapphire substrates for enhancing the efficiency of GaN-based light-emitting diodes*, RSC Advances, 10(28), 16284 (2020); https://doi.org/10.1039/d0ra01900c.

[4] A.V. Volkov, O.G. Istinova, N.L. Kazanskiy, G.F. Kostyuk, *Research and development of technology of DOE microrelief formation on sapphire substrates*, Computer Optics, 24, 70 (2002);

[5] N. R. Gottumukkala, M.C. Gupta, *Laser processing of sapphire and fabrication of diffractive optical elements*, Applied Optics, 9(61), 2391 (2022); https://doi.org/10.1364/AO.452810.

[6] D.Smith, S.H. Ng, M.Han, *Imaging with diffractive axicons rapidly milled on sapphire by femtosecond laser ablation*, Appl. Phys. B, 127, 154 (2021); https://doi.org/10.1007/s00340-021-07701-x.

[7] V.V. Petrov, Zichun Le., A.A. Kryuchyn, S.M.Shanoylo, M.Fu, Ie.V. Beliak, D.Yu.Manko, A.S. Lapchuk, E.M. Morozov, Long-term storage of digital information (2018); https://doi.org/10.15407 / Akademperiodyka. 360.148ISBN: 9789663603605.

[8] V.V.Petrov, V.P.Semynozhenko, V.M.Puzikov, A.A. Kryuchyn, A.S.Lapchuk, Ye.M.Morozov, Y.O.Borodin, O.V.Shyhovets, S.M.Shanoylo, *Method of aberration compensation in sapphire optical discs for the long term data storage*, Functional Materials, 1(21), 105 (2014); http://dx.doi.org/10.15407/fm21.01.105.

[9] C.-M. Chang, M.-H. Shiao, D. Chiang, C.-T. Yang, M.-J. Huang, C.-T. Cheng, W.-J. Hsueh, *Submicron Patterns on Sapphire Substrate Produced by Dual Layer Photoresist*, Complimentary Lithography Applied Mechanics and Materials V. 284-287, 334 (2013); https://doi.org/10.4028/www.scientific.net/AMM.284-287.334.

[10] E.G..Shustin, N.V. Isaev, I.L. Klykov, & V. V. Peskov, Control of the energy of ion flow affecting electrically insulated surface in plasma processing reactor based on a beam plasma discharge. Vacuum, 85(6), 711 (2011); https://doi.org/10.1016/j.vacuum.2010.11.004.

[11] V.A. Babaev, A.E. Muslimov, A.V. Butashin, *Atomic force microscopy in the study of the roughness of a supersmooth crystalline surface and the development of technology for sapphire substrates with a regular microrelief*, Bulletin of the Social and Pedagogical Institute, 1(6). (2013), [in russian].

[12] I. V. Gorbov, D. Yu. Manko, A. A. Kryuchyn, Zichun Le, Minglei Fu, and A. V. Pankratova, *Optical Disc for Long-Term Data Storage Based on Chromium Film*, Металлофизика и новейшие технологии. 2(38). 267 (2016); http://dx.doi.org/10.15407/mfint.38.02.0267. [in russian]

[13] N. Khamnualthong, & Siangchaew, Krisda & P. Limsuwan, *Study of Chromium Hard Mask Formation and Wall Angle Control for Deep Etching Application*, Procedia Engineering. 32. 922 (2012); https://doi.org/10.1016/j.proeng.2012.02.033.

[14] I.V. Gorbov, V.V. Petrov, A.A. Kryuchyn, *Using ion beams for creation of nanostructures on the surface of high-stable materials*, Semiconductor Physics Quantum Electronics & Optoelectronics, 1(10), 27 (2007); http://dx.doi.org/10.15407/spqeo10.01.027.

[15] K.R. Williams, K. Gupta , M. Wasilik, *Etch Rates for Micromachining Processing—Part II,* Journal of Microelectromechanical systems, 6(12), 761 (2003); https://doi.org/10.1109/JMEMS.2003.820936.

[16] V. Korolkov, A. Malyshev, A. Nikitin, V. Poleshchuk, A. Kharissov, A.Cherkashin, W. Chuck, *Application of gray-scale LDW-glass masks for fabrication of high-efficiency DOEs*, Proc SPIE, 3633. (1999); https://doi.org/10.1117/12.349316.

В.В. Петров, А.А. Крючин, І.В. Горбов, А.В. Панкратова, Д.Ю. Манько, Ю.О. Бородін, О.В .Шиховець

Формування субмікронних рельєфних структур на поверхні сапфірових підкладок

Інститут проблем реєстрації інформації НАН України, Київ, Україна, kryuchyn@gmail.com

Проведено аналіз технологій, які дозволяють створювати мікрорельєфні структури на поверхні сапфірових підкладок. Показано, що найбільш ефективним методом формування рельєфних структур із субмікронними розмірами є йонно-променеве травлення через сформовану методом фотолітографії захисну маску. Основні проблеми при створенні мікрорельєфу на поверхні сапфірових підкладок полягають у видаленні статичного електричного заряду в процесі йонно-променевого травлення підкладок, а також отриманні захисної маски з вікнами заданих розмірів, через яку здійснюється травлення сапфірової підкладки.

Ключові слова: сапфирові підкладки, селективне травлення, мікрорельефні структури, захисна маска, прямий лазерний запис.

PHYSICS AND CHEMISTRY OF SOLID STATE
V. 24, No. 2 (2023) pp. 304-311
Section: Chemistry

DOI: 10.15330/pcss.24.2.304-311

Vasyl Stefanyk Precarpathian National University

ФІЗИКА І ХІМІЯ ТВЕРДОГО ТІЛА
Т. 24, № 2 (2023) С. 304-311
Хімічні науки

UDC: 539.216., 543.32/34., 543.38., 669.056.9., 621.894., 539.893 ISSN 1729-4428

O.V. Komashko, H.O. Sirenko, M.B. Skladaniuk

The features of chemo-mechanical activation technology of polymer composite materials production

Vasyl Stefanyk Precarpathian National University, Ivano-Frankivsk, Ukraine, oks.pavlykivska@gmail.com

The paper deals with the study of the processes of obtaining polymer composites by chemo-mechanical activation technology (CMA-technology). The methods of research and testing of composite materials based on polytetrafluoroethylene (PTFE) and carbon fibers are analyzed and generalized. The influence of CMA technology on the structure and properties of PTFE composite was determined.

Keywords: polymer composite, polytetrafluoroethylene, carbon fibers, chemo-mechanical activation technology.

Received 1 February 2023; Accepted 2 June 2023.

Introduction

Nowadays, the production of new polymer composite materials with improved performance properties is crusial [1]. Fluorine-containing materials are among the most popular in various industries [2].

The object of study of this work is the technology of obtaining composites based on polytetrafluoroethylene and carbon fibers. The use of PTFE as a matrix affects the antifriction properties of the resulting composite materials.

PTFE composites are widely used due to the unique characteristics of polytetrafluoroethylene. Among its advantages are high heat resistance, high friction coefficient, the highest chemical resistance among thermoplastics, the ability to be used at low temperatures, and durability [3].

Among all the fillers, carbon fibers are the most effective because of their mechanical properties and light weight [4]. The use of carbon fibers significantly improves the wear resistance and increases the heat resistance of the composite material.

Generally, according to already known technologies, to obtain composites polytetrafluoroethylene powder is mechanically mixed with fillers, followed by pressing and sintering. However, this method has a number of disadvantages due to the high melt viscosity of PTFE. Therefore, it is reasonable to develop the technology of consecutive chemo-mechanical activation of PTFE and carbon fiber samples before their mixing [5].

Technological progress shows that the use of chemo-mechanical activation technology is promising for improving the antifriction properties [6, 7] of polymer composite materials, as it increases their toughness, stiffness, thermal conductivity, and heat resistance, which increases the reliability and durability of products made from such materials.

According to the CMA technology, carbon fiber was pretreated with a 20 % aqueous solution of flame retardants, annealed at high temperatures (723-2673 K), surface intermediate compounds were removed, pressed, kept at a special temperature, conditioned, crushed, and mixed with polytetrafluoroethylene at ultra-high speeds (5000-25000 rpm) in crushers, mills, dismembrators, or disintegrators [8]. At the last stages, the PTFE composite blanks were pressed and sintered.

For the mechanical activation of carbon materials, we used a crusher KDU-2.0 "Ukrainka" (with a knife speed of n = 1440 rpm), a crusher MRP-1 (with a knife speed of n = 7000 rpm), and MRP-1M (with a knife speed of n = 7350 rpm). The MPP-1 and MPP-1M were used for ultrafine grinding of the components and mixing the composition [9].

I. Technological parameters for matrix preparation and modification

Polytetrafluoroethylene (PTFE-4) with fibrous, spherical, and scaly particle shapes was used for the study.

First, PTFE blanks obtained by pressing are molded in the cold and then sintered in an electric furnace at 365-385 ^{0}C. This helps to harden the polymer and increases its strength under friction.

PTFE samples obtained by pressing and injection molding have the following physicomechanical properties at room temperatures [10]: density 2150-2220 kg/m^3, tensile strength 14-35 MPa, bending strength 14-18 MPa, compressive strength 10-12 MPa, elongation at break 250-500 %, compressive elastic modulus 700-800 MPa, bending elastic modulus 470-850 MPa, specific impact strength without notching > 100 kD/m^2, HB hardness 30-40 MPa, Vick's heat resistance 373-383 K, brittleness temperature < 4 K, glass transition temperature 153 K, melting point 590 K, decomposition temperature > 688 K.

Polytetrafluoroethylene is also undergoing structural modification [11]. The polymer passes mechanical activation, shock wave and electromagnetic treatment, and radiation exposure.

For the mechanical grinding of dry PTFE powder, the MRP-1M crusher was used with the following parameters: sample load: 120 ± 20 g, productivity - 0.6 kg/h, chamber volume - 0.4 m^3, knife diameter - 0.345 m, maximum linear knife speed Vmax = 130 m/s. The number of rotations of the knife (working body) was: n = 5000 min^{-1}, n = 7000 min^{-1}, n = 9000 min^{-1}, crushing time: 3 min, 5 min, 8 min. It was determined that the optimal rotation frequency is equal to n = 9000 min^{-1} and the time interval is equal to τ = 5 min (Table 1), at which the maximum indicators of the physicomechanical and tribotechnical properties of the polymer are obtained.

As a result of mechanical activation, the tensile strength increases by 2.6 times, the relative elongation at break by 4.3 times, and the wear rate decreases by 1.85 times compared to non-activated PTFE [12].

II. Chemical, thermal and mechanical activation of the filler

It is known that the introduction of carbon fibers as fillers affects the tribotechnical properties of polytetrafluoroethylene, which was studied in [13]. It was found that the wear resistance is higher compared to that of pure PTFE.

The carbonized carbon fibers obtained from organic hydrate cellulose (HC) tissue were studied. The carbon fiber dispersions were pretreated with a mixture of flame retardants $Na_2B_4O_7 \cdot 10\ H_2O$ and $(NH_4)_2HPO_4$, taken in equal amounts. Next, the carbon fiber was heat-treated in an environment of natural gas CH_4 by passing through a Tammany Furnace and dry nitrogen N_2, gradually increasing the temperature from 723 K to 2673 K, and the types of fibers were obtained, which are given in (Table 2), where HC is hydrate cellulose, Tc is the final temperature of carbonization or graphitization, LM is low-modulus carbon fiber. The classification of fibers is given in [14].

Thus, from the initial hydrate cellulose fabric at a temperature of 723 K in methane (CH_4), a partially carbonized UT-4 fabric with the following characteristics was obtained (Table 3). By further annealing the UT-4 fabric at 1123 K in a CH_4 atmosphere, a carbonized UTM-8 fabric with the following characteristics was obtained (Table 3). The UTM-8 fabric was heat-treated at 2673 K in an N_2 atmosphere and a graphitized TGN-2m fabric was obtained. The resulting fabric had the following characteristics (Table 3). After the heat treatment, the carbon fiber fabric TGN-2m contained the most carbon (99.2 %) compared to UT-4 and UTM-8.

After grinding in MRP-1, the dispersions of UTM-8 carbon fibers were treated with a solution of $Na_2B_4O_7 \cdot 10H_2O + (NH_4)_2HPO_4$ in a 1:1 ratio and heat-treated sequentially at temperatures 1123 K, 1473 K, 1623 K, 1873 K, 2273 K, 2573 K, 2673 K in a dry nitrogen environment and carbon fibers TGN-T850, TGN-T1200, TGN-T1350, TGN-T1600, TGN-T2000, TGN-T2300, TGN-T2400 were obtained, accordingly. Graphitized TMP-3 fibers were obtained from TGN-2m by applying a pyrocarbon coating in N_2 at 2673 K. However, filling with such a fiber leads to a decrease in the antifriction

Table 1.

The effect of mechanical activation on PTFE properties

Modes of mechanical activation	Tensile strength,, σ_{pp}, MPa	Relative elongation at break δ, %	Wear rate I·10^{-6}, mm^3/N·m
Not activated	9.5	96	1133
τ = 3 min, n = 5000 rpm	10.2	240	1080
τ = 5 min, n = 5000 rpm	21.6	416	930
τ = 8 min, n = 5000 rpm	17.3	280	800
τ = 3 min, n = 7000 rpm	10.7	270	970
τ = 5 min, n = 7000 rpm	23.5	423	820
τ = 8 min, n = 7000 rpm	18.2	358	717
τ = 3 min, n = 9000 rpm	19.6	290	890
τ = 5 min, n = 9000 rpm	24.8	415	610
τ = 8 min, n = 9000 rpm	18.0	340	720

Table 2.

Carbon fibers

Mark	Source organic fiber	Type of carbon fiber	Tк, K
UT-4	HC	LM	723
UTM-8	HC	LM	1123
TGN-2m	HC	LM	2673
TMP-3 (Pc: 12% pyrocarbon)	HC	LM	2673
TKK-1 (Pk: 0,2-3,0 % SiC)	HC	LM	2673
TKC-1 (Pk: 0.8-4.0 % ZrC)	HC	LM	2673
TGN-T850	HC	LM	1123
TGN-T1200	HC	LM	1473
TGN-T1350	HC	LM	1623
TGN-T1600	HC	LM	1873
TGN-T2000	HC	LM	2273
TGN-T2300	HC	LM	2573
TGN-T2400	HC	LM	2673

Table 3.

Characteristics of carbon fibers at the stage of their production [6].

Fiber characteristics	UT-4	UTM-8	TGN-2m
tensile load of the fabric (on the warp), N/cm	100-160	70-240	150-160
breaking load of the fabric (by weft), N/cm	15-30	20-100	25-35
Carbon content, %.	60-70	66-72	99.1-99.3
Hydrogen content, %.	-	-	0.2-0.4
Boron compounds content, %.	0.2	3.0-3.6	0.4
Phosphorus content, %.	0.5	3.0-3.6	0.002
Sols content, %	1.5	21-26	0.45-0.55
Fiber strength at break, GPa	0.2-0.3	0.5-0.6	0.45-0.50
Tensile modulus of elasticity, GPa	3-4	30-50	30-50
Relative elongation at break, %.	4.5-6.5	4.5	1.2-1.3
Fiber diameter, μm	11-14	10-12	8-9
Thermal conductivity, W/(m·K)	0.08-0.09	0.08-0.12	0.14-0.16

properties of composites [15].

To fill the composite, carbon fiber material (CFM) in the form of fabric and fiber was introduced into the matrix material at a certain temperature regime (T_k=723-3073 K) [16].

Mechanical activation. Previously, the CFM in the form of fabric or ribbon was crushed in a crusher KDU-2.0 "Ukrainka" (number of crushing hammers - 90, number of knives - 3, number of rotations of working bodies n = 1440 rpm, capacity - 200 kg/h). The obtained fiber fractions were 3.0-15.0 or 0.5-8.0 mm. [17].

According to the CMA technology, the carbon fibers were mainly crushed in the MRP-1 (knife diameter - 0.205 m, maximum linear knife speed V_{max} = 78 m/s, knife rotation frequency f = 120 s^{-1} (117 s^{-1}), knife rotation number n = 7000 rpm).

Mechanical crushing of the fiber was also carried out in a crusher MRP-1M (sample load: 120 ± 20 g, productivity - 0.6 kg/h, knife speed n = 7350 rpm, chamber volume - 0.4 m^3, knife diameter - 0.345 m, maximum linear knife speed V_{max} = 130 m/s). The MRP-1M was also used as a composition mixer.

The CMA technology is based on high knife speeds, which crush both the fiber and the composition; the tests were carried out from 2000 to 12000 rpm.

The carbon fibers pre-ground in MRP-1 or MRP-1M (to a bulk density of 40-160 kg/m^3) were subjected to fine grinding in a ball mill. For grinding, the carbon fiber dispersion was loaded into the ball mill chamber, the working part of which had a volume of 92.66 cm^3 of steel, a diameter of 65.5 mm, and a height of 27.5 mm. Thirty-five balls of steel SCH-15 with a diameter of 12.7 mm were placed in the mill chamber (filling the working part of the mill with 48 volume %). The number of mill rotations ranged from 20-30 to 125-175 per minute. The tests were carried out for 5-2050 hours in a humid air environment.

The carbon fibers were also subjected to intensive mechanical grinding in a D-160 Z crusher from Alpine (capacity - 20-40 kg/h, rotor diameter 0.160 m, number of pins (fingers) on the rotor disk - 316). RPM range: 3000 rpm, 5000 rpm, 7000 rpm, 9000 rpm, 11000 rpm,

14000 rpm, 17000 rpm, 19000 rpm, 22500 rpm. The length of the carbon fiber is $\ell_0 \leq 5$ mm, ℓ_τ = 40-150 μm. [18]. However, it was found that the grinding of carbon fiber in a dismemberer is not effective.

The technology and final heat treatment temperature have an impact on pH. For example, for partially carbonized fibers, the pH is in the range of 4.8-6.4, for carbonized fibers 6.4-7.8, and for graphitized fibers 7.3-8.3. The pH is also affected by the time of fiber crushing. As the crushing time increases, the pH decreases.

During the heat treatment of fibers, the flame retardants applied to the fibers decompose (above 373 K) according to the scheme:

$$(NH_4)_2HPO_4 \rightarrow H_3PO_4 + 2NH_3\uparrow$$

With a gradual increase in temperature, H_3PO_4 loses water and polymers of the composition $(HPO_3)_n$ are formed.

Filling composites with low modulus carbon fibers increases the isotropic roughness of the contact metal surfaces by $\sqrt{m_0}$ = 0,043 – 0,143μm [19].

The activation of carbon fibers by zirconium dioxide ZrO_2 + 3 % Y_2O_3 at 700^0C significantly affects the intensity of volumetric wear of fluoroplastic carbon fiber reinforced plastic [20].

III. Mixing of components and technology of composite materials production

For mixing polymer powders and fibers, a crusher with high-speed submersible working knives MRP-1 with n = 7000 rpm was used. To do this, in one case, long fibers 0.6-6 mm long were added to the polymer composition, which was crushed in a crusher KDU-2.0 "Ukrainka". And in the second case, the fibers, after being crushed in the KDU-2.0 "Ukrainka" for 3-30 minutes before mixing the polymer composites, were crushed in the MRP-1 to lengths of 20-500 μm, and then mixed with PTFE powder and molybdenum disulfide in the MRP-1 for 5 minutes.

This mixing technology results in not only mechanical mixing. Due to the additional grinding of the polymer composition components, triboactivation of the mixture particles occurs [21].

The resulting slurry was subjected to cold pressing under a pressure of Pp = 50.0-70.0 MPa to obtain blanks. The next process was sintering the blanks in air at 638 K. The heating-cooling rate was 40 K/h.

The resulting material (GOST 12015-66, GOST 12019-66) was left at room temperature for 15 days for testing. After aging, the material was conditioned for 24 hours.

IV. Research of physical and mechanical properties

The physico-mechanical properties of the composite material based on polytetrafluoroethylene are influenced by the parameters of carbon fiber distribution [22], technological parameters [23], the content of the components of the composite material [24, 25].

A study of the influence of technological parameters on the physical and mechanical properties of composite samples is given in [26]. Using the methods of mathematical planning of the experiment, it was found that the intensity of wear is most affected by the mixing time of the composition. The content of low-modulus carbon fiber, the time of its preliminary grinding, and the mixing time also affect the friction coefficient, tensile strength, impact strength, and mechanical properties. The content of solid lubricant in the composition affects the tensile strength.

It has been found that the type [27] and shape of carbon fiber [28], composition and degree of preliminary deformation [29] affects the wear resistance and thermal conductivity and, accordingly, the thermal properties of PTFE composites. The orientation of the fibers also affects the thermophysical properties [30,31].

The concentration of fillers in the composite has a significant impact on the wear rate. With an increase in the content of carbon fiber in the polymer matrix, an increase in wear resistance is observed, but, having reached a certain optimal concentration, it begins to decrease due to the gradual destruction of components [32]. Amorphization processes occur when the concentration of carbon fiber is in the range of 3-4 %, the maximum wear resistance is achieved at a content of 15 % [33].

The study of physical and mathematical properties by UV spectroscopy [12] showed an increased concentration of CF_2 groups in PTFE after mechanical activation. The tests were performed on a Specord 75 IR spectrophotometer. An increase in the speed during the activation of PTFE contributes to an increase in the end groups of CF_2 in its composition.

The pH-metric analysis of the aqueous extracts of carbon fibers UT-4 (T_k = 723 K), UTM-8 (T_k = 1123 K), and TGN-2m (T_k = 2673 K) is given in [8]. The studies have shown that the pH change is most affected by the time of crushing and the type of fiber. The pH of the aqueous extracts of the initial carbon fibers have the following values (Fig. 1). After additional grinding for 5 minutes to a bulk density of 80 kg/m^3 in MRP-1, the pH of the aqueous extracts of carbon fibers decreases relative to the original fibers by 0.3, 0.43, 0.50, respectively, for UT-4, UTM-8, and TGN-2m. Thus, any thermomechanical activation of carbon fiber leads to a decrease in the pH of aqueous fiber extracts.

Work [34] found a linear relationship between the wear resistance and friction coefficient of PTFE-based carbon fiber reinforced plastics filled with short, randomly arranged carbon fibers and the mechanical and thermophysical properties of adjacent surfaces. Wear intensity studies were conducted at the HTI-72 installation [18]. The analysis of the test results shows that wear resistance does not depend on the hardness of adjacent friction surfaces, but is significantly affected by the plastic deformation energy of the adjacent surface of the counterbody and the tensile deformation energy.

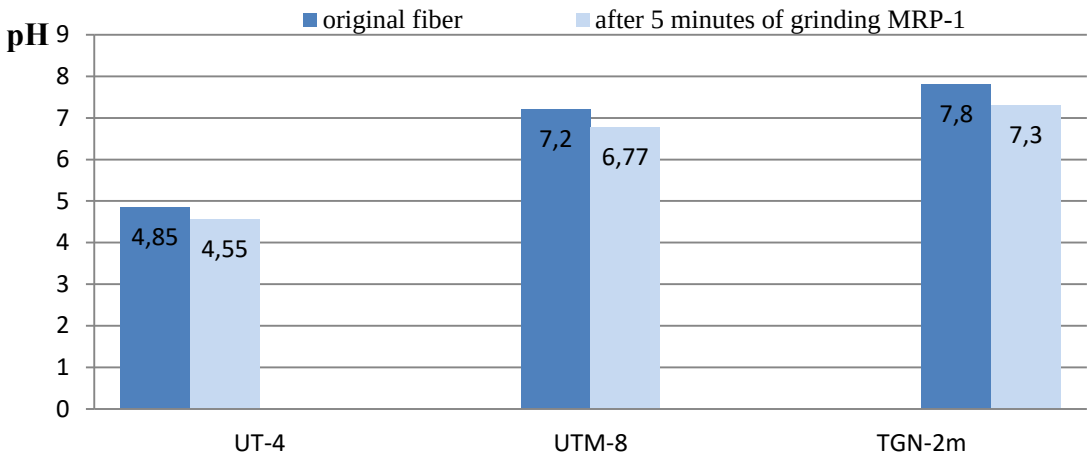

Fig. 1. pH of water extracts from the initial carbon fibers (exposure for 15 min. at 293 K, tub modulus 33) and after 5 min. grinding in MRP-1.

The thermographic analysis. Carbon fibers with a final heat treatment temperature of 1123, 1473, 1623, 1873, 2273, 2573 K, which were previously crushed in a crusher to a bulk density of 0.04 g/cm^3, were studied. These fibers were annealed in the temperature range of 293-953 K. Additionally, the fibers were ground for 200 hours in a ball mill and also annealed at 293-953 K. The results of the thermographic analysis are given in Table 4 and Table 5.

After annealing the initial fiber, the temperatures of the exo-effect onset T_{0max} (Table 4) and peak T_{max} (Table 5) shift to the high-temperature region. After an additional 200 hours of dispersion of the original carbon fiber, these indicators shift to the low-temperature region, but after annealing the chopped fibers, there is a shift of these indicators to the high-temperature region. Probably, the complexes formed on the surface of carbon fibers are converted into gas as a result of thermal effects.

Table 4.

The temperature of the onset of the exo-effect (T_{0max}) of the studied carbon fibers TGN-T

Final heat treatment temperature of carbon fiber, K	T_{0max}			
	Before annealing		After annealing	
	Starting point	After 200 h of grinding	Starting point	After 200 h of grinding
1123	406	386	520	510
1473	543	390	640	540
1623	582	396	662	545
1873	610	400	680	550
2273	645	405	700	600
2573	675	410	729	610

Table 5.

The temperature of the peak exo-effect (T_{max}) of the studied carbon fibers of TGN-T

Final heat treatment temperature of carbon fiber, K	T_{max}			
	Before annealing		After annealing	
	Starting point	After 200 h of grinding	Starting point	After 200 h of grinding
1123	620	542	757	713
1473	798	584	795	728
1623	825	605	825	735
1873	870	615	860	742
2273	876	635	878	760
2573	880	650	903	770

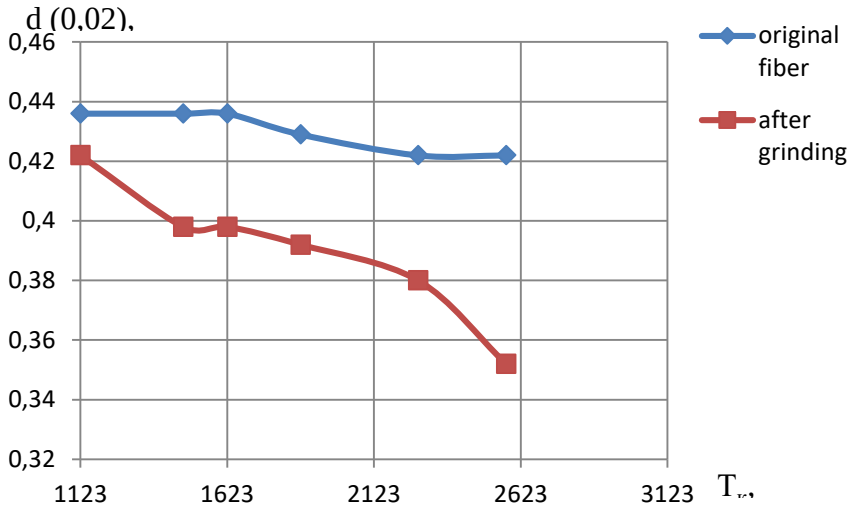

Fig. 2. Dependence of the interlayer distance on the final heat treatment temperature of the initial fibr of TGN-T and the fiber after 200 h of grinding in a ball mil.

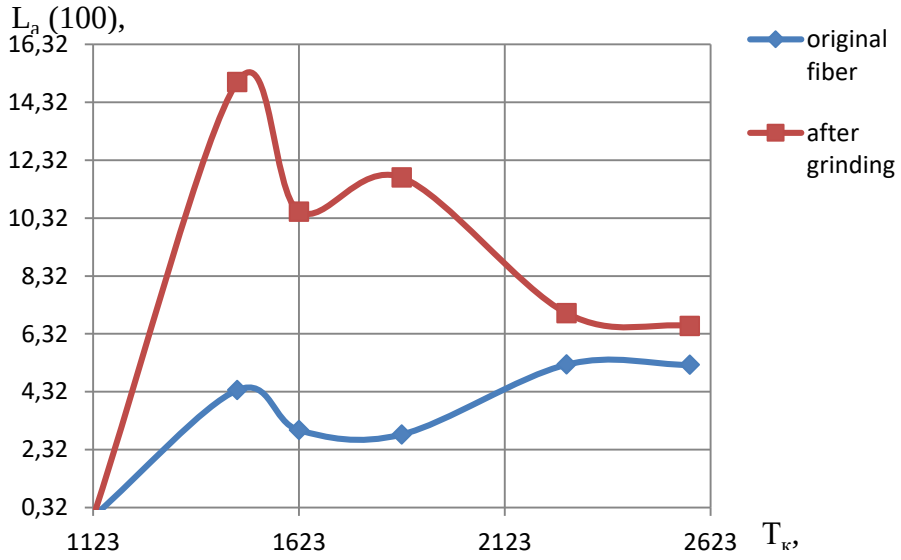

Fig. 3. Dependence of the thickness of the hexagonal layer package on the final heat treatment temperature of carbon fibers TGN-T.

Mechanical grinding and the temperature of the final heat treatment (T_k) of carbon fibers lead to the improvement of the turbostrata structure. Fig.2 shows that with an increase in the final heat treatment temperature of TGN-T carbon fibers from 1123 to 2673 K, the interlayer distance d (002) decreases for the original fiber and significantly decreases after 200 hours of mechanical activation in a ball mill. The length of the package of layers of L_a(100) hexagons (Fig.3) increases significantly after 200 h of mechanical dispersion but decreases with increasing T_k. Therefore, thermomechanical activation contributes to the formation of an ordered two-dimensional structure of carbon fibers and increases the wear resistance of the polymer composite.

Conclusions

It has been summarized the impact of CMA technology on the properties of composite materials, which are obtained by the authors and many researchers in this scientific area.

The complex application of chemical treatment, mechanical grinding and activation of fillers and matrix have a positive effect on the mechanical and tribotechnical properties of the polymer composite.

Composite materials obtained by CMA technology have higher strength and wear resistance than materials produced using traditional technology.

It was revealed that chemo-mechanical activation increases the thermal stability of composites based on polytetrafluoroethylene, and also affects its

supramolecular structure, changing from disordered to more organized.

It is determined that the mechanical activation of carbon fibers and PTFE polymer matrix increases by 10-25 % the physico-mechanical properties of the composition as a whole, which has a further effect on friction and wear.

A comparative analysis of tribotechnical parameters, tensile strength characteristics before and after chemo-mechanical activation was carried out.

The optimal temperature conditions of operation were found.

Thus, CMA technology is effective and can be used for industrial realization.

Komashko O.V. **–** postgraduate student of the Department of Chemistry;
Skladaniuk M.B. **–** Candidate of Physical and Mathematical Sciences;
Sirenko H.O. **–** Honored Scientist of science and technology of Ukraine, Academician of the Academy of Technological Sciences of Ukraine, Professor, Doctor of Technical Sciences, Professor of the Department of Chemistry.

[1] Handbook of engineering polymeric materials edited by Nicholas P. Cheremisinoff (Marcel Dekker inc., New York, 1997); https://doi.org/10.1201/9781482292183.
[2] Sina Ebnesajjad, Fluoroplastics. Volume 2: Melt Processible Fluoropolymers - the Definitive User's Guide and Data Book (Elsevier Inc, 2016); https://doi.org/10.1016/C2012-0-05998-4
[3] Sina Ebnesajjad, Introduction to Fluoropolymers. Materials, Technology, and Applications (Elsevier, 2021); https://doi.org/10.1016/C2018-0-04702-7
[4] X. Huang, *Fabrication and Properties of Carbon Fibers*, Materials, 2(4), 2369 (2009); https://doi.org/10.3390/ma2042369
[5] K.O. Dyadyura, P. P. Savchuk, P.V. Rudenko, V. P. Kashyckiy, K.V. Berladir, *The method of obtaining a polymer composition based on polytetrafluoroethylene*, Patent 110989 Ukraine, MPK C08J 5/00, C08L 27/00, opubl. 25.10.2016, Bul. № 20 (2016).
[6] H.O. Sirenko, Antifriction carboplastics (Technika, Kiev, 1985).
[7] E. Dhanumalayan, G.M. Joshi, *Performance properties and applications of polytetrafluoroethylene (PTFE)—a review*, Advanced Composites and Hybrid Materials,1, 247(2018); https://doi.org/10.1007/s42114-018-0023-8
[8] H.O. Sirenko, L.M. Soltys, L.Y. Midak, I.V Kravets, Physico-chemistry of the surface of carbonized and graffitized fibers obtained by chemo-mechanical activation technology: 1. theoretical part and test methods, Herald of Vasyl Stefanyk Precarpathian National University. Series Chemistry, (XIV), 149 (2012).
[9] A.F. Budnik, H.V. Berladir, P.V. Rudenko, V.A. Sviders'kij, Patent 101976 U Ukraine, MPK C08J5/04, opubl. 12.10.2015, Bul. № 19 (2015).
[10] L.V. Baziuk, H.O. Sirenko, A.F. Budnyk, S.P. Shapovalov, Seventh International Scientific and Practical Conference "Development of Scientific Research" (InterGraphics, Poltava, 2011) 48.
[11] O.A Budnyk., K.V. Berladir, A.F. Budnyk, P.V. Rudenko, *Structural changes in the matrix of PTFE-composites*, Herald of Belarusian State Technical University named after V. H. Shukhov, (4), 104 (2015).
[12] H.V. Berladir, T.P. Hovorun, S.G. Rudenko, O.A. Bilous, S.V. Varenyk, V.V. Kravets, D.V. Shvetsov, *Mechanically activated polytetrafluoroethylene: morphology and supramolecular structure*, Journal of Nano- and Electronic Physics, 14 (1), 01030 (2022); https://essuir.sumdu.edu.ua/handle/123456789/87465.
[13] Y. Sujuan, Z. Xingrong. Tribological properties of PTFE and PTFE composites at different temperatures, Tribology Transactions, 57(3), 382 (2014).
[14] H.O. Sirenko, L.M. Soltys, M.B. Skladanyuk, *Properties of carbon fibers (review*), Herald of Vasyl Stefanyk Precarpathian National University. Series Chemistry, (XIX), 63 (2015); http://lib.pnu.edu.ua/files/Visniki/chemical/chemikal_2015_19.pdf
[15] A.F. Budnyk, *Method of Producing Carbon Fiber Filler of PTFE-Matrix Composite*, Patent 40960; Ukraine,MPK S08L27/00, 27 April 2009.
[16] H.O. Sirenko, H.M. Sorokyn , A.F. Budnyk, O.M. Sirenko, Antifriction material: A.s. 1467893 (USSR), MKI B32B3/12; D04C5/00; F16C33/12/, №4261265, Published in 1989. - Bulletin № 11.
A.F. Budnyk, O. A. Budnyk, , *Technological processes filler preparation and composition in production composite materials based on polytetrafluoroethylene*, East-European Journal of Advanced Technologies, ¾ (27), 9 (2007).
[17] Application of synthetic materials: conference materials, Editor-in-chief R.I. Silin. Kishinev: Cartea Moldoveiasca, P. 199 (1975).
[18] H.O. Sirenko, L.M. Soltys, V.P. Svidersky, B.O. Talankin, Regularities of Change the Microroughness of Conjugated Surfaces the Polymer Composite – Metal in Mechano-physicalchemical Processes of Friction and Wear, Herald of Vasyl Stefanyk Precarpathian National University. Series Chemistry, (XV), 150 (2012).
[19] V.P. Sviderskyi, L.M. Kyrychenko, A.I. Mishchyshyn, *Increasing the wear resistance and mechanical characteristics of antifriction fluoroplastic carboplastics modified with zirconium oxide nanopowders*, Increase of Machine and Equipment Reliability, 32 (2019); http://elar.khmnu.edu.ua/jspui/handle/123456789/8629.

[20] A.F. Budnyk, H.V. Berladir,V.A. Svidersky, O.A. Budnyk, P.V. Rudenko, A.A. Ilyinik, *Physicochemical aspects of mechanical activation of polytetrafluoroethylene composition during production and recycling*, Eastern European Journal of Advanced Technologies, 2/11 (68), 9 (2014); http://journals.uran.ua/eejet/article/view/23381/21034
[21] K.V. Berladir, T.P. Hovorun, V.A. Sviderskiy, P.V. Rudenko, M.E. Vyshehorodtseva, Nanostructural Modification of Polytetrafluoroethylene and its Composition by Energy Influence, Journal of Nano- and Electronic Physics, 8 (1), 01033(5) (2016); https://doi.org/10.21272/jnep.8(1).01033
[22] O. A. Bilous, T. P. Hovorun, K. V. Berladir, S. I. Vorobiov, V. V. Simkulet, *Mathematical modeling of the mechanical characteristic of the activated PTFE-matrix using the method of planning the experiment*, Journal of Engineering Sciences, 5(1), C1 (2018), https://doi.org/10.21272/jes.2018.5(1).c1
[23] K. Berladir, D. Zhyhylii, O. Gaponova, J. Krmela,V. Krmelová, A. Artyukhov, *Modeling of Polymer Composite Materials Chaotically Reinforced with Spherical and Cylindrical Inclusions*, Polymers, 14(10), 2087 (2022); https://doi.org/10.3390/polym1410208
[24] M. A. Markova, P. N. Petrova, Influence of Carbon Fibers and Composite Technologies on the Properties of PCM Based on Polytetrafluoroethylene, Inorganic Materials: Applied Research, 12, 551 (2021); https://doi.org/10.1134/S2075113321020362
[25] O. A. Bilous, T. P. Hovorun, K. V. Berladir., S. I. Vorobiov., V. V. Simkulet, Mathematical Modeling of the Mechanical Characteristic of the Activated PTFE-Matrix Using the Method of Planning the Experiment, Journal of Engineering Sciences, 5 (1), 1 (2018); https://doi.org/10.21272/jes.2018.5(1).c1
[26] P.N. Grakovich, V.A . Shelestova, V.J . Shumskaja, et al. *Influence of the Type of Carbon Fiber Filler on the Physical–Mechanical and Tribological Properties of PTFE Composites*, J. Frict. Wear 40, 11 (2019); https://doi.org/10.3103/S1068366619010069
[27] L.V. Bazyuk, V.P. Svidersky, *Influence of Type and Form of the Fillers on Therm ophysical Properties for composite M aterials on the base of the Polytetrafluoroetelene and Aromatic Polyam ide*, Herald of Vasyl Stefanyk Precarpathian National University. Ser. Chemistry, (V), 47 (2008); http://elar.khmnu.edu.ua/jspui/handle/123456789/4475
[28] H.A.Sirenko, V.P.Sviderskiy, L.Ya.Midak, L.V.Karavanovich, Influence of temperature to a creep of composite materials because of polytetraftorethilene for want of by constant to a load, Polymer Journal 27 (3), 167 (2005).
[29] H.O. Sirenko, V.P. Sviderskyi, L.V. Karavanovych. *Influence of polymer composition on wear rate and thermal conductivity coefficien*t, Proc. of V International Scientific and Technical Conference "Wear resistance and reliability of friction units of machines (ZNM-2003), 27 (2003).
[30] O.A.Budnik, A.F.Budnik, K.V.Berladir, P.V.Rudenko, V.A.Sviderskiy, Influence of mechanical activation of polytetrafluoroethylene matrix of tribotechnical composites on its structural and phase transformations and properties, Funct. Mater., 22 (4), 499 (2015); http://dx.doi.org/10.15407/fm22.04.499
[31] A.F. Budnyk, V.A. Sviderskyi, A.O. Thomas, P.V. Rudenko, H.V. Berladir, *Design of polymer composite modeled by spheres and ellipsoids by the criterion of coordination of properties*, East-European Journal of Advanced Technologies, 2/5 (62), 20 (2013); http://journals.uran.ua/eejet/article/view/12397/10286
[32] H.V. Berladir, V.A. Sviderskyi, Physical Modification fluoroplast-4 in order to improve tribotechnical properties of composites based on it, VI International scientific and technical conference of students, graduate students that young scientists "Chemistry and modern technologies", Dnepropetrovsk, 150 (2013).
[33] H.O. Sirenko, L.M. Soltys, M.F. Semenyuk, The Specific Square of Gaussian Anisotropic and Isotropic Rough Surfaces, Herald of Vasyl Stefanyk Precarpathian National University. Ser. Chemistry, (XII), 134 (2011).

О.В. Комашко, Г.О. Сіренко, М.Б. Складанюк

Особливості хемо-механо-активаційної технології одержання полімерних композитних матеріалів

Прикарпатський національний університет імені Василя Стефаника вул. Шевченка, 57, м. Івано-Франківськ, 76018, Україна, oks.pavlykivska@gmail.com

Проведено огляд робіт по дослідженню процесів одержання полімерних композитів за хемо-механо-активаційною технологією (ХМА-технологією). Зроблено аналіз та узагальнення методів дослідження і випробування композиційних матеріалів на основі політетрафторетилену (ПТФЕ) і вуглецевих волокон. Встановлено вплив ХМА- технології на структуру і властивості ПТФЕ-композиту.

Ключові слова: полімерний композит, політетрафторетилен, вуглецеві волокна, хемо-механо-активаційна технологія.

PHYSICS AND CHEMISTRY OF SOLID STATE
V. 24, No. 2 (2023) pp. 312-322
Section: Technology

DOI: 10.15330/pcss.24.2.312-322

Vasyl Stefanyk Precarpathian National University

ФІЗИКА І ХІМІЯ ТВЕРДОГО ТІЛА
Т. 24, № 2 (2023) С. 312-322
Технічні науки

PACS: 63.70.+h ISSN 1729-4428

Hussam Raad[1], Emad Kadum Njim[2], Muhsin J. Jweeg[3], Muhannad Al-Waily[1]

Sandwiched Plate Vibration Analysis with Open and Closed Lattice

[1]*Department of Mechanical Engineering, Faculty of Engineering, University of Kufa, Iraq*
[2]*Ministry of Industry and Minerals, State Company for Rubber and Tires Industries, Iraq*
[3]*Al-Farahidi University, College of Technical Engineering, Iraq*

This work attempts to replace the sandwich core's traditional shape and material with a cellular pattern, where the cells have a regular shape, distribution, and size. The contribution of this paper is to design two structures, one open-celled and the other closed, and to evaluate the performance of sandwich plates with lattice cell core as it is used for many industrial applications, particularly in automobile engineering. The new theoretical formulations are constructed for two structures to find the free vibration characteristics. The results of the new design are compared with the traditional shape. Derivation of equations to predict mechanical properties based on relative density with the chosen shapes, specific vibration equation of three-layer sandwich plate, and substitution by equation using excel sheet. Results are promising, and the effectiveness of cellular pattern theoretical analysis estimation. Limitations and error rates for the mechanical properties come through the empirical equations, and their ratio to the relative density values are higher depending on the behavior of the core material. Findings reveal, with open cell decrease in modulus of elasticity by (PLA: -90.4%) and (TPU: -90.4%), increases natural frequency by (PLA: 44.5%) and (TPU: 46.4%), as for closed-cell decreases in the modulus of elasticity by (PLA: -66.9%) and (TPU: -64.4%), increases natural frequency by (PLA: 36%) and (TPU: 37.7%). Converting a solid substance or replacing a foam form with a cellular pattern is one way to better performance and save weight through the selected cell pattern in absorbing the energy of the vibration wave.

Keywords: sandwich plate, free vibration, lattice structural, strut section, closed and open cell, relative density.

Received 17 November 2022; accepted 8 June 2023.

Introduction

Composite structures are essential in energy absorption, weight reduction, and structure protection. Hence such arrangements received attention for their potential to resolve the instability problem. Various studies have revealed the mechanical behavior of sandwich structures using different techniques, such as using the reinforcement of polymer core materials and functionally graded materials [1-2]. Abud Ali et al. [3] presented a review of the behavior of composite structures. Cellular materials are widely used in nature to build structures that can withstand heavy loads while being lightweight [4]. Industrially, some of the most common engineerings utilize cellulosic materials, including those in the aviation and automotive sectors and building and industry packaging; the low density and excellent stiffness- and strength-to-weight ratios make them ideal for various applications [5]. These cells comprise interconnecting plates or struts that create the cell's borders and faces. The simplest are honeycomb and corrugated, 2D arrays of forms that pack to occupy a planar space, and 3D cellular materials, such as foam, which are used more often [6].

Foams are solid-gas mixtures after manufacture, a cellular solid with many sizes and forms results. High mechanical qualities and low density make foams useful [7]. Open-cell foams are utilized as sound absorbers, filtering, and mattresses. Closed-cell foams are stiffer and used in construction, such as sandwich panels and thermal insulation [8]. Usually, structures include minor faults that differ in size and dispersion based on the material and how it was treated [9]. The structures change depending on cell parameters such as relative density, size, shape, geometrical, wall thickness, and distribution between

struts and faces. Numerous previous studies have revealed the compressive and tensile strength properties of polyurethane foam and polyurethane rigid foam [10]. Maiti et al. (2016) used compressive strain coupled with a time-temperature superposition utilizing a minimum arc length-based method to forecast the long-term performance of the two types of foams [11]. Three-dimensional (3D) printing has recently been highly used to analyze sandwich structures with various applications [12]. 3D printing was explored for creating the lattice cores of these sandwich structures [13]. Lipton and Lipson (2016) presented a method for causing viscous thread instability while implicitly extruding material to produce cellular architectures. Cellular structures manufacture foams for applications ranging from bioengineering to robotics and food printing [14].

Ge et al. (2018) designed cellular structures model that was 3D printed with thermoplastic polyurethane. Flexibility & energy absorption of 3d printed foam were evaluated experimentally [15]. The mechanical behavior of octet-truss microstructures of three distinct octet structures is examined experimentally and numerically by Bagheri et al. [16]. Elasticity modulus increases with increasing strut radius. Results were found to be consistent. Moreover, Guo et al. (2019) presented a new technique to study pyramid lattice core sandwich plates. Theoretical analysis with Hamilton's concept establishes motion's equation. The design of lattice cells will benefit from the new technique [17]. The octahedrons, truncated octahedrons & stellated octahedrons as porous cells are made by selective laser melting. It's experimental, and simulations work. The results indicated that the octahedron configuration has the highest mechanical performance [18].

Lei et al. (2019) created two kinds of multi-layer cores using AlSi10Mg materials, performed numerically and experimentally. Strut position and constructed angle change in strut diameter deviation [19]. Wang et al. (2019) experimental work examine the behavior of sandwich panels with different types of lattice cores using galvanized sheet metal and 3d printed lattice cores. Lattice & graded lattice cores absorb more energy than solids [20]. In their experimental work, Azmi et al. (2019) checked the damage amount & position to see how it affects the natural frequencies of the lattice structure. Increasing damage reduces the natural frequency, and natural frequency values rise as it moves away from the clamped edge [21]. Qi et al. (2020) designed an innovative hybrid sandwich composite of pyramidal truss core reinforced by carbon fiber using finite element models. The study verifies an improvement in the characteristic of the hybrid joining insert [22]. Bonthu et al. (2020) created a 3D-P of a syntactic foam cored sandwich (skin-core-skin printing in sequence at once). This study included optimizing printing conditions and producing high-quality sandwich structures without flaws [23].

Monteiro et al. (2021) found out how sandwich panels' flexural behavior is affected by lattice topology with numerical and experimental methodologies. Relative density constant (0.3). Several lattice geometries have a potential alternative to standard construction [24]. Ma et al. (2021) reported a review study on sandwich panels' features and impact behavior based on cores lattice and loading conditions as compression. Application and future development have been forecasted [25]. Wei et al. (2021) explored the vibration properties of an octahedral lattice core sandwich, representing theoretical and numerical study. Outcomes coincide perfectly with an octahedron core's natural frequencies by adjusting its cell [26]. Guo et al. (2021) investigated vibration analyses and passive control of sandwiched beams by 3D printed lattice. Theoretical results confirmed empirically, literature findings and simulation showed how 3D printing could create complex lattice cores [27]. The optimal design of core characteristics and skins is also discussed for inhomogeneous [28] and soft polymers [29]. To predict the stability of isotropic composite plates reinforced by different types of powder, Chiad et al. (2020) developed a combined finite element and experimental work [30]. A three-dimensional FEA model predicts the flexural behavior of sandwich structures adhesively bonded to a polymeric foam core consisting of fiber-composite skins (also termed face sheets) [31].

Moreover, studies have been conducted to analyze static and dynamic behaviors of composite structures such as plates and shells [32-34]. Ambreen Kalsoom et al. (2021) investigated the stiffness and damping characteristics of the sandwich beam with 3D printed thermoplastic composite face sheets using higher-order beam theory based on various parameters such as support conditions, non-homogeneous magnetic flux, geometrical properties [35]. Roman Lewandowski et al. (2021) conducted numerical studies on dynamic characteristics for composite sandwich beams made from elastic and viscoelastic layers based on refined zig-zag theory [36]. Al-Waily et al. proposed a dynamic analytical model of the composite plates reinforced with hybrids nanomaterials additives [37]. Studies also focus on static and dynamic experimental works of specific components of the sandwich structure [38]. Recently, many investigations have been proposed to improve the sandwich panel design methods using isotropic face sheets and functionally graded cores. Njim et al. (2021) investigated analytical and numerical investigation of free vibration behavior for sandwich plates with functionally graded porous metal cores and homogenous skins based on classical plate theory [39] and the finite element using the Rayleigh-Ritz [40].

Among the literature on sandwich panels with composite faceplate and foam core, most studies focus on the behavior of core material. However, previous research investigated low-density cellular structures and their application as an alternative to solid materials concentrating on maintaining or improving performance.

The current research includes the experimental and theoretical study of free vibration analysis of a sandwich plate with two sides of aluminum metal and foam core. The study aims to replace the irregular cells foam of the core with a regular cellular structure, where the cells have a standard shape, distribution, and size. Two configurations are employed, one open-cell and the other closed. The theoretical analysis of the two structures is carried out to obtain the free vibration characteristics based on various parameters using mechanical properties obtained from the experimental work. The findings of this study are essential in the automobile industry. The

numerical results presented herein for the cellular core sandwich plate are not available in the literature and hence, should be of interest to future research directions.

I. Structural core

For the structural core to differ from the solid, values of the modulus of elasticity and the poison ratio, need to be derived as an equation in a different direction. The geometrical structure of cellular solids is defined by the cells' form, size, and distribution. 3D cellular solids like foams have greater complexity than 2D honeycomb structures. But studying two-dimensional structures helps us comprehend three-dimensional structures like foams. The relative density ρ_r of a cellular solid is one of its most essential properties [41],

$$\rho_r = \frac{\rho^*}{\rho_o} \tag{1}$$

Where, ρ^* and ρ_o are the cellular and outer (connected solidly) material densities, respectively. The cell wall thickens with relative density. The outer material's volume fraction is shown in Fig. 1,

$$p_o = \frac{V_o}{V^*} \tag{2}$$

As the density of the foam $\rho^* = \frac{m^*}{V^*}$ and density of the outer material $\rho_o = \frac{m_o}{V_o}$, Since that $m^* = m_o$. The outer material's volume fraction po can be written as,

$$p_o = \frac{m_o}{\rho_o}/\frac{m^*}{\rho^*} = \frac{\rho^*}{\rho_o} = \frac{V_o}{V^*} \tag{3}$$

The inner material's relative density matches the outer material's volume fraction $p_i = \frac{V_i}{V^*}$, Also, note that,

$$p_o = \frac{V^* - V_i}{V^*} = 1 - V_i = 1 - \frac{V_i}{V^*} \tag{4}$$

It will seem more like a solid substance with isolated pores if the relative density is more significant than, $p_o > 0.3$.

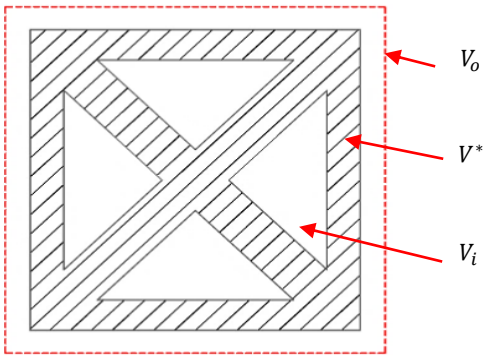

Fig. 1. One cell of cellular structure.

Closed Cell Design

Closed-cell foams have walls, unlike open-cell foams. The proposed for the close cell cubic is symmetric in all directions, as illustrated in Fig. 2. The way of defining the relative young's modulus is,

$$E_r = \frac{E_c^*}{E_c} \tag{5}$$

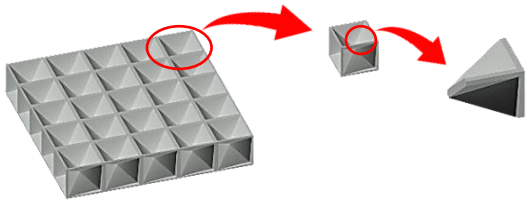

Fig. 2. Closed cell structure.

Where E_c^* and E_c represents Young's modulus of the cellular and solid materials of the closed structure, respectively. The cells are designed to be having same mechanical properties in the x and y directions, as illustrated in Fig. 3. The cell of the foam is symmetric, as shown in Fig. 4, and the characteristics of a rectangular strut with lengths (t) are,

$$\frac{\rho^*}{\rho_o} = 1 - \frac{V_i}{V^*} = 1 - \frac{24V_{is}}{8c^3} = 1 - \frac{3V_{is}}{c^3} \tag{6}$$

$$V_{is} = \frac{1}{3}Ah = \frac{1}{3}(c - t\cos\gamma)^3 \tag{7}$$

So, the final equation would look like this,

$$\frac{\rho^*}{\rho_o} = 1 - \frac{(c - t\cos\gamma)^3}{c^3} \tag{8}$$

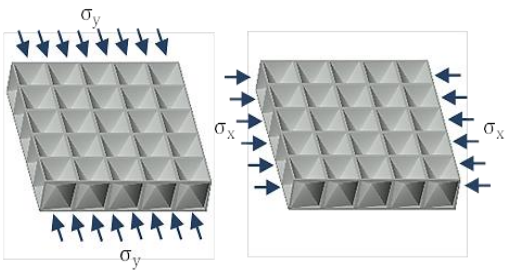

Fig. 3. Closed-cell in x-y direction to conclude young's modulus.

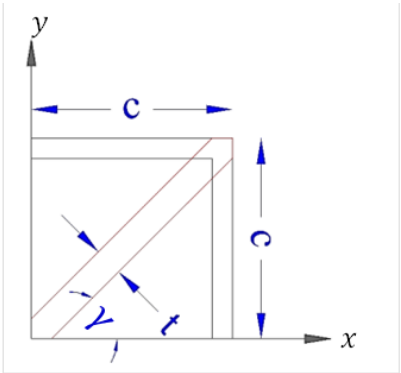

Fig. 4. The closed-cell area (eighth cells).

Modeled an isotropic closed-cell foam and provided an estimated foam Young's modulus linked to the solid

Young's modulus as a function of the proportion of solid material in struts φ by [8],

$$\frac{E_c^*}{E_c} \approx C_1 \varphi^2 \left(\frac{\rho^*}{\rho_o}\right)^2 + C_1'(1-\varphi)\frac{\rho^*}{\rho_o} + \frac{p_{at}(1-2\nu^*)}{E_o\left(1-\frac{\rho^*}{\rho_o}\right)} \quad (9)$$

$$G_c^* = \frac{E_f^*}{2(1+\nu_f^*)} \quad (10)$$

$C_1 \approx C_1' \approx 1$ and the last term in Eq. (9) can be neglected as it almost equals zero, also atmospheric pressure $p_{at} =$ 0.1 Mpa, then the equation goes,

$$\frac{E_c^*}{E_c} \approx \varphi^2 \left(\frac{\rho^*}{\rho_o}\right)^2 + (1-\varphi)\frac{\rho^*}{\rho_o} \quad (11)$$

By substitution Eq. (8) in Eq. (11), get,

$$\frac{E_c^*}{E_c} \approx \begin{pmatrix} \varphi^2 \left(1 - \frac{(c - t\cos\gamma)^3}{c^3}\right)^2 + \\ (1-\varphi)\left(1 - \frac{(c-t\cos\gamma)^3}{c^3}\right) \end{pmatrix} \quad (12)$$

And since the cell is symmetrical in the x and y direction then, the equation becomes,

$$E_{c2}^* = E_{c1}^* = E_c^* = \begin{pmatrix} \varphi^2 \left(1 - \frac{(c-t\cos\gamma)^3}{c^3}\right)^2 + \\ (1-\varphi)\left(1 - \frac{(c-t\cos\gamma)^3}{c^3}\right) \end{pmatrix} E_c \quad (13)$$

Percentage of the strut from the total material forming the solid part of the core structure (φ). To obtain the following equation, the free vibration equation was derived based on Kirchhoff's theory of a three-layer sandwich plate (two faces of plates and a core) [42, 43],

$$\omega_{mn} = \sqrt{\frac{\left(\frac{\pi}{a}\right)^4 \left(2\left(\frac{2E_s}{1-\nu_s^2}\left(\frac{h_s^3}{3} + \frac{h_s^2 h_f}{2} + \frac{h_s h_f^2}{4}\right) + \frac{E_f}{1-\nu_f^2}\left(\frac{h_f^3}{12}\right)\right) + \left(\frac{4E_s}{(1+\nu_s)}\left(\frac{h_s^3}{3} + \frac{h_s^2 h_f}{2} + \frac{h_s h_f^2}{4}\right) + G_f\left(\frac{h_f^3}{3}\right)\right)\right)}{2\rho_s h_s + \rho_f h_f}} \quad (14)$$

The new modified equation, instead of after the back substitution of the equations,

$$\omega_{mn} = \sqrt{\frac{\left(\frac{\pi}{a}\right)^4 \left(2\left(\frac{2E_s}{1-\nu_s^2}\left(\frac{h_s^3}{3} + \frac{h_s^2 h_f}{2} + \frac{h_s h_f^2}{4}\right) + \frac{E_c^*}{1-\nu_c^{*2}}\left(\frac{h_f^3}{12}\right)\right) + \left(\frac{4E_s}{(1+\nu_s)}\left(\frac{h_s^3}{3} + \frac{h_s^2 h_f}{2} + \frac{h_s h_f^2}{4}\right) + G_c^*\left(\frac{h_f^3}{3}\right)\right)\right)}{2\rho_s h_s + \rho_f^* h_f}} \quad (15)$$

Open Cell Design

Most open-cell foams lack walls. Procedures remove cell membranes physically or chemically. Applying the same approach for open cells, proposing cell cubic symmetric in two directions as illustrated in Fig. 5. They were using the same equation only by adopting mechanical properties for open-cell. The same way in defining relative young's modulus as mechanical the same in x and y directions as illustrated in Fig. 6. As shown in Fig. 7, the chosen open cell has three areas,

$$\frac{\rho^*}{\rho_o} = \frac{V_o}{V^*} = \frac{4(V_{os})}{4c^2 h} = \frac{V_{os}}{c^2 h} \quad (16)$$

$$V_{os} = \begin{pmatrix} t\left(\left(c^2 - \left(c - \frac{t}{2}\right)\right) + \left(c^2 - (c-t)\right)\right) \\ +t^2\left(\sqrt{2c^2 + (h-2t)^2} - \frac{t}{\tan\gamma}\right) \end{pmatrix} \quad (17)$$

So, the final equation is going to be,

$$\frac{\rho^*}{\rho_o} = \frac{1}{c^2 h}\begin{pmatrix} t\left(\left(c^2 - \left(c - \frac{t}{2}\right)\right) + \left(c^2 - (c-t)\right)\right) \\ +t^2\left(\sqrt{2c^2 + (h-2t)^2} - \frac{t}{\tan\gamma}\right) \end{pmatrix} \quad (18)$$

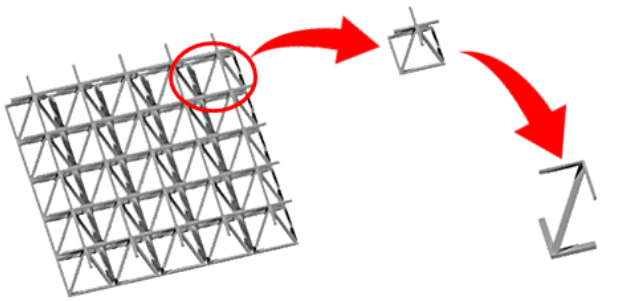

Fig. 5. The open cell structure.

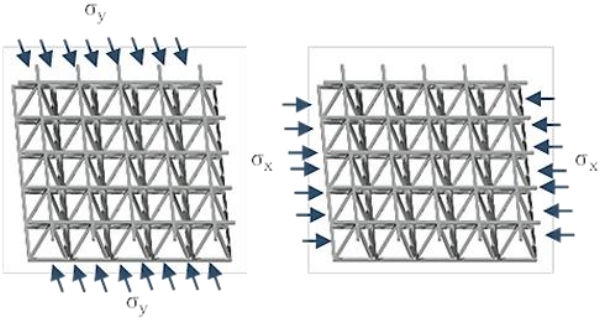

Fig. 6. Open the cell in the x-y direction to conclude young's modulus.

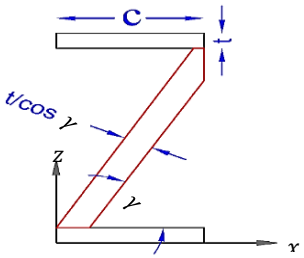

Fig. 7. closed-cell (quarter cell).

As a result, [8] calculated the open-cell foam's elastic constants using the cubic model,

$$\frac{E_c^*}{E_c} \approx C_1 \left(\frac{\rho^*}{\rho_o}\right)^2 \tag{19}$$

$$G_c^* = \frac{E_f^*}{2(1+\nu_f^*)} \tag{20}$$

As $C_1 \approx 1$ and $\nu^* = 0.3$, the equation goes,

$$\frac{G_c^*}{E_c} \approx \frac{3}{8}\left(\frac{\rho^*}{\rho_o}\right)^2 \tag{21}$$

$$\frac{E_c^*}{E_c} \approx \left(\frac{1}{c^2 h}\left(t\left(\left(c^2 - \left(c - \frac{t}{2}\right)\right) + [c^2 - (c-t)]\right) + t^2\left(\sqrt{2c^2 + (h-2t)^2} - \frac{t}{\tan\gamma}\right)\right)\right)^2 \tag{22}$$

And since the cell is symmetrical in the x and y direction then, the equation becomes,

$$E_{c2}^* = E_{c1}^* = E_c^* = \left(\frac{1}{c^2 h}\left(t\left(\left(c^2 - \left(c - \frac{t}{2}\right)\right) + (c^2 - (c-t))\right) + t^2\left(\sqrt{2c^2 + (h-2t)^2} - \frac{t}{\tan\gamma}\right)\right)\right)^2 E_c \tag{23}$$

Using the same equations (14) and (15) to compete for the natural frequency.

II. Results

For a rectangular sandwich plate, $a = b = 30\text{cm}$. Using two Faces with a thickness of $h_s = 1\text{mm}$ of aluminum alloy (Al 1100-H12) has $E_s = 68.9$ Gpa, $\rho_s = 2710\ \text{kg/m}^3$ & $\nu_s = 0.33$. The core part with a thickness of $h_f = 14\text{mm}$. The material to be adopted in the core structure is polylactic acid (PLA) and Thermoplastic polyurethane (TPU). The tensile test is carried out to find mechanical properties according to ASTM. Hence, standard specimens for PLA and TPU material are used as raw materials in 3D printing machines to make structural foam, depending on ASTM D638 for plastic materials [44, 45]. Two types of samples adopted rigid and non-rigid plastic specimens for the record, as illustrated in Fig. 8. According to the standards, five samples of each material, with the dimensions listed in Table 1.

Table 1.
ASTM D638 for plastic rigid (PLA) and non-rigid (TPU).

Measurements	PLA (mm)	TPU (mm)
Lo	165	115
L	33	20
Wo	20	19
W	12.5	6
R	76	14
Ri	-	25
Thickness	3	3
Gauge length	50	25

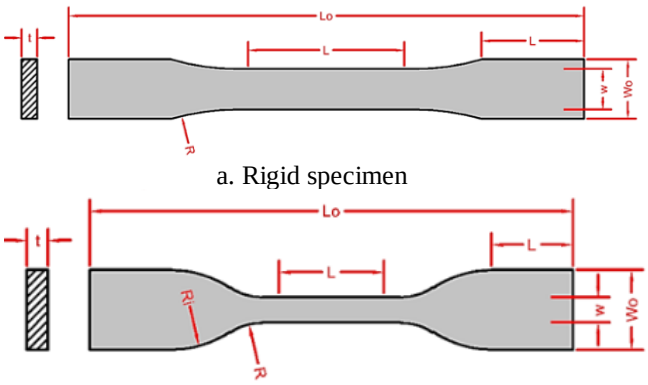

a. Rigid specimen

b. Non- rigid specimen

Fig. 8. ASTM D638 specimens.

Table 2.
Printing parameters of all specimens.

Printing setting	PLA filament	TPU filament
Nozzle dia.	0.40mm	0.50mm
Layer thickness	0.28mm	0.25mm
Infilling density	100%	100%
Infilling pattern	lines	lines
Printing temp.	200° C	228° C
Bed temp.	60° C	65° C
Printing speed	50mm/sec.	25mm/sec.

As the average results, PLA has a young's modulus magnitude of 1.175 Gpa and a density of 1360 kg/m^3, while TPU has a young's modulus magnitude of 0.833 Gpa and a density of 1450 kg/m^3. Printed specimens are illustrated in Fig. 9 before and after testing. First,

choose the cell dimension to build the core for open and closed cells. The selected cell is cubic in shape with a length of 14mm. The other dimension to be calculated like strut thickness, with a critical relative density as $\rho_r > 0.3$. Table 3 shows the selected strut thickness results as well as the calculated young modulus. In comparison with PLA, the stiffness of TPU polymer type decreases with thickness.

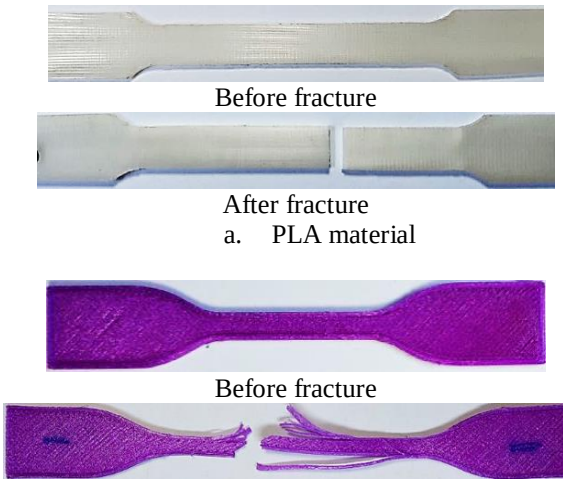

Before fracture

After fracture

a. PLA material

Before fracture

After fracture

b. TPU elongation 300 % material

Fig. 9. Tensile specimen before and after testing .

As can be seen from the results, the fundamental natural frequency increases as a function of relative density. Table 4 compares the natural frequency results between the traditional shape with open and closed cells at h_c 0.014 (m). Based on the results, it is evident that the new design has a distinct improvement in natural frequency. According to Table 5, closed-cell designs adopting varying strut thicknesses produce different results. According to the table, natural frequency and Young modulus increase as the proportion of solid material in struts φ decreases, furthermore the PLA samples showing significantly higher stiffness than TPU samples.

The natural frequency to elasticity modulus relation is illustrated in Fig. 10 for open cells and Fig. 11 for closed cells, while the connection to relative density is presented in Fig. 12 for available cells and Fig. 13 for closed cells. Fig. 14 shows the strut thickness effect on the natural frequency.

III. Discussion

With the Derivation of equations for extracting and converting mechanical properties from relative density, Young's modulus, stiffness modulus, and Poisson ratio. Relying on the equation for extracting the natural frequency, we discuss the results as follows,

Figures (10) and (11) show the relationship between the natural frequency and the modulus of elasticity. The connection is inverse with the decrease in the modulus of elasticity, so the natural frequency increases, and this decrease comes after converting the solid material into

Table 3.

Open cell design results adopting varying strut thickness ranges

Mat	t, mm	ρ_r	E_c^*, Gpa	v_c^*	G_c^*, Gpa	ρ_c^* ,kg/m^3	ω, rad/sec
PLA	1.1	0.163	0.031	0.3	0.012	222.21	6046.38
	1.2	0.181	0.038	0.3	0.015	245.68	5933.88
	1.3	0.198	0.046	0.3	0.018	269.59	5825.61
	1.4	0.216	0.055	0.3	0.021	293.91	5721.44
	1.5	0.234	0.064	0.3	0.025	318.64	5621.23
	1.6	0.253	0.075	0.3	0.029	343.73	5524.85
	1.7	0.271	0.087	0.3	0.033	369.17	5432.16
	1.8	0.290	0.099	0.3	0.038	394.94	5343.01
	1.9	0.310	0.113	0.3	0.043	421.02	5257.27
	2	0.329	0.127	0.3	0.049	447.38	5174.80
TPU	1.1	0.163	0.022	0.3	0.009	236.91	5973.81
	1.2	0.181	0.027	0.3	0.010	261.93	5858.01
	1.3	0.198	0.033	0.3	0.013	287.43	5746.78
	1.4	0.216	0.039	0.3	0.015	313.36	5639.96
	1.5	0.234	0.046	0.3	0.018	339.72	5537.38
	1.6	0.253	0.053	0.3	0.020	366.48	5438.88
	1.7	0.271	0.061	0.3	0.024	393.60	5344.27
	1.8	0.290	0.070	0.3	0.027	421.08	5253.41
	1.9	0.310	0.080	0.3	0.031	448.88	5166.13
	2	0.329	0.090	0.3	0.035	476.99	5082.28

Table 4.

Comparison the result of the traditional shape with the open and closed cells at h_c 0.014 (m).

Mat.	E_c^* , Gpa	ρs (kg/m3)	ρ_r	νc	ρc (kg/m^3)	ω (rad/s)
PLA	1.175	1360	1	0.38	1360	5239.38
TPU	0.833	1450	1	0.35	1450	5080.74

Table 5.

Closed-cell design results adopting varying strut thickness

Mat	t mm	φ	ρ_r	E_c^* Gpa	ν_c^*	G_c^* Gpa	ρ_c^* kg/m^3	ω rad/sec
PLA	1.1	0.22	0.298	0.236	0.3	0.091	404.85	5321.43
	1.2	0.24	0.321	0.249	0.3	0.096	437.04	5217.62
	1.3	0.26	0.344	0.262	0.3	0.101	468.51	5121.86
	1.4	0.28	0.367	0.274	0.3	0.105	499.25	5033.24
	1.5	0.30	0.389	0.285	0.3	0.110	529.27	4951.00
	1.6	0.32	0.411	0.296	0.3	0.114	558.59	4874.48
	1.7	0.34	0.432	0.305	0.3	0.117	587.21	4803.14
	1.8	0.36	0.452	0.315	0.3	0.121	615.14	4736.48
	1.9	0.38	0.472	0.324	0.3	0.125	642.39	4674.07
	2	0.40	0.492	0.333	0.3	0.128	668.97	4615.55
TPU	1.1	0.22	0.298	0.236	0.3	0.091	431.64	5233.64
	1.2	0.24	0.321	0.249	0.3	0.096	465.96	5128.41
	1.3	0.26	0.344	0.262	0.3	0.101	499.51	5031.51
	1.4	0.28	0.367	0.274	0.3	0.105	532.28	4941.98
	1.5	0.30	0.389	0.285	0.3	0.110	564.30	4859.01
	1.6	0.32	0.411	0.296	0.3	0.114	595.56	4781.93
	1.7	0.34	0.432	0.305	0.3	0.117	626.07	4710.13
	1.8	0.36	0.452	0.315	0.3	0.121	655.85	4643.12
	1.9	0.38	0.472	0.324	0.3	0.125	684.90	4580.46
	2	0.40	0.492	0.333	0.3	0.128	713.24	4521.75

foam that permeates every air cell, as seen in fig. (12) and (13). The difference between the rigid material (PLA) and the non-rigid (TPU) is evident as the tough material comes at a higher frequency.

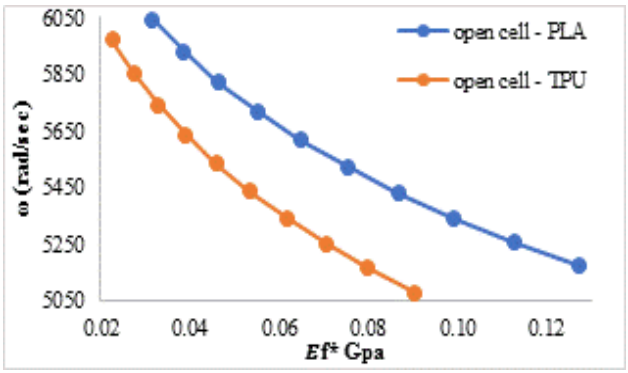

Fig. 10. Natural frequency to elasticity modulus for open cell.

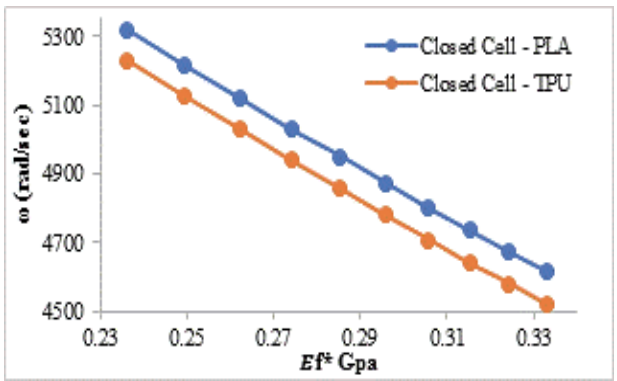

Fig. 11. Natural frequency to elasticity modulus for closed cell.

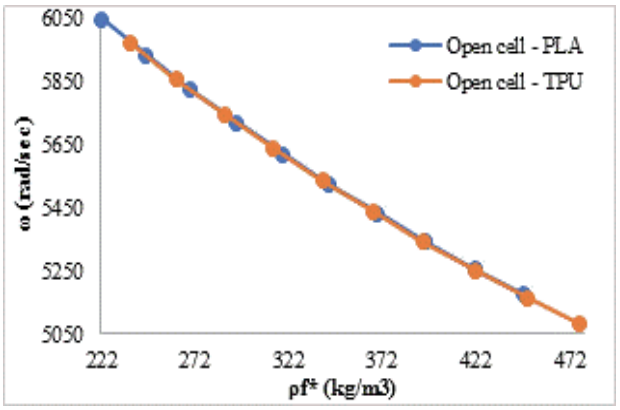

Fig. 12. Natural frequency to relative density for open cell.

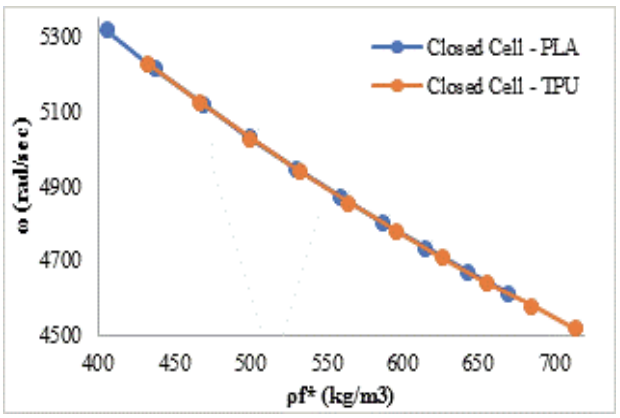

Fig. 13. Natural frequency relation relative density for closed-cell.

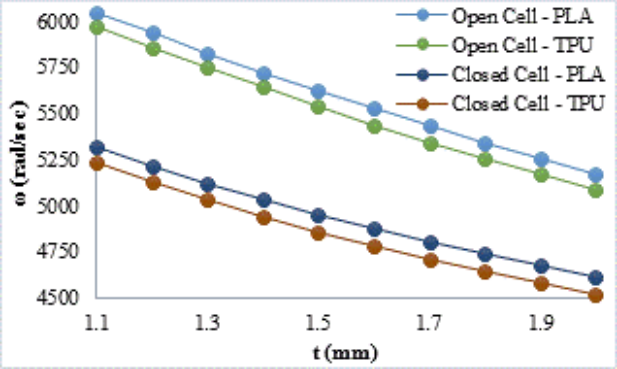

Fig. 14. Natural frequency to strut thickness with two cell types (Open & Closed) and two materials (PLA & TPU).

For open lattice cells, depending on the relative density as a regulator. When the relative density (0.3) at (t = 1.9mm) compared to solid matter, the percentage decrease in the modulus of elasticity by (PLA: -90.4%) and (TPU: -90.4%), increases the natural frequency by (PLA: 44.5%) and (TPU: 46.4%). One more time, a closed lattice cell with the same relative density (0.3) at (t = 1.5mm) compared to solid matter. Percentage decrease in the modulus of elasticity by (PLA: -66.9%) and (TPU: -64.4%) increases the natural frequency by (PLA: 36%) and (TPU: 37.7%). Converting a solid material into a cellular one to reduce weight loses some properties. The properties can be compensated by adding a nanomaterial or by filling the cellular part with another material and turning it into a hybrid structure.

Conclusions

After reviewing the results in tables and charts and discussing the results as in the previous text, the following is concluded,

The effect of converting a solid material or replacing a foam form with a cellular pattern is very effective.

The choice of cell shape and pattern determines their performance. The regular shape in both directions makes the material isotropic and homogeneous

Selection between closed and open-cell depends on the application, and it is preferable to use a closed-cell in the sandwich because it offers much performance.

The open-cell structure can be converted into a closed one by filling the attached space with another material, such as foam, which makes the core a hybrid shape that offers the performance the engineer aspires to.

Effectiveness of cellular pattern theoretical analysis estimation and possible use in various applications

The results of this investigation can be used in various engineering applications such as retractable car roofs, the floor of electric cars to isolate the cabin from the battery placed under the vehicle, and electric motor covers for electric cars.

Nomenclature

Symbols	Definition
a	Plate length in x-direct (m)
b	Plate width in y-direct (m)
c	Half of the cell length or width (m)
E_s	face layer young's modulus (Pa)
E_f	core layer young's modulus (Pa)
E_c^*	cellular core material young's modulus (Pa)
Ec	solid material young's modulus (Pa)
G_f	core layer rigidity modulus (Pa)
G_c^*	cellular core layer rigidity modulus (Pa)
h_s	Upper face layer height (m)
h_f	lower face layer height (m)
p_i	Inner volume fraction
p_o	Outer volume fraction
t	The thickness of the cell frame (m)
V^*	cellular material Volume (m^3)
V_o	outer (connected solid) material Volume (m^3)
V_i	inner (air) Volume (m^3)
V_{is}	Inner air volume (m^3)
V_{os}	Outer frame volume (m^3)
ω_{mn}	Natural frequency $(rad/s.)$
vs	face layer Poisson's ratio
v_c^*	cellular Poisson's ratio
ρ_r	Relative density
ρ^*	cellular material density $(kg/m3)$
ρ_f	face layer density $(kg/m3)$
ρ_s	core layer density $(kg/m3)$
ρ_o	outer (connected solid) material density $(kg/m3)$
φ	the proportion of solid material in struts

Hussam Raad – M.Sc. researcher (Applied Mechanics) raadhussam4@gmail.com;
Emad Kadum Njim – Ph.D. researcher (Applied Mechanics) emad.njim@gmail.com;
Muhsin J. Jweeg – Prof. Dr. (Applied Mechanics) muhsinjj@gmail.com;
Muhannad Al-Waily – Prof. Dr. (Applied Mechanics) muhanedl.alwaeli@uokufa.edu.iq.

[1] E.K. Njim, S.H. Bakhy, M. Al-Waily, *Analytical and numerical flexural properties of polymeric porous functionally graded (PFGM) sandwich beams*, Journal of Achievements in Materials and Manufacturing Engineering 110 (1), 5 (2022); https://doi.org/10.5604/01.3001.0015.7026.

[2] E.K. Njim, S.H. Bakhy, M. Al-Waily, *Free vibration analysis of imperfect functionally graded sandwich plates: analytical and experimental investigation*, Archives of Materials Science and Engineering 111 (2), 49 (2021); https://doi.org/10.5604/01.3001.0015.5805.

[3] ZAA Abud Ali, A.A. Kadhim, R.H. Al-Khayat, M. Al-Waily, *Review Influence of Loads upon Delamination Buckling in Composite Structures*, Journal of Mechanical Engineering Research and Developments 44 (3), 392 (2021).

[4] A. Öchsner, G.E. Murch, M.J.S. de Lemos, Cellular and Porous Materials: Thermal Properties Simulation and Prediction, Wiley-VCH Verlag GmbH & Co. KgaA (2008).
[5] A. Karakoç, *Effective stiffness and strength properties of cellular materials in the transverse plane*, Aalto University publication series (2013). https://doi.org/10.1002/9783527621408.
[6] L.J. Gibson, M. F. Ashby, Cellular solids: Structure and properties, second edition, Lorna J. Gibson and Michael F. Ashby (1997).
[7] P. Stevenson, Foam Engineering: Fundamentals and Applications, John Wiley & Sons (2012).
[8] V. Shulmeister, Modelling of the Mechanical Properties of Low-Density Foams, Shaker (1997).
[9] H. Altenbach, A. Öchsner, *Cellular and Porous Materials in Structures and Proceses*, Springer Nature Switzerland AG (2012). https://doi.org/10.1007/978-3-7091-0297-8.
[10] A. Koyama, D. Suetsugu, Y. Fukubayashi, H.. Mitabe, *Experimental study on the dynamic properties of rigid polyurethane foam in stress-controlled cyclic uniaxial tests*, Construction and Building Materials, 321(2022); https://doi.org/10.1016/j.conbuildmat.2022.126377.
[11] A. Maiti, W. Small, J.P Lewicki, T.H. Weisgraber, E.B. Duoss, S.C. Chinn, *3D printed cellular solid outperforms traditional stochastic foam in long-term mechanical response*, Scientific Reports 6 (2016); https://doi.org/ 10.1038/srep24871.
[12] E.K. Njim, S.H. Bakhy, M. Al-Waily, *Experimental and numerical flexural analysis of porous functionally graded beams reinforced by (Al/Al2O3) nanoparticles*, International Journal of Nanoelectronics and Materials 15 (2), 94 (2022).
[13] A. Fadeel, H. Abdulhadi, G. Newaz, R. Srinivasan, A. Mian, *Computational investigation of the post-yielding behavior of 3D-printed polymer lattice structures*, In Journal of Computational Design and Engineering, 9 (1), 263 (2022), https://doi.org/10.1093/jcde/qwac001.
[14] J.I. Lipton, H. Lipson, *3D Printing Variable Stiffness Foams Using Viscous Thread Instability*, Scientific Reports 6 (2016).
[15] C. Ge, L. Priyadarshini, D. Cormier, L. Pan, J. Tuber, *A preliminary study of cushion properties of a 3D printed thermoplastic polyurethane Kelvin foam*, Packaging Technology and Science 31(5) (2018); https://doi.org/10.1002/pts.2330.
[16] A. Bagheri, I.B. Corral, M. Ferrer, M.M. Pastor, F. Roure, *Determination of the elasticity modulus of 3D printed octet-truss structures for use in porous prosthesis implants*, Materials 11(12), (2018) https://doi.org/10.3390/ma11122420.
[17] Z. Guo, C. Liu, F. Li, *Vibration analysis of sandwich plates with lattice truss core*, Mechanics of Advanced Materials and Structures, 26(5) (2019); https://doi.org/10.1080/15376494.2017.1400616.
[18] C. Tian, X. Li, S. Zhang, G. Guo, S. Ziegler, J.H. Schleifenbaum, *Porous structure design and fabrication of metal-bonded diamond grinding wheel based on selective laser melting (SLM*), International Journal of Advanced Manufacturing Technology. 100 (5–8) (2019); https://doi.org/10.1007/s00170-018-2734-y.
[19] H. Lei, C. Li, J. Meng, H. Zhou, Y. Liu, X. Zhang, *Evaluation of compressive properties of SLM-fabricated multi-layer lattice structures by experimental test and μ-CT-based finite element analysis*, Materials and Design 169 (2019). https://doi.org/10.1016/j.matdes.2019.107685.
[20] S. Wang, Y. Xu, W. Zhang, *Low-velocity impact response of 3D-printed lattice sandwich panels*, IOP Conference Series: Materials Science and Engineering 531 (2019).
[21] MS Azmi, R. Ismail, R. Hasan, A. Putra, M.N. Nurdin, Effect of damage on FDM printed lattice structure material vibration characteristics, Proceedings of Mechanical Engineering Research Day (2019).
[22] G. Qi, Y.L. Chen, P. Richert, L. Ma, K.U. Schröder, *A hybrid joining insert for sandwich panels with pyramidal lattice truss cores*, Composite Structures 241 (2020); https://doi.org/10.1016/j.compstruct.2020.112123.
[23] D. Bonthu, H.S. Bharath, S. Gururaja, P. Prabhakar, M. Doddamani, *3D printing of syntactic foam cored sandwich composite*, Composites Part C: Open Access 3 (2020); https://doi.org/10.1016/j.jcomc.2020.100068.
[24] J.G. Monteiro, M. Sardinha, F. Alves, A.R. Ribeiro, L. Reis, A. M. Deus, *Evaluation of the effect of core lattice topology on the properties of sandwich panels produced by additive manufacturing*, *Proceedings of the Institution of Mechanical Engineer*s, Part L: Journal of Materials: Design and Applications 235 (6) (2021); https://doi.org/10.1177/1464420720958015.
[25] Q. Ma, M.R.M. Rejab, J.P. Siregar, Z. Guan, *A review of the recent trends on core structures and impact response of sandwich panels*, Journal of Composite Materials 55 (18) (2021); https://doi.org/10.1177/0021998321990734.
[26] N. Wei, H. Ye, X. Zhang, J. Li, B. Yuan, *Vibration Characteristics Research of Sandwich Structure with Octet-truss Lattice Core*, Journal of Physics: Conference Series 2125 (1) (2021); https://iopscience.iop.org/article/10.1088/1742-6596/2125/1/012059.
[27] Z. Guo, G. Hu, J. Jiang, L. Yu, X. Li, J. Liang, *Theoretical and Experimental Study of the Vibration Dynamics of a 3D-Printed Sandwich Beam With an Hourglass Lattice Truss Core*, Front Mech Eng, 7 (2021); https://doi.org/10.3389/fmech.2021.651998.
[28] E.K. Njim, S.H. Bakhy, M. Al-Waily, *Optimisation Design of Functionally Graded Sandwich Plate with Porous Metal Core for Buckling Characterisations*, Pertanika Journal of Science & Technology, 29(4), 3113 (2021; https://doi.org/10.47836/pjst.29.4.47.

[29] E.K. Njim, S.H. Bakhy, M. Al-Waily, *Optimization design of vibration characterizations for functionally graded porous metal sandwich plate structure*, Materials Today: Proceedings (2021); https://doi.org/10.1016/j.matpr.2021.03.235.
[30] J.S. Chiad, M. Al-Waily, M.A. Al-Shammari, Buckling Investigation of Isotropic Composite Plate Reinforced by Different Types of Powders, International Journal of Mechanical Engineering and Technology 9 (9), 305 (2018).
[31] H. Liu, J. Liu, Ci. Kaboglu, J. Zhou, Xi.o Kong, Sh. Li, B. R.K. Blackman, A. J. Kinloch, J. P. Dear, *Modelling the quasi-static flexural behaviour of composite sandwich structures with uniform- and graded-density foam cores*, Engineering Fracture Mechanics, 259 (2022); https://doi.org/10.1016/j.engfracmech.2021.108121.
[32] M. Al-Waily, A.M. Jaafar, *Energy balance modelling of high velocity impact effect on composite plate structures*, Archives of Materials Science and Engineering, 111(1), 14 (2021).
[33] E.N. Abbas, M.J. Jweeg, M. Al-Waily, *Analytical and Numerical Investigations for Dynamic Response of Composite Plates Under Various Dynamic Loading with the Influence of Carbon Multi-Wall Tube Nano Materials*, International Journal of Mechanical & Mechatronics Engineering, 18(6), 1 (2018).
[34] M. Al-Waily, M.A. Al-Shammari, M.J. Jweeg, *An Analytical Investigation of Thermal Buckling Behavior of Composite Plates Reinforced by Carbon Nano Particles*, Engineering Journal 24(3) (2020); https://doi.org/10.4186/ej.2020.24.3.11.
[35] A. Kalsoom, A. N. Shankar, I. Kakaravada, P. Jindal, V. V. K. Lakshmi, and S. Rajeshkumar, *Investigation of dynamic properties of a three-dimensional printed thermoplastic composite beam containing controllable core under non-uniform magnetic fields*, Journal of Materials: Design and Applications.; 236 (2), 404 (2021) https://doi.org/10.1177/14644207211045943.
[36] R. Lewandowski, P. Litewka, P. Wielentejczyk, *Free vibrations of laminate plates with viscoelastic layers using the refined zig-zag theory – Part 1*. Theoretical background, Composite Structures, 278, (2021); https://doi.org/10.1016/j.compstruct.2021.114547.
[37] M. Al-Waily, M.J. Jweeg, M.A. Al-Shammari, K.K. Resan, A.M. Takhakh, *Improvement of Buckling Behavior of Composite Plates Reinforced with Hybrids Nanomaterials Additives*, Materials Science Forum 1039 23 (2021);
[38] E.K. Njim, M. Al-Waily, S.H. Bakhy, *A Review of the Recent Research on the Experimental Tests of Functionally Graded Sandwich Panels*, Journal of Mechanical Engineering Research and Developments 44(3), 420 (2021).
[39] E.K. Njim, S.H. Bakhy, M. Al-Waily, *Analytical and Numerical Investigation of Free Vibration Behavior for Sandwich Plate with Functionally Graded Porous Metal Core*, Pertanika Journal of Science & Technology 29(3), 1655 (2021); https://doi.org/10.47836/pjst.29.3.39.
[40] E. K. Njim, S. H. Bakhy, M. Al-Waily, *Analytical and numerical free vibration analysis of porous functionally graded materials (FGPMs) sandwich plate using Rayleigh-Ritz method*, Archives of Materials Science and Engineering 110 (1), 27 (2021); https://doi.org/10.5604/01.3001.0015.3593.
[41] D. Lukkassen A. Meidell, Advanced materials and structures and their fabrication processes, Book manuscript, Narvik University College, HiN 2 (2007).
[42] S.S. Rao, Vibration of continuous systems, John Wiley & Sons, Inc. (2019).
[43] A.W. Leissa, Vibration of Plates, NASA, Washington, DC (1984).
[44] E. K. Njim, S. H. Bakhy, M. Al-Waily, *Analytical and numerical investigation of buckling load of functionally graded materials with porous metal of sandwich plate*, Materials Today: Proceedings (2021); https://doi.org/10.1016/j.matpr.2021.03.557.
[45] E.K. Njim, S.H. Bakhy, M. Al-Waily, *Analytical and Numerical Investigation of Buckling Behavior of Functionally Graded Sandwich Plate with Porous Core*, Journal of Applied Science and Engineering. 25(2), 339 (2022); http://dx.doi.org/10.6180/jase.202204_25(2).0010.

Hussam Raad, Emad Kadum Njim, Mushin J. Jweeg, Muhannad Al-Waily
,
Х. Раад[1], Е.К. Нжім[2], М.Д. Джвіг[3], М. Аль-Вейлі[1]

Аналіз вібрації багатошарової пластини із відкритою та закритою комірками

[1]Кафедра механічної інженерії, інженерний факультет, університет Куфи, Ірак
[2]Міністерство промисловості та мінералів, Державна компанія виробництва гуми та шин, Ірак
[3]Університет Аль-Фарахіді, коледж технічної інженерії, Ірак

У роботі здійснено спробу замінити традиційну форму та матеріал серцевини сендвіча стільниковою формою, у якій клітини мають правильні форму, розподіл та розмір. Ідея цієї статті полягає в розробці двох структур, одна із яких з відкритою коміркою, а інша із закритою, а також в оцінці ефективності сендвіч-пластини із гратковою коміркою серцевини, що використовується для багатьох промислових застосувань, зокрема в автомобілебудуванні. Нові теоретичні формулювання побудовані для двох структур для знаходження характеристик вільних коливань. Результати такої моделі порівнюються із традиційною формою. Виведені рівняння для прогнозування механічних властивостей на основі відносної густини з вибраними формами, специфічне рівняння вібрації тришарової сендвіч-плити та розв'язано за допомогою таблиць Excel. Багатообіцяючими є і результати, і оцінка ефективності теоретичного аналізу клітинної структури. Обмеження та частота похибок для механічних властивостей випливають з емпіричних рівнянь, і їх співвідношення до значень відносної густини є вищим залежно від поведінки матеріалу серцевини. Висновки вказують, що при відкритих комірках спостерігається зниження модуля пружності на (PLA: -90,4%) і (TPU: -90,4%) та збільшення власної частоти на (PLA: 44,5%) і (TPU: 46,4%), тоді як для закритих комірок модуль пружності зменшується на (PLA: -66,9%) і (TPU: -64,4%), а також збільшується власна частоту на (PLA: 36%) і (TPU: 37,7%). Перетворення твердої речовини або заміна пінопластової форми стільниковою формою є одним із способів покращити продуктивність і заощадити вагу завдяки вибраній стільниковій конфігурації при поглинанні енергії вібраційної хвилі.

Ключові слова: сендвіч-плита, вільні коливання, конструкція комірки, розпірна секція, закриті та відкриті комірки, відносна щільність.

PHYSICS AND CHEMISTRY OF SOLID STATE
V. 24, No. 2 (2023) pp. 323-334
Section: Physics

DOI: 10.15330/pcss.24.2.323-334

Vasyl Stefanyk Precarpathian National University

ФІЗИКА І ХІМІЯ ТВЕРДОГО ТІЛА
Т. 24, № 2 (2023) С. 323-334
Фізико-математичні науки

‘UDK 53.08/.07:620.3. ISSN 1729-4428

Ya.I. Lepikh, I.K. Doycho

Properties of silica porous glasses with the nanoparticle ensembles of some compounds. Review

Interdepartmental scientific and educational physical and technical center of MES and NAS of Ukraine at I.I.Mechnikov Odesa national university, Odesa, ndl_lepikh@onu.edu.ua

Properties porous silica glasses are systemized in this review. Also the methods of formation of the nanoparticles’ ensembles of the substances, which are useful for the microelectronics, are described. Porous silica glasses are perspective due to their chemically resistance, mechanical strength and development of their inner surface. Own electrical resistance is too big for the porous glasses’ specimens with standard sizes, that’s why ones use them as matrixes for luminescence type of sensors mainly. The luminescent properties’ dependence on the molecular structure of investigate substances (such as dyes and metal oxides), as well as on the nanoparticle ensemble technological formation condition is studied. It is revealed to which certain gases dyes of the specified type are sensitive and why it occurs in such manners. It is shown due to which of the described nano-size systems’ properties sensitivity is appeared. Besides, one can embed a conductive phase into the pores of glass due to features of its structure. After such treatment one can use the porous glasses as matrix for formation of resistance type sensors.

Keywords: silica porous glass, luminescence, gas sensors, humidity sensors, carbon treatment, ohmic contacts, dyes.

Received 7 February 2023; Accepted 14 June 2023.

Introduction

Typically, the luminescent centers of the materials suitable for use as active elements of fluorescent gas sensors are located near the surface. This is understandable, because the changes in the gas composition of the environment primarily affect the near-surface matter layers. Therefore, in order to achieve these changes best registration, it is necessary to strive for the maximum possible development of the substance surface, which is able to be an active element of the gas sensor. This development can be achieved by dispersing the substance to nanometers (or almost molecular level in the case of a molecular crystal), because it is known that the total surface area of many small particles is always much larger than the surface of one large particle of the same volume. It should be emphasized that it is impossible to work fruitfully with nanometer size individual particle, so they should be placed in a system of some test tubes of appropriate size. The role of such a system of nano-sized tubes can be played by a matrix that contains small voids in the through pores form. This forms an ensemble of nanoparticles, consisting of these matter small particles and the matrix in which they are placed. Since the matrix is a part of the ensemble, it must meet certain restrictions, due to which its presence will not affect the test substance gas sensitivity and, moreover, will positively affect its luminescent properties. One of the main such limitations is chemical inertness, i.e. the matrix should not chemically interact with the test substance and change its (or its own) chemical composition. Secondly, it must have a fairly strong skeleton, which will prevent both the nanoparticle ensemble aggregation and the created system mechanical destruction. Finally, it should be non-luminescent (or glow in areas of the spectrum that are not relevant to the test substance). Some authors use polymers [1-2] or gelatin [1, 3] as a matrix. These compounds do not luminesce and are quite chemically inert. Due to their structure peculiarities, they are able to hold the clusters of the substance formed

inside them. However, these clusters can have arbitrary sizes and shapes, and their growth will not be restraining by polymer or gelatin, but on the contrary, they themselves will uncontrollably form the matrix skeleton. Porous silicate glass with nanometer-sized through voids is devoid of this defect. The interpenetrating pores size, can vary from a few nanometers to several hundred nanometers. In addition, compound quartz skeleton is quite durable, and therefore limits the particle size that are formed, because they cannot exceed the pores size. The glass columnar structure allows influencing both the pores inner surface and the nanoparticles created inside them. In most cases, these nanoparticles are conveniently created by saturating the matrix with certain substances solutions. Thus, porous silicate glass perfectly meets the requirements for the matrix, but it does not exist in nature. However, it can be obtained from two-phase sodium-boron-silicate glass by a not very sophisticate technology [4].

I. The porous silicate glass types and their creation technology

Two-phase sodium boron silicate glass has a rather complex chemical formula $SiO_2\times$ $[Na_2O\times B_2O_3]$. Such glass melting temperature exceeds 750°C. In addition, the melting temperature of the glass silicate component is much higher than the melting temperature of the sodium borate complex, and therefore there exists a temperature at which the glass sodium borate component is in a liquid state, while its silicate component is simply very hot. This state corresponds to a temperature of 650°C. If the burden for two-phase glass melting, which is brought to 750°C, is cooled adiabatically to 650°C, so that the phase separation occurs at the indicated temperature, the sodium borate complex will still melt, forming large bubbles, which will form a silicate skeleton. Due to the melt viscosity, it is kept in such conditions for several hundred hours, until the two phases are completely dissolved in each other, and then slowly cooled to room temperature. The obtained two-phase glass is enough large (up to hundreds of nanometers) areas of interposed silicate and sodium borate phases. These phases, specifically, show unequal chemical resistance, so that a mixture of hydrofluoric, nitric and glacial acids can completely erode the sodium borate phase, with almost no effect on the silicate phase, which leaves a quartz skeleton with through voids in place of etched borate phase. These voids are quite large, however, due to mutual dissolution, rather small, sandy SiO_2 particles got into the sodium borate phase, which after its etching must settle inside the resulting pores. Such settled sandy particles are called residual silica gel. Chemically, they are completely identical to the quartz skeleton and differ from it only in fineness. The resulting glass is conventionally called porous glass type *C*. Such glass is unsuitable for a number of applications, because due to large enough holes it will form test substance particles of significant size, so to achieve significant deployment of its surface will remain impossible.

To form smaller pores in the glass, it is necessary to change slightly the two-phase glass technological modes creating. The burden, for its melt should be adiabatically cooled to a lower temperature, which is close to the sodium borate phase melting temperature, but some lower than it (about 490°C). If the burden is kept at this temperature for hundreds of hours, it will lead to the formation of sodium-borate phase of relatively small bubbles and, after cooling to room temperature, the phases will separate, resulting in two-phase glass with small (about tens of nanometers) areas of interwoven silicate and sodium borate phases. After etching the unstable sodium borate phase as described above, enough fine-grained silicate glass is formed, which will also contain residual silica gel in the pores. The resulting glass is conventionally called porous glass type A.

The presence of silica gel inside the pores, depending on a particular scientific problem conditions, can be both desirable and harmful. Thus, the presence of silica gel makes the glass more fine-grained, but at the same time reduces the free space for the nanoparticle test substance formation. On the other hand, the presence of silica gel improves the glass adsorption properties, but deteriorates its mechanical properties (due to gel swelling in a humid environment, the sample may deform [5-7]). Although special treatment can improve the glass mechanical properties, but it will not always have a positive effect on its other properties [8]. Within the problem of the surface substance suitable expansion as some sensor active element, the separative ability of silica gel is certainly useful, which prevents the aggregation process of particles formed an ensemble in the pores [1, 9]. However, for cases where the presence of silica gel in the pores is harmful, the lixiviate techniques, have been developed in [10], can be used. In this manner the glass can be depleted with silica gel or this technique quite deprive the glass of this formation. According to this technique, the finished glass is etched in an alkaline etchant based on KOH. This etchant interacts enough quickly with finely divided silica gel and acts much more slowly on solid (at least porous) matrix walls. Due to this, most of the silica gel is removed, while the walls of the matrix skeleton are only slightly etched [4, 11]. The type A glass treated in this way is conventionally called the type B glass, and the type C glass is called the type D glass.

Figure 1 shows the results of the structure of all 4 the above noted types glasses investigation using an electron microscope. It is noticeable that of *A* and *B* type glasses are fine-porous ones, while the pores in *C* and *D* type glasses are much larger. Residual silica gel particles in the images corresponding to *A* and *C* glasses look like white spots. In *C* type glass they are larger, in B type glasses they are almost imperceptible (this confirms that the leaching technique leads only to the depletion of glass by silica gel [4, 11]), and in type *D* glasses they do not exist at all.

Figure 2 shows the pore-sizes distribution spectra for all these types of glasses. One can see that two main fractions of pore sizes exist for every type of glass. However, anyone of types contents a small amount of pores with size from about 10 nm to more 100 nm.

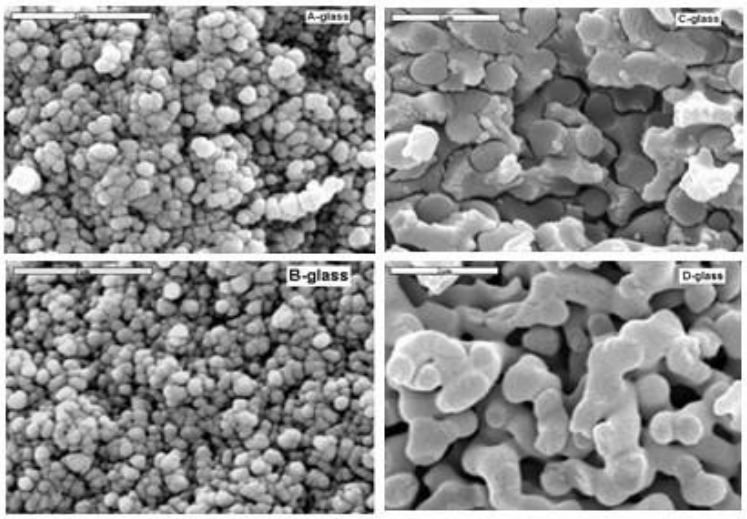

Fig. 1. Electron microscopic images of structures for four types of porous glass.

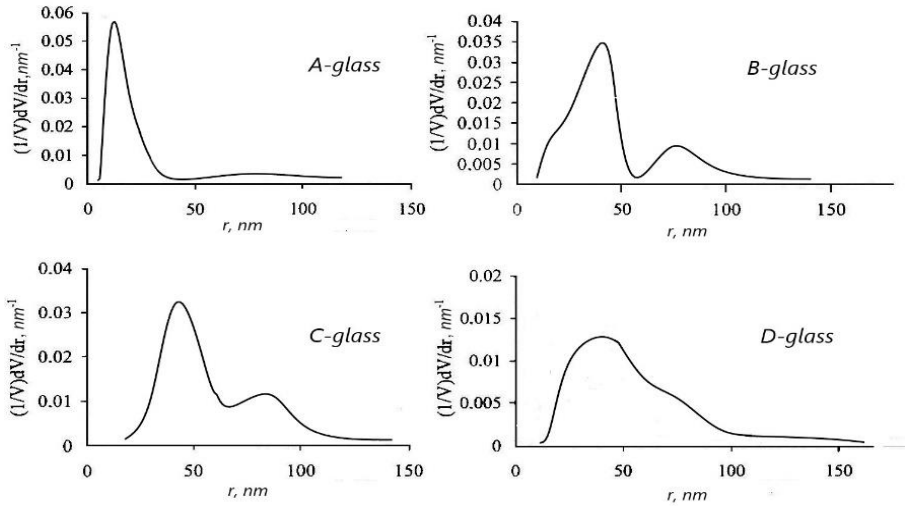

Fig. 2. Typical pore-size distribution for four types of porous glass.

II. The structure of the dyes based on the 4-valent tin

It's useful to pay special attention to the dyes based on the 4-valent tin among the materials, which can be used as active elements for the luminescence gas sensors. According to [12], these macromolecular compounds are the most sensitive to the environment gaseous composition. The molecules of this group dye consist of a coordination node with a ligand, which may show different dentition, and a hydrazide fragment with a certain type substituent. It is expedient to consider the dye molecule in this way, because the coordination node is a more stable formation and remains unchanged during chemical transformations, while the substituent composition and its placement in the hydrazide fragment can be changed by simple chemical reactions. Coordination nodes can be of two types: tetradimethylaminobenzaldehyde and dihydroxynaphthaldehyde (denoted by the ligand $\{SnCl_4ON\}$ and $\{SnCl_3O_2N\}$, respectively). Ligand $\{SnCl_4ON\}$ is single-dentate and has a zwitter-ionic structure with a negative charge, which is delocalized in the fragment N=C–O, and ligand $\{SnCl_3O_2N\}$ is double-dentate with a negative charge, which is concentrated in the O-Sn-O area. The structural formulas of both coordination nodes are shown in Figure 3 [13].

The hydrazide fragment in Fig.3 is not indicated. It is a conventional benzene ring with a substituent of nicotinoyl or benzoyl type. In the first case, a certain nitrogen group is built directly into the benzene ring (i.e., one of the benzene ring carbon is actually replaced by nitrogen). This, of course, leads to the appearance of a localized charge near the substitution, which is compensated by the opposite charge in the coordination node; therefore, the corresponding molecule will exhibit the properties of the dipole. In the second case, the hydrogen atom in one of the benzene ring positions is replaced by an amine or hydroxyl group, which is also accompanied by a charge redistribution within the coordination node to maintain the electro-neutrality of the molecule. Isomeric dyes that differ only in the substituent position relative to the hydrazide fragment are called dyes with different tautomeric form. The substituent position in each tautomeric form is indicated by a number. For this all

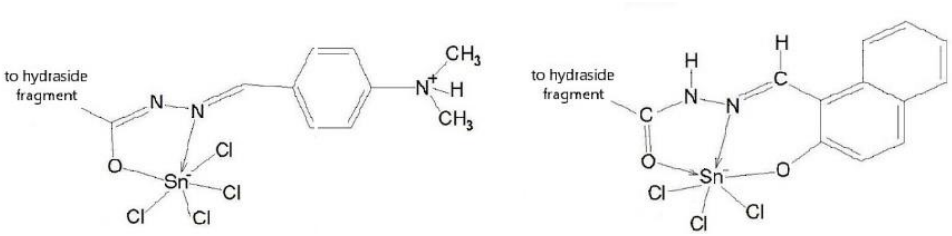

Fig. 3. Coordination nodes structural formulas of {$SnCl_4ON$} *(left)* and {$SnCl_3O_2N$} *(right).*

6 carbon atoms in the corresponding benzene ring are numbered, as "1" is a carbon atom having a bond that connects the hydrazide fragment with the coordination node. Other positions are successively denoted by numbers from the natural series from "2" to "6" counterclockwise. Therefore, substitution cannot occur at position "1", because it will destroy the molecule. The results obtained in [4] show that the dye molecules have no intramolecular bonds (at least hydrogen ones), so the tautomeric forms are invariant with respect to the reading direction of carbon atoms in the benzene ring of the hydrazide fragment. Therefore, the dyes in which the substitution took place at position "2" or at position "6" are completely equivalent and have the same photoluminescence spectra. The same is true of dyes with substitutions at positions "3" or "5". A direct consequence of this equivalence is the dye molecule additional rotational symmetry, which leads to additional electron-rotational levels suitable for the radiative transition. Because of this, the dyes luminescence intensity with a substituent in position "4" is the lowest, because there are no additional levels for them. In addition, the interaction of the substituent with the coordination node also increases the luminescence intensity and the stronger the closer is the substituent to the coordination node. Therefore, the dyes luminescence with substitution in position "2" (or "6") is always more intense than when substituted in position "3" (or "5") [14].

The dyes luminescence is a consequence of the radiative transitions between the electron-vibrational sublevels of the first excited and ground singlet dye molecule electronic states. These states system occurs when the molecules are sufficiently mobile relative to each other, which occurs in solutions due to the interaction of the dye molecule (or its part) with the surrounding solvent molecules. The solvent does not affect the energy of the radiation, but, depending on the solvent absorbency, can affect its intensity. As demonstrated in [4, 13], the absorption capacity of the standard organic chemistry solvent dimethylformamide $(CH_3)_2NCO$, which is usually abbreviated as DMFA, is the lowest, so it is in it that dyes based on tetravalent tin complexes glow most intensely. But the dye molecules in the solution are separated from the environment by the vessel and, with the exception of those on the surface of the solution, passivate each other. Thus, only a small part of the dye molecules has direct contact with the environment and this should significantly reduce the sensitivity of their luminescence to the composition of the surrounding atmosphere. Thus, the dye in solution is unsuitable for use as an active element in gas sensors.

However, dyes can glow not only in solutions but also in the dry state, if the dye is dispersed in a suitable model environment. As a model medium, it is advisable to use porous silicate glass, in which the average size of the pores is comparable to the size of the dye molecules. When the pores in such glass are saturated with a dye solution in DMFA, it disperses almost to the molecular level, and its nanoparticle glow centers will come into direct contact with the particles of gas contained in the environment, so they can react to changes in its composition. In this case, the presence of residual silica gel inside the pores, which will play the role of separation material between the dye molecules, will allow to get rid of the effect of its molecules mutual matching. From the above it is clear (and confirmed by the results of a number of works [9, 15-19]) that the role of the model medium will be best played by porous *A* type silicate glass. In this case, the glow will occur due to the dye molecules interaction with the model medium inner surface and silica gel particles penetrate between the dye molecules, leading to the formation of aggregations, which are the centers of non-radiative recombination through the source channels. In addition, for more nanoparticle uniform distribution in the pores, majority of the solvent is removed after impregnation with additional low-temperature annealing, and due to its almost absence, the emitted light quanta possible absorption is eliminated. Therefore, the dye nanoparticle ensemble luminescence intensity inside the acceptable type porous matrix always exceeds the photoluminescence intensity of the same dye in the corresponding solution.

We investigated the photoluminescence spectra excited by the ultraviolet laser LCS-DTL-374QT (wavelength $\lambda = 355$ nm, power 15 mW) and recorded on a standard setup, which consisted of a quartz monochromator SF-4, a photomultiplier PEM-79 with sensitivity 280÷850 nm, as a photodetector, and a selective amplifier that was synchronized with the excitation laser frequency. The result was transmitted to the computer monitor via an analog-to-digital converter using USB-oscillography software. In order to ensure obtained results comparability in terms of intensity, the installation in each measurement was calibrated with a mineral origin luminophore by type LDP-2mA, which is characterized by constant luminescence and complete degradation absence. The width of the monochromator slot and the enhancement limits were kept constant, therefore, it can be argued that the obtained spectra were comparable in relative units, if the unit luminescence intensity is considered to be the luminophore luminescence.

Analysis of the photoluminescence spectra of dyes based on the 4-valent tin both in DMFA solution and in the form of nanoparticle ensembles in a porous matrix showed that they in all cases have a Gaussian shape with

one maximum and are almost entirely determined by their intensity and its maximum position. As mentioned above, the luminescence intensity of any dye in the form of a nanoparticle ensemble has always exceeded its intensity in solution. The greatest increase in luminescence was observed in the case of the benzoyl type hydroxyl substituent. The spectra remained hyperchromic relative to the dye in solution, whereas in the case of a benzoyl type amine substituent or nicotinoyl substitution there was a spectrum shift in one direction or another. This explains the highest glow intensity for dyes with hydroxyl substitution. For them, the additional energy that arises during the nanoparticle ensemble formation is spent entirely on the luminescence intensity amplifying, while in the case of amine substitution, part of it is spent on the photoluminescence spectrum maximum shifting. The detailed analysis of the luminescence spectra of all tautomeric forms for dyes with both types of coordination nodes and any substituent is given in [4].

III. Concentration dependence of luminescence for the dye nanoparticles ensemble

The dye nanoparticle ensemble luminescence intensity depends on the concentration of the solution used to create the specified ensemble. To identify this dependence regularity, consider how the luminescence intensity of the dye solution in DMFA changes with increasing concentration. There are two competing processes: illumination and light absorption. The first process causes an increase in the luminescence intensity due to an increase in the luminescence center quantity (see, for example, [20]) due to the greater of the dye molecule number in the concentrated solution. This process is almost linear and at low concentrations the luminescence intensity increases from zero to some limit value, which is called the saturating solution limit concentration. After this concentration excess, the second process associated with concentration quenching begins to prevail [20-21]. There are so many molecules in the solution that they begin to merge into aggregations, which are centers of nonradiative recombination through the source channels. The solution luminescence intensity decreases according to the parabolic law. Fig.4 *(left)* shows a model image of the described dependence. It should be noted that according to the Frank-Condom principle, both processes occur simultaneously, and therefore the dye concentration intensity dependence in solution at low concentrations is almost linear, and after excess the concentration limit is almost parabolic.

When the matrix is saturated with dye solutions of appropriate concentration to create an ensemble of nanoparticles, similar processes occur in the obtained system. However, for the case of a nanoparticle ensemble, there are certain changes in the described dependence. An almost linear curve section at concentrations below the limit is converted to a "piece-linear". Such a "piecewise linear" increase in the dye nanoparticle ensembles photoluminescence intensity in a porous matrix at low saturating solution concentrations may be due to the inhomogeneity the different sizes pores fraction filling in porous glass during this ensemble formation. At impregnating solution relatively low concentration in the matrix pores there is a relatively small quantity of nanoparticles. They will enter the smallest pores alone, dispersed to an almost molecular level, so they will not aggregate (i.e. no leakage channels will appear). As far as even in fine-grained *A* type glass there is always a certain number of rather large pores, many dye nanoparticles will get into them, but their fusion in aggregation will prevent the surrounding on all sides silica gel particles, and they will settle separately on the pores' walls. The luminescence intensity increases rather slowly with concentration increasing. When the impregnating solution concentration reaches certain "average" values, similar processes continue, but the dye molecules' quantity increases [21]. Therefore, more radiative recombination centers appear inside the pores, and this leads to the luminescence intensity increase acceleration with increasing concentration (see, for example, [4, 21]). The solution limiting concentration in the case of the nanoparticle ensemble remains the same as it was in the solution, and its excess again leads to the absorption processes in the system prevalence. However, due to the solvent practical absence inside the pores of the matrix, this can hardly be explained by the concentration quenching. At such high concentration impregnating solution, small particles in large pores will be so many that they will merge into aggregation at the stage of their formation [22-23], and silica gel particles will not have time to interfere with this process, but will envelop the already existing aggregations (see e.g. [9, 22]). In this case, the largest (about hundreds of nanometers) pores will be filled, in which the silica gel will only partially passivate the dye molecules surface. Solvent residues after annealing will also be concentrated mainly in the specified size pores. Therefore, most of the dye found in large pores will behave as if in solution, i.e. there will be the photoluminescence intensity decrease, which will approach the value typical for the solution. A comparison of the luminescence intensity of the $2NH_3\{SnCl_4ON\}$ dye concentration dependences in DMFA solution and in the form of the nanoparticle ensemble in *A* type porous silicate glass is shown in Fig. 4 and testifies to their complete similarity.

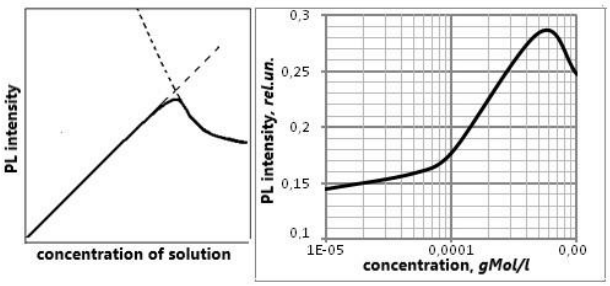

Fig. 4. The $2NH_3\{SnCl_4ON\}$ dye nanoparticle ensemble luminescence concentration intensity dependence in DMFA solution *(left, model curve)* and as a nanoparticle ensemble *(right, experimental curve).*

It can be seen that at solution low concentrations the nanoparticle ensemble glow intensity is insignificant;

then, through the different size pores unequal filling rate (see e.g. [4, 21]), it increases nonlinearly and the corresponding curve slope changes. At a concentration of $0{,}5\times10^{-3}$ gmol/l (the saturating solution limiting concentration), luminescence becomes maximum. When the solution saturating concentration exceeds the limiting one, the photoluminescence intensity decreases, as in the case of the solution.

IV. The dye nanoparticle ensemble gas sensitivity

The luminescence properties of obtained ensemble of nanoparticles of the dyes based on the 4-valent tin complexes can differ sufficiently depending on technological conditions of it formation and on structure of dye molecules. Taking this fact in to account it's useful to observe which species of dyes are sensitive to one of other gas and why it's so for further use of these systems as active elements of gas sensors. One of such sensor important properties is the reproducibility of their properties, which should ensure their reusability. Therefore, it is undesirable to be based on direct chemical interaction of the dye substance with gaseous impurities present in the environment, and should proceed from these dyes molecular structure and the peculiarities of the nano-size system formation based on their chemical composition. The gaseous contaminant presence will be fixed by changing the ensemble photoluminescence intensity, therefore, we will consider such nano-size systems that have the highest initial glow. Therefore, taking into account the above-described properties of dyes and matrices, we will form ensembles of nanoparticles in porous *A* type silicate glass and use DMFA solutions of dyes with tautomeric form "2".

Nanoparticle ensembles in this sense can be used as active sensor elements not of any gases, but of gases which contain the same chemical elements, as in a dye molecule. Such gases will not chemically interact with the nanoparticle ensemble elements, however, their presence in the atmosphere will create artificial conditions for changing the system luminescent properties. In this case, after entering the unpolluted atmosphere, these artificial conditions will disappear, and the system alone or with the help of simple processing will restore its original glow.

As is clear from the studied dye structure description, their molecule consists mainly from benzene rings assemblage. The rings that make up the coordination node are perfect and therefore chemically quite inert, while in the only ring of the hydrazide fragment there is a substitution of a hydrogen (benzoyl) or carbon (nicotinoyl) atom for a certain amine or hydroxyl complex. Thus, the substituent in the hydrazide fragment is a certain analog of the substitution impurity in the semiconductors, so it can be a luminescently active center. In turn, between the coordination node perfect benzene rings contains a ligand based on Sn and Cl. It is a certain analogue of interstitial impurities in semiconductors and can also be luminescently active and sensitive to some gaseous substances in the environment. Due to its zwitter-ionic structure, the ligand provides a certain charge distribution within the coordination node, and hence the entire dye molecule.

Thus, the dye nanoparticle ensemble based on a tetravalent stannum in a *A* type porous glass can, by changing its luminescence intensity, detect the gas presence in the environment that can affect the substituent or cause the charge redistribution in the dye molecule. There are two such gases: ammonia, which is very similar in structure and chemical composition to the benzoyl-type amine substituent, and hydrogen chloride vapor, which dissociates perfectly in water, forming negatively charged Cl^- ions. We were able to detect sensitivity namely to these gases in our study.

As can be seen from the right part of Fig. 4, sensitivity to ammonia should be expected from a nanoparticle ensemble based on $2NH_3\{SnCl_4ON\}$, if it is created by *A* type porous glass impregnation with a solution in DMFA with a concentration of 0.5×10^{-3} gMol/l. In this case, the luminescence intensity achieves the maximum value and the specified concentration exceeding leads to a luminescence weakening. However, the ingress of the sample formed under these conditions into the ammonia medium should lead to an increase in the nitrogen concentration in the pores, which is equivalent to the creation of a nanoparticle ensemble at a saturating solution concentration exceeding the limit. This will reduce the luminescence intensity of the sample [4, 24-25].

To experimentally confirm these considerations, the initial luminescence intensity of the sample $2NH_3\{SnCl_4ON\}$ in the form of a nanoparticle ensemble formed under these conditions was first measured, and then it was immersed in an atmosphere containing ammonia. Measurements were repeated immediately after immersion and after 10 minutes in the specified atmosphere. Then the sample was transferred to a pure atmosphere and kept in it for 24 hours. Next, its luminescence intensity was measured again, immediately and after 10 minutes of low-temperature (at 240°C) annealing. The result in the form of a histogram is shown in Fig. 5. Histograms show that the dye after immersion in the atmosphere containing ammonia sharply and steadily reduces luminescence intensity and it is possible to restore initial intensity only after annealing.

To explain this result, it should be mentioned that the nitrogen inside the coordination node is in an inactive state. Therefore, we can assume that the dye $2NH_3\{SnCl_4ON\}$ initially contains active nitrogen only in the substituent, its amount in the ensemble is determined by the impregnating solution concentration, which is the limit and corresponds to the maximum luminescence. After immersion in ammonia, the amount of active nitrogen in the system increases, and it behaves as if it was formed from a solution with a higher concentration, which corresponds to a lower luminescence intensity (as is well seen in Fig.4). The change durability is probably due to the formation of ammonia-stable bridges within the pores, which is equivalent to the aggregation formation that are leakage channels. Short-term low-temperature annealing breaks these bonds and the system luminescence is practically restored. This model is confirmed by an attempt to perform the same experiment with the $2OH\{SnCl_4ON\}$ dye nanoparticle ensemble. This ensemble shows almost complete insensitivity to ammonia, because the dye on the basis of which it is

formed, initially does not contain active nitrogen, so it does not interact with ammonia [24-25].

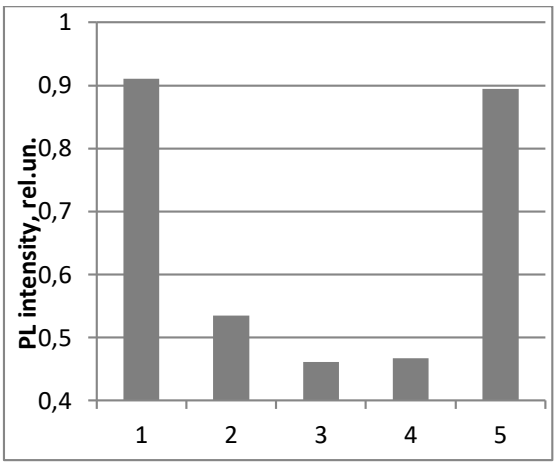

Fig. 5. Sensitivity of the photoluminescence intensity of the $2NH_3\{SnCl_4ON\}$ dye nanoparticle ensemble to ammonia:
1 - initial sample in a pure atmosphere;
2 - in an atmosphere containing ammonia;
3 - for 10 minutes in ammonia;
4 - 1 day after returning to pure atmosphere;
5 - after 10 minutes of low-temperature annealing

Ammonia sensor was patented recently [26] works on described principle.

It should be noted that the hydrazide fragment is resistant to other aggressive media, so it is impossible to detect any other gases that may be present in the environment by their interaction with the hydrazide fragment.

The influence of the environment composition on the ligands in the coordinated nodes may be traced by the changes of glow intensity of dye nanoparticles' ensemble if the atmosphere contents the HCl vapors. Recall that chlorine is contained only in the ligands of dye coordination nodes, moreover in different amounts for different types of forms and choose a dye-based system that it will glow the brightest, so it will be easiest to notice changes in its luminescence. Such system is the dye nanoparticle ensembles with a benzoyl type hydroxyl substituent with a tautomeric form "2". Fig. 6 shows the luminescence spectra of $2OH\{SnCl_3O_2N\}$ *(left)* and $2OH\{SnCl_4ON\}$ *(right)* dyes in a pure atmosphere and in one containing hydrogen chloride vapor. These dyes coordination nodes differ in the ligand dentance hence the charge distribution in the molecule. Ligands are as a whole an electro-neutral molecule placed between the coordination node benzene rings, which in some of its parts carries both a negative and a positive charge, which is localized on non-neighboring atoms. Thus, a specific ligand in the system creates a certain charge balance in it. In the HCl vapors presence in the atmosphere, which are enriched in negative Cl^- ions, this balance is disturbed [24-25], which determines the sensitivity of the system to these vapors.

The spectra in Fig. 6. show that the initial luminous intensity of the $2OH\{SnCl_3O_2N\}$ dye exceeds the glow intensity of the $2OH\{SnCl_4ON\}$ dye almost three times, and both are sensitive to the presence of HCl vapors in the atmosphere. However, if the $2OH\{SnCl_4ON\}$ dye reduces the intensity of its luminescence slightly (about 20%), the luminescence of the $2OH\{SnCl_3O_2N\}$ dye decreases significantly and becomes approximately the same as that of the $2OH\{SnCl_4ON\}$ dye in a pure atmosphere.

The study of the glow decrease kinetics of the samples in the atmosphere of HCl vapors showed that the decrease of the luminescence intensity of both nanosize systems occurs abruptly after a short latency period. Measurements were performed at a wavelength corresponding to the maximum of glow (as can be seen from Fig. 6, for $2OH\{SnCl_3O_2N\}$ it is 468 nm, and for $2OH\{SnCl_4ON\}$ it is 510 nm). Fig. 6 shows the corresponding kinetic spectra.

The vertical line on the graph corresponds to the moment when the charge redistribution in the system based on the $2OH\{SnCl_3O_2N\}$ dye begins. It can be seen that to the left of it the decrease in glow intensity for both systems is insignificant and almost the same. But for a system with a two-dentate ligand, it is smoother, and for a system with a one-dentate ligand, it occurs a little earlier and a sharp jump.

The presence of a latent period is probably due to the fact that, unlike the substituent, the ligand is inside the molecule and is shielded on all sides by perfect chemically inert benzene rings. So until the HCl molecules begin to interact with it and change the charge distribution, it takes

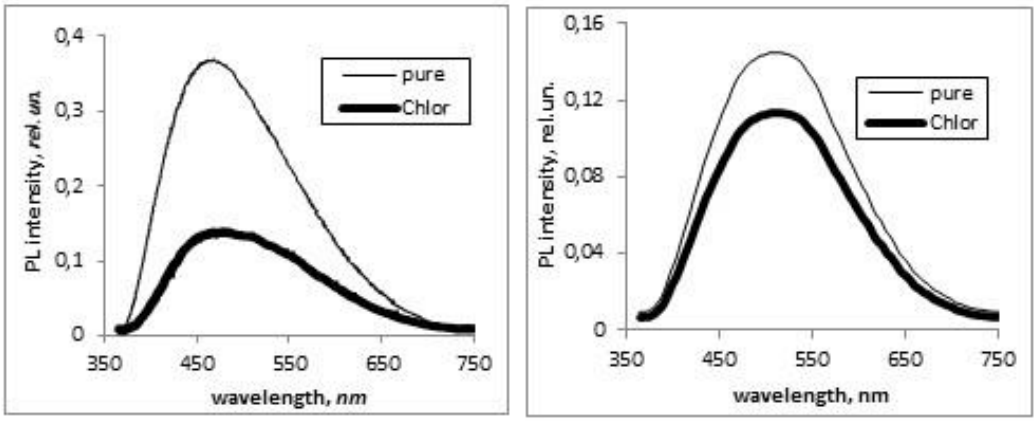

Fig. 6. Luminescence spectra of nanoparticle ensembles of $2OH\{SnCl_3O_2N\}$ *(left)* and $2OH\{SnCl_4ON\}$ *(right)* dyes in a pure atmosphere and in one containing HCl.

minutes. For the 2OH{$SnCl_3O_2N$} dye with a two-dentant ligand, this time is slightly longer, because the interaction with HCl in this case is to saturate the system with a negative charge to a state that is typical for 2OH{$SnCl_4ON$} dyes with a single-dentate ligand. After reaching this state, the system begins to glow as a 2OH{$SnCl_4ON$} dye, i.e. abruptly reduces its luminescence intensity. In the case of a nanoscale system based on the 2OH{$SnCl_4ON$} dye, no significant charge redistribution occurs, so for it the latency period is less long and the decrease in intensity is insignificant.

It would seem that similar processes should take place in dyes with an amine substituent, but for this type dyes the charge redistribution is mostly compensated by the luminescence maximum shift in one or another direction at a constant intensity. And such a shift can be caused not only by charge redistribution, but also by many other factors [4], so if it occurs, it does not necessarily indicate the appearance of HCl vapor in the atmosphere, and such systems are not suitable for fixing these vapors.

In conclusion, we note that the initial charge distribution for both systems can be restored by the sample heat treatment in the same mode as in the case of $2NH_3${$SnCl_4ON$} dye nanoparticle ensemble interaction with ammonia. Apparently, this treatment is sufficient to remove foreign gases from any porous system to get rid of their impact.

From the above results, it is cl clear that the role of the HCl vapor sensor active element will be best played by the 2OH{$SnCl_4ON$} dye nanoparticle ensemble in porous *A* type silicate glass. The sensor of HCl vapor in the environment was discovered on the base of such nanoparticles' ensemble exactly [27].

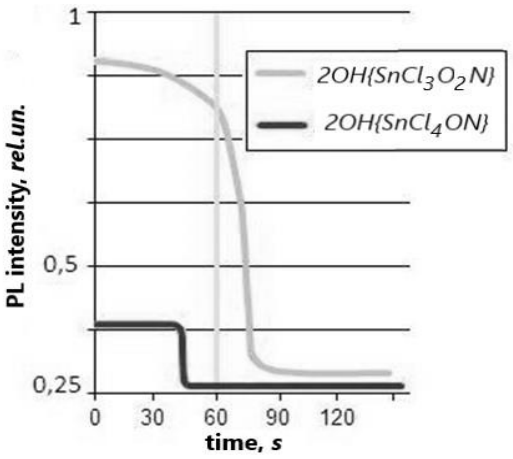

Fig. 7. Photoluminescence intensity reducing kinetics for the dye nanoparticle ensemble of dyes with one-dentant (2OH{$SnCl_4ON$}) and two-dentant (2OH{$SnCl_3O_2N$}) ligand in the presence of HCl vapors in the environment.

V. Carbon treatment of the porous glass and it using in sensors

Carbon treatment method [28-29] is an alternative way to get rid of porous glass from silica gel. It is based on the fact that porous glass is almost pure silicon dioxide, and because carbon is similar in chemical properties to silicon, but is more active, it is able to displace it from the oxide at appropriate temperatures. Silica gel and silicate skeleton, are chemically identical and differ only in dispersion. Thus, under certain conditions, carbon will displace silicon from the oxide, primarily in silica gel, as a more dispersed formation. Carbon treatment consists of two stages: primary and secondary. In the initial stage, anyone type of glass is saturated with a solution of a substance containing carbon. The best in this case is glucose: it is well soluble in water and when heated to 180°C is easily reduced simply in the voids of matrix to carbon in the form of highly dispersed graphite with the release of water. The process is described by a known equation

$$C_6H_{12}O_{6\text{ - (t)}} \rightarrow 6C + 6H_2O,$$

lasts about a day and its completion can be judged visually by the sample blackening. *A* type glass treated in this way is conventionally called *α* type glass, and *C* type glass is called *γ* glass. B and D types of glass, which was lixiviated, are initially removed of silica gel, so these glasses don't require total carbon treatment. However, primary carbon treatment is able to reduce the electrical resistance of pore glass specimens by several orders of magnitude due to the inbuilt of conductive phase consisting of graphite nanoparticles into it. Such a conductivity increasing may be useful for the certain applications of this type of glasses. One designates these glasses after the primary carbon treatment as B_1 and D_1, respectively.

The porous glasses, as every other porous system, are able to soak spontaneously with water vapors due to the atmosphere always contains some amount of humidity. The water vapour reduces the electrical resistance of the system sufficiently, and this fact suggests to use of porous glass as an active element of resistive humidity sensor. It confirms by the fact every type of glass contains some amount of pores of size-range from about 10 to more 100 nm (see Fig.2). Presence such large size-range of pores corresponds to condition of hydrophilicity of system at large humidity range [30]. However, electrical resistance of the porous glasses is too big and it hinders to use a nanosize system on their base in such manner. This resistance can reach some teraohms for the standard size specimens 1×0,5×0,1 cm^3 and its decreasing due to humidity change will be invisible in this background. That's where the primary carbon treatment helps us, that's why it reduce the system resistance by several orders of magnitude due to conductive properties of graphite.

It must be noted that not any type of glasses suitable for using as matrix for active element of humidity sensor. So, the A-glass isn't appropriate one that's why the resistance of *α* glass, which was formed after annealing, keeps it high value, if amount of the soaked glucose is too less. At the other hand, excess of soaked glucose together with big amount of residual silica gel will score the pores after annealing and the system will lose it moisture sensibility. In the case of *γ*-glass, in addition, it's difficult to obtain a reliable contact due to high roughness of surface [31]. Inside D_1-glass the conductive phase is able to shunt the specimen. So, namely B_1-type of glasses appropriate to use as matrix for humidity sensor. This

glass contains fine pores mainly and it is depleted with silica gel. Besides its surface haven't high roughness. After formation of graphite nanoparticles' ensemble in B-glass a graphite layer creates on the surface of obtained B_1-glass. A reliable contact may be putting in to this layer with help of conductive paste. The change of the resistance of obtained system will quite correlate with moisture of environment.

Fig.8 shows a typical dependence of resistance of the graphite nanoparticles' ensemble in B_1-glas on moisture. This ensemble was formed by immersion of glass in the 40% water solution of glucose during a day with following anneal by 180°C during 2 hours. Contact for such system was putting in with silicone paste. All measurements was performed at the room temperature. One can see that the reduce of the system resistance by increase of relative moisture of environment from 10% to 99% achieve two order of magnitude.

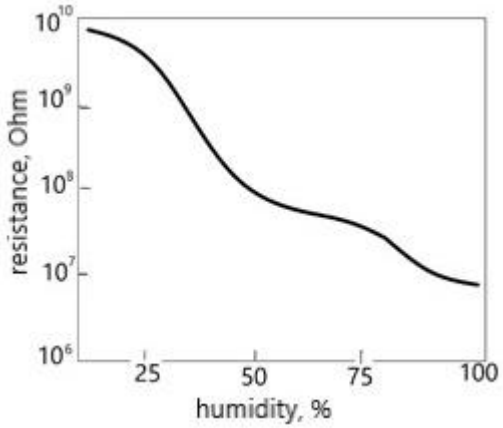

Fig. 8. Resistance dependence of graphite nanoparticles' ensemble in ***B₁*** porous glass on humidity of environment at the room temperature.

It can be note that similar isotherms may be graphed at some temperature and they almost don't change. This statement is true just at negative temperature, because at such temperature the moisture of the air determines by ice sublimation. And besides the separate nanoparticles of water, which was absorbed by system, are divided with silica gel and graphite nanoparticles, that's why temperature of environment is indifferent for them and the state of aggregation doesn't exist for such nanoparticles' ensembles.

Formation of ohmic contact to the pore glass specimen is another application of the primary carbon treatment. It could investigate correlation between luminescence properties of nanosize system in the pore matrix and electrically ones. Primary carbon treatment may be particular to reach such aim.

Using primary carbon treatment a standard specimen deeps with butts $5 \times 0.5\ mm^2$ into glucose solution on the depth 0.5÷1 mm with the help of clamp-like holder. It creates the conditions, which almost respond to the tusk of diffusion from a constant source. According to the second Fick's low on the step of dopant spin-on into the system there arises concentration of glucose C_x on the distance x during the time t:

$$C_x = C_0 \mathrm{erfc}\left(\frac{x}{2\sqrt{Dt}}\right).$$

Here C_0 is initial concentration of soaked solution. Factor D is certain analog of diffusion coefficient, which is called saturation coefficient. It's different from diffusion coefficient sufficiently, that's why in contrast with last one it describes infiltration of enough big glucose molecules into voids of of porous glass. These voids are very big in comparison with interatomic distances (see Fig.2). Corresponding coefficient depends on type of glass, namely on of it porosity, pore-size distribution, presence of residual silica gel and amount of this substance, as well as on temperature of soaking.

Fig.9 shows us schematically the glucose distribution inside wafer of the porous glass after soaking of specimen at both butts with this substance. Depth of immersion of the wafer into solution indicates with dotted line. Let's note that both curves don't show the configuration of profile of soaked glucose, but they image the reduce of it concentration by distance from source of soaking only.

Let's note also that the error function complement convergences too slow by an attempt of series expansion. That's why one usually applies the McLaurin series expansion to estimate analytically of concentration of glucose, which was soaked on a small distance from it source. However, one must use asymptotic mapping of this function for the case of big distances. The first case gives us:

$$C_x = C_0\left[1 - \frac{2}{\sqrt{\pi}}\sum_{n=0}^{\infty}\frac{(-1)^n\left(\frac{x}{2\sqrt{Dt}}\right)^{2n+1}}{n!(2n+1)}\right],$$

and by the second one

$$C_x = C_0\frac{\exp\left(-\left(\frac{x}{2\sqrt{Dt}}\right)^2\right)}{\left(\frac{x}{2\sqrt{Dt}}\right)\sqrt{\pi}}\left[1 + \sum_{n=1}^{\infty}(-1)^n\frac{(2n)!}{n!\left(\frac{x}{\sqrt{Dt}}\right)^{2n}}\right].$$

Although the convergence of these series is too slow, it's able to keep some first terms only in these cumbersome expression for any specific tusk. So we have for small x:

$$C_x \approx C_0\left[1 - \frac{2}{\sqrt{\pi}}\left(\frac{x}{2\sqrt{Dt}} - \frac{x^3}{6\sqrt{(Dt)^3}}\right)\right],$$

and for big ones:

$$C_x \approx C_0\frac{\exp\left(-\left(\frac{x}{2\sqrt{Dt}}\right)^2\right)}{\left(\frac{x}{2\sqrt{Dt}}\right)\sqrt{\pi}}\left[1 - \frac{2Dt}{x^2} + \frac{12(Dt)^2}{x^4}\right].$$

Furthermore, the wafer of porous glass, which was soaked from both butts with glucose according above manner, must be annealed to decompose penetrated glucose in pores thermally. Simultaneously drive-in step of graphite diffusion takes place. It's certain analogue of the tusk about diffusion from a limited source. If the glucose concentration at the butts of the wafer coincided with C_0 before the thermal decomposition, and the concentration in the arbitrary point x determined by above equation and was equal C_x, then new concentration at the time t will determine by expression:

$$C_{x1} = C_x \exp\left(-\frac{x^2}{4Dt}\right).$$

Fig.10 shows graphite nanoparticles' distribution in ensemble, which was formed by the above annealing. These curves don't correspond again to graphite configuration in porous glass. They shows just the reduce of graphite amount by drifting apart the butts of wafer.

Comparison of the Fig.9 and Fig.10 shows us that the graphite particles in ensemble in contrast of glucose nanoparticles are concentrated near the butts of wafer mainly. And specified concentration quickly fade away by drifting apart them. Thus, areas with heightened conductivity arise at the butts of wafer. Presence of these areas don't affect to the conductivity of remaining part of specimen anyhow. Treating these areas of the wafer with silicone paste or other one we can form an ohmic contact to the pore glass specimen. Arising conductive areas present an *α*-glass, which smoothly passes into *A*-glass (or in case of other types of glass we have a pass B_1 into *B* or *γ* into *C* or D_1into D).

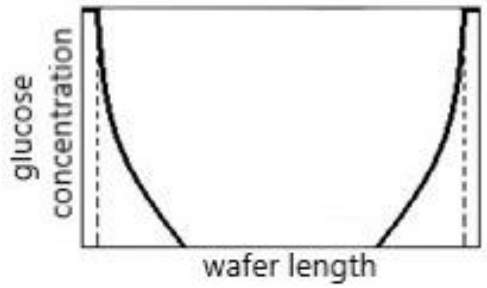

Fig. 9. Glucose distribution in in the porous glass wafer.

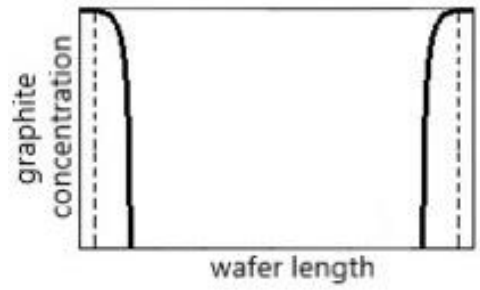

Fig. 10. Distribution of graphite nanoparticles in the formed ensemble.

It must be noted that the glasses of *α*- and *γ*-types are not currently used by themselves: they cannot serve as a matrix to create ensembles of nanoparticles, because their pores are completely filled with carbon. As carbon conducts electricity well, they are actually just constant resistors, with indefinite resistance. However, they give an opportunity to dispose of residual silica gel, if they will anneal additionally, in other words will perform secondary carbon treatment.

This annealing temperature regime corresponds to the silicon displacement from the oxide without simultaneous pores' collapse (i.e. within 300 ÷ 400ºC). This produces chemically inert carbon dioxide. This gas is heavier than air and therefore lingers in the pores for a while, preventing oxygen from entering there. As a result, the reduced silicon atoms, which are unable to oxidize, will begin to crystallize into silicon nanocrystallites, which will settle on the dangle bonds, which will appear on the walls of pores in the "stem" form due to the etching of the silicate skeleton. The completion of the reaction can be fixed visually by restoring of the sample transparency. During secondary carbon treatment, almost all silica gel is converted into silicon clusters, while the leaching technique application leads only to the original glass depletion with silica gel to almost complete sample dissolution, if the leaching lasts long enough [4, 11]. Thus, carbon treatment is an alternative way to remove silica gel from pores. After secondary treatment, *α* glass is called *β*-type glass, and *γ* glass is called *δ*-type glass. It should be noted that these types of glasses differ in many respects from type *B* or *D* glasses, respectively [11]. This is, in particular, due to the change in the matrix structure during carbon treatment (as opposed to leaching): as a result, silicon clusters appear on the slot walls, similar in structure to porous silicon obtained by laser ablation [32]. As a result, extraneous peaks appear in the glass luminescence spectra, which correspond to porous silicon and are located in areas of the spectrum that may be significant for the test substance. Therefore, *β* and *δ* type glasses are not usually used as a matrix to create nanoparticle ensembles of, although their absorption properties are applicable to other applications, such as ophthalmic bioprosthetics [33-34].

Conclusion

Photoluminescence of dyes based on tetravalent stannum complexes is possible not only in solutions but also in the dry state, if they are formed in the form of a nanoparticle ensemble inside a fine-porous matrix containing residual silica gel in the porous. Silica gel inhibits the formation of aggregations and this leads to an increase in the glow intensity compared to the solution.

The luminescence intensity of all tautomeric forms of this type dyes increases when the substituent of any nature approaches to the coordination node due to the emergence of additional electron-rotational levels suitable for the radiative transition. This effect does not depend on the coordination node and is true for both solutions and nanoparticles.

When forming an ensemble of the dye nanoparticles in a porous matrix, the increase in the concentration of the impregnating solution first leads to an increase in the intensity of the glow, and after exceeding the concentration limit, photon absorption processes begin to prevail over their radiation, and the luminescence weakens to typical for solution.

There are two types of luminescence centers in the dye molecule: a substituent in the hydrazide fragment, which is analogous to the substitution impurity in the semiconductor, and a ligand in the coordination node, which plays the role of the interstitial impurity. The substituent is responsible for the sensitivity to ammonia and the ligand is responsible for the sensitivity to HCl vapors.

The dye nanoparticle ensemble sensitivity to ammonia shows itself in the luminescence intensity decrease in comparison with photoluminescence in a pure atmosphere, if the dye contains an amine substituent of the

benzoyl type. The effect is probably related to the formation of bridges within the matrix pores, which are the leakage channels.

The dye nanoparticle ensemble sensitivity to HCl vapors shows itself in the switching of the system's luminescence to a lower intensity due to the negative charge redistribution in it under the action of excess chlorine ions if the dye contains a benzoyl-type hydroxyl substituent.

In both cases, in the extraneous gases presence, the attenuation of glow compared to photoluminescence in a pure atmosphere is quite stable, however, the initial intensity can be restored by short-term low-temperature annealing, which provides multiple use of active dyes nanoparticle ensembles as gas sensor active elements.

Through carbon treatment of porous glass, which consists of two steps, one can dispose of the residual silica gel from the pores of glasses. It concerns to the glasses, with contain this substance. Residual silica gel transforms into silicon clusters, which settle on the walls of pores.

Primary carbon treatment leads on creation of the conductive layer inside all the types of porous glasses. It allows to reduce own electrical resistance of standard-size specimens sufficiently. After such treatment these specimens may be used as active element of resistive humidity sensors.

Partial primary carbon treatment of the standard specimens of porous glass allows to form ohmic contacts on the butts of the sample for subsequent applications.

Lepikh Ya.I. – DSc, Professor;
Doycho I.K. – PhD, Senior Researcher**.**

[1] I.K. Meshkovsky. The Composite Optical Materials Based on Porous Matrices (Sankt-Petersburg, 1998).
[2] V.A. Smyntyna, V.M. Skobeeva, N.V Malushin. *The Boundary Influence on the Optical and Luminescent Properties of the Quantum Dots of the CdS In A Polymer*, Fizika i Khimiya Tverdogo Tela, 12(2), 355 (2011).
[3] V.A.Smyntyna, V.M. Skobeeva, N.V. Malushin. *Influence of the Surface on the Spectrum of Luminescence NC CdS in Gelatine Matrix*, Photoelectronics, 21, 50 (2012).
[4] I.K. Doycho. *Study of the Photoluminescent Properties of Nanoparticles Ensembles of Dyes*, In book: Non Equilibrious Processes in the Sensor Structures, p.120 (Ed. V.A. Smyntyna, ONU, Odesa, 2015).
[5] S.A. Gevelyuk, I.K. Doycho, E. Rysiakiewicz-Pasek, K. Marczuk. *Relative Changes of Porous Glass Dimensions in Humid Ambiance*, Journal of Porous Materials, 7, 465 (2000).
[6] S.A. Gevelyuk, I.K. Doycho, D.V. Lishchuk, L.P. Prokopovich, E.D. Safronsky, E. Rysiakiewicz-Pasek, Ya.O. Roizin. *Linear Extension of Porous Glasses with Modified Internal Surface in Humid Environment*, Optica Applicata, 30(4), 605 (2000).
[7] S.A. Gevelyuk, I.K. Doycho, L.P. Prokopovich, E. Rysiakiewicz-Pasek, E.D. Safronsky. *Humidity Dependencies of Porous Sol-Gel and Silica Glass Linear Sizes*, Material Science, 20(2), 23 (2002).
[8] E. Rysiakiewicz-Pasek, V.A. Vorobyova, S.A. Gevelyuk, I.K. Doycho, V.T. Mak. *Effect of Potassium Nitrate Treatment on the Adsorption Properties of Silica Porous Glasses*, Journal of Non-Crystalline Solids, 345, 260 (2004).
[9] O.V. Tyurin, Y.M. Bercov, S.O. Zhukov, T.F. Levitskaya, S.A. Gevelyuk, I.K. Doycho, E. Rysiakiewicz-Pasek. *Dye Aggregation in Porous Glass*, Optica Applicata, 40 (2), 311 (2010).
[10] O.V. Mazurin, G.P. Roskova, V.I. Averianov, T.V. Antropova. Biphasic Glasses: Structure, Properties, Applications (Nauka, Leningrad, 1991).
[11] I.K. Doycho, V.S. Grinevych, and L.M. Filevska. *Porous Silica Glasses as a Model Medium for the Formation of Nanoparticles Ensembles: Review*, Advanced Nanomaterials for Detection of CBRN, NATO Science for Peace and Security Series A: Chemistry and Biology, 283 (2020); https://doi.org/10.1007/978-94-024-2030-2_21.
[12] I.D.Tolmachov, O.V. Stronsky. *Optical Nonlinearities in Chalcogenides Vitreous Semiconductors. Review*, In book: Optoecectronics and semiconductor technique, 45, 27 (2010).
[13] V.M. Mitsa, R. Golomb, O. Kondrat, N. Popovich. *Synchrotron XPS Studies of Illuminated and Annealed Flash Evaporated a Ge253 Films*, J. Non-cryst. Solids, 401, 258 (2014).
[14] I.K. Doycho, S.A. Gevelyuk, E. Rysiakiewicz-Pasek. *Photoluminescence of Tautomeric Forms of Nanoparticle Ensembles of Dyes Based on the 4-valence Stannum Complexes in Porous Silica Glass*, Photoelectronics, 24, 30 (2015).
[15] S.A. Gevelyuk, V.S. Grinevych, I.K. Doycho, L.M. Filevska. *The Active Environment Influence on the Luminescence of SnO_2 Nanoparticles' Ensembles in a Porous Matrix*, Applied Physics A, 126(12) , 919 (2020); https://doi.org/10.1007/s00339-020-04101-4.
[16] S.A. Gevelyuk, V.S. Grinevich, I.K. Doycho, Ya.I. Lepikh, L.M. Filevska. *The Radiation Peculiarities of Nanoscale SnO_2 in a Porous Matrix*, Journal of Nano- and Electronic Physics, 12(3), 03020(2020); https://doi.org/10.21272/jnep.12(3).03020.
[17] Ya.I. Lepikh, T.I. Lavrenova, N.M. Sadova. Structural-phase and Electrophysical Properties of Nanocomposits Based on the "glass-Ni_3B" system, Recived by the Catode Beam Annealing, Journal of Nano- and Electronic Physics, 9(5), 05005(2017); https://doi.org/10.21272/jnep.9(5).05005.
[18] Ya.I. Lepikh, T.I. Lavrenova. Influence of a Glass Properties and Structural-phase Transformations on Electrophysical Parameters of Semiconductor Systems "glass-$Pb_2Ru_2O_6$, Ru", Radioelectronics & Info Communications, IEEE 11-16 Sept. 2016, 259 (2016); https://doi.org/10.1109/UkrMiCo.2016.7739616. http://eeexplore.ieeeorg/document/7739616/.

[19] Ya.I. Lepikh, T.I. Lavrenova, T.N. Bogdanova, N.P. Zatovska, P.O. Snegur. *Annealing Temperature Modes Influence on Properties of Heterophase Nanocomposites Basssеddd on Ceramics "glass – Ag-Pd*" Systems, J.Functional Materials, 21(3), 297 (2014).
[20] N.V. Shmatkova, I.I. Seifullina, I.K. Doycho, S.A. Gevelyuk, V.A. Smyntyna, R.V. Viter. 2-nd International Conference «Applied Physics and Non-organic Chemistry», (DIP, Simferopol, 2013), 197.
[21] S.A. Gevelyuk, E. Rysiakiewicz-Pasek, I.K. Doycho. *Dependence of Photoluminescence of Nanoparticle Ensembles of Stannum (IV) Complexes in Silica Porous Matrix on Concentration of Saturating Solution, Photoelectronics*, 25, 40 (2016).
[22] O.V. Tyurin,.V.P. Churashov, S.O. Zhukov, L.I.Manchenko, T.F. Levitska, O.I. Sviridova. *Interaction between Molecular Dyes and Polymolecular Formations*, Optika I Spektroskopija, 104 (1), 97 (2008).
[23] W. Cooper. *Electronic Adsorption, Luminescence and Related Properties of Resolved J-aggregates of 1,1'-diethyl-2,2'-cyanine Adsorbed to Silver Halide*, Photographic Science and Engineering, 17 (2), 217 (1973).
[24] I.K. Doycho, S.A. Gevelyuk, Ya.I. Lepikh, E. Rysiakiewicz-Pasek. *Gas Sensibility Features of Dyes on the Base of Sn(IV) Complexes*, SEMST, 14 (1), 31 (2017).
[25] I.K. Doycho, S.A. Gevelyuk, Ya.I. Lepikh, E. Rysiakiewicz-Pasek. *Nature of Gas Sensitivity of Dyes on the Base of Sn(IV) Complexes*, Optica Applicata, 49 (3), 427 (2019).
[26] Patent of Ukraine №119092, Ammonia sensor: IPC G01N 21/64 (2006.01); Gevelyuk S.A., Doycho I.K. Lepikh Ya.I.; registered in State Register of invention patents 25.04.2019.
[27] Patent of Ukraine №118415, HCl vapours sensor: IPC G01N 21/76 (2006.01); Lepikh Ya.I., Doycho I.K., Gevelyuk S.A.; registered in State Register of invention patents 10.01.2019.
[28] S.A. Gevelyuk, I.K. Doycho, L.P. Prokopovich, E. Rysiakiewicz-Pasek, K. Marczuk. *The Influence of Anneal of Incorporated Carbon on the Photoluminescence Properties of Porous Glass and Porous Silicon*, Polish Ceramic Bulletin 19, Ceramics 57, Porous and Special Glasses, p.59 (Ed. L.Stoch, Polish Ceramic Society, Krakow, Poland, 1998).
[29] S.A. Gevelyuk, I.K. Doycho, L.P. Prokopovich, E. Rysiakiewicz-Pasek, E.D. Safronsky. *Influence of Carbon Multiple Treatments on the Photoelectrical Properties of Porous Glasses*, Radiation Effects & Defects in Solids, 158, 427(2003); https://doi.org/10.1080/1042015022000037292.
[30] Hubert Grange, Jean-Sebastien Danel, Brigitte Desloges, and Vincent Jousseaume. US patent 8739622 B2, Jun.3, 2014, G01N27/00.
[31] E.D. Safronsky, Y.O. Roizin, E. Rysiakiewicz-Pasek. *Application of Porous Glasses for Humidity Control*, Optical Materials, 5, 217 (1996).
[32] S.A. Gevelyuk, I.K. Doicho, L.P. Prokopovich, D.P. Savin. *The Structural and Luminescent Properties of the Porous Silicon, Obtained by the Laser Ablation Method*, Photoelectronics, 8, 18 (1999).
[33] E. Rysiakiewicz-Pasek, S.A. Gevelyuk, I.K. Doycho, L.P. Prokopovich, E.D. Safronsky. *Antibiotic Hentamicini Sulphate Effect on Photoluminescent Properties of the Silicate Porous Glasses, which Are Suitable for Ophthalmologic Prosteting*, Optica Applicata, 33 (1), 33 (2003).
[34] E. Rysiakiewicz-Pasek, S.A. Gevelyuk, I.K. Doycho, V.A. Vorobjova. *Application of Porous Glasses in Oftalmic Prostetic Repair*, Journal of Porous Materials, 11, 21 (2004).

Я.І. Лепіх, І.К. Дойко

Властивості кремнеземних пористих стекол з ансамблями наночастинок деяких сполук. Огляд

Міжвідомчий науково-навчальний фізико-технічний центр МОН та НАН України при Одеському національному університеті імені І.І.Мечникова, м. Одеса, Україна, ndl_lepikh@onu.edu.ua

У цьому огляді систематизовано властивості шпаристих силікатних стекол. Описано методи формування у шпаринах ансамблів наночастинок речовин, що використовуються у мікроелектроніці. Шпаристі силікатні стекла є перспективними в цьому сенсі завдяки власній хімічній стійкості, механічній тривкості та гарній розгорнутості своєї внутрішньої поверхні. Проте, власний електричний опір стандартних зразків цієї речовини є надто великим, і через це у сенсориці її, зазвичай, використовують переважно як матрицю для сенсорів люмінесцентного типу. Досліджено залежність люмінесцентних властивостей системи як від молекулярної будови досліджуваних речовин (на кшталт барвників або оксидів металів), так і від технологічних умов формування ансамблів наночастинок. Виявлено, до яких саме газів є чутливими барвники конкретного типу і чому вони поводять себе саме таким чином. Продемонстровано, завдяки яким властивостям розглянутих нанорозмірних систем виникає зазначена газочутливість. До того ж, завдяки особливостям будови шпаристих силікатних стекол, у їхні шпарини можна вбудовувати провідну фазу шляхом спеціальної обробки. Після зазначеної обробки стекла можуть використовуватися як матриця для формування сенсорів резистивного типу.

Ключові слова: кремнеземне пористе скло, люмінесценція, сенсори газу, сенсори вологості, обробка вуглецем, омічні контакти, барвники.

PHYSICS AND CHEMISTRY OF SOLID STATE
V. 24, No. 2 (2023) pp. 335-340
Section: Physics

DOI: 10.15330/pcss.24.2.335-340

Vasyl Stefanyk Precarpathian National University

ФІЗИКА І ХІМІЯ ТВЕРДОГО ТІЛА
Т. 24, № 2 (2023) С. 335-340
Фізико-математичні науки

PACS: 68.35.bj, 81.05.Gc ISSN 1729-4428

V.M. Rubish[1], V.K. Kyrylenko[1], M.O. Durkot[1], V.V. Boryk[2], R.O. Dzumedzey[2], I.M.Yurkin[3], M.M.Pop[1,3], Yu.M. Myslo[3]

The influence of mercury vapor on the electrical resistance of chalcogenide amorphous films

[1]*Institute for Information Recording, NAS of Ukraine, Uzhgorod Ukraine, center.uzh@gmail.com*
[2]*Vasyl Stefanyk Precarpathian National University, Ivano-Frankivsk, Ukraine*
[3]*Uzhgorod National University, Uzhgorod, Ukraine*

Using the planar structures "Ni layer - chalcogenide amorphous film - Ni layer" and "graphite probe - chalcogenide amorphous film graphite probe" samples, the influence of mercury vapor on the electrical resistance of amorphous films of the Se-Te, Se-Sb and Se-As systems was investigated. It was established that exposure of samples in mercury vapor leads to a decrease in their electrical resistance by 4-7 orders of magnitude. As the temperature and mercury concentration increase, the transition time from a high-resistance state to a low-resistance state decreases. When introducing Te, Sb, and As into amorphous selenium and increasing their concentration in the composition of the films, the transition time increases, and the value of the change in resistance decreases. It was established that the change in resistance is mainly determined by the change in surface conductivity of chalcogenide films. A decrease in the electrical resistance of selenium-containing amorphous films modified with mercury is caused by the formation of HgSe crystalline inclusions in their matrix.

Keywords: chalcogenide amorphous films, electrical resistance, mercury film modification, mercury selenide, mercury vapor sensors.

Received 28 January 2023; Accepted 6 June 2023.

Introduction

While studying the electrical and optical properties of semiconductor materials, it was found that the exposure of amorphous selenium films in mercury vapor leads to an increase in their electrical conductivity in 5–6 orders of magnitude [1]. The revealed impact is evidence of the possibility of using this material as an active element of sensitive sensors for detecting mercury vapor. The author of this academic study considers that the reason for the significant increase in the electric conductivity is most likely stipulated by the formation of crystalline inclusions of mercury selenide (HgSe) in the Se amorphous matrix. At the same time, it is assumed mercury selenide that appears because of the interaction of mercury with amorphous selenium is a non-stoichiometric compound (Se atoms predominate). A similar conclusion suggests itself upon the results of the study we have conducted with the structure and morphology of the surface of amorphous selenium films, which are modified with mercury by methods of the X-ray diffraction analysis, Raman spectroscopy and scanning electronic microscopy (SEM) [2-4]. On diffraction patterns of the Se amorphous films exposed to mercury vapor, we have found the reflections whose intensity is growing with increasing exposure time [2, 4]. The position of these reflections well agrees with the position of reflections on diffraction patterns of HgSe crystal received via the hydrochemical method using aqueous solutions of various substances such as $HgCl_2$, $SeCl_4$ and $(N_2H_4{\cdot}H_2O)$ [5], $Hg(CH_3COO)_2$ і $SeCl_4$ [6] in the presence of $N_2H_4{\cdot}H_2O$, $Hg(NO_3)_2$ and Na_2SeSO_3 [7]. In Raman spectra of the Se amorphous films modified with mercury, we have found weak bands [3] typical of similar spectra of HgSe Nanocrystals that were obtained by chemical deposition of Hg and Se vapors in zeolite matrix with the mostly spherical pores of Nd-Y [8]. Inclusions of

another phase also clearly appear on SEM images of surfaces that are modified with mercury from the selenium amorphous films [2]. The research results presented in scientific papers [2-4], with considerable reliability, allow us to state that the structure of the phase, which is forming in the matrix of Se amorphous films upon their modification with mercury, corresponds to the HgSe structure in cubic modification.

The Se-Te, Se-Sb and Se-As amorphous films, with a low content of Te, Sb and As (up to 15 at. %), may be used as promising materials for creating sensors for detecting mercury vapor in the environment. In comparison with the Se films, the films of these systems have higher softening and crystallization temperatures and, respectively, they are more stable and resistant to spontaneous crystallization [9-11].

We should note that the results of the studies presented in [1-4] concern the static mode of mercury modification of the selenium amorphous films. The measurements were done in a certain period, after exposure to the amorphous films in the mercury vapor. In terms of the practical application of selenium-containing amorphous films, the study of their electrical properties in the process of modification with mercury is of the most interest. In addition, we should specify that the rate of mercury evaporation and, respectively, mercury concentration and saturated vapor pressure in a certain volume shall be determined by the size of the open surface of a mercury drop and temperature [12]. Respectively, these parameters will significantly affect the formation rate of HgSe inclusions and the electrical resistance of the films.

In connection with the above, the study of the impact of temperature, mercury concentration, and chemical composition on the electrical characteristics of the amorphous Se-Te (Sb, As) system is of certain interest. We devote this scientific paper to solving these precise issues.

I. Experimental Methodology

We have conducted the studies of the graphs of dependency of the electrical resistance (R) of the amorphous films of the Se-Te, Se-Sb and Se-As systems (with low content of Te, Sb and As) on the time (t) of exposure in mercury vapors, using special hermetic containers, in the temperature range of 287-296 K, on planar structures such as the "Ni layer - amorphous chalcogenide film (ACF) – Ni layer" and structures such as the "graphite probe (GP) - amorphous chalcogenide film (ACF) –graphite probe (GP)". The pressure of saturated mercury vapor at such temperatures is 0.066-0.152 Pa, while the concentration is 5.6-13.3 mg/m^3.

To study the electrical properties of structures such as the "Ni layer-ACF-Ni layer", we have used a combined method [13], which makes it possible to measure the $R(t)$ dependency of films at changing the time of their modification with mercury. The sequence of operations for making planar samples such as the "Ni layer-ACF-Ni layer" is as follows. On the glass substrate, we applied the semi-transparent Ni layer, which is 50-150 nm thick. The 0.3-0.4 mm gap was forming on the layer by scribing. For this, an elliptical scriber was applied. Amorphous Se and $Se_{100-x}Te_x$ films, which are 150-300 nm thick, were applied to the gap area via a mask. We obtained the amorphous films of these compositions by a method of vacuum evaporation of vitreous Se and polycrystalline alloys such as $Se_{100-x}Te_x$ ($3 \le x \le 15$) from quasi-closed effusive cells on glass substrates with a nickel layer.

In several experiments to study the impact of mercury vapor on the electrical resistance of amorphous films of systems such as Se-Sb and Se-As we applied such structures as "GP-ACF-GP". The probes' diameters were 0.5 mm while the distance between them could be variable from 2 to 5 mm. Such structures have the advantages of the simplicity of high-quality cleaning of contact surfaces in the measuring system and constructively built-in stability of the distance between probes. It is important to simplify the structure of samples such as "GP-ACF-GP" because of the absence of the stage of sputtering of metal cords. In this structure of the measuring cell, the thickness of the chalcogenide film was approximately 1 mcm.

II. Experimental Results

Fig. 1. shows the graphs of dependence of the electrical resistance of planar samples such as the "Ni layer-Se film-Ni layer" from the time of their modification with mercury at various ambient temperatures and mercury concentration (the beginning of activating the amorphous selenium by mercury is marked on figures with an up arrow (↑)). The thickness of the selenium film (d_{Se}), the surface area of the mercury drops (S_{Hg}) and the temperature, at which we measured the dependency of samples' resistance at the time of their modification with mercury, are specified directly in the figures. The thickness of the Ni layer was 60-70 nm. In the experiments, we applied the vessels in which the surface drop area was 7 and 70 mm^2.

As you can see from Fig. 1., there is a latent period during which the resistance of the planar sample remains almost unchangeable. The period duration depends on mercury concentration and temperature and ranges from several minutes to one hour. Later, the resistance of the planar samples reduces sharply (by 4–6 orders of magnitude). For some structures of samples, we found a reduction in resistance by almost 7 orders of magnitude [14]. With the temperature rise, the duration of the latent period reduces and the rate of resistance increases. The same picture is also observed with an increase in mercury concentration. We got similar results (a sharp reduction in resistance by 4–6 orders of magnitude) while using samples such as "Cr layer - Se film - Cr layer" [15]. Such a course of dependency $R(t)$ may be explained from the point of structural changes, which occur in the Se amorphous films at their modification with mercury. In [16, 17], based on Raman studies, we concluded that the matrix of the Se amorphous film is built both by elements of the Se_8 rings and the elements of the helical Se_n chains. During the latent period, the interaction of the Se and Hg atoms occurs. Such interaction ends with the formation of the HgSe 'island-bridge' structure in the Se subsurface layer. The studies' results of the Se amorphous films, which are modified with mercury, [2-4] do not negate this

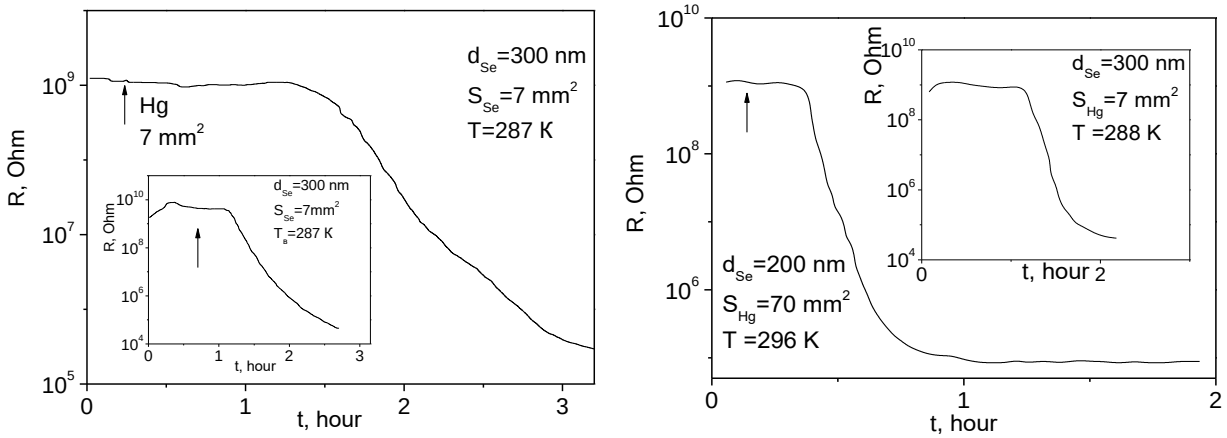

Fig. 1. The graph showing the dependence of the electrical resistance of planar samples such as the "Ni layer – Se amorphous film - Ni layer" from the time of exposure to the mercury vapour (there are explanations in the figure and in the text).

conclusion. Subsequently, the increase in the time of exposure of films in the mercury vapor leads to a significant increase in the islands' sizes and strengthening of the bridge connection between them. By this, we can explain the impact of a sharp reduction in the electrical resistance in samples such as the "Ni(Cr)layer - Se amorphous film - Ni(Cr)layer" modified with mercury.

Fig. 2. shows the graph showing the dependence of the sample resistance from the time of activation by mercury, for the case when the mercury concentration changed within the measuring (vessels with different S_{Hg} were alternately introduced in and removed from the measuring container). The moment of the vessel's removal in Fig. 2. is marked by an arrow down (↓). We can see that when the vessels with mercury are introduced into the measuring container, the graph showing dependence *R(t)* shows the sections where the resistance of the sample reduces sharply. The rate of changing the resistance of the sample decreases significantly at a reduction in the dynamic concentration of mercury, i.e. when we change the vessel with the Hg surface area of 70 mm^2 for the vessel with S_{Hg}=7 mm^2. On the graph showing the dependence of the electrical resistance of the sample such as the "Ni layer - Se film - Ni layer" from the time of its exposure to mercury vapor, some sectors are available where the resistance practically does not change (after removing the vessels with Hg), allows us to assert about the ability to keep in "memory" the mercury concentration, which the sample has absorbed before removing the vessels with mercury from measuring container.

Fig. 3. depicts the graph showing dependence R(t) for the samples such as the "Ni layer - $Se_{100-x}Te_x$ film - Ni layer". Just like for the Se amorphous films, modification with mercury of the amorphous films such as the $Se_{100-x}Te_x$ (x=3, 5, 10 and 15) leads to a reduction in their electrical resistance by 4-6 orders of magnitude. We can see that with an increase in the Te concentration in the composition of films of the Se-Te system, the resistance variation value reduces during the transition from a high-resistance state to a low-resistance state while the transition time and latent period increase. This may show a reduction in the instability of the structural network of films in the Se-Te system when the Se atoms are replaced by the Te atoms. As we have noted above, the structural network of the selenium amorphous film is built up by elements of Se_8 rings and S_{en} chains. When the Se atoms replace the Te atoms in $Se_{100-x}Te_x$ films, the tellurium atoms statically and uniformly replace the Se atoms in these chain groups. This, in turn, leads to a reduction in the Se_n length and, consequently, to a reduction in the quantity of Se atoms, which can interact with mercury. As in the case of the selenium amorphous films, HgSe [17] inclusions are formed in the amorphous matrix if the $Se_{100-x}Te_x$ films are exposed to the mercury vapor. Such formation leads to a sharp decrease in the electrical resistance of planar structures such as the "Ni layer - $Se_{100-x}Te_x$ film - Ni layer". According to Raman studies, we did not find the HgTe inclusions in the $Se_{100-x}Te_x$ films modified with mercury [17].

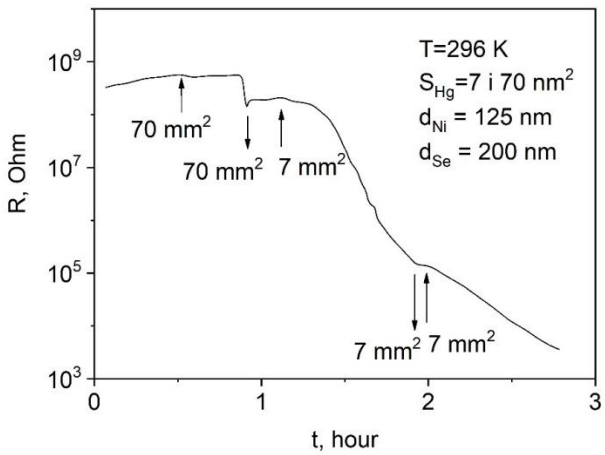

Fig. 2. The graph showing the dependence of the electrical resistance of planar samples such as the "Ni layer-Se film-Ni layer" for the case when the concentration of mercury changed within the resistance measuring (there are explanations in the figure and in the text).

Experiments proved that the course of the graph showing the dependence of planar structures such as the "Ni(Cr) layer-ACF-Ni(Cr) layer" practically does not depend on the thickness of the chalcogenide film. We

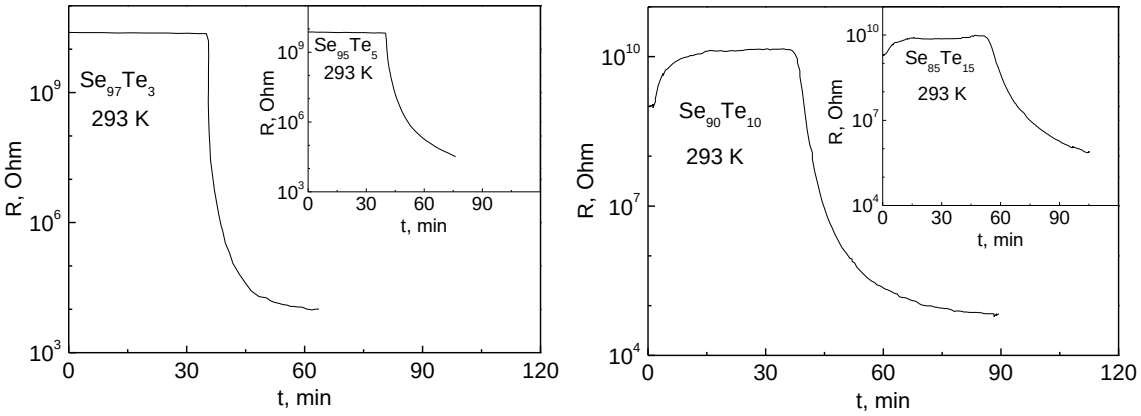

Fig. 3. The graph showing the dependence of the electrical resistance from planar samples such as the "Ni layer –$Se_{100-x}Te_x$ film – Ni layer" from the time of exposure to mercury vapour.

remind that the thickness of chalcogenide films such as $Se_{100-x}Te_x$ ($0 \le x \le 15$) in these experiments was 150-300 nm. This allows us to conclude that the change in the electrical resistance of such planar structures is mainly determined by changes in the surface electrical conductivity of chalcogenide films. This conclusion is confirmed by the results of studies of the impact of mercury vapor on the electrical resistance of chalcogenide films while using the samples such as "GP- ACF-GP". The thickness of chalcogenide films such as the $Se_{100-x}Sb(As)_x$ (x=0, 3, 7) was 1 mcm in these experiments.

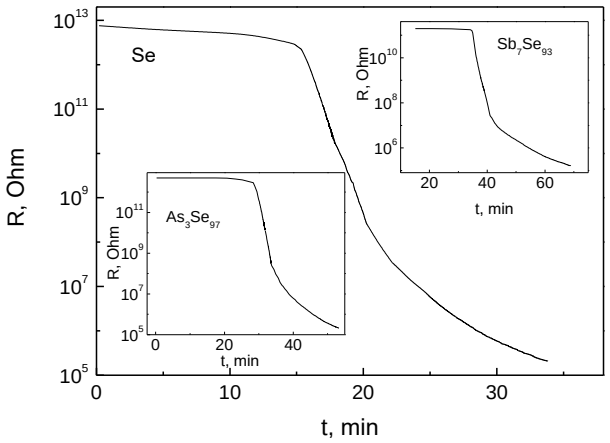

Fig. 4. The graph showing the dependence of the electrical resistance from planar samples such as "GP- ACF-GP" from the time of exposure to mercury vapor.

The graph showing the dependence of the electric resistance of some samples such as the "GP-$Se_{100-x}Sb(As)_x$ film- GP" from the time of their exposure to the mercury vapor at the temperature of 283-287 K are shown in Fig. 4. We can see that the graph showing dependency $R(t)$ of samples such as the "GP-$Se_{100-x}Sb(As)_x$ films-GP" are similar to the same graphs of the dependency shown in Fig. 1 and Fig. 3. Given the results of above studies, we may assume that the reduction in the electrical resistance of such samples as the "GP-ACF- GP", which are modified with mercury, is stipulated by the formation of the HgSe crystalline inclusions at the surface layer of chalcogenide film. It is seen from Fig. 4, that with an increase in the content of Sb and As in the composition of films, the latent period, during which the resistance practically does not change, increases. In this case, the time of transition from the high-resistance state to the low-resistance state also increases. As for the $Se_{100-x}Te_x$ films, this fact is stipulated by the reduction in the length of the Se_n chains due to the formation of such structural elements as $Sb(As)Se_{3/2}$ [10], in which the heteropolar Sb-Se bonds and As-Se bonds have more stability than homopolar Se-Se bonds of. Respectively, the quantity of the Se atoms, which may interact with Hg atoms to form HgSe, is much fewer.

Conclusions

Having studied the graphs of dependence of electric resistance of amorphous films such as the Se, $Se_{100-x}Te_x$, $Se_{100-x}Sb_x$ and $Se_{100-x}As_x$ from the time of exposure to mercury vapor, we have found as follows.

There is a latent period during which the resistance of the samples is practically unchanged. Depending on the mercury concentration, the temperature and the chemical composition of the films, the above duration period may range from several minutes to one hour.

A further increase in exposure time of chalcogenide films in mercury vapor leads to a reduction in their electrical resistance by 4–7 orders of magnitude. Reduction in electrical resistance is mainly determined by an increase in the electrical conductivity of the films because of forming crystalline inclusions of mercury selenide in their surface layers.

The time of the film's transition from a high-resistance state to a low-resistance state reduces with increasing the temperature and mercury concentration. When the content of Te, Se and As increases in the films, the time of transition increases while the value of the variable resistance reduces.

The obtained results show the possibility of using amorphous films of the Se-Te, Se-Sb and Se-As systems as sensitive elements of the electric sensors for detecting the mercury vapor.

Rubish *V.M.* – Head of Uzhhorod Laboratory of Optoelectronics and Photonics Materials of the Institute for Information Recording of the National Academy of Science of Ukraine, doctor of physics and mathematics sciences, professor;
Kyrylenko *V.K.* – leading design engineer of Uzhhorod Laboratory of Optoelectronics and Photonics Materials of the Institute for Information Recording of the National Academy of Science of Ukraine,
Durkot *M.O.* – leading engineer-technologist of Uzhhorod Laboratory of Optoelectronics and Photonics Materials of the Institute for Information Recording of the National Academy of Science of Ukraine;

Boryk V.V. – PhD in chemical sciences, associate professor;
Dzumedzey R.O. – PhD in physical and mathematical sciences;
Yurkin I.M. – associate professor of the Engineering and Technical Department of Uzhhorod National University, a candidate in physical and mathematical sciences;
Pop M.M. – doctoral student of the Department of Physics of Uzhhorod National University, a candidate in physical and mathematical sciences;
Myslo Yu.M. – associate professor of the Department of Solid State Electronics & Information Security Uzhhorod National University, candidate of physical and mathematical sciences.

[1] M.I. Korsunskyi, Anomalous photoconductivity and spectral memory in semiconductor systems, Moscow: Nauka, 319 (1978).
[2] L.I. Makar, S. Mudry, L. Nykyruy, R.P. Pisak, V.M. Rubish, I. Shtablavyi, S.A. Bespalov, A.M. Solomon, R.S. Yavorskyi, *Formation of HgSe nanocystalline inclusions in the matrix of amorphous selenium films*, Mat. Intern. Meeting "Clusters and nanostructured materials (CNM-6)", Uzhgorod, Ukraine, 267 (2020).
[3] O.M. Hreshchuk, V.O. Yukhymchuk, L.I. Makar, V.M. Rubish, M.M. Pop, T.I. Yasinko, Y.V. Bendzo, T.M. Zaiats, *Study of amorphous Se-films modified with mercury by Raman spectroscopy technique*, Materials of school-conference of young scientists "Modern materials science: physics, chemistry, technology (MMSPCT – 2021)», Uzhgorod, Ukraine, 211 (2021).
[4] A.M. Solomon, V.M. Rubish, R.P. Pisak, X-ray studies of amorphous selenium films modified with mercury, Proc. of the jubilee conf. "The 30th years Institute of Electron Physics National Academy of Science of Ukraine", 220 (2022)
[5] M. Esmaeili-Zare, M. Salavati-Niasari, A. Sobhani, *Simple sonochemical synthesis and characterization of HgSe nanoparticles*, Ultrasonics Sonochemistry, 19, 5, 1079 (2012); https://doi.org/10.1016/j.ultsonch.2012.01.013.
[6] M. Salavati-Niasari, M. Esmaeili-Zare, A. Sobhani, *Cubic HgSe nanoparticles: sonochemical synthesis and characterisation*, Micro & Nano Letters, 7, 12, 1300 (2012); https://doi.org/ 10.1049/mnl.2012.0709.
[7] M.A. Sozanskyi, V.Y. Stadnik, P.Y. Shapoval, Y.Y. Yatchyshyn, R.I. Hlad, *Hydrochemical synthesis of mercury selenide (HgSe) on glass substrates*, Materials of the 4th All-Ukrainian Scientific and Practical Conference of young scientists and students "Physics and chemistry of solid bodies. Status, achievements and prospects", Lutsk, 73 (2016).
[8] A.M.M. Abeykoon, M. Castro-Colin, E.V. Anokhina, M.N. Iliev, W. Donner, M. Brunelli, A.J. Jacobson, S.C. Moss, *X-Ray scattering studies of HgSe nanoclusters in zeolite*, Metallurgical and materials transactions A, 39 A, 3179 (2008); https://doi.org/10.1007/s11661-008-9563-9.
[9] J. Sarrach, J.P. Neufville, W.L. Haworth, *Studies of amorphous Ge-Se-Te alloys. I Preparation and calorimetric observations*, J. Non-Cryst. Solids, 22, 2, 245 (1976); https://doi.org/10.1016/0022-3093(76)90057-0.
[10] A.P. Shpak, V.M. Rubish, *Glass formation and properties of alloys in chalcogenide systems based on arsenic and antimony*, K.: IMP NASU, 120 (2006).
[11] D.G. Georgiev, P. Boolchand, *Rigidity transitions and molecular structure of As_xSe_{1-x} glasses*, Phus. Rev. B, 62, 14, R9228 (2000); https://doi.org/10.1103/PhysRevB.62.R9228.
[12] V.M. Rubish, V.K. Kyrylenko, M.O. Durkot, L.I. Makar, A.A. Tarnai, L. Nykyrui, *The impact of mercury vapor on the electric properties of amorphous selenium films*; Materials of the 4th International Scientific conference "Actual Problems of Fundamental Science", Lutsk, 96-97 (2021)
[13] V.K. Kyrylenko, V.M. Marian, M.O. Durkot, V.M. Rubish, *Study of amorphous chalcogenide materials of the memory elements based on phase transitions*, Data recording, storage & processing, 16, 2, 7 (2014).
[14] V.M. Rubish, V.K. Kyrylenko, L.I. Makar, M.O. Durkot, M.M. Pop, *Electrical conductivity of mercury-modified amorphous films of selenium-tellurium system*, Sourcebook of the jubilee conference "The 30th years Institute of Electron Physics National Academy of Science of Ukraine", 222 (2022)
[15] V.K. Kyrylenko, V.M. Rubish, L.I. Nykyruy, R.P. Pisak, M.O. Durkot, Z.R. Zapukhlyak, V.I. Fedelesh, V.N. Uvarov, *Electrical properties of mercury modified amorphous selenium*, Mat. Intern. Meeting "Clusters and nanostructured materials (CNM-6)", Uzhgorod, Ukraine, 138 (2020).
[16] V.M. Rubish, O.M. Hreshchuk, M.O. Durkot, L.I. Makar, M.M. Pop, I.M. Yurkin, V.O. Yukhymchuk, T.I. Yasinko, *Structural studies of photosensitive composites "NP Au/ selenium film*", Data recording, storage & processing, 22, 4, 12-18 (2020).
[17] V.M. Rubish, S.M. Hasinets, M.O. Durkot, L.I. Makar, R.P. Pisak, V.O. Stefanovych, T.I. Yasinko, S.A. Kostiukevych, K.V. Kostiukevych, Impact of laser radiation and mercury vapor on the structure of amorphous $Se_{100-x}Te_x$ films, Registration, storage and processing of the data, 24, 2, 3-10 (2022).

В.М. Рубіш[1], В.К. Кириленко[1], М.О. Дуркот[1], В.В. Борик[2], Р.О.Дзумедзей[2],
І.М. Юркін[3], М.М. Поп[1,3], Ю.М. Мисло[3]

Вплив парів ртуті на електричний опір халькогенідних аморфних плівок

[1]Інститут проблем реєстрації інформації НАН України, Ужгород, Україна, center.uzh@gmail.com
[2]Прикарпатський національний університет ім. В. Стефаника, Івано-Франківськ, Україна
[3] Ужгородський національний університет, Ужгород, Україна

З використанням планарних структур «шар Ni-халькогенідна аморфна плівка-шар Ni» та зразків «графітовий зонд-халькогенідна аморфна плівка-графітовий зонд» досліджено вплив парів ртуті на електричний опір аморфних плівок систем Se-Te, Se-Sb і Se-As. Встановлено, що витримка зразків в парах ртуті призводить до зменшення їх електричного опору на 4-7 порядків. З підвищенням температури і концентрації ртуті час переходу з високоомного стану в низькоомний зменшується. При введенні в аморфний селен Te, Sb та As і збільшенні їх концентрації у складі плівок час переходу зростає, а величина зміни опору зменшується. Встановлено, що зміна опору визначається в основному зміною поверхневої електропровідності халькогенідних плівок. Зменшення електричного опору селеновмісних аморфних плівок, модифікованих ртуттю, викликане формуванням в їх матриці кристалічних включень HgSe.

Ключові слова: халькогенідні аморфні плівки, електричний опір, модифікування плівок ртуттю, селенід ртуті, сенсори наявності ртутних парів.

PHYSICS AND CHEMISTRY OF SOLID STATE
V. 24, No. 2 (2023) pp. 341-347
Section: Technology

DOI: 10.15330/pcss.24.2.341-347

Vasyl Stefanyk Precarpathian National University

ФІЗИКА І ХІМІЯ ТВЕРДОГО ТІЛА
Т. 24, № 2 (2023) С. 341-347
Технічні науки

UDK: 669.66.011 ISSN 1729-4428

C.A. Imamalizade

Manufacturing of nitinol-based alloys by using modern technology: A short review

Azerbaijan State Oil and Industry University, Baku, Azerbaijan, cimamelizade@gmail.com

The paper provides a brief review of literature data on the synthesis, processing, structure, mechanical properties, and application of nitinol and alloys based on it, which are promising functional materials found application in a number of high technologies. In addition, machine learning methods were applied to predict the temperatures of phase transformations.

Keywords: shape memory alloys, nitinol, and alloys based on it, machine learning, microstructure, thermomechanical behavior.

Received 16 January 2023; accepted 8 June 2023.

The purpose of the article is to discuss the methods of synthesis and thermomechanical processing, structural features, as well as the use of alloys based on nitinol in modern high technologies.

A very extensive literature review of works in the field of research of materials with a memory effect does not allow us to consider them all in detail. Therefore, the following is only a brief part of all available literature in this area.

Modern scientific progress is unthinkable without the search and creation of new materials with functional properties. Such promising materials include shape-memory alloys. This contributed to the extensive popularity of this material for a wide range of applications [1-5].

Shape memory alloys (SMAs) are such kinds of alloys whose technical properties contribute to solve complicated challenges in the modern world. SMAs have 2 main technical properties used in modern industry: shape memory effect and superelasticity. The shape memory effect helps SMAs to recover their initial shape during the thermomechanical cycle. Superelasticity helps SMAs to resist extra-large loads without plastic deformation during only mechanical cycles [1-3].

SMAs are used in a wide variety of applications in modern industries. They are used as dental wires, in joining broken bones using metal plates, and in the construction of sensitive medical devices in bioengineering applications [4]. They are also used as tubes and wires in applications with hot fluids. SMAs are ideal as they can return to their original shape even in a heated environment [1,2].

SMAs are applied also in civil engineering, for instance, in bridge construction. SMAs reduce vibrations, hence damping the natural frequency of different structures. This vibration-damping property has also been used in jet engines and launch vehicles [4]. One potential application for SMAs with high working temperatures is decreasing airplane noise [5]

Fig. 1 shows the application of SMAs in medical and jet engines aerospace engineering.

Nitinol (NiTi) is one the most famous alloy among the SMAs family and consist of a nearly equal amount of nickel and titanium. Despite the fact that the region of homogeneity of this alloy is 50-56 at %Ni, from a technical point of view, alloys from the region of 50-52 at% Ni are the most applicable (Fig. 2) [6].

Therefore, in the literature, there are a number of works devoted to the study of alloys from this range of compositions [6-12]. Usually, to improve the thermomechanical properties, these alloys are alloyed with a third element: hafnium, zirconium, and silicon [13-17]. More complex compositions are also used [18, 19].

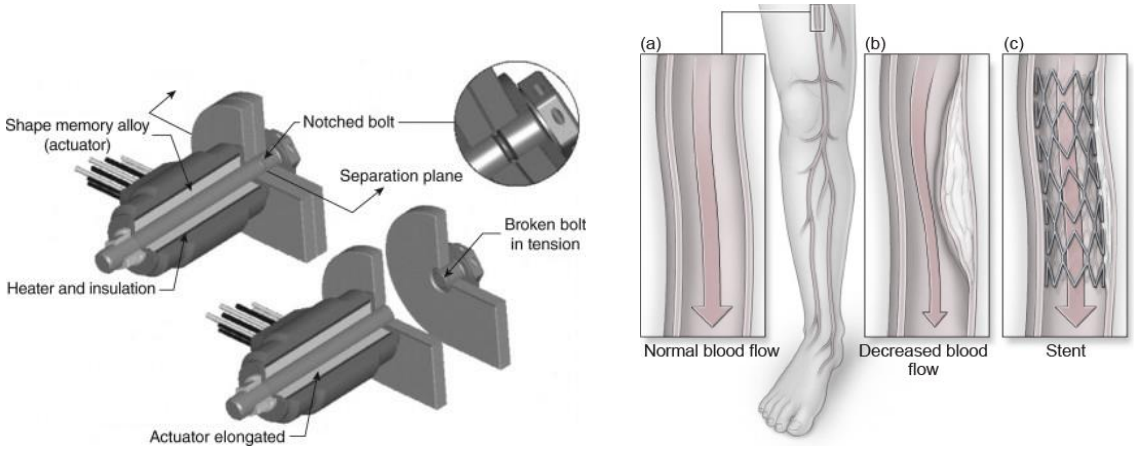

Fig 1. Application of shape memory alloys [4,5].

The rapid development of new technologies imposes the most important and diverse requirements on materials. However, traditional methods for discovering new materials, such as empirical trial and error and density functional theory (DFT), usually require a long research time. Machine learning (ML) can significantly reduce computational costs and reduce research time; i.e. it is one of the most efficient ways to replace DFT calculations and repetitive lab experiments. Machine learning is used to discover new materials, predict material and molecular properties, study quantum chemistry, and design drugs [20-23].

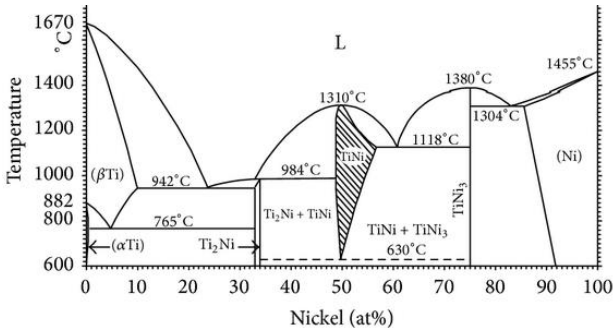

Fig 2. Phase diagram of the Ni-Ti binary system [6].

A number of investigations are devoted to manufacturing and applications of NiTi-based alloys by using ML. In [7, 22-25], the dependences of transition temperatures from features were investigated in NiTiHf and NiTiFeCuPd alloys by using various ML methods. In [22] Gauss Process Regression was used to predict transition temperatures of nitinol-based alloys. Authors of [23] used the artificial neural network to find the best parameters for manufacturing NiTi-based alloys. It was found that cutting parameters, such as feed rate, cutting speed, and depth of cut have a significant influence on the machining process of this alloy. Deep Learning was applied to predict the conventional yield strength, conventional tensile strength, and unit elongation of binary nitinol [24]. It was obtained that, Deep Learning showed higher performance as compared with Random Forest which also was used in this article.

The study [25] presents the optimization of cutting parameters, such as feed rate, cutting speed, and depth of cut, to obtain appropriate and acceptable values for critical outputs, such as cutting forces, tool wear, surface roughness, and dimensional deviation of machined parts. This study showed that the developed empirical model can predict the main results of turning operations with high accuracy. Cutting speed has been shown to play a critical role in controlling output data such as tool wear, surface roughness, and cutting forces (Fig. 3). With a lower cutting speed, relatively higher feed, and depth of cut, material removal rate can be maximized when machining NiTiHf HTSMA.

The optimization of parameters of electrochemical machining was investigated by using a deep neural network, Taguchi regression, and response surface method. The results obtained by the authors were compared among each other and discussed in the work [7].

In the literature, there is a huge number of works devoted to various methods of manufacturing and heat treatment [27-35], the study of the influence of chemical composition on phase formation and transformation [35-41], crystal structure [41-46], thermomechanical properties [45-48], improving and optimization of manufacturing parameters [30, 49-53].

Let's briefly discuss some of these works.

The machinability of Ti–rich $Ni_{49.8}Ti_{30.2}Hf_{20}$ and Ni-rich $Ni_{50.8}Ti_{29.2}Hf_{20}$ high-temperature shape memory alloy (HTSMA) wires were investigated in the 750-825°C temperature range [8]. Tensile testing and differential scanning calorimetry have been used to determine the thermomechanical behavior of hot-rolling alloy solutionized and then aged NiTiHf wires. It was obtained that, the ideal temperature of rolling for Ni-rich NiTiHf wires is over H-phase dissolution temperature (about 800° C). The reason for such a temperature is to prevent the wire from getting more brittle because of the H-phase effect and restrict compositional instability at the surface of the wire caused by HfO_2. The properties of oxide layers created during the rolling process and then heat treatments have been compared to solve several problems related to NiTiHf wire processing.

A new combinatorial alloy synthesis method (suspended droplet alloying- SDA) has been proposed for effective alloy discovery [26]. In this method, a laser is used to melt alloyed or elemental wires fed at a controlled rate to get a specific chemistry. The synthesized sample

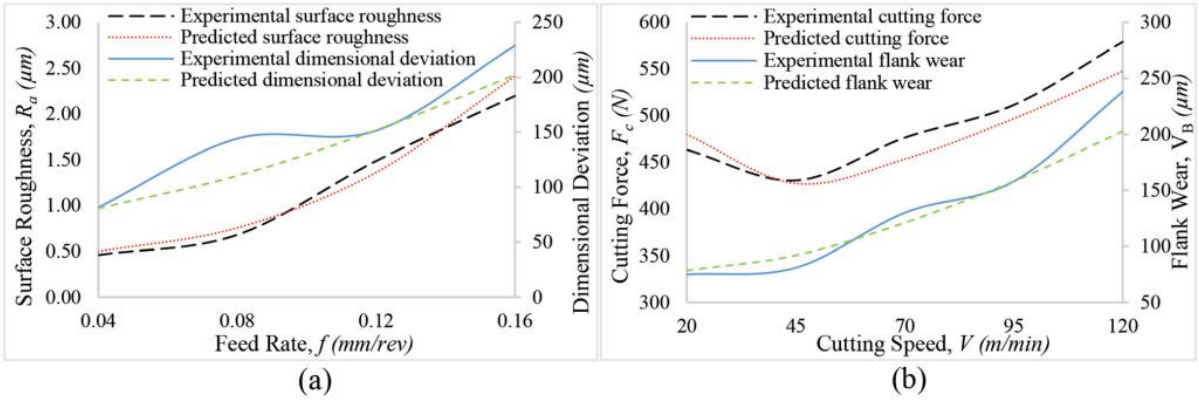

Fig. 3. Experimental and predicted values depending on cutting speed (constant f = 0.12 mm/rev, ap = 0.8 mm) (a) and feed rate (constant V = 70 m/min, ap = 0.8 mm) (b) [25].

was subjected to heat treatment for various periods of time. The microstructural and chemical inhomogeneity was assessed using quantitative electron microscopy and X-ray diffraction. In addition, the phase transition temperatures of the samples were compared to cast and heat-treated (reference) samples (Fig. 4). As a rule, long-term annealed samples showed a limited local deviation from the target chemical composition (±1 wt.%) while showing an expected phase distribution with the fairly homogeneous microstructure**.** According to this work, the original sample has a lower temperature of transformations due to chemical inhomogeneity, while the heat-treated samples have a similar transformation temperature to the reference sample.

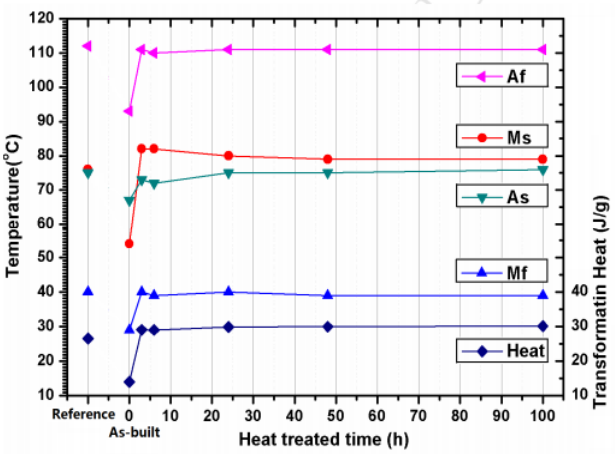

Fig. 4. Influence of the heat treatment time on the transformation temperatures and peak height, in comparison to the reference $Ti_{50.4}Ni_{49.6}$ sample (marked as a reference on the left of the figure) [26].

NiTi-20Hf HTSMA with the composition of 50-51%Ni has been manufactured and tested by using thermal cycling, heat treatments, and hardness testing [49]. For all conditions, transformation temperatures have been measured, and has been observed negative correlation between transformation temperature and Ni content up to 50.5%. However, above 50.5% Ni content, transformation temperature has increased or has been stable depending on the homogenized condition or age. Similar behavior has been observed in hardness test results. Above 50.5% Ni contents, NiTi-20Hf alloys have illustrated higher hardness results in 550°C for 3 h aging conditions

Laser powder bed fusion was extensively investigated in the shape memory alloys field, primarily NiTi alloys to adapt microstructures and create complex geometries [30]. However, according to the authors, the processing of HTSMA still remains unknown. This paper investigated the dependence of the functionality of this alloy on the effect of process parameters (PP). Microstructure and the shape memory properties of additively fabricated high-temperature NiTiHf alloys were characterized over a large range of PP (hatch spacing, scan speed, and laser power,) and correlation with energy density was found. The results will help for optimizing fabrication parameters in future works related to HTSMA.

Authors of [34], for the first time, laser welding has been used to increase the strength of Ni-rich NiTiHf HTSMA. Initial material aged at 500 °C for 3 h, then air cooled. After these heat treatments, defectless joints with conductive weld conditions were obtained. Microstructural properties, facilitated by using synchrotron X-ray diffraction and microscopy, showed that at room temperature, the melting zone consists of a single-phase martensitic structure. However, in base material melting zone consists of martensite and H-phase precipitates. Loading at constant temperatures (30 °C for martensite, 200 °C for austenite) both of phases showed equal strength and nearly perfect superelasticity.

In [41], the microstructure and mechanical properties of rapidly solidified $Ti_{50-x/2}Ni_{50-x/2}Hf_x$ (x = 0, 2, 4, 6, 8, 10, and 12 at.%) and $Ti_{50-y/2}Ni_{50-y/2}Si_y$ (y = 1, 2, 3, 5, 7, and 10 at.%) shape memory alloys (SMAs) were investigated. The sequence of the phase formation and transformations in dependence on the chemical composition is established. Rapidly solidified Ti-Ni-Hf or Ti-Ni-Si SMAs are found to show relatively high yield strength and large ductility for specific Hf or Si concentrations, which is due to the gradual disappearance of the phase transformation from austenite to twinned martensite and the predominance of the phase transformation from twinned martensite to detwinned martensite during deformation as well as to the refinement of dendrites and the precipitation of brittle intermetallic compounds. The authors show a formation of continuous series of solid solutions exists between the

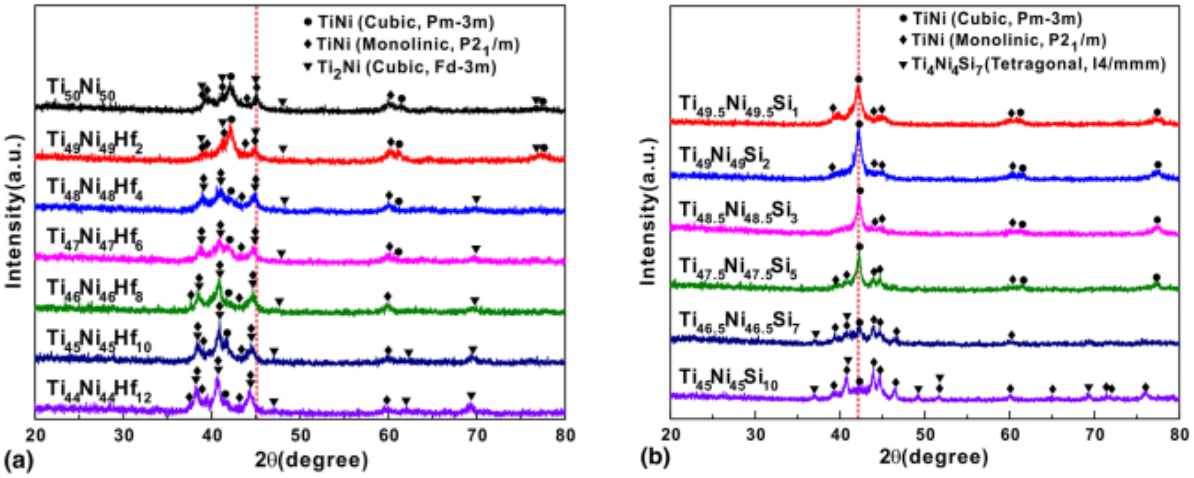

Fig. 5. Powder XRD difractoqrams of the rapidly solidified (a) Ti-Ni-Hf and (b) Ti-Ni-Si samples [41].

HfNi and NiTi phases at the high temperatures (> 1448 K) (Fig. 5).

Scanning electron microscopy, transmission electron, and X-ray diffraction (XRD) were used to investigate how the amount of zirconium (0-20%) affects to morphological features of martensitic transformation and phase composition of ternary Ni-Ti-Zr alloys [44]. In a large range of temperatures, the electrical resistivity of ternary Ni-Ti-Zr alloys was measured and critical temperatures were calculated. In addition, based on XRD data the complete diagram of martensitic transformations B2 ↔ B19' of ternary Ni-Ti-Zr HTSMA which occurs in a range between 32-50 K has been constructed. It was shown that the increasing amount of Zr in alloys results in increasing martensitic transformation temperature.

Conclusion

In this article, a number of works on nitinol-based alloys, their synthesis, heat treatment, crystal structure, and thermomechanical properties are considered and analyzed. However, the presence of a large number of unexplored problems requires further research in these areas.

Chingiz Abbas Imamalizade – doctoral student, Azerbaijan State Oil and Industry University.

[1] Shape Memory Alloy Engineering For Aerospace, Structural, and Biomedical Applications. 2^d Edition. Ed.: A.Concilio, V.Antonucci, F.Auricchio, L.Lecce, E. Sacco, 934 (2021).

[2] A. Wadood, *Brief Overview on Nitinol as Biomaterial*, Advances in Materials Science and Engineering., 4173138 (2016); https://doi.org/10.1155/2016/4173138.

[3] J.J. Mohd, M. Leary, A. Subic, M.A. Gibson, *A review of shape memory alloy research, applications and opportunities*, Materials & Design, 56, 1078 (2014); https://doi.org/10.1016/j.matdes.2013.11.084.

[4] D. Kapoor. *Nitinol for Medical Applications: A Brief Introduction to the Properties and Processing of Nickel Titanium Shape Memory Alloys and their Use in Stents*, Johnson Matthey Technology Review, 61(1), 66 (2017); http://dx.doi.org/10.1595/205651317X694524.

[5] T. Ikeda, *The use of shape memory alloys (SMAs) in aerospace engineering*. Shape Memory and Superelastic Alloys, Applications and Technologies. Woodhead Publishing Series in Metals and Surface Engineering, 125, (2011); https://doi.org/10.1533/9780857092625.2.125.

[6] M.H. Elahinia, M. Hashemi, M. Tabesh, S.B. Bhaduri, *Manufacturing and processing of NiTi implants: A reviews*, Progress in Materials Science. Sci., 57(5), 911 (2012); https://doi.org/10.1016/j.pmatsci.2011.11.001.

[7] W.J. Song, S.G. Choi, E.-S. Lee, *Prediction and Comparison of Electrochemical Machining on Shape Memory Alloy(SMA) using Deep Neural Network(DNN)*, Journal of Electrochemical Science and Technology, 10(3), 276 (2019); https://doi.org/10.33961/jecst.2019.03174.

[8] A.W. Young, R.W. Wheeler, N.A. Ley, O. Benafan, M.L.Young, *Microstructural and Thermomechanical Comparison of Ni-Rich and Ni-Lean NiTi-20 at.% Hf High Temperature Shape Memory Alloy Wires*, Shape Memory and Superelasticity, 5, 397 (2019); https://doi.org/10.1007/s40830-019-00255-0.

[9] D.E. Nicholson, O. Benafan, S.A. Padula, B.Clausen, R.Vaidynathan, *Loading Path and Control Mode Effects During Thermomechanical Cycling of Polycrystalline Shape Memory NiTi*, Shape Memory and Superelasticity, 4, 143 (2018); https://doi.org/10.1007/s40830-017-0136-x.

[10] O. Benafan, R.D. Noebe, S.A. Padula, D.J. Gaydosh, B.A. Lerch, A.Garg, R. Vaidyanathan, *Temperature-dependent behavior of a polycrystalline NiTi shape memory alloy around the transformation regime*, Scripta Materialia., 68(8), 571 (2013); https://doi.org/10.1016/j.scriptamat.2012.11.042.

[11] S. Manchiraju, D. Gaydosh, O. Benafan, R. Noebe, R. Vaidyanathan, *Thermal cycling and isothermal deformation response of polycrystalline NiTi: Simulations vs. experiment*, Acta Materialia, 59 (13), 5238 (2011); https://doi.org/10.1016/j.actamat.2011.04.063.

[12] O. Benafan, A. Garg, R.D. Noebe, H.D. Skorpenske, K. An, N. Schell, *Deformation characteristics of the intermetallic alloy 60NiTi*, Intermetallics, 82, 40 (2017); https://doi.org/10.1016/j.intermet.2016.11.003.

[13] K. Safaei, M. Nematollahi, P. Bayati, H. Dabbaghi, O. Benafan, M. Elahinia, *Torsional behavior and microstructure characterization of additively manufactured NiTi shape memory alloy tubes*, Engineering Structures, 226, 111383 (2021); https://doi.org/10.1016/j.engstruct.2020.111383.

[14] M. Nematollahi, G. Toker, S.E. Saghaian, J. Salazar, M. Mahtabi, O. Benafan, *Additive manufacturing of Ni-rich nitihf 20: Manufacturability, composition, density, and transformation behavior*, Shape Memory and Superelasticity, 5 (1), 113-124 (2019); https://doi.org/10.1007/s40830-019-00214-9.

[15] M. Elahinia, N.S. Moghaddam, A. Amerinatanzi, S. Saedi, G.P. Toker, *Additive manufacturing of NiTiHf high temperature shape memory alloy*, Scripta Materialia, 145, 90 (2018); https://doi.org/10.1016/j.scriptamat.2017.10.016.

[16] G.S. Bigelow, A. Garg, O. Benafan, R.D. Noebe, S.A. Padula II, D.J. Gaydosh, *Development and testing of a $Ni_{50.5}Ti_{27.2}Hf_{22.3}$ high temperature shape memory alloy*, Materialia, 21, 101297 (2022); https://doi.org/10.1016/j.mtla.2021.101297.

[17] O. Karakoc, K.C. Atli, O. Benafan, R.D. Noebe, I. Karaman, *Actuation fatigue performance of NiTiZr and comparison to NiTiHf high temperature shape memory alloy*s, Materials Science and Engineering, 829, 142154 (2022); https://doi.org/10.1016/j.msea.2021.142154.

[18] D.E. Nicholson, S.A. Padula II, R.D. Noebe, O. Benafan, R. Vaidyanathan, *Thermomechanical behavior of NiTiPdPt high temperature shape memory alloy springs*, Smart materials and structures 23(12), 125009 (2014); http://iopscience.iop.org/0964-1726/23/12/125009.

[19] D. Xue, D. Xue, R.Yuan, Y. Zhou, P.V. Balachandran, X. Ding, J. Sun, T. Lookman, *An informatics approach to transformation temperatures of NiTi based shape memory alloys*, Acta Materialia, 125, 532 (2017); https://doi.org/10.1016/j.actamat.2016.12.009.

[20] J. Wei, X. Chu, X. Sun, K. Xu, H. Deng, J. Chen, J., Z. Wei, M. Lei, *Machine learning in materials science*, InfoMat, 1(3), 338 (2019); https://doi.org/10.1002/inf2.12028.

[21] A. Agrawal, A. Choudhary, *Perspective: Materials informatics and big data: Realization of the "fourth paradigm" of science in materials science*, APL Mater., 4, 053208 (2016); https://doi.org/10.1063/1.4946894.

[22] S. Liu, B.B. Kappes, B.A. Ahmadi, *Physics-informed machine learning for composition –process –property design: Shape memory alloy demonstration*, Applied Materials Today, 22, 100898 (2021); https://doi.org/10.1016/j.apmt.2020.100898.

[23] H. Abedi, K.S. Baghbaderani, A. Alafghani, *Neural Network Modeling of NiTiHf Shape Memory Alloy Transformation Temperature*s, Research Squrae, 1 (2021); https://doi.org/10.21203/rs.3.rs-952869/v1.

[24] R. A. Aliev, J. Kacprzyk, W. Pedrycz, M. Jamshidi, M. Babanli, & F. M. Sadikoglu (Eds.). 14th International Conference on Theory and Application of Fuzzy Systems and Soft Computing – ICAFS-2020. Advances in Intelligent Systems and Computing. (Budva, Montenegro, 2021), p.467–471. https://doi.org/10.1007/978-3-030-64058-3_58.

[25] A.O. Kabil, Y. Kaynak, H. Saruhan, O. Benafan, *Multi-objective Optimization of Cutting Parameters for Machining Process of Ni-Rich NiTiHf High-Temperature Shape Memory Alloy Using Genetic Algorithm*, Shape Memory and Superelasticity, 7, 270 (2021); https://doi.org/10.1007/s40830-021-00328-z.

[26] S. Li, N.J.E. Adkins, S. McCain, M.M. Attallah, *Suspended droplet alloying: A new method for combinatorial alloy synthesis; Nitinolbased alloys as an example*, Journal of Alloys and Compounds., 768, 392 (2018); https://doi.org/10.1016/j.jallcom.2018.07.260.

[27] O. Benafan, G.S. Bigelow, A. Garg, R.D. Noebe, D.J. Gaydosh, R.B. Rogers, *Processing and Scalability of NiTiHf High-Temperature Shape Memory Alloys*, Shape Memory and Superelasticity, 7(1), 109 (2021); https://doi.org/10.1007/s40830-020-00306-x.

[28] G.P. Toker, M. Nematollahi, S.E. Saghaian, K.S. Baghbaderani, O. Benafan, *Shape memory behavior of NiTiHf alloys fabricated by selective laser melting*, Scripta Materialia, 178, 361 (2020); https://doi.org/10.1016/j.scriptamat.2019.11.056.

[29] O. Benafan, G.S. Bigelow, D.A. Scheiman, *Transformation behavior in NiTi-20Hf shape memory alloys – Transformation temperatures and hardness*, Scripta Materialia, 146, 251 (2018); https://doi.org/10.1016/j.scriptamat.2017.11.050.

[30] M. Nematollahi, G.P. Toker, K. Safaei, A. Hinojos, S.E. Saghaian, O. Benafan, Laser Powder Bed Fusion of NiTiHf High-Temperature Shape Memory Alloy: Effect of Process Parameters on the Thermomechanical Behavior, Metals, 10(11), 1522 (2020); https://doi.org/10.3390/met10111522.

[31] N. Babacan, M. Bilal, C. Hayrettin, J. Liu, O. Benafan, I. Karaman, *Effects of cold and warm rolling on the shape memory response of $Ni_{50}Ti_{30}Hf_{20}$ high-temperature shape memory alloy* Acta Materialia, 157, 228 (2018); https://doi.org/10.1016/j.actamat.2018.07.009.

[32] B. Amin-Ahmadi, T. Gallmeyer, J.G. Pauza, T.W. Duerig, R.D. Noebe, A.P. Stebner, *Effect of a pre-aging treatment on the mechanical behaviors of $Ni_{50.3}Ti_{49.7-x}Hf_x$ (x ≤9 at. %) shape memory alloys*, Scripta Materialia, 147, 11 (2018); https://doi.org/10.1016/j.scriptamat.2017.12.024.

[33] M. Moshref-Javadi, S.H. Seyedein, M.T. Salehi, M.R. Aboutalebi, *Age-induced multi-stage transformation in a Ni-rich NiTiHf alloy*, Acta Materialia, 61(7), 2583 (2013); https://doi.org/10.1016/j.actamat.2013.01.037.

[34] J.P. Oliveira, N. Schell, N. Zhou, L. Wood, O. Benafan, Laser welding of precipitation strengthened Ni-rich NiTiHf high temperature shape memory alloys: Microstructure and mechanical properties, Materials & Design, 162, 229 (2019); https://doi.org/10.1016/j.matdes.2018.11.053.

[35] G.S. Bigelow, O. Benafan, A. Garg, R.D. Noebe, *Effect of Hf/Zr ratio on shape memory properties of high temperature $Ni_{50.3}Ti_{29.7}$ (Hf, Zr)$_{20}$ alloys*, Scripta Materialia, 194, 113623 (2021); https://doi.org/10.1016/j.scriptamat.2020.11.008.

[36] G.S. Bigelow, O. Benafan, A. Garg, R. Lundberg, R.D. Noebe, *Effect of Composition and Applied Stress on the Transformation Behavior in Ni_xTi_{80-x} Zr_{20} Shape Memory Alloys*, Shape Memory and Superelasticity,, 5 (4), 444 (2019); https://doi.org/10.1007/s40830-019-00259-w.

[37] N.A. Ley, R.W. Wheeler, O. Benafan, M.L. Young, *Characterization of Thermomechanically Processed High-Temperature Ni-Lean NiTi–20 at.% Hf Shape Memory Wires*, Shape Memory and Superelasticity. 5, 476 (2019); https://doi.org/10.1007/s40830-019-00254-1.

[38] P.S. Chaugule, O. Benafan, J.B. le Graverend, Phase transformation and viscoplasticity coupling in polycrystalline nickel titanium-hafnium high-temperature shape memory alloys Acta Materialia, 221, 117381 (2021); https://doi.org/10.1016/j.actamat.2021.117381.

[39] O. Benafan, G.S. Bigelow, D.A. Scheiman, *Transformation behavior in NiTi-20Hf shape memory alloys Transformation temperatures and hardness*, Scripta Materialia, 146, 251 (2018); https://doi.org/10.1016/j.scriptamat.2017.11.050.

[40] N. Zarkevich, O. Benafan, J. Lawson, *Controlling properties by chemistry in doped shape memory alloys*, APS March Meeting, abstract id.S41.006 (2021).

[41] L. Han, K.K. Song , L.M. Zhang, H. Xing, B. Sarac, F. Spieckermann, T. Maity, M. Muhlbacher, L. Wang, I. Kaban, and J. Eckert, *Microstructures, Martensitic Transformation, and Mechanical Behavior of Rapidly Solidified Ti-Ni-Hf and Ti-Ni-Si Shape Memory Alloys*, Journal of Materials Engineering and Performance, 27, 1005 (2018) https://doi.org/10.1007/s11665-018-3209-x.

[42] S.M. Kornegay, M. Kapoor, B.C. Hornbuckle, D. Tweddle, M.L. Weaver, O. Benafan, G. Bigelow, R. Noebe, G. Thompson, *Influence of H-phase precipitation on the microstructure and functional and mechanical properties in a Ni-rich NiTiZr shape memory alloy*, Materials Science and Engineering: A., 801, 140401 (2021); https://doi.org/10.1016/j.msea.2020.140401.

[43] J.P. Oliveira, J. Shen, J.D. Escobar, C.A.F. Salvador, N. Schell, N. Zhou, *Laser welding of H-phase strengthened Ni-rich NiTi-20Zr high temperature shape memory alloy*, Materials & Design, 202, 109533 (2021); https://doi.org/10.1016/j.matdes.2021.109533.

[44] N.N. Kuranova, A.V. Pushin, V.G. Pushin, N.I.Z. Kourov, *Structure and Thermoelastic Martensitic Transformations in Ternary Ni–Ti–Zr Alloys with High-Temperature Shape Memory Effects*, *Physics* of *Metals* and *Metallography*, 119, 582 (2018); https://doi.org/10.1134/S0031918X18060091.

[45] A. N. Titenko, L. D. Demchenko, M. B. Babanli,I. V. Sharai, Ya. A. Titenko, *Effect of thermomechanical treatment on deformational behavior of ferromagnetic Fe–Ni–Co–Ti alloy under uniaxial tension*, Applied Nanoscience, 9, 937 (2019); https://doi.org/10.1007/s13204-019-00971-0.

[46] O Benafan, R.D. Noebe, S.A. Padula II, D.W. Brown, S. Vogel, *Thermomechanical cycling of a NiTi shape memory alloy-macroscopic response and microstructural evolution*, International Journal of Plasticity, 56, 99 (2014); https://doi.org/10.1016/j.ijplas.2014.01.006.

[47] O. Benafan, G.S. Bigelow, A. Garg, *Thermomechanical Behavior of NiTi-8Hf Low-Temperature Shape Memory Alloys*, Shape Memory and Superelasticity, 7, 314 (2021); https://doi.org/10.1007/s40830-021-00325-2.

[48] O. Karakoc, K.C. Atli, A. Evirgen, J. Pons, R. Santamarta, O. Benafan, R. Noebe, I. Karaman, *Effects of training on the thermomechanical behavior of NiTiHf and NiTiZr high temperature shape memory alloys*, Materials Science and Engineering: A., 794(5), 139857 (2020); https://doi.org/10.1016/j.msea.2020.139857.

[49] O. Benafan, A. Garg, R.D. Noebe, G.S. Bigelow, S.A. Padula II, D.J. Gaydosh, N. Schell, J.H. Mabe, R. Vaidyanathan, *Mechanical and functional behavior of a Ni-rich $Ni_{50.3}Ti_{29.7}Hf_{20}$ high temperature shape memory alloy*, Intermetallics, 50, 94 (2014); https://doi.org/10.1016/j.intermet.2014.02.006.

[50] H.E. Karaca, S.M. Saghaian ,G. Ded , H. Tobe, B. Basaran , H.J. Maier , R.D. Noebe , Y.I. Chumlyakov, Effects of nanoprecipitation on the shape memory and material properties of an Ni-rich NiTiHf high temperature shape memory alloy, Acta Materialia, 61(19), 7422 (2013); https://doi.org/10.1016/j.actamat.2013.08.048.

[51] O. Benafan, D.J. Gaydosh, *Machined helical springs from NiTiHf shape memory alloy* ,Smart Materials and Structures., 29(12), 125001(2020); https://doi.org/10.1088/1361-665X/abbec9.

[52] K.E. Kirmacioglu, Y. Kaynak, O. Benafan, *Machinability of Ni-rich NiTiHf high temperature shape memory alloy*, Smart Materials and Structures., 28(5), 055008(2019); https://doi.org/10.1088/1361-665X/ab02a2.

[53] O. Benafan, D.J. Gaydosh, *Constant-torque thermal cycling and two-way shape memory effect in $Ni_{50.3}Ti_{29.7}Hf_{20}$ torque tubes*, Smart Materials and Structures, 27(7), 075035 (2018); https://doi.org/10.1088/1361-665X/aac665.

[54] O. Benafan, R.D. Noebe, T.J. Halsmer, S.A. Padula, G.S. Bigelow, G.J. Gaydosh, A. Garg, *Constant-Strain Thermal Cycling of a $Ni_{50.3}Ti_{29.7}Hf_{20}$ High-Temperature Shape Memory Alloy*. Shape Memory and Superelasticity, 2, 218 (2016); https://doi.org/10.1007/s40830-016-0068-x.

Ч.А. Імамалізаде

Виробництво сплавів на основі нітинолу на основі сучасних технологій: короткий огляд

Азербайджанський державний університет найти та промисловості, Баку, Азербайджан, cimamelizade@gmail.com

У статті подано короткий огляд літературних даних щодо синтезу, переробки, структури, механічних властивостей і практичного застосування нітинолу та сплавів на його основі, які є перспективними функціональними матеріалами та знайшли застосування в ряді високих технологій. Для прогнозування температур фазових перетворень застосовано метод машинного навчання.

Ключові слова: сплави з пам'яттю форми, нітінол та сплави на його основі, машинне навчання, мікроструктура, термомеханічна поведінка.

PHYSICS AND CHEMISTRY OF SOLID STATE
V. 24, No. 2 (2023) pp. 348-353
Section: Physics

DOI: 10.15330/pcss.24.2.348-353

Vasyl Stefanyk Precarpathian National University

ФІЗИКА І ХІМІЯ ТВЕРДОГО ТІЛА
Т. 24, № 2 (2023) С. 348-353
Фізико-математичні науки

PACS: 61.43.Gt, 81.05.Uw, 82.47.Uv ISSN 1729-4428

S. A. Lisovska[1, 2], R. V. Ilnytskyy[1], R. P. Lisovskyy[2, 3], N. Ya. Ivanichok[1, 3], Kh. V. Bandura[2], B. I. Rachiy[1]

Structural and sorption properties of nanoporous carbon materials obtained from walnut shells

[1]*Vasyl Stefanyk Precarpathian National University, Ivano-Frankivsk, Ukraine, bogdan_rachiy@ukr.net*
[2]*Ivano-Frankivsk National Medical University, Ivano-Frankivsk, Ukraine, rlisovsky@ifnmu.edu.ua*
[3]*Joint Educational and Scientific Laboratory for Physics of Magnetic Films of G. V. Kurdyumov Institute for Metal Physics of the National Academy of Sciences of Ukraine and Vasyl Stefanyk Precarpathian National University, Ivano-Frankivsk, Ukraine, lesrom2000@gmail.com*

Using the method of low-temperature nitrogen adsorption/desorption, the porous structure of nanoporous carbon materials obtained by alkaline activation of light industry waste (walnut shells) with subsequent thermal modification was investigated. The optimal relationship between temperature and modification time has been established. It is shown that an increase in the modification temperature reduces the transition time of micropores into mesopores and leads to a decrease in the specific surface area and total pore volume. Thus, the material obtained at a modification temperature of 400 ºC and a holding time of 120 min is characterized by the maximum specific surface area of 940 m^2/g. It has been investigated that an increase in the time of temperature modification leads to an increase in specific electrical conductivity.

Keywords: nanoporous carbon material, thermochemical activation, specific surface area, pore size distribution, specific electrical conductivity.

Received 28 February 2023; Accepted 2 June 2023.

Introduction

The study of sorption properties of materials with a highly developed surface is currently receiving the greatest attention of researchers due to the wide scope of their application [1-3]. The main advantage in this type of research is precisely those materials that, along with a highly developed surface, would have such characteristics as a wide range of applications, variability between the possibility of controlling their properties both during acquisition and adjusting certain parameters in subsequent modification. Activated carbon materials obtained from raw materials of vegetable origin (wood sawdust, nuts, fruit stones, rice husks, etc.) have an undeniable advantage when used in such research. Along with the properties mentioned above, these materials also have such an important property as environmental friendliness [4]. And this property is currently the main advantage of these materials and makes them practically the main materials for research. Among the numerous advantages of this raw material, one should also include the wide-scale scope of their application: from the medical field (sorbents, blood purification, etc. [5]) to industrial applications (purification of drinking water, material for electrochemical power sources, etc. [6,7]).

The aim of the research is to obtain carbon materials based on food industry waste with controlled sorption properties and to adjust their properties using thermochemical activation for use as electrodes of electrochemical capacitors.

I. Materials and methods of research

Depending on the fields of application, researchers try to achieve specific properties of the developed surface, such as the ratio of the sizes of macro-, meso- and

micropores of carbon materials during the carbonization of raw materials. However, the correction of these ratios is usually acquired during their further modification through chemical and thermal activations. This is primarily related to the structure of the raw material, subsequent modification and composition of the precursor during chemical processing and thermal activation of the finished material [8]. Heat treatment and chemical activation usually take place at different temperature and time regimes depending on the raw material using dehydrating agents (phosphoric acid, zinc chloride, potassium hydroxide) [9].

Preparation of nanoporous carbon materials (NCM) was carried out by the method of thermochemical activation. At the first stage, mechanically crushed walnut shells were poured into an autoclave and heated to 300-350 ºC at a heating rate of 10 ºC/min and held at this temperature for 30 min. The obtained carbonate was mechanically crushed to a fraction of 250 μm and mixed with water and potassium hydroxide in a weight ratio of 1:1:0.5. The resulting mixture was stirred for 30 minutes and dried in vacuum oven at a temperature of 70-80 ºC for 48 hours. After complete drying, the obtained material was poured into an autoclave, placed in a furnace and heated to 900 ºC at a heating rate of 10 ºC/min and held at this temperature for 30 min. Cooling was carried out with the furnace turned off. After complete cooling, the carbon material was washed with distilled water to neutral pH. In this way, we obtained thermochemically activated carbon material (L). Additional thermal activation was performed to open the internal porosity and increase the specific surface area of the carbon material. At the next stage, the obtained carbon material was subjected to thermal activation in an air atmosphere. Activation was carried out at a temperature of 400 ºC for different time intervals from 30 to 240 min in steps of 30 min. The samples were numbered according to the time of thermal activation (LH30-LH240). For example, sample LH90 is a material thermally activated for 90 min at a temperature of 400 ºC. According to the described method, series of carbon materials activated at a temperature of 450 ºC (series – LD) and 500 ºC (series – LH) were obtained.

Nitrogen adsorption/desorption isotherms for evaluating the porous structure of the carbon material were obtained using a Quantachrome Autosorb Nova 2200e sorbtometer. Calculations were performed using the Brunauer-Emmet-Teller (BET) method for specific surface area, complementary Barrett-Joyner-Halenda (BJH) methods, Density Functional Theory (DFT), and the t-method for pore size distribution.

The content of chemical compounds in the studied materials was determined by burning the carbon material at a temperature of 1000 ºC. The analysis of the composition of the obtained ash was carried out using the "EXPERT 3L" alloy elemental composition analyzer.

II. Results and discussion

The basis for calculating the values of the specific surface area (S_{BET}), the specific surface area of micropores (S_{micro}) and mesopores (S_{meso}), as well as the value of the total pore volume (V_{Σ}) and the volume of micropores (V_{micro}), as well as the distribution of pores by the dimensions were the analysis of sorption isotherms [10-12]. Before the measurements, the samples were degassed at a temperature of 180 °C for 18 hours. Nitrogen adsorption/desorption isotherms for the studied carbon materials obtained by thermal treatment at a temperature of 400 °C with different exposure times of this treatment are shown in Fig. 1. All isotherms belong to the II type of isotherms according to the IUPAC classification and are characteristic of the formation of a polylayer on the surface with a high adsorption potential. A hysteresis loop is observed on almost all isotherms, which is associated with sorption processes in sub-nanopores (pore size between 0.1 and 1 nm according to the IUPAC classification [13]). The presence of a hysteresis loop for the investigated carbon materials and changes in its dimensions also indicate the presence of a relative number of mesopores. There is an open hysteresis loop, that is, a divergence of the adsorption/desorption curves in the region of low pressures for the carbonized material that was not subjected to heat treatment. It is characteristic of materials that retain the adsorbate over the entire range of relative pressures. Changes in the shape of adsorption/desorption curves indicate the development of a porous structure during heat treatment of carbon materials. Isotherms of other series with different temperatures and time of heat treatment have similar shapes, so they are not given in this paper.

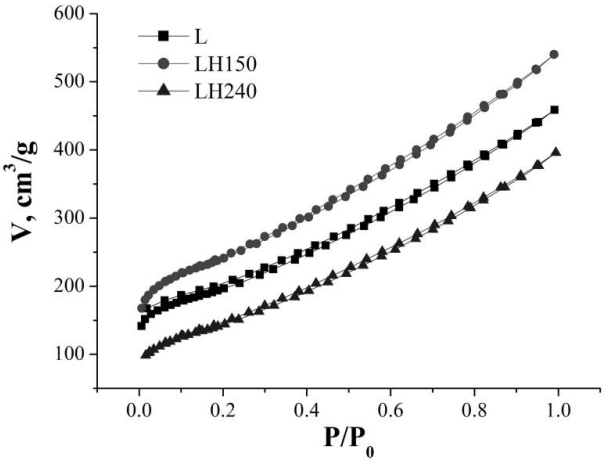

Fig. 1. Nitrogen adsorption isotherms of the obtained samples.

The parameters of the porous structure of the obtained materials are shown in the table 1. The specific surface area was determined by the BET method [14]. Several complementary methods were used to estimate the pore size distribution. The BJH method is usually used to determine the size distribution of mesopores (correctness interval is 3-60 nm), while using the desorption curve in the pressure range of (0.4-0.967) p/p_0 [15]. The mesoporous structure was developed for all the investigated materials of the LH series. The share of mesopores in the total volume of pores calculated by the t-method is 72-95 %. For samples of the LH series, the growth of micropores occurs up to 120 min, after the

Table 1.

Parameters of the porous structure of the obtained materials of the LH series

Sample	Specific surface area			V_Σ, cm^3/g	V_{micro}, cm^3/g	V_{meso}, cm^3/g	V_{micro}/V_Σ, %	V_{meso}/V_Σ, %	d, nm
	S_{BET}, m^2/g	S_{meso}, m^2/g	S_{micro}, m^2/g						
L	707	528	179	0.709	0.081	0.628	0.114	88.6	4.016
LH 30	831	460	371	0.709	0.156	0.553	0.220	78.0	3.411
LH 60	868	445	423	0.695	0.173	0.522	0.249	75.1	3.203
LH 90	897	419	478	0.708	0.196	0.512	0.277	72.3	3.156
LH 120	940	443	497	0.727	0.201	0.526	0.276	72.4	3.092
LH 150	875	636	239	0.835	0.101	0.734	0.121	87.9	3.819
LH 180	782	576	206	0.761	0.086	0.675	0.113	88.7	3.896
LH 210	707	624	83	0.764	0.039	0.725	0.051	94.9	4.32
LH 240	511	511	–	0.613	–	0.613	0.000	100.0	4.795

specified time, the total volume of micropores decreases due to their burnout and transition to mesopores, the volume fraction of which increases by 40 %. At the same time, a decrease in the total specific surface area is observed both due to the transition of mesopores into macropores and due to the combustion of carbon material (Fig. 2). A further increase in exposure time leads to an uneven redistribution of macro- and mesopores. For the sample aged for 240 min, there are practically no micropores, and the percentage of material yield by mass is 33 %. The maximum volume of mesopores is observed for materials with a heat treatment time of 150-210 min. The decrease in the percentage mass of the material for the sample of the LH series is presented in Fig. 2.

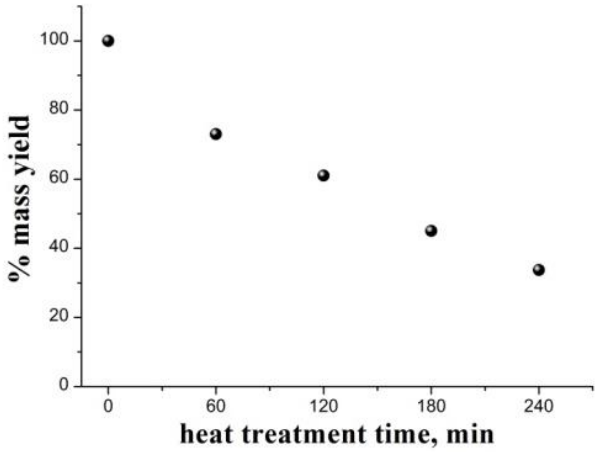

Fig. 2. Dependence of the mass of the obtained NCM on the time of temperature exposure (LH series).

For series of materials with a higher temperature of thermal modification, a decrease in the time of temperature influence on the maximum value of the specific surface area and the maximum volume of mesopores is observed. Thus, the peak value of the specific surface area with increasing activation temperature shifts toward decreasing activation time. For the LD series, the maximum value of the specific surface area is 910 m^2/g (heat treatment time 90 min), and for the LF series it is 870 m^2/g (heat treatment time 60 min). However, the maximum value of the specific surface area for higher activation temperatures is not reached.

The characteristics of the mesoporous structure were described using the BJH method. For samples of the LH series, the maximum mesopore volume in the range of V_{meso} = 0.11 – 0.12 cm^3/g is reached at 150–210 min. For practically all samples of the LH series, the maximum of the differential pore volume falls on the pores in the interval d = 3.3-3.7 nm. With the growth of the pore diameter a sharp decrease in the differential pore volume is observed, and for d = 30-60 nm in all the studied samples it changes monotonically in the interval (1-2) · 10^{-3} cm^3/g. For samples of the LD, LF series, the peak of the differential pore volume falls on a similar pore diameter interval. The maximum mesopore volume for samples of the LD and LF series is in the range of V_{meso} = 0.11-0.12 cm^3/g at 30-60 min, respectively. The dependence of the differential pore volume on their diameter for materials with the maximum value of the total pore volume in each of the series is shown in Fig. 3.

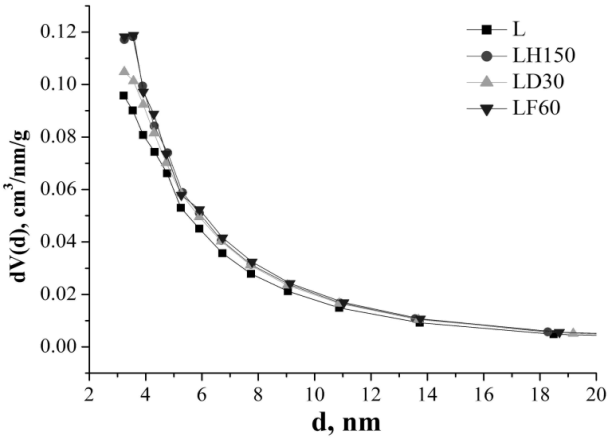

Fig. 3. Dependencies of the maximum values of the differential pore volume on the diameter for different series of the obtained materials.

To describe the size distribution of micropores, the QSDFT (Quenched Solid DFT) method of Density Functional Theory (DFT) [16] was used, which takes into account the structural heterogeneity of the surface of slit-like pores. The carbonized material is characterized by the presence of a peak in the region d=1.0-1.2 nm with a maximum d=1.1 nm (Fig. 4). A peak in the region of sub-nanopores (up to 1 nm) is clearly distinguished in the samples of the LH series, for all times of temperature exposure. With increasing temperature exposure time (up to 120 min), a peak shift from d = 0.7 nm (for sample LH-30) to d = 0.8-0.9 nm (for samples LH-90 – LH-120) is observed, which is also accompanied by an increase in the differential volume of pores (Fig. 4). That is, probably, at the given times of temperature exposure, the formation and burnout of pores of the specified diameter takes place. An increase in the time of temperature exposure leads to a monotonous decrease in the differential pore volume, and the LH-240 sample shows a wide and homogeneous micropores size distribution and a relatively low value of $dV(d) \leq 0{,}15$ $cm^3/nm/g$. Samples of the LD series (Fig. 5) are characterized by the presence of peaks in a similar range. The difference is an insignificant increase in the differential volume of pores and the formation of peaks at shorter times of temperature exposure. For samples of the LF series (Fig. 6), the peak at d = 0.9 nm is present for the sample with a temperature exposure time of 30 min. A further increase in the time of temperature exposure leads to a decrease in the differential pore volume and a shift of the peak to the region d = 0.6-0.7 nm. That is, an increase in temperature probably leads to the combustion of carbon particles, which is manifested in a decrease in the volume of sub-nanopores. Thus, the time of temperature exposure is one of the determining factors for the formation of a mesoporous structured.

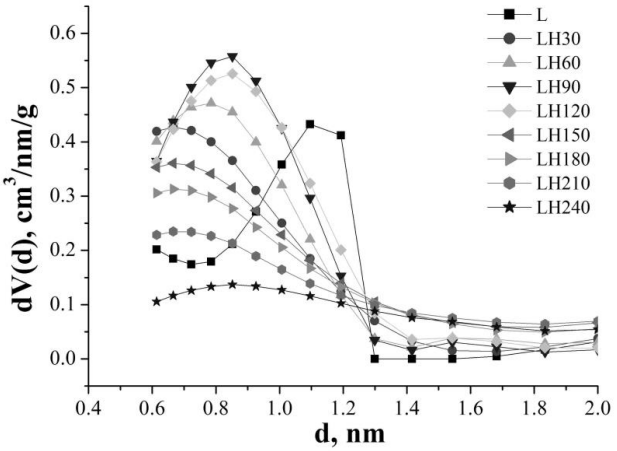

Fig. 4. Size distribution of micropores for LH series carbon materials (QSDFT method).

The dependence of the specific electrical conductivity on the time of temperature exposure is shown in Fig. 7. The carbon material was pressed at a pressure of 1.5 MPa. A further increase in pressing pressure leads to insignificant deviations in the changes in specific electrical conductivity values. An increase in the time of temperature exposure leads to an increase in specific electrical conductivity, which is probably due to a change in the structure of carbon particles, a significant burnout of the carbon material, which in turn leads to densification and arrangement of its structure.

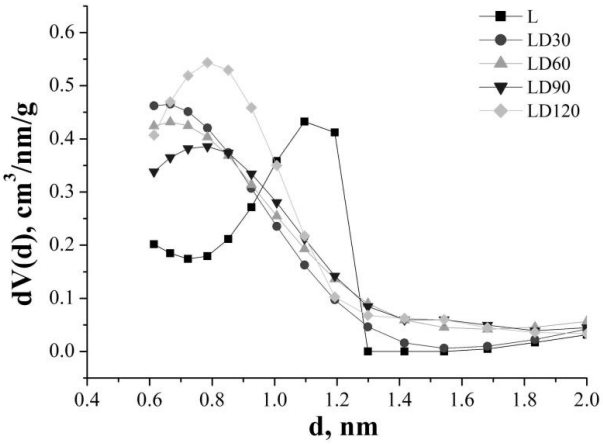

Fig 5. Micropores size distribution for LD series carbon materials (QSDFT method).

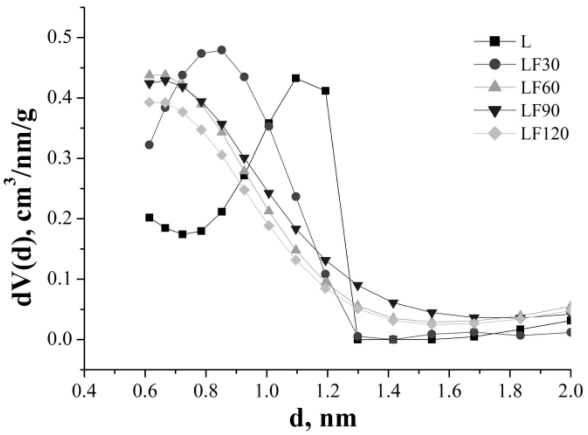

Fig. 6. Micropores size distribution for LF series carbon materials (QSDFT method).

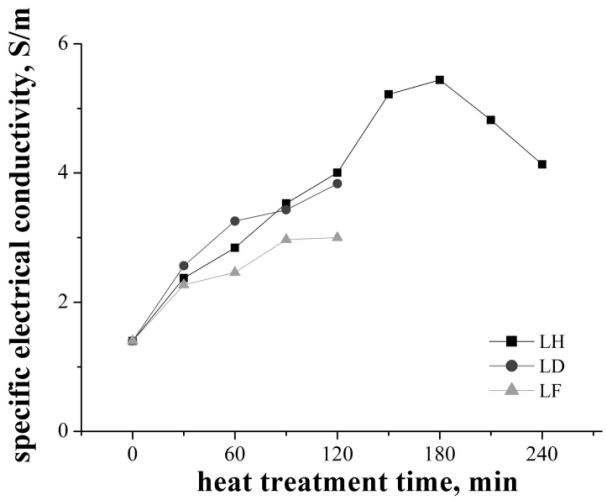

Fig. 7. Dependence of specific electrical conductivity on time of temperature exposure.

The content of chemical compounds in the obtained carbon materials was evaluated by burning it at a temperature of 1000 °C. Table 2 shows a number of existing compounds found in ash. An insignificant amount

(about 1.5%) of potassium oxide in the ash is due to the specificity of the method of obtaining porous carbon material.

Table 2.
The content of chemical compounds in carbon material

Chemical compound	The concentration of the compound in the ash, %	Mass of compound in ash, mg	The concentration of the compound in the carbon material, %
Al_2O_3	3.032	5.49	0.164
SiO_2	1.544	2.79	0.083
K_2O	27.288	49.39	1.474
CaO	15.363	27.81	0.830
Cr_2O_3	0.637	1.15	0.034
Ni_2O_3	0.224	0.41	0.012
MnO_2	0.297	0.54	0.016
Fe_2O_3	50.33	91.10	2.719
CuO	0.885	1.60	0.048
SO_3	0.248	0.45	0.013
SrO	0.095	0.17	0.005

Conclusions

The technique of obtaining nanoporous carbon material from light industry waste (wallnut shells) by thermochemical alkaline activation with subsequent temperature exposure to form an optimal pore size ratio was studied. A clear correlation was found between the volume and surface of micropores and the temperature and time of NCM modification. It was established that changing the modes of modification of carbon materials is an effective tool for regulating their porous structure, which makes it possible to obtain samples with a predetermined morphology.

It was established that an increase in the treatment temperature leads to a decrease in the maximum specific surface area from 940 m^2/g for the LH 120 sample to 870 m^2/g for the LF 60 sample and a decrease in the temperature exposure time to reach the specified peak values.

Lisovska S. A. – teacher of the specialized medical college of Ivano-Frankivsk National Medical University, PhD student of the Department of Materials Science and New Technologies, Vasyl Stefanyk Precarpathian National University;
Ilnytskyy R. V. – professor of the Department of Materials Science and New Technologies, Vasyl Stefanyk Precarpathian National University;
Lisovskyy R. P. – professor of the Department of Medical Informatics, Medical and Biological Physics, Ivano-Frankivsk National Medical University, leading specialist of Joint Educational and Scientific Laboratory for Physics of Magnetic Films of G. V. Kurdyumov Institute for Metal Physics of the National Academy of Sciences of Ukraine and Vasyl Stefanyk Precarpathian National University;
Ivanichok N. Ya. – leading specialist of Joint Educational and Scientific Laboratory for Physics of Magnetic Films of G. V. Kurdyumov Institute for Metal Physics of the National Academy of Sciences of Ukraine and Vasyl Stefanyk Precarpathian National University;
Bandura Kh. V. – assistant of the Department of Medical Informatics, Medical and Biological Physics, Ivano-Frankivsk National Medical University;
Rachiy B. I. – professor of the Department of Materials Science and New Technologies, Vasyl Stefanyk Precarpathian National University.

[1] P. Karmanova, A. P. Voznyakovsky, L. S. Kochevac, N. G. Rachkovaa, N.I. Bogdanovich, *Sorption properties of carbonized biopolymers of plant origin panel*, Carbon Resources Conversion, 6(1), 34 (2023); https://doi.org/10.1016/j.crcon.2022.10.004.
[2] M. Zgrzebnicki, A. Kałamaga, R. Wrobel, *Sorption and Textural Properties of Activated Carbon Derived from Charred Beech Wood*, Molecules, 26(24), 7604 (2021); https://doi.org/10.3390/molecules26247604.
[3] T.Y. Boychuk, I.M. Budzulyak, N.Y. Ivanichok, R.P. Lisovskiy, B.I. Rachiy, *Electrochemical properties of hybrid supercapacitors formed from nanosized spinel* $LiMn_{1.5}Fe_{0.5}O_4$, Journal of Nano- and Electronic Physics, 7 (1), 01019 (2015).
[4] S. Mandal, J. Hu, S.-Q. Shi, *A comprehensive review of hybrid supercapacitor from transition metal and industrial crop based activated carbon for energy storage applications*, Materials Today Communications, 34, 105207 (2023); https://doi.org/10.1016/j.mtcomm.2022.105207.
[5] X. Ye, Q. Fana, L. Shang, F. Ye, *Adsorptive carbon-based materials for biomedical applications*, Engineered Regeneration, 3(4), 352 (2022); https://doi.org/10.1016/j.engreg.2022.08.001.
[6] J. Suresh Babu, Bhavani Naga Prasanna, Satish Babu, Yamarthi Narasimha Rao, and Surafel Mustefa Beyan, *Environmental Applications of Sorbents, High-Flux Membranes of Carbon-Based Nanomaterials*, Adsorption Science & Technology, 2022, Article ID 8218476, 13 pages https://doi.org/10.1155/2022/8218476.
[7] B. I. Rachiy, B. K. Ostafiychuk, I. M. Budzulyak, N. Y. Ivanichok, *Specific energy characteristics of nanoporous carbon activated by orthophosphoric acid*, Journal of Nano- and Electronic Physics, 7(4), 04077 (2015).
[8] Yu. Starchuk, N. Ivanichok, I. Budzulyak, S.-V. Sklepova, O. Popovych, P. Kolkovskyi, B. Rachiy, *Electrochemical properties of nanoporous carbon material subjected to multiple chemical activation*, Fullerenes Nanotubes and Carbon, Nanostructures, 30(9), 936 (2022), https://doi.org/10.1080/1536383X.2022.2043285.
[9] I.F. Myronyuk, V.I. Mandzyuk, V.M. Sachko, R.P. Lisovsky, B.I. Rachiy, *Morphological and electrochemical properties of the lactose-derived carbon electrode materials*, Journal of Nano- and Electronic Physics, 8 (4), 04006 (2016), https://doi.org/10.21272/jnep.8(4(1)).04006.

[10] M. A. HouriehI, M. N. Alaya, M. Youssef and F. El-SejariahI, *Analysis of Nitrogen Sorption Data of Chemically Activated Carbon by the Application of Adsorption Models Based on Surface Coverage and Volume Filling of Micropores,* Adsorption Science & Technology, 17(8), 675 (1999); https://journals.sagepub.com/doi/pdf/10.1177/026361749901700806.
[11] B. K. Ostafiychuk N. Ya. Ivanichok, S.-V. S. Sklepova, O. M. Ivanichok V. O. Kotsyubynsky, P. I. Kolkovskyy, I. M. Budzulyak, R. P. Lisovskiy, *Influence of plant biomass activation conditions on the structure and electrochemical properties of nanoporous carbon material,* Materials Today: Proceedings, 62, 5712 (2022); https://doi.org/10.1016/j.matpr.2022.01.486.
[12] V. I. Mandzyuk, N. I. Nagirna, R. P. Lisovskyy, *Morphology and Electrochemical Properties of Thermal Modified Nanoporous Carbon as Electrode of Lithium Power Sources*, Journal of Nano- and Electronic Physics, 6(1), 01017 (2014).
[13] M. Thommes, K. Kaneko, A.V. Neimark, J.P. Olivier, R. Francisco, J. Rouquerol, K.S.W. Sing, *Physisorption of gases, with special reference to the evaluation of surface area and pore size distribution (IUPAC Technical Report),* Pure and Applied Chemistry 87(9-10), 1051 (2015); https://doi.org/10.1515/pac-2014-1117.
[14] S. Brunauer, P.H. Emmett, E. Teller, *Adsorption of Gases in Multimolecular Layers,* Journal of the American Chemical Society, 60(2), 309 (1938); https://doi.org/10.1021/ja01269a023.
[15] E.P. Barret, L.C. Joyner, P.P. Halenda, *The Determination of Pore Volume and Area Distributions in Porous Substances. I. Computations from Nitrogen Isotherms,* Journal of the American Chemical Society, 73(1), 373 (1951); http://dx.doi.org/10.1021/ja01145a126.
[16] P. I. Ravikovitch A. V. Neimark, *Density functional theory model of adsorption on amorphous and microporous silica materials,* Langmuir, 22, 11171 (2006); https://doi.org/10.1021/la0616146.

С. А. Лісовська[1, 2], Р. В. Ільницький[1], Р.П. Лісовський[2, 3], Н. Я. Іванічок[1, 3], Х.В. Бандура[2], Б. І. Рачій[1]

Структурно-сорбційні властивості нанопористих вуглецевих матеріалів, отриманих зі шкаралупи горіха

[1]Прикарпатський національний університет імені Василя Стефаника, Івано-Франківськ, Україна, bogdan_rachiy@ukr.net
[2]Івано-Франківський національний медичний університет, Івано-Франківськ, Україна, rlisovsky@ifnmu.edu.ua
[3]Спільна навчально-наукова лабораторія фізики магнітних плівок Інституту металофізики ім. Г.В. Курдюмова НАН України і Прикарпатського національного університету імені Василя Стефаника, Івано-Франківськ, Україна, lesrom2000@gmail.com

Методом низькотемпературної адсорбції/десорбції азоту досліджена пориста структура нанопористих вуглецевих матеріалів, отриманих лужною активацією відходів легкої промисловості (шкаралупи горіха) з подальшою термічною модифікацією. Встановлено оптимальну залежність між температурою та часом модифікації. Показано, що зростання температури модифікації зменшує час переходу мікропор в мезопори та призводить до зменшення площі питомої поверхні і загального об'єму пор. Так, максимальною питомою площею поверхні 940 м^2/г володіє матеріал, отриманий при температурі модифікації 400 ºС та часі витримки 20 хв. Досліджено, що зростання часу температурної модифікації призводить до збільшення питомої електропровідності.

Ключові слова: нанопористий вуглецевий матеріал, термохімічна активація, питома площа поверхні, розподіл пор за розмірами, питома електропровідність.

PHYSICS AND CHEMISTRY OF SOLID STATE
V. 24, No. 2 (2023) pp. 354-360
Section: Technology

DOI: 10.15330/pcss.24.2.354-360

Vasyl Stefanyk Precarpathian National University

ФІЗИКА І ХІМІЯ ТВЕРДОГО ТІЛА
Т. 24, № 2 (2023) С. 354-360
Технічні науки

PACS:75.60.Ch, 75.70.Kw, 68.37.Rt, 75.70.-i, 77.80.Dj, 76.30.Fc ISSN 1729-4428

S.I.Yushchuk[1], S.A. Yuryev[1], V.V. Moklyak[2,3]

The epitaxial iron-yttrium garnet films with homogeneous properties and narrow FMR line width

[1]*National University ''Lviv Polytechnic", Department of Physics, Lviv, Ukraine, s.o.yuryev@gmail.com*
[2]*G.V. Kurdyumov Institute for Metal Physics, N.A.S. of Ukraine, Kyiv, Ukraine ,mvvmcv@gmail.com*
[3]*Ivano-Frankivsk National Technical University of Oil and Gas, Ivano-Frankivsk, Ukraine, volodymyr.mokliak@nung.edu.ua*

The growth of iron-yttrium garnet $Y_3Fe_5O_{12}$ (YIG) films with of 1...15 μm thicknesses on single-crystal substrates of gallium-gadolinium garnet $Gd_3Ga_5O_{12}$ (GGG) was carried out using the method of liquid phase epitaxy (LPE). The influence of the composition and mass of the charge, the temperature regimes, the rates of movement and the substrate rotation on the films parameters were studied. The layered structure caused by the heterogeneity of the chemical composition in the film thickness was determined and studied. The dependence of the degree impurity of Pb^{2+} and Pt^{4+} ions in YIG films and their influence on the ferromagnetic resonance (FMR) line width ΔH on the films growth conditions was investigated. It's shown that in order to obtain by the LPE method the series of defect-free films with low magnetic losses and reproducible parameters, it's necessary to use melt-solutions of large mass (6...12 kg) and apply their additional mixing during the growth process.

Keywords: iron-yttrium garnet, ferrite-garnet films, liquid phase epitaxy, ferromagnetic resonance.

Received 16 March 2023; accepted 6 June 2023.

Introduction

The monocrystalline iron-yttrium garnet $Y_3Fe_5O_{12}$ films are a perspective material for the making of passive integrated ultrahigh-frequency (UHF) circuits working on the spin and magnetostatic waves (MSW) [1,2,3]. For these purposes is required a material with a certain set of parameters: the ferrite layer thickness (d), saturation magnetization ($4\pi M_S$), the anisotropy field, the FMR line width ΔH etc. This is achieved by selecting the optimal chemical composition of the charge and the technological process for growing high quality films with a minimum number of defects [4].

To obtain the specified working parameters of MSW devices the YIG films with a homogeneous distribution of the internal magnetic field and the narrow FMR line width are required. The narrower the FMR line width, the lower the magnetic losses. The saturation magnetization and the magnetic anisotropy field determine the value of the operating frequency. The quality of the ferrite film also depends on the homogeneities of her thickness, magnetic parameters over the area of the ferrite epitaxial structure (FES), mechanical stresses, impurities and growth defects. Most defects in YIG films are due to defects in GGG substrate [5].

In bulk YIG single crystals it is possible to obtain the FMR ΔH value of the order of 0.2...0.3 Oe. It's quite problematic to achieve such values for monocrystalline YIG films with the thickness of 1...15 μm.

The purpose of this work was to determine of the charge composition and growing conditions for obtaining of the high-quality monocrystalline YIG films, similar in magnetic parameters to bulk YIG single crystals.

I. Experimental techniques

Currently the method of liquid-phase epitaxy is the most recognized for obtaining the monocrystalline YIG films.

YIG films were grown by isothermal dipping of GGG single crystalline substrates of (111) orientation in the oversaturated melt -solution (MS) of ferrite charge using

$PbO-B_2O_3$ solvent. The ratio between of the quantity composition of components in the charge was selected taking into account the Blank-Nielson molar coefficients [6]:

$$R_1 = Fe_2O_3/Y_2O_3;$$

$$R_3 = PbO/B_2O_3; \quad (1)$$

$$R_4 = \frac{Fe_2O_3+Y_2O_3}{\Sigma \text{ oxides}}.$$

Melting of the charge, its homogenization and films growth were carried out in platinum crucibles. The saturation temperature (T_s) of the melt-solution was determined as the temperature of the beginning of film growth on the substrate.

The substrates with a diameter of 50,8 mm were cut from the GGG single crystal of cylindrical form. It's known that the GGG crystal lattice parameter a_s = 12.382 Å and for YIG a_f = 12.376 Å. The thickness of the substrates was 0.5 mm, and the density of defects on their area did not exceed 0.5 cm^{-2}. The substrates were mechanically ground and polished to 14- purity class. Such treatment does not completely eliminate the defects of the substrate surface layer. The defects appear after their etching in hot orthophosphoric acid. The presence of defects in the substrate leads to the increase ΔH parameter of YIG films to 8.2...8.9 Oe.

Therefore the substrates else were subjected to chemical-mechanical polishing using the colloidal suspension. After that, the substrates were chemically polished in orthophosphoric acid at the temperature of 438 K.

An automated installation was used for epitaxial growth. The temperature in the furnace zones was maintained with an accuracy of ±0.1 K. The thickness of the grown films was 1...15 μm. Optical interference method was used to measure their thickness. The interference pattern is formed by measuring the transmission spectra when a light stream is incident on the sample in a direction close to normal. The measurement error of the film thickness did not exceed 2 %.

The transmission spectra of FES were obtained using Specord M-40 and Specord 75 IR spectrophotometers. The line width ΔH of films was measured by the "magnetic gup" method [7] in which the area of localization of measurements is 0,4 mm. The saturation magnetization $4\pi M_s$ of films was measured using a vibrating magnetometer [8]. The structure and composition of epitaxial films were studied using an electron microscope with a Comebax X-ray microanalyzer.

II. Results of experiments and their discussion

The purpose of the technology of growing monocrystalline YIG films is to minimize to the acceptable level from the numbers of negative factors, which influence on the ΔH value, the homogeneity of ΔH over the film area, the repeatability of the main films parameters during the growth of the series films. Therefore, to obtain high-quality films suitable for practical use, it's necessary to control the composition and weight of the starting charge and the technological conditions of their growth.

For the small thicknesses of ferrite film (1...15 μm), the influence of the film-substrate (FS) transition layer and the film-air (FA) surface layer on its main parameters becomes significant. These layers have a defective structure compared to the film itself [9-11] and obviously contribute to the anisotropic properties of the film [12-16].

In the process of forming a ferro-garnet film the transition FS layer grows on the boundary between the YIG layer and the GGG substrate enriched with Ga^{3+} and Gd^{3+} ions.

These ions migrate into the melt-solution. As the result, the acid of the $Gd_3Ga_5O_{12}$ substrate in the $PbO-B_2O_3$ solvent at the beginning growth stage. The FS transition layer is a solid solution of YIG and nonmagnetic GGG. The Gd^{3+} and Ga^{3+} ions in this solid solution are introduced into the dodecahedral and tetrahedral positions of the ferro - garnet film, respectively. This transition layer has a lower saturation magnetization and a higher ΔH value than the YIG. Since Gd^{3+} ions contribute to the increase of the ΔH value through the mechanism of ionic relaxation. Consequently, the heterogeneity of the YIG film composition in the FS layer leads to the increase of the ΔH parameter.

The decrease in the FS layer of Gd^{3+} and Ga^{3+} ions carried out by means of the selected molar ratio R_3 in the charge. The experiments with the $PbO - B_2O_3$ solvent for value R_3 = 12.4; 14; 15.6; 16 showed that the degree of solubility of GGG substrates linearly increases with increasing concentration of B_2O_3 in the solvent. It is necessary to use solvents with the lower content of B_2O_3.During the films growth from the different charge compositions it was found that the most optimal for decreasing of Gd^{3+} and Ga^{3+} ions in the FS layer are MS with R_3 = 15.6.

The select of the R_4 ratio (1) was based on the need to decrease the quantity of Pb^{2+} and Pt^{4+} ions in the structure of the YIG films. The Pb^{2+} ions are introduced into the YIG film from the $PbO-B_2O_3$ solvent and Pt^{4+} ions - from the crucible material [17].The quantity of $Pb^{2+}$and Pt^{4+} ions is increases with the increase of the film growth rate, which is proportional to the overcooling degree ΔT of the MS. The ΔT is equal to the difference between the saturation temperature T_s and the film growth temperature T_g, which is lower than T_s: $\Delta T = T_s - T_g$. For each MS composition there is a growth rate at which the film has a minimum value of the ΔH parameter. The appearance of these minimums is explained by the same content of $Pb^{2+}$and Pt^{4+} ions in the YIG films. With equal in ratio of the Pb^{2+} and Pt^{4+} ions in the film, the charge compensation is realized. That eliminating is causes of the appearance of Fe^{4+} and Fe^{2+} ions in the films. The exchange of electrons between Fe^{4+} and Fe^{2+} ions leads to the increase of ΔH parameter.

The coefficient R_1 (1) should be such that only the garnet phase crystallizes from the melt - solution. From the results of phase analysis of charges it was obtained that this requirement realized when R_1 = 11...30.

The Table 1 shows the growth technological

parameters for two FES with a thickness of 5 μm and different values of ΔH.

Table 1 shows that the minimum value of ΔH = 0.22 Oe has film No. 2 with almost the same contents of lead (0.23 mass. %) and platinum (0.21 mass. %). According to the data of Table 1, it can also be observed that with the increase the growth rate to 0.54 μm/min, the concentration of lead in the YIG film increases more quickly than the concentration of platinum. As the result, the also increases the ΔH to ΔH = 0.61 Oe.

Consequently, to obtain YIG films with minimal values of ΔH, it's necessary to set the rate of their growth at which the same concentrations of Pb^{2+} and Pt^{4+} ions are generated in the films, i.e. charge compensation is created. This growth rate must be supported constant when growing a series of films.

We have found that at the substrate rotation rate with ω =100 rpm/minthe impurity of Pt^{4+} ions into the film structure increases with the increase of the overcooling degree of the MS. The concentration of Pb^{2+} ions in the YIG films also increases with increasing growth rate and decreases with decreasing of the MS overcooling degree. This means that it's possible to create such technological regimes when the platinum and lead ions in the film have certain ratio concentrations. This way it is possible to influence on the ΔH line width.

At the first moment when the substrate is introduced into the melt-solution of the liquid phase epitaxy process the diffusion border layer is formed near the substrate. Further growth of the film is caused by mass transport of garnet-forming components through this layer [18]. The thickness δ of the diffusion layer depends on the growth parameters. With a stationary substrate this layer has a maximum thickness. When the substrate rotates, its thickness decreases with increasing rotation rate:

$$\delta = 1{,}58\ D^{1/3}\ \gamma^{1/6}\ \omega^{-1/2}, \qquad (2)$$

D – diffusion coefficient; γ – kinematic viscosity; ω – the angular rotation rate.

This equation is valid if the laminar flows, arising due to convection, forms the homogeneous in thickness the flat diffusion layer along the crystallization front. The heterogeneity of the film thickness over its area influences on magnetic properties [19] and degree of practical use of the growing film.

At the growth of YIG films with the thickness of 1…15 μm using one-sided horizontal rotation of the substrate, the heterogeneity of the film thickness equal to 30...50 % and the FMR line width ΔH - > 100 % are observed (Table 2).

This heterogeneity is due to the formation of a convex diffusion layer at the crystallization front. The thickness of the diffusion layer increases to the center of the substrate. As can be seen from the Table 2 the ΔH increases with increase of the diffusion layer thickness. During reverse rotation, the shape and thickness of the diffusion layer change periodically. In this case, the heterogeneity of the film thickness over the area equal to 20...30 %, the ΔH ~ 50 %. The such periodic change is formed of a layered film structure with different lead content in the layers. Therefore, one-sided and reversed rotation of the substrate does not form a flat diffusion layer, which is necessary for growing YIG films with homogeneous parameters in over the area of film.

To include the total bulk of the melt-solution in the

Table1.

Technological parameters, contents of lead and platinum, the FMR line width of YIG films

№ of the sample	Molar coefficients			Overcooling degree ΔT, K	Growth rate fg, μm/min	Content of Pb, mass. %	Content of Pt, mass. %	FMR line width ΔH, Oe
	R_1	R_3	R_4					
1	11.698	15.606	0.08	15	0.54	0.50	0.34	0.61
2	25.0	15.603	0.13	10	0.35	0.23	0.21	0.22

Table 2.

Dependence of the ferrite film thickness and the FMR line width ΔH on the method of substrate rotation

№ of the sample	Thickness of the YIG film, μm at the distance from the edge, cm					FMR line width ΔH, Oe at the distance from the edge, cm				
	0.5	1.5	2.5	3.5	4.5	0.5	1.5	2.5	3.5	4.5
One-sided rotation of the substrate										
1	6.1	5.5	4.9	5.4	6.1	0.51	1.15	1.47	0.81	0.62
2	8.8	7.8	6.9	7.9	8.8	0.75	1.43	1.87	1.33	0.90
3	14.6	12.4	9.5	12.1	14.5	1.03	2.10	2.50	2.20	1.70
Reverse rotation of the substrate										
1	5.9	5.1	5.0	5.2	5.8	0.45	0.52	0.81	0.93	0.34
2	8.7	7.3	7.2	7.4	8.8	0.56	0.77	1.10	0.72	0.41
3	14.3	12.4	11.3	12.5	14.5	1.04	0.95	1.73	2.15	0.98
One-sided rotation of the substrate with mixer										
1	6.2	6.3	6.1	6.1	6.2	0.31	0.30	0.31	0.32	0.31
2	9.2	9.1	9.5	9.1	9.1	0.38	0.40	0.41	0.40	0.40
3	15.3	15.1	14.8	15.0	15.3	0.60	0.61	0.61	0.62	0.60

film growth process and to form a flat diffusion layer the method of additional mixing of the melt-solution with a special mixer was used. The mixer was attached to the holder substrate and rotates with substrate [20].The mixer grips fresher liquid from the depths of the crucible and moves it to the surface of the grown film. At the same time, removes the used melt-solution, which is degraded on ferro-garnet components. Table 2 shows that when using a mixer the difference of the thickness over the films area does not exceed of 4% and the value of ΔH – 8 %.

Fig. 1 shows the FMR spectra of the YIG films grown by reverse rotation (1) of the substrate and by one-sided rotation (2) of the substrate together with the mixer. From Fig. 1 we can see that the FMR spectrum of the YIG film grown using reverse rotation has a distorted shape. The FMR resonance curve (2) for the YIG film grown with the use of a mixer has good resolution.

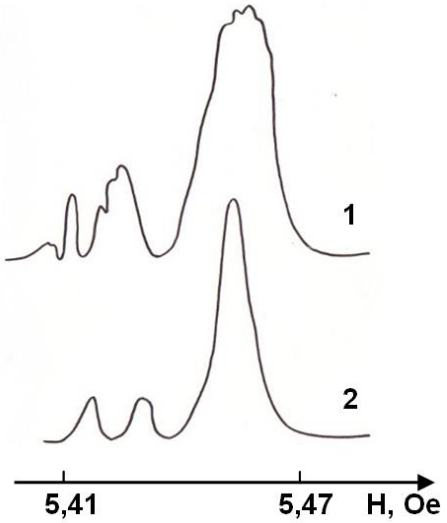

Fig. 1. The FMR spectra of the YIG films grown by reverse rotation (1) of the substrate and by one-sided rotation (2) of the substrate together with the mixer.

Using the method of X-ray spectral electron microanalysis, we studied the layered structure of YIG films of (111) orientation with thicknesses up to 5 μm. To investigate the FS and FA transition layers and their influence on the magnetic properties of the epitaxial ferrite films structures were subjected these structures to layer-by-layer chemical etching in a mixture of concentrated orthophosphoric and sulfuric acids in the temperature range 353...423 K. The etching rate was 0.05...0.20 μm/min. After each etching the ferrite film thickness, saturation magnetization, and ΔH parameter were measured.

Table 3 shows the values of $4\pi M_s$, ΔH and film thicknesses d of the three YIG films after etching in the acid mixture. Table 3 shows that the ferrite film has a layered structure in relation to the values of ΔH and $4\pi M_s$ parameters. This layered film structure is forms during the growth process. These layers have different thicknesses, are characterized by lower or higher saturation magnetization compared to YIG (for the YIG $4\pi M_s$ = 1750 Gs) and much higher values of the ΔH parameters. For example, films 1 and 3 had a magnetization of 1780 Gs. After two etchings, their magnetization decreased to 1700 Gs. The increased magnetization of the FA layer of these films is due to the presence of a large number of Pb^{2+} ions in this layer, which displace Fe^{3+} ions from the octahedral positions of the garnet. In the transition FS layers with the thickness of 0.2 μm, there are large number of Ga^{3+} ions that displace Fe^{3+} ions from the tetrahedral positions of the garnet, decreasing the magnetization to 1470 and 1510 Gs, respectively (Table 3).

As noted above, in order to decrease the etching of the $Gd_3Ga_5O_{12}$ substrate in the MS and, consequently, the decrease of Gd^{3+} and Ga^{3+} ions content in the MS, it's necessary to decrease the boron oxide content in the solvent. However, a decrease of boron oxide content in the MS, along with positive factors also has negative ones - the compositional stability of the garnet phase is decreased and the volatility of lead oxide is increases. The highly volatility of PbO also leads to significant etching of substrates and films as they are lowering or lifting out of the growth furnace. Fig. 2 shows the surface of the YIG film etched by PbO vapor. To minimize of substrates and film etching the platinum screen should be attached below the substrate to the substrate holder. In our experiments the platinum mixer served as a screen.

The dependence of the thickness of the transition layers on the technological regimes was investigated. The thicknesses of the FS and FA layers are decreased if the substrate holder together with the mixer rotates at a frequency of ~ 50 rpm/min during the dipping of the substrate into the MS and the FES drawing from the MS after the end of the growing process. This can be explained by the removal of Gd^{3+}, Ga^{3+} and Pb^{2+} ions from the substrate by the upward flow of fresh MS and supply the YIG components to the substrate.

The thickness of the FA layer also dependent on the rate of vertical movement of the substrate during its dipping and post growth removal from the melt-solution. Experiments have shown that the removal of FES from the

Table 3.

Thicknesses and magnetic parameters of three samples of YIG films during the etching process

№ 1	d, μm	4.1	3.2	2.4	1.5	0.8	0.5	0.2
	ΔH, Oe	0.9	0.83	0.80	0.64	0.73	1.40	2.11
	$4\pi M_s$, Gs	1780	1780	1700	1710	1650	1600	1470
№ 2	d, μm	3.8	3.0	2.2	1.4	0.7	0.6	0.4
	ΔH, Oe	0.80	0.85	0.71	0.47	0.7	1.34	1.92
	$4\pi M_s$, Gs	1740	1710	1680	1590	1530	1460	1390
№ 3	d, μm	3.7	2.8	1.9	1.2	0.6	0.4	0.3
	ΔH, Oe	1.10	1.00	0.86	0.78	0.93	1.38	2.14
	$4\pi M_s$, Gs	1780	1780	1700	1720	1670	1580	1510

MS at a rate of ~ 20 cm/min minimizes the thickness of the surface layer of the FA and the change in the parameter ΔH.

When growing the series of films from the one MS the following reasons cause the depletion of the MS:

a) lead evaporation during homogenization and growth processes;

b) depletion of the MS into garnet-forming components during of the film growth process;

c) reducing of MS quantity due to the formation of droplets and small melt marks on the FES and equipment.

Based on our research, it was concluded that when growing YIG films it's necessary to use a large mass of MS to minimize the change in the saturation temperature. This makes it possible to grow a larger number of films with identical parameters from one MS.

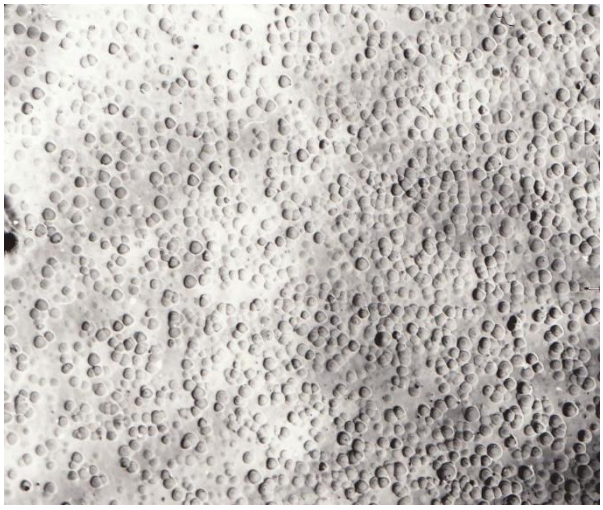

Fig. 2. The surface of the YIG film etchedby PbO vapor, zoom: x200.

Fig. 3 shows the influence of MS depletion on the ΔH of YIG films grown from the melt-solution of 6 kg. It can be seen that the ΔH increases with the number N of grown films. This increase of ΔH is associated with a change in the starting ratio between the quantities of Fe_2O_3 and Y_2O_3 oxides in the melt-solution. This ratio which given by the coefficients R_1 and R_4, leading to a change in the growth parameters (T_S, T_g, ΔT, f_g) and the increase in the content of Pb^{2+} and Pt^{4+} ions in the film structure. The greater of the MS mass the greater the numbers N of films with similar parameters can be grown. The research results showed that the most favorable charge for growing the YIG films with the thickness of up to 15 μm and a diameter of 50,8 mm is a charge with the mass of 12.0 kg.

As the result of the research, the optimal weight composition of the melt-solution in which the solubility of GGG at growing temperatures is insignificant:
PbO – 90.34 %; B_2O_3 – 1.81 %; Fe_2O_3 – 7.13%; Y_2O_3 – 0.72 %. The YIG films with a thickness of 1...10 μm grown from this melt-solution on GGG substrates with a diameter of 50,8 mm have a FMR line width ΔH = 0.3...0.5 Oe and are suitable for use in microwave devices.

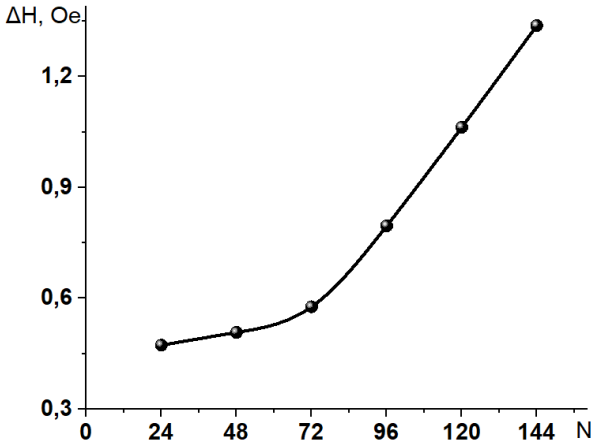

Fig 3. The dependence of the ΔH FMR line width on the number N of grown films.

Conclusions

The optimal composition of the charge for growing YIG films by liquid-phase epitaxy is determined by the molar coefficients R_1, R_3 and R_4, which must have values: $11 \le R_1 \le 30$; $R_3 = 15.6$ and $R_4 = 0.13$.

When growing a series of YIG films with similar parameters, it's necessary to use melt solution of large mass (6...12 kg) with a high content of garnet-forming oxides and the use additional mixing.

To decrease the concentration of lead in the YIG films it's necessary to grown the films at small overcooling.

The film-substrate layer is enriched with Ga^{3+} and Gd^{3+} ions and the surface layer of the YIG film is enriched with Pb^{2+} ions. Transition layers have different magnetizations from the main YIG film and have a higher FMR line width ΔH.

To obtain YIG films with narrow values of ΔH it is necessary to set the growth rate at which similar concentrations of Pb^{2+} and Pt^{4+} ions are formed in the films.

The use of additional mixing of the melt-solution during the growing process decrease the thickness heterogeneity to 4 % and the ΔH to 8 %.

Yushchuk S.I. – Doctor of Technical Sciences, Professor, Professor of the Department of General Physics, Institute of Applied Mathematics and Fundamental Sciences, National University "Lviv Polytechnic";
Yur`ev S.A. – PhD, Docent, Associate Professor of the Department of General Physics, Institute of Applied Mathematics and Fundamental Sciences, National University "Lviv Polytechnic";
Moklyak V.V.– Doctor of Physical and Mathematical Sciences, Senior Research, Leading Researcher of Laboratory of Magnetic Film PhysicsG.V. Kurdyumov Institute for Metal Physics, N.A.S. of Ukraine, Professor of the Department of General and Applied Physics, Institute of Architecture, Construction and Power Engineering, Ivano-Frankivsk National Technical University of Oil and Gas.

[1] A.G. Gurevich, G.A. Melkov, Magnetic vibrations and waves (Nauka, Moscow, 1994).
[2] L.V. Lutsev, A.M. Korovin, V.E. Bursian, S.V. Gastev, V.V. Fedorov, S.M. Suturin, N.S. Sokolov, *Low-relaxation spin waves in laser-molecular-beam epitaxy grown nanosized yttrium iron garnet films*, Appl. Phys. Lett., 108 (18), 182402, (2016); https://doi.org/10.1063/1.4948304.
[3] Y.V. Khivintsev, V.K. Sakharov, A.V. Kozhevnikov, G.M. Dudko, Y.A. Filimonov, A. Khitun, *Spin waves in YIG based magnonic networks: Design and technological aspects*, J. Magn. Magn. Mater., 545, 168754, (2022); https://doi.org/10.1016/j.jmmm.2021.168754.
[4] S.I. Yushchuk, S.A. Yur'ev, P.S. Kostyuk, V.K. Bondar, *Application of Epitaxial Garnet Ferrite Structures in Microwave Electronics*, Tekhn. Konstr. Elektron. Appar., 57, 22 (2005).
[5] S.I. Yushchuk, P.S. Kostyuk, V.I. Loboyko, *The influence of substrates on the ferromagnetic resonance line width of iron- yttrium garnet epitaxial films*, Inorganic Materials, 38 (2), 233 (2002).
[6] [S.L. Blank, J.W. Nielson, *The growth of magnetic garnets by liquid phase epitaxy*, Journ. Cryst. Growth, 17, 302 (1972).
[7] S.I. Yushchuk, S.A. Yur'ev, P.S. Kostyuk, V.I. Nikolaychuk, *Aproximate and nondestructive quality control of epitaxial ferrogarnet films*, Instr. and Exp. Techniq, 54 (5), 712 (2011); https://doi.org/10.1134/S0020441211050083.
[8] S.I. Yushchuk, S.O. Yuryev, I.R. Zachek, V.V. Moklyak, *Diagnostics of Ferrogarnet Films Magnetization*, Physics and Chemistry of Solid State, 15 (3), 643 (2014).
[9] V.V. Moklyak, *Features Crystal Structure LaGa - Substituted Epitaxial Films Yttrium Iron Garnet. Determination of Defects,*Physics and Chemistry of Solid State, 16 (1), 68 (2015); https://doi.org/10.15330/pcss.16.1.68-73.
[10] A.O. Kotsyubynsky, V.V. Moklyak, I.M. Fodchuk, *The Magnetic Microstructure of YIG / GGG Films: Mossbauer Studies in the External Magnetic Fields*, Physics and Chemistry of Solid State, 20 (2), 202 (2019); https://doi.org/10.15330/pcss.20.2.202-208.
[11] I. Fodchuk, I. Hutsuliak, V. Dovganyuk, A. Kuzmin, Y. Roman, M. Solodkyi, P. Pynuk, P. Lytvyn, O. Gudymenko, I. Syvorotka, M. Barchuk, Fifteenth International Conference on Correlation Optics (Chernivtsi, Ukraine, 2021), p. 408; https://doi.org/10.1117/12.2615833.
[12] V.V. Moklyak, *Evaluation of structural perfection of epitaxial films yttrium iron garnet*, Journal of Surface Physics and Engineering, 13 (1), 34 (2015); https://periodicals.karazin.ua/pse/article/download/4492/4062.
[13] V.V. Moklyak, *A study of magnetic and electronic hyperfine interactions in epitaxial film of yttrium-iron garnet by the method of conversion electron Mössbauer spectroscopy*. Russian Microelectronics, 45, 587 (2016); https://doi.org/10.1134/S1063739716080114.
[14] A. O. Kotsyubynsky, V. V. Moklyak, I. M. Fodchuk, V. O. Kotsyubynsky, P. M. Lytvyn, A. B. Grubyak, *Magnetic Microstructure of Epitaxial Films of LaGa-Substituted Yttrium Iron Garnet*,Metallofiz. Noveishie Tekhnol.,41 (4), 529 (2019); https://doi.org/10.15407/mfint.41.04.0529.
[15] M.A. Popov, I.V. Zavislyak, Measurements of the Cubic Anisotropy Field in the (111) Thin Magnetic Films. IEEE 3rd Ukraine Conference on Electrical and Computer Engineering (UKRCON, Lviv, Ukraine, 2021), p. 27 https://doi.org/10.1109/UKRCON53503.2021.9575262.
[16] V. Koronovskyy, Y. Vakyla, *Magnetoelectric properties of micromagnetic structural inhomogeneities of ferrite garnet films with uniaxial magnetic anisotropy*, Ferroelectrics, 577 (1), 214 (2021); https://doi.org/10.1080/00150193.2021.1916364.
[17] V.G. Kostishyn, V.V. Medved, L.M. Letyuk, *Magnetic microstructure and properties of $Y_3Fe_5O_{12}$ epitaxial films witn the various contents of Pb ions*, J. Magn. Magn. Mater., 215, 519 (2000).
[18] A. Eschenfelder, Physics and Technique of Cylindrical Magnetic Domains: Translated from English (Mir, Moscow, 1983).
[19] Y. Rao, D. Zhang, H. Zhang, L. Jin, Q. Yang, Z. Zhong, M. Li, C. Hong, B.o. Ma, *Thickness dependence of magnetic properties in submicron yttrium iron garnet films*, Journal of Physics D: Applied Physics, 51 (43), 435001 (2018); https://doi.org/10.1088/1361-6463/aade43.
[20] Device for the growth of monocrystalline films of iron- yttrium garnet. A.c. № 1137785 (1983), authors: P.S. Kostyuk, N.I. Buben, L.M. Letyuk, O.D. Lototsky, P.A. Matskevich, S.I. Khomin.

С.І. Ющук[1], С.А. Юр'єв[1], В.В. Мокляк[2,3]

Епітаксійні плівки залізо-ітрієвого гранату з однорідними властивостями та вузькою шириною лінії ФМР

*[1]Національний університет "Львівська політехніка", фізичний факультет,Львів, Україна*s.o.yuryev@gmail.com
[2]Інститут металофізики ім. Г.В. Курдюмова, НАН України, Київ, Україна, mvvmcv@gmail.com
[3]Івано-Франківський національний технічний університет нафти і газу, Івано-Франківськ, Україна,
volodymyr.mokliak@nung.edu.ua

Методом рідкофазної епітаксії (РФЕ) проведено вирощування плівок залізо-ітрієвого гранату $Y_3Fe_5O_{12}$ (YIG) товщиною 1...15 мкм на монокристалічних підкладках галій-гадолінієвого гранату $Gd_3Ga_5O_{12}$ (GGG). Досліджено вплив складу та маси шихти, температурних режимів, швидкостей руху та обертання підкладки на параметри плівок. Визначено та досліджено шарувату структуру, зумовлену неоднорідністю хімічного складу в товщині плівки. Досліджено залежність ступеня забруднення іонів Pb^{2+} та Pt^{4+} у плівках YIG та їх вплив на ширину лінії феромагнітного резонансу (ФМР) ΔH від умов росту плівок. Показано, що для отримання методом РФЕ серії бездефектних плівок з малими магнітними втратами та відтворюваними параметрами необхідно використовувати розчини-розплави великої маси (6...12 кг) та застосовувати їх додаткове змішування під час процесу росту.

Ключові слова: залізо-іттрієвий гранат, ферит-гранатові плівки, рідкофазна епітаксія, феромагнітний резонанс.

PHYSICS AND CHEMISTRY OF SOLID STATE
V. 24, No. 2 (2023) pp. 361-366
Section: Chemistry

DOI: 10.15330/pcss.24.2.361-366

Vasyl Stefanyk Precarpathian National University

ФІЗИКА І ХІМІЯ ТВЕРДОГО ТІЛА
Т. 24, № 2 (2023) С. 361-366
Хімічні науки

UDC 546+548.734+669.017.1 ISSN 1729-4428

L. Zinko, G. Nychyporuk, O. Matselko, R. Gladyshevskii

The ternary system Hf–Re–Al at 1000°C

Ivan Franko National University of Lviv, Lviv, Ukraine, lianazinko@gmail.com

The interaction of the components in the Hf–Re–Al system was investigated by X-ray powder diffraction and scanning electron microscopy with energy-dispersive X-ray spectroscopy. The isothermal section of the phase diagram at 1000 °C was constructed in the full concentration range. A new ternary compound ~$Hf_5Re_2Al_2$, isostructural with Ti_5Ga_4 (*hP*18, *P*6$_3$/*mcm*), and two extended solid solutions Hf(Re,Al)$_2$ were found.

Keywords: hafnium, rhenium, aluminum, X-ray powder diffraction, energy-dispersive X-ray spectroscopy, phase diagram, isothermal section, crystal structure.

Received 18 February 2023; Accepted 20 June 2023.

Introduction

Ternary systems involving *d*-elements of groups IV and VII and *p*-elements of group III of the periodic table have been studied for more than 50 years. Isothermal sections of the phase diagrams have been constructed for the Ti–Mn–B [1], Zr–Mn–B [2], Ti–Re–B [3], Hf–Re–B [4], Ti–Mn–Al [5-8], Ti–Mn–Ga [9], Zr–Mn–Ga [9, 10], Hf–Mn–Ga [10, 11], and Zr–Mn–In [12, 13] systems. T^{IV}–T^{VII}–M^{III} systems are characterized by no or few ternary compounds [14-17]. Some of the systems have been investigated for the formation of compounds of particular compositions, isostructural to known types. Information about the compounds found in the systems {Ti, Zr, Hf}–{Re, Mn}–{B, Al, Ga, In} is summarized in Table 1. Other T^{IV}–T^{VII}–M^{III} systems, probably due to the

Table 1.

Ternary compounds in T^{IV}–T^{VII}–M^{III} systems [17]

System	Phase	Structure type	Pearson symbol	Space group
Ti–Re–B	Ti_2ReB_2	Mo_2FeB_2	*tP*10	*P*4/*mbm*
Zr–Re–B	Zr_9Re_4B	Hf_9Mo_4B	*hP*28	*P*6$_3$/*mmc*
Hf–Re–B	Hf_9Re_4B	Hf_9Mo_4B	*hP*28	*P*6$_3$/*mmc*
Ti–Mn–Al	$Ti_{7.25}Mn_{7.25}Al_{14.5}$	$Mg_6Cu_{16}Si_7$	*cF*116	*Fm*-3*m*
Zr–Mn–Al	$ZrMn_6Al_6$	$ThMn_{12}$	*tI*26	*I*4/*mmm*
Ti–Mn–Ga	$TiMn_{0.5}Ga_{2.5}$	Cu_3Au	*cP*4	*Pm*-3*m*
	$Ti_{2.75}Mn_{3.25}Ga_5$	Ti_6Sn_5	*hP*22	*P*6$_3$/*mmc*
Zr–Mn–Ga	$Zr_6Mn_{10.5}Ga_{12.5}$	Th_6Mn_{23}	*cF*116	*Fm*-3*m*
	$ZrMn_{0.5}Ga_{2.5}$	Cu_3Au	*cP*4	*Pm*-3*m*
	$Zr_3Mn_2Ga_6$	$Hf_3Mn_2Ga_6$	*oP*22	*Pmmn*
	$Zr_3Mn_2Ga_4$	$Zr_3V_2Ga_4$	*oP*72	*Pnma*
Hf–Mn–Ga	$HfMnGa_2$	$HfFeGa_2$	*oP*48	*Pnma*
	$Hf_3Mn_2Ga_6$	$Hf_3Mn_2Ga_6$	*oP*22	*Pmmn*
	$Hf_3Mn_2Ga_4$	$Zr_3V_2Ga_4$	*oP*72	*Pnma*
Zr–Mn–In	$ZrMn_{0.7}In_{2.3}$	Cu_3Au	*cP*4	*Pm*-3*m*

difference between the melting temperatures of the components and the complexity of the synthesis, remain little studied.

The aim of this work was to investigate the interaction of the components in the Hf–Re–Al system at 1000 °C.

It should be noted that the binary systems Hf–Re, Hf–Al, and Re–Al, which border the ternary system under investigation, have been studied quite thoroughly. The phase diagrams have been constructed [18] and the crystal structures of several compounds have been determined [17].

I. Experimental

The interaction of the components in the Hf–Re–Al system was investigated on 2 binary and 35 ternary samples. The alloys were synthesized from high-purity metals (Hf ≥ 99.9 mass %, Re ≥ 99.9 mass % (pressed pellets), Al ≥ 99.999 mass %) by arc melting with a tungsten electrode, a water-cooled copper hearth and a Ti getter, under an argon atmosphere. After the synthesis, the ingots were sealed in quartz ampoules under vacuum, annealed at 1000 °C for 1 week and quenched into cold water. Phase analysis and structure refinements were carried out using X-ray powder diffraction (XRPD) data collected on diffractometers DRON-2.0M (Fe $K\alpha$ radiation) and STOE Stadi P (Cu $K\alpha_1$ radiation). The phase analysis was performed using Powder Cell [19] and STOE WinXPOW [20] programs. The profile and structural parameters were refined by the Rietveld method, using the WinCSD [21] program packages. The overall compositions of the samples and of the individual phases, in particular for the determination of the solubilities of the third component in the binary phases, were investigated by means of energy-dispersive X-ray spectroscopy (EDXS; scanning electron microscope Tescan Vega 3 LMU equipped with an X-MaxN^{20} silicon drift detector).

II. Results and discussion

As a result of the phase analysis by X-ray diffraction and EDXS of the samples of the Hf–Re–Al system at 1000°C, we confirmed the existence of 13 of the 20 known binary compounds, the compositions and crystallographic parameters of which are given in Table 2. The results are in good agreement with literature data on the interaction of the components and phase diagrams of the binary systems Hf–Re, Hf–Al, and Re–Al [18, 22-25].

According to the results of the local X-ray spectral analysis, the binary compounds $HfAl_3$, Hf_2Al_3, HfAl, Hf_4Al_3, Hf_3Al_2, Hf_2Al, and $Re_{14}Al_{54.75}$ do not dissolve significant amounts of the third component. The maximum solubility of Hf in the compounds Re_4Al_{11} and Re_2Al is ~5 at.%. Approximately the same amount of Al is soluble in the compound $Hf_{21}Re_{25}$.

The formation of two extended solid solutions based on the compounds $HfRe_2$ (a certain region of homogeneity exists) and $HfAl_2$ is expected, given the isostructurality of the parent compounds (see Table 2) and the similar sizes of the rhenium and aluminum atoms (r_{Hf} = 0.1564, r_{Re} = 0.1370, r_{Al} = 0.1431 nm [26]). A continuous series

Table 2.

Crystallographic parameters of binary compounds in the Hf–Re, Re–Al, Hf–Al systems [17] (binary phases stable at 1000 °C are highlighted)

Compound	Structure type	Pearson symbol	Space group	Cell parameters, nm		
				a	*b*	*c*
$Hf_{21}Re_{25}$	$Zr_{21}Re_{25}$	*hR*276	*R*-3*c*	2.5773	–	0.8760
$HfRe_2$	$MgZn_2$	*hP*12	*P*6$_3$/*mmc*	0.5239	–	0.8584
Hf_5Re_{24}	Ti_5Re_{24}	*cI*58	*I*-43*m*	0.9708	–	–
Re_2Al	$CuZr_2$	*tI*6	*I*4/*mmm*	0.29802	–	0.95796
ReAl	CsCl	*cP*2	*Pm*-3*m*	0.288	–	–
$Re_{1.8}Al_{22}$	$Re(Re_{0.4}Al_{0.6})_2Al$	*tP*4	*P*4/*mmm*	0.30785	–	0.59515
Re_4Al_{11}	Mn_4Al_{11}	*aP*15	*P*-1	0.5172	0.5154	0.8959
				α = 74.83°; β = 90.43°; γ = 80.24°		
$Re_{14}Al_{54.75}$	$Re_{14}Al_{54.75}$	*aP*71	*P*-1	0.5159	0.9106	2.3755
				α = 100.94°; β = 90.30°; γ = 93.00°		
$Re_8Al_{32.07}$	$Re_8Al_{32.07}$	*aP*43	*P*-1	0.5153	0.90782	1.3727
				α = 96.852°; β = 95.521°; γ = 92.392°		
$ReAl_6$	$MnAl_6$	*oS*28	*Cmcm*	0.7599	0.6606	0.9029
$ReAl_{12}$	WAl_{12}	*cI*26	*Im*-3	0.7527	–	–
$HfAl_3$ rt	$ZrAl_3$	*tI*16	*I*4/*mmm*	0.3989	–	1.7155
$HfAl_3$ ht	$TiAl_3$	*tI*8	*I*4/*mmm*	0.3893	–	0.8925
$HfAl_2$	$MgZn_2$	*hP*12	*P*6$_3$/*mmc*	0.525	–	0.868
Hf_2Al_3	Zr_2Al_3	*oF*40	*Fdd*2	0.9529	1.3763	0.5522
HfAl	TlI	*oS*8	*Cmcm*	0.3253	1.0822	0.4280
Hf_4Al_3	Zr_4Al_3	*hP*7	*P*6/*mmm*	0.5334	–	0.5429
Hf_3Al_2	Zr_3Al_2	*tP*20	*P*4$_2$/*mnm*	0.7535	–	0.6906
Hf_5Al_3	Mn_5Si_3	*hP*16	*P*6$_3$/*mcm*	0.8052	–	0.5690
Hf_2Al	$CuAl_2$	*tI*12	*I*4/*mcm*	0.6776	–	0.5372

of solid solutions is likely to form at higher temperatures.

At the temperature of the study, in the region of high hafnium content in samples with the element ratio Hf:Re:Al = 9:4:1 according to the EDXS analysis, the existence of a new compound of approximate composition ~$Hf_5Re_2Al_2$, isostructural with the compound Ti_5Ga_4 (*hP*18, $P6_3/mcm$) [27], was discovered. A detailed description of this compound will be the subject of a separate publication.

Table 3 shows the compositions, and Fig. 1 presents

Table 3.

Compositions of the samples shown in Fig. 1

Sample	Composition		Sample	Composition	
	nominal	from EDXS		nominal	from EDXS
1	$Hf_{10}Re_{80}Al_{10}$	$Hf_{11.0(5)}Re_{86.2(5)}Al_{2.8(7)}$	6	$Hf_{25}Re_{30}Al_{45}$	$Hf_{28.0(4)}Re_{33.7(4)}Al_{38.3(9)}$
2	$Hf_{15}Re_{40}Al_{45}$	$Hf_{13.4(3)}Re_{40.5(2)}Al_{46.1(8)}$	7	$Hf_{40}Re_{15}Al_{45}$	$Hf_{42.1(5)}Re_{10.6(5)}Al_{47.4(8)}$
3	$Hf_{20}Re_{40}Al_{40}$	$Hf_{22.1(6)}Re_{49.5(6)}Al_{28.4(9)}$	8	$Hf_{50}Re_{30}Al_{20}$	$Hf_{53.3(8)}Re_{28.8(8)}Al_{17.9(9)}$
4	$Hf_{25}Re_{10}Al_{65}$	$Hf_{22.2(2)}Re_{8.4(2)}Al_{69.4(8)}$	9	$Hf_{75}Re_{10}Al_{15}$	$Hf_{73.4(7)}Re_{11.3(7)}Al_{15.3(6)}$
5	$Hf_{20}Re_{65}Al_{15}$	$Hf_{25.9(7)}Re_{67.4(6)}Al_{6.7(9)}$			

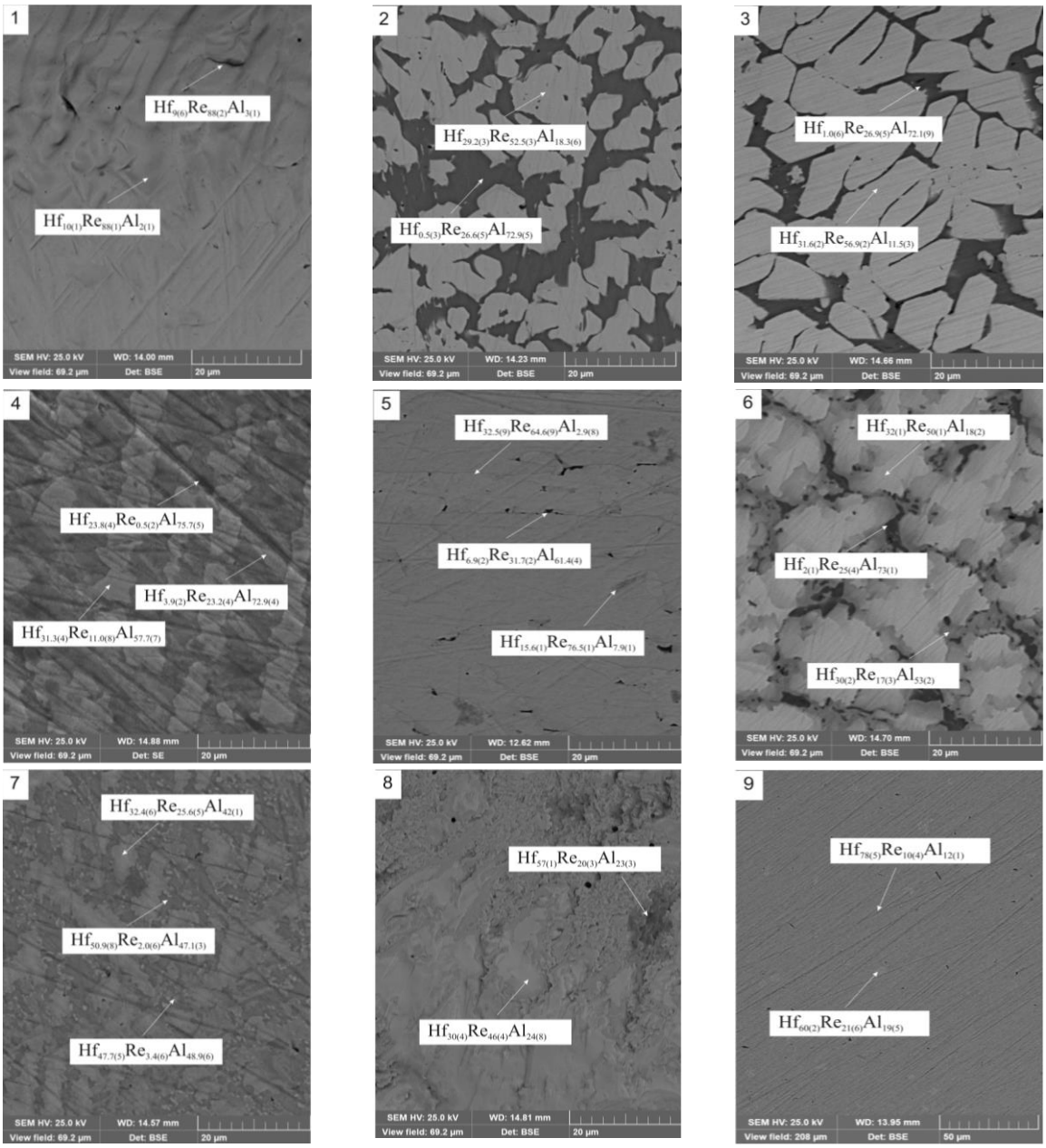

Fig. 1. Microstructures of selected samples and compositions of the detected phases.

Table 4.
Results of the phase analysis of the samples shown in Fig. 1, compositions from EDXS, cell parameters from XRPD

Sample	Phase	Pearson symbol, space group	Cell parameters, nm		
			a	*b*	*c*
1	**Hf_5Re_{24}** $Hf_{10(1)}Re_{88(1)}Al_{2(1)}$	*cI*58, *I*-43*m*	0.96621(3)	–	–
	$Hf_{9(6)}Re_{88(2)}Al_{3(1)}$	not detected by XRPD			
2	**$Hf(Re,Al)_2$** $Hf_{29.2(3)}Re_{52.5(3)}Al_{18.3(6)}$	*hP*12, *P*6$_3$/*mmc*	0.52294(3)	–	0.85248(9)
	Hf_5Re_{24}	*cI*58, *I*-43*m*	0.96694(9)	–	–
	Re_4Al_{11} $Hf_{0.5(3)}Re_{26.6(5)}Al_{72.9(5)}$	*aP*15, *P*-1	0.5213(2)	0.5132(2)	0.9010(3)
			$\alpha = 74.98(2)°$; $\beta = 91.28(3)°$; $\gamma = 80.32(3)°$		
3	**$Hf(Re,Al)_2$** $Hf_{31.6(2)}Re_{56.9(2)}Al_{11.5(3)}$	*hP*12, *P*6$_3$/*mmc*	0.52327(2)	–	0.85345(4)
	Re_4Al_{11} $Hf_{1.0(6)}Re_{26.9(5)}Al_{72.1(9)}$	not detected by XRPD			
4	**$Hf(Al,Re)_2$** $Hf_{31.3(4)}Re_{11.0(8)}Al_{57.7(7)}$	*hP*12, *P*6$_3$/*mmc*	0.52573(3)	–	0.85710(7)
	$HfAl_3$ rt $Hf_{23.8(4)}Re_{0.5(2)}Al_{75.7(5)}$	*tI*16, *I*4/*mmm*	0.39907(3)	–	1.7164(2)
	Re_4Al_{11} $Hf_{3.9(2)}Re_{23.2(4)}Al_{72.9(4)}$	*aP*15, *P*-1, >5 % by XRPD			
5	**$Hf(Re,Al)_2$** $Hf_{32.5(9)}Re_{64.6(9)}Al_{2.9(8)}$	*hP*12, *P*6$_3$/*mmc*	0.52450(3)	–	0.85774(9)
	Hf_5Re_{24} $Hf_{15.6(1)}Re_{76.5(1)}Al_{7.9(1)}$	*cI*58, *I*-43*m*	0.97154(8)	–	–
	$Hf_{6.9(2)}Re_{31.7(2)}Al_{61.4(4)}$	not detected by XRPD			
6	**$Hf(Re,Al)_2$** $Hf_{32(1)}Re_{50(1)}Al_{18(2)}$	*hP*12, *P*6$_3$/*mmc*	0.52485(3)	–	0.85404(8)
	$Hf(Al,Re)_2$ $Hf_{30(2)}Re_{17(3)}Al_{53(2)}$	not detected by XRPD			
	Re_4Al_{11} $Hf_{2(1)}Re_{25(4)}Al_{73(1)}$	not detected by XRPD			
7	**$Hf(Re,Al)_2$** $Hf_{32.4(6)}Re_{25.6(5)}Al_{42(1)}$	*hP*12, *P*6$_3$/*mmc*	0.52592(4)	–	0.8554(1)
	Hf_4Al_3 $Hf_{47.7(5)}Re_{3.4(6)}Al_{48.9(6)}$	*hP*7, *P*6/*mmm*	0.53282(8)	–	0.5435(2)
	HfAl $Hf_{50.9(8)}Re_{2.0(6)}Al_{47.1(3)}$	*oS*8, *Cmcm*	0.3318(6)	1.116(2)	0.4185(7)
8	**$Hf(Re,Al)_2$** $Hf_{30(4)}Re_{46(4)}Al_{24(8)}$	*hP*12, *P*6$_3$/*mmc*	0.52747(7)	–	0.8603(2)
	~$Hf_5Re_2Al_2$ $Hf_{57(1)}Re_{20(3)}Al_{23(3)}$	*hP*18, *P*6$_3$/*mcm*	0.8091(2)	–	0.5689(2)
	Hf	*hP*2, *P*6$_3$/*mmc*	0.3170(1)	–	0.5038(3)
9	**Hf** $Hf_{78(5)}Re_{10(4)}Al_{12(1)}$	*hP*2, *P*6$_3$/*mmc*	0.31599(3)	–	0.50208(9)
	~$Hf_5Re_2Al_2$ $Hf_{60(2)}Re_{21(6)}Al_{19(5)}$	*hP*18, *P*6$_3$/*mcm*	0.8076(1)	–	0.5730(2)

photographs of the surfaces of individual samples. Table 4 summarizes the results of the phase analyses. Fig. 2 shows the isothermal section of the Hf–Re–Al phase diagram at 1000 °C. The ternary phase ~$Hf_5Re_2Al_2$ forms equilibria with Hf_3Al_4, Hf_2Al, (Hf), $Hf_{21}Re_{25}$ and the extended solid solution of $HfRe_2$.

If we compare the Hf–Re–Al system with previously studied T^{IV}–T^{VII}–M^{III} systems, we can see that they differ both in the nature of the phase fields and in the number and types of ternary compounds that exist in the systems [1-17]. In most of the systems involving boron, compounds are either absent or a single compound is formed. The systems with aluminum and indium are characterized by the presence of one or two compounds. Slightly more compounds (2-4) are formed in the systems with gallium. The Ti–Mn–Al system has been studied at various temperatures.

Similarly to the system studied by us, hexagonal phases isostructural to the $MgZn_2$ type with regions of homogeneity of different size are also known in the systems {Ti, Zr, Hf}–Mn–Al and {Zr, Hf}–Mn–Ga, whereas in the system Hf–Re–B the binary phase $HfRe_2$ does not dissolve significant amounts of the third component. In contrast to the Hf–Re–Al system, no ternary compound with a structure of the Ti_5Ga_4 or Hf_5CuSn_3 types [28] has been reported in the systems considered here.

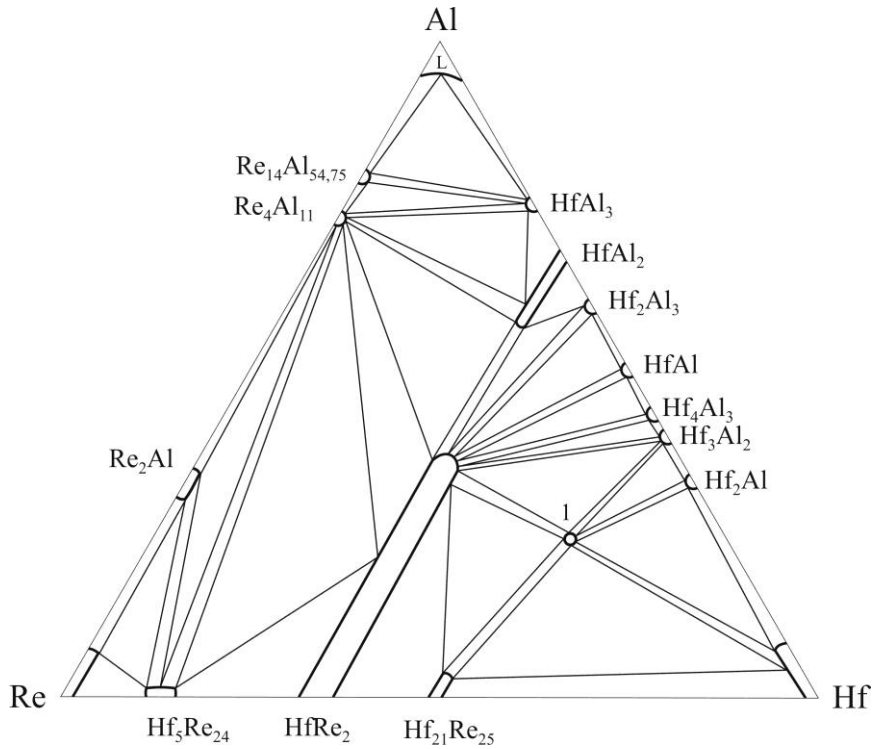

Fig. 2. Isothermal section of the Hf–Re–Al phase diagram at 1000 °C (1 – ~$Hf_5Re_2Al_2$).

Conclusions

Ternary systems involving *d*-elements of groups IV and VII and *p*-elements of group III of the periodic system are characterized by either the absence, or a low number of ternary compounds. The isothermal section of the phase diagram of the Hf–Re–Al system at 1000 °C was investigated in the full concentration range using X-ray powder diffraction, scanning electron microscopy, and energy-dispersive X-ray spectroscopy. Under the conditions of the study, the existence of 13 previously reported binary compounds was confirmed. Approximately 5 at.% of Hf can be dissolved in the compounds Re_4Al_{11} and Re_2Al, and about the same amount of Al in $Hf_{21}Re_{25}$. A new ternary compound of the approximate composition ~$Hf_5Re_2Al_2$, adopting a Ti_5Ga_4-type structure (*hP*18, $P6_3/mcm$), and two extended solid solutions based on the hexagonal Laves-type ($MgZn_2$) binary compounds $HfRe_2$ and $HfAl_2$ were found.

The Hf–Re–Al system differs from previously studied T^{IV}–T^{VII}–M^{III} systems, both in the nature of the phase fields and in the number and structures of the ternary compounds. Hexagonal Laves-type phases also form in the {Ti, Zr, Hf}–Mn–Al and {Zr, Hf}–Mn–Ga systems, however, no ternary compound with a Ti_5Ga_4-(or Hf_5CuSn_3-) type structure was found in these systems.

Acknowledgments

The authors are grateful to research fellow Vasyl Kordan for assistance in the study of microstructures and to senior research assistant Pavlo Demchenko for obtaining X-ray diffractograms.

Zinko L. – Ph.D. Student;
Nychyporuk G. – Ph.D., Laboratory Chief Manager;
Matselko O. – Ph.D., Research Fellow;
Gladyshevskii R. – Doctor of Sciences, Professor, Member of the NAS of Ukraine.

[1] Y. B. Kuz'ma, T. P. Paitash, S. I. Baidala, *Phase equilibria in the systems titanium–vanadium–boron and titanium–manganese–boron*, Visn. Lviv Univ., Ser. Chem., 11, 18 (1969).
[2] Y. V. Voroshylov, Y. B. Kuz'ma, *Phase equilibria in the ternary systems zirconium–vanadium–boron, zirconium–niobium–boron, zirconium–manganese–boron*, Powder Metall. Met. Ceram., 6(6), 466 (1967).
[3] Y. B. Kuz'ma, *The systems Ti–Co–B and Ti–Re–B*, Neorg. Mater., 7, 514 (1971).
[4] Y. B. Kuz'ma, B. I. Lakh, B. I. Stadnyk, D. A. Kovalyk, *The systems hafnium–tungsten–boron, hafnium–rhenium–boron and niobium–rhenium–boron*, Powder Metall. Met. Ceram., 9(12), 1003 (1970).
[5] V. Raghavan, *Al–Mn–Ti (Aluminum-Manganese-Titanium)*, J. Phase Equilib. Diffus., 32(5), 465 (2011); https://doi.org/10.1007/s11669-011-9926-6
[6] X. Huang, J. Tan, Y. Guo, G. Xu, Y. Cui, *Experimental Diffusion Research on BCC Ti–Mn Binary and Ti–Al–Mn Ternary Alloys*, J. Phase Equilib. Diffus., 39, 702 (2018); https://doi.org/10.1007/s11669-018-0675-7
[7] X. M. Huang, G. M. Cai, J. Zhang, F. Zheng, H. S. Liu, Z. P. Jin, *Phase relation and transition in the Ti–Al–Mn system*, J. Alloys Compd., 861, 158578 (2021); https://doi.org/10.1016/j.jallcom.2020.158578

[8] X. L. Yan, X. Q. Chen, A. V. Grytsiv, P. Rogl, R. Podloucky, H. G. Schmidt, G. Giester, X. Y. Ding, *On the ternary Laves phases $Ti(Mn_{1-x}Al_x)_2$ with $MgZn_2$-type*, Intermetallics, 16, 16 (2008). https://doi.org/10.1016/j.intermet.2007.07.005
[9] V. Y. Markiv, A. I. Skripka, *Examination of the phase equilibria in Ti–Mn–Ga and Zr–Mn–Ga alloys*, Russ. Metall. (Engl. Transl.), 4, 196 (1981).
[10] N. Belyavina, A. I. Skripka, V. Y. Markiv, *The systems Zr–{Sc, Ti, Mn, Nb}–Ga and Hf–{Sc, Mn, Zr, Nb}–Ga*, Phase Equilibria in Metal Alloys, Nauka, M., 154 (1981).
[11] N. N. Belyavina, V. Y. Markiv, *Isothermal section of the phase diagram of Hf–Mn–Ga system at 500 °C*, Visn. Kyiv. Univ., Ser. Phys., 21, 17 (1980).
[12] L. D. Gulay, V. I. Zaremba, *Investigation of the interaction between the components in the Zr–Mn–In system at 870 K*, J. Alloys Compd., 347, 184 (2002); https://doi.org/10.1016/S0925-8388(02)00776-4
[13] L. Gulay, V. Zaremba, Y. Kalychak, *Crystal structure of $ZrMn_{0.7}In_{2.3}$ compound*, Visn. Lviv Univ., Ser. Chem., 39, 101 (2000).
[14] A. E. Dwight, *Alloying behavior of zirconium, hafnium and the actinides in several series of isostructural compounds*, J. Less-Common Met., 34, 279 (1974); https://doi.org/10.1016/0022-5088(74)90170-2
[15] H. Mabuchi, K. I. Hirukawa, Y. Nakayama, *Formation of structural $L1_2$ compounds in $TiAl_3$-base alloys containing Mn*, Scr. Metall., 23, 1761 (1989); https://doi.org/10.1016/0036-9748(89)90357-8
[16] V. Y. Markiv, V. V. Burnasheva, *New ternary compounds in the systems (Sc, Ti, Zr, Hf)–(V, Cr, Mn, Fe, Co, Ni, Cu)–(Al, Ga)*, Dopov. Akad. Nauk Ukr. RSR, Ser. A: Fiz.-Mat. Tekh. Nauki, 463 (1969).
[17] P. Villars, K. Cenzual (Eds.), Pearson's Crystal Data – Crystal Structure Database for Inorganic Compounds, Release 2021/22, ASM International, Materials Park, OH (2021).
[18] P. Villars, H. Okamoto, K. Cenzual (Eds.), ASM Alloy Phase Diagram Database, Release 2006/2018, ASM International, Materials Park, OH (2018).
[19] W. Kraus, G. Nolze, Powder Cell for Windows, Berlin (1999).
[20] STOE WinXPOW, Version 1.2, STOE & CIE GmbH, Darmstadt (2001).
[21] L. Akselrud, Y. Grin, *WinCSD: software package for crystallographic calculations (Version 4)*, J. Appl. Crystallogr., 47, 803 (2014).
[22] L. A. Cornish, M. J. Witcom, *An investigation of the Al–Re phase diagram*, J. Alloys Compd., 291, 117 (1999); https://doi.org/10.1016/S0925-8388(99)00248-0
[23] J. L. Murray, A. J. McAlister, D. J. Kahan, *The Al–Hf (Aluminum–Hafnium) system*, J. Phase Equilib., 19(4), 376 (1998).
[24] H. Boller, H. Nowotny, A. Wittmann, *The crystal structure of some hafnium-containing phases*, Monatsh. Chem., 91, 1174 (1960).
[25] A. Taylor, B. J. Kagle, N. J. Doyle, *The constitution diagram of the rhenium–hafnium system*, J. Less-Common Met., 5(1), 26 (1963); https://doi.org/10.1016/0022-5088(63)90041-9
[26] J. Emsley, The Elements (2nd Ed.), Clarendon Press, Oxford (1991).
[27] K. Schubert, H. G. Meissner, M. Pötzschke, W. Rossteutscher, E. Stolz, *Some structural data of metallic phases (7)*, Naturwissenschaften, 49, 57 (1962).
[28] W. Rieger, H. Nowotny, F. Benesovsky, *Phases with octahedral elements of transition metals*, Monatsh. Chem., 96, 232 (1965); https://doi.org/10.1007/BF00912313

Л. Зінько, Г. Ничипорук, О. Мацелко, Р. Гладишевський

Потрійна система Hf–Re–Al при 1000°C

Львівський національний університет імені Івана Франка, Львів, Україна, lianazinko@gmail.com

Взаємодію компонентів у системі Hf-Re-Al досліджено методами рентгенівської порошкової дифракції, скануючої електронної мікроскопії та енергодисперсійної рентгенівської спектроскопії. Побудовано ізотермічний переріз діаграми стану при 1000 °C в повному концентраційному інтервалі. Визначено існування нової тернарної сполуки ~$Hf_5Re_2Al_2$, ізоструктурної до типу Ti_5Ga_4 (*hP*18, *P*6$_3$/*mcm*), і двох протяжних твердих розчинів складу $Hf(Re,Al)_2$.

Ключові слова: гафній, реній, алюміній, рентгенівська порошкова дифракція, енергодисперсійна рентгенівська спектроскопія, діаграма стану, ізотермічний переріз, кристалічна структура.

PHYSICS AND CHEMISTRY OF SOLID STATE
V. 24, No. 2 (2023) pp. 367-373
Section: Physics

DOI: 10.15330/pcss.24.2.367-373

Vasyl Stefanyk Precarpathian National University

ФІЗИКА І ХІМІЯ ТВЕРДОГО ТІЛА
Т. 24, № 2 (2023) С. 367-373
Фізико-математичні науки

PACS: 78.66.Jg, 68.35.bj, 89.75.Fb. ISSN 1729-4428

Mykhaylo Mar'yan[1*], Nataliya Yurkovych[1], Vladimir Seben[2]

Low-temperature anomalies and nanosized levels formation of self-organized structures in the non-crystalline solids of As(Ge)-S(Se) systems

[1*]*Uzhhorod National University, Uzhhorod, Ukraine, mykhaylo.maryan@uzhnu.edu.ua*
[2]*University of Presov, Presov, Slovakia*

The relationship between low-temperature anomalies of physical and chemical properties and the formation of self-organized structures in non-crystalline solids of the As(Ge)-S(Se) systems is discussed. Obtained temperature dependences for the specific heat capacity and coefficient of linear expansion in the temperature domain T < 100 K, detailing the linear and nonlinear contributions. The influence of the obtaining conditions of non-crystalline solids on the low-temperature behavior of physico-chemical properties and the change in the ratios of various contributions and temperature intervals is considered. The correlation and common features of the formation of self-organized structures of non-crystalline materials in the region of low temperatures and softening temperatures, manifested in the presence of nanolevels of structuring, are analyzed.

Keywords: low-temperature anomalies, nanosized effects, non-crystalline materials, self-organized structures, synergetics, soft atomic configurations, two-level states.

Received 15 March 2023; Accepted 21 June 2023.

Introduction

Non-crystalline solids of systems As(Ge)-S(Se) are very interesting objects with wide practical and fundamental applications [1,2]. The fundamental researches using ideas of synergetics for the self-organizing processes and formation of self-organized structures in them, also is extremely also important and unique [2]. In the region of low temperatures (T < 50 K), the behavior of a number of thermal properties (the heat capacity, the coefficient of thermal expansion, the velocity of sound propagation) for non-crystalline solids is different from the temperature characteristics of the crystalline compounds. The low-temperature anomalies of physical properties for non-crystalline solids are described at present on the basis of representations of two-level tunnel states and soft atomic configurations without a single interpretation of their microscopic nature [3-5]. An interesting application of such phenomena is also the Bose & Einstein condensation, which is being studied intensively studied over the past decades [6]. Processes of self-organization and a synergetic approach to low-temperature anomalies can cardinally change the views and methods of implementation without dissipative dissemination of information through the realization of fractal structures [7].

In order to explain the nature of the low-temperature phenomena of non-crystalline materials of As(Ge)-S(Se,Te) systems in a wide temperature range, it is necessary to consider the behavior of physical-mechanical properties in conjunction with the features of the structure and factors that determine it. These factors include the conditions for obtaining non-crystalline materials and the effect of external fields (electromagnetic radiation, external noise). Non-crystalline materials are characterized by the presence of self-organized and fractal structures [2, 7-10], whose parameters, due to influence on the near and medium order, are largely determined by the conditions of obtaining. For example, such factors include the synthesis temperature, cooling rate, annealing regimes, which determine the spatial fluctuations of structural parameters. In addition, the self-consistent consideration

of the dynamics of atomic oscillations, the reorganization of local atomic potentials, and the spectrum of low-frequency excitations of non-crystalline materials in terms of conditions for their obtaining is of fundamental interest. The nature of the transition to a non-crystalline state as a self-organized process and low-temperature anomalies also have much in common [7, 11]. From this perspective, the study of the formation processes of orderly self-organized structures in non-crystalline solids continues to arouse constant interest in the synergetic approach and their practical application in the creation of non-volatile memory and technologies, the development of intelligent non-crystalline materials of artificial intelligence [7]. The above-mentioned approaches are discussed in this article.

I. Model of system

Let's consider the relationship between the behavior of physical properties (mean-square displacements and frequency of oscillations of atoms, heat capacity and thermal expansion) of non-crystalline solids in the region of low temperatures T < 100 K with the conditions for their obtaining. The fluctuations of the parameters of the non-crystalline structure, which are described at the near-order level by the dispersion of the interatomic distances and angles between the bonds, cause the local heterogeneity of the matrix and lead to the formation of regions with different levels of ordering. The Hamiltonian H of such a system can be given as follows

$$H = \sum_f \sum_l \left(\frac{\left(P_l^f\right)^2}{2m} + U_f(\vec{r}_l) \right) \sigma_l^f + \frac{1}{2} \sum_{f,f'} \sum_{l,l'} \Phi_{f,f'}(\vec{r}_l - \vec{r}_{l'})\, \sigma_l^f \sigma_{l'}^{f'} \ . \tag{1}$$

Here $U_f(\vec{r}_l) = \sum_{f,f'} \Phi_{f,f'}(\vec{r}_l - \vec{r}_{l'})$ is the single-particle potential, $\Phi_{f,f'}(\vec{r}_l - \vec{r}_{l'})$ is the paired interaction potential, σ_l^f are the local characteristic functions. Effective Hamiltonian $\widetilde{H}$ of two-level states ($f = 1,2$) the system has the look:

$$\widetilde{H} = \sum_l \widetilde{H}_f, \widetilde{H}_f = \sigma_f \sum_l \left(\frac{\left(\vec{P}_l^f\right)^2}{2m} + U_f(\vec{r}_l) - \mu \right) + \frac{A_f}{2} \sum_{l,l'} \Phi_f(\vec{r}_l - \vec{r}_{l'}) \ . \tag{2}$$

Where $A_1 = 1 - \sigma_2^2, A_2 = \sigma_2^2,\ \sigma_1 + \sigma_2 = 1$. In the future, we will introduce the notation $\sigma \equiv \sigma_2$. Configuration entropy $dS_i = -k_B ln\left[\prod_f \left\{ \frac{g_f^!}{N_f^!(g_f - N_f)!} \right\}\right]$, associated with fractal regrouping the regions of soft-atomic configurations inside the system, is determined for this case by the number of distribution methods N_f atoms in f possible states with degrees of degeneracy g_f. Degree of degeneracy g_f takes into account the splitting of the corresponding energy level due to the influence of neighbors, and $g_f > N_f$. So, $g_2 > N_{2max}$ $(N_{2max} = (10^{-4} \div 10^{-2}) \cdot N)$(is the density of possible soft atomic configurations in non-crystalline material, which is determined by its structure and conditions of obtaining [11]) and $g_1 \geq N_{1max} \cong N$, which gives an estimation $g_2/g_1 = 10^{-4} \div 10^{-2}$. Since in the non-crystalline material the proportion of atoms contained in soft atomic configurations is significant $(\sigma \cong 10^{-4} \div 10^{-2})$, and the displacement of the atoms for the system near the order $(10 \div 30)\%$ the interatomic distances, then for the study of the temperature behavior of the non-crystalline system, it is necessary to involve methods that take into account strongly non-harmonic effects and structural rearrangements. We use the self-consistent pseudo-harmonic approximation, which enables us to determine the renormalization of the force constants and local potentials as a result of the anharmonicity of atomic oscillations [11-14].

Let's consider the solution of the variational problem [11, 12] for the functional of energy

$$\partial F/\partial \sigma = a_e \cdot (\sigma - \sigma_e),$$
$$F = \sum_f F_f - T \cdot dS, \quad dS = dS_i + dS_e, \tag{3}$$
$$a_e = (\partial^2 F/\partial \sigma_e)_e \ .$$

Where $dS_i \geq 0$ is a flow of entropy within a non-crystalline system, $dS_e < 0$ is a flow of synentropy from the external environment [7], σ_e is an equilibrium value σ. The variational problem leads to self-consistent equations:

$$\sigma = \frac{\tilde{\Lambda}_1 - \tilde{\Lambda}_2 - \vartheta ln \frac{g_2/N_2 - 1}{g_1/N_1 - 11} - a_e \cdot (\sigma - \sigma_e)}{2(\tilde{\Phi}_2 - \tilde{\Phi}_1)},\ \tilde{\Lambda}_f = \langle \sum_l \frac{\left(\vec{P}_l^f\right)^2}{2m} \rangle,\ \tilde{\Phi}_f = \langle \sum_{l,l'} \Phi_f(\vec{r}_l - \vec{r}_{l'}) \rangle. \tag{4}$$

The system of equations with respect to renormalized power constants $\tilde{v}_f(l)$ and mean-square displacements $\widetilde{D}(l) = \langle \frac{[\{u(l) - u(0)\}l]^2}{l^2} \rangle$ in the approximation of the pair interaction of near neighbors Z, it is possible to investigate the temperature behavior of the non-crystalline system and has the form

$$z\widetilde{D}_f(l) = \frac{\hbar}{N} \sum_k \frac{\omega(k)}{\tilde{v}_f(l)} cth \frac{\hbar\omega(k)}{2\vartheta}, \quad \tilde{v}_f(l) = A_f \frac{\partial^2}{\partial r_l^2} \left[exp\left\{ \frac{1}{2} \widetilde{D}_f \frac{\partial^2}{\partial r_l^2} \right\} \Phi_f\left(r_l - r_{l'}\right) \right] \tag{5}$$

Describing the effective interaction of atoms with the Morse potential, we find for a self-consistent interaction

potential:

$$\widetilde{\Psi}_f(l) = A_f V_{0f} exp\{-Q^*\}\left[exp\{-2\alpha(l-\alpha_0)\}exp\left\{2y_f\right\} - 2exp\{-\alpha(l-\alpha_0)\}exp\left\{y_f/2\right\}\right], \quad (6)$$

where $\alpha = \alpha_0 + 3Q^*/2\alpha$ is an averaged interatomic distance taking into account the static disordering of equilibrium positions characterized by a parameter $Q^* = \alpha^2 Q^2$; $y_f = \alpha^2 \widetilde{D}_f(l)$ are given reduced mean-square displacements of atoms; α and V_{0f} are the parameters of the potential. Thus, according to the principle of the local quasi-equilibrium of non-crystalline material in the presence of external applied pressure P, the average inter atomic distance is equal

$$l_f = \alpha_0 + \frac{3y_f}{2\alpha} + \delta_f, \quad \delta_f = -\frac{P^* \exp(y_l)}{\left(3\alpha(1-\xi\sigma_2^2)\right)},$$

$$\xi = 1 - \frac{V_{02}exp\{y_1 - y_2\}}{V_{01}} \ll 1, \quad P^* = \frac{6P\alpha\alpha_0^2}{zf}$$

is the reduced pressure, $f = 2\alpha V_{0f} exp\{-Q^*\}$ is the power constant in a harmonic approximation, then the potential energy and force constants in the region of low temperatures ($\theta \ll k_B T_D$, where T_D is a Debye's temperature) are defined by expressions

$$\widetilde{\Psi}_f\left(l_f\right) = -A_f V_{0f} exp\{-Q^*\}exp\left\{-y_f\right\},$$

$$\tilde{v}_f\left(l_f\right) = A_f f\left(exp\left\{-y_f\right\} + \frac{P^*}{1-\xi\sigma_2^2}\right) \quad (7)$$

$$y_f = \frac{\beta_f}{A_f^2 \lambda_f}\vartheta^4\left(1 + \frac{5\beta_f}{2A_f^2\lambda_f}\vartheta^4 + \cdots\right)$$

where $\lambda_f = \frac{V_{0f}\alpha_0(1+P^*)\cdot V \cdot exp\{-Q^*\}}{\pi^2\hbar v_{0f} S_{0f}}$, $\beta_f = \frac{\alpha^4}{60(\hbar S_{0f})^4}$, $S_{0f}^2 = zf\alpha_0^2(1 + \frac{P^*}{1-\xi\sigma_2^2})/2m$ is a sound speed in harmonic approximation, v_{0f} is a geometric structural factor $\left(0 < v_{0f} < 1\right)$. The system of equations (4) - (7) allows us to investigate the behavior of the mean-square displacements, the atomic fraction in soft atomic configurations and a number of other physical properties that are determined through $y_f(T)$ and $\sigma_f(T)$ in the temperature range $T < 100°K$. Because $A_f\widetilde{\Phi}_f = zN\widetilde{\Psi}_f(l)/2$, $\sigma_f\tilde{\Lambda}_f = zN\tilde{v}_f(l)/\alpha^2$, Then equation (4) using the relation (7) is rewritten in this way:

$$\sigma = \frac{V_{02}y_2\sigma\left(exp\{-y_2\}+\frac{P^*}{1-\xi\sigma^2}\right) - V_{01}y_1(1+\sigma)\left(exp\{-y_1\}+\frac{P^*}{1-\xi\sigma^2}\right) + \vartheta ln\frac{\frac{g_2}{\sigma}-N}{\frac{g_1}{1-\sigma}-N}exp\{Q^*\}+\alpha_e\cdot(\sigma-\sigma_e)}{V_{01}exp\{-y_1\}-V_{02}exp\{-y_2\}} \quad . \quad (8)$$

In particular, taking into account (7), for $T < 10°K$ we get

$$\sigma = \frac{(1+P^*)\vartheta^4}{2\varepsilon}\left(\frac{\beta_2 V_{02}}{\lambda_2\sigma^3} - \frac{\beta_1 V_{01}}{\lambda_1(1-\sigma^2)(1+\sigma^2)}\right). \quad (9)$$

From here we have $\sigma \cong \gamma\theta$, $\gamma^4 = \frac{\beta_2(1+P^*)V_{02}}{2\lambda_2\varepsilon} \ll 1$, $\varepsilon = V_{01} - V_{02}$.

Internal energy and volume

$$\tilde{E} = (1-\sigma^2)\widetilde{\Phi}_1 + \sigma^2\widetilde{\Phi}_2 + \sigma\tilde{\Lambda}_2 + (1-\sigma)\tilde{\Lambda}_1, \quad V = N\left((1-\sigma)\cdot v_1 + \sigma\cdot v_2\right), \qquad v_f = v_{0f}l_f^3, \quad (10)$$

there are functions σ, $y_{1,2}$ and given this way:

$$\tilde{E} = \frac{z}{2}exp\{-Q^*\}\times\left[-V_{01}e^{-y_1} + \sigma^2(V_{01}e^{-y_1} - V_{02}e^{-y_1}) + V_{01}y_1(1-\sigma^2)\left(e^{-y_1} + \frac{P^*}{1-\xi\sigma^2}\right) + V_{02}y_2\sigma^2\left(e^{-y_2} + \frac{P^*}{1-\xi\sigma^2}\right)\right], \quad (11)$$

$$\frac{V}{N} = (1-\sigma)v_{01}\left(\alpha + \frac{3\cdot y_1}{2\alpha} - \frac{P^*e^{y_1}}{3\alpha(1-\sigma^2)}\right) + \sigma v_{02}\left(\alpha + \frac{3\cdot y_2}{2\alpha} - \frac{P^*e^{y_2}}{3\alpha(1-\xi\sigma^2)}\right) \quad . \quad (12)$$

Thus, the low-temperature thermal capacity and the coefficient of thermal expansion of the system are described by the relations

$$C_p = \frac{M_\alpha}{m}\cdot\frac{\partial\left(\frac{(\tilde{E}+PV)}{N}\right)}{\partial T}\Bigg|_2 = \frac{z}{2}\frac{M_\alpha}{m}\cdot e^{-Q^*} \quad .$$

$$\left([V_{01}e^{-y_1}(1-y_1) - V_{02}e^{-y_2}(1-y_2) - (V_{01}y_1 - (V_{02}y_2]\frac{P^*}{1-\xi\sigma^2}\frac{\partial(\sigma^2)}{\partial T} + V_{01}e^{-y_1}(1-\sigma^2)(2-y_1)\frac{\partial y_1}{\partial T} + V_{02}e^{-y_2}\cdot\sigma^2\cdot(2-y_2)\frac{\partial y_2}{\partial T} + \left[V_{01}(1-\sigma^2)\frac{\partial y_1}{\partial T} + V_{02}\sigma^2\frac{\partial y_2}{\partial T}\right]\frac{P^*}{1-\xi\sigma^2} + P^*(v_2-v_1)\frac{\partial\sigma}{\partial T} + P^*\frac{\partial v_1}{\partial T} + P^*\sigma\frac{\partial}{\partial T}(v_2-v_1)\right), \quad (13)$$

$$\alpha_T = \frac{1}{V}\frac{\partial V}{\partial T}\Big|_P = \frac{1}{V}\left[(v_2 - v_1)\frac{\partial \sigma}{\partial T} + \frac{\partial v_1}{\partial T} + \sigma\frac{\partial}{\partial T}(v_2 - v_1)\right] \quad .$$

Here M_α is molar mass. Using (11), (12) for E and V in the temperature range $T < 10°K$ we will get:

$$\tilde{E} = \frac{z}{2}e^{-Q^*}\left[-V_{01} + \gamma^2\vartheta^2\left(\varepsilon + \frac{\beta_2 V_{02}(2+P^*)}{\lambda_2\gamma^4}\right) + \frac{\beta_1 V_{01}\vartheta^4}{\lambda_1(1-\gamma^2\vartheta^2)^2}(2 + P^* - \gamma\vartheta(1 + P^*\gamma^2\vartheta^2)\right], \qquad (14)$$

$$\frac{V}{N} = \alpha_0^3(1 - \frac{P^*}{3\alpha\alpha_0(1-\xi\gamma^2\vartheta^2)})^3 \times \left\{v_{01}(1-\gamma\vartheta)\left[1 + \frac{\beta_1\vartheta^4}{6\alpha\alpha_0\lambda_1(1-\gamma^2\vartheta^2)^2}(9 - \frac{2P^*}{(1-\xi\gamma^2\vartheta^2)}\right]^3 + v_{02}\gamma\vartheta\left[1 + \frac{3\beta_2}{2\alpha\alpha_0\gamma^4\lambda_2} - \frac{\beta_1 P^*\vartheta^4}{6\alpha\alpha_0\lambda_1(1-\gamma^2\vartheta^2)^2(1-\xi\gamma^2\vartheta^2)}\right]^3\right\}.$$

The corresponding thermal capacity and thermal expansion coefficient of the system will look like

$$C_P = a_1 T + a_2 T^2 + a_3 T^3, \; a_T = -b_1 T + b_2 T^3, \qquad (15)$$

Where

$$a_1 = z\gamma^2 k_B^2 \cdot \frac{M_\alpha}{m}\left\{e^{-Q^*}\left[\varepsilon + \frac{\beta_2 V_{02}(2+P^*)}{\lambda^2\gamma^4}\right] - \frac{2\xi v_{01} V_{01} P^*}{3}\right\},$$

$$a_2 = \frac{M_\alpha}{m} \cdot \frac{zf(v_{01}-v_{02})P^*\gamma^3 k_B^3}{3\alpha^3},$$

$$a_3 = 3z\beta_1 k_B^4 \frac{M_\alpha}{m}\left[\frac{V_{01}(2+P^*)e^{-Q^*}}{2\lambda_1} + \frac{fP^*}{\alpha^2\lambda_1}\right],$$

$$b_1 = \frac{2P^*\xi\gamma^2 k_B^2}{\alpha a_0}, \qquad b_2 = \frac{18\beta_1 k_B^4}{\alpha a_0\lambda_1}.$$

II. Results and discussions

Solutions of the self-consistent system of equations (8, 9) in the temperature region T < 100 K calculated numerically using the iterative method [11] (model parameters for non-crystalline solids of As(Ge)-S(Se) systems
($P^* = 0.1,\ \varepsilon = 10^{-4}\,eV,\ f = (10^4 \div 10^5\ dynes/cm,$
$g_1/g_2 = 11 \div 15, \alpha \cdot a_0 = 6$). The parameter Q* is taken into account based on the results of the study of inelastic neutron scattering of chalcogenide glasses as the magnitude of the amplitude of continuum disorder: *Q^*=0.15÷0.18* [10, 11]. Linear temperature dependence of the fraction of atoms in soft atomic configurations at $T < 1°K$ which the temperature rises it becomes nonlinear ($\sigma \approx T^k, k < 1$), saturated ($\sigma_{max} \approx 10^{-4} \div 10^{-2}$) about $T \approx 10 \div 10^2$ K (Fig. 1). Anomalous temperature behavior of changes in the fraction of atoms in soft atomic configurations $\partial\sigma/\partial T$ (Fig. 1) manifests itself in the temperature range *(3÷30) K* and correlates with the position of the frequency domain of the boson peak ν_{bp} of chalcogenide glasses [3, 8, 15]. The presence of a boson peak confirms the formation of nanoscale ordered structures in chalcogenide glasses [3, 15]. One of the variants of such an implementation is the formation through the processes of self-organization of soft atomic configurations of a fractal structure, which precisely realizes the minimum of energy dissipation [7, 14].

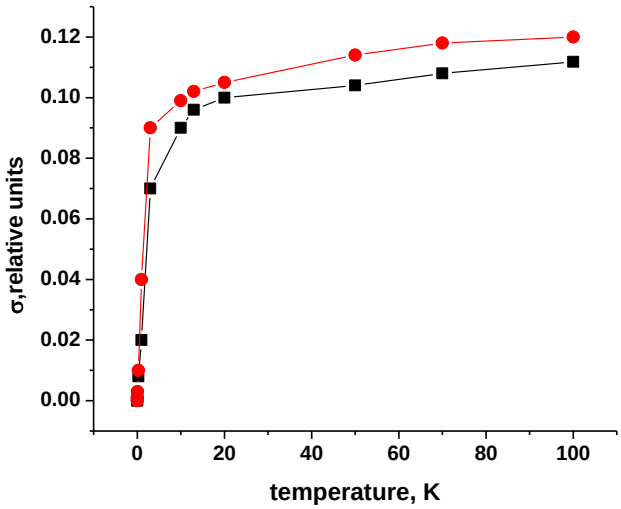

Fig. 1. Temperature dependence of the fraction of atoms in soft atomic configurations σ. Q^*=0.15 (black square), Q^*=0.18 (red circle).

Within the synergetic model, the structure of non-crystalline solids can be described as a linear contribution to thermodynamic functions C_p and α_T, caused by fluctuation transitions of atoms or their groups between soft atomic configurations, and cubic, due to phonons (Fig. 2). Since the coefficient of the linear part of the temperature dependence α_T is negative (15), then in the low temperature region α_T of the system initially decreases with heating, and then, due to the growth of the contribution of phonons ($\approx b_2 T^3$), begins to grow (Fig. 2). The nature of the effect of temperature compression of non-crystalline solids in the region $T \leq 1°K$ is as follows. Structural heterogeneity at the level of the near and middle orders determines for the heterogeneity of the phonon subsystem (the anharmonicity of the atomic oscillations is most pronounced for weak links). Accumulated in the local areas of the non-crystalline system energy is stored in the form of elastic deformations $\approx P^* exp(y_2)/(1 - \xi\sigma^2)$. With the growth of the fraction atoms in soft atomic configurations, elastic deformations will also increase, causing the sample to compress. At higher temperatures (1÷10) K cubic contribution to α_T becomes decisive (Fig. 2). The obtained result is consistent with the experimental data [4] on the temperature dependence of the Grüneisen coefficient (*G= – 1*) for a number of non-crystalline solids in the temperature range T ≤ 10 K.

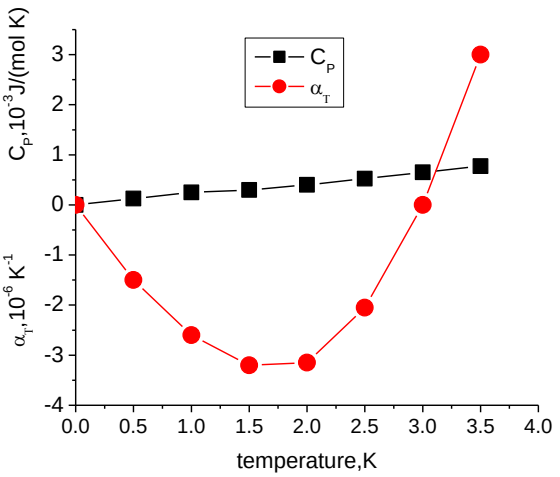

Fig. 2. Low-temperature dependences of the heat capacity C_p (black square) and the coefficient of thermal expansion α_T (red circle) for non-crystalline As_2S_3, $Q^* = 0.18$.

This model explains the quasilinear temperature dependence of heat capacity $C_p \approx T^{\delta}$ $(\delta = 0.1 \div 0.4)$, taking into account the self-consistent way along with the contribution of purely phonon excitations, their renormalization as a result of interaction with low-energy structural states (Fig. 3). This contribution, due to the interaction of phonons with soft configurations, has the order $a_2 \cdot T^2$ and is essential in the temperature range T ≤ (1÷3) K. The temperature dependence of the heat capacity, including not very low temperatures and calculated in accordance with (14), is presented in Fig. 3. In Fig. 3 shows experimental data of the dependence of the heat capacity C_p of glass As_2S_3 in the temperature range T = (0÷12) K <<T_D = 161 K, where T_D is the Debye's temperature, which is in good agreement with the theoretically obtained ones (15). For T = (3÷10) K this dependence C_p/T^3 have a wide maximum ("hump"), which is due to the interaction of atoms in soft atomic configurations with the matrix of the soft atomic state, which leads to a self-consistent renormalization of the force constants, the distribution of low-energy states and its nonlinear temperature dependence.

We analyze the influence of the conditions of obtaining on the nature of low temperature anomalies of the thermal properties of non-crystalline solids. The influence of technological regimes of obtaining (changes in the temperature of synthesis T_0) was taken into account as follows: an increase in the synthesis temperature causes an increase in the continuum disorder of the framework Q^*, which is described by the dispersion of distortion of the short order and causes the change in atomic potentials (11), the frequency of oscillations of the atoms and thermodynamic functions E, V (14). So, for non-crystalline material As_2S_3 obtained by cooling the melt from the synthesis temperatures in the range T = (870÷1370) K (the boundaries are determined by the minimum and maximum temperature of synthesis of this composition at a rate *q=1.8 K/s* [1]), there is a change in the dispersion of interatomic distances, which is coordinated in order of magnitude with experimental data [11]. It should be noted that the variation of the conditions of synthesis does not change the universal nature of low-temperature anomalies C_p and α_T of non-crystalline solids, but causes a change in the ratios of different contributions and temperature intervals. The growth of the dispersion of the fluctuations of the interatomic distances of the material obtained at the synthesis temperature T = 1370 K, causes an increase in the atomic share in soft atomic configurations and a shift in the temperature interval of saturation to a region of lower values in comparison with those for a material obtained at a temperature T = 870 K. This result is consistent with the results obtained by the authors [7] in studies of the growth of the density of low-energy states with a decrease in the transition temperature to a non-crystalline state (an increase in the synthesis temperature at $q = const$ for As_2S_3 causes a decrease in the temperature interval of softening-glass transition). Correspondingly, the change Q^* affects the nature of the dependence C_p/T^3 from T, which qualitatively agrees with the experimental studies on the influence of the conditions of obtaining As_2S_3 to low-temperature heat capacity in the temperature range $(2 \div 10)°K$ [16].

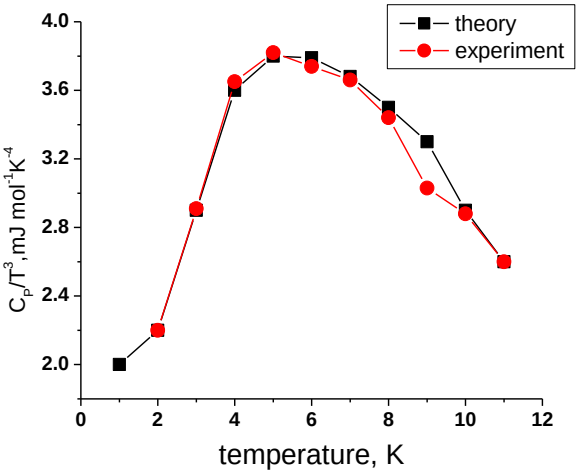

Fig. 3. Low-temperature dependence of the heat capacity of vitreous As_2S_3. Red circle – experiment [8], black square – calculation according to (15), $Q^* = 0.18$.

It should be noted that the correlation studies of low-temperature anomalies of physical properties (mean-square displacements, heat capacity, and coefficient of thermal expansion) of non-crystalline solids with the conditions of their obtaining indicate the common features of the transition to state of the non-crystalline solids [10, 17]. The authors of [1, 5] established empirical relations between the softening temperature and the density of soft low-temperature states. In particular, it is shown that the coefficient for the linear part of the temperature dependence of the heat capacity is a function of the softening temperature $a_1 = f(T_g)$. Since the softening temperature depends on the conditions for obtaining in particular the synthesis temperature, using (15) it will be rewritten as follows:

$$a_1 = z\gamma^2 k_B^2 \cdot \frac{M_a}{m}\left\{e^{-Q^*}\left[\varepsilon + \frac{\beta_2 V_{02}(2+P^*)}{\lambda^2\gamma^4}\right] - \frac{2\xi\nu_{01}V_{01}P^*}{3}\right\} = c' + \frac{c''}{\exp(Q^*)} = c' + \frac{c''}{\mathrm{f(q,}T_{0)}} = f(T_g). \quad (16)$$

That is, the ratio (16) for the coefficient of thermal dependence of the heat capacity allows us to obtain an empirical relation $a_1 = f(T_g)$, which describes the correlation between low-temperature anomalies and the transition to the state non-crystalline solids [15-18].

Conclusions

Analytical relations for the specific heat capacity, the coefficient of linear expansion of non-crystalline solids, which provide an opportunity to describe the linear and cubic contributions and their nature in the temperature range T < 100 K, have been obtained. The self-consistent dynamics of atomic oscillations, renormalization of local atomic potentials, and the spectrum of low-frequency excitations of non-crystalline materials are analyzed in detail from the point of view of the conditions of their obtaining. The common features of the transition of the system into a non-crystalline state and the realization of low-temperature anomalies as a manifestation of the formation of self-organized structures are discussed.

Mar'yan Mykhaylo – Doctor of Sciences (Physics & Mathematics), Professor of the Department Solid-State Electronics & Information Security Faculty of Physics Uzhhorod National University;
Yurkovych Nataliya – PhD (Physics & Mathematics), Ass. Prof. of the Department Solid-State Electronics & Information Security Faculty of Physics Uzhhorod National University;
Seben Vladimir – PhD, Ass. Prof. of the Department of Physics, Mathematics & Technics Faculty of Humanities and Natural Science University of Presov.

[1] J.L. Adam, X. Zhang. Chalcogenide Glasses: Preparation, Properties and Applications (Elsevier Science, London, 2014).
[2] M. Mar'yan, N. Yurkovych & V. Seben. *Formation and Modeling of Nanosized Levels of the Self-Organized Structures in the Non-Crystalline Thin Films of Ge-As-Te(S,Se) Systems*, Journal of Nano- and Electronic Physics, 11 (5), 05028:1(2019); https://doi.org/10.21272/jnep.9(5).05020.
[3] M.I. Klinger., *High-pressure effects in low temperature fundamental optical absorption and photoluminescence of glassy semiconductors*, Phys. Status Sol. B, 211(1), 207 (1999); https://doi.org/10.1002/(SICI)1521-3951(199901)211:1<207::AID-PSSB207>3.0.CO;2-7.
[4] O.B. Wright., *Thermodynamics of irreversible heat generation in glasses at low temperatures*, Physica B: Condensed Matter, 263(1), 321(1999); https://doi.org/10.1016/S0921-4526(98)01368-4.
[5] S.A. Dembovsky, *Quasimolecular defects as a unified microscopic basis of the glassy state,* J. Non-Cryst. Solids 90(1), 355 (1987); https://doi.org/10.1016/S0022-3093(87)80444-1.
[6] M. A. Nielsen, I.L. Chuang. Quantum Computation and Quantum Information (Cambridge University Press, NY, 2010).
[7] M. Mar'yan, N. Yurkovych & V. Seben, *Nanosized levels of the self-organized structures in the non-crystalline semiconductors As-S(Se) system*, Semiconductor physics, quantum electronics and optoelectronics, 22(3), 299 (2019); https://doi.org/10.15407/spqeo22.03.299.
[8] X. Liu, H.V, Lohneysen, *Low-temperature thermal properties of amorphous* As_x Se_{1-x}, Physical review. B, Condensed matter, 48(18), 13486 (1993); https://doi.org/10.1103/PhysRevB.48.13486.
[9] V.T. Maslyuk, *A model for maxima in the heat capacities of chalcogenide glasses*, Journal of Non-Crystalline Solids, 212(1), 80 (1997); https://doi.org/10.1016/S0022-3093(97)00003-3.
[10] E. Bartsch, F. Fujura, M. Kichel and H. Sillescu, *Inelastic neutron scattering experiments on Van der Waals glasses – A test of recent microscopic theories of the glass transition*, Phys. Chem., 93(11), 1252(1989); https://doi.org/10.1002/bbpc.19890931121.
[11] M. Mar'yan, N. Yurkovych, *Influence on disorder structure of the non-crystalline materials and synergetic effects*, Scientific Herald of Uzhhorod University. Series Physics, 35, 17 (2014); https://doi.org/10.24144/2415-8038.2014.36.17-24.
[12] P. Shuster, Stochasticity in Processes: Fundamentals and Applications to Chemistry and Biology (Springer, London, 2016); https://doi.org/10.1007/978-3-319-39502-9.
[13] D. Sornette. Critical Phenomena in Natural Sciences. Chaos, Fractals, Self-organization and Disorder: Concepts and Tools (Springer, NY, 2006); https://doi.org/10.1007/3-540-33182-4.
[14] M. Mar'yan, V. Seben, N. Yurkovych. Synergetics, Fractality and Information. Application to the Self-Organized Sructures and Intelligent Materials (Presov: University of Presov Publ., 2020).
[15] M.I. Klinger., *Soft atomic motion modes in glasses: Their role in anomalous properties*, Physics Reports, 492(4):111 (2010); https://doi.org/10.1016/j.physrep.2010.03.004.
[16] E. Vateva, B. Terziyska, D. Arsova, *Low-temperature specific heat and thermal conductivity of ternary chalcogenide glasses*, Journal of Optoelectronics and Advanced materials, 9, 1965 (2007).

[17] M. Mar'yan, N. Yurkovych, V. Seben, *Self-organized structures induced by external white noise and nanosized levels of their formation in the non-crystalline As-S(Se) semiconductor systems*, Semiconductor physics, quantum electronics and optoelectronics, 25 (4), 402 (2022); https://doi.org/10.15407/spqeo25.04.402.
[18] P. Baloh, V. Tkac, R. Tarasenko, M. Orendac *et al*., *Relation between nanocluster approximation and Soft-Potential Model, the role of keystone nanocluster in the thermal conductivity*, Journal of Non-Crystalline Solids, 600(1), 122040 (2023); https://doi.org/10.1016/j.jnoncrysol.2022.122040.

Михайло Мар'ян[1*], Наталія Юркович [1], Володимир Шебень[2]

Низькотемпературні аномалії та нанорозмірні рівні формування самоорганізованих структур в некристалічних тілах систем As(Ge)-S(Se)

[1]Ужгородський національний університет, Ужгород, Україна, mykhaylo.maryan@uzhnu.edu.ua*
[2]Пряшівський університет, Пряшів, Словаччина

Дискутується взаємозв'язок низькотемпературних аномалій фізико-хімічних властивостей та формування самоорганізованих структур у некристалічних тілах систем As(Ge)-S(Se). Отримані температурні залежності для питомої теплоємності та коефіцієнта лінійного розширення в області температур $T < 100^{o} K$, які деталізують лінійні та нелінійні вклади. Розглянуто вплив умов одержання некристалічних тіл на низькотемпературну поведінку фізико-хімічних властивостей та зміну співвідношень різних вкладів і температурних інтервалів. Обговорюється кореляція та спільні риси формування самоорганізованих структур некристалічних матеріалів в області низьких температур і температур розм'якшення, що проявляється у наявності наноріvнів структурування.

Ключові слова: низько-температурні аномалії, нанорозмірні ефекти, некристалічні матеріали, м'які атомні конфігурації, самоорганізовані структури, синергетика, дворівневі стани.

PHYSICS AND CHEMISTRY OF SOLID STATE
V. 24, No. 2 (2023) pp. 374-384
Section: Chemistry

DOI: 10.15330/pcss.24.2.374-384

Vasyl Stefanyk Precarpathian National University

ФІЗИКА І ХІМІЯ ТВЕРДОГО ТІЛА
Т. 24, № 2 (2023) С. 374-384
Хімічні науки

UDC 544.47

ISSN 1729-4428

Ivan Mironyuk[1], Nazarii Danyliuk[2], Liliia Turovska[3], Ihor Mykytyn[1], Volodymyr Kotsyubynsky[4]

Structural, morphological and photocatalytic properties of nanostructured TiO_2/AgI photocatalyst

[1]*Department of Chemistry, Vasyl Stefanyk Precarpathian National University, Ivano-Frankivsk, Ukraine, myrif555@gmail.com*
[2]*Educational and Scientific Center of Material Science and Nanotechnology, Vasyl Stefanyk Precarpathian National University, Ivano-Frankivsk, Ukraine, danyliuk.nazariy@gmail.com*
[3]*Department of Medical Informatics, Medical and Biological Physics, Ivano-Frankivsk National Medical University, Ivano-Frankivsk, Ukraine, lturovska@ifnmu.edu.ua*
[4]*Department of Materials Science and New Technologies, Vasyl Stefanyk Precarpathian National University, Ivano-Frankivsk, Ukraine, kotsuybynsky@gmail.com*

Nanostructured TiO_2/AgI photocatalyst under the action of ultraviolet or visible electromagnetic radiation effectively neutralizes organic pollutants in the aqueous environment. It is a nanostructure in which micro- and small mesopores of anatase TiO_2 are filled with silver iodide in the superionic state. The content of the α-AgI ion-conducting phase in the volume of TiO_2 pores can be ~20 wt %.

To obtain a photocatalyst, titanium dioxide is synthesized by the sol-gel method, using a titanium aquacomplex solution $[Ti(OH_2)_6]^{3+}\bullet 3Cl^-$ and a Na_2CO_3 modifier additive as a precursor. The modifying additive during synthesis ensures the fixation of $=O_2CO$ carbonate groups on the surface of oxide material particles. The presence of these groups leads to an increase in both the pore volume and the specific surface area of TiO_2. The specific surface area of carbonized titanium dioxide is 368 $m^2\bullet g^{-1}$, the pore volume is 0.28 $cm^3\bullet g^{-1}$, and their size is 0.9-4.5 nm.

To fill the micro- and small mesopores of TiO_2 with the superionic α-AgI phase, Ag^+ cations are first adsorbed from the $AgNO_3$ solution on the titanium dioxide surface, and then the oxide material is contacted with the KI solution.

Compared to the Evonik P25-TiO_2 photocatalyst, the nanostructured TiO_2/AgI photocatalyst demonstrates a significantly higher efficiency of photodegradation of organic dyes Congo Red and Methyl Orange in visible and ultraviolet radiation. The most active TiO_2/40AgI sample achieved complete degradation of the CR dye (5 mg/L) in 6 minutes of UV irradiation (λ = 365 nm), while the efficiency of commercial P25-TiO_2 over the same time was only 42%.

Keywords: titania, Congo Red, Methyl Orange, photocatalyst.

Received 19 January 2023; Accepted 20 June 2023.

Introduction

To improve the spatial separation of photogenerated charges and increase the quantum yield of photocatalytic transformations, nanostructured binary photocatalysts are used. The coordinated energy of the conduction band and the valence band of these nanostructures contributes to the irreversible interfacial transfer of photogenerated electrons and holes.

In binary photocatalysts based on TiO_2, metal oxide [1–4] or chalcogenide semiconductors [5–7], conductive polymers [8–10], carbon materials such as graphite, fullerenes, graphene [11–14], etc. can perform the co-catalyst function.

The components of photocatalysts based on TiO_2 are also solid-state electrolytes, in particular, silver halides [15–17]. TiO_2/AgBr nanostructures have a photocatalytic effect in dye oxidation reactions, they are characterized by photobactericidal properties.

TiO_2-AgI nanocomposites obtained by mixing the corresponding sols exhibit photocatalytic activity in the reduction reactions of methylviologen [17].

TiO_2/AgI nanoheterostructures should be more efficient photocatalysts than nanocomposites of this composition. By definition, in a nanostructured photocatalyst, nanometer-scale components must be interconnected and placed in a certain order relative to each other. The large area of phase contact in these nanostructures and the ionic conductivity of AgI ensure the removal of photogenerated holes of the valence band of titanium dioxide and prevent their recombination with the electrons of the conduction band.

In this work, our goal was to synthesize a nanoheterostructural photocatalyst in which TiO_2 is combined with silver iodide in the superionic state, to study the structural and morphological characteristics of the photocatalyst, and to study its activity in dye oxidation reactions in ultraviolet and visible electromagnetic radiation.

I. Experimental

1.1. Preparation of TiO_2/AgI nanostructures

Nanostructured TiO_2/AgI photocatalyst was obtained by filling titanium dioxide mesopores with silver iodide during the reaction between $AgNO_3$ and KI. Ag^+ cations were adsorbed from the $AgNO_3$ solution on the surface of the oxide material for AgI to enter the TiO_2 pores, and only then the oxide material was brought into contact with the KI solution. Due to the high Laplace pressure, AgI nanoparticles in the pores of the oxide material pass from the dielectric state (β-AgI phase) to the superionic state (α-AgI phase). The ionic conductivity of the α-AgI phase is 10^8 times higher than the ionic conductivity of the β-AgI phase.

The synthesis of anatase nanoparticle TiO_2 is based on the sol-gel method, in which a solution of the $[Ti(OH_2)_6]^{3+}\cdot 3Cl^-$ aquacomplex is used as a precursor. In order to increase the pore volume of TiO_2, its specific surface area, and adsorption activity with respect to metal cations on the surface of the oxide material, carbonate groups $=O_2CO$ were grafted during synthesis [18]. To implement this process, the modifying reagent Na_2CO_3 was introduced into the titanium precursor solution. Its percentage was 8 wt.% relative to TiO_2.

The mixture of reagents was diluted with water and kept at a temperature of 70°C for 30-40 minutes. After heating, the pH of the reaction medium was adjusted to 6-7 with a 10% NaOH solution. The resulting TiO_2 particles were removed from the reaction medium using a vacuum filter, then washed from adsorbed Na^+ and Cl^- ions with distilled water and dried at a temperature of 120-140°C.

With a pore size of 0.9-4.5 nm and a pore volume of 0.28 $cm^3\cdot g^{-1}$, the specific surface area of the synthesized TiO_2 was 370 $m^2\cdot g^{-1}$.

Table 1 shows the morphological characteristics (specific surface area, pore volume) of base and modified TiO_2. The base titanium dioxide in the table is designated α-TiO_2, and the modified one is 8C-TiO_2. Morphological characteristics indicate that the modified TiO_2 exceeds the base one in terms of specific surface area and pore volume. The carbonated TiO_2 obtained by this method is an effective adsorbent for the extraction of metal cations from an aqueous medium.

To obtain nanoheterostructured photocatalysts, silver cations Ag^+ were adsorbed on the 8C-TiO_2 surface. To do this, an adsorbent was introduced into the $AgNO_3$ solution and kept for 30-40 minutes. It was removed from the dispersion medium and mixed with the KI solution. After 10-20 minutes of contact, the precipitate of the solid product was separated from the reaction medium, washed with distilled water, and dried at a temperature of 140-150^{0}C for 2 hours.

Studies of the adsorption of silver cations by carbonized TiO_2 showed that 1 g of the 8C-TiO_2 adsorbent extracts 190-210 mg of silver ions from an $AgNO_3$ solution.

To optimize the phase composition of the photocatalyst in the specified way, three test samples of the photocatalyst containing 20, 30, and 40 wt.% of silver iodide were obtained. These samples are designated TiO_2/20AgI, TiO_2/30AgI, and TiO_2/40AgI, respectively.

1.2. Characteristics of methods

Phase analysis of the TiO_2 samples and TiO_2/AgI nanostructures was carried out on an XRD-7000 Shimadzu X-ray diffractometer in copper anode radiation. Crystal phases were identified using the Mateh 3.0 software.

The morphological characteristics of powder materials, namely, their specific surface area, pore volume, and pore size distribution, were calculated from N_2 adsorption/desorption isotherms. Adsorption was studied at the boiling point of liquid nitrogen (T = 77 K) on an automatic sorbometer Quantachrome Autosorb (Nova 2200 e). Before radiation, the test samples were calcined in vacuum at a temperature of 180^{0}C for 24 hours. The pore size distribution was calculated using the density functional theory [19].

Images of TiO_2 particles and TiO_2/AgI nanostructures

Table 1.

Morphological characteristics of test samples (average value of specific surface area and pore volume)

Test samples	Porous structure parameters							
	S, $m^2\cdot g^{-1}$	S_{micro} $m^2\cdot g^{-1}$	S_{meso} $m^2\cdot g^{-1}$	S_{meso}/S, %	V $cm^3\cdot g^{-1}$	V_{micro} $cm^3\cdot g^{-1}$	V_{meso} $cm^3\cdot g^{-1}$	V_{meso}/V, %
a-TiO_2	239	100	139	58	0.15	0.054	0.098	64.4
8C-TiO_2	370	6	364	98	0.28	0.001	0.279	99.6
TiO_2/40AgI	222	-	222	100	0.20	-	0.20	100

were obtained using a JSM-2100F transmission electron microscope and a REMMA-102 scanning electron microscope. The scanning electron microscope is connected to an energy-dispersive X-ray spectrometer. This allowed us to control the elemental composition of the test samples.

1.3. Evaluation of photocatalytic performance

The photocatalytic activity of nanostructured TiO_2/AgI composites was evaluated by studying the photodegradation of dye solutions: Congo Red (CR) and Methyl Orange (MO) under the influence of UV and visible electromagnetic radiation. The source of electromagnetic radiation was LEDs with a wavelength of 365, 395 and 430 nm. The power of each LED was 5 W. The design of the photoreactor is described in detail in [20].

Before the start of the experiment, a suspension containing 30 mg of photocatalyst and 20 ml of an aqueous solution of CR or MO dye (5 mg/L) was stirred with a magnetic stirrer for 30 minutes in the dark to ensure the establishment of an adsorption-desorption equilibrium between the dye molecules and the photocatalyst surface at room temperature. After that, the suspension with its continuous stirring was irradiated with electromagnetic radiation with a given wavelength. The photodegradation kinetics of the dyes was recorded with a DT-1309 light meter. The final concentration of the dye in the solution was determined with a Ulab 102UV spectrophotometer. A detailed description of this technique and calibration dependences are given in [21]. The percentage of dye degradation was determined by equation (1):

$$\% \text{ degradation dye} = C_0\text{-}C/C_0 \cdot 100\%, \quad (1)$$

where % degradation dye is the percentage of dye degradation, C_0 is its initial concentration, and C is the dye concentration at time t. A commercial P25-TiO_2 photocatalyst from Evonik was also studied under these conditions.

II. Results and discussion

2.1. Morphological condition of the samples

The liquid-phase method for obtaining carbonated TiO_2 makes it possible to obtain an oxide material with small mesopores and their large total volume (Table 1). The image of the microstructure of the 8C-TiO_2 sample with a resolution of 5 nm (Fig. 1a) makes it possible to see the primary particles of the oxide material, which are anatase nanocrystallites. Their size is 3-7 nm, and they have a faceted shape. Rows of TiO_6 octahedra are visible on the faces of individual crystallites. White dots in the rows indicate the absence of titanium atoms in them. Defects in the structure of crystallites are micropores < 1.5 nm in size.

During the sol-gel synthesis, the primary particles-crystallites are combined into aggregates. The aggregate

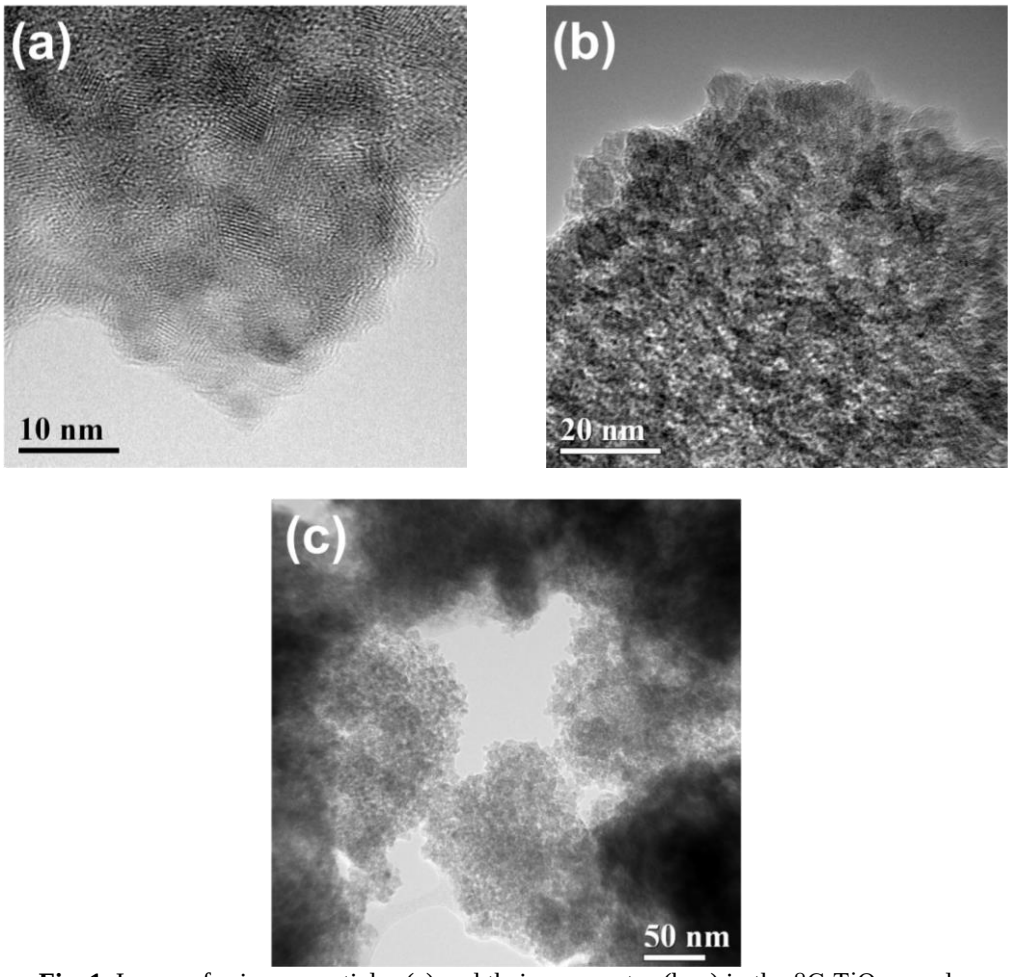

Fig. 1. Image of primary particles (a) and their aggregates (b, c) in the 8C-TiO_2 sample.

size is 180-360 nm (Fig. 1c). The image of the aggregate with a resolution of 20 nm (Fig. 1b) shows numerous white areas 1-4 nm in size, which are mesopores.

Filling the pore volume of carbonated TiO_2 with silver iodide leads to a decrease in its specific surface area and pore volume. Thus, the specific surface area of the TiO_2/40AgI test sample is 222 $m^2 \cdot g^{-1}$, and that of the 8C-TiO_2 sample is 370 $m^2 \cdot g^{-1}$ (Table 1). The pore volume of this nanostructured material decreases from 0.28 $cm^2 \cdot g^{-1}$ to 0.2 $cm^2 \cdot g^{-1}$ compared to carbonated TiO_2. The contact area between titanium dioxide and the α-AgI phase is 148 $m^2 \cdot g^{-1}$. An analysis of the pore size distribution in carbonated TiO_2 and in the TiO_2/40AgI sample shows (Fig. 3) that silver iodide in the nanostructured material is localized only in small mesopores 2.4-3.2 nm in size and micropores, and these pores are half filled with AgI. The absence of silver iodide in pores with a diameter of 3.2-4.5 nm is due to the fact that during the AgI formation reaction, pressure arises that displaces reaction products from the volume of these pores, so the condensation of silver iodide molecules occurs outside the pore volume of the oxide material. The formation of AgI crystallites in the volume of small mesopores and micropores is probably due to their small necks, which limit the extraction of AgI molecules from their volume.

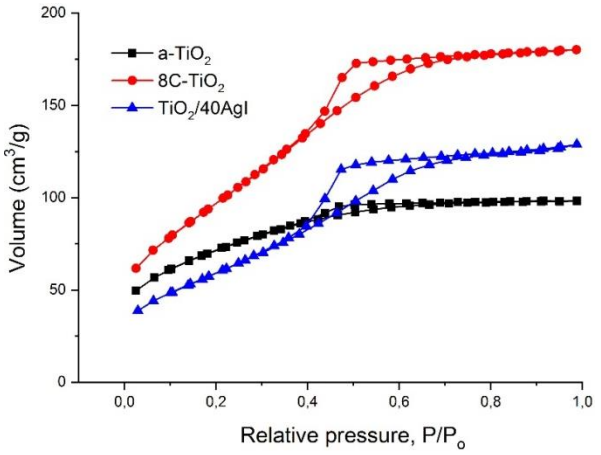

Fig. 2. Isotherms of adsorption/desorption of N_2 molecules by test samples.

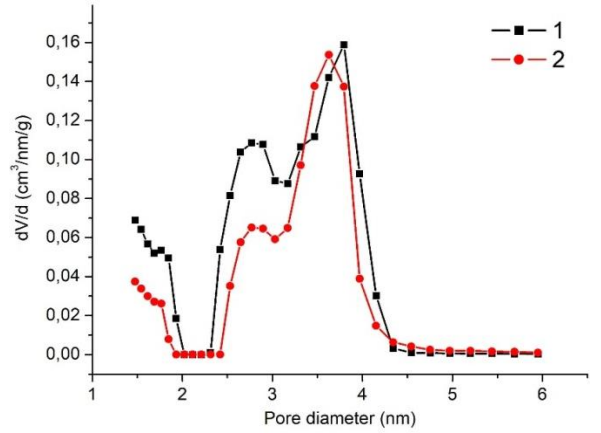

Fig. 3. Pore size distribution in carbonated titanium dioxide 8C-TiO_2 (1) and photocatalyst TiO_2/40AgI (2).

Fig. 4 shows an image of TiO_2/40AgI sample particles obtained using a scanning electron microscope. We can see that the mixture with large xerogel-like particles of TiO_2/40AgI of black color contains small particles of AgI of white color. The elemental composition of TiO_2/AgI and AgI particles is confirmed by the spectra of energy-dispersive X-ray microanalysis (Fig. 5 a, b).

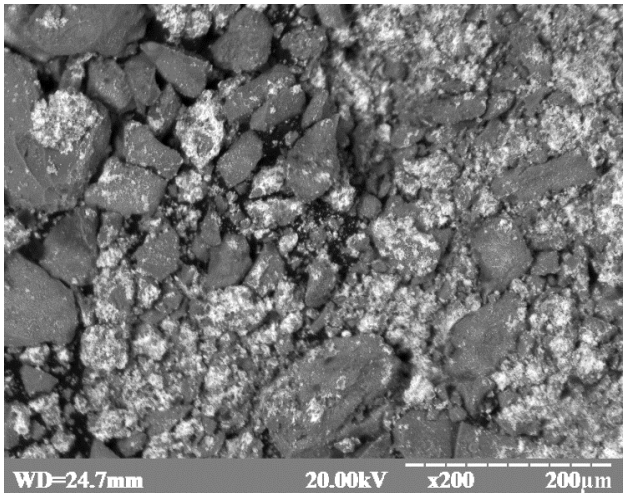

Fig. 4. Image of TiO_2/40AgI particles. Black particles are TiO_2/AgI heterostructure xerogel, white particles are AgI.

2.2. Phase composition of the photocatalyst

Silver iodide belongs to the class of solid electrolytes, which are characterized by ionic conductivity. At room temperature and normal pressure, the crystalline state of silver iodide corresponds to the β-AgI phase [22]. In some cases, a metastable γ-AgI phase may also be present along with this phase.

At normal pressure, according to the phase diagram [22] (Fig. 6), at a temperature of 146^0C, the β-AgI phase undergoes phase transition into the α-AgI phase. As a result of this phase transition, AgI passes from the dielectric to the superionic state. In the superionic state, the electrical conductivity L of the α-AgI phase is 1.38 $S \cdot cm^{-1}$ [22]. This value is close to the L value of concentrated liquid electrolytes. At room temperature, the electrical conductivity of the β-AgI phase is 10^{-8} $S \cdot cm^{-1}$.

The phase diagram of AgI indicates that with increasing pressure, the temperature of the β→α-phase transition decreases. At a pressure of 270 MPa, AgI acquires a superionic state already at room temperature. It is important to note that the temperature of AgI transition to the superionic state depends on the particle size. Very small nanocrystallites in the superionic state can exist at room temperature. This phenomenon is due to the action of Laplace pressure. Phenomenologically, the Laplace pressure P_L arises due to the action of surface tension σ and its value depends on the curvature of the surface of the solid. For spherical particles

$$P_L = \frac{4\sigma}{d} \qquad (2),$$

where d is the effective particle diameter.

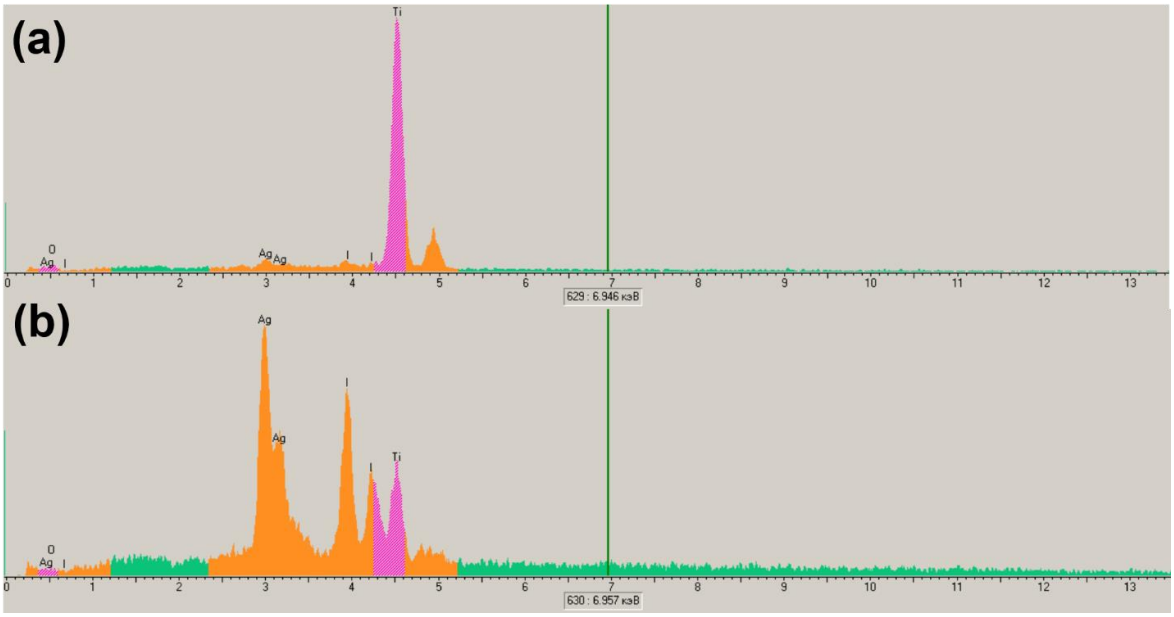

Fig. 5. Energy-dispersive spectra of TiO_2/AgI heterostructure particles (a) and AgI particles (b) of the TiO_2/40AgI test sample.

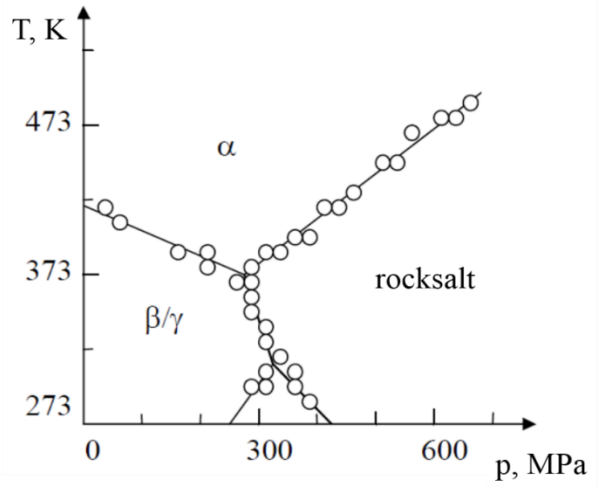

Fig. 6. Phase diagram of AgI.

The calculation shows that silver iodide particles in pores of the photocatalyst with a diameter of 2.4 nm at an AgI surface tension of 0.18 $J \cdot m^{-2}$ are under pressure of 300 MPa. At this pressure, AgI particles localized in small titanium dioxide mesopores pass into the superionic state.

Phase analysis of the test samples of TiO_2/20AgI, TiO_2/30AgI and TiO_2/40AgI by X-ray diffractometry revealed an anatase modification of TiO_2 and two phases of silver iodide – α-AgI and β-AgI in each sample. The diffraction patterns of the test samples are shown in Fig. 7.

Table 2 shows the space symmetry groups of the phases, their content and lattice parameters. The α-AgI phase is localized in small mesopores and micropores of anatase, while the β-AgI phase is located outside the pore volume of TiO_2. It can be seen from the presented data that with an increase in the content of silver iodide in the samples from 20% to 40%, the content of the α-AgI phase in the pores of the oxide material increases from 6.17 wt.% to 20.17 wt.%. Characteristically, with an increase in the content of the current-conducting phase, the efficiency of the nanostructured photocatalyst increases.

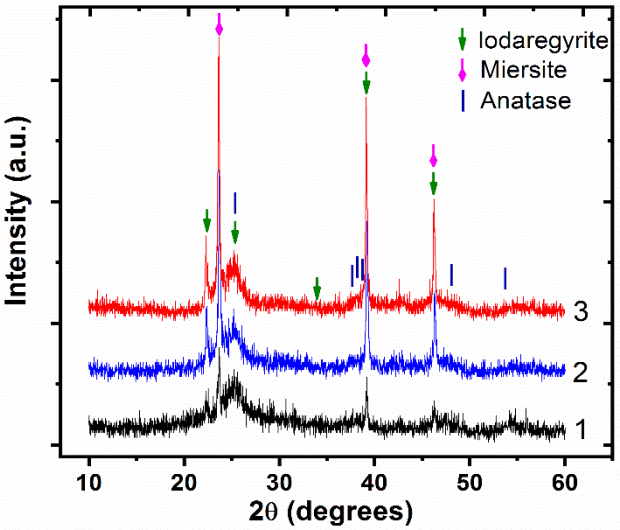

Fig. 7. X-ray diffraction patterns of TiO_2/20AgI (1), TiO_2/30AgI (2), and TiO_2/40AgI (3) samples.

2.3. Discussion of the results

2.3.1 Effect of AgI loading percentage

AgI effectively absorbs in the visible light region [23], so the percentage of AgI incorporation into titanium dioxide pores should have a significant effect on the activity of nanostructured photocatalysts. The photocatalytic activity of AgI/TiO_2 photocatalysts was evaluated by their ability to affect the degradation of dyes under the action of UV and visible electromagnetic radiation. Figs. 8-11 show that the efficiency of destruction of molecules of CR and MO dyes increases with an increase in the percentage of AgI in the nanostructured photocatalyst. The maximum efficiency of CR and MO removal is achieved in the TiO_2/40% AgI photocatalyst.

Table 2.

Phase composition of samples and lattice parameters of anatase TiO_2, α-AgI and β-AgI.

Sample	TiO_2 (Anatase) ICSD # 44882 Tetragonal, I41/amd			β −AgI (Iodaregyrite) ICSD # 65063 Hexagonal, P6mm			α −AgI (Miersite) ICSD # 52361 Cubic, F-4 3m	
	Content, %	a, Å	c, Å	Content, %	a, Å	c, Å	Content, %	a, Å
TiO_2/40AgI	60.0± 4.4	3.7839± 0.0024	9.4432± 0.0089	19.83± 7.73	4.5651± 0.0679	7.5191± 0.2779	20.17± 0.61	6.4914± 0.0035
TiO_2/30AgI	70.0± 4.11	3.7365± 0.0046	9.39322 0.05712	19.26± 0.48	4.5765± 0.0030	7.4828± 0.0108	10.74± 0.39	6.4889± 0.0017
TiO_2/20AgI	80.0± 3.29	3.7752± 0.0034	9.4015± 0.01634	13.83± 0.51	4.5687± 0.0016	7.4782± 0.0091	6.17± 0.73	6.4924± 0.00132

As shown in Figs. 8-11, the CR and MO dyes were effectively degraded as a result of the action of test samples of photocatalysts. Accordingly, with an increase in the mass fraction of AgI from 20% to 40%, the efficiency of dye degradation increases, while the reaction rate constants increase from 0.1277 min^{-1} to 0.1844 min^{-1} for CR and from 0.0640 min^{-1} to 0.1051 min^{-1} for MO when irradiated with visible light (λ= 430 nm). The photocatalytic reaction occurs on the surface of the catalyst; therefore, the adsorption capacity of the 8C-TiO_2 base has a significant effect on the rate of degradation of the CR and MO dyes.

It is known that the combination of AgI and TiO_2 leads to a shift of the absorption spectra to the visible light region [24]. AgI nanoparticles act as a sensitizer [25]. Accordingly, the nanostructured TiO_2/AgI composite efficiently absorbs visible light during photocatalytic reactions. The obtained samples of photocatalysts were studied at wavelengths of electromagnetic radiation of 365, 395, and 430 nm. Among all the samples, the TiO_2/40AgI photocatalyst at an irradiation wavelength of 365 nm destroyed the CR and MO dyes four times faster than the P25-TiO_2 photocatalyst.

2.3.2 Photocatalytic degradation of Congo Red

The kinetics of photodegradation of Congo Red by test samples of the photocatalyst is shown in Fig. 8. The obtained kinetic curves are described by a pseudo-first order equation, since the function of dependence of $\ln(C/C_0)$ on the reaction time (t) shows linearity with high correlation coefficients in the range from 0.9016 to 0.9983 (Table 3), where C_0 is the initial concentration of CR before irradiation, C is the concentration of CR at reaction time t, k is the reaction rate constant. The calculated photodegradation rate constants of Congo Red are shown in Fig. 9. Self-photodegradation of CR dye under irradiation with LEDs is not observed. The efficiency of the degradation of Congo Red for all samples decreases with increasing irradiation wavelength from 365 to 430 nm. For the TiO_2/40AgI sample, the reaction rate constants are 0.4099 min^{-1} and 0.1844 min^{-1}, respectively.

In particular, the incorporation of AgI into TiO_2 mesopores contributes to an increase in the activity of the photocatalyst in the visible light spectrum. The TiO_2/40AgI sample during irradiation at a wavelength of 430 nm showed almost 5 times higher efficiency

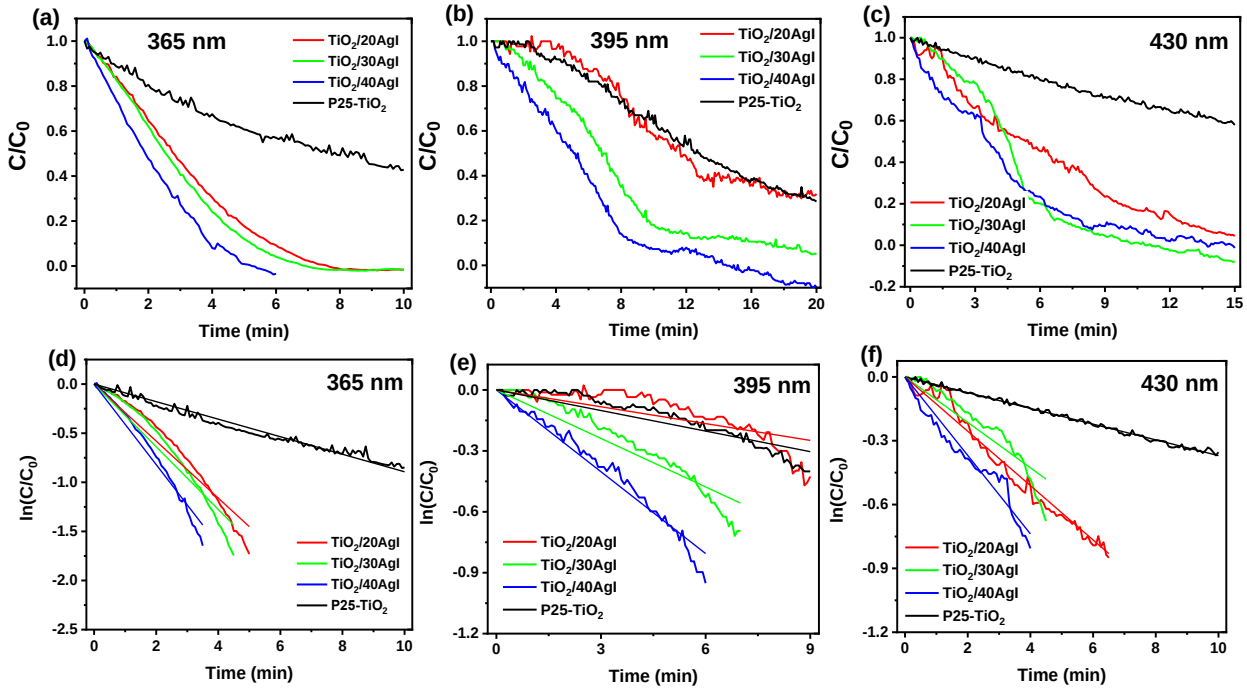

Fig. 8. (a-c) Effect of AgI concentration on CR dye degradation; (d-f) experimental lines transformed according to first-order kinetics.

Table 3.

Rate constants of the first order kinetic model of CR photodegradation on TiO_2/AgI and P25-TiO_2 samples (experimental conditions: solution volume 20 ml, dye concentration 5 mg/L).

λ, nm	**TiO_2/20AgI**		**TiO_2/30AgI**		**TiO_2/40AgI**		**P25-TiO_2**	
	k, min^{-1}	R^2	k, min^{-1}	R^2	k, min^{-1}	R^2	k, min^{-1}	R^2
365	0.2903	0.9794	0.3191	0.9753	0.4099	0.9885	0.0892	0.9933
395	0.0275	0.9016	0.0795	0.9631	0.1342	0.9901	0.0337	0.9362
430	0.1277	0.9881	0.1068	0.9462	0.1844	0.9843	0.0369	0.9983

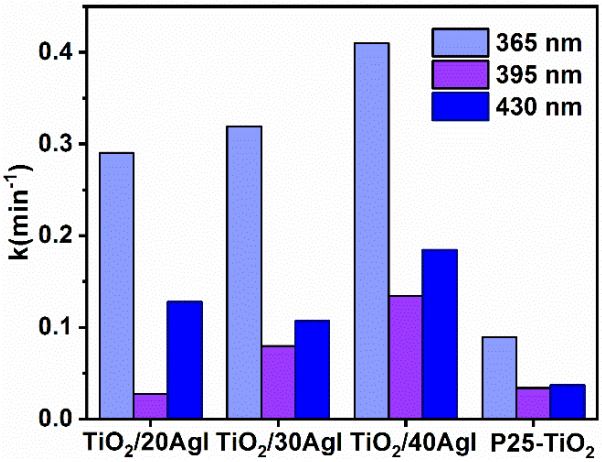

Fig. 9. Rate constants of the first-order kinetic model of CR dye photodegradation on TiO_2/20AgI, TiO_2/30AgI, TiO_2/40AgI, and P25-TiO_2 samples.

compared to P25-TiO_2 with reaction rate constants of 0.1844 min^{-1} and 0.0369 min^{-1}, respectively. Test samples show increased photocatalytic activity when illuminated with visible light (430 nm) for 15 minutes. In the photodegradation of CR dye by TiO_2/20AgI, TiO_2/30AgI, and TiO_2/40AgI samples when irradiated with a wavelength of 365 nm and 430 nm, the efficiency is 96%, 100%, and 100%, respectively. The resulting nanostructured TiO_2/AgI composites showed better efficiency when irradiated with 365 nm light compared to commercial P25-TiO_2. For example, the TiO_2/40AgI sample achieved complete degradation of CR in 6 minutes of irradiation, while P25-TiO_2 destroyed the dye by only 42% during the same period of time. According to the efficiency of CR photodegradation, test samples can be arranged as follows:

P25-TiO_2 < TiO_2/20AgI < TiO_2/30AgI < TiO_2/40AgI.

Thus, at 40% AgI, the photocatalytic activity was the highest. A further increase in the content of AgI in a nanostructured composite is unreasonable since it entails electron-hole recombination [26]. A similar result was described in [24]. The 0.2Ag@AgI/TiO_2 photocatalyst showed the highest efficiency of RhB removal (91%) in 90 min. As the content of AgI increases, its activity decreases.

2.3.3 Photocatalytic degradation of Methyl Orange

To illustrate that the resulting TiO_2/AgI nanostructures can degrade various organic toxicants, their photocatalytic activity was measured by monitoring the decomposition of Methyl Orange dye in aqueous solution under the same conditions as Congo Red. Changes in the MO concentration during the experiments were recorded using a DT-1309 light meter. The color of MO gradually decreases and the color of the solution changes from orange to colorless within 20 minutes of the reaction, indicating that the chromophore groups of the MO molecules are destroyed, and the corresponding color change can be registered using a light meter. For comparison, similar MO photodegradation experiments were carried out in the presence of commercial P25-TiO_2. The efficiency of MO photodegradation in 10 min of photooxidation at a wavelength of 365 nm reaches 95%, 100%, 100%, and 59% for TiO_2/20AgI, TiO_2/30AgI, TiO_2/40AgI, and P25-TiO_2 samples, respectively. The efficiency of MO degradation in 20 min of the irradiation reaction at a wavelength of 395 nm is 99%, 100%, 100%, and 74% for TiO_2/20AgI, TiO_2/30AgI, TiO_2/40AgI, and P25-TiO_2 samples, respectively. The efficiency of MO degradation in 20 min of 430 nm light irradiation is 67%, 84%, 99%, and 44% for TiO_2/20AgI, TiO_2/30AgI, TiO_2/40AgI, and P25-TiO_2 samples, respectively. The TiO_2/40AgI sample showed the highest photocatalytic activity among the test samples. According to the efficiency of MO degradation, the samples can be arranged as follows:

P25-TiO_2 < TiO_2/20AgI < TiO_2/30AgI < TiO_2/40AgI.

The photocatalytic degradation of MO is described by a first order equation (Fig. 10), as is the photodegradation of most organic substances [20,27,28]. Linear transformations of kinetic curves are shown in Figs. 10 d-f in the coordinates of $\ln(C/C_0)$ versus reaction time t. The reaction rate constants of MO photodegradation for various photocatalysts TiO_2/20AgI, TiO_2/30AgI, TiO_2/40AgI, and P25-TiO_2 are shown in Fig. 11. The value of k for the process of MO photodegradation by TiO_2/40AgI photocatalyst was the highest compared to other samples. The reaction rate constant was 0.3698 min^{-1}, 0.1885 min^{-1}, 0.1051 min^{-1} for light energy sources with wavelengths of 365, 395, and 430 nm, respectively. It was determined that the photocatalytic activity of TiO_2/40AgI significantly exceeds the activity of P25-TiO_2, especially

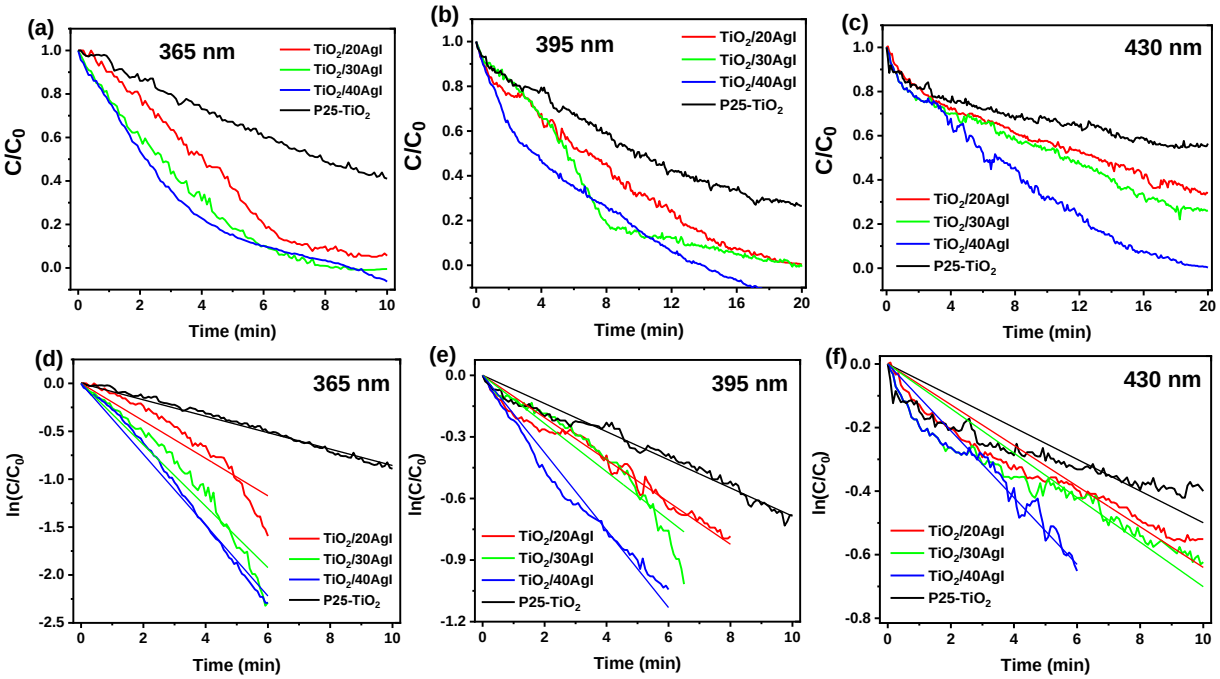

Fig. 10. (a-c) Effect of AgI concentration on MO dye degradation; (d-f) experimental lines transformed according to first-order kinetics.

Table 4.

Rate constants of the first order kinetic model of MO photodegradation on the TiO_2 sample (experimental conditions: solution volume 20 ml, dye concentration 5 mg/L).

λ, nm	**TiO_2/20AgI**		**TiO_2/30AgI**		**TiO_2/40AgI**		**P25-TiO_2**	
	k, min^{-1}	R^2	k, min^{-1}	R^2	k, min^{-1}	R^2	k, min^{-1}	R^2
365	0.1956	0.9578	0.3204	0.9826	0.3698	0.9963	0.0857	0.9965
395	0.1028	0.9917	0.1173	0.9757	0.1885	0.9931	0.0685	0.9928
430	0.0640	0.9786	0.0700	0.9687	0.1051	0.9838	0.0499	0.9457

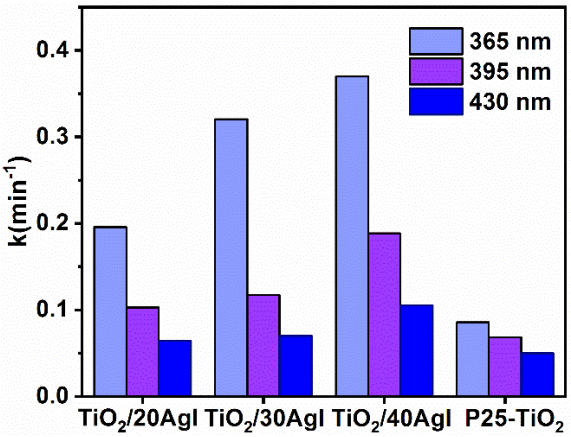

Fig. 11. Rate constants of the first-order kinetic model of MO dye photodegradation on TiO_2/20AgI, TiO_2/30AgI, TiO_2/40AgI, and P25-TiO_2 samples.

when irradiated at a wavelength of 430 nm, the reaction rate constant is twice as high, which is explained by the presence of AgI nanoparticles in TiO_2 mesopores. Thus, the TiO_2/40AgI photocatalyst can provide effective degradation of MO under UV and visible light irradiation.

Table 5 shows the results of the efficiency of similar photocatalysts based on TiO_2 and AgI in the photodegradation of various organic dyes. Under optimized experimental conditions, the activity of the resulting TiO_2/AgI nanostructures significantly exceeded the efficiency of the nanocomposites presented in Table 5. Thus, nanostructured TiO_2/AgI photocatalysts obtained by this method can be used to neutralize organic pollutants in an aqueous medium.

Efficient separation of electron-hole pairs in the nanostructured TiO_2/AgI composite increases its photocatalytic activity in photodegradation reactions of CR and MO dyes under UV and visible irradiation.

Table 5.

Comparison of photoactivity of nanocomposites based on TiO_2 and AgI

Photocatalyst	Light source	Experimental conditions	Photodegradation efficiency	Ref
0.2Ag@AgI/TiO_2	Xe (1000 W)	Catalyst = 50 mg [RhB] = 10 mg/L	91% in 90 min	[24]
0.2-AgI–TiO_2	Xe ($\lambda > 420$ nm)	Catalyst = 10 mg [BDE209] = $1.0 \cdot 10^{-5}$ mol·L^{-1}	70% in 180 min	[27]
TiO_2 QDs/CDs/Ag	50W LED	Catalyst = 100 mg [RhB] = $1.0 \cdot 10^{-5}$ mol·L^{-1}	97% in 20 min	[25]
30AgI@TiO_2/U6N	Hg lamp (500W, $\lambda > 400$ nm)	Catalyst = 20 mg [RhB] = 20 mg/L	100% in 30 min	[29]
Ag-AgI(4%)-TiO_2/CNFs	Xe (300 W)	Catalyst = 100 mg [MO] = 10 mg/L	97% in 180 min	[30]
AgI–TiO_2–cotton	Xe (1000 W) ($\lambda > 400$ nm)	[MO] = 5 mg/L	56% in 120 min	[31]
AgI-TiO_2/PAN	Xe (300 W)	Catalyst = 200 mg [MO] = 50 mg/L	87.8% in 270 min	[32]
TiO_2/40AgI	10 W LED ($\lambda = 430$ nm)	Catalyst = 30 mg [CR] = 5 mg/L	100% in 15 min	This work
TiO_2/40AgI	10 W LED ($\lambda = 430$ nm)	Catalyst = 30 mg [MO] = 5 mg/L	100% in 20 min	This work

Conclusions

This paper describes the synthesis and properties of nanostructured TiO_2/AgI photocatalysts. Filling micro- and mesopores of TiO_2 with AgI nanoparticles in the superionic state is an effective strategy for obtaining photocatalysts efficient in ultraviolet and visible electromagnetic radiation. Synthesis of TiO_2 has been carried out by the sol-gel method using a solution of the titanium aquacomplex $[Ti(OH_2)_6]^{3+} \cdot 3Cl^-$ and a Na_2CO_3 additive-modifier as a precursor. The presence of carbonate groups $=O_2CO$ on the surface of TiO_2 leads to an increase in the pore volume and specific surface area of the photocatalyst. The specific surface area of carbonated titanium dioxide is 368 $m^2 \cdot g^{-1}$, the pore volume is 0.28 $cm^3 \cdot g^{-1}$, and their size is 0.9-4.5 nm. The process of filling micro- and small mesopores of TiO_2 with the superionic α-AgI phase consists in the adsorption of Ag^+ cations on the surface of titanium dioxide, followed by the interaction of the oxide material with the KI solution. Among the studied nanostructured composites, the TiO_2/40AgI sample was the most effective, destroying CR and MO dyes four times faster than commercial P25-TiO_2 under UV irradiation ($\lambda = 365$ nm). According to the photodegradation efficiency of CR and MO, the studied samples can be arranged as follows: P25-TiO_2<TiO_2/20AgI<TiO_2/30AgI<TiO_2/40AgI under UV and visible irradiation. The high efficiency of the nanostructured TiO_2/40AgI photocatalyst will make it possible to use it to neutralize toxic organic substances in the aqueous environment.

Acknowledgements

The authors thank the Ministry of Education and Science of Ukraine for financial support in the framework of project 0120U102035.

Mironyuk Ivan – Doctor of Chemical Sciences, Head of the Department of Chemistry, Vasyl Stefanyk Precarpathian National University;
Danyliuk Nazarii – PhD student, leading specialist at the Educational and Scientific Center of Material Science and Nanotechnology, Vasyl Stefanyk Precarpathian National University;
Turovska Liliia – Associate Professor of the Department of Medical Informatics, Medical and Biological Physics, Ivano-Frankivsk National Medical University;
Mykytyn Ihor – Associate Professor of the Chemistry Department, Vasyl Stefanyk Precarpathian National University;
Kotsyubynsky Volodymyr – Doctor of Physical and Mathematical Sciences, Vasyl Stefanyk Precarpathian National University.

[1] M.K.I. Senevirathna, P.K.D.D.P. Pitigala, K. Tennakone, *Water photoreduction with Cu_2O quantum dots on TiO_2 nano-particles*, J. Photochem. Photobiol. A Chem. 171, 257 (2005); https://doi.org/10.1016/j.jphotochem.2004.10.018.

[2] D.L. Liao, C.A. Badour, B.Q. Liao, *Preparation of nanosized TiO_2/ZnO composite catalyst and its photocatalytic activity for degradation of methyl orange*, J. Photochem. Photobiol. A Chem. 19, 11 (2008); https://doi.org/10.1016/j.jphotochem.2007.07.008.

[3] L.C. Chen, F.R. Tsai, S.H. Fang, Y.C. Ho, *Properties of sol-gel SnO_2/TiO_2 electrodes and their photoelectrocatalytic activities under UV and visible light illumination*, Electrochim. Acta. 54, 1304 (2009); https://doi.org/10.1016/j.electacta.2008.09.009.

[4] E. V. Skorb, L.I. Antonouskaya, N.A. Belyasova, D.G. Shchukin, H. Möhwald, D. V. Sviridov, *Antibacterial activity of thin-film photocatalysts based on metal-modified TiO_2 and TiO_2: In_2O_3 nanocomposite*, Appl. Catal. B Environ. 84, 94 (2008); https://doi.org/10.1016/j.apcatb.2008.03.007.

[5] J.S. Jang, H.G. Kim, U.A. Joshi, J.W. Jang, J.S. Lee, *Fabrication of CdS nanowires decorated with TiO_2 nanoparticles for photocatalytic hydrogen production under visible light irradiation*, Int. J. Hydrogen Energy. 33; 5975 (2008); https://doi.org/10.1016/j.ijhydene.2008.07.105.

[6] W. Ho, J.C. Yu, *Sonochemical synthesis and visible light photocatalytic behavior of CdSe and CdSe/TiO_2 nanoparticles*, J. Mol. Catal. A Chem. 247, 268 (2006); https://doi.org/10.1016/j.molcata.2005.11.057.

[7] D. Jing, L. Guo, *WS_2 sensitized mesoporous TiO_2 for efficient photocatalytic hydrogen production from water under visible light irradiation*, Catal. Commun. 8, 795 (2007); https://doi.org/10.1016/j.catcom.2006.09.009.

[8] G. Liao, S. Chen, X. Quan, Y. Zhang, H. Zhao, *Remarkable improvement of visible light photocatalysis with PANI modified core-shell mesoporous TiO_2 microspheres*, Appl. Catal. B Environ. 102, 126 (2011); https://doi.org/10.1016/j.apcatb.2010.11.033.

[9] H.C. Liang, X.Z. Li, *Visible-induced photocatalytic reactivity of polymer-sensitized titania nanotube films*, Appl. Catal. B Environ. 86, 8 (2009); https://doi.org/10.1016/j.apcatb.2008.07.015.

[10] D. Wang, Y. Wang, X. Li, Q. Luo, J. An, J. Yue, *Sunlight photocatalytic activity of polypyrrole-TiO_2 nanocomposites prepared by "in situ" method*, Catal. Commun. 9, 1162 (2008); https://doi.org/10.1016/j.catcom.2007.10.027.

[11] J. Zhong, F. Chen, J. Zhang, *Carbon-Deposited TiO_2: Synthesis, Characterization, and Visible Photocatalytic Performance*, J. Phys. Chem. 933 (2010); https://doi.org/10.1021/jp909835m.

[12] R. Sellappan, J. Zhu, H. Fredriksson, R.S. Martins, M. Zäch, D. Chakarov, *Preparation and characterization of TiO_2 / carbon composite thin films with enhanced photocatalytic activity*, J. Mol. Catal. A. Chem. 335, 136 (2011); https://doi.org/10.1016/j.molcata.2010.11.025.

[13] S. Mu, Y. Long, S. Kang, J. Mu, *Surface modification of TiO_2 nanoparticles with a C 60 derivative and enhanced photocatalytic activity for the reduction of aqueous Cr (VI) ions*, Catal. Commun. 11, 741 (2010); https://doi.org/10.1016/j.catcom.2010.02.006.

[14] T. Graphene, T. Different, Y. Zhang, Z. Tang, X. Fu, Y. Xu, *TiO_2-Graphene Nanocomposites for Gas-Phase Photocatalytic Degradation of Volatile Aromatic Pollutant: Is TiO_2-graphene truly different from other TiO_2-carbon composite materials*, ACS Nano. 4, 7303 (2010); https://doi.org/10.1021/nn1024219.

[15] Y. Zang, R. Farnood, *Photocatalytic activity of AgBr/TiO_2 in water under simulated sunlight irradiation*, Appl. Catal. B. 79, 334 (2008); https://doi.org/10.1016/j.apcatb.2007.10.019.

[16] J. Yu, G. Dai, B. Huang, *Fabrication and Characterization of Visible-Light-Driven Plasmonic Photocatalyst Ag/AgCl/TiO_2 Nanotube Arrays*, J. Phys. Chem. C., 16394 (2009); https://doi.org/10.1021/jp905247j.

[17] D. Fitzmaurice, H. Frei, *Time-resolved optical study on the charge carrier dynamics in a TiO_2/AgI sandwich colloid*, J. Phys. Chem., 9176 (1995); https://doi.org/10.1021/j100022a034.

[18] I. Mironyuk, T. Tatarchuk, M. Naushad, H. Vasylyeva, I. Mykytyn, *Highly efficient adsorption of strontium ions by carbonated mesoporous TiO_2*, J. Mol. Liq., 285, 742 (2019); https://doi.org/10.1016/J.MOLLIQ.2019.04.111.

[19] V.M. Gun'ko, V.V. Turov, *Nuclear magnetic resonance studies of interfacial phenomena*, CRC Press. Boca Rat., (2013); https://doi.org/10.1201/b14202.

[20] T. Tatarchuk, N. Danyliuk, A. Shyichuk, W. Macyk, M. Naushad, *Photocatalytic degradation of dyes using rutile TiO_2 synthesized by reverse micelle and low temperature methods: real-time monitoring of the degradation kinetics*, J. Mol. Liq. 342, 117407 (2021); https://doi.org/10.1016/j.molliq.2021.117407.

[21] N. Danyliuk, T. Tatarchuk, I. Mironyuk, V. Kotsyubynsky, V. Mandzyuk, *Performance of commercial titanium dioxide samples in terms of dye photodegradation assessed using smartphone-based measurements*, Phys. Chem. Solid State., 3, 582 (2022); https://doi.org/10.15330/pcss.23.3.582-589.

[22] S. Yamasaki, T. Yamada, H. Kobayashi, H. Kitagawa, *Preparation of Sub-10 nm AgI Nanoparticles and a Study on their Phase Transition Temperature*, 73 (2013); https://doi.org/10.1002/asia.201200790.

[23] K. Ullah, A. Ullah, A. Aldalbahi, J. Do Chung, W.C. Oh, *Enhanced visible light photocatalytic activity and hydrogen evolution through novel heterostructure AgI-FG-TiO_2 nanocomposites*, J. Mol. Catal. A Chem. 410, 242 (2015); https://doi.org/10.1016/j.molcata.2015.09.024.

[24] W. Liu, C. Wei, G. Wang, X. Cao, Y. Tan, S. Hu, *In situ synthesis of plasmonic Ag@AgI/TiO_2 nanocomposites with enhanced visible photocatalytic performance*, Ceram. Int. 45, 17884 (2019); https://doi.org/10.1016/j.ceramint.2019.06.004.

[25] A. Shoja, A. Habibi-yangjeh, M. Mousavi, S. Vadivel, *Preparation of novel ternary TiO_2QDs/CDs/AgI nanocomposites with superior visible-light induced photocatalytic activity*, J. Photochem. Photobiol. A Chem. 385, 112070 (2019); https://doi.org/10.1016/j.jphotochem.2019.112070.

[26] E. Liu, Y. Zhang, Y. Cong, *Highly enhanced photocatalytic reduction of Cr (VI) on AgI/TiO_2 under visible light irradiation: influence of heat pretreatment*, Elsevier B.V. (2015); https://doi.org/10.1016/j.jhazmat.2015.12.050.

[27] Q.W. Ying-Ying Shao, Wei-Dong Ye, Chun-Yan Sun, Chu-Lin Liu, *Visible-light-induced degradation of polybrominated diphenyl ethers with AgI–TiO_2*, RSC Adv. 7, 39089 (2017); https://doi.org/10.1039/C7RA07106J.

[28] I. Mironyuk, N. Danyliuk, L. Turovska, I. Mykytyn, *Structural, morphological and photocatalytic properties of TiO2 obtained by thermolytic decomposition of the* $[Ti(OH_2)_6]^{3+}\bullet 3Cl^-$ *aquacomplex*, Phys. Chem. Solid State. 23, 741 (2022); https://doi.org/10.15330/pcss.23.4.741-755.

[29] F. Fazlali, A. Hajian, A. Afkhami, H. Bagheri, *A superficial approach for fabricating unique ternary AgI@*TiO_2*/Zr-MOF composites: An excellent interfacial with improved photocatalytic light-responsive under visible light*, J. Photochem. Photobiol. A Chem., 112717 (2020); https://doi.org/10.1016/j.jphotochem.2020.112717.

[30] D. Yu, J. Bai, H. Liang, J. Wang, C. Li, Fabrication of a novel visible-light-driven photocatalyst Ag-AgI-TiO_2 nanoparticles supported on carbon *nanofibers*, Appl. Surf. Sci. 349, 241 (2015); https://doi.org/10.1016/j.apsusc.2015.05.019.

[31] D. Wu, M. Long, *Enhancing visible-light activity of the self-cleaning* TiO_2*-coated cotton fabrics by loading AgI particles*, Surf. Coatings Technol. 206, 1175 (2011); https://doi.org/10.1016/j.surfcoat.2011.08.007.

[32] D. Yu, J. Bai, H. Liang, T. Ma, C. Li, *AgI-modified* TiO_2 *supported by PAN nanofibers: A heterostructured composite with enhanced visible-light catalytic activity in degrading MO*, Dye. Pigment. 133, 51 (2016); https://doi.org/10.1016/j.dyepig.2016.05.036.

Іван Миронюк[1], Назарій Данилюк[2], Лілія Туровська[3], Ігор Микитин[1], Володимир Коцюбинський[4]

Структурні, морфологічні та фотокаталітичні властивості наноструктурованого TiO_2/AgI фотокаталізатора

[1]*Кафедра хімії Прикарпатського національний університет імені Василя Стефаника, Івано-Франківськ, Україна, myrif555@gmail*

[2]*Навчально-науковий центр матеріалознавства і нанотехнологій Прикарпатського національного університету імені Василя Стефаника, Івано-Франківськ, Україна, danyliuk.nazariy@gmail.com*

[3]*Кафедра медичної інформатики, медичної та біологічної фізики Івано-Франківського національного медичного університету, Івано-Франківськ, Україна, lturovska@ifnmu.edu.ua*

[4]*Кафедра матеріалознавства та нових технологій Прикарпатського національного університету імені Василя Стефаника, Івано-Франківськ, Україна, kotsuybynsky@gmail.com*

Наноструктурований фотокаталізатор TiO_2/AgI, при дії ультрафіолетового або видимого електромагнітного випромінювання, ефективно знешкоджує у водному середовищі органічні забруднювачі. Він являє собою наноструктуру в якій мікро- та дрібні мезопори анатазного TiO_2 наповнені йодитом срібла в суперйонному стані. Вміст йонопровідної фази α-AgI в об'ємі пор TiO_2 може становити ~ 20 мас.%. Діоксид титану, для одержання фотокаталізатора, синтезують золь-гель методом, використовуючи, як прекурсор розчин титанового аквакомплексу $[Ti(OH_2)_6]^{3+}\bullet 3Cl^-$ та добавку-модифікатор Na_2CO_3. Модифікуюча добавка в процесі синтезу забезпечує вкорінення на поверхні частинок оксидного матеріалу карбонатних групувань $=O_2CO$. Наявність цих групувань приводить до зростання як об'єму пор так і питомої поверхні TiO_2. Питома поверхня карбонатованого діоксиду титану 368 $м^2\bullet г^{-1}$, об'єм пор 0.28 $см^3\bullet г^{-1}$, а їх розмір 0.9-4.5 нм. Для заповнення мікро- та дрібних мезопор TiO_2 суперйонною α-AgI фазою спочатку на поверхні діоксиду титану з розчину $AgNO_3$ адсорбують катіони Ag^+, а після цього здійснюють контактування оксидного матеріалу з розчином KI. Створений наноструктурований фотокаталізатор TiO_2/AgI в порівнянні з фотокаталізатором концерну Evonik марки P25-TiO_2 демонструє суттєво вищу ефективність щодо фотодеградації органічних барвників Конго червоного та Метилоранжу в видимому та ультрафіолетовому випромінюванні. Найактивніший зразок TiO_2/40AgI досягав повного руйнування барвника КЧ (5 мг/л) за 6 хвилин УФ-опромінення (λ = 365 нм), тоді як ефективність комерційного P25-TiO_2 становила всього 42%, за цей самий проміжок часу.

Ключові слова: титан (IV) оксид; Конго червоний; Метилоранж; фотокаталізатор.

PHYSICS AND CHEMISTRY OF SOLID STATE
V. 24, No. 2 (2023) pp. 385-391
Section: Physics

DOI: 10.15330/pcss.24.2.385-391

Vasyl Stefanyk Precarpathian National University

ФІЗИКА І ХІМІЯ ТВЕРДОГО ТІЛА
Т. 24, № 2 (2023) С. 385-391
Фізико-математичні науки

UDK 621.362 ISSN 1729-4428

R.G. Cherkez[1,2], V.A. Semeshkin[2], A.S. Zhukova[2], V.V. Stefiuk[2]

The influence of the plates on the effectiveness of penetrating thermoelements in the cooling regime

[1]*Institute of Thermoelectricity, Chernivtsi, Ukraine*
[2]*Yuriy Fedkovych Chernivtsi National University, Chernivtsi, Ukraine, r.cherkez@chnu.edu.ua*

This paper describes the physical model of the penetrating thermoelement with the developed surface of warmth exchange for the cooling of the air's flow. It presents the theory of the calculation and the method of the computer modeling of the temperature's and potential's allocation, the definition of the effectiveness of the energy's transformation – the cooling factor and the cooling efficiency. This work researches the 3D temperature's and materials' allocation for the material of the branches of the thermoelement based on Bi_2Te_3.

Key words: penetrating thermoelement, cooling coefficient, cooling capacity, 3d model.

Received 23 February 2023; Accepted 21 June 2023.

Introduction

The thermoelectrical coolers are widely used for the cooling of the electronics in different fields of usage, starting with consumer goods and ending with the designing of the spaceships. The thermoelectrical elements are widely used in cooling technics. Detailed, theoretical and experimental researches and optimization of the process of the thermoelectric cooling are conducted mainly for the stationary mode of the coolers' (modules). The results of these researches contributed to the massive industrial production of the thermoelectrical modules for the various needs [1,2].

The process of the thermoelectric cooling is not well explored nowadays. That's why specifically with the help of computer modelling we can more precisely explore it, create new thermoelectric modules and devices based on them [3,4]. We researched the model of the penetrating thermoelement with the developed system of the heat exchange for the cooling of the flow in order to find the optimal functions of the inhomogeneity of the material of the supports in combination with the search of the optimal parameters, with which the thermodynamic efficiency of the capacity of conversion will be maximal. Such thermoelectric model in perspective might be used in the future researches in this field of study, with different constructional peculiarities of the thermoelectric equipment, which, in turn, makes possible the research of the new thermoelectric materials in order to improve the conversion of energy and the cost of the thermoelectric equipment on its base.

So, the aim of the work is the verification of the influence of the geometry on the effectiveness of the penetrating element in the cooling regime.

I. The physical model of the penetrating thermoelectric cooling thermoelement

While using the material with the high penetration, the inner surface of the heat exchange might be developed. In such case the intensity of the heat exchange will highly increase and the temperature drop of the environments which exchange the heat will decrease. As the result, the beneficial temperature drop on the element will increase, what positively influences on the effectiveness of the heat transformation.

When we change the conditions of the heat exchange along the twig, we influence the volumetric distribution of the heat sources in the penetrating thermoelement. That's why we have wide opportunities to influence the energetic characteristics of the thermoelement – coefficient of

efficiency or capacity and the cooling coefficient. The penetrating thermoelement consists of coherent and parallel arranged on the distance plates of the twigs N- and P- types of conduction, which are connected by switching plates. The coolant is pumped through the channel of the penetrating thermoelement. It cools by means of the heat exchange with the branch's material, where the gradient of the temperature is set up due to thermoelectric Peltier effect and the existence of the electric flow. The upper spikes are thermostatized by the heat exchangers in consequence of pumping of the coolant, the rest of the surface is adiabatically isolated. The temperature of the coolant at the entrance of the thermoelement is set.

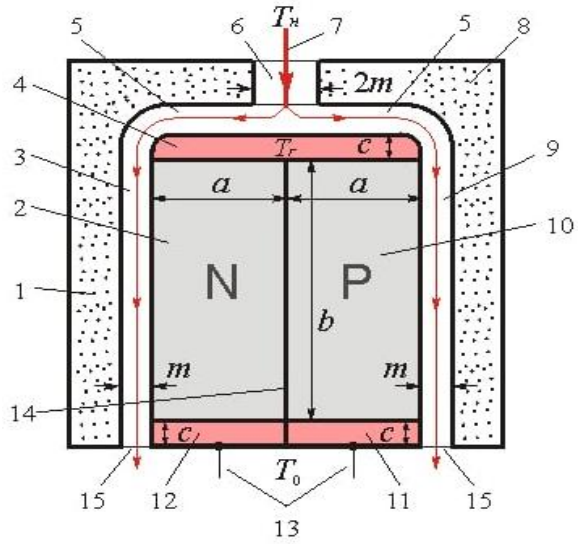

Fig.1. The physical model of the thermoelement in which the heat flows are formed because of heat exchange with the coolant, where 1 – adiabatic isolation, 2 – n-type branch, 3 – channel, 4 – commutation plate, 5 – 6 channels, 7 – coolant, 8 – adiabatic isolation, 9 – channel, 10 – branch p-type, 11 – 12 – commutation plates, 13 – electric contacts. Branches 2, 10 are embraced of the adiabatic isolation with 1, 8 and form channels 5, 6, 9. Through the channel 6 the heat carrier 7 with the temperature T_H is brought, which flows equally through channels 3, 5 and 5, 9.

The branches are made of the homogeneous material based on Bi – Te, where the temperature's dependence Z should be counted. The commutation plates are made of copper, the commutation resistance – 10^{-6} (Om • cm^2). The temperature T_0 of the lowest commutation plates is – 20°C. Branches N, P are connected with the thin layer 14, heat conductivity, electric conductivity and the thickness, which we neglect. The size of the thermoelement in the direction which is perpendicular to the picture's plane – d, magnitude d = a. Magnitude d = 0 and d = a are adiabatic isolations, which form the channels 5, 6, 9. The friction between the coolant and the adiabatic isolations 1, 8 is absent.

II. Mathematic description of the model

The existence of the heat exchange of the thermoelectric materials with the coolant negotiates the need of solutions of the problems of the temperature's allocation, electric potential and the heat's flow in the material, which are associated with the equations of motion and the heat transfer of the coolant. The movement of the coolant in the channels should be described by Navier Stokes equation and continuity equations. The equation of the heat conductivity should be explored in order to distribute temperature in the coolant. Navier Stokes equation:

$$\left.\begin{aligned} \rho\frac{d\vec{\vartheta}}{dt} = \rho\vec{F} - \vec{\nabla}P + \mu\overrightarrow{\nabla^2}\vec{\vartheta} + \frac{1}{3}\mu\vec{\nabla}\left(div\vec{\vartheta}\right), \\ div\rho\vec{\vartheta} = 0. \end{aligned}\right\} \quad (1)$$

Where the left side of the first equation (1) is the force of inertia, the first additive at the right side of the given equation – massive force, second – the effect of surface pressure forces (normal stresses), the two last additives – the effect of tangential components of surface forces (internal friction forces).

The heat exchange in the liquid is described by the equation of heat conductivity:

$$\rho C_p\left(\frac{\partial T}{\partial t} + \left(\vec{\vartheta}\vec{\nabla}\right)T\right) = -\left(\vec{\vartheta}\vec{q}\right) + \Sigma_{i,j}\,\tau_{ij}\,S_{ij} - \frac{T}{\rho}\frac{\partial\rho}{\partial T}\Big|_p\left(\frac{\partial\rho}{\partial T} + \left(\vec{\vartheta}\vec{\nabla}\right)P + Q\right. \quad (2)$$

Where ρ – density, C_p – heat capacity, T – temperature, $\vec{\vartheta}$ - liquid velocity vector, q – heat flow density, P – pressure, τ_{ij} - viscous stress tensor, η – viscosity, I – unit tensor, S_{ij} - deformation rate tensor, Q – inner heat sources.

Generalized mathematic model is based on the equation of the heat balance of the solid phase, equation of mass transfer of the gas component, equation of continuity, dynamics of filtration liquid and equation of state. Besides, it is necessary to formulate the appropriate boundary conditions. In order to solve this problem with help of computer, it is recommended to use special program, e.g. COMSOL Multiphysics.

The results of such researches where conducted for the penetrating thermoelement in 3D model and where received in the work [8] for the flow of the cooling liquid and air. This work investigates the influence of the speed of coolant's pumping and thermocouple supply voltage on the difference of temperatures and characteristics of energy penetration. It describes the optimal definition of the water's (air's) usage at the entrance of the channel and the difference of the potentials on the thermocouple, in order to achieve the maximal cooling ability during the cooldown. Optimization of the other parameters in 3D model is a great challenge.

III. Method of solving the formulated problem

Due to the diversity of applications, thermoelectric coolers can have many different configurations. With the help of COMSOL Multiphysics this package describes the basic construction of the single-stage thermoelectric cooler of different sizes with different thermocouples and other geometric characteristics. The modeled penetrating couple also can be used as the starting point for the more detailed calculations. The additional parameters of input might be extended on multi-stage thermoelectric coolers and be used in different conditions [9]. While using Peltier equation, the flow of the current from one end of thermoelectric elements to the other, creates orthogonal heat flows, which causes the temperature's drop between the plates, which gives the opportunity to calculate the productivity parameters. Afterwards this model can be used to search the best penetrating element with better productivity, equipment on its base, for the specific program or producer to optimize the construction and to provide the productivity.

In this paper is used the generalized theory of calculations of penetrating thermocouples taking into account the changes of appropriate parameters of the branch's material from the temperature and concentration of the charge's carriers and conditions of heat exchange along the height of the branch. This method of modeling of the distribution of temperature and heat's flow in 1D and 3D models of osmotic thermocouples, the improved theory of calculated osmotic thermocouples, is used to solve the tasks of multifactor optimization to achieve maximal energetic effectiveness in the viability of thermoelectric conversion. Since the penetrating couple is the element of thermocouple, so the heat exchange with the source of heat (extractor) takes place not only at the surface of spike, but also inside the branch of thermocouple [10]. In this case the extensive material becomes penetrated (with channels and pores), in order to pump the heat carrier through it (liquid or gas).

By mean of usage of highly penetrating materials, we can develop the inner surface of the heat exchange, increase the intensity of heat exchange, decrease the difference of temperature between the environments which exchange the heat. It urges to the increase of useful temperature's difference on the thermocouple, which can increase the effectivity of energy's transformation [5-7]. The volumetric distribution of the heat source (flow) in the penetrating branch of the thermocouple also might be influenced by the mean of change of the conditions of the heat transfer through the height of the branch. That's why we can influence on the energetic characteristics of the thermocouple – the cooling coefficient of the cooler or air conditioner.

IV. Calculation of the main characteristics of the penetrating thermoelement with the help of computer modeling

Thermocouple consists of two different conductors (stems), which contact with each other at one point (junction). When the temperature is set, the voltage appears between them across the connection. That's why the thermocouple is calibrated with the temperature sensor, and this can transform temperature gradients into the electric streams.

In order to estimate the characteristics of the penetrating thermoelectric thermoelement during the cooling regime using the COMSOL Multiphysics, first of all the geometry of thermoelement during the cooling regime was modeled. Let's describe more precisely geometry (fig. 2-3) of the modeled model.

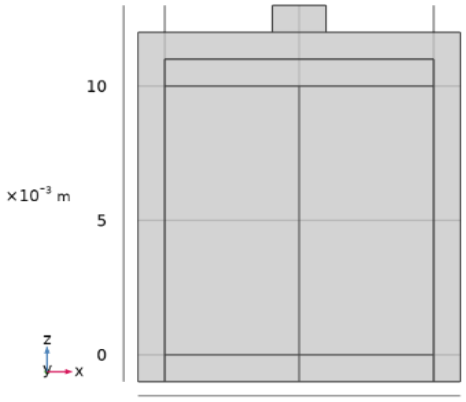

Fig. 2. One of the variations of thermoelement's geometry.

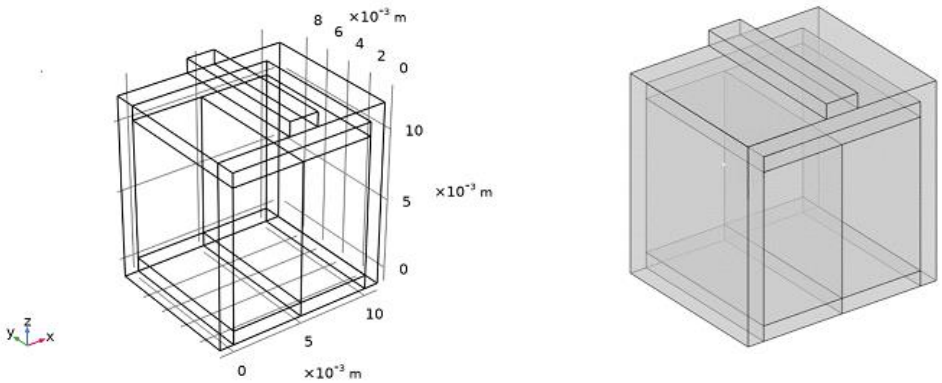

Fig. 3. Geometry of the penetrating thermoelement.

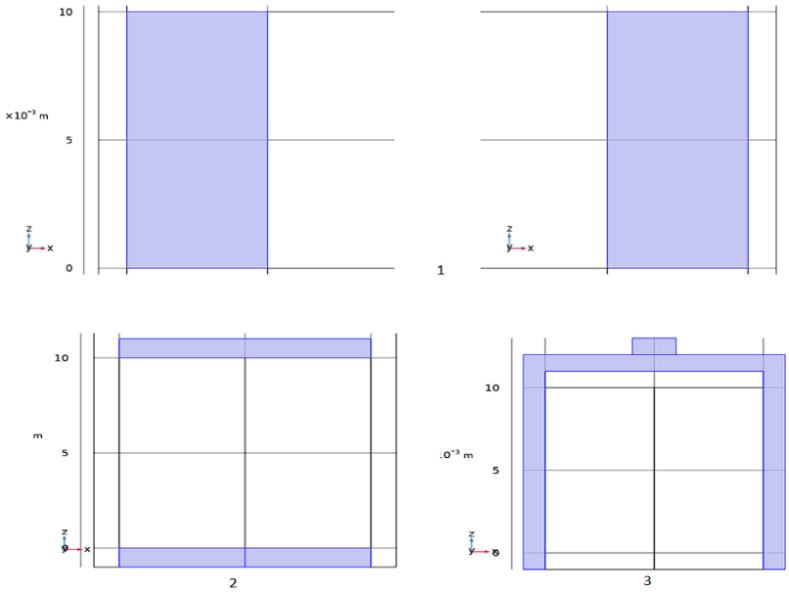

Fig. 4. Geometry of thermoelectric material – 1; commutation plates – 2; heat carrier – 3.

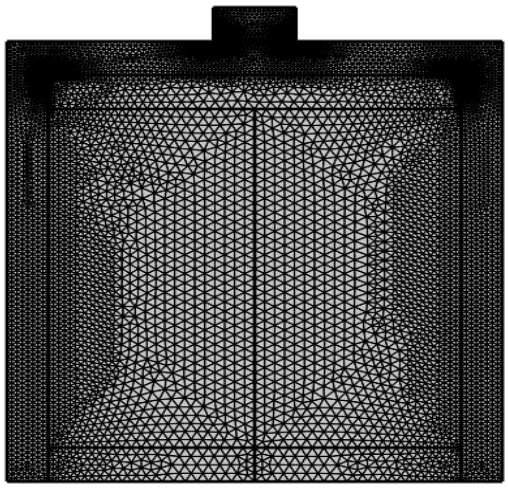

Fig. 5. Geometric grid.

Let's look at geometry of thermoelectric material with quality $Z = 0.002(\frac{1}{K})$.

On the figures (2 – 5) we can see the detailed visualization of geometry of the modeled thermoelement, where every detail of the created model is shown very precisely.

So, with the help of COMSOL Multiphysics we can observe the temperature distribution in the thermoelectric cooling module.

At the figure 6 we can clearly observe that isothermal surfaces and heat flow are shown relentlessly in the module itself and in the coolant. The distribution of speed in the coolant (fig. 7), distribution of electric potential of the penetrating thermoelement (fig. 8) and distribution of thermoelectric field of the penetrating thermoelement

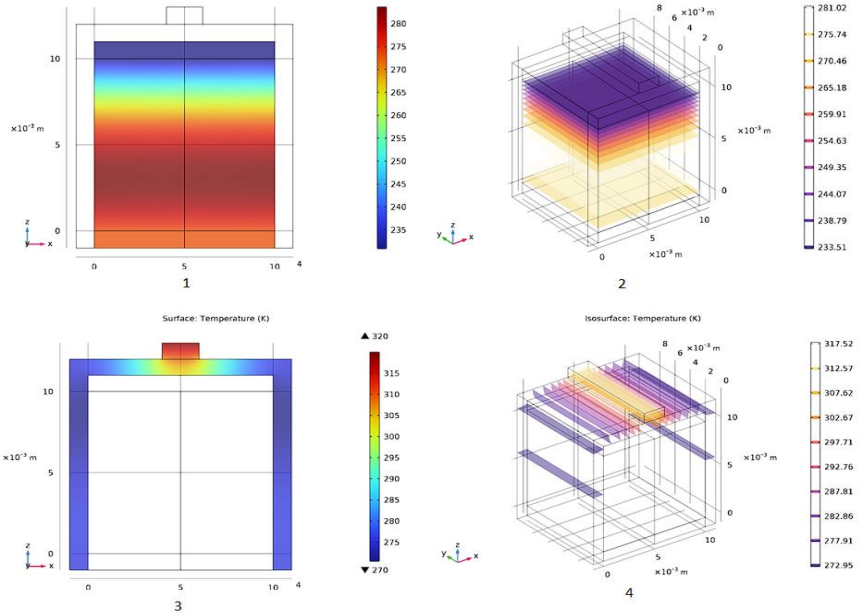

Fig. 6. Computer model of temperature distribution in the module – 1; isothermal surface of thermoelement – 2; distribution of temperature in the heat carrier – 3; isothermal surface of thermoelement – 4.

Table 1.

Parameters of the penetrating thermoelement in the cooling regime

H	1 (cm)	2 (cm)	3 (cm)	4 (cm)	5 (cm)
U, V	0.0355	0.0355	0.0355	0.0355	0.0355
T_x, K	230.01	230.3	230.62	230.95	231.28
$T_{пов}$, K	265.39	273.84	268.67	269.88	270.64
Q_c, W	0.96038	0.48661	0.32848	0.24934	0.20182
I, A	13.29	6.72	4.5173	3.3956	2.7165
G, m/s	7.7259E-4	8.2136E-4	8.2738E-4	8.3124E-4	8.3277E-4
W, W	0.95107	0.47727	0.31911	0.23997	0.19247
COP	2.03558749	2.039780349	2.04833811	2.068459763	2.092792351

Table 2.

The comparative characteristics of classic and penetrating thermoelement

	Classic thermoelement	**Penetrating thermoelement**
H, cm	1 cm	1 cm
U, V	0.0355	0.0355
T_x, K	241.14	230.01
$T_{пов}$, K	0	265.39
***Q_c*, W**	0.79542	0.96038
I, A	12.14	13.29
***G*, m/s**	0	7.7259E-4
***W*, W**	0.89741	0.95107
COP	1.846	2.036

(fig. 9) are shown with the help of computer modeling.

The results of the modeling are put in the table. The parameters of the penetrating cooling thermoelement for different height of branches, which were calculated with the help of computer modeling, are given in the table 1. Where H – height of thermoelement, U – output voltage, T_x – temperature of cold junction of thermoelement, Q_c – cooling capacity, I – input voltage, G – speed of the coolant, W – consumed power, COP – coefficient of thermoelement productivity is defined as

$$COP = \frac{Q}{UI} \qquad (3)$$

Formula (3) gives the most effective indicators of thermoelectric cooling, when the heat, which is consumed already allocated to the input voltage, reaches the maximum.

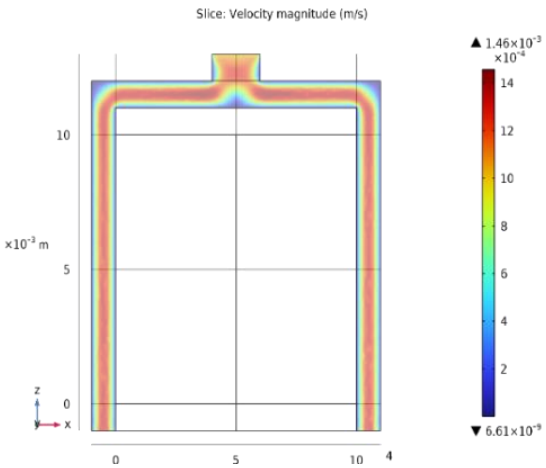

Fig. 7. Distribution of speed in thermoelement.

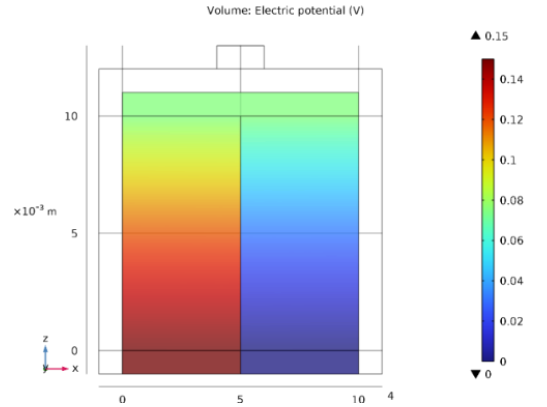

Fig. 8. Allocation of electric potential of thermoelement

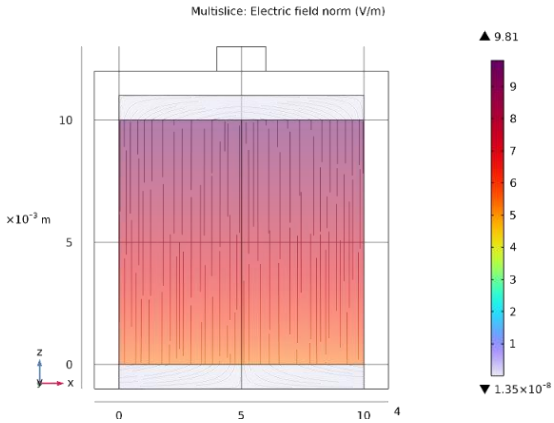

Fig. 9. Allocation of electric field in thermoelement.

When we compare parameters with the classic thermoelement, the theoretical calculations show that the usage of such allocators at the optimal conditions increases the cooling coefficient at 10-30%. The comparative characterization is shown in chart 2.

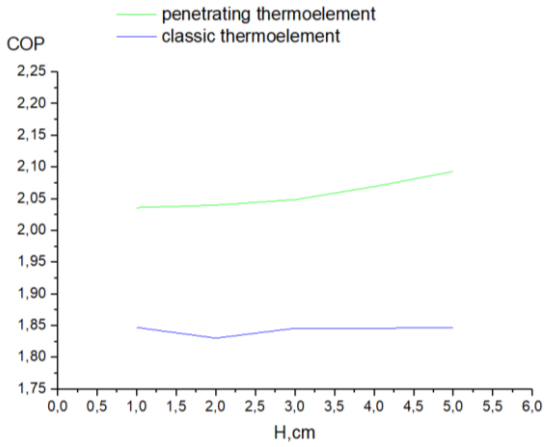

Fig. 10. Graphic of dependence of COP on height of thermoelement.

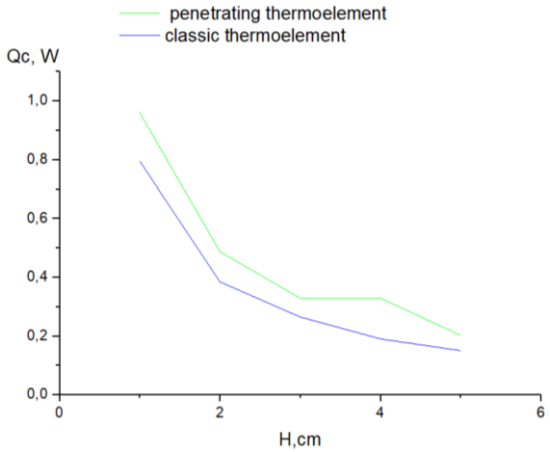

Fig 11. Graphic of dependence of cooling capacity to height of thermoelement.

The obtained results proved the perspectivity of the researches and creation of penetrating thermoelectric modules, and show that in case of geometry and height (1cm) for two modules, the advantage of the penetrating thermoelement is in the better coefficient of productivity of thermoelement at 9.33%. On the base of calculations from table 1, the graphics of dependence of COP (fig. 10) and cooling capacity (fig. 11) on height of thermoelement where built.

Based on the given model of thermoelectric cooler, the mathematic description of the basic processes is given. These processes lead to the mutual transformation of thermal and electric energy in the thermoelectric refrigerators with the help of computer modeling at the COMSOL Multiphysics. With the help of modeling is proved that while changing the conditions of the heat exchange along the height of the branch, we can influence at the volumetric distribution of the sources of heat in the branches of the penetrating thermoelement.

Conclusions

The usage of the penetrating thermoelectric coolers of such transformers of the energy allows to increase the cooling coefficient by 10-30%. The received results demonstrate the perspectivity of the researches and creation of the penetrating cooling thermoelements. They show that, as in case of the height of branch at 1cm, the advantage of the penetrating thermoelement is at the higher cooling productivity of thermoelement at 9.3%.

Cherkez R.G. – Doctor of Physics and Mathematics Sciences, professor of the department of thermoelectricity and medical physics of the Chernivtsi National University named after Yu. Fedkovicha;
Semeshkin V.A. – Postgraduate student of the Department of Thermoelectricity and Medical Physics of the Chernivtsi National University named after Yu. Fedkovicha;
Zhukova A.S. – student of the Department of Computer Sciences of the Chernivtsi National University named after Yu. Fedkovicha;
Stefiuk V.V. – student of the department of thermoelectricity and medical physics of the Chernivtsi National University named after Yu. Fedkovicha.

[1] E. K. Iordanishvili, B. E-Sh. Malkovich, M.N. Veish, *Experimental research of nonstationary thermoelectric cooling. 2. Regime of extremal voltage*, Journal of Engineering and Physics, 22, (2), 220 (1972).
[2] L. F. Ioffe, L. S. Stilbans, E. K. Iordanishvili, T. S. Stavitskaia, Thermoelectric cooling, Moscow; Leningrad, Publisher AofS USSR, 108 p., 1956.
[3] A. F. Ioffe, Semiconductor thermocouples, Moscow; Leningrad, Publisher AofS USSR, 188 p. (1960).
[4] L.I. Anatychuk, Thermoelectric power converters, Thermoelectricity. Volume II. Chernivtsi: Bukrek, 2003. 376 p.
[5] V. N. Kozliuk, H. M. Shchegolev, *Thermodynamic analysis of the penetrating thermoelectric refrigerators*, Thermophysics and thermal engineering. Ed. 25, 96 (1973).
[6] G. K. Kotyrlo, V. N. Kozliuk, Y. N. Lobunets, *Thermoelectric generator with the developed surface of the heat exchange*, Thermal problems of the straight transformation of energy, Ed.7., 85 (1975).
[7] Y. N. Lobunets Methods of calculation and engineering of thermoelectric procreators of energy, Kyiv, Scientific thought (1989).
[8] Cherkez R. G., Feniak P. P., Demianiuk D. D. *Computer modeling of the penetrating thermoelement of cooling*, Thermoelectricity, 5, 64 (2013).
[9] L.I. Anatychuk, R.G. Cherkez, *On the Properties of Permeable Thermoelements*, Proc. of XXII Intern. Conf. on thermoelectrics(France), 480 (2003).

[10] L.I. Anatychuk, L. N. Vihor, *Computer engineering of cascade modules for generators*, Thermoelectricity, 4, 19 (2002).

Р.Г. Черкез[1,2], В.А. Семешкін[2], А.С. Жукова[2], В.В. Стефюк[2]

Вплив висоти пластин на ефективність проникного термоелемента в режимі охолодження

[1]*Інститут термоелектрики НАН та МОН України, м. Чернівці, Україна,*
[2]*Чернівецький національний університет ім. Ю. Федьковича, м. Чернівці, Україна, r.cherkez@chnu.edu.ua*

У роботі описано фізичну модель проникного термоелемента з розвиненою поверхнею теплообміну для охолодження потоку повітря. Представлено теорію розрахунку та метод комп'ютерного моделювання розподілу температур та потенціалів, визначення ефективності перетворення енергії - холодильного коефіцієнту та холодопродуктивності, досліджено 3D розподіл температур та потенціалів для матеріалу віток термоелемента на основі Bi_2Te_3.

Ключові слова: проникний термоелемент, холодильний коефіцієнт, холодопродуктивність, 3D-модель.

PHYSICS AND CHEMISTRY OF SOLID STATE
V. 24, No. 2 (2023) pp. 392-402
Section: Chemistry

DOI: 10.15330/pcss.24.2.392-402

Vasyl Stefanyk Precarpathian National University

ФІЗИКА І ХІМІЯ ТВЕРДОГО ТІЛА
Т. 24, № 2 (2023) С. 392-402
Хімічні науки

PACS:78.30.Er; 75.50.Vv ISSN 1729-4428

Farhana Naaz[1], Preeti Lahiri[1*], Chanda Kumari[1], Hemant Kumar Dubey[2]

Spectroscopic, Magnetic and Morphological studies of $MgFe_2O_4$ Nanopowder

[1]*Department of Chemistry, Institute of Science, MMV, Banaras Hindu University, Varanasi-221005, India* plahiri16@yahoo.com
[2]*Department of Chemistry BRD PG College, Deoria-274001, India*

Spinel type nano ferrite compound $MgFe_2O_4$ was synthesized through sol gel technique using metal nitrates as precursors. The phase composition, morphology and elemental analysis of magnesium ferrite ($MgFe_2O_4$) were performed by X-ray diffraction, fourier transform infrared, atomic force microscopy, energy dispersive x-ray and scanning electron microscopy, analyses.

The sample's X-ray diffraction pattern verifies the existence of single phase material, with the size of its crystallites estimated to be 39.9 nm. Fourier transform infrared examination supported metal-oxygen vibrations corresponding to tetrahedral and octahedral sites, respectively. From scanning electron microscopy image, grain size obtained about 97.7 nm. Raman spectra of the sample shows five Raman active modes ($A_{1g} + E_g + 3F_{2g}$), which is compatible with the spinel structure. Magnetic measurement study at room temperature shows a hysteresis loop behaviour with a low saturation magnetization value, 27.192 emu g^{-1} and a small coercivity value. The optical band gap determined using UV-visible transmittance spectra. Additionally, X-ray photoelectron spectroscopy are used to confirm oxidation states and explore the chemical composition of the sample.

Keywords: Spinel ferrite, Nanocrystalline, X-ray diffraction, Raman spectra, Magnetic properties.

Received 17 January 2023; Accepted 20 June 2023.

Introduction

Ferrites belong to ferromagnetic materials. Ferrite nanomaterials have shown applications in various ways, such as music recording heads, core materials for power transformer in electronics and telecommunications [1,2]. Importantly, magnetic oxide nano-based materials differently from bulk material in terms of their physical, chemical, magnetic and electrical properties [3]. Advantages of nanomaterials rest on their superior thermal stability, environmental and economic advantages to regular counterparts. Owing to their finite size effect, high surface to volume ratio, unique crystal structures, and magnetic characteristics, spinel ferrites nanoparticles have generated a lot of attention in recent years. The general formula for spinel ferrites is AFe_2O_4, where A and Fe are divalent and trivalent metal cations, respectively, with Fe serving as the major constituent. Spinel ferrites are represented by the general formula AFe_2O_4, where A and Fe are divalent and trivalent metal cations, respectively with Fe as major constituent. Due to their interesting magnetic and electrical properties, they have drawn significant attention to the researchers. Structurally, the spinel ferrite is a cubic closed packed organization of oxygen atoms with 8 formula units per unit cell. Since the radius of oxygen ion is greater than that of metal ion, the oxygen touches each other and form a closed packed Face centered cubic (FCC) lattice. The spreading of cations between A or B site of the lattice depends on both parameters such as preparation routes and heat treatment [4-6].

$MgFe_2O_4$ is the most adaptable, vital and multipurpose spinel ferrites due to unique and reproducible characteristics. They include high saturation magnetization value, and electrical resistivity [7]. Through these magneto-electrical properties $MgFe_2O_4$ show a great utility in the area of catalysis, sensors, high-density recording media and other magnetic technologies [8]. Overall, it is a n-type semiconducting as well as soft

magnetic material. Both photocatalytic activity and catalytic effect of magnesium ferrite in a heterogeneous Fenton-like reaction have been studied [9,10]. Magnesium ferrites typically have the structural formula $(Mg_{1-x}^{2+}Fe_x^{3+})_A[Mg_x^{2+}Fe_{2-x}^{3+}]_B O_4$,is stated as the percentage of the (A) sites occupied by Fe^{3+}cations, where A , B stand for the cationic sites of tetrahedral and octahedral co-ordinations respectively, where x represents the degree of inversion. The structural and magnetic properties of $MgFe_2O_4$ obtained from transmission electron microscopy, XRD, Mossbauer spectroscopy, and magnetometry have been reported [11]. Numerous studies [12,13] on $MgFe_2O_4$ nanoparticles described their nanostructures and many properties, including IR, XRD, SEM, and VSM. N-Suresh kumar [14] synthesized nickel substituted magnesium ferrites by auto combustion method and also studied dielectric and magnetic properties. Magnetic and structural properties of $MgFe_2O_4$ nanopowder synthesized by EDTA-based sol–gel reaction has been reported by Shaban I. Hussein [15]. The electronic structure of $MgFe_2O_4$ nanoparticles created chemically has also been examined by Singh et al [16]. Nanoparticles of $MgFe_2O_4$ have good photoelectrical properties [17]. The synthesis of spinel magnetic oxide involves different chemico-physical approaches that include co-precipitation [18], sol-gel method [19], wet chemical method [20], combustion method [21], hydrothermal method [22], microwave assisted [23], micro-emulsion [24], and ceramic technique [25]. Each method has its own merits and demerits in terms of its ease, efficiency, yield, and costs.

Considering these criteria, we find the sol gel method is effective and can work at low temperatures. Briefly, the sol–gel is a process for developing solid materials from small molecules. In this case, monomers are converted into colloidal solution (sol) that acts as a precursor for an integrated network (or gel) of discrete particles or network polymers. This approach is applicable for the production of metal oxides, like silicon and titanium. Metal alkoxides are common precursors. This chemical technique yields a "sol" which develops into a diphasic system with a liquid phase and solid phase that can have different morphologies, such as discrete particles or continuous polymer networks. Metal alkoxides are typical precursors. Several other names of the sol-gel method are low-temperature self-combustion, auto-ignition, self-propogation, and gel thermal decomposition methods.

We explain, in this paper, the characterization of single phasic cubic spinel ferrites using a sol gel technique by systematic examinations on the structural and physiochemical properties of magnesium ferrites nanoparticles based on several characterization parameter like XRD, SEM, FT-IR, EDX, and magnetic. AFM was utilized to determine the nanoparticles surface roughness and also to obtain 2D and 3D images. Moreover, Raman spectroscopic studies was added to understand the vibrational modes and structural studies of the materials, the optical behaviour of the nano-particles was investigated to determine the absorbance range 300-780 nm, which spans the visible region and is important for various photovoltaic and photocatalytic properties. Moreover, the chemical and elemental state of the nano-particles was concluded by using XPS analysis.

Furthermore, we found that the sol gel technique is the most suitable for creating good molar ratio control with small particle size distribution due to molecular-level mixing, fast processing time, lower temperatures and inexpensive.

I. Experimental Procedure

$MgFe_2O_4$ was prepared via the auto-combustion aided sol-gel method. The energy required to produce the ferrite nano-particles is provided in this procedure by a redox process using a thermal precursor and citric acid as a fuel [26]. Metal nitrates were served as a source of soluble cations and the oxidant [27]. Citric acid ($C_6H_8O_7$) was employed as both a fuel and a chelating agent, forming interactions with metal ions and preventing the precipitation of hydroxilated compounds [28]. Analytical reagent grade, Merck India, used in this work were: iron nitrate ($Fe(NO_3)_3 \cdot 9H_2O$, 99%) magnesium nitrate ($Mg(NO_3)_2 \cdot 6H_2O$, 98%) and citric acid ($C_6H_8O_7$). The desired composition was obtained by taking stoichiometric molar ratio (2:1) of $Fe(NO_3)_3.9H_2O$ (0.032 mol) and $Mg(NO_3)_2.6H_2O$ (0.016 mol) dissolved in 20 ml of double distilled water. To promote homogeneity, an equimolar amount of citric acid (0.046 mol) was added to an aqueous mixture, which was magnetically agitated while the reaction temperature was kept at 60^0C.The pH was optimize to 7.0 by adding ammonia solution drop by drop under steady stirring until the mixture was neutralised and turned into sol. The sol developed into a black gel after 8 hours of stirring, releasing a huge amount of gases (CO_2, H_2O, N_2) in the process. The gel was dried for 12 hours at 100 ^{0}C, with its volume swelling by nearly five times, yielding a fluffy, abundant powder. At end, the dried gel was grounded and annealed at 500 ^{0}C for 3 h to get a dark brown ferrite nanoparticle as a final product. The Flow chart of the sol-gel synthesis process of $MgFe_2O_4$ nanoparticles is given below.

The structural investigations (crystal structure and phase analysis) of the synthesized nanomaterial were performed by using XRD, Rigaku Miniflex 600, Japan technique with Cu-Kα radiation (λ=1.5406 A^0) within 2θ range 20-80º. The FTIR spectrum was obtained in the range 400 cm^{-1} to 4000 cm^{-1} employing a FTIR spectrometer, Perkin Elmer. SEM, (ZEISS model EVO-18 research, Germany) and AFM, model NTEGRA PRIMA, NT-MDT, Russia was used to determine microstructure and surface roughness of nanomaterial respectively. The quantitative elemental analysis was carried out by means of EDAX analyser (EDX, Oxford instrument USA). The magnetic behaviour of the produced sample was investigated using a SQUID-based magnetometer (MPMS 3) in the magnetic field range of 20 kOe. Raman spectra was recorded to estimate the frequency mode of tetrahedral and octahedral sites of cubic spinel at frequency range of 100-800 cm^{-1}, using the model RENISHAW In-VIA Raman microscope. UV–VIS diffuse reflectance spectra were acquired by UV-VIS Spectrophotometer SHIMADZU in the wavelength range of 200–600 nm (UV-1700 Pharma Spec), chemical and elemental state analysis of the investigated surface were indicated by XPS, Thermo scientific K-ALFHA Surface Analysis.

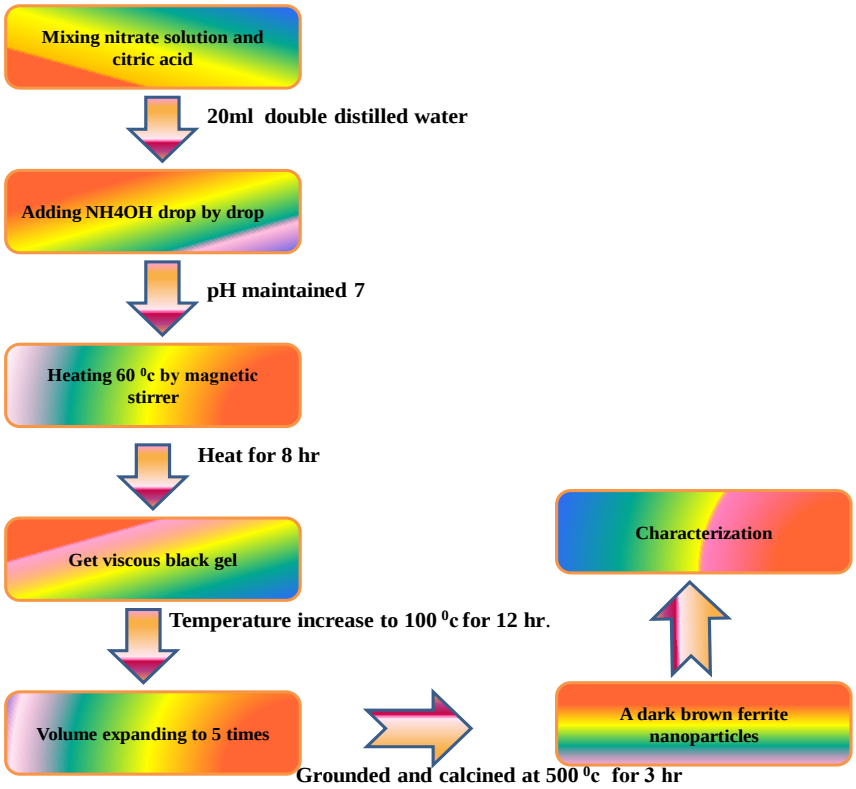

Flow chart of the sol-gel synthesis process of $MgFe_2O_4$ nanoparticles.

II. Results and Discussion

2.1 FTIR analysis

Figure 1 illustrates room temperature IR spectrum of the magnesium ferrite sample determined in the range 400 to 4000 cm^{-1}. The calcined $MgFe_2O_4$ magnetic nanoparticle exhibits two main absorption bands at around 630 and 441 cm^{-1}. The higher frequency band (ν_1) and the lower frequency band (ν_2), specify the metal-oxygen intrinsic stretching vibration of the spinel unit cell in the tetrahedral (A) and octahedral (B) sites [29] respectively. The observed variance in band positions is due to the distance between the metal-oxygen ions connected to the octahedral and tetrahedral complexes. This indicates bond formation and the phase stability of synthesized material. TheFTIR results confirmed that the sample has spinel structure of $MgFe_2O_4$, which was revealed by the XRD results. The strong signature band observed at 3420 cm^{-1} is assigned to the symmetric streching vibrations of O-H groups [30]. The symmetric stretching vibration of hydrogen bonded water molecules is responsible for the perturbations in the absorption band between 1030 and 1630 cm^{-1}, indicating the existence of absorbed or free water molecules in a sample. The force constant (k) was evaluated from the equation [31],

$$k = 4\pi^2 c^2 m\nu^2 \quad (1)$$

where, c is the velocity of light (2.99×10^8 m/sec), v is the vibrational frequency of the A and B sites, m is the reduced mass for the metal-oxygen ions. Values obtained for force constant are shown in Table 1.

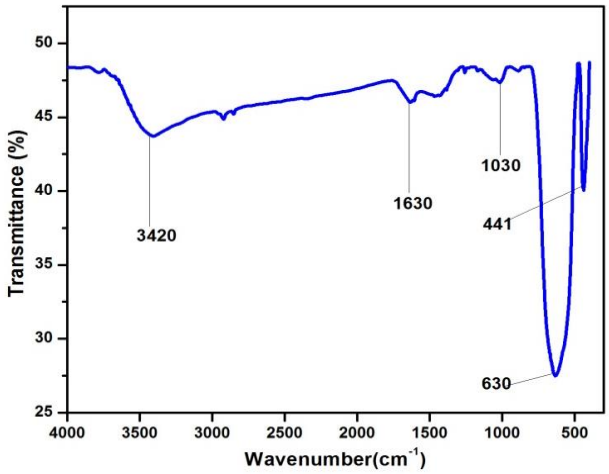

Fig. 1. The FT-IR spectra of Magnesium ferrite nanoparticles.

2.2 X-ray diffraction analysis

Powder X–ray diffraction studies are helpful in determining the structure and particle size of nanoparticles produced. The XRD of powdered sample of $MgFe_2O_4$ obtained by sol-gel method is illustrated in Fig. 2. The XRD pattern reveals formation of monophase face centered cubic (fcc) spinel structure. All Bragg reflections have been indexed as (111), (220), (311), (222), (400), (422), (511) and (440). All observed sharp diffraction peaks were compared with magnesium ferrite JCPDS card number 89-3084. The most intense peak at 2θ=35.55 degree corresponds to crystalline plane of

magnesium ferrite which indicates a fine particle nature of the particles.

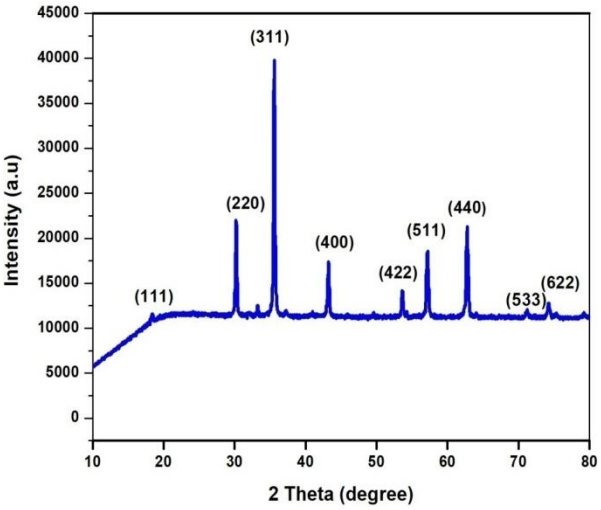

Fig. 2. X-ray diffraction patterns of Magnesium ferrites nanoparticles.

The average crystallite size (D) was estimated from the XRD peak broadening of the most intense peak (311) using the Scherrer's relation [32],

$$D = \frac{k\lambda}{\beta \cos\theta} \quad (2)$$

where, k is Scherrer's constant (0.91), λ is wavelength (λ=1.5406 A^0). The parameters D and θ are taken as crystallite size and Bragg's angle respectively. Here β is the full width at half maxima (FWHM) of XRD peaks. Table 1 shows the calculated values for crystallite size, x-ray density ,lattice constant, and cell volume based on x-ray data. The average crystallite size (D) of the synthesized material was found to be 39.9 nm (Table I) for $MgFe_2O_4$. The lower value (36.6 nm) was reported for the same sample synthesized by co-precipitation method [33].

The lattice constant 'a' was calculated for prominent (311) peak using the following relation,

$$a = d\sqrt{h^2 + k^2 + l^2} \quad (3)$$

where d is interplanar distance and *h,k,l* are the miller indices of the diffraction plane. The calculated lattice parameter 'a' (8.35 A^0) for $MgFe_2O_4$ agrees well with the reported value of 8.37A^0 [34]. Following relation was used to calculate x-ray(ρ_x) density,

$$\rho_x = ZM/N_A a^3 \quad (4)$$

where *Z* is the number of molecules per unit cell (Z = 8), M is the molecular mass of the sample, and N is the Avogadro's number ($N_A = 6.026 \times 10^{23}$ atoms mol^{-1}). The sample of ferrite was determined to have a density of 4.554 g/cm^3 (Table 1).

Utilizing the following formula, the volume of the unit cell was computed,

$$V = a^3 \quad (5)$$

in$(A^0)^3$ units. Relationships were used to determine the distance between magnetic ions and the hopping length (L) in the A sites (tetrahedral) and B sites (octahedral) [35],

$$L_A = \frac{a\sqrt{3}}{4} \text{ and } L_B = \frac{a\sqrt{2}}{4} \quad (6)$$

It was observed that the hopping lengths for two sites were 3.615 A^0 and 2.951 A^0 respectively in Table 1.

2.3 SEM and EDX analysis

The surface morphologies and elemental composition of magnesium ferrite nano powder were examined by SEM, coupled with EDX analysis. In Fig. 3 (a) SEM image of calcined $MgFe_2O_4$ sample is illustrated. Agglomerates and non-uniformity are evident in the sample. The grain size was estimated using AIL [36]. The number of grain boundaries intersected by a randomly chosen straight line of length L drawn on micrographs was counted, and the average grain diameter (G), which is around 98 nm, was computed, N is the total number of the complete sample, and M is the magnification.

$$G = 1.5L/MN \quad (7)$$

The elemental analysis of the prepared $MgFe_2O_4$ nano powder was obtained by EDX analysis and weight % and atomic % of elements were shown in the Table 2. The estimated ferrite composition is confirmed by EDX data, which is reinforced by the good agreement between experimental and theoretical Mg/Fe molar ratio (Table 2). The sample's EDX pattern, which displays the presence of Mg, Fe, and O without precipitating cations, is demonstrated in Fig. 3(b).

Table 1.

Some structural parameters; crystalline size, lattice parameter, X-ray density, unit cell volume, hopping length for A-Site (d_A) and B-Site (d_B) and force constants for octahedral (k_o) and tetrahedral (k_t) sites of Magnesium ferrite nanoparticles

Sample	Crystalline size (nm)	Lattice parameter (A^0)	X-ray density (g/cc)	Unit cell volume $(A^0)^3$	Force constant $k_o \times 10^5$ (dyne/cm)	Force constant $k_t \times 10^5$ (dyne/cm)	A site d_A (A.u)	B Site d_B (A.u)
$MgFe_2O_4$	39.9	8.35	4.554	583.79	1.414	2.886	3.615	2.951

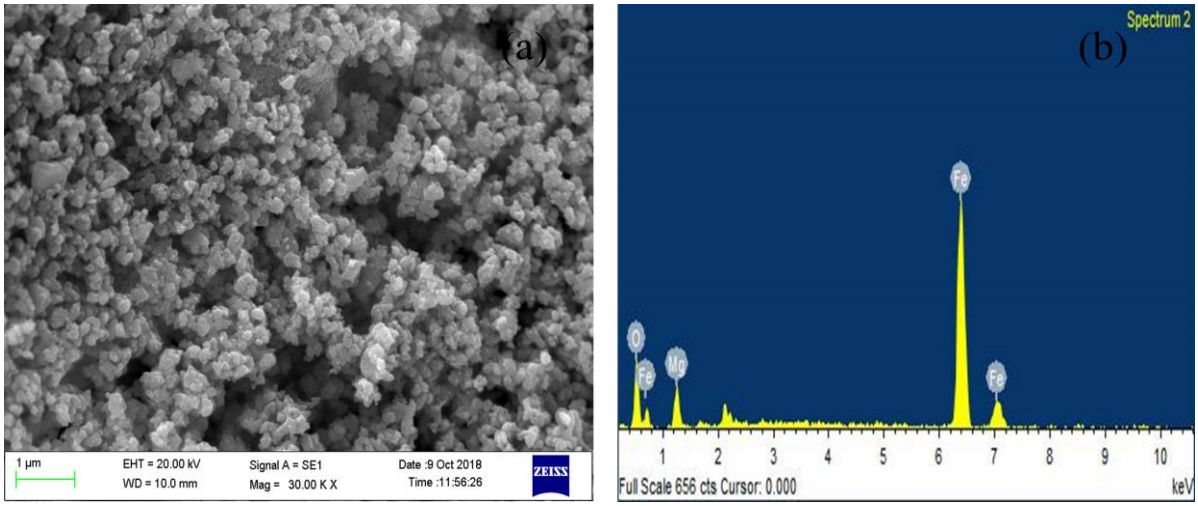

Fig. 3. (a) SEM image and (b) EDX analysis of Magnesium ferrite nanoparticles.

Table 2.

The observed and theoretical elemental composition value of $MgFe_2O_4$ obtained from EDX analysis

Element	Experimental value		Theoretical value	
	Weight %	Atomic %	Weight %	Atomic %
O	21.51	44.41	31.98	57.15
Mg	11.95	16.23	12.15	14.26
Fe	66.54	39.35	55.84	28.57
TOTAL	100.0			

2.4 AFM analysis

Thin film topography of $MgFe_2O_4$ nanoparticles obtained by AFM (atomic force microscopy). This microscopic technique has several advantages for characterising nanoparticle. Images obtained via AFM display data in two and three dimensions, allowing for the quantitative generation of information on both individual particles and groups of particles. Fig. 4. display the 2D and 3D AFM images of $MgFe_2O_4$ respectively and its related histogram and size distribution. The average roughness (Rq) and root mean square roughness (RMS) values obtained about 5.982 nm and 7.541 nm respectively. Also, the maximum height (R_p) and a maximum depth (R_v) observed as 35.645 nm and 27.449 nm respectively.

2.5 Raman analysis

Raman spectroscopic technique is a powerful technique to identify the structural and vibrational properties of the material $MgFe_2O_4$ spinel. $MgFe_2O_4$ crystallises as an AB_2O_4 type spinel structure with eight formula units per unit cell in Fd3m space group.According to results from group theoretical calculations, AFe_2O_4 type spinel structures consist of five raman active phonon modes, namely $A_{1g}+E_g+3F_{2g}$, which are made up of the motion of O ions and both A and B site ions [37,38]. Figure 5 displays the $MgFe_2O_4$ sample's raman spectra in the frequency range of 100–800 cm^{-1}. In Table 3 and Fig. 5, several peaks have been identified. The A_{1g} (1) mode is caused by the symmetric stretching of oxygen atoms along Fe–O (or M–O) tetrahedral bonds. The E_g & F_{2g}(3) modes are caused by the symmetric and asymmetric bending of oxygen with respect to Fe respectively. The F_{2g} (2) mode is caused by the asymmetric stretching of the Fe–O bond, F_{2g} (1) is due to translational movement of the whole tetrahedron (FeO_4) [39], while F_{2g}(2) and F_{2g}(3) related to the vibrations of octahedral group.

Table 3.

Raman modes of spinel $MgFe_2O_4$ and their assignments

Raman Modes (cm^{-1})	Assignment
209	F_{2g}(1)
330	E_g
479	F_{2g}(2)
549	F_{2g}(3)
707	A_{1g}

In our system, $MgFe_2O_4$ nanopowder contains five peaks at 209, 330, 479, 549 and 707 cm^{-1} (Table 3). These bands are given the following designations: F_{2g} (1), E_g, F_{2g} (2), F_{2g} (3) and A_{1g} (1) correspondingly. These modes match the reported [40] values of 217, 333, 486, 554, and 715 cm^{-1} for magnesium ferrites. It agrees well with the current strong band location for $MgFe_2O_4$ at 707 cm^{-1}, which J. Chandradass [41] attributed to the A_{1g} mode in $MgFe_2O_4$.

2.6 VSM analysis

To investigate the magnetic behaviour of spinel $MgFe_2O_4$, SQUID based magnetometer has been employed under magnetic field upto 20 kOe.By applying a magnetic field to a material that becomes magnetized by the magnetic field, the M-H loop or hysteresis curve is

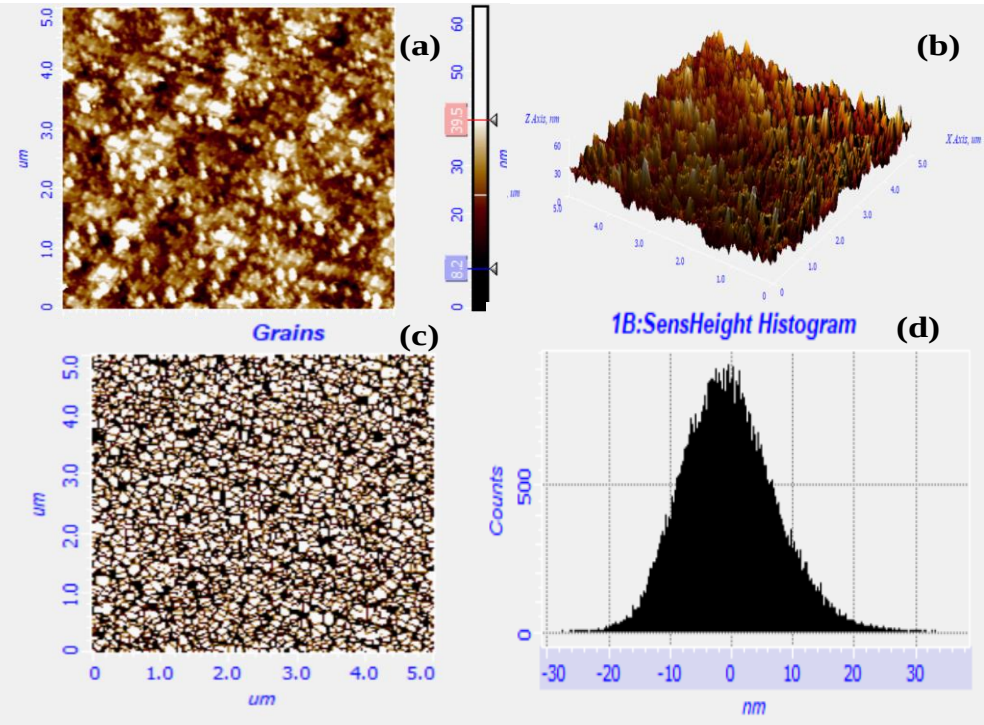

Fig. 4. AFM images of $MgFe_2O_4$ nanoparticles. (a) Two dimension (2D) (b) Three dimension (3D) (c) examination of grain size (d) histogram of $MgFe_2O_4$ nanoparticles.

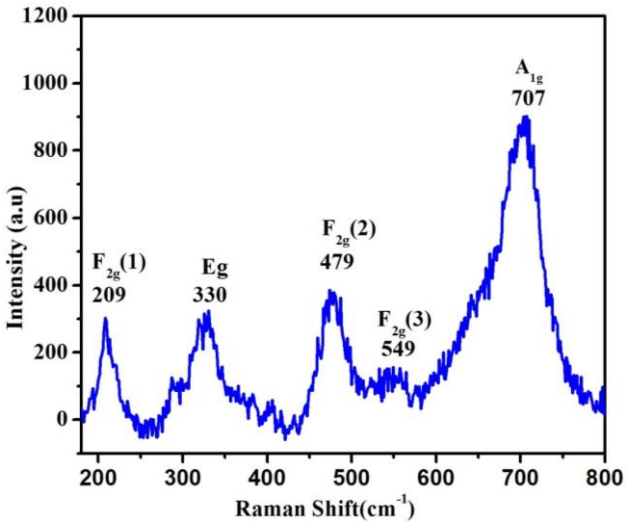

Fig. 5. Raman spectra of synthesized spinel $MgFe_2O_4$ nanoparticles.

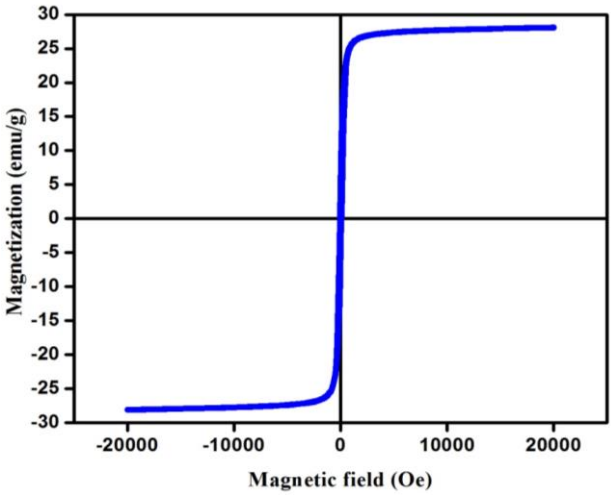

Fig. 6. Magnetisation curve of $MgFe_2O_4$ nanopowder under applied magnetic field of 20 kOe.

formed. Remanence magnetization is the value of magnetization at which field is zero. The point on the curve where the magnetization is zero and the field is negative is referred to as the coercive field, and the saturation magnetization is the point at which the magnetising force stops increasing the magnetic induction in a magnetic material. The room temperature magnetization curve of the calcined $MgFe_2O_4$ nanoparticle obtained from M-H loop is depicted in Fig. 6. This curve denotes hysteresis ferromagnetism and is typical for soft magnetic materials.

Magnetic parameters such as saturation magnetization (M_s), coercivity (H_c), retaintivity (M_r) and remanent ratio (R) values; 27.192 emu g^{-1}, 36.0 Oe, 0.4646 emu g^{-1}, 0.0170 respectively of ferrite nanoparticles are listed in Table 4. It was observed that the saturation value of

Table 4.

The coercivity (H_c), saturation magnetization (M_s), retaintivity (M_r), remanant ratio (R), and magnetic moment (μ_B) obtained at a magnetic field at 20 k Oe at room temperature

Sample	M_s (emu/g)	H_c (Oe)	M_r (emu/g)	M_r/M μ_B
$MgFe_2O_4$	27.192	36.00	0.4646	0.0170 0.9737

27.192 emu/g obtained in the sample calcined at 500^0C (crystallite size of 39.9 nm) is close to the values of 33.4 emu g^{-1} for bulk $MgFe_2O_4$ [42] and 30.6 emu g^{-1} for sol-gel/combustion synthesized $MgFe_2O_4$ (crystallite size of 78 nm) [43], while it is higher than the values of 14.09 emu g^{-1} for co-precipitation synthesized $MgFe_2O_4$ nanoparticles (diameters of 34.4 nm) [44]. Remanent magnetisation (M_r) value for the sample was obtained from the Fig. 6. The $MgFe_2O_4$ nanopowder's Mr/Ms ratio, which measures remanent magnetization to bulk saturation magnetization, was calculated to be 0.0170. A significant portion of superparamagnetic particles are indicated by the low Mr/Ms value. The coercivity (H_c) was found to be 36 Oe (Table 4) for the $MgFe_2O_4$ nanaparticle. The value is less than the value of 165 Oe for $MgFe_2O_4$ produced by sol–gel/combustion but is comparable to the value of 48.86 Oe for nanoparticles made by coprecipitation.

Sub-lattices A and B are magnetised in opposing directions by the spins of the A and B site ions, producing a magnetic moment that is equal to the difference between the magnetic moments of the A and B site ions [45]. The magnetic moment per formula unit is given by the equation,

$$M = M_B - M_A \quad (8)$$

where M_B and M_A stand for the B- and A- sublattice magnetic moments in uB, respectively. This formula is based on Neel's two sub-lattice model of ferrimagnetism [46]. The Ms value is typically determined by the net magnetic moment. According to the literatures [47,48], the octahedral positions are preferentially occupied by Mg^{2+} cations in the bulk magnesium ferrite, which has an inverted spinel structure. The cationic distribution on tetrahedral and octahedral lattice sites has a significant impact on the Ms of spinel ferrite nanoparticles [49].

The following relation [50] was used to compute the magnetic moment per formula unit in Bohr magneton (B) of the sample,

$$\mu_B = M_w \times M_s / 5585 \quad (9)$$

where M_S is the saturation magnetization in the electromagnetic unit and M_w is sample's molecular weight. Table 4 displayed the magnetic moment's value.

2.7 Optical studies

The UV-vis spectra of $MgFe_2O4$ were conducted using dil HCl as a solvent in order to examine the optical characteristics of the prepared nanoparticles. The absorbance extends around 300-600 nm shows visible region which is important for numerous application in photo-catalytic and photo voltaic activity. Fig. 7(a) displays the UV-visible absorbtion spectra of 500°C-calcined magnesium ferrite nanopowder as a function of wavelength (nm). Typical band throughout 300-500 nm is proclaimed in optical absorption spectra of $MgFe_2O_4$ nanoparticles. These bands results from octahedral coordination of Fe^{3+} ions [51]. The absorption cutoff wavelength is 427.5 nm. The optical band gap energy (Eg) of magnetic nanoparticles sample was calculated according to the Tauc relationship as given below [52],

$$Ahv = A(hv - Eg)^n \quad (10)$$

where (α) absorption coefficient, (Eg) the energy gap, (A) is constant for different transition, (h) is Plank constant ($6.62.10^{-34}$ J s^{-1}photon $^{-1}$), (hν) are the energy of photon and the value of n is either ½ for indirect band gap or 2 for direct band gap. The intercept on the (hν) axis can be found by projecting the plot to the point where $(\alpha hv)^2 = 0$ as shown in Fig. 7(b). The intercept of the straight line at α=0 was used to calculate the band gap energy, which was found to be 2.91eV, somewhat higher than the stated value range of 2.0-2.2 [53,54].

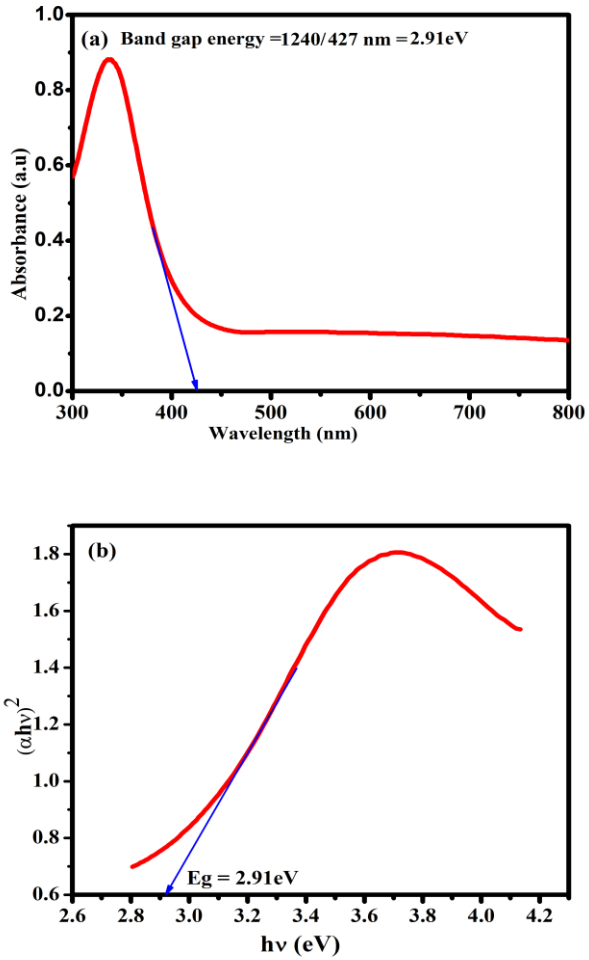

Fig. 7. (a) UV visible absorbtion spectra of the $MgFe_2O_4$. (b) $(\alpha h\upsilon)^2$ $[eVcm^{-1}]^2$ versus photon energy (hυ) graphs for $MgFe_2O_4$.

2.8 XPS analysis

XPS is used to study the chemical and elemental state analysis at the depth of about 5-10 nm of the investigated surface of the sample. XPS is that technique which not only shows elements are present but also what other elements they are bounded to. Also it examined the energy of the component.

XPS spectrum displayed in Fig. 8, the spectrum reveals chemical composition of the sample $MgFe_2O_4$ nanoparticles attributed to element Mg, Fe, O and unintentional element like carbon. As shown in Fig. 8 (a) two characteristic peaks at 724.88 eV and 711.28 eV indicated as binding energy which corresponds to $Fe^{3+}2p_{1/2}$ and Fe^{2+} $2p_{3/2}$ orbital which is similar to the

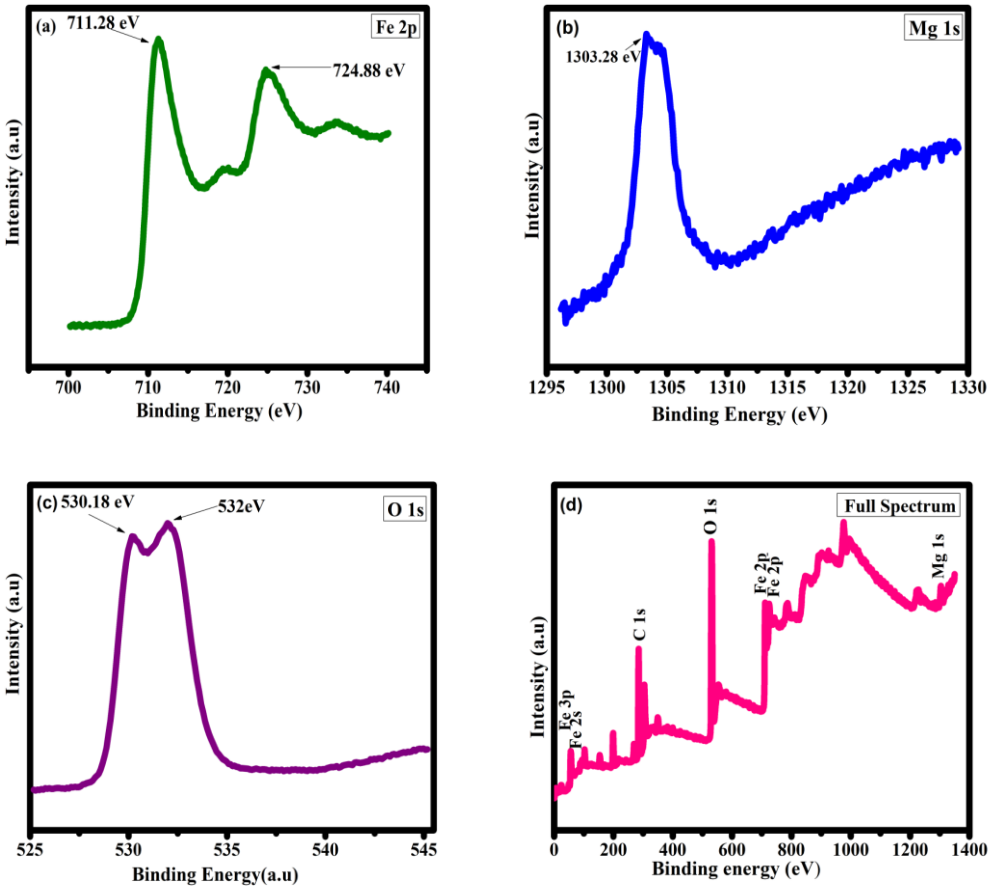

Fig. 8. XPS spectra of $MgFe_2O_4$ nanoparticles (a) Fe 2p (b) Mg 1s (c) O 1s (d) Full spectrum.

reported earlier by Hengli Xiang [55]. The single peak located at 1303.28 eV would be attributed to Mg 1s which reveal the oxidation state Mg^{+2} in the sample which is shown in Fig. 8 (b)that is in fine agreement with some earlier results [56].The peak located at 530.18 eV is attributed to O 1s region which appears due to metal-oxygen bonding and the peak at 532.00 eV as shown in Fig. 8 (c) represents oxygen vacancies or metal hydroxyl bonds at the surface, full spectrum of the sample are shown in Fig. 8d. Table 5 shows the elements and its peak position of Fe 2p, O 1s, Mg 2p of the sample.

Table 5.

Peak position in (eV) of Fe2p, O1s, Mg2p, spectra of $MgFe_2O_4$ nanoparticles.

Peak	Peak position (eV)
Fe 2p	724.88
	711.28
O 1s	530.18 532.00
Mg 2p	1303.28

Conclusions

In this study, we present evidence that sol-gel-produced magnesium ferrites nanoparticles can form a single-phase cubic spinel structure. Surface morphology image illustrated with some agglomerated size particles. The synthesized composition's Mg, Fe, and O content are confirmed by the EDX analysis spectrum. Five Raman active modes E_g, $3F_{2g}$, A_{1g} in the range of 209-707 cm^{-1}, which are anticipated in the spinel structure, were validated by a Raman investigation. Raman study confirmed the existence of five Raman active modes E_g, $3F_{2g}$, A_{1g} in the range of 209-707 cm^{-1} which are predictable in the spinel structure. Magnetic measurement shows soft magnetic behaviour of the sample with the M_s value 27.129 emu/g. AFM is utilized to estimate the height, grain size, and average roughness of the particles. The band gap energy at 2.91eV are obtained by UV-VIS absorbance spectra while chemical composition and elemental states are determined by X-ray photoelectron spectroscopy (XPS).

Acknowledgement

For financial support, authors are sincerely grateful to CSIR [No.09/013(0823)/2018-EMR-1] New Delhi, India. We appreciate Prof. Ranjan Kumar Singh from the Department of Physics at the BHU Institute of Science in Varanasi for providing the Raman spectral facility, and we also appreciate CIF from the IIT for giving technical assistance with XRD, SEM, EDX, and XPS.

Conflicts of Interest

There are no conflicts of interest, according to the authors.

Farhana Naaz – M.Sc, Research Scholar;
Preeti Lahiri – Ph.D., Professor;
Chanda Kumari – Ph.D., Senior Research Scholar;
Hemant Kumar Dubey – Ph.D., Assistant Professor.

[1] 1. J. D Adam, L. E Davis, G. F.Dionne, E. F Schloemann, S. N. Stitzer, *Ferrite Devices and Materials*,IEEE Transactions on Microwave Theory and Techniques, 50, 721 (2002); https://doi.org/10.1109/22.989957.

[2] V.G. Harris,A. Geiler, Y. Chen, S.D. Yoon, W. Mingzhong, A. Yang, Z. Chen, H. Peng, V. Patanjali, X. Zuo, Parimi,ManasoriAbe, O. Acher and C.Vittoria, *Recent advances in processing and applications of microwave Ferrites*, Journal of Magnetism and Magnetic Materials, 321, 2035 (2009); https://doi.org/10.1016/j.jmmm.2009.01.004.

[3] J. Balavijayalakshmi and Greeshma, *Synthesis and Characterization of Magnesium ferrite nanoparticles by Co-precipitation method*, Journal Environ. Nanotechnology, 2, 53 (2013), https://doi.org/10.13074/jent.2013.06.132015.

[4] V.B. Kawade, G.K. Bichile and K.M. Jadhav, *X-ray and infrared studies of chromium substituted magnesium*,Material Letters 42, 33 (2000);https://doi.org/10.1016/S0167-577X(99)00155-X.

[5] C.J. Kriessman and S.E. Harrison, *Cation Distributions in Ferrospinels Magnesium-Manganese Ferrites*, Physical Review, 103, 1 (1956); https://doi.org/10.1103/PhysRev.103.857.

[6] E.W. Gorter. *Magnetization in Ferrites: Saturation Magnetization of Ferrites with Spinel Structure*, Nature, 165, 78 (1950); https://doi.org/10.1038/165798a0.

[7] S.K. Pradhan, S. Bid, M. Gateshki and V. Petkov, *Microstructure characterization and cation distribution nanocrystalline magnesium ferrite prepared by ball milling*, Material Chemistry Physics, 93, 224 (2005); https://doi.org/10.1016/j.matchemphys.2005.03.017.

[8] R.J. Willey, P. Noirclerc and G. Busca, *Preparation and characteriation of magnesium chromite and magnesium aerogels*. Chemical Engineering Communication, 123, 1 (2013); https://doi.org/10.1080/00986449308936161.

[9] R. Dom , R. Subasri, K. Radha and P.H. Borse, *Synthesis of solar active nanocrystalline ferrite, MFe2O4 (M: Ca, Zn, Mg) photocatalyst by microwave irradiation*, Solid. State communication, 151, 470-473, (2011); https://doi.org/10.1016/j.ssc.2010.12.034.

[10] C. Xiong, Q. Chen, W. Lu, H. Gao, W. Lu and Z. Gao, *Novel Fe-based complex oxide catalysts for Hydroxylation of phenol*, Catalysis Letters, 69, 231 (2000); https://doi.org/ 10.1023/A:1019042527870.

[11] S.A. Oliver, R. J. Willey, H.H. Hamdeh,G. Oliveri ,G. Busca, *Structure and magnetic properties of magnesium ferrite fine powder*, Scripta Metallurgica et Materialia, 33, 1695 (1995); https://doi.org/10.1016/0956-716X(95)00412-O.

[12] R. Paulsingh and C. Venkataraju, *Effect of calcinations on the structural and magnetic properties of magnesium ferrite nanoparticles prepared by sol gel method*, Chinese Journal Physics, 56, 2218 (2018);https://doi.org/10.1016/j.cjph.2018.07.005.

[13] A.Tariq , U. Ullah, I. Ahmad, M. Asif, I. Sadiq, H. *Haleem.Comparative analysis of the Magnesium Ferrite ($MgFe_2O_4$) nanoparticles synthesized by three different routes*. IET Nanobiotechnology, 137, 697 (2019); https://doi.org/10.1049/iet-nbt.2018.5032.

[14] N.S Kumar, N. Das, K. Devlal, S. Seema, M.S. Shekhawat, M. Hidayath and A.S. Khader,*Dielectric and Magnetic Studies of Ni-Mg Mixed ferrites by combustion Method,AIP Conference Proceeding*, 2220, 1 (2020);https://doi.org/10.1063/5.0001907.

[15] S.I. Hussein, A.S. Elkady, M.M. Rashad, A.G. Mostafa and R.M. Megahid, *Structural and magnetic properties of magnesium ferrite nanoparticles prepared via EDTA-based sol–gel reaction*, Journal of Magnetism and Magnetic Materials, 379, 9 (2015); https://doi.org/10.1016/j.jmmm.2014.11.079.

[16] 16. J.P. Singh, S.O. Won, W.C. Lim, I.J. Lee and K.H. Chae, *Electronic structure studies of chemically synthesized $MgFe_2O_4$ nanoparticles*, Journal Molecular Structures 1108, 444 (2016); https://doi.org/10.1016/j.molstruc.2015.12.002.

[17] Y. He, X. Yang, J. Lin, Q. Lin and J. Dong. *Mössbauer Spectroscopy, Structural and Magnetic Studies of Zn2+ Substituted Magnesium Ferrite Nanomaterials Prepared by Sol-Gel Method*, Journal Nanomaterials, 1, 1 (2015); http://dx.doi.org/10.1155/2015/854840.

[18] S. Thankachan, S. Xavier, B. Jacob and E.M. Mohammed, *A comparative study of structural electrical and magnetic properties of magnesium ferrite nanoparticles synthesised by solgel and co- precipitation techniques*.J. Exper. Nanosc. 8, 347 (2013); https://doi.org/10.1080/17458080.2012.690892.

[19] R.P. Singh and Venkataraju, *Effect of calcinations on the structural and magnetic properties of magnesium ferrite prepared by sol gel method*, Chinese. J. Phys. 56, 2218 (2018); https://doi.org/10.1016/j.cjph.2018.07.005.

[20] M. Kurain, S. Thankachan, D.S. Nair, E.K. Aswathy, A. BABU, A. Thomas and B.K Krisjna, *Structural, magnetic, and acidic properties of cobalt ferrite nanoparticles synthesised by wet chemical methods*, Journal Advance Ceramic, 4, 199 (2015); https://doi.org/10.1007/s40145-015-0149-x.

[21] S. Hasan, B. Azhdar, *Facile synthesis of nanocrystalline zinc ferrite via a self propagatin combustion method* Material Letters, 61, 347 (2007); https://doi.org/10.1016/j.matlet.2006.04.06.

[22] S.Verma, P.A. Joy, Y.B. Khollam, H.S. Potdar and S.B. Deshpande, *Synthesis of nanosized MgFe2O4 powders by microwave hydrothermal method*, Material Letters58, 1092, (2004);https://doi.org/10.1016/j.matlet.2003.08.025.

[23] K.K. Zeynep, R. Boncukcuoglu, I.H. Karakas and M. Ertugru, *The effects of heat treatment on the synthesis of nickel ferrite (NiFe2O4) nanoparticles using the microwave assisted combustion method*,Journal of Magnetism and Magnetic Materials, 298-306, (2015); https://doi.org/10.1016/j.jmmm.2014.08.045.

[24] P. Holec, J. Plocek, D. Niznansky, Poltierova and J. Vejpravova. *Preparation of MgFe2O4 nanoparticles by microemulsion method, J. Sol-Gel*, ScienceTechnology, 51, 301 (2009); https://doi.org/10.1007/s10971-009-1962-x.

[25] La Agusu, Alimin, L. O. Ahmad, M. Z. Firihu, S. Mitsudo, H. Kikuchi, *Crystal and microstructure of MnFe2O4 synthesized by ceramic method using manganese ore and iron sand as raw materials*, Journal Physics Conference, 1153, 1 (2019); https://doi.org/10.1088/1742-6596/1153/1/012056.

[26] S. S. Jagtap, M.R. Sopan. *Synthesis and characterization of Mg-Ni ferrite prepared by Sol gel autocumbustion method*, Appl. Res. Devl. Inst. J. 8, 1, (2013);

[27] A. Gaffoor , D. Ravinder. *Characterization of Nano-Structured Nickel-Cobalt Ferrites Synthesized By Citrate-Gel Auto Combustion Method*, Journal Engineering Res. Applied, 4, 73 (2014).

[28] A.A Thant, S. Srimala, P. Kaung, M. Itoh, Radzali and M.N.A. Fauzi, *Low temperature synthesis of MgFe2O4 soft ferrite nanocrystalline*, Journal of Australian Ceramic Society, 46, 11, (2010);

[29] N. Kaur and M. Kaur. *Comparative studies on impact of synthesis methods on structural and magnetic properties of magnesium ferrite nanoparticles* Processing and Application of Ceramics 8, 137 (2014); https://doi.org/10.2298/PAC1403137K.

[30] N. Sivakumara, A. Narayanasamya, J.M. Greneche, R. Murugaraj, Y.S, Leed. *Electrical and magnetic behaviour of nanostructured $MgFe_2O_4$ spinel ferrite*, journal of alloys and compound, 504, 395 (2010); https://doi.org/10.1016/j.jallcom.2010.05.125.

[31] K.B. Modi, M.K. Rangolia, M.C. Chhantbar and H.H. Joshi, *Study of infrared spectroscopy and elastic properties of fine and coarse grained nickel–cadmium ferrites*, Journal of Material Science,41, 7308 (2006); https://doi.org/10.1007/s10853-006-0929-3.

[32] B.D. Cullity, Stock SR. *Elements of X-Ray diffraction*, 3rd ed. Hampshire (NJ), USA*: Prentice Hall.*167 (2006).

[33] N. Farhana, H.K. Dubey, C. Verma, P. Lahiri, *Structural and magnetic properties of $MgFe_2O_4$ Nanopowder synthesized via co-precipitation route*,SN Applied Sci*ence*, 2, 808, (2020);https://doi.org/ 2611-9.

[34] P.P. Hankare, V.T. Vader, N.M. Patil, SDJB Sankpal, M.R. Kadam, B.K. Chougule, N.S. Gajbhiye. *Synthesis, characterization and studies on magnetic and electrical propertiesof Mg ferrite with Cr substitution*, Material Chemistry Phys*ics*, 113, 233 (2009); https://doi.org/10.1016/j.matchemphys.2008.07.066.

[35] A.T. Pathan, S.N. Mathad and A.M. Shaikh. *Infrared spectral studies of nanostructured Co^{2+} substituted Li- Ni Zn ferrites*, International Journal Self-Prop High Temp Synthesis, 3, 112 (2014);https://doi.org/10.3103/S1061386214020083.

[36] E.D. Case, J.R. Smyth, V. Monthei. *Grain size determinations*, Journal American Ceramic Society, 64 24(1981).

[37] R. Gupta, A.K. Sood, P. Metcalf and J.M. Honig, *Raman study of stoichiometric and Zn-doped Fe_3O_4.* Physics Review, B 65, 1 (2002); https://doi.org/10.1103/PhysRevB.65.104430.

[38] L.V. Gasparov and D.B. Tanner, *Infrared and Raman studies of the Verwey transition in magnetite*, Journal American Physics, Society, 62 1-7, (1999); https://doi.org/10.1103/PhysRevB.62.7939.

[39] G.V.M. Jacintho, A.G. Brolo, P. Corio, P.A.Z. Suarez and J.C. Rubim, *Structural Investigation of MFe_2O_4 (M= Fe,Co) Magnetic Fluids,J. Phys. Chem.* 113, 7684 (2009); https://doi.org/10.1021/jp9013477.

[40] Z. Wang , P. Lazor , S.K. Saxena and HSC Neill, *High pressure Raman spectroscopy of ferrite $MgFe_2O_4$.* Material research Bulletin, 37, 1589 (2002); https://doi.org/10.1016/S0025-5408(02)00819-X.

[41] 41. J. Chandradass, A.H. Jadhav, K.H. Kim and H. Kim, *Influence of processing methodology on the structural and magnetic behavior of $MgFe_2O_4$ nanopowders*, Journal of Alloys Compound, 517, 164 (2012); https://doi.org/10.1016/j.jallcom.2011.12.071.

[42] V. Sepelak, I. Bergmann, D. Menzel, A. Feldhoff, P. Heitjans, F.J. Litterst and K.D. Becker. *Magnetization enhancement in nanosized MgFe2O4 prepared by mechanosynthesis*, Journal of Magnetism and Magnetic Materials, 316, 764 (2007); https://doi.org/10.1016/j.jmmm.2007.03.087.

[43] Y. Huang, Y. Tang, J. Wang and Q. Chen, Synthesis of MgFe2O4 nanocrystallites under mild conditions. Material Chemistry Physics, 97, 394 (2006); https://doi.org/10.1016/j.matchemphys.2005.08.035.

[44] M.M. Rashad, *Magnetic properties of nanocrystalline magnesium ferrite by co-precipitation assisted with ultrasound irradiation*, Journal Material Science, 42, 5248 (2007);https://doi.org/10.1007/s10853-006-0389-9.

[45] B. Viswanathan, V.R.K. Murthy, *Ferrite Materials Science and Technology*. I ed., Toppan company(s) Pte. Ltd, Singapore. 2-16, (1990).

[46] M.A. Gabal, M. Reda, R.M. El-Shishtawy and Y.M. Al Angari, *Structural and magnetic properties of nano-crystalline Ni- Zn ferrites synthesized using egg-white precursor*, Journal of Magnetism and Magnetic Materials324, 2258 (2012); https://doi.org/10.1016/j.jmmm.2012.02.112.

[47] A.Pradeep, P. Priyadharsini, G. Chandrasekaran, *Sol–gel route of synthesis of nanoparticles of $MgFe_2O_4$ and XRD, FTIR and VSM study*, Journal of Magnetism and Magnetic Materials, 320, 2774 (2008);https://doi.org/10.1016/j.jmmm.2008.06.012.

[48] Y. Ichiyanagi, M. Kubota, S. Moritake, Y. Kanazawa, T. Yamada and T. Uehash, *Magnetic properties of Mg Ferrite nanoparticles*, Journal of Magnetism and Magnetic Materials, 310, 2378 (2007); https://doi.org/10.1016/j.jmmm.2006.10.737.

[49] S. Rahman, K. Nadeem, M.A. Rehman, M. Mumtaz, S. Naeem, I.L. Papst, *Structural and magnetic properties of ZnMg-ferrite nanoparticles prepared using the co-precipitation method*, Ceramic International, 39, 5235 (2013); http://dx.doi.org/10.1016/j.ceramint.2012.12.023.

[50] 50. R.C. Kambale, P.A. Shaikh, C.H. Bhosale, K.Y. Rajpure, Y.D. Kolekar, *The effect of Mn substitution on the magnetic and dielectric properties of cobalt ferrite synthesized by an autocombustion*, Smart. Material Structure18, 1 (2009); https://doi.org/10.1088/0964- 1726/18/11/115028.

[51] S.K. Durrania, S. Naz, M. Mehmood, M. Nadeem and M. Siddique, *Structural, impedance and Mössbauer studies of Magnesium ferrite synthesized via sol-gel auto- combustion Process*, Journal Saudi Chemstry Society, 21, 1, (2017); https://doi.org/10.1016/j.jscs.2015.12.006.

[52] C. Kumari, H.K. Dubey, F. Naaz, P. Lahiri, *Structural and optical properties of nanosized Co substituted Ni ferrites by coprecipitation method,*Phase Transition, 93, 1 (2020); https://doi.org/10.1080/01411594.2019.1709120.

[53] G.D. Nipan, V.A. Ketsko, A.I. Stognij, A.V. Trukhanov, T.N. Koltsova, M.A. Kopeva, L.V. Elesina, N.T. Kuznetsov, *Properties of $Mg(Fe_{1-x}Ga_x)_2O_4$ Solid Solutions in Stable and Metastable States*, Inorganic Material, 46, 490 (2010);

[54] H.G. Kim, P.H. Borse, J.S. Jang, E.D. Jeong, O.S. Jung, Y.J. Suh, J.S. Lee, *Fabrication of $CaFe_2O_4/MgFe_2O_4$ bulk heterojunction for enhanced visible light photocatalysis* Chemistry Communication, 39, 5889 (2009).

[55] H. Xiang, X. Peng, D. Xu, X. Yang, G. Ren, Z. Zhang, Y. Zhong and X. Wang. *One-pot solvent-free synthesis of MgFe2O4 nanoparticles from ferrous sulfate waste*, Material and Manufacturing Processes, 35,590 (2020); https://doi.org/10.1016/j.mtcomm.2020.101516.

[56] V.K. Mittal, S. Bera, R. Nithya, M.P. Srinivasan, S. Velmurugan, S.V. Narasimhan, *Solid State Synthesis of Mg–Ni Ferrite and Characterization by XRD and XPS*,Journal Nuclear Material, 335, 302 (2004);http://dx.doi.org/10.1016%2Fj.jnucmat.2004.05.010.

Ф.Нааз[1], П. Лахірі[1*], Ч. Кумарі[1], Х. Кумар Дубей[2]

Спектроскопічні, магнітні та морфологічні дослідження нанопорошку $MgFe_2O_4$

[1]*Кафедра хімії, Інститут наук, ММВ, Університет Банараса Хінду, Варанас-221005, Індія, plahiri16@yahoo.com*
[2]*Кафедра хімії, коледж BRDPG, Деорія-274001, Індія*

Нано феритову сполуку типу шпінелі $MgFe_2O_4$ синтезовано золь-гель методом із використанням нітратів металів як прекурсорів. Фазовий склад, морфологію та елементний аналіз фериту магнію ($MgFe_2O_4$) здійснено методами дифракції Х-променів, перетворення Фур'є в інфрачервоному діапазоні, атомно-силової мікроскопії, енергодисперсійної Х-променевої та скануючої електронної мікроскопії.

Х-променева дифракційна картина зразка підтверджує існування однофазного матеріалу, для якого оцінка розмірів кристалітів склала 39,9 нм. Дослідження в інфрачервоному діапазоні із використанням перетворенням Фур'є підтвердило наявність коливань метал-кисень, що відповідають тетраедричним і октаедричним вузлам, відповідно. Із результатів скануючої електронної мікроскопії отримано розмір зерене, який склав приблизно 97,7 нм. Спектри комбінаційного розсіювання зразка демонструють п'ять активних мод раманівського розсіювання ($A_{1g} + E_g + 3F_{2g}$), що сумісно зі структурою шпінелі. Дослідження магнітних характеристик при кімнатній температурі показує поведінку петлі гістерезису з низьким значенням намагніченості насичення, 27,192 $emug^{-1}$і незначним значенням коерцитивної сили. Ширину забороненої зони визначено за допомогою спектрів пропускання в УФ-діапазону. Крім того, для підтвердження ступенів окислення та дослідження хімічного складу зразка використано методи рентгенівської фотоелектронної спектроскопії.

Ключові слова: феритова шпінель, нанокристали, дифракція Х-променів, спектри комбінаційного розсіювання, магнітні властивості.

PHYSICS AND CHEMISTRY OF SOLID STATE
V. 24, No. 2 (2023) pp. 403-409
Section: Physics

DOI: 10.15330/pcss.24.2.403-409

Vasyl Stefanyk Precarpathian National University

ФІЗИКА І ХІМІЯ ТВЕРДОГО ТІЛА
Т. 24, № 2 (2023) С. 403-409
Фізико-математичні науки

UDC: 544.6; 661.66 ISSN 1729-4428

I.M. Budzulyak, L.S. Yablon, M.M. Khemii, V.O. Kotsyubynsky, B.I. Rachiy, R.V. Ilnytskyi, R.I. Kryvulych

Stimulation of the metal doping process of nanoporous carbon material by laser irradiation

Vasyl Stefanyk Precarpathian National University, Ivano-Frankivsk, Ukraine, ivan.budzuliak@pnu.edu.ua

It has been established that the doping of activated carbon material with chromium and manganese increases the specific capacitance of storage devices based on the charge-discharge mechanism of a double electric layer (DEL) by ~70 % and leads to a decrease in their internal resistance by 30-35 %. The main reason for this rise is the transformation of the electron energy spectrum due to an increase in the density of electronic states, as a result of which a much larger number of electrolyte ions (primarily positive ones) participate in the formation of DEL and cause an increase in the specific capacitance of these devices. It has been shown that laser irradiation stimulates the metal penetration into the bulk of carbon material.

Keywords: nanoporous carbon material, doping, chromium, manganese, laser irradiation.

Received 31 January 2023; Accepted 28 June 2023.

Introduction

Traditional electrochemical energy storage devices (supercapacitors), whose specific capacitance can reach ~200 F/g when using aqueous electrolytes, operate on the principle of charge/discharge of the DEL, which is formed at the electrode/electrolyte interface.

The main factors influencing the increase in the specific characteristics of DEL are the higher density of electronic states due to changes in the Fermi level of the surface layers of activated carbon and the involvement of as much of the developed surface as possible in charge/discharge processes. One of the possibilities to influence the properties of porous carbon material (PCM) for these purposes is to incorporate metals with a high density of electronic states into its matrix [1, 2].

The use of porous carbon material is due to the fact that, in addition to being low-cost and accessible, PCM is relatively easy to modify, which can be used to control not only the amount of the developed surface, but also its state, pore size distribution, conductivity, etc., which are important for its application.

However, the specific capacitance of the DEL formed by the PCM and electrolyte does not always satisfy the requirements for the appropriate charge storage devices, due to the fact that PCM, being a semiconductor, contains a low concentration of free charge carriers (electrons) compared to metals.

One of the solutions to this problem is to increase the density of electronic states in the PCM matrix. This idea can be realized by modifying the PCM by doping it with metals with a high density of electronic states, which makes it possible to significantly increase the capacitance of DEL, and, accordingly, of capacitors formed on the basis of PCM modified in this way.

I. Experimental, discussion of the results

An important characteristic of an electronic system is the density of states, i.e., the number of states in a unit energy interval. Since electrons are governed by the Pauli principle, the density of states determines the maximum number of electrons that can be accommodated in a certain energy range.

Considering the fact that the choice of electrolyte concentration is determined by its maximum conductivity,

it is possible to increase the amount of accumulated charge of DEL by increasing the density of electronic states near the Fermi level in the electrode material. Thus, the aim was to purposefully increase the electron density of the valence band of activated carbon by doping. The study [3] shows that 3d transition metals and rare earth elements have the highest density of electronic states near the Fermi level. We focused on 3d transition elements Mn and Cr.

Fig. 1 (*a*) shows the valence band spectrum of the non-doped activated carbon material, which demonstrates that it has a double-hump structure with a significant decrease in intensity when the binding energy approaches the Fermi level.

When doped with manganese, the appearance of the valence band changes significantly (Fig. 1(b)). It becomes almost single-humped with a significant increase in intensity at the Fermi level.

The results obtained indicate that the doping of PCM with manganese most significantly affects the intensity of its valence band spectra at the Fermi level, and, accordingly, the electronic density, which is displayed in the value of the specific capacitance. In particular, the specific capacitance of ECs based on manganese-doped PCM is ~ 65 % higher than the similar capacitance of ECs formed from non-doped PCM.

The change in the intensity of the valence band spectra of non-doped HFM is also significantly affected by various technological treatments (thermal, chemical, etc.). However, in this case, the spectral pattern of the band remains practically the same (Fig. 2). Obviously, in order to improve the performance parameters of ECs, it is necessary to apply the established procedures in a complex manner.

In the two-dimensional (2D) structure, which is

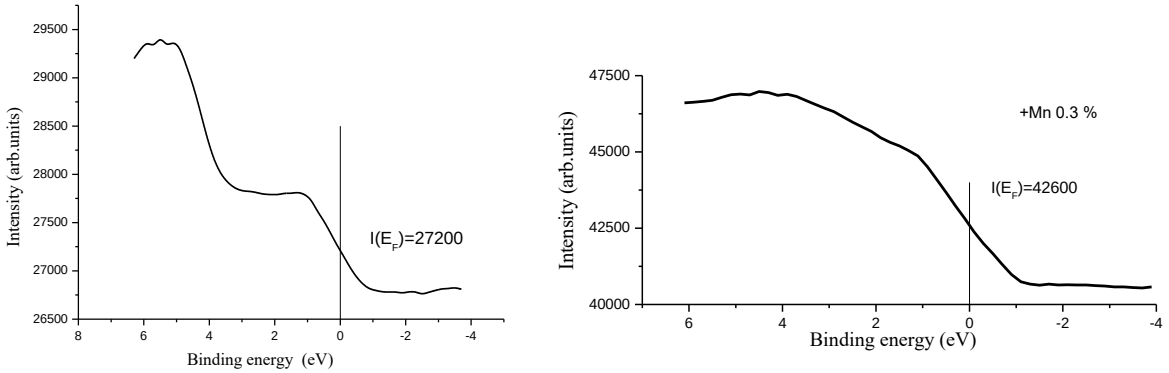

a *b*

Fig.1. Valence band spectrum of PCM: *a* - non-doped PCM; *b* - PCM doped with manganese.

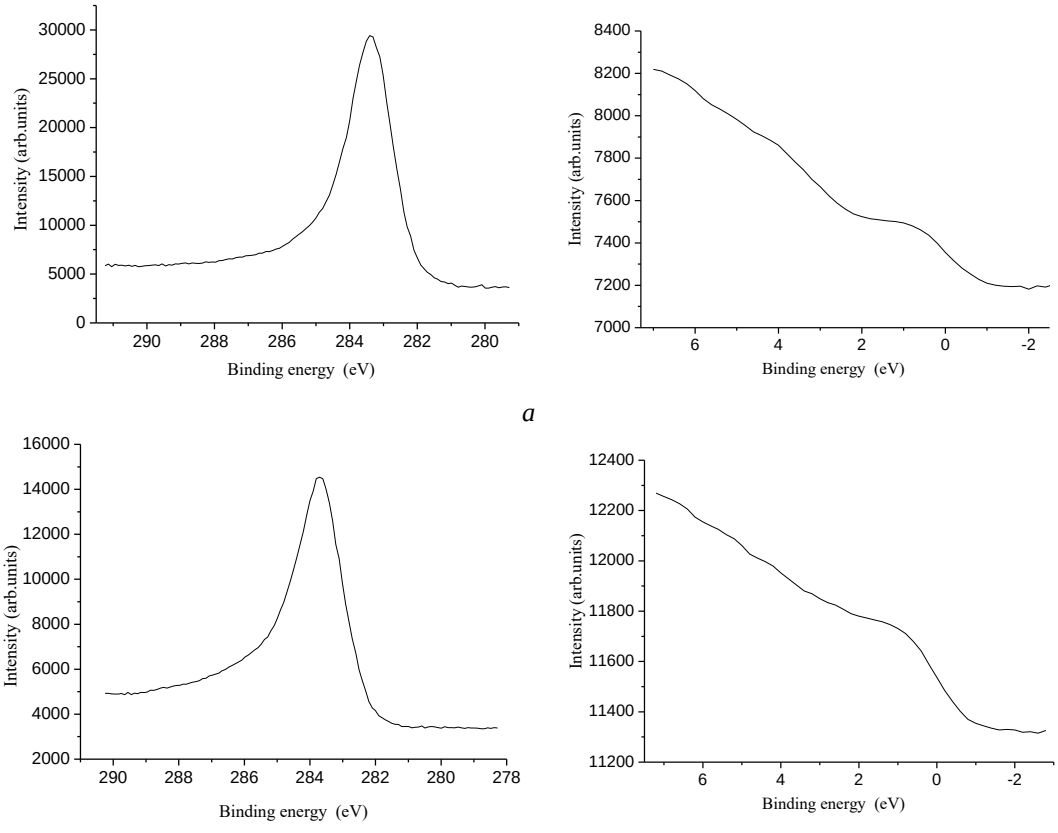

a

b

Fig.2. Intensity of the valence band spectra: *a* - carbonized PCM; *b* - carbonized and heat-treated PCM.

typical for our case, when the large area of the developed surface is of major importance, for each quantum level with energy E_i the total number of states

$$Z(E) = \frac{m_e(E-E_i)S}{(2\pi k)^2},$$

where S – is the sample area.

The state density, which in this case is calculated per unit area, is determined by the sum of the numbers of all levels whose energies E_i are lower than E [4]:

$$D_{2D}(E) = \frac{2}{S}\sum_i \frac{dZ(E_i)}{dE}.$$

The PCM was chemically doped with chromium by reducing it from an aqueous solution of $Cr_2(SO_4)_3 \cdot 6H_2O$. For this purpose, a weight of salt dissolved in distilled water was mixed with PCM to a homogeneous mixture, hydrochloric acid was added to create an acidic environment in which to carry out the reduction, and finely dispersed zinc was added. The resulting precipitate was dissolved in water in appropriate ratios, mixed with PCM, and dried at 140 °C to a constant weight. $KMnO_4$ was used as a manganese doping agent, where Mn has the highest oxidation degree, which is 7^+. For this, ethanol was added to a 5% solution of $KMnO_4$ and, after the reaction was completed, HNO_3 was added and heated to a temperature of 80 °C. The resulting precipitate was washed with water deionization until NO^-_3 ions were removed, and dried to a constant weight at room temperature. After that, the precipitate was dissolved in water in appropriate ratios, mixed with PVM and dried at 140 °C to a constant weight.

The influence of injected metals on the behavior of electrochemical capacitor systems formed on the basis of PCM + metal was studied by impedance spectroscopy. The dependence of the specific capacitance of the doped PCM on the content of chromium and manganese is shown in Fig. 3.

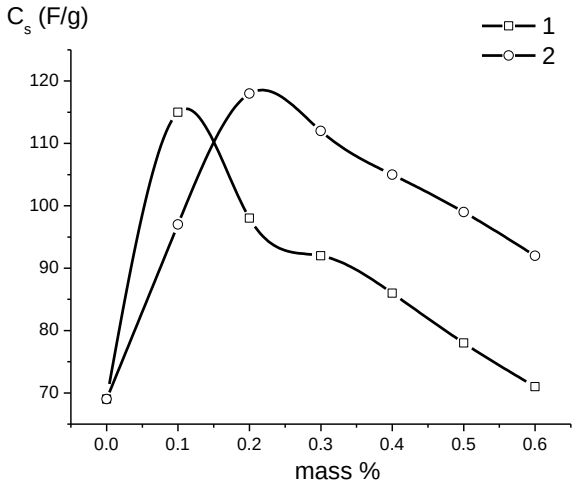

Fig.3. Dependence of the specific capacitance of PCM on the content of chromium (1) and manganese (2).

To obtain the Nyquist diagrams, a three-electrode electrochemical cell was used (Fig. 4), in which PCM with the appropriate content of chromium or manganese was used as the working electrode. The impedance measurements were performed using an Autolab PGSTAT / FRA-2 spectrometer (Netherlands) in the frequency range 10^{-2} – 10^5 Hz.

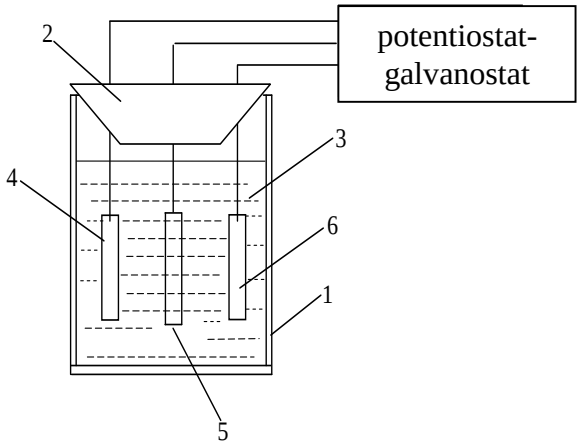

Fig.4. Electrochemical cell: 1 - glass cell; 2 - sealing lid; 3 - electrolyte; 4 - working electrode; 5 - reference electrode; 6 auxiliary electrode.

Cyclic voltammograms of carbon material electrodes were obtained in the potential range of -1 ÷ 0.2 V using the above three-electrode cell with a chlorine-silver reference electrode; the scan rate was 5, 8, 10, 20, 30, 40, and 50 mV/s, respectively.

The impedance curves obtained at potentials of -1 ÷ 0.2 V (in this case, the potential difference between the working electrode and the reference electrode) and the automatic calculation of the parameters of the equivalent circuit (primarily, the capacitance) made it possible to plot the volt-faradic dependencies for the studied activated carbon material with different dopant concentrations (Fig. 5, a, b). The criterion for selecting the interval of applied potentials is to change the parameters of the equivalent circuit by no more than 10%. In addition, in the negative potential region, the maximum of the curve $C = f(E)$ is also one of the factors in choosing the applied potential.

As follows from these dependencies, an increase in the percentage of manganese leads to both an increase in the specific capacitance of the active material and a certain symmetry of the C-U dependencies, i.e., the penetration of manganese into the nanoporous carbon material allows for the grafting of OH^-groups of the solvent in the positive potential region, resulting in an increase in the capacitance in the positive potential region. When chromium is incorporated, on the $C = f(U)$ dependence, chromium doping does not align both branches of the C-U dependence, resulting in a capacitance of such materials in the positive potential region that is even lower than that of pure PCM.

Fig. 5 shows the DEL capacitance at the electrode-electrolyte interface, so the mismatch of both curves in the positive potential region indicates an additional contribution to the total capacitance, pseudocapacitance due to Faraday processes involving functional groups (e.g., COOH > C = H, OH). It is known [5-7] that the existence of functional groups can affect the capacitance of ECs, both due to the possible occurrence of redox Faraday reactions involving these groups and due to changes in the specific capacitance by the specific value

Table 1.

Specific capacitance of PCM (F/g) in aqueous electrolyte (30% KOH solution in water)

Material	Method of research		
	impedance spectroscopy	voltammetry	chronoamperometry
PCM	156	164	169
PCM + 0,2 % Cr	204	206	215
PCM + 0,3 % Cr	185	188	194
PCM + 0,4 % Cr	180	185	190
PCM + 0,2 % Mn	188	191	197
PCM + 0,3 % Mn	205	210	218
PCM + 0,4 % Mn	200	205	212

of the interfacial surface.

A characteristic feature of the process of chemical modification of PCM with the above metals is that chromium and manganese significantly reduce the value of the Warburg diffusion impedance *W* (Fig. 6) compared to the unmodified material. Due to the fact that for all samples there is a general tendency to decrease *W* when the potential changes to the negative region, this parameter can be associated with diffusion processes involving K^+ ions in the carbon matrix [8, 9].

From the results obtained, it follows that an increase in the percentage of chromium increases the specific capacitance of PCM compared to pure PCM. The material with 0.2% Cr content by weight has the highest capacitance; further increase in Cr content leads to a decrease in capacitance. Most probably, this fact is associated with a decrease in the specific surface area of the carbon material due to the blocking of pores by chromium ions, as a result of which less potassium ions are involved in the formation of DEL.

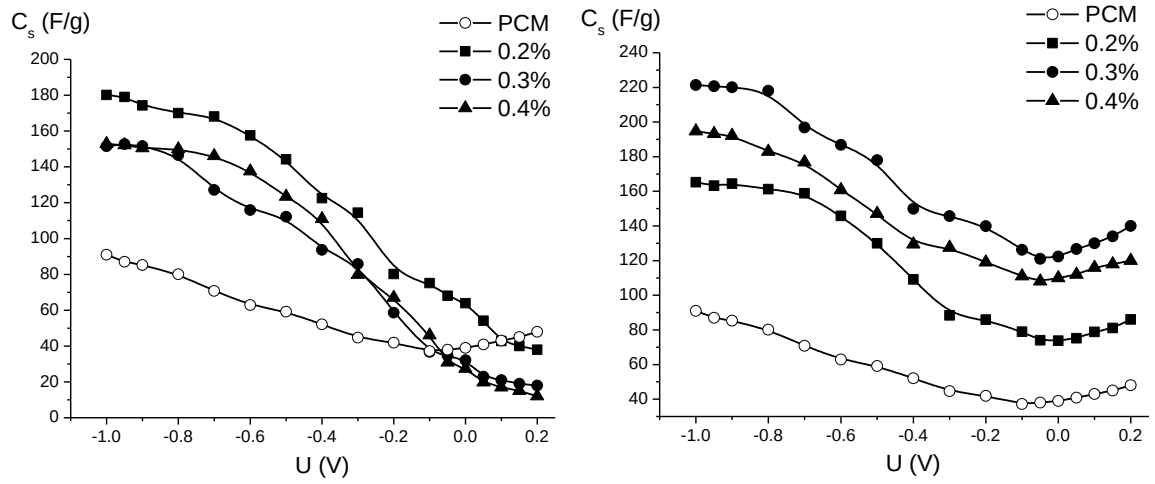

a *b*

Fig.5. Volt-faradic dependences for PCM with different percentage of: a - chromium; b – manganese.

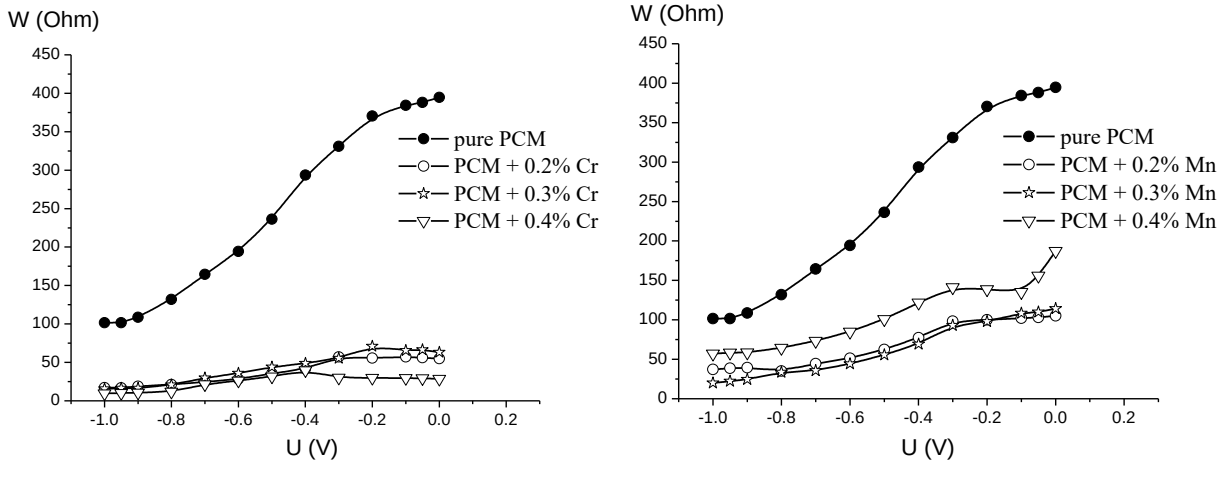

a *b*

Fig.6. Dependence of Warburg impedance on the applied potential for PCM with different percentage of chromium (a) and manganese (b).

The implementation of manganese also leads to an increase in the specific capacitance. However, the dependence of the last one on the scan rate, in comparison to Cr-doped PCM, is non-monotonic with respect to the percentage of Mn ions (Table 1).

Thus, the chemical modification of PCM with chromium and manganese leads to an increase in the specific capacitance of PCM [1, 10, 11]. The main reason for this increase, according to previous studies, is the transformation of the valence band of the carbon material due to the introduction of additional electronic states from the incorporated metals, as a result of which a much larger number of ions participate in the formation of the DEL, and thus causes an increase in the specific capacitance.

However, the doping technique does not provide metal localization on the surface of the PCM. As a result, during repeated cycling of electrochemical capacitors, metal atoms are removed by the electrolyte and the EC parameters become worse. In order to prevent this phenomenon, we carried out additional treatment of the doped PCM by irradiation with a neodymium laser operating in a pulsed mode.

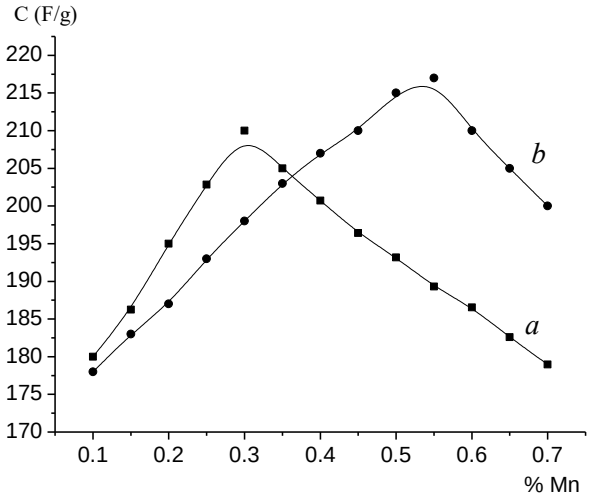

Fig.7. Dependence of the specific capacitance of the electrolyte/Mn-doped PCM system on the amount of manganese introduced before (a) and after (b) laser irradiation.

Laser irradiation leads to a reduction in the size of such fragmentary formations in the PCM matrix, which makes it possible to doping with more metal without blocking the pores of the developed PCM surface. As a result of irradiation with laser pulses, the maximum specific capacitance is shifted toward higher metal fractions (Fig. 7, b).

The decrease in the size of the "metallic" fragments should obviously be accompanied by a certain decrease in the electron density at the Fermi level.

The distribution of individual elements in the depth of the sample was determined for three types of samples in which chromium and manganese were incorporated. Fig. 8 shows a typical profile of element distribution in the samples of PCM doped with manganese to the level of 0.5 wt. %.

In Fig. 8, the etching time is proportional to the etching depth, and the shape of the obtained dependence at the qualitative level reflects the concentration distribution of elements by thickness in the near-surface region.

Due to the etching speed, the surface layers with a thickness of no more than 50-100 nm are available for analysis with an analysis time of about 7200 s.

As can be seen from Fig. 8, a, the distribution of manganese over the depth of the sample is quite irregular. An increase in the amount of manganese introduced above 0.5 wt. % leads to the fact that the signal intensity from manganese becomes greater than the signal intensity of carbon and oxygen. Therefore, we do not present the other profiles, although they, similarly to the profile in Fig. 8, a, there is an uneven distribution of manganese.

Laser irradiation (E = 0.1 J/cm^2, τ = 15 ns, pulse repetition rate f = 56 Hz, irradiation time 180 s) leads to a significant redistribution of the analyzed elements along the depth of the sample (Fig. 8, b). In particular, the depth h_m, which corresponds to the main maximum of the manganese distribution profile, practically does not change when the sample is irradiated. At the same time, manganese atoms both from the near-surface region $x < h_m$ and from a depth greater than h_m are concentrated in the neighborhood of h_m. In addition, laser irradiation leads to

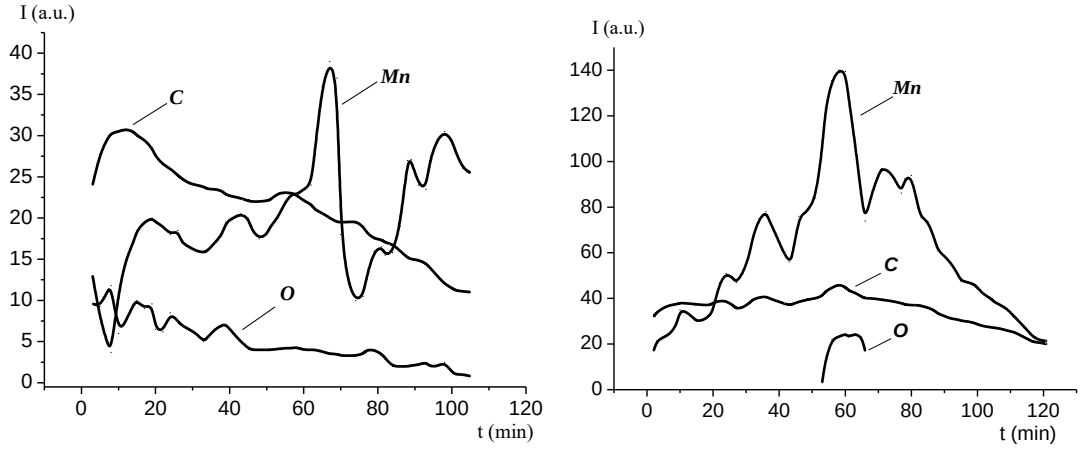

a b

Fig.8. Depth distribution profile of C, O, Mn elements of manganese-doped PCM depending on the etching time t for non-irradiated (a) and irradiated (b) samples.

a slight appearance of oxygen compared to the non-irradiated sample, and then only in the region of the maximum intensity of the manganese peak, which may be due to the formation of Mn_xO_y oxide [12].

As for samples of chromium-doped nanoporous carbon, studies by other methods have shown that the dielectric constant in such samples increases several times, which leads to an increase in the background of the useful mass spectrum signal as a result of electrification of the sample surface. Therefore, it was impossible to obtain high-quality mass spectra of laser-irradiated samples with a chromium content exceeding 0.1 wt. %.

Conclusions

1. The optimal method for producing carbon electrode material for electrochemical capacitors from plant-based raw materials (fruit pits) is hydrothermal treatment at high pressure $(6 \div 8)\cdot 10^5$ Pa. Additional thermal vacuum annealing of the resulting activated carbon at a temperature of 723-743 K in a chamber with a residual pressure of no more than 1.33 Pa for 60-70 minutes increases the specific capacitance of the corresponding capacitors by 10-15 % due to the desorption of uncontrolled impurities from the formed pores.

2. The total capacitance of the non-doped PCM/electrolyte system is a component of two capacitances - the PES capacitance (94 - 97 %) and the pseudocapacitance (6 - 3 %). The increase in the specific capacitance of electrochemical capacitors based on chemically modified activated carbon is due to an increase in the contribution of these components by 88 - 92 % and 12 - 8 %, respectively. On the basis of doped activated carbon material, laboratory samples of ECs were formed in 2525-size cases, the maximum specific capacitance of which is 150 F/g for aqueous electrolyte (30% solution of KOH in water).

Acknowledgments

This work was funded by the National Research Foundation of Ukraine (2020.02/0043).

Budzulyak I.M. – Doctor of Physical and Mathematical Sciences, Professor;
Yablon L.S. – Doctor of Physical and Mathematical Sciences, Professor;
Khemii M.M. – postgraduate student;
Kotsyubynsky V.O. – Doctor of Physical and Mathematical Sciences, Professor;
Rachiy B.I. – Doctor of Physical and Mathematical Sciences, Professor;
Ilnytskyi R.V. – Doctor of Physical and Mathematical Sciences, Professor;
Kryvulych R.I. – postgraduate student.

[1] A. P. Shpak, I. M. Budzulyak, R. P. Lisovskii, *Preparation and modification of nanoporous carbon for molecular storage of electric energy*, (Naukove vydannya, Kyiv, 2006). ISBN 966-360-029-2.
[2] Michała Bembenek, Volodymyr Kotsyubynsky, Volodymyra Boychuk, Bogdan Rachiy, Ivan Budzulyak, Łukasz Kowalski, Liubomyr Ropyak, *Effect of Synthesis Conditions on Capacitive Properties of Porous Carbon Derived from Hemp Bast Fiber*, Energies 15(22), 8761 (2022); https://doi.org/10.3390/en15228761.
[3] V. V. Nemoshkalenko, X-ray emission spectroscopy of metals and alloys (Naukova dumka, Kyiv, 1972).
[4] V. V. Pohosov, Yu. A. Kunytskii, A. V. Babich, A. V. Korotun, A.P. Shpak, Nanophysics and nanotechnology: textbook (ZNYU, Zaporijjya, 2011).
[5] Yu. M. Volfkovych, T. M. Seredyuk, *Electrochemical capacitors*, Electrochemistry 38(39), 1043 (2002).
[6] V. Kotsyubynsky, B. Rachiy, V. Boychuk, I. Budzulyak, L.Turovska, M. Hodlevska, *Correlation between structural properties and electrical conductivity of porous carbon derived from hemp bast fiber*, Fullerenes Nanotubes and Carbon Nanostructures 30 (8), 873 (2022); https://doi.org/10.1080/1536383X.2022.2033729.
[7] O.M. Ivanichok, N.Ya Ivanichok, P.I.Kolkovskyi, I.M. Budzulyak, B.I. Rachiy, R.P. Lisovskiy, Proceedings of the 2021 IEEE 11th International Conference "Nanomaterials: Applications and Properties", NAP 2021.
[8] I. M. Budzulyak, B. I. Rachii, V. O. Kotsyubynskii, L. S. Yablon, O. V. Morushko, *Synthesis, structure and electrochemical properties of nanoporous carbon material and composites based on it* (Ivano-Frankivsk, 2021).
[9] B.K. Ostafiychuk, N.Ya. Ivanichok, S.-V.S. Sklepova, O.M. Ivanichok, V.O. Kotsyubynsky, P.I. Kolkovskyy, I.M. Budzulyak, R.P. Lisovskiy, *Influence of plant biomass activation conditions on the structure and electrochemical properties of nanoporous carbon material*, Materials Today: Proceedings 62(9), 5712 (2022); https://doi.org/10.1016/j.matpr.2022.01.486.
[10] I. M. Budzulyak, V. I. Mandzyuk, R. P. Lisovskii, *Electrochemical characteristics of capacitor systems formed on the basis of chemically modified carbo*, Nanosystems, nanomaterials, nanotechnologies 4(3), 569 (2006).
[11] Y. Starchuk, N. Ivanichok, I. Budzulyak, S.V. Sklepova, O. Popovych, P. Kolkovskyi, & B. Rachiy, *Electrochemical properties of nanoporous carbon material subjected to multiple chemical activation*, Fullerenes, Nanotubes and Carbon Nanostructures 30(9), 936 (2022); https://doi.org/10.1080/1536383X.2022.2043285.
[12] M. V. Berkeshchuk, I.M. Budzulyak, Ya.T. Solovko, D.I. Popovych, *Redistribution of impurities in activated carbon due to laser exposure*, Electrochemical energy 6(2), 92 (2006).

І.М. Будзуляк, Л.С. Яблонь, М.М. Хемій, В.О. Коцюбинський, Б.І. Рачій, Р.В. Ільницький, Р.І. Кривулич

Стимуляція процесу легування металами нанопористого вуглецевого матеріалу лазерним опроміненням

Прикарпатського національний університет імені Василя Стефаника, Івано-Франківськ Україна,
ivan.budzuliak@pnu.edu.ua

Встановлено, що легування активованого вуглецевого матеріалу хромом і марганцем збільшує питому ємність пристроїв накопичення заряду, що працюють за принципом заряду-розряду подвійного електричного шару (ПЕШ), на ~70 % та призводить до зменшення їх внутрішнього опору на 30-35 %. Основною причиною такого зростання є трансформація енергетичного спектру електронів за рахунок збільшення густини електронних станів, в результаті чого значно більша кількість іонів електроліту (насамперед, позитивних) приймає участь у формуванні ПЕШ і зумовлює ріст питомої ємності даних пристроїв. Показано, що лазерне опромінення стимулює проникнення металів у об'єм вуглецевого матеріалу.

Ключові слова: нанопористий вуглецевий матеріал, легування, хром, марганець, лазерне опромінення.

Всеукраїнський науковий журнал

ФІЗИКА І ХІМІЯ ТВЕРДОГО ТІЛА

Ukrainian Scientific Journal

PHYSICS AND CHEMISTRY OF SOLID STATE

Том 24, № 2
Volume 24, No. 2

Комп’ютерна верстка **Юрчишин Л.Д.**

Підписано до друку 28.06.2023 р. Формат 60×84/8.
Гарн. Times New Roman. Умовн. друк. аркушів 12,65
Тираж 100 екземплярів.

Друк: підприємець Голіней О.М.
вул. Галицька, 128, м. Івано-Франківськ, 76008
Тел. +38(0342) 58-04-32